Order Number 9108442

Nature and origin of variations in late-glacial and Holocene atmospheric ^{14}C as revealed by global carbon cycle modeling

Braziunas, Thomas Frank, Ph.D.

University of Washington, 1990

U·M·I
300 N. Zeeb Rd.
Ann Arbor, MI 48106

Nature and Origin of Variations in Late-glacial and Holocene Atmospheric ^{14}C as Revealed by Global Carbon Cycle Modeling

by

Thomas F. Braziunas

A dissertation submitted in partial fulfillment

of the requirements for the degree of

Doctor of Philosophy

University of Washington

1990

Approved by Minze Stuiver

(Chairperson of Supervisory Committee)

Program Authorized

to Offer Degree Geological Sciences

Date July 11, 1990

Doctoral Dissertation

In presenting this dissertation in partial fulfillment of the requirements for the Doctoral degree at the University of Washington, I agree that the Library shall make its copies freely available for inspection. I further agree that extensive copying of this dissertation is allowable only for scholarly purposes, consistent with "fair use" as prescribed in the U. S. Copyright Law. Requests for copying or reproduction of this dissertation may be referred to University Microfilms, 300 North Zeeb Road, Ann Arbor, Michigan 48106, to whom the author has granted "the right to reproduce and sell (a) copies of the manuscript in microform and/or (b) printed copies of the manuscript made from microform."

Signature Thomas Brayshaw

Date 7/11/90

University of Washington

Abstract

Nature and Origin of Variations in Late-glacial and Holocene Atmospheric ^{14}C as Revealed by Global Carbon Cycle Modeling

by Thomas F. Braziunas

Chairman of the Supervisory Committee: Professor Minze Stuiver
Department of Geological Sciences

Simulations with a global box-diffusion ^{14}C model indicate that the millennium- and century-scale atmospheric $\Delta^{14}C$ variations during the Holocene are more likely explained by fluctuations in ^{14}C production rate (Q) than by changes in air-sea CO_2 exchange rate (F) or internal ocean mixing (parameterized as an "eddy diffusivity" K_Z). The ^{14}C reservoir model deconvolves histories for each of these three processes that are compatible with a 9600-yr bi-decadal atmospheric (tree-ring) $\Delta^{14}C$ record assuming alternative pre-Holocene ^{14}C conditions. Holocene microparticle concentrations in ice cores and dust grain sizes in marine sediment cores disagree with the model-derived global wind speeds necessary to explain (through F variations) the millennium-scale trends in atmospheric $\Delta^{14}C$. Alternately, foram ^{14}C data do not support the history in the oceanic ventilation index generated by millennium-scale K_Z variations. Coral ^{14}C data for recent centuries conflict with the marine $\Delta^{14}C$ history associated with century-scale variations in F or K_Z but are consistent with changes in ^{14}C production rate.

The ^{14}C production rates derived theoretically from an 11,000-yr record of averaged global dipole moments strongly correlate with the Q history required to explain tree-ring $\Delta^{14}C$. Several pre-Holocene Q histories were calculated from limited dipole moment data available for the past 30,000 yrs and do not contradict $^{234}U/^{230}Th$-calibrated coral ^{14}C

measurements. Relative variations in Greenland ice-core ^{10}Be concentrations (reflecting changes in ^{10}Be production) over the past 9000 yrs also correlate strongly with tree-ring Q fluctuations except for a 4500-3500 BC discrepancy.

Simulations of transient variations in Q, F, and K_Z supplement previous studies of alternative steady-state ^{14}C situations. The modeling of combined climate and production rate scenarios (ie. $F+K_Z$, F+Q, K_Z+Q) incorporates "feedback" effects which depend on the instantaneous marine ^{14}C profile and atmosphere/surface ocean ^{14}C disparity.

Spectral analyses of the 9600-yr tree-ring Q history generally produce power at or near harmonics of a 420-yr cycle. Century-scale Q periodicities may reflect harmonic or nonsinusoidal solar processes. Residual ^{14}C production and bi-decadal sunspot numbers from AD 1700 to 1840 define a preliminary history of relative sunspot numbers back to 7730 BC. "Fine-tuned" Q periodicities are used to forecast future solar behavior.

TABLE OF CONTENTS

ACKNOWLEDGEMENTS

I am deeply grateful to Minze Stuiver for his guidance and generosity (of time, ideas, and funding) during my graduate studies and dissertation work. His integrity and dedication to science as well as his accessibility and benevolent support of student efforts have been an inspiration to me.

It is also a pleasure to acknowledge Paul Quay for his helpful suggestions and advice during many discussions related to my studies; my carbon models are based on his original programs. Along with Minze and Paul, Steve Emerson provided a diligent critique of the dissertation draft with many valuable suggestions. Steve Porter and Bob Charlson, also on my committee, have provided help and encouragement throughout my graduate studies. I was very fortunate to know and learn from these five dedicated educators and from Fred Anderson in my undergraduate years at the University of Chicago. On a daily basis, the technical support of Travis Saling and Paula Reimer in the Quaternary Isotope Laboratory is much appreciated.

I especially thank my wife, Jane, for sharing the burdens and joys of graduate life as a parent and for making these busy years a very special time. My children Erik and Kristin keep my life in perspective everyday with their love. Finally, I am very grateful to my parents, Edward and Dolores, whose hard work and care allowed me early on to follow my goals.

Financial support for this research was provided by National Science Foundation grants ATM-8318665 and BNS-8701720.

CHAPTER 1. GLOBAL ^{14}C RESERVOIR MODELING

1.1 Introduction and objectives

The ^{14}C isotope is one member of a global array of sensitive biogeochemical "tracers" whose abundance and distribution in various natural archives (eg. tree rings, ice cores, lake and marine sediments, corals) contain valuable information on the geophysical and climatic history of this planet (Oeschger 1988). The carbon cycle alone teems with chemical species (eg. CO_2, CH_4, CO) of several isotopic labels (^{14}C, ^{13}C, ^{12}C) whose records have proven instrumental in unraveling the interplay of local and global processes that operate during, for example, the dramatic glacial/interglacial cycling of the recent Quaternary period (eg. Broecker and Denton 1989, Curry and Crowley 1987, Genthon et al. 1987, Oppo et al. 1990, Raynaud et al. 1988, Shackleton and Pisias 1985, Shackleton et al. 1988).

No single biogeochemical tracer can provide the global integration necessary to explain the mechanisms of glacial/interglacial climate transitions. Such an integration requires an interdisciplinary approach that incorporates, at the least, comparisons of contemporaneous histories of different tracers from the same archive, of contemporaneous histories of the same tracer from different archival sources, and of regionally distinct tracer records. Accurate absolute (or at least relative) dating will help untangle phase relationships in biogeochemical signals and allow causes, effects, and fortuities in global changes to be properly assigned. An important first step, however, is the identification of the source(s) of variations in each tracer signal itself.

Within the Holocene epoch, digressions in atmospheric ^{14}C might be expected to be

limited and more easily analyzed; after all, variations in carbon reservoir burdens and exchange properties are likely to be more restricted within a relatively homogeneous climatic regime. Indeed, by focusing on this time period in the natural ^{14}C system, some potential influences on the ^{14}C signal can be de-emphasized (eg. major sea level variations, tectonic-scale trends in volcanic CO_2 degassing, fossil fuel emissions) even though a multitude of influences remain (see below and Table 3 in Damon et al., 1978). Still, carbon modeling studies that concentrate on recent human impacts on the carbon (eg. $^{14}CO_2$, $^{13}CO_2$, $^{12}CO_2$) and climate systems implicitly treat the preanthropogenic Holocene (ie. prior to the last few centuries) as a natural steady state (eg. Oeschger et al. 1975, Siegenthaler and Oeschger 1987).

However, dramatic millennium-, century-, and decade-scale variations in atmospheric $\Delta^{14}C$ have occurred throughout the past 10,000 yrs (eg. figure 1.1) and this proverbial "steady state" appears not to be truly maintained on any of these timescales. Thus, as hopefully demonstrated below, enough complications remain during the "stable" Holocene epoch to provide interest and challenge to the proper identification of the nature and origin of atmospheric ^{14}C variations.

I have focused on four potential sources of atmospheric and oceanic ^{14}C variations. Two geophysical processes involve the geomagnetic and solar modulation of the ^{14}C production rate; two climate-related mechanisms, ie. variations in air-sea CO_2 exchange and in oceanic ventilation rate, can redistribute ^{14}C amongst the global carbon reservoirs. The essential and influential role of each of these processes on ^{14}C dynamics is briefly noted here.

The ^{14}C isotope is produced in the atmosphere, primarily in the lower stratosphere through the nuclear reaction $^{14}N(n,p)^{14}C$. This reaction represents the capture by atmospheric nitrogen of thermal (low-energy) neutrons which originate as spallation

products from the interaction of incoming cosmic ray particles and atmospheric constituents. The geomagnetic field limits the influx of cosmic rays by trapping positively charged particles of certain classes of trajectories along field lines (eg. Merrill and McElhinny 1983). The ability of a particle to penetrate to the earth's surface is a function of its magnetic rigidity, the geomagnetic latitude and the global dipole moment. In this way, variations in the global dipole moment in theory correlate inversely with the atmospheric influx of cosmic rays and the rate of ^{14}C production. Discussion of geomagnetic modulation is continued in sections 2.1, 2.3 and 2.4.

The magnetic properties of the solar wind also theoretically interact with incoming galactic cosmic rays and a similar inverse relationship is expected between solar activity and ^{14}C production rate (eg. Stuiver and Quay 1980). Details on solar modulation of ^{14}C production are presented in sections 2.3, 2.4, 3.3 and 4.4.

After production, ^{14}C quickly oxidizes to $^{14}CO_2$ and mixes throughout the atmospheric CO_2 reservoir. Each $^{14}CO_2$ molecule resides 3.3 yrs on average in the atmospheric reservoir before decay or transfer to either the terrestrial biosphere or surface ocean reservoir (assuming recent preanthropogenic conditions and correcting for fractionation effects in the model described below). At steady state, the net atmospheric ^{14}C flux into the ocean and terrestrial biosphere must balance the rate of new ^{14}C production in the atmosphere (neglecting a nominal decay). Atmospheric ^{14}C content will vary in response to changes in any of these fluxes.

The atmospheric $\Delta^{14}C$ response to higher-frequency (eg. decadal, century-scale) fluctuations in ^{14}C production is significantly attenuated; lower-frequency (eg. millennium-scale or longer) fluctuations in ^{14}C production more effectively change atmospheric (and oceanic) ^{14}C content but with a strong delay. Fluctuations in atmospheric ^{14}C produced by changes in rates of air-sea CO_2 exchange and/or internal

oceanic mixing also have a set of attenuation and lag "factors". In recent preanthropogenic times, surface ocean $^{14}C/^{12}C$ was only slightly depleted (ca. 5%) with respect to atmospheric $^{14}C/^{12}C$; the difference in the $^{14}C/^{12}C$ signatures of these two reservoirs limits the power of air-sea and internal ocean CO_2 flux changes to alter the atmospheric ^{14}C content.

A global ^{14}C reservoir model is required to simulate the attenuations and the delays in reservoir $\Delta^{14}C$ histories that accompany sudden or gradual variations in these four processes. The model described below reconstructs the histories of these forcing mechanisms necessary to produce the observed millennium- and century-scale variations in atmospheric $\Delta^{14}C$ (chapters 2 and 3). With this model, the relative sensitivity of atmospheric ^{14}C content to these forcings and the adjustment time in its response can be accurately quantified.

Several excellent modeling studies have already assessed the sensitivity of ^{14}C content in atmospheric and oceanic reservoirs to changes in ^{14}C production rate and climatic variables. Using 2- and 3-box global carbon reservoir models, Houtermans et al. (1973) systematically calculate the frequency-dependent attenuations and lags associated with atmospheric $\Delta^{14}C$ variations forced by hypothetical ^{14}C production rate cycles (see section 2.1). With a global box-diffusion ^{14}C model, Siegenthaler et al. (1980) and Bard (1988) define the steady-state relationships of atmospheric and oceanic $\Delta^{14}C$ levels to climatic and ^{14}C production rate conditions. These authors also consider the transient variations in ^{14}C reservoirs during transitions in climate and production rate in the context of glacial/interglacial cycles. Using an elegantly simple 4-box reservoir model, Wenk and Siegenthaler (1985) and Toggweiler and Sarmiento (1985) investigate the implications for reservoir $^{12}CO_2$, $^{13}CO_2$, and $^{14}CO_2$ contents of glacial/interglacial changes in high-latitude oceanic processes; the latter authors reconstruct the steady-state carbon and

nutrient chemistry of the glacial atmosphere and ocean from the present knowledge of boundary conditions.

A few modeling studies have focused on the observed atmospheric (tree-ring) ^{14}C history during the Holocene and the identification of its major influences. With a simple 3-box carbon model, Grey (1969) finds strong correlations between the observed atmospheric ^{14}C variations and model-derived millennium-scale and century-scale ^{14}C fluctuations forced by geomagnetic and solar changes, respectively. In contrast, Lal (1985) concludes in his sensitivity analysis using 2 versions of a 5-box carbon model that the observed Holocene-scale trend in atmospheric $\Delta^{14}C$ is better explained by climate-related reservoir changes occurring since the last glacial stage. These processes include sediment dissolution and more effective oceanic mixing and high-latitude air-sea CO_2 exchange during the Holocene. Lal emphasizes the uncertainties in the geomagnetic data and notes the lack of a sinusoidal trend in early Holocene atmospheric $\Delta^{14}C$ and the contrariety of the ice-core ^{10}Be data. All these points are addressed in this dissertation (sections 2.2, 2.3, 2.4). Toggweiler and Sarmiento (1985) also find that oceanic conditions (rather than ^{14}C production changes) may explain much of the late glacial/early Holocene $\Delta^{14}C$ elevation but the transient simulations shown here indicate that the long-term decline in Holocene $\Delta^{14}C$ would not be expected if climate alone controls the initially high Holocene reservoir ^{14}C levels (section 2.2).

Stuiver and Quay (1980) utilize a global box-diffusion ^{14}C model to deconvolve century-scale ^{14}C production rate variations (assuming constant climate conditions) from high-precision atmospheric (tree-ring) ^{14}C measurements spanning 850 years; the model production rates are regressed against solar activity records (sunspot numbers, geomagnetic Aa indices) to quantify and extrapolate the solar modulation associated with ^{14}C variations. With a 2-box model, Sternberg and Damon (1983) similarly deconvolve

^{14}C production rates to focus on the geomagnetic signal in the long-term ^{14}C record. This dissertation expands on these previous deconvolution model approaches by employing new methods, assumptions, and data in order to build on (and sometimes reinterpret) the earlier findings (eg. sections 2.3 and 4.4).

The objectives of this current study are to deconvolve the histories of four alternative mechanisms for millennium- and century-scale atmospheric ^{14}C variations during the Holocene, compare the implications of each scenario with the available geophysical and paleoclimatic evidence, and, in this way, identify and quantify the primary origins of the ^{14}C signal (chapters 2 and 3). Combinations of processes will be simulated and other potential influences on reservoir ^{14}C variations will be assessed. After identifying the main components of the ^{14}C signal, spectral techniques are applied to search for patterns and periodicities in the model-derived ^{14}C production rate curve (concluded to be the primary explanation for reservoir $\Delta^{14}C$ variations), and the implications of the spectral and pattern analyses for past, present, and future solar behavior are considered (chapter 4).

1.2 Atmospheric (tree-ring) $\Delta^{14}C$ database

The Holocene bi-decadal $\Delta^{14}C$ history shown in figure 1.1 can be divided into five distinct segments related to measurement sources. The derivation of the ^{14}C record for each segment is summarized below; supplementary details on the tree-ring (ie. "dendro-") chronologies can be found in several review articles (cf. Ferguson 1970, Pilcher et al. 1984, Stuiver and Pearson 1986 Table 2). The term "cal" is used extensively in this dissertation to distinguish the time measurements (such as dendro-years and varve-years)

Figure 1.1: Bi-decadal tree-ring $\Delta^{14}C$ from 7760 BC to AD 1980 (bar curve). The 7760 to 7220 BC portion has subsequently been revised by ca. -9 ‰. The $\Delta^{14}C$ values for AD 1840 to 1980 are "natural" variations (without the Suess effect) as reconstructed from a relationship between ^{14}C production rates and sunspot numbers. The long-term trend (heavy line) is a spline approximating a 400-yr moving average of the data. The dotted line is the sinusoidal curve which best fits the 9740-yr $\Delta^{14}C$ record. The "M" labels denote Maunder-type century-scale $\Delta^{14}C$ fluctuations; the "S" labels signify Spörer-type century-scale $\Delta^{14}C$ fluctuations. These features are discussed in the text.

(inset) Tree-ring $\Delta^{14}C$ measurements used to calculate the main figure's bi-decadal averages between 7220 to 5220 BC. Vertical lines are ±1 sigma ranges.

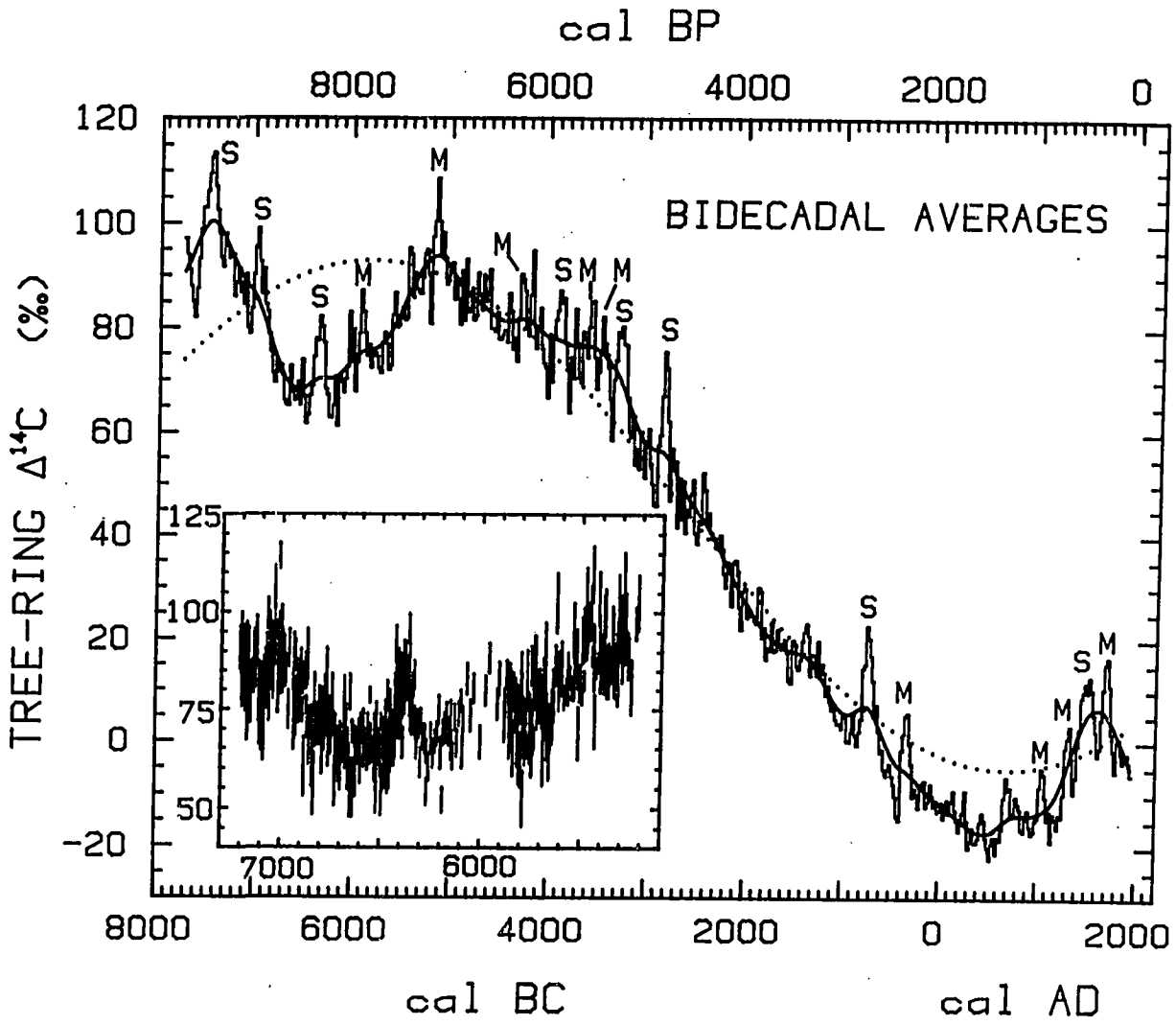
cal BP
8000
6000
4000
2000
0
120
100
80
60
40
20
0
-20
TREE-RING Δ14C (‰)
BIDECADAL AVERAGES
S
M
125
100
75
50
7000
6000
8000
6000
4000
2000
0
2000
cal BC
cal AD

that have been calibrated to the calendar timescale from those time references based on ^{14}C ages.

(1) For the period of 2500 BC to AD 1840 (ie. "bi-decades" 2490 BC to AD 1830), the ^{14}C record is calculated from the combined high-precision tree-ring measurements of the Seattle and Belfast laboratories (Stuiver and Pearson 1986, Pearson and Stuiver 1986). Measurement precision is ca. 2 °/oo (16 ^{14}C yrs) for each laboratory with respect to all aspects of laboratory reproducibility; interlaboratory agreement is excellent with no systematic ^{14}C age difference on average for contemporaneous samples. The close Belfast/Seattle agreement is underscored by the fact that 90% of the standard deviation of 25.6 ^{14}C yrs for interlaboratory differences on contemporaneous samples is explained by the precision error alone.

A nominal systematic correction of ca. -2 to -3 °/oo for the Seattle ^{14}C measurements (due to radon influence) is currently being defined and implemented but has not been applied to any of the Seattle $\Delta^{14}C$ data discussed here. A similar adjustment is anticipated for the Belfast data (G. Pearson, pers. comm. with M. Stuiver) so that the interlaboratory agreement will remain strong. These secondary improvements will minimally affect the model results discussed below.

The wood samples were collected from diverse geographic locations which are compiled here to provide a convenient overview of the entire Holocene tree-ring database. For AD 940 to 1840, the bi-decadal $\Delta^{14}C$ record is an average of decadal (ie. ten-ring) measurements from Pacific Northwest Douglas firs (Washington, Oregon, and British Columbia) with the bi-decadal (ie. 20-ring) Irish oak chronology (Ireland, Scotland, and England). From 150 BC to AD 940, the ^{14}C history is an average of decadal

measurements on California sequoias and the bi-decadal Irish oak chronology (with some supplementary oak measurements from northern and southern Germany). For 2500 to 150 BC, $\Delta^{14}C$ measurements from the south German oak and Irish oak chronologies are combined.

Contemporaneous wood samples from geographically distant locations (eg. eastern Europe, western North America) sometimes show nominal systematic age differences of several ^{14}C years. A portion of such an offset may derive from natural spatial patterns in atmospheric $^{14}CO_2$ as suggested by preliminary 3-D atmospheric tracer modeling (Braziunas and Fung, in progress).

(2) From 5220 to 2500 BC, the $\Delta^{14}C$ record consists solely of the Irish oak chronology as reported in Pearson et al. (1986). These bi-decadal values have a standard deviation of ca. 2 ‰.

(3) Between 7220 and 5220 BC, bi-decadal $\Delta^{14}C$ values are a composite of results from several laboratories (Linick et al. 1985, Linick et al. 1986, Kromer et al. 1986, Stuiver et al. 1986a). Whereas the post-5220 BC ^{14}C measurements discussed above have a high precision and uniform tree-ring coverage for each bi-decadal interval, the data mixture for this earlier time period generally has less precision and an uneven distribution (figure 1.1 inset). Thus the combined results (grouped in 20-yr intervals) have a greater standard deviation of 5 ‰. Most outliers are the data of Linick et al. (1985) with quoted precisions averaging to 6 ‰. The weighted-average bi-decadal ^{14}C record derived here from all reported measurements differs slightly from the ^{14}C curve presented in Stuiver et al. (1986b) for which I preferentially selected only the laboratory results with higher precision. A 200-yr interval around 6000 BC has limited data coverage; therefore, less

import must be assigned to this particular Maunder-type ("M") atmospheric $\Delta^{14}C$ fluctuation as deduced from the limited measurements (see chapter 3).

Wood samples, although analyzed in different laboratories, are primarily from the south German oak chronology. Between 6560 and 5340 BC, the data also include sporadic wood samples from the cross-dated Bristlecone pine chronology (White Mountains in California).

(4) From 7760 to 7220 BC, bi-decadal $\Delta^{14}C$ values were derived from a floating south German oak tree-ring segment ("M9" curve in figure 5 of Kromer et al. 1986) tentatively matched with the dated German oak chronology.

Recently, reliable cross-dating has shown that the "Heidelberg Main 9" tree is 74 years younger than its original age assignment (B. Kromer, pers. comm. with M. Stuiver). This shortening of the calendar age of the tree translates into a corresponding average drop in the calculated atmospheric $\Delta^{14}C$ (pre-decay tree-ring ^{14}C content) of about 9 ‰; the lower calculated *initial* ^{14}C content for each wood sample is required to compensate for the reduced time available for natural decay to contribute to the *measured* ^{14}C age. The $\Delta^{14}C$ values for specific bi-decades can change by +1 to -26 ‰ because of the shift in absolute time of high-frequency fluctuations in the tree-ring ^{14}C history.

All model simulations discussed below were performed using the original age assignment for the Main 9 tree before the 74-yr adjustment (and without supplementary measurements supplied recently by B. Kromer, pers. comm. with M. Stuiver). The revisions, however, should not significantly alter the model results presented in the following chapters (see section 2.1 for specifics). Only one century-scale $\Delta^{14}C$ fluctuation is modified to a degree.

(5) After AD 1850 the observed tree-ring $\Delta^{14}C$ record has been influenced by the release of ^{14}C-deficient fossil fuel CO_2. This "industrial effect" produces a sharp 16 ‰ decline in atmospheric $\Delta^{14}C$ by AD 1950 in addition to the natural variations imposed by solar and geomagnetic modulation of ^{14}C production rates (Stuiver and Quay 1981). The dramatic decline in post-AD 1850 tree-ring measurements is displayed in figures 1 and 2 of Stuiver et al. (1986b).

In order to properly portray the most recent natural trend in atmospheric $\Delta^{14}C$, the industrial effect must be removed from the post-AD 1850 tree-ring record. Therefore, for the AD 1850 to 1970 time interval, I used the bi-decadal averages of a reconstructed "natural" history for atmospheric $\Delta^{14}C$ (Stuiver and Quay 1981) derived from an empirical relationship between sunspot numbers (averaged over 11-yr solar cycles between AD 1720 and 1860) and contemporaneous model-derived ^{14}C production rates. This reconstruction extends the pre-AD 1840 tree-ring record to AD 1980 (figure 1.1). The bi-decade AD 1830 (ie. 1820-1840) is considered the last tree-ring $\Delta^{14}C$ measurement without an industrial effect. As a first approximation, I assigned the same "natural" $\Delta^{14}C$ level to bi-decade AD 1970 as 1950.

A bi-decadal Q/sunspot relationship was calculated as part of the modeling efforts here (as described in section 4.4). This new relationship can be applied, as part of an iterative process, to modify the post-AD 1840 "natural" $\Delta^{14}C$ values. However, the original relationship of Stuiver and Quay (1981) properly regenerates the observed tree-ring record when natural and anthropogenic influences are simulated in a forward model so that any "improvements" in the relationship would be expected to be secondary. A complete discussion is presented in section 4.4.

A cubic spline function was fit to the bi-decadal $\Delta^{14}C$ record to represent its long-

term trend (thick curve in figure 1.1); an arbitrary average standard deviation was assigned to the bi-decadal data in order to generate a smoothing spline (Reinsch 1967) that closely resembles a 400-yr moving average. I preferred a spline to a moving average for the millennium-scale trend because the resulting curve is smoother and remains centered more closely on the data. For example, two large positive fluctuations in $\Delta^{14}C$ within 400 years of one another will pull a moving-average curve away from the less positive data between the fluctuations while a spline is less affected.

The purpose of the 400-yr trend line is to remove the gradual geomagnetic or climatic influence on atmospheric $\Delta^{14}C$ so as to look at the residual higher-frequency solar and/or climatic signal. Major features of the $\Delta^{14}C$ record are the century-scale fluctuations of about 20 ‰ that resemble either the recent $\Delta^{14}C$ excursion contemporaneous with the Maunder Minimum in sunspots (variations marked "M" on figure 1.1) or the excursion contemporaneous with the longer Spörer Minimum in solar activity (variations are marked "S"). I judged a 400-yr curve to best remove the longer-term trend while retaining the essential characteristics of these shorter-term solar-related variations. The identification and implications of these century-scale features are the topics of chapters 3 and 4.

Some researchers have characterized the long-term $\Delta^{14}C$ trend after 6500 BC as sinusoidal with a period of ca. 11,300 yrs and an amplitude around 50 ‰ (e.g. Bruns et al. 1983, Damon and Linick 1986). Prior to 6500 BC, however, the $\Delta^{14}C$ record deviates from a simple sinusoid. The sinusoid that yields the best chi-squared fit to the full 9700-yr $\Delta^{14}C$ record has a longer period of 13,100 yrs, an amplitude of 49 ‰ and a phase shift of 160° (dotted line in figure 1.1 is equation: $\Delta^{14}C = 44+\cos((2\pi/13100)(T+5850))$ where T is the calendar year as BC (negative) or AD (positive)). The sinusoidal representation of the long-term data trend is no longer satisfactory, especially for the early and late portions of the data record.

Although long-term geomagnetic influence on atmospheric $\Delta^{14}C$ is sometimes treated as inherently sinusoidal, geomagnetic dipole-moment data covering the past 30,000 yrs show a general rise with no apparent cyclicity (figure 4.9 in Merrill and McElhinny 1983; Tauxe and Valet 1989). This observation has a "reasonable" rating and implies that non-linear processes operate in producing the Earth's magnetic field (Merrill and McElhinny 1983, Table 10.1). In addition, because the geomagnetic data have a limited geographic extent, regional non-dipole disturbances may significantly bias the paleointensity measurements (Aitken et al. 1989). Because of these complexities, the empirical spline approximation was selected to represent the long-term $\Delta^{14}C$ trend rather than a sinusoid or theoretically-based curve (see section 2.3).

1.3 Early- and pre-Holocene atmospheric $\Delta^{14}C$

Radiocarbon ages of terrestrial macrofossils from Swiss lake-core sediments (Zbinden et al. 1989) appear to indicate significantly reduced atmospheric $\Delta^{14}C$ levels during much of the 4000 years prior to the start of the tree-ring record discussed above (figure 1.2). The measured radiocarbon ages were converted into atmospheric $\Delta^{14}C$ values for specific calendar years by: (1) accepting the evidence from the Swedish varve chronology (Tauber 1970) for the durations in varve (calendar) yrs of pollen zones observed in the Swiss lake cores; (2) assuming constant sedimentation rates within the pollen zones of the Swiss lake sediments; and (3) assigning an absolute date to the Younger Dryas/Holocene transition of 10,700 cal BP in accord with the revised dating of ice recessional features in the Swedish varve chronology (Strömberg 1985). This time marker agrees perfectly with the 10,720 cal BP date determined by ice-layer counting for a

Figure 1.2: Atmospheric $\Delta^{14}C$ values derived from the radiocarbon ages and assigned calendar ages of: (1) the post-7220 BC bi-decadal tree-ring record (bar curve), (2) the spline curve of the revised "Heidelberg Main 9" tree-ring $\Delta^{14}C$ record (solid line covering the bi-decades 7950 to 7170 BC), (3) laminae in lake sediments from Lake of the Clouds in Minnesota (squares with one-sigma error bars), (4) terrestrial macrofossils from sediments of two Swiss lakes (x = core RL305 from Rotsee, o = cores from Lobsigensee, dashed line = trend line as derived by Zbinden et al.,1989), and (5) the end of the *Juniperus* pollen zone in Scandinavia and the assumably synchronous $\delta^{18}O$ transition in the Greenland ice core, dated by ice-layer counting (shaded rectangle indicating ±1 sigma ranges). The dotted lines signify the calendar years for the Allerød/Younger Dryas and Younger Dryas/Holocene boundaries as specified in Zbinden et al. (1989).

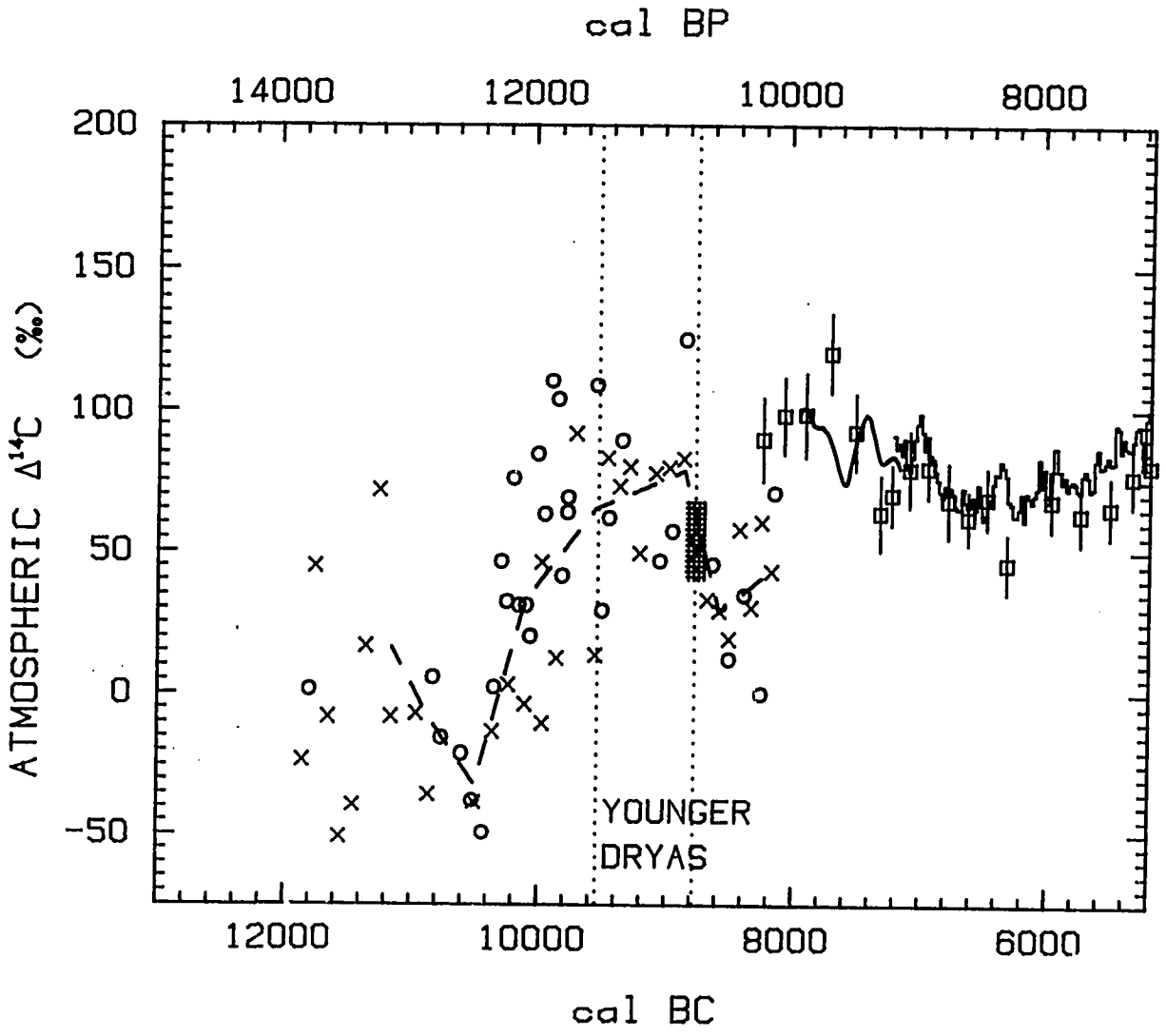
cal BP
14000
12000
10000
8000
200
150
100
50
0
-50
ATMOSPHERIC Δ14C (‰)
YOUNGER
DRYAS
12000
10000
8000
6000
cal BC

definitive Younger Dryas/Holocene transitional signal in $\delta^{18}O$ in the Dye 3 ice core from Greenland (Hammer et al. 1986).

The atmospheric $\Delta^{14}C$ trend calculated from the macrofossil radiocarbon ages and assigned calendar ages (Zbinden et al. 1989, and figure 1.2) is offset from the trend associated with tree-ring radiocarbon ages (described above) and from radiocarbon ages of organic carbon in the laminated sediments of Lake of the Clouds in Minnesota (Stuiver 1970). Calendar ages were determined for the Lake of the Clouds samples by counting laminae; the derived atmospheric $\Delta^{14}C$ levels agree closely with the tree-ring record back to 7960 cal BC (incorporating the revised Main 9 tree-ring curve). Also displayed on figure 1.2 as dotted lines are the Allerød/Younger Dryas and Younger Dryas/Holocene boundaries at 9550 cal BC and 8750 cal BC, respectively, as established by the Swedish varve chronology utilized by Zbinden et al. (1989). Interestingly, the 13,100-yr sinusoidal curve of figure 1.1 passes through the scatter of the macrofossil $\Delta^{14}C$ points.

The shaded rectangle in figure 1.2 represents the match between the calendar age for the ice-core $\delta^{18}O$ transition of 10,720 ± 75 cal BP determined through ice-layer counting (of seasonal variations in $\delta^{18}O$, dust, and acidity) and the radiocarbon age of 10,000 ± 75 ^{14}C yrs for the termination of the *Juniperus* pollen zone in southern Scandinavia, a climate change believed to be synchronous with the strong $\delta^{18}O$ event (Hammer et al. 1986). These two age estimates together translate into an atmospheric $\Delta^{14}C$ of 53 ±14 ‰ at the Younger Dryas/Holocene boundary. The full estimated error in ice-layer counts is ±150 yrs, half being considered as "one sigma" (Hammer et al. 1986).

To connect the trends of the macrofossil and lamina/tree-ring ^{14}C records requires either a sharp increase in $\Delta^{14}C$ around 8300 BC or a correction in the calendar ages of some of the data. A "floating" (ie. without fixed calendar ages) German pine record yields

a ca. 950 dendro-year trend in radiocarbon ages that overlaps these other records (Becker and Kromer 1986 Table 2; Becker and Kromer unpublished results, pers. comm. with M. Stuiver). The German pine data do not display the requisite ^{14}C increase and thus indicates that a correction in calendar ages is necessary for either the Swiss lake or Lake of the Clouds samples.

Whereas the Lake of the Clouds $\Delta^{14}C$ values generally concur with the tree-ring $\Delta^{14}C$ record, the Swiss lake results have several inherent limitations which might create a significant calendar-age (and associated atmospheric $\Delta^{14}C$) displacement. The conversion of radiocarbon ages to atmospheric $\Delta^{14}C$ values is sensitive to the assigned calendar age for the demise of the organic material (ie. the absolute time since its last exchange with the atmospheric or oceanic reservoir). Zbinden et al. estimate uncertainties ≤ 200 calendar yrs for ages of pollen zone boundaries and uncertainties ≤ 600 yrs on specific pollen zone durations. An earlier starting time of 200 calendar years in their chronology (a shift of data points to the left in figure 1.2) also raises the associated $\Delta^{14}C$ values by ca. 25 ‰. In such a case, the increased calendar time for ^{14}C decay after death (ie. ^{14}C aging) requires that the calculated initial ^{14}C contents be higher in order to produce the measured radiocarbon ages of the samples. If the Allerød pollen zone (12,300 to 11,500 cal BP in figure 1.2) lasted 600 calendar years longer than originally estimated, the $\Delta^{14}C$ rise during the Allerød would disappear. In this case, the lengthened calendar time for ^{14}C decay substitutes for the increase in atmospheric $\Delta^{14}C$ otherwise required to explain the measured radiocarbon ages (ie., 600 yrs of decay is the equivalent of ca. 75 ‰).

The laboratory uncertainties of ±120-200 ^{14}C yrs in the radiocarbon ages themselves translate into errors in $\Delta^{14}C$ of ±15-25 ‰. Such large uncertainties result from the small sample sizes on which ^{14}C content was measured through accelerator mass spectrometry (AMS). This lack of precision is reflected in the scatter of the data points

(figure 1.2), an indication that little weight should be given to the value of any single point alone.

The atmospheric $\Delta^{14}C$ levels calculated from the Lake of the Clouds laminae are about 40 o/oo (equivalent to "320 calendar yrs") higher than the most recent Swiss lake values. The measured radiocarbon ages for the $\Delta^{14}C$ data shown on figure 1.2 are plotted with their assumed calendar ages in figure 1.3. The dashed line indicates ^{14}C/calendar-age equivalence. The Younger Dryas/Holocene boundary occurs at 10,000 ^{14}C yrs by definition (Holocene Commission of INQUA). On such a diagram, a correction in calendar age corresponds to a horizontal shift in the data point; the vertical placement is fixed by the reported radiocarbon age. I fit a smoothing spline to the macrofossil data (all points assigned one sigma of ±200 ^{14}C yrs) to replace the jagged trend line in Zbinden et al. (1989). A shift of 250 calendar yrs to older ages (to the left) would align the macrofossil curve with the Lake of the Clouds/tree-ring trend and still permit it to overlap the ice-layer result (although the Younger Dryas/Holocene pollen zone boundary in the Swiss lake core would now precede the $\delta^{18}O$ event by 250 calendar years).

The floating German pine data of Becker and Kromer, with average uncertainties of only 27 ^{14}C yrs (3.5 o/oo), will best fit both the macrofossil ^{14}C trend and Lake of the Clouds data if: (1) the German pine ^{14}C data span the time period of 9200 to 8250 BC, and (2) the macrofossil ages are older by *450* calendar yrs. This fit is shown in figure 1.4 with the added trend (heavy line) of the floating German pine data. If the pine radiocarbon trend is matched to the original Swiss lake curve (figure 1.2), it is discrepant with the Main 9 tree-ring results. Also, the floating pine curve cannot be matched to a 250-yr macrofossil shift and the lamina/tree-ring trend. The final fit was determined by horizontally shifting the macrofossil and German pine curves until a good visual match with the tree-ring and Lake of the Clouds data is achieved.

Figure 1.3: The measured radiocarbon ages and assigned calendar ages associated with the $\Delta^{14}C$ values of figure 1.2. A smooth spline through the terrestrial macrofossil data (solid line from 11,850 to 8160 BC) replaces the jagged trend line in figure 1.2. The beginning of the Holocene is defined as 10,000 ^{14}C yrs BP (dotted line). The dashed line represents equivalence of ^{14}C and calendar ages. Other symbols and lines are identified in figure 1.2.

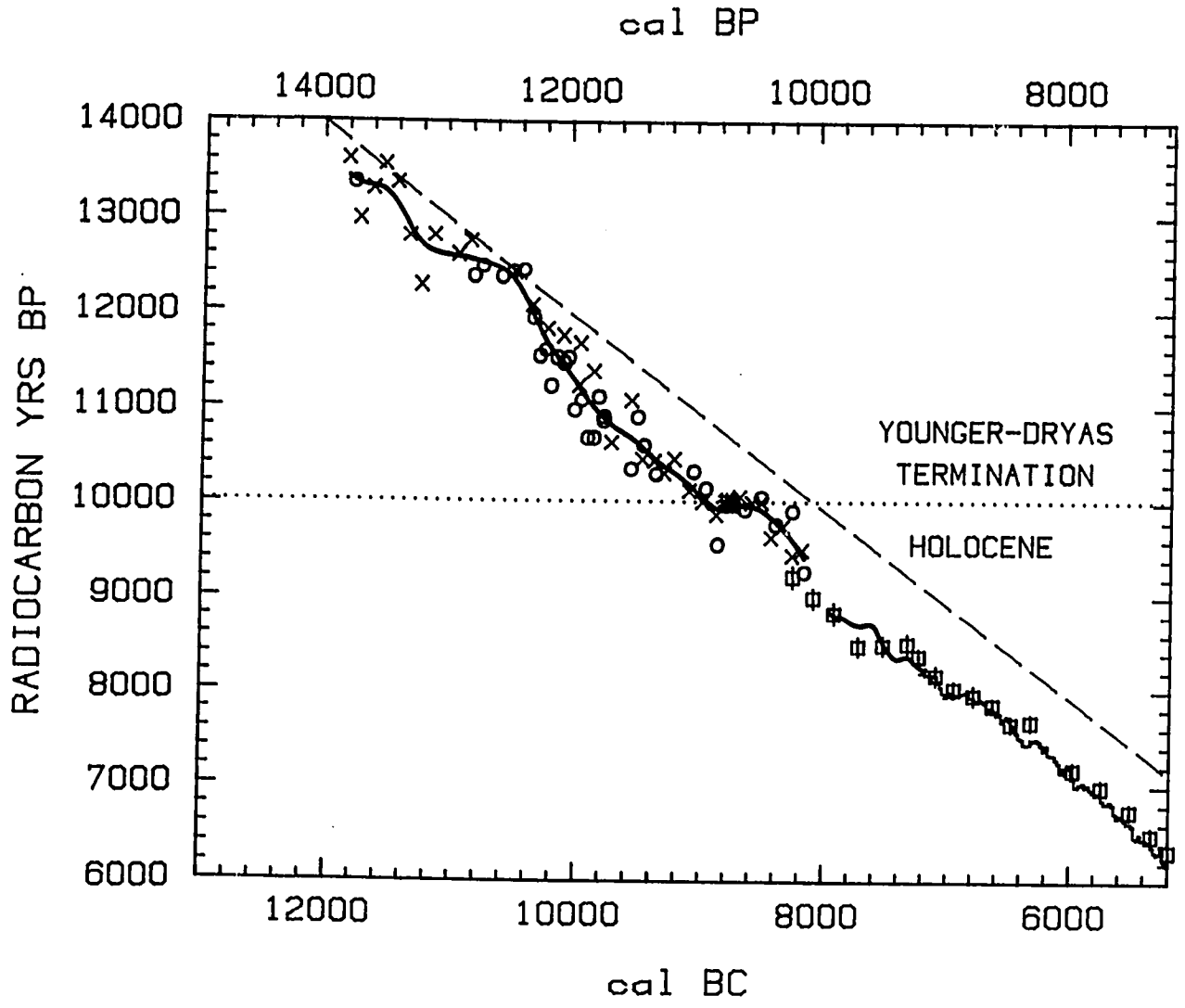
cal BP
14000
12000
10000
8000
14000
13000
12000
11000
10000
9000
8000
7000
6000
RADIOCARBON YRS BP
YOUNGER-DRYAS
TERMINATION
HOLOCENE
12000
10000
8000
6000
cal BC

Figure 1.4: The measured radiocarbon ages presented in figure 1.3 with *re-assigned* calendar ages for the terrestrial macrofossil data. The spline through the terrestrial macrofossil data has been shifted by 450 calendar yrs (light solid line from 12,300 to 8610 BC). A smooth spline through the radiocarbon age measurements on a floating German pine (Becker and Kromer, pers. comm.) is assigned the calendar interval of 9170 to 8250 BC (heavy solid line). Other symbols and lines are identified in figure 1.2.

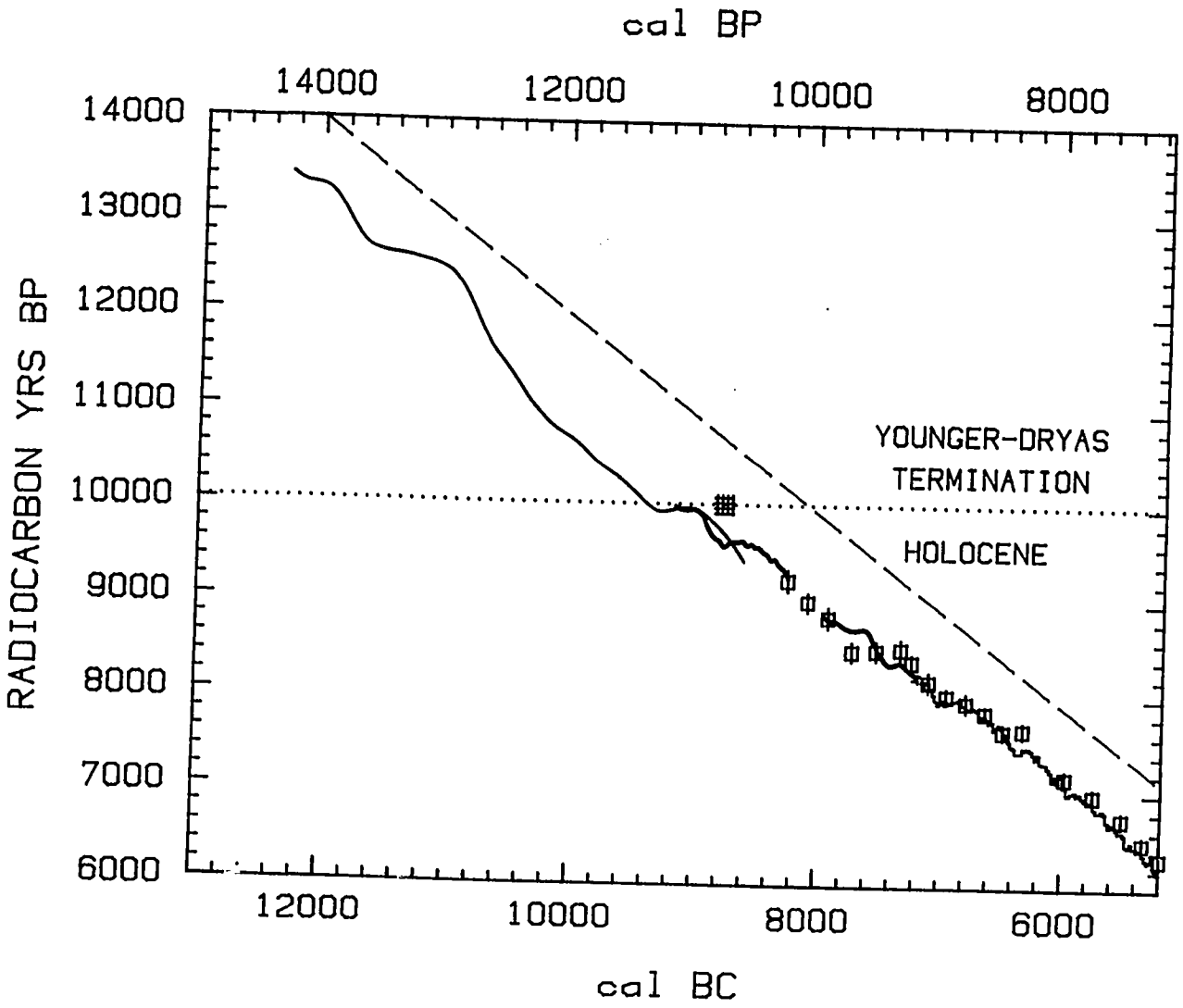
cal BP
14000
12000
10000
8000
RADIOCARBON YRS BP
14000
13000
12000
11000
10000
9000
8000
7000
6000
YOUNGER-DRYAS
TERMINATION
HOLOCENE
12000
10000
8000
6000
cal BC

For the reasons above, the adjusted radiocarbon chronology displayed in figure 1.4 with the 450-yr shift in macrofossil data is here considered the most acceptable. The Swiss lake calendar ages are based on the Swedish varve chronology; a conjectured addition of 450 calendar yrs, together with an earlier revision of +465 yrs (discussed in Strömberg 1985), would produce a total +915 yr adjustment in the original (Tauber 1970) Swedish varve chronology. The possibility of such an adjustment was expressed 20 yrs ago (Stuiver 1970, Stuiver et al. 1986a).

A 450-yr shift in calendar ages for the Swiss lake data, however, does not necessitate that great an adjustment in the Swedish varve chronology. The potential for time lags between vegetation changes in Swiss lakes and glacial fluctuations in Sweden, as well as the blurred resolution of the Swiss pollen record, produce an estimated uncertainty of ±200 yrs in the *calendar* ages of the macrofossil samples (Zbinden et al. 1989) independent of the accuracy of the varve chronology.

An independent chronology of radiocarbon variations during the last 30,000 yrs has been derived from corals dated using ^{234}U-^{230}Th mass spectrometry. These measurements (Bard et al. 1990) are consistent with the Holocene tree-ring record but are contrary to the pre-Holocene Swiss macrofossil evidence. A *minimum* shift of 450 calendar years in the macrofossil ages is necessary to bring the post-12,000 BP data near the coral results.

A complication in the interpretation of the coral radiocarbon measurements, however, is the application of a "reservoir correction" in order to convert these surface ocean radiocarbon ages to atmospheric values for comparison with the other chronologies. A "reservoir correction" of 400 ^{14}C yrs is selected as a first approximation. If, as an extreme example, no reservoir correction was required, that is, surface ocean $\Delta^{14}C$ levels

were identical to atmospheric $\Delta^{14}C$ levels during the pre-Holocene time under consideration rather than deficient by 50 ‰ ("aged" ca. 400 ^{14}C yrs), then a 50-yr shift in the calendar ages of the macrofossils is still necessary to place them near the post-12,000 BP coral data. The elegantly simple 4-box atmosphere/ocean model of Toggweiler and Sarmiento (1985) simulates a deficiency of ca. 75 ‰ (ie. 600 ^{14}C yrs) in the glacial surface ocean (discussed more below); a greater reservoir correction like this increases the discrepancy between the macrofossil and coral data. The chronologies prior to 12,000 BP are more discrepant and clearly involve a more complex scenario (including variable production rates, climate change, and reservoir corrections) than will be considered here.

A dilemma apparent in figure 1.4 is the shifted chronology's disagreement with the ice-layer evidence (shaded rectangle). The shaded area expands if the full error of ±150 calendar yrs in ice-layer counts is displayed. If the $\delta^{18}O$ transitional event in the Greenland ice core originally considered simultaneous with the Scandanavian *Juniperus* zone termination (Hammer et al. 1986) instead occurred after this termination, the shaded area could drop vertically to a younger ^{14}C age in figure 1.4. Direct ^{14}C dating of the Dye 3 ice core points to a younger radiocarbon age for the $\delta^{18}O$ transitional event, but this AMS dating application is presently fraught with difficulties (Andrée et al. 1986a). Citing this evidence, however, Fairbanks (1989) concludes that the $\delta^{18}O$ fluctuation at issue is some 500 ^{14}C yrs younger than the Younger Dryas/Holocene boundary and proposes that a pulse in meltwater discharge is responsible for the $\delta^{18}O$ signal rather than a temperature event. Such a scenario, based on sea-level changes inferred from Caribbean corals, would make the ice-core results consistent with the adjusted ^{14}C chronology.

The radiocarbon chronologies as shown in figure 1.4 are converted to atmospheric $\Delta^{14}C$ values in figure 1.5. The macrofossil curve $\Delta^{14}C$ levels are ca. 60 ‰ above the original determinations of Zbinden et al. in figure 1.2. The shaded area between 11,400

Figure 1.5: Atmospheric $\Delta^{14}C$ values associated with the measured radiocarbon ages and re-assigned calendar ages of figure 1.4. Symbols and lines have the same identity as in figure 1.4. Diagonal shading between 11,400 and 10,900 cal BP covers the calendar interval corresponding to 10,000 ± 100 ^{14}C yrs in the radiocarbon ages of the macrofossil trend line. Diagonal shading between 12,250 and 11,950 cal BP is positioned 800 ± 150 calendar yrs prior to the highest $\Delta^{14}C$ value in the Younger Dryas termination zone.

(inset) Spline approximating a 400-yr moving average of the combined $\Delta^{14}C$ data in the main figure.

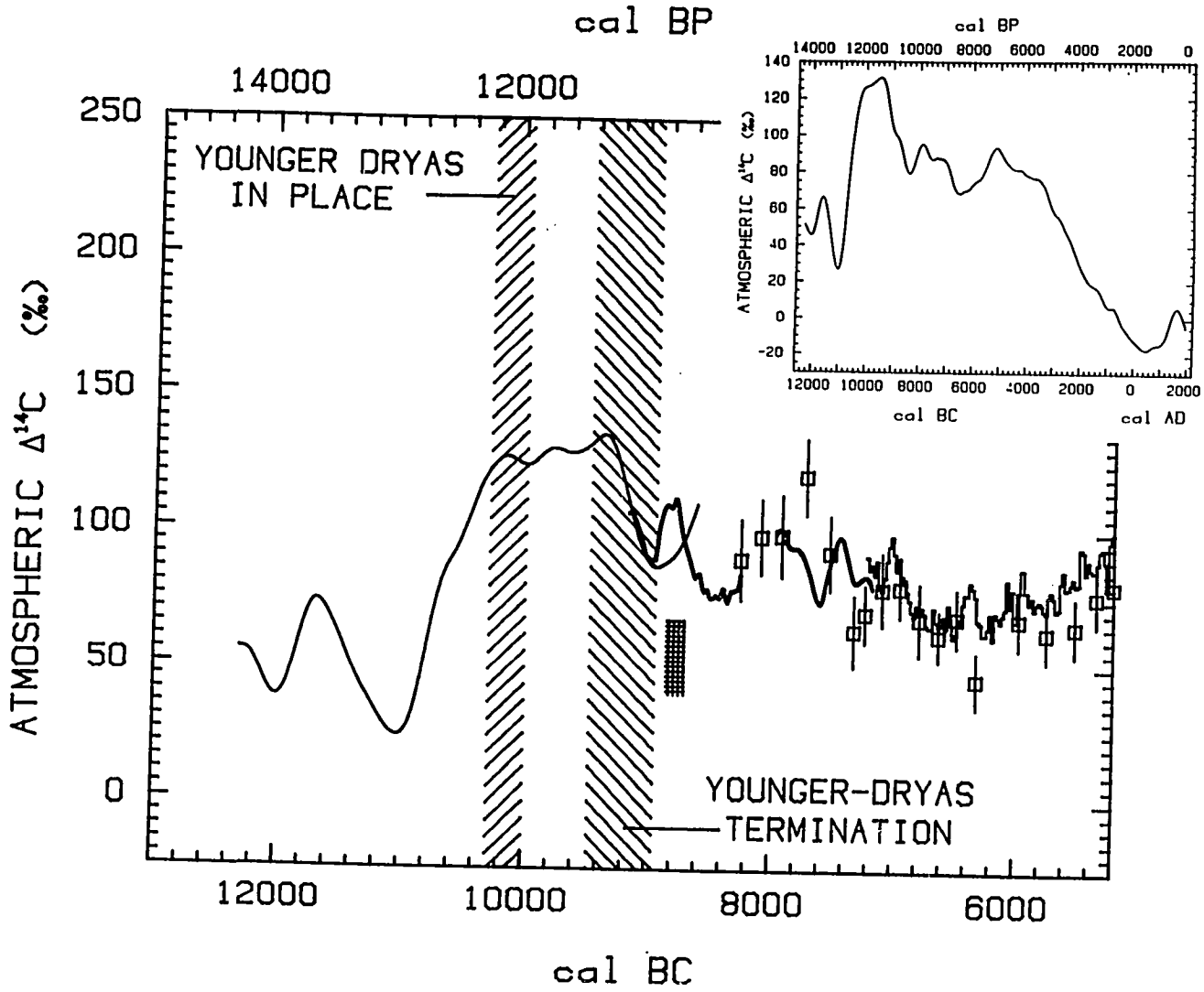
cal BP
14000
12000
250
200
150
100
50
0
ATMOSPHERIC Δ14C (‰)
YOUNGER DRYAS
IN PLACE
YOUNGER-DRYAS
TERMINATION
12000
10000
8000
6000
cal BC
cal BP
14000 12000 10000 8000 6000 4000 2000 0
140
120
100
80
60
40
20
0
-20
ATMOSPHERIC Δ14C (‰)
12000 10000 8000 6000 4000 2000 0 2000
cal BC
cal AD

and 10,900 cal BP represents the time interval during which the trend in the radiocarbon chronology (figure 1.4) is within ±100 ^{14}C yrs of 10,000 ^{14}C yrs BP, the radiocarbon age defined as the beginning of the Holocene. Because of the apparent drop in atmospheric $\Delta^{14}C$ during this time interval at a rate similar to ^{14}C decay, the Younger Dryas termination (equivalent here to the start of the Holocene) cannot be as sharply defined in *calendar* years. In fact, the radiocarbon time scale appears to underestimate substantially the duration of this transition and makes it difficult to determine the true synchrony of events at this time.

The ice-layer results are not compatible with the conjectured $\Delta^{14}C$ curve of figure 1.5. A 500-yr correction in ^{14}C age, a possibility mentioned above, raises the shaded rectangle vertically about 60 °/oo. A correction in the ice-layer counts of 450 shifts the rectangle vertically and to the left as both calendar age and calculated initial ^{14}C content change. In both cases the ice-layer result would then be consistent with the proposed atmospheric $\Delta^{14}C$ curve. In the first case, however, a time lag exists between the major floral change at the end of the Younger Dryas and the dramatic $\delta^{18}O$ signal in the Greenland ice core. With the insensitive radiocarbon time scale at 10,000 ^{14}C yrs BP and the possibility that ice-core $\delta^{18}O$, glacial fluctuations in Sweden, and pollen transitions in Scandinavia and Switzerland may not be synchronous, the definition for the Younger Dryas/Holocene transition may require reconsideration.

All calendar dates within the shaded region between 11,400 and 10,900 cal BP qualify as valid times for the termination of the Younger Dryas if defined as 10,000 ± 100 ^{14}C yrs BP. The pollen zone transition reflecting this termination in the Swiss lakes has shifted 450 calendar yrs to specifically 11,150 cal BP. One might also choose the 135 °/oo peak in $\Delta^{14}C$ at 11,300 cal BP prior to the dramatic 50 °/oo fall in atmospheric $\Delta^{14}C$

to denote the "true" termination. Using this definition and accepting the varve counts of 800 ± 150 varve yrs for the duration of the Younger Dryas (Tauber 1970), the Younger Dryas would commence at 12,100 ± 150 cal BP (shaded region on left in figure 1.5). This date corresponds with the 125 ‰ apex of a dramatic 100 ‰ rise in atmospheric $\Delta^{14}C$. The timing of these two major digressions in atmospheric $\Delta^{14}C$, coinciding with glacial and biological events, strongly implies that the atmospheric $\Delta^{14}C$ trend at this time is related to reservoir (climate) changes rather than production rate variations.

The origin of the "Younger-Dryas excursion" in atmospheric $\Delta^{14}C$ is not addressed in detail in this dissertation. The explanation appears intricate because the dramatic 100 ‰ rise in atmospheric $\Delta^{14}C$ begins at ca. 13,000 cal BP, well before the start of the "cold" Younger Dryas pollen zone and near the start of the "warm" Allerød pollen period (assumed to cover the 800 calendar years just prior to the Younger Dryas per Tauber 1970). If the Younger Dryas climate event is related to a decrease in northern Atlantic ventilation, because of a meltwater influx and/or other "climatic mode switch" (Broecker et al. 1985b, 1988a), then for this reason alone more ^{14}C should indeed remain in the atmosphere (section 2.2); but the secondary $\Delta^{14}C$ elevation between 10,900 and 10,500 cal BP in the German pine chronology more closely agrees with the timing and rapidity of climate change for at least one other calibration of the Younger Dryas event (figure 11 in Broecker et al. 1988a). Another complication is that the general rise in atmospheric $\Delta^{14}C$ levels is contemporaneous with the strong atmospheric CO_2 increase between 14,000 and 11,000 cal BP (Neftel et al. 1988) countering the expectation that greater atmospheric pCO_2 will lower atmospheric ^{14}C content (section 2.2). The influences of these carbon system changes on atmospheric $\Delta^{14}C$ are addressed more quantitatively in section 2.2. The conflicting evidence at present from the lake sediments, corals (see also section 2.3), and ^{10}Be implications (section 2.4) prevent a more definitive analysis of the origin for the

Younger Dryas climate event.

The magnitude of this 800-yr "Younger Dryas excursion" in atmospheric $\Delta^{14}C$ can be compared to the rest of the 14,000-yr $\Delta^{14}C$ record in the inset of figure 1.5. The curve in the inset is a spline (approximating a 400-yr moving average) of the combined data in the main figure. In combining the individual $\Delta^{14}C$ records, the macrofossil curve was linked to the beginning of the German pine trend at 9170 cal BC and the gap between the German pine and Main 9 trends was interpolated (passing through the Lake of the Clouds data points). The combined ^{14}C data can also be utilized to calibrate radiocarbon ages beyond 8300 ^{14}C yrs BP. This preliminary ^{14}C/calendar age calibration is presented in Table 1.1. For radiocarbon ages older than 11,000 BP, we prefer the calibration scenarios calculated from pre-Holocene dipole records (see section 2.3 and Table 2.1). These alternative calibrations contrast sharply with the lake sediment record before 11,000 ^{14}C yr BP but are in good agreement with the independently calibrated coral ^{14}C data (Bard et al. 1990).

The modeling efforts detailed below indicate that the century-scale and millennium-scale fluctuations in atmospheric $\Delta^{14}C$ during the Holocene result from ^{14}C production rate changes related to solar and geomagnetic behavior, respectively. The Younger Dryas $\Delta^{14}C$ excursion, however, appears to be induced by climate change. This conclusion is critical in selecting the initial conditions of the model ^{14}C simulations. As demonstrated in chapter 2, the pre-Holocene history of the geomagnetic field (and sun) has a more persistent influence on the subsequent 10,000 yrs of the global ^{14}C system than pre-Holocene climatic events. A prolonged enhanced level of ^{14}C production will be retained in the oceanic system and influence model results for several ^{14}C half-lives (ie. 20,000 yrs) after the production rate declines; the memory of a redistribution in ^{14}C during a climate disturbance will affect later ^{14}C behavior only up to the mixing (ventilation) time

TABLE 1.1

CALENDAR YR - RADIOCARBON YR AGE-CALIBRATION DERIVED FROM ADJUSTED LAKE-SEDIMENT AND TREE-RING RECORDS

^{14}C AGE	CAL AGE	^{14}C AGE	CAL AGE
11000	12250	9600	10550
10900	12200	9500	10400
10800	12100	9400	10300
10700	12000	9300	10200
10600	11900	9200	10150
10500	11800	9100	10100
10400	11700	9000	10000
10300	11600	8900	9950
10200	11500	8800	9800
10100	11400	8700	9550
10000	11350	8600	9500
9900	10900	8500	9450
9800	10850	8400	9400
9700	10850	8300	9200

of the oceanic reservoir (<2000 yrs). Therefore, it is more important to properly establish the pre-Holocene history in the geomagnetic field than in climate change in order to accurately model all the influences on Holocene variations in atmospheric and oceanic $\Delta^{14}C$. These maxims will be illustrated in the sensitivity tests of alternative initial conditions for Holocene simulations in the next chapter.

1.4 Global ^{14}C reservoir model

The basic structure and parameterization of the global ^{14}C box-diffusion ("BD") model replicates the original design of Oeschger et al. (1975, figure 1) as implemented by Stuiver and Quay (1980). The global atmospheric carbon reservoir exchanges with a global surface ocean carbon reservoir and two terrestrial reservoirs representing shorter- and longer-lived biota. The oceanic reservoir is subdivided vertically into a 75-meter surface mixed layer, 37 thermocline layers each 25 meters thick, and 5 identical deep ocean partitions extending to a total depth of 3800 meters. Figure 1.6 illustrates the vertical resolution of the box-diffusion model ocean with each "horizontal line" representing the $\Delta^{14}C$ time history of one ocean reservoir. The surface mixed layer is the top "horizontal line" of the ^{14}C profiles. The shape and transient changes of the depicted ocean ^{14}C distribution are discussed below.

The ^{14}C contents of each reservoir (except the two terrestrial boxes -- see below) areconsidered "well mixed" with all ^{14}C atoms having equal probability of removal at any specified time (Bolin and Rohde 1973) and reservoir exchanges are governed by first-order donor-controlled differential equations (Oeschger et al. 1975). The model equations

are simple linear approximations of these fluxes (the "Euler approach") calculated at time intervals short enough (.04 yr or less) to insure consistent model results.

In the rest of this section, I first describe the parameterization of the model constants (all reservoir ^{12}C contents, terrestrial ^{12}C exchanges) and model variables (reservoir ^{14}C contents, atmosphere/ocean and oceanic ^{12}C exchanges, ^{14}C production rate). Then the concept of ventilation index is presented as an important tool for comparison of model ^{14}C time series with oceanic ^{14}C data. Finally, other modeling designs are briefly discussed.

Constant model reservoir contents and exchange parameters

The ^{12}C contents of all model reservoirs are assumed to remain constant throughout the Holocene. The ice-core CO_2 record from Byrd Station, Antarctica, indicates that the major rise in atmospheric pCO_2 occurred between 14,000 and 11,000 BP (Neftel et al. 1988), more than 1000 calendar yrs prior to the start of the Holocene ^{14}C simulations conducted here. I have assumed that the ^{14}C and ^{12}C reservoirs recover from climatic perturbations within such a time frame (as discussed in detail in section 2.2). The ice-core CO_2 measurements also indicate that atmospheric pCO_2 may have varied ±20 ppm (±7%) *during* the Holocene but, as demonstrated below, these variations in themselves will have only a secondary impact on the Holocene record of atmospheric ^{14}C.

Pre-industrial atmospheric pCO_2 is set at 280 ppm, equivalent to 594 gigatons (GT) of carbon. This pCO_2 level was chosen to agree with ice-core measurements (eg. Oeschger and Stauffer 1986) although the more recently published data from the Byrd core indicate a slightly lower average value for atmospheric pCO_2 during the Holocene (Neftel et al. 1988). An average pre-industrial atmospheric pCO_2 level of 270 ppm for the past 2000 calendar yrs was deconvolved using a global ^{13}C model which translated the ^{13}C signal in tree rings into past deforestation and fossil fuel fluxes (Stuiver and Braziunas

1986). As a simplification, atmospheric pCO_2 remains constant throughout the recent centuries of the model simulation as well.

The terrestrial biosphere is partitioned into two reservoirs (B_1 and B_2) with residence times of $\tau_1 = 2.7$ yr and $\tau_2 = 80$ yr, comprising 10.6% and 89.4% of the total model land mass, respectively. The dual biospheric division mimics the structure of the original Oeschger et al. BD model but the specifications are based on the estimated biospheric reservoirs of AD 1970 in Emanuel et al. (1981, 1984). The reservoir with fast turnover combines ground vegetation, leaves and detritus while the other reservoir contains tree wood and active soil carbon. The quantification of deeper soil carbon pools is often confused by choice of definitions and remains uncertain (eg. discussion in Olson et al. 1985). The less active soil carbon and peat are not modeled here; the sensitivity of the model results to incorporation of such longer-storage terrestrial carbon reservoirs is considered in section 2.1.

The total mass of the pre-industrial terrestrial biosphere is set at 1903 GT of carbon, an increase of nearly 150 GT from the estimates of the standing crop in AD 1970 (Olson et al. 1978, Emanuel et al. 1981). The additional carbon is assumed not to alter the proportional distribution of the two reservoirs calculated above. The carbon increase for the natural biospheric burden was derived from the estimated cumulative deforestation flux deconvolved from a global ^{13}C model (Stuiver and Braziunas 1986) and agrees closely with independent estimates based on historical data of land-use changes (Olson et al. 1978, Houghton et al. 1983).

Each terrestrial reservoir exchanges directly with the atmosphere as a fixed delay line according to its assigned residence time (see Oeschger et al. 1975). Thus, unlike the other model boxes, the terrestrial biosphere is not simulated by well-mixed ^{14}C reservoirs. The parameterization of atmosphere-terrestrial exchanges is complex because, during

deforestation, air-to-biomass CO_2 uptake depends not only on atmospheric CO_2 content but also the changing size of the terrestrial reservoir. A simple donor-controlled first-order exchange process will always (unrealistically) attempt to restore the original carbon content of the terrestrial biosphere after a deforestation perturbation (Siegenthaler et al. 1978). This difficulty is, however, not relevant here because the ^{12}C contents of the atmosphere and biosphere do not change in the simulations and thus the two biospheric fluxes (B_1/τ_1 = 21 GT C/yr and B_2/τ_2 = 75 GT C/yr) remain constant. But I still preferred the "fixed delay" approach as a way to simulate biospheric residence as an "expected length of life" rather than an "average age" (Bolin and Rodhe 1973). A more refined biospheric structure with more complex interchanges between terrestrial compartments is especially important to consider when modeling the variable biosphere of recent centuries (eg. Siegenthaler and Oeschger 1987).

The carbon reservoirs of the model ocean contain dissolved inorganic carbon (ΣCO_2 = $CO_2 + HCO_3^- + CO_3^=$) but lack organic carbon. Without a biologically-mediated particulate flux of carbon to the deeper ocean, the vertical ΣCO_2 profile shows no depletion in the upper ocean. The ΣCO_2 contents of each oceanic layer is set identically at ca. 2.31 moles m^{-3} (2254 μmol kg^{-1}) in agreement with the global ocean average calculated from GEOSECS data (Takahashi et al. 1981). The surface ocean depth containing the same quantity of carbon as the atmosphere, ie. Z_{EQ} or the "equivalent mixed layer depth" (Bacastow and Bjorkstrom 1981), is 59 meters, similar to the value assigned by Oeschger et al. (1975). Alternatively, the vertically constant [ΣCO_2] of the model ocean can be set at 2.04 moles m^{-3} (2002 μmol kg^{-1}), as in Siegenthaler (1983), to realistically simulate the carbon contents of the upper ocean where CO_2 exchange with the atmosphere occurs. The effect of this alternative parameterization is minimal for the natural ^{14}C simulations discussed here and is addressed in section 2.1.

Although the living marine biomass is estimated to be ca. 3 GT C, the mass of the particulate and especially dissolved organic carbon may be several orders of magnitude greater (eg. Mopper and Degens 1979). The total marine organic reservoir thus may be equivalent to a substantial fraction of the inorganic carbon pool in our model (38,200 GT C). Depending on its residence time, marine organic carbon may contain a notable portion of the total marine ^{14}C burden (estimated at ca. 4% in Damon, 1988). This potential but uncertain ^{14}C reservoir has not been incorporated into the present model.

A discussion of the sensitivity of atmospheric $\Delta^{14}C$ to changes in atmospheric pCO_2 is included in section 2.2 under the heading: "Alternative roles for climate in long-term reservoir $\Delta^{14}C$ change". A 7% increase (decrease) in atmospheric pCO_2 is found to lower (raise) atmospheric $\Delta^{14}C$ by only 3.5 ‰ at steady state.

Variable model reservoir contents and exchange parameters

Unlike the ^{12}C contents in the model reservoirs, their ^{14}C contents do vary with changes in the global carbon system. The effect on atmospheric and oceanic $\Delta^{14}C$ levels of variations in three flux parameters (the ^{14}C production rate Q, the air-sea CO_2 exchange rate F, and the internal ocean mixing diffusion parameter K_z) is investigated in chapters 2 and 3; the process of deriving transient histories in these parameters is discussed below after their attributes are summarized.

The rate of air-sea $^{12}CO_2$ gas exchange F depends on several potentially inconstant factors. The equation for F has been simplified as:

$$F = k_w \beta pCO_{2(atm)} = k_w \beta pCO_{2(surf\ oc)} \qquad (1.1)$$

where k_w represents the wind- and temperature-dependent piston velocity (m yr^{-1}), β

is the temperature-dependent CO_2 solubility (moles CO_2 m^{-3} atm^{-1}), and $pCO_{2(atm)}$ and $pCO_{2(surf\ oc)}$ are the partial pressures (atm) of CO_2 in the atmosphere and surface ocean respectively. The F parameter (in moles CO_2 m^{-2} yr^{-1}) represents either the air-to-sea CO_2 invasion rate (left side of equation 1.1) or the sea-to-air CO_2 evasion rate (right side of equation 1.1), these fluxes being equivalent since all of the ^{12}C reservoirs remain constant in the following simulations ($pCO_{2(atm)} = pCO_{2(surf\ oc)}$ at all times). The wind-dependence of k_w will be quantified in chapter 2 in order to associate hypothetical variations in global wind speeds with deconvolved changes in F.

Substituting F for the individual terms above, the full equation for the net transfer of $^{14}CO_2$ from the atmosphere into the surface ocean becomes (after Siegenthaler and Münnich 1981):

$$^{14}F_{net} = (^{14}k_w/k_w)\,(^{14}\beta/\beta)\,(^{14}C/^{12}C)_{atm}\ F\ A\ -$$
$$(^{14}k_w/k_w)\,(^{14}\Omega_{\Sigma CO2})\,(^{14}C/^{12}C)_{surf\ oc}\ F\ A \qquad (1.2)$$

where $(^{14}k_w/k_w)$ is the ratio of piston velocities for $^{14}CO_2$ and $^{12}CO_2$ which determines kinetic fractionation during air-sea transfer, $(^{14}\beta/\beta)$ is the ratio of solubilities for $^{14}CO_2$ and $^{12}CO_2$ which determines the equilibrium fractionation associated with the invasion flux, $(^{14}\Omega_{\Sigma CO2})$ is the equilibrium fractionation between the dissolved CO_2 species and ΣCO_2, $(^{14}C/^{12}C)_{atm}$ and $(^{14}C/^{12}C)_{surf\ oc}$ are the carbon ratios in atmospheric CO_2 and surface ocean ΣCO_2 respectively, and A represents the surface area of the model ocean (3.61×10^{14} m^2). The standard simulations ignore the fractionation terms by calculating $^{14}C/^{12}C$ ratios from fractionation-corrected $\Delta^{14}C$ levels (more below). Although the net air-sea $^{12}CO_2$ flux is zero throughout all the simulations, the $^{14}F_{net}$ flux (moles $^{14}CO_2$ yr^{-1}) is zero only if the $^{14}C/^{12}C$ ratios of the atmospheric and

surface ocean carbon reservoirs are equal.

To represent standard pre-industrial conditions, the two exchange terms F and K_z (see below) were together calibrated to produce in AD 1830: (1) a fractionation-corrected $(^{14}C/^{12}C)_{surf\ oc}$ that is 5% less than the fractionation-corrected $(^{14}C/^{12}C)_{atm}$ and (2) a similarly-corrected average $(^{14}C/^{12}C)$ for the model ocean reservoir below the surface layer that is 16% deficient relative to the atmospheric ratio. These $\Delta^{14}C$ levels of -50 ‰ for the surface ocean and -160 ‰ for the global average ocean conform to the pre-bomb marine ^{14}C data (eg. Oeschger et al. 1975, Siegenthaler 1989). The calibrated natural air-sea exchange rate of 19 moles CO_2 m^{-2} yr^{-1} (k_w = 4.6 m day^{-1}) falls within a range of published estimates (Broecker et al. 1980) and the results of ^{14}C simulations that assume constant F conditions during the Holocene are relatively insensitive to alternative F choices within this range (see section 2.1).

Although the reconstructed surface ocean $\Delta^{14}C$ is -50 ‰ prior to nuclear weapons testing after AD 1945, the post-AD 1830 anthropogenic input of fossil fuel CO_2 ($\Delta^{14}C$ = -1000 ‰) precipitated an "unnatural" decline in surface ocean $\Delta^{14}C$ of perhaps 10 ‰ as estimated from available coral ^{14}C data (Druffel and Suess 1983) and global ^{14}C modeling (Stuiver et al. 1986b). The proper pre-industrial surface ocean $\Delta^{14}C$ then is closer to -40 ‰. However, recent compilations and extrapolations of pre-bomb surface ocean $\Delta^{14}C$ measurements (Broecker and Peng 1982, Broecker et al. 1985a) yield by my calculations an area-average pre-bomb ("post-industrial") surface ocean $\Delta^{14}C$ of ca. -60 ‰. Therefore the original calibration of Oeschger et al. (1975) was retained.

The F parameter is variable in some simulations. An indication of the "F sensitivity" of atmospheric ^{14}C can be derived by simple mass balance considerations. If the production of new ^{14}C in the atmosphere remains constant, then at steady-state the net flux of ^{14}C into the ocean reservoir must also not change. The fractionation-corrected net

^{14}C flux into the terrestrial biosphere is extremely small and does not influence these calculations; the biospheric return of ^{14}C-tagged carbon is relatively rapid before any significant ^{14}C decay occurs. If F were to increase by 7% (ie. either k_w, s, or pCO_2 in equation 1.1 increases 7%), then the $^{14}C/^{12}C$ ratios in equation 1.2 must respond to prevent $^{14}F_{net}$ from changing. The large ocean reservoir maintains the same ^{14}C content if ^{14}C production is constant. Assuming $(^{14}C/^{12}C)_{surf\ oc}$ remains at 95% relative to the original atmosphere, the new $(^{14}C/^{12}C)_{atm}$ ratio decreases by .35% (3.5 ‰). This (in)sensitivity factor of -1/20 will be further considered in chapters 2 and 3. I chose an F variation of 7% because $pCO_{2(atm)}$ may have varied to this degree during the Holocene (Neftel et al. 1988; see section 2.2).

Vertical exchange within the model ocean is parameterized by an "eddy diffusivity" K_Z. Although diffusion is not the predominant process in oceanic mixing, K_Z represents the approximation that "the many large- and small-circulation cells that perform mixing, taken together, exert an effect statistically similar to molecular diffusion, only on a much larger scale" (Baes et al. 1985). Such diverse processes as turbulent mixing, Ekman pumping, polar convection, and the thermohaline circulation are simulated by this single parameter.

The particulate flux of organic carbon (representing about 20% of the carbon transport to the deep ocean where remineralization to $\sum CO_2$ occurs) is determined by the supply of nutrients to the marine surface waters; this supply, in turn, would be controlled by the oceanic circulation rate in this one-dimensional BD ocean model. Thus, for natural ^{14}C simulations during the Holocene, the particulate ^{14}C flux would (if explicitly included) vary with the single ocean mixing parameter K_Z. High-latitude oceanic processes complicate this simple correlation and the storage or release of nutrients during major pre-Holocene climatic transitions is an independent influence on the supply of

nutrients to surface waters. Such factors are assumed to be less influential within the Holocene climatic epoch (see below and section 2.2 for further discussion). In effect, the organic ^{14}C flux is incorporated here into the calibration of K_Z.

As also presented in Oeschger et al. (1975), the exchange equations governing marine ventilation are:

$$^{14}F_{oc} = - K_Z \, \partial ^{14}CO_2/\partial z \tag{1.3}$$

$$\partial ^{14}CO_{2(z)}/\partial t = K_Z \, \partial^2 \, ^{14}CO_{2(z)}/\partial z^2 - \lambda \, ^{14}CO_{2(z)} \tag{1.4}$$

such that the ^{14}C flux $^{14}F_{oc}$ (in moles m^{-2} yr^{-1}) depends on the eddy diffusivity (in m^2 yr^{-1}) and the $^{14}CO_2$ concentration gradient at that depth z; and the time rate of change in ^{14}C at a given depth (in moles m^{-3} yr^{-1}) is related to the change in the slope of the vertical gradient as well as the rate of ^{14}C decay (λ = 1/8267 yr^{-1}).

In figure 1.6, the oldest vertical ^{14}C profile (at the first tree-ring ^{14}C bi-decade at 7750 cal BC) essentially depicts the assumed natural steady-state distribution of oceanic $\Delta^{14}C$ which initiates the standard ^{14}C simulations considered below. The exponential ^{14}C decline reflects the decay of ^{14}C during its diffusive transport into the deeper ocean away from its atmospheric production source. In the simulation displayed in figure 1.6, the ^{14}C profile fluctuates during the Holocene as the marine carbon system responds to a variable ^{14}C production rate (see next subsection).

As stated before, the exchange parameters F and K_Z are together calibrated to produce an oceanic ^{14}C profile with fractionation-corrected ^{14}C activities in the surface layer and average below-surface reservoir that are 95% and 84% of the atmospheric ^{14}C activity in AD 1830. A modeling inconsistency arises because Oeschger et al. (1975) calibrate F and

Figure 1.6: The history of the oceanic vertical $\Delta^{14}C$ profile associated with variations in ^{14}C production rate required to produce the observed Holocene record of atmospheric (tree-ring) $\Delta^{14}C$. Each "horizontal" line represents one of the 43 model ocean boxes. The time intervals between "vertical" lines span 200 yrs.

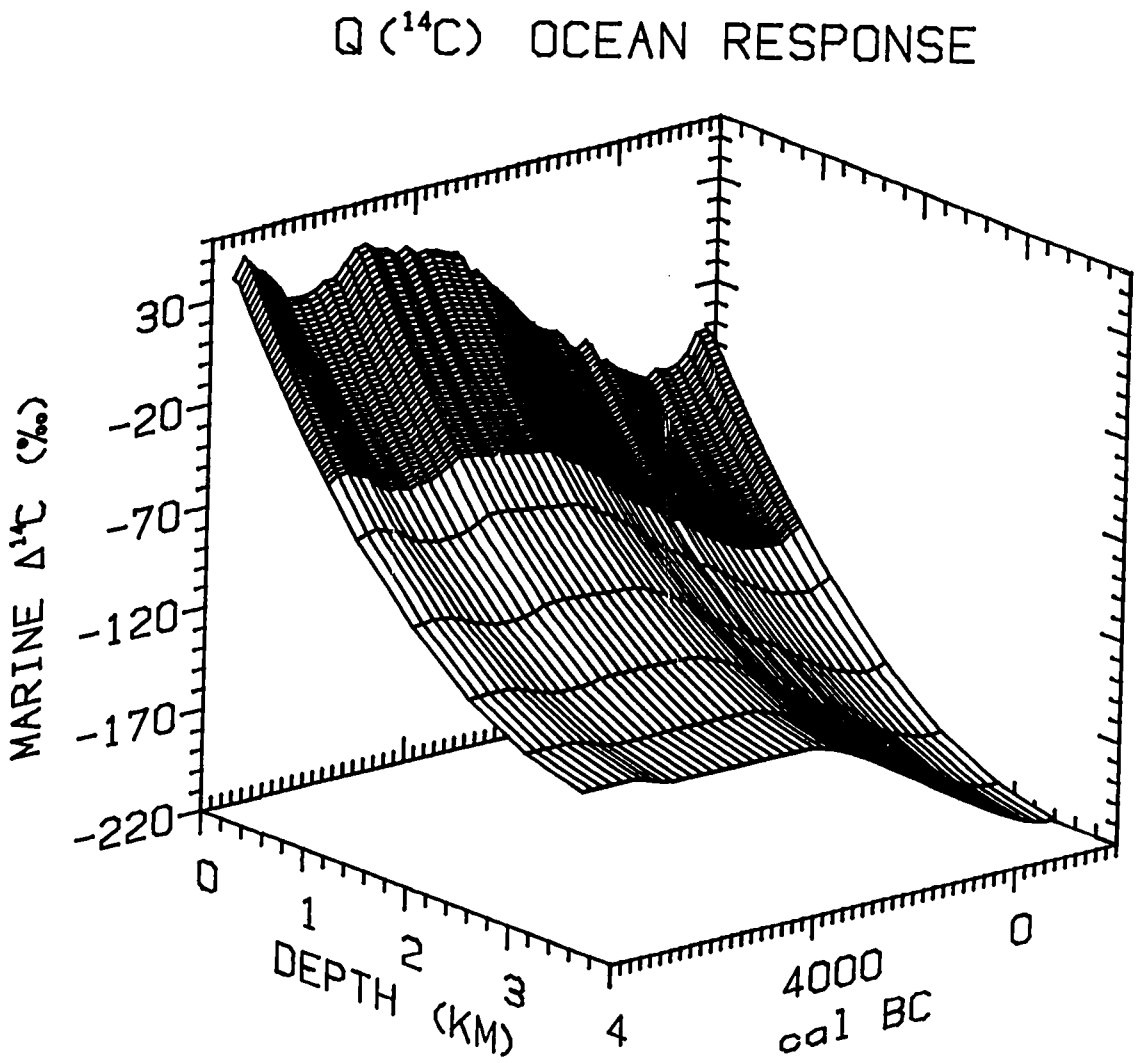
Q (^{14}C) OCEAN RESPONSE
MARINE Δ^{14}C (‰)
30
-20
-70
-120
-170
-220
0
1
2
3
4
DEPTH (KM)
4000
0
cal BC

K_Z to produce a steady-state pre-industrial (ie. AD 1860) ^{14}C profile with the above ^{14}C specifications while, in the present Holocene-length simulation, these specifications are associated instead with a transient ^{14}C system in the early 19th century (youngest ^{14}C profile in figure 1.6). The distinction appears minor because the $\Delta^{14}C$ histories of the ocean layers are relatively steady for the past millennium (figure 2.3); fortuitously, the parameterization of F and K_Z to produce an initial steady-state oceanic ^{14}C profile (at 7750 BC) with the above ^{14}C specifications also provides a nearly identically-shaped profile in AD 1830 (when F and K_Z remain constant during the Holocene simulation).

The above ^{14}C specifications constrain F to be 19 moles CO_2 m^{-2} yr^{-1} and K_Z to be 4000 m^2 yr^{-1} (1.27 cm^2 s^{-1}). The K_Z value is lower than independent parameterizations using ^3H and bomb ^{14}C (compiled in Broecker et al. 1980) but basic modeling conclusions are relatively insensitive to alternative combinations of F and K_Z within a reasonable range of choices. Although absolute numbers may change, relative model-derived ^{14}C production variations and the high-frequency (century-scale) $\Delta^{14}C$ fluctuations and $\Delta^{14}C$ trends in oceanic reservoirs are only minimally affected (see chapter 2).

Production of ^{14}C occurs in the model atmosphere, considered as a single well-mixed reservoir without latitudinal or vertical ^{14}C distinctions. Although the modulation of ^{14}C production by the 11-yr solar activity cycle and the influence on ^{14}C distribution by latitude-specific stratosphere/troposphere and troposphere/ocean exchange processes may produce persistent latitudinal gradients in atmospheric ^{14}C (eg. Lerman et al. 1970, Fan et al. 1983), these potential complications were not considered in the global simulations.

The ^{14}C production rate Q is calculated at steady-state to balance the total ^{14}C decay

in the carbon model reservoirs. Since the ^{14}C contents of all other reservoirs are fixed relative to the atmospheric reservoir by the parameterizations of F, K_Z, B_1/τ_1 and B_2/τ_2, the assumed initial steady-state atmospheric $\Delta^{14}C$ value determines all other ^{14}C terms. In the simulation depicted in figure 1.6, the initial atmospheric $\Delta^{14}C$ is assumed to be 90 ‰ (ie. elevated 9% relative to an AD 1890 level of 0 ‰; as a result, all other reservoirs and the ^{14}C production rate are elevated 9% from values that would be in equilibrium with the ^{14}C content of the AD 1890 atmosphere. This choice of initial steady-state conditions is discussed in section 2.1.

The deconvolution of Q, F, and K_Z

Several versions of the basic global BD model described above were designed in order to deconvolve alternative exchange parameter variations compatible with the observed atmospheric (tree-ring) $\Delta^{14}C$ record.

In the Q-deconvolution model version, the ^{14}C production rate is calculated to balance small changes in atmospheric $\Delta^{14}C$ (interpolated from the bi-decadal tree-ring record to the spacing of the model time step) with pre-change net atmospheric ^{14}C fluxes to the other model reservoirs. Using the new atmospheric $\Delta^{14}C$ at the end of the model time step, the reservoir exchanges are updated and the deconvolution procedure is repeated. The deconvolution equation that involves these calculations is:

$$Q(^{14}C) = (\Delta R_a/\Delta t)\,{}^{12}C_a + {}^{14}F_{net} + (B_1/\tau_1)(R_a - R_{a(\tau 1)}) + (B_2/\tau_2)(R_a - R_{a(\tau 2)}) + \lambda R_a\,{}^{12}C_a \qquad (1.5)$$

where R_a is the $^{14}C/^{12}C$ ratio in atmospheric CO_2 at the start of the model time step, $\Delta R_a/\Delta t$ is the rate of change in R_a during the model time step, $^{12}C_a$ represents moles of

atmospheric CO_2, $R_{a(\tau 1)}$ and $R_{a(\tau 2)}$ are the $^{14}C/^{12}C$ ratios in atmospheric CO_2 at τ_1 and τ_2 yrs ago, and the other variables have been identified above. The ^{14}C production function is usually expressed, after appropriate conversion, in units of ^{14}C atoms cm_E^{-2} s^{-1} where cm_E represents a centimeter of earth surface.

Analogously, the F- and K_Z-deconvolution model versions calculate the variation in each respective exchange parameter required to balance atmospheric $\Delta^{14}C$ change and a specified ^{14}C production rate with a compensatory atmosphere/ocean ^{14}C exchange. The F-deconvolution model directly varies the air-sea ^{14}C transfer while the K_Z-deconvolution model first determines the surface ocean $\Delta^{14}C$ change required, with constant F, to produce the specified atmospheric $\Delta^{14}C$ change. The model equations then deconvolve the K_Z value that will provide the necessary change in surface layer/thermocline ^{14}C transfer to produce that surface ocean $\Delta^{14}C$ change. An iterative process of updating reservoir ^{14}C contents and recalculating exchange parameters is again followed in these model versions.

The relevant equation for the F-deconvolution model is:

$$F(^{14}C) = ((\Delta R_a/\Delta t)\ ^{12}C - Q + \lambda R_a\ ^{12}C + {}^{14}F_B\ ) /\ (R_{so} - R_a) \qquad (1.6)$$

where $^{14}F_B$ represents the two terrestrial exchanges shown in figure 1.5 and R_{so} is the $(^{14}C/^{12}C)$ ratio of the surface ocean reservoir. The K_Z parameter is constant in this model version; Q may represent a constant ^{14}C production rate or an independently assumed production history (such as derived from the geomagnetic dipole record in section 2.3).

The two pertinent equations in the K_Z-deconvolution model are:

$$R'_{so} = ((\Delta R_a/\Delta t)\ {}^{12}C_a - Q + R_a F + {}^{14}F_B + \lambda R_a\ {}^{12}C_a) / F \qquad (1.7)$$

$$K_z({}^{14}C) = ((R_a - R_{so}) - \lambda R_{so}\ {}^{12}C_{so} - (\Delta R_{so}/\Delta t)\ {}^{12}C_{so}) / ((R_{so}\ {}^{12}C_{so} / Z_{so} - R_{th1}\ {}^{12}C_{th1} / Z_{th}) / (Z_{th}/2)) \qquad (1.8)$$

where R'_{so} is the new ($^{14}C/^{12}C$) ratio of the surface ocean required to balance the observed change in atmospheric $\Delta^{14}C$, R_{so} and R_{th1} are the pre-change ($^{14}C/^{12}C$) ratios of the surface ocean and uppermost thermocline boxes respectively, $^{12}C_{so}$ and $^{12}C_{th1}$ are the $\sum CO_2$ contents (expressed as moles m^{-2}) of the surface ocean and uppermost thermocline respectively, and Z_{so} and Z_{th} are the thicknesses of the surface layer and upper thermocline box respectively. The terms in the main denominator of the equation represent the linearization of the $^{14}CO_2$ gradient at the mixed layer/thermocline boundary. The $\sum CO_2$ contents of every oceanic layer are equivalent in the model since the particulate flux is zero. The units of $K_z(^{14}C)$ for this equation are $m^2\ yr^{-1}$.

Because $K_z(^{14}C)$ governs all the oceanic exchanges associated with the vertical ^{14}C profile, the required changes in ^{14}C transfer at the mixed layer/thermocline boundary have significant implications for the ^{14}C distribution throughout the entire oceanic reservoir. The deconvolved $K_z(^{14}C)$ history is a bit tremulous even when forced by smoothed long-term trends in atmospheric $\Delta^{14}C$ and Q (eg. figure 2.30), and $K_z(^{14}C)$ often becomes undefined when required to compensate for short-term (bi-decadal) variations in the atmospheric ^{14}C contents. The adjustment of ^{14}C fluxes throughout the ocean interior creates a very unsettled situation at the surface layer/thermocline interface where the variable ^{14}C signals from above and below combine in the recalculation of K_z at each time step. A simultaneous variation in circulation at all oceanic depths is indeed an extreme scenario but this simple case can still provide basic insights into the influence of global

oceanic processes on transient atmospheric ^{14}C contents.

A fourth model version, the F,K_Z-deconvolution model, was programmed to derive the simultaneous and equivalent relative changes in air-sea CO_2 exchange rate and eddy diffusivity that together will balance the assumed atmospheric $\Delta^{14}C$ and ^{14}C production rate histories. More information on this model is presented in section 2.2 in association with its application.

The validity of the deconvolution process is tested by applying each deconvolved parameter history as a forcing function in a conventional model version which determines the consequent $\Delta^{14}C$ variations in the atmosphere and other model reservoirs. A model-derived atmospheric $\Delta^{14}C$ record that replicates or closely resembles the original (tree-ring-related) atmospheric $\Delta^{14}C$ curve confirms that the responsible parameter history has been accurately deconvolved. Such a ^{14}C model of "forward" calculations is described by the basic equations in Oeschger et al. 1975. The model version programmed here will accept any combination of variable or constant Q, F, and/or K_Z functions. In addition to its use in verifying the deconvolution results, the "forward" model has also been utilized to simulate the implications of sudden (century-scale) climatic switches (ie. step changes in F or K_Z) for atmospheric and oceanic ^{14}C variations (section 3.3).

Potential insights from oceanic ventilation indices

In the four deconvolution models described above, the atmospheric $\Delta^{14}C$ record serves to force variations in specified flux parameters. The consequential $\Delta^{14}C$ variations in the model oceanic reservoirs furnish an independent means of evaluating the likelihood of each simulated ^{14}C scenario. In the following chapters, the comparison of modeled marine results with the ^{14}C data from corals and forams will be an important method for assessing model assumptions. Therefore, several useful definitions involving modeled or

observed oceanic ^{14}C levels are presented here prior to their extensive application in the modeling analyses in following chapters.

The apparent ^{14}C age difference between surface and deep ocean reservoirs provides an indication of the deep sea ventilation rate (ie. the renewal or turnover time of the deep ocean reservoir). The equations relating ^{14}C age to radiocarbon activity (Stuiver and Polach 1977) translate this ^{14}C age difference into the equation:

$$t_V = 8033 \ln (A_{so} / A_{do}) = 8033 \ln (R_{so}/R_{do}) \qquad (1.9)$$

where t_V is the deep sea ventilation time in ^{14}C yrs, A_{so} and R_{so} are the ^{14}C activity and ($^{14}C/^{12}C$) ratio respectively associated with the surface ocean, and A_{do} and R_{do} are the ^{14}C activity and ($^{14}C/^{12}C$) ratio respectively associated with the deep ocean reservoir. This latter reservoir must be defined with respect to a particular depth or depth interval. In this way, the direct ^{14}C measurements of marine water samples, as part of the GEOSECS ^{14}C sub-program, were utilized to estimate replacement times for abyssal ocean basins (Stuiver et al. 1983).

Using accelerator mass spectrometry (AMS), Andrée et al. (1986b) measured the ^{14}C activity of foraminifera in sediment cores from the South China Sea that span the last 12,000 yrs. These authors defined the apparent ^{14}C age difference between contemporaneous benthic and planktonic (*Globigerinoides sacculifer*) foraminfera as a "foram ventilation index" (FVI). Although this FVI has limitations as a *global* ventilation index because it is regionally biased and restricted to one depth level, it still provides important (and rare) information on long-term oceanic ventilation rates. Andrée et al. conclude that no significant digressions in ocean circulation are apparent over the last 10,000 yrs (discussion continued in section 2.1).

The FVI provides an oceanic ^{14}C history without the need to determine the $\Delta^{14}C$ time series of the surface and deep ocean individually. As in the case of the terrestrial ^{14}C samples discussed in section 1.3, each measured foram ^{14}C age can derive from an infinite combination of initial ^{14}C contents and calendar ages. Without an independent calibration of the foram calendar ages, the oceanic $\Delta^{14}C$ levels associated with this "floating" record cannot be identified. The difference between ^{14}C age of surface and deep waters does not depend on calibration of the synchronous time at which the planktonics and benthics were living.

A "model ventilation index" (MVI) is analogously defined here as the ^{14}C age difference between model surface ocean ^{14}C and average model deep ocean ^{14}C (below the thermocline at 1 km depth). With respect to the $\Delta^{14}C$ signatures of the reservoirs, the equation for this index can be written as:

$$MVI = 8033 \ln ((1000+\Delta^{14}C_{so})/(1000+\Delta^{14}C_{do})) \qquad (1.10)$$

where the subscripts "so" and "do" refer to the surface ocean reservoir and the average deep ocean below 1 km respectively. As an option, $\Delta^{14}C_{do}$ can refer to the average ocean below the surface layer (ie. the model thermocline and deep ocean) in order to compare MVI directly with the third ventilation index KVI defined below.

At standard steady-state conditions the model surface ocean R_{so} is approximately equal to .95 R_a and the average model ocean (below the surface) R_{th+do} is .84 R_a (see calibration above). The latter ratio weighs the steady-state average thermocline R_{th} of .91 R_a with the average deep ocean R_{do} below the thermocline of .81 R_a. These relative values yield a steady-state MVI of 1275 ^{14}C yrs according to equation 1.10. When, alternatively, the ^{14}C contents of the entire ocean *below the surface* are compared to the

surface ocean, MVI is 1025 ^{14}C yrs (using precise numbers for the ratios).

The analytical solution for the steady-state oceanic ^{14}C profile in the global BD model also defines a ventilation index which is directly related to the strength of the ocean mixing parameter K_Z. The model ocean diffusivity is linked to the ^{14}C activities of surface and deep waters through the equation (Oeschger et al. 1975):

$$A_{do} = A_{so} \ (\tanh (\sqrt{(\lambda/K_Z)}\ hd)) \ / \ (\sqrt{(\lambda/K_Z)}\ hd) \qquad (1.11)$$

where A_{do} refers to the average ^{14}C activity of the model ocean below the surface layer and hd is the depth of the model ocean below the surface layer (3725 m).

Equations 1.9 and 1.11 are combined here to define a K_Z-related ventilation index KVI directly reflecting model ocean mixing rate at any specified time:

$$KVI = -8033 \ln (\tanh (\sqrt{(\lambda/K_Z)}\ hd) \ / \ (\sqrt{(\lambda/K_Z)}\ hd)) \qquad (1.12)$$

As in the cases of FVI and MVI, the time associated with KVI is measured in ^{14}C yrs. According to this equation, the standard K_Z value of 4000 $m^2\ yr^{-1}$ defines a KVI of 1025 ^{14}C yrs, in agreement with the alternative definition of MVI above.

Although MVI and KVI are identical when the model ocean is at steady state, these two ventilation indices can differ notably when external (or even internal) forces produce changes in the ^{14}C contents of the ocean reservoirs. For example, figure 1.6 displays the variations in the oceanic ^{14}C profile associated with the observed atmospheric (tree-ring) $\Delta^{14}C$ record when the atmospheric $\Delta^{14}C$ variations are assumed to be forced by changes in the ^{14}C production rate under constant climatic conditions. Because K_Z remains constant in this simulation, KVI is constant at 1025 ^{14}C yrs. However, the attenuations

and delays that accompany the transmission of Q-forced atmospheric ^{14}C variations into the oceanic realm produce changes in the oceanic ^{14}C profile that *falsely* suggest fluctuations in ventilation rate as measured by MVI (quantified in section 2.1). Thus, whereas variations in KVI reflect the "true" oceanic mixing history, MVI (and FVI) only provide "apparent" ventilation histories which can be misleading especially when the oceanic ^{14}C system is not near equilibrium.

Still, FVI and MVI are the only long-term ^{14}C ventilation indices available and, when analyzed in conjunction with other recorded signals in the climate system, their interpretation can become more robust. To illustrate the complications (and merits) of analyzing FVI and MVI together with other ^{14}C records, I utilized the conventional global BD model version to delineate the potential implications of an FVI digression in a hypothetical scenario. To lend interest to this illustration, the scenario is based on actual foram ^{14}C data that show significant late-glacial FVI variations (Shackleton et al. 1988). This BD model is neither structured nor parameterized to authentically portray late-glacial ^{14}C changes but an accurate model analysis is not sought here. This exercise is presented only to demonstrate the distinctions between KVI and MVI and the importance of additional databases for their interpretation.

Figure 1.7 displays the model-derived atmospheric and oceanic ^{14}C response to a 40% decline in ^{14}C production rate spanning 2000 yrs (upper left panel). The atmospheric $\Delta^{14}C$ response entails a significant decline (nearly 20%) but a more gradual recovery (solid line in upper right panel) than the return of Q to initial conditions. The oceanic mixing rate K_z remains constant in this simulation and thus KVI also is steady (dashed line in lower panel). However, the lag in the response of the deep ocean ^{14}C reservoir to the Q perturbation in comparison to the timing of the surface ocean ^{14}C response produces an *apparent* 500-yr digression in oceanic ventilation time as

Figure 1.7: Responses in model ^{14}C reservoirs to a hypothetical change in ^{14}C production rate during the late-glacial transitional period. The upper left panel shows the assigned ^{14}C production rate (Q) history that forces reservoir $\Delta^{14}C$ changes in the conventional global box-diffusion (BD) model. The upper right panel displays the atmospheric $\Delta^{14}C$ variations that are derived either from the BD model (solid line) or from ^{14}C ages of macrofossils from Swiss lake sediments as calibrated by Zbinden et al. (1989) and previously shown in figure 1.2. The lower panel shows the associated variations in model and K_Z ventilation indices (MVI and KVI respectively) and the history of a foram ventilation index (FVI) derived from Pacific forams by Shackleton et al. (1988). FVI (squares) and MVI (solid line) are based on the difference (in ^{14}C yrs) between the ^{14}C contents of the surface marine reservoir and the deeper ocean reservoirs. KVI (dashed line) is defined by the instantaneous eddy diffusivity K_Z. For the purposes of simplifying this illustration, the FVI points (dated in ^{14}C yrs) are plotted on the same calendar timescale as the other indices (see text).

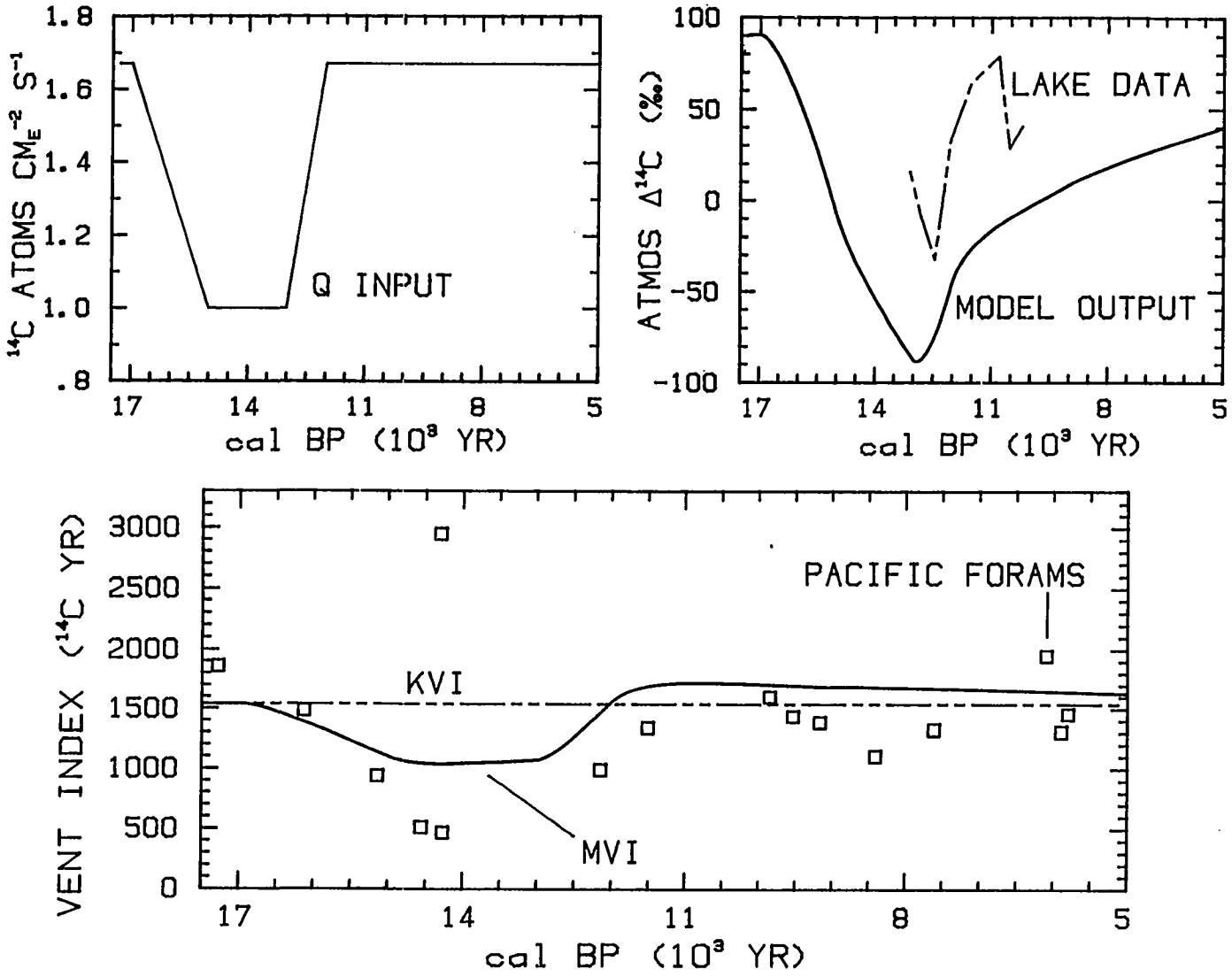
1.8
1.6
1.4
1.2
1.0
.8
^{14}C ATOMS CM_E^{-2} S^{-1}
Q INPUT
17
14
11
8
5
cal BP (10^3 YR)
100
50
0
-50
-100
ATMOS $\Delta^{14}C$ (‰)
LAKE DATA
MODEL OUTPUT
17
14
11
8
5
cal BP (10^3 YR)
3000
2500
2000
1500
1000
500
0
VENT INDEX (^{14}C YR)
PACIFIC FORAMS
KVI
MVI
17
14
11
8
5
cal BP (10^3 YR)

represented by MVI (solid line in lower panel). The initial conditions for this simulation are the standard choices discussed in detail in the following chapters. The global MVI trend was adjusted by a multiplication factor of ca. (1535 ^{14}C yrs/1275 ^{14}C yrs) in order to match the absolute "base-line" values of the regional FVI points (squares).

The FVI record is derived from the ^{14}C ages, measured by AMS, of planktonic and benthic (3120 m depth) foraminifera in a core from the eastern equatorial Pacific (Shackleton et al. 1988). For the purpose of simplifying this illustration, I have assumed an equivalence between calendar yrs and the reported ^{14}C ages of planktonic forams (minus a constant 580-yr reservoir correction); this timescale corresponds to the graphical presentation by the original authors. In order to reconstruct the original magnitude and true timing (in calendar yrs) of the FVI excursion, a preliminary calibration of the surface ocean ^{14}C ages might be ventured by applying the ^{14}C/calendar age associations in Table 1.1 (in section 1.3) and Table 2.1 (in section 2.3); a variable reservoir correction representing the changing atmosphere-surface ocean ^{14}C difference is a complicating factor. An appropriately parameterized ^{14}C model is necessary for a detailed analysis of this foram data. The late-glacial transgression in FVI is actually only a secondary component in a 30,000 ^{14}C-yr FVI record whose major feature is a significantly slower (apparent) ventilation time for the Pacific during the last glacial stage (Shackleton et al. 1988).

Figure 1.8 shows an alternative mechanism that generates the same digression in FVI and MVI as does the Q perturbation. In this second hypothetical scenario, the oceanic eddy diffusivity is the forcing function in the conventional BD model. When K_Z is enhanced 90% during a 2000 yr interval (upper left panel), the true ventilation index KVI (dashed line in lower panel) *and* "apparent" ventilation index MVI (solid line in lower

Figure 1.8: Responses in model ^{14}C reservoirs to a hypothetical change in oceanic mixing (eddy diffusivity) during the late-glacial transitional period. The upper left panel shows the assigned K_z history that forces reservoir $\Delta^{14}C$ changes in the conventional global box-diffusion (BD) model. The other displayed features are defined in the caption for figure 1.7.

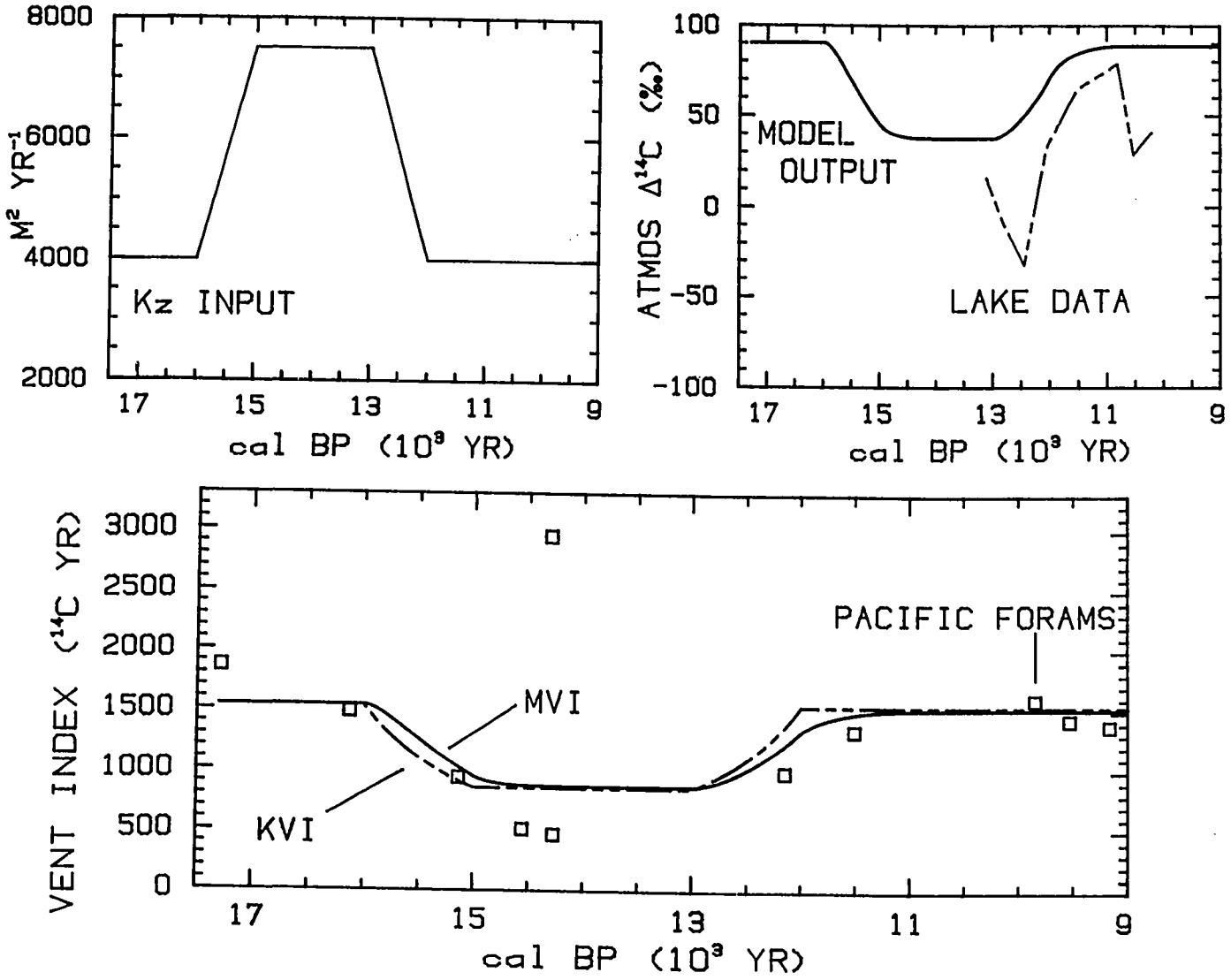
8000
6000
4000
2000
M² YR⁻¹
Kz INPUT
17
15
13
11
9
cal BP (10³ YR)
100
50
0
-50
-100
ATMOS Δ¹⁴C (‰)
MODEL OUTPUT
LAKE DATA
17
15
13
11
9
cal BP (10³ YR)
3000
2500
2000
1500
1000
500
0
VENT INDEX (¹⁴C YR)
PACIFIC FORAMS
MVI
KVI
17
15
13
11
9
cal BP (10³ YR)

panel) both deviate similarly from pre-disturbance conditions. However, even when MVI genuinely reflects changes in oceanic mixing, a lag in MVI of up to 200 yrs is apparent in comparison to the actual history of the KVI (ie. K_Z) digression.

To identify the mechanism that produces the MVI or FVI record, evidence from other sectors of the global ^{14}C system must be pursued. The Q and K_Z perturbation have distinctive effects on the atmospheric ^{14}C reservoir (upper right panel in figures 1.7 and 1.8). The redistribution of global ^{14}C by a change in oceanic mixing rate leaves a more modest and shorter-term mark on the atmospheric reservoir in comparison to a Q perturbation that acts to deplete ^{14}C throughout the entire system. Both model curves show a surface similarity to the macrofossil ^{14}C data of Zbinden et al. (1989) from Swiss lakes (dashed line). With our favored adjustment in this data trend (450 cal yrs older with, as a consequence, $\Delta^{14}C$ greater by ca. 55 ‰, as discussed in section 1.3), the similarity between the data and the K_Z-forced atmospheric $\Delta^{14}C$ curve is even stronger. The lack of evidence from corals (Bard et al. 1990) or geomagnetic data (Merrill and McElhinny 1983) for a sharp decline in ^{14}C production rate in the late glacial also contradicts the first hypothetical scenario. These additional records will be discussed in detail in section 2.3.

The distinctive effects of climate and ^{14}C production variation on reservoir $\Delta^{14}C$ histories during the Holocene will be analyzed closely in the following chapters. As in this introductory illustration, the evidence from model and foram ventilation indices for oceanic ^{14}C changes will be weighed against the observed atmospheric ^{14}C signal and proxy records of ^{14}C production rate fluctuations to assess the likely origins for millennium- and century-scale digressions in the ^{14}C system.

Alternative model parameterizations

A few complications to the basic box-diffusion ^{14}C model described above are discussed here.

The standard model versions do not incorporate fractionation factors in the exchanges between the atmospheric, oceanic, and terrestrial reservoirs because the $\Delta^{14}C$ values are corrected for such fractionation. Applying the definition of $\Delta^{14}C$ (Stuiver and Polach 1977), the conversion of these Δ values into $^{14}C/^{12}C$ ratios for the model equations normalizes all carbon reservoirs to possess the same $^{13}C/^{12}C$ ratio ($\delta^{13}C$ = -25 o/oo for all reservoirs in the standard simulations). This homogenization simplifies the model without altering the exchanges between reservoirs. However, two flux terms, the ^{14}C production and decay rates, do depend on the true absolute ^{14}C contents of the reservoirs.

In order to quantify the secondary consequences of this dependence, fractionation factors were included in one version of the box-diffusion model. Constant $\delta^{13}C$ contents were assigned to each major reservoir: the atmosphere was fixed at -7 o/oo, the ocean at 0.92 o/oo, and the terrestrial biosphere at -25 o/oo. Fractionation factors for air-sea exchange conformed to estimates of Siegenthaler and Münnich (1981); fractionation during atmosphere-to-terrestrial exchange was assumed to completely account for their ^{13}C disparity whereas no fractionation occurred during the return flux. The precise equations of Stuiver and Robinson (1974) for conversion of $\Delta^{14}C$ into absolute $^{14}C/^{12}C$ ratios were required for a proper steady state in the model. The results of this sensitivity analysis is noted near the end of section 2.1.

Reservoirs of ^{14}C with very long residence times are not included in the standard ^{14}C model versions. Damon (1988) estimates that sediments may hold ca. 25% of the ^{14}C in the global system. Soils on land, coastal wetland environments, and marine sediments may each have substantial ^{14}C contents, despite long residence times and

substantial decay, because of their large carbon reservoirs. Damon's estimates allow the global ^{14}C decay rate to match independent estimates of recent ^{14}C production rates, although an equivalence is not strictly necessary.

In this model analysis, *relative* variations in ^{14}C production are emphasized rather than absolute scales. However, simulations with longer-storage terrestrial reservoirs were performed and the results are presented at the end of section 2.1. The implications of a significant oceanic ^{14}C reservoir are also discussed.

Polar marine processes have a significant control on atmospheric pCO_2 and are expected to play important roles in glacial/interglacial carbon reservoir changes (eg. Toggweiler and Sarmiento 1985, Wenk and Siegenthaler 1985). The inclusion of high-latitude marine boxes allows a carbon model to more realistically portray ocean-induced ^{14}C changes. A transient model with high-latitude processes has not been developed here; however, the effects of alternative *steady-state* oceanic conditions on atmospheric $\Delta^{14}C$, as simulated by the box models with polar marine reservoirs and by the one-dimensional box-diffusion model, are compared below and found to be basically consistent (last part of section 2.2).

Siegenthaler (1983) designed an "outcrop-diffusion" model to investigate the importance of a high-latitude oceanic sink for removal of fossil-fuel CO_2 from the atmosphere. This model does not have an explicit polar oceanic reservoir but, instead, appends onto the box-diffusion structure an additional direct interchange between the atmosphere and subsurface model ocean layers. This model demonstrates that the polar ocean can effectively diminish excess atmospheric CO_2 while insignificantly modifying the accompanying "industrial effect" on atmospheric ^{14}C (ie. the ca. 20 ‰ decline in $\Delta^{14}C$ between AD 1850 and 1950 created by the input of the "dead" carbon in fossil fuels). Because the atmospheric $\Delta^{14}C$ history is insensitive to this extra feature, the Q

record derived from the simpler box-diffusion ^{14}C model should also be robust with respect to this alternative model design.

The contrary responses of atmospheric $^{12}CO_2$ and $^{14}CO_2$ to a direct deep-ocean sink reflect the different chemical equilibration times for the two carbon isotopes in the surface ocean. Surface ocean pCO_2 equilibrates with atmospheric pCO_2 on the timescale of a month whereas for $^{14}CO_2$ complete isotopic equilibrium is required, with a timescale of a decade, among dissolved CO_2, HCO_3^-, and $CO_3^=$ (Broecker and Peng 1974). Thus the excess $^{12}CO_2$ in the global surface ocean is ca. 85% in equilibrium with the excess $^{12}CO_2$ in the atmosphere (as modeled by Oeschger et al. 1975) and the high-latitude circumvention of the rate-limiting exchange between the surface and deep oceans produces a significant increase in marine uptake. The global surface ocean is only ca. 50% in equilibrium with the ^{14}C "industrial effect" (eg. Druffel 1982) and, therefore, the polar outcrop has a much less dramatic effect on the atmospheric ^{14}C perturbation.

CHAPTER 2. MODEL ANALYSIS OF ORIGINS FOR MILLENNIUM-SCALE $\Delta^{14}C$ VARIATIONS

The deconvolution models described in section 1.4 were utilized to assess several potential causes for the longer-term features observed in Holocene atmospheric and oceanic $\Delta^{14}C$ histories. Climate and production-rate sources for the measured atmospheric (tree-ring) $\Delta^{14}C$ record invoke contrary responses in oceanic $\Delta^{14}C$ which allow a critical appraisal of their credibilities. In addition, data records of natural phenomena (eg. geomagnetic and ^{10}Be fluctuations) tied to relative ^{14}C production rate variations permit the evaluation of a production-rate origin for reservoir $\Delta^{14}C$ trends. If such records and their relationships to ^{14}C production rates are treated as indisputable, then the secondary climatic contributions to observed $\Delta^{14}C$ variations can also be quantified. Here climate-related changes in air/sea CO_2 gas exchange and oceanic vertical mixing are considered.

2.1 Implications of a production rate origin for reservoir $\Delta^{14}C$ variations

Deconvolved model ^{14}C production rate

The Q-deconvolution carbon reservoir model described in section 1.4 was utilized to derive the ^{14}C production rate required to generate the observed atmospheric (tree-ring) ^{14}C record for the past 9700 yrs with assumed constant climate conditions, i.e. with constant reservoir exchange parameters and burdens. A "steady state" atmospheric $\Delta^{14}C$ value of 90 ‰ prior to 7750 BC was assumed, as noted in chapter 1 and considered

more extensively below.

The deconvolved production rate variations, $Q(^{14}C)$, are averaged over the same bi-decadal intervals as the atmospheric $\Delta^{14}C$ data and are displayed in figure 2.1. Analogous to our treatment of the atmospheric $\Delta^{14}C$ record, a smoothing spline that approximates a 400-yr moving average was chosen to represent the long-term trend in production rate (thick curve in figure 2.1). A curve with this level of detail can be used to differentiate the ^{14}C variations of duration greater than 500 yrs which are often attributed to geomagnetic causes from the higher-frequency $\Delta^{14}C$ fluctuations often discussed in terms of solar origins (eg. Damon and Linick 1986). Such a spline distinguishes the typical century-scale prominences from the more subdued trends in ^{14}C. The 17 century-scale Maunder- and Spörer-type oscillations in production rate, marked as "M" and "S" respectively in figure 2.1, will be discussed in the next chapter.

The deconvolved production rate curve (figure 2.1) is similar to the original atmospheric ^{14}C curve (figure 1.1) but with stronger high-frequency variations relative to the long-term change (see also figure 2.2). The atmosphere acts as a low-pass filter, attenuating higher frequency perturbations in production rate more than the gradual rate changes. An "attenuation coefficient" H is defined as the relative change in reservoir $\Delta^{14}C$ divided by the causal relative change in ^{14}C production rate. This coefficient is a function of the duration and nature of the forcing (e.g. pulses or harmonic variations in ^{14}C production) but is independent of the absolute magnitude of the perturbation.

Based on a simple global two-box $^{14}CO_2$ model for the atmosphere and ocean, Houtermans (1966) derived theoretical attenuation factors of .0055, .045, .07 and .43 for harmonic (cyclic) ^{14}C production rate changes with periods of 10^1, 10^2, 10^3 and 10^4 yrs, respectively. In other words, a change in atmospheric $\Delta^{14}C$ of 10 ‰ (ie. 1 %) on each of these time scales requires a respective change in Q of ca. 180%, 22%, 14%, and

Figure 2.1: Bi-decadal ^{14}C production rates (bar curve) between 7740 BC and AD 1960 necessary to generate, without climate intervention, the atmospheric $\Delta^{14}C$ variations depicted in figure 1.1. The production rates, in ^{14}C atoms per second per cm^2 of Earth surface, are derived from the Q-deconvolution model assuming constant reservoir burdens and exchange parameters. The right-hand axis scales these $Q(^{14}C)$ variations relative to the average model-derived $Q(^{14}C)$ of 1.546 for the last ca. 500 years (AD 1440 to 1980). A spline (heavy line) approximating a 400-yr moving average represents the long-term trend, Q_t, in ^{14}C production. The century-scale Maunder- and Spörer-type $Q(^{14}C)$ variations (labelled "M" and "S" respectively) are discussed in the text.

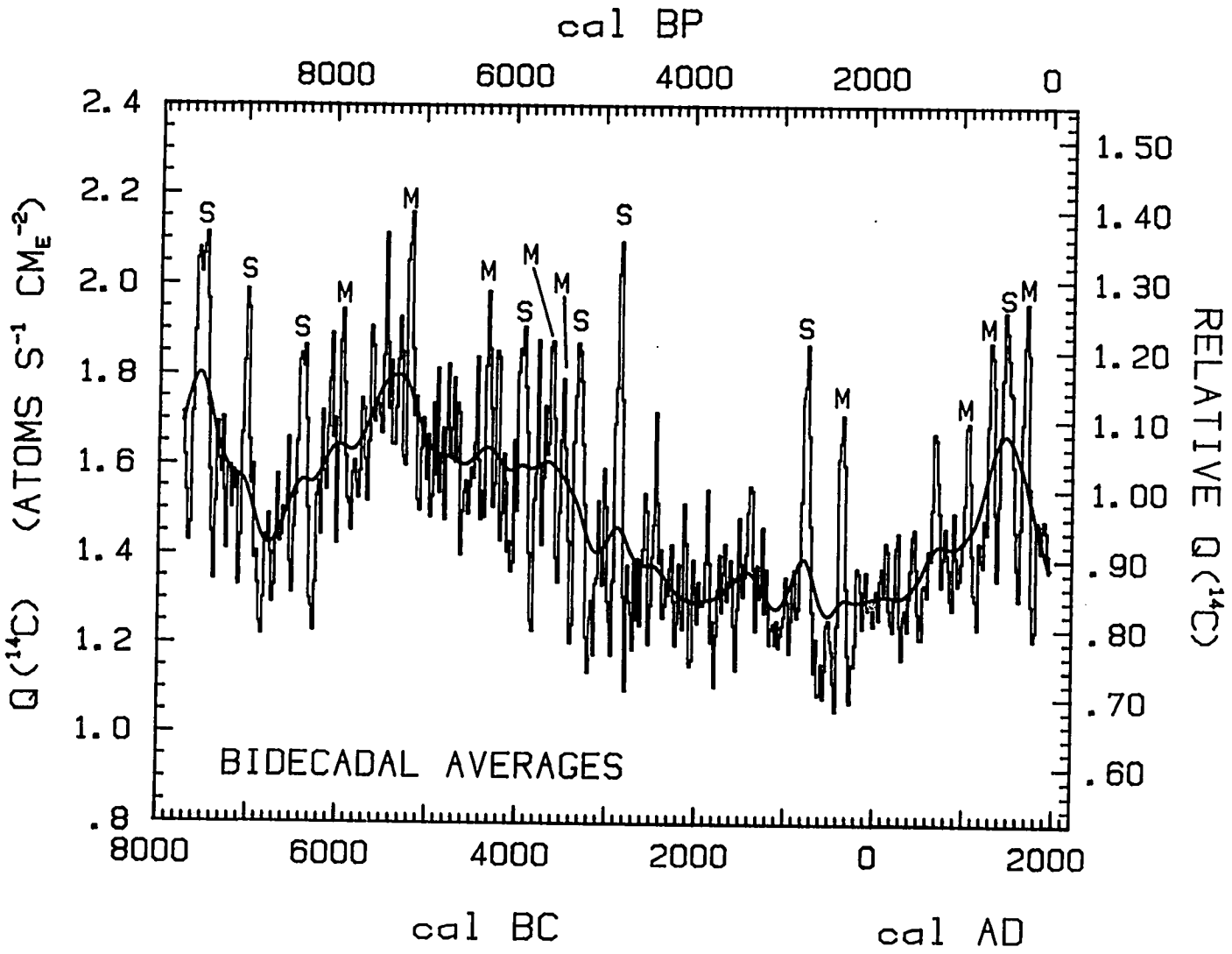
cal BP
8000
6000
4000
2000
0
2.4
2.2
2.0
1.8
1.6
1.4
1.2
1.0
.8
Q (^{14}C) (ATOMS S^{-1} CM$_E^{-2}$)
1.50
1.40
1.30
1.20
1.10
1.00
.90
.80
.70
.60
RELATIVE Q (^{14}C)
S
M
BIDECADAL AVERAGES
8000
6000
4000
2000
0
2000
cal BC
cal AD

2.3%.

Houtermans et al. (1973) calculated similar H values with a more sophisticated 3-box global model but found that the inclusion of distinct surface and deep ocean reservoirs (each with atmospheric exchange) creates somewhat weaker attenuations for harmonic perturbations faster than 10^2 yrs. However, the models respond similarly for longer-term perturbations which have time to be distributed throughout the ocean regardless of the model structure.

The box-diffusion model utilized in this study, with the parameterization of reservoir burdens, exchanges and fractionation processes described in chapter 1, yields attenuation coefficients of .0082, .044, .088, and .27 for sinusoidal fluctuations in Q with periods of 10^1, 10^2, 10^3, and 10^4 yr, respectively. That is, to produce a 10 ‰ change in atmospheric $\Delta^{14}C$ maintained for each respective time period listed, the causal production rate must change ca. 120%, 23%, 11%, and 4%. The associated phase lags are 2, 10, 120 and 1200 yr.

The magnitudes of attenuation factors for the box-diffusion model compare well with the corresponding factors for the 2-box model suggesting that the essential nature of the ^{14}C system is ably simulated in Houtermans' elegantly simple study. The greater oceanic resolution and diffusive vertical mixing of the box-diffusion model significantly limit the capacity of the ocean to attenuate the atmospheric responses to high-frequency ^{14}C production changes, but our H values still fall within the uncertainty ranges of attenuation factors provided by the model analysis of Houtermans et al. (1973).

A mass balance calculation demonstrates the basic principle behind this attenuation phenomenon. Since the atmosphere contains about 100 yrs of ^{14}C production (eg. (800 kg ^{14}C burden) / (6 kg/yr production) according to our model parameterization), a specific

Q increase lasting 1 yr will only raise the atmospheric burden by 1/100th, or 1% of the Q increase (H = .01). A more permanent Q increase lasting 10,000 yrs, however, should raise the atmospheric burden proportionately (H=1.0) because the time equivalence of the ^{14}C burden is greatly exceeded.

The $^{14}CO_2$ reservoir exchanges and transient redistribution of newly produced ^{14}C complicate this static explanation. The residence time of atmospheric CO_2 is ca. 7.2 yrs with respect to oceanic exchange (eg. (600 GT burden) / (80 GT/yr air-sea exchange) according to our model parameterization where GT denotes gigatons or 10^{15} gm of carbon); the residence time of atmospheric $^{12}CO_2$ and $^{14}CO_2$ is ca. 3.3 yrs with respect to oceanic *and* terrestrial exchanges (eg. (600 GT)/(180 GT/yr)). The attenuation is still high (ie. H is low at ≈.01) for decadal-scale production variations because the rapid exchange of CO_2 with surface ocean waters and terrestrial leaves and grasses acts to effectively more than double the ^{14}C reservoir absorbing the new production. On century scales, the attenuation is still high (H ≈ .04) because of indirect exchange with the huge deep ocean reservoir. The long 100-yr "time equivalence" for the atmospheric $^{14}CO_2$ burden, as compared to the residence time of 3.3 yrs, stems from the net oceanic flux of $^{14}CO_2$ (eg. 113 kg ^{14}C/yr invasion - 107 kg ^{14}C /yr evasion according to our model parameterization) which is about 20 times weaker than the gross oceanic flux of ^{14}C.

The ^{14}C production rate declines about 25% ((1.7 - 1.3)/1.5) on average in transition from the early to late Holocene (figures 2.1, 2.2). The deconvolved century-scale perturbations in Q show similar relative excursions. The attenuation factors for Q fluctuations of 10^2 and 10^4 yrs indicate that the atmospheric $\Delta^{14}C$ responses to the former perturbations will shrink to 1/6th (H=.044 / H=.27) of the magnitude of the Holocene-scale atmospheric $\Delta^{14}C$ change. Thus atmospheric $\Delta^{14}C$ signals are weakened to 1.1 % (11 ‰) and 6.5 % (65 ‰) for 25% Q forcings with periods of 10^2 and 10^4 yr,

respectively. In this way, the long-term decline in atmospheric $\Delta^{14}C$ (with an amplitude of 50 ‰ for a peak-to-trough difference of 100 ‰) becomes more prominent than the century-scale $\Delta^{14}C$ variations (≈ 15 ‰) driven by comparable changes in ^{14}C production rate.

Specifically, as illustrated in figures 1.1, 2.1, and 2.2, an average Maunder-type Q variation of 25% lasts 200 yrs and produces a fluctuation in atmospheric $\Delta^{14}C$ of 13 ‰ (H = .052) while an average Spörer-type Q variation of 31% lasts 300 yrs and produces an atmospheric $\Delta^{14}C$ change of 17 ‰ (H = .055). A detailed discussion of these century-scale variations is presented in chapter 3.

The decline in $Q(^{14}C)$ commences 300 yrs before the drop in atmospheric $\Delta^{14}C$ and concludes at 2000 BC, that is 2500 yrs prior to the nadir in atmospheric $\Delta^{14}C$ (cf. splines in figures 1.1 and 2.1). The greatest rate of descent in $Q(^{14}C)$ centers on 3000 BC, approximately 1000 yrs prior to the midpoint of the atmospheric $\Delta^{14}C$ drop. These $Q(^{14}C)$ characteristics broadly accord with the phase lag (30° or 800 yrs) predicted by Houtermans et al. (1973) for a 10,000 yr periodic disturbance. The contrast between the abrupt decline in ^{14}C production rate and the gradual descent in atmospheric $\Delta^{14}C$ is discussed more in the next subsection.

The ^{14}C production rate varies about a constant level of $1.34 \pm .01$ ^{14}C atoms s^{-1} cm_E^{-2} between ca. 3000 BC and AD 500 (where cm_E^2 denotes a square centimeter of earth surface). This stability compares well with the trend in contemporaneous ^{10}Be concentrations in Greenland ice cores which may more directly reflect variations in cosmogenic production rates (see section 2.4).

The model-derived ^{14}C production rate is 1.36 ^{14}C atoms s^{-1} cm_E^{-2} in AD 1950 (ie. 1940 - 1960). Independent estimates for ^{14}C production based on theoretical calculations and limited neutron-flux data vary from 1.75 for the rate in AD 1950 (O'Brien 1979) to

2.2 ± 0.4 for the average production during several recent 11-year solar cycles (Lingenfelter and Ramaty 1970; Damon 1988). The strong bi-decadal variability exhibited by $Q(^{14}C)$ (figure 2.1) hinders the comparison of model results with other estimates of average production rates over short time scales. Yet the model fluxes generally fall more than 20% below the independently-calculated ^{14}C production rates. The uncertainties and distinctions involved in the theoretical and model estimates are considered in detail in sections 2.4 and 4.4.

Enhancement of the model's carbon reservoir sizes and the inclusion of sedimentary storages increase the deconvolved ^{14}C production appropriate to balance the total decay in the global ^{14}C system. The relative variations in production rate will remain essentially unchanged (see below). The reference level for the relative scale in figure 2.1 (right axis) was chosen to be 1.546 ^{14}C atoms s^{-1} cm_E^{-2}, the average model $Q(^{14}C)$ back to 500 cal BP (AD 1450). This selection is not entirely arbitrary in that it expedites the comparison of "long-term" $Q(^{14}C)$ to ^{14}C production derived from time-averaged geomagnetic data in later sections.

The modeling procedure and analysis detailed above was replicated for the 4500-yr (2500 BC - AD 1950) *decadal* tree-ring $\Delta^{14}C$ record of Stuiver and Becker (1986). The model simulations utilized a pre-2500 BC atmospheric $\Delta^{14}C$ record comprised of the previously described bi-decadal $\Delta^{14}C$ data set and pre-Holocene "steady-state" conditions. The natural atmospheric $\Delta^{14}C$ levels for the decades after AD 1855 (ie. 1850 - 1860) were reconstructed from the sunspot-derived curve of Stuiver and Quay (1981) as described in chapter 1. Figure 2.2 does not show the decadal features and splined trends for this artificial extension.

The decadal versions for the atmospheric $\Delta^{14}C$, the deconvolved $Q(^{14}C)$, and their long-term trends (ie. cubic splines approximating 400-yr moving averages) closely

Figure 2.2: Decadal ^{14}C production rates (upper bar curve) between 2500 BC and AD 1860 necessary to generate, without climate intervention, the measured decadal atmospheric (tree-ring) $\Delta^{14}C$ variations (lower bar curve). The production rates, in ^{14}C atoms s^{-1} cm_E^{-2}, are derived as in figure 2.1 with the same bi-decadal $\Delta^{14}C$ record assumed prior to 2500 BC. Splines apprximating 400-yr moving averages represent the long-term trends in ^{14}C production and atmospheric $\Delta^{14}C$ (upper and lower heavy line, respectively).

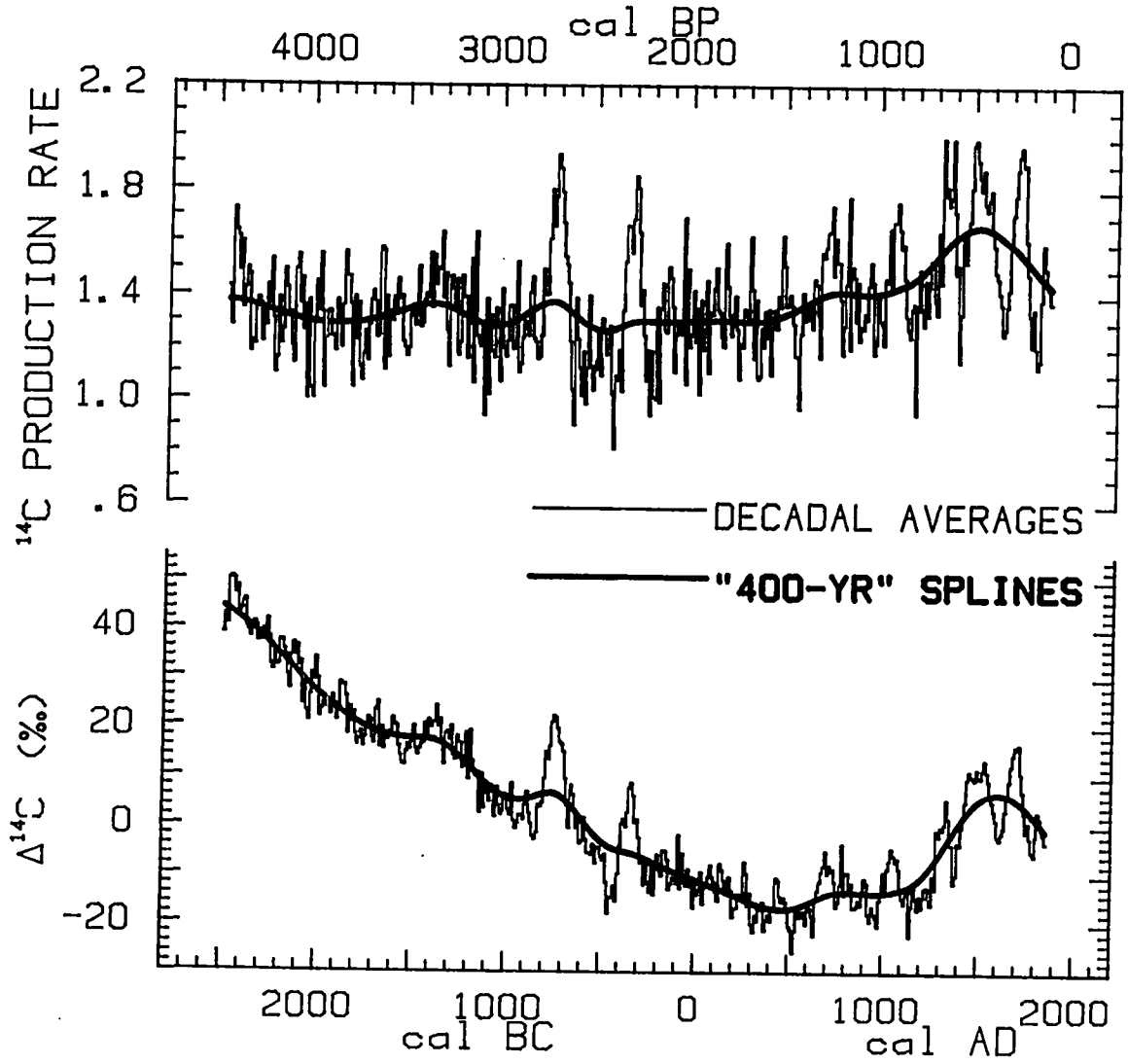
cal BP
4000
3000
2000
1000
0
2.2
1.8
1.4
1.0
.6
^{14}C PRODUCTION RATE
DECADAL AVERAGES
"400-YR" SPLINES
40
20
0
-20
Δ^{14}C (‰)
2000
1000
0
1000
2000
cal BC
cal AD

resemble their bi-decadal counterparts (figure 2.2). The residual features of both the bi-decadal and decadal records are displayed and discussed in more detail elsewhere (Stuiver and Braziunas 1988). The finer resolution of the decadal records does not impact the basic spectral analysis presented in chapter 4. The deconvolved decadal Q(^{14}C) record is currently being utilized to compare finer scale features of the ^{14}C curve with contemporaneous high-resolution climate records (Stuiver, work in progress).

As a final remark, the derived ^{14}C production rate histories are based on atmospheric Δ^{14}C measurements strictly from the northern hemisphere. Lerman et al. (1970) presented ca. 40 ^{14}C measurements on tree rings that indicate a consistent 4-5 °/oo depletion in the ^{14}C content of the natural atmosphere of the southern hemisphere relative to the northern hemisphere Δ^{14}C record during the current millennium. An interhemispheric box-diffusion model (Stuiver and Braziunas, in progress) indicates that the true "global" ^{14}C production rate history is, on average, <1% reduced in absolute magnitude from the Q history deconvolved from the northern hemisphere record alone.

Ocean Δ^{14}C response to Q-forcing

The variations in atmospheric ^{14}C also affect the oceanic carbon reservoir through the model exchange equations described in chapter 1. In the functional scenario considered here, the model ocean is "driven" by the atmosphere which, in turn, is responding to a changing ^{14}C production rate under static climatic conditions (constant reservoir burdens and exchange parameters). The impact of this external forcing on the distribution of oceanic Δ^{14}C has already been illustrated in figure 1.6.

The 90 °/oo decline in atmospheric Δ^{14}C from 3000 BC to AD 500 is echoed in similar drops of 85, 80, and 75 °/oo for the surface ocean mixed layer, thermocline, and

deep ocean, respectively (figure 2.3). However, the oceanic response lags the atmospheric decline increasingly with depth. For example, only the model deep sea does not yet reflect the recent rise in $\Delta^{14}C$ apparent in the other reservoirs in response to the recent upswing in ^{14}C production rate. The depth-dependent lag in oceanic response changes the relative distribution of ^{14}C among the reservoirs. The strength of the vertical ^{14}C profile wanes in the mid-Holocene as the upper ocean $\Delta^{14}C$ declines more quickly than the marine reservoirs below 1000 meters but waxes again in the current millennium (figure 1.6).

An important component of the 4500-yr mid-Holocene decline in atmospheric and oceanic $\Delta^{14}C$ is the long-term memory of the global ^{14}C system for past ^{14}C production rates. With a decay half-life of 5730 yrs, the ^{14}C created during the extended high levels of ^{14}C production early in the Holocene persists in the system well beyond the more rapid Q drop that begins around 4000 BC. Figure 2.4 demonstrates this persistence by comparing the observation-dependent reservoir $\Delta^{14}C$ curves (light lines) with the declining $\Delta^{14}C$ histories imparted by an instantaneous drop in ^{14}C production rate at 4000 BC. Except for the recent observed $\Delta^{14}C$ rise, the match with the hypothetical curves is excellent. At least several half-lives (ie. 17,000 yrs) are required for the ^{14}C in the reservoirs to stabilize and reflect the new "steady state" level of ^{14}C production. Because reservoir $\Delta^{14}C$ integrates the past history of ^{14}C production, the timing and magnitude of the specific sources responsible especially for long-term $\Delta^{14}C$ trends is obscured in the $\Delta^{14}C$ record and more easily revealed in deconvolved ^{14}C production rate or climate curves (see following sections for further discussion).

As a consequence of the nearly parallel intra-oceanic $\Delta^{14}C$ trends, the surface/deep ocean ^{14}C age-differences remain relatively constant. Because vertical mixing (ie. K_z) does not vary in this solely Q-forced model scenario, the true oceanic ventilation rate KVI

Figure 2.3: Reservoir $\Delta^{14}C$ histories associated with the Q-deconvolution model. The model thermocline history represents the average for the 37 vertical thermocline layers; the model deep sea history represents the average for the 5 deep sea layers. The atmospheric input curve is the tree-ring $\Delta^{14}C$ record.

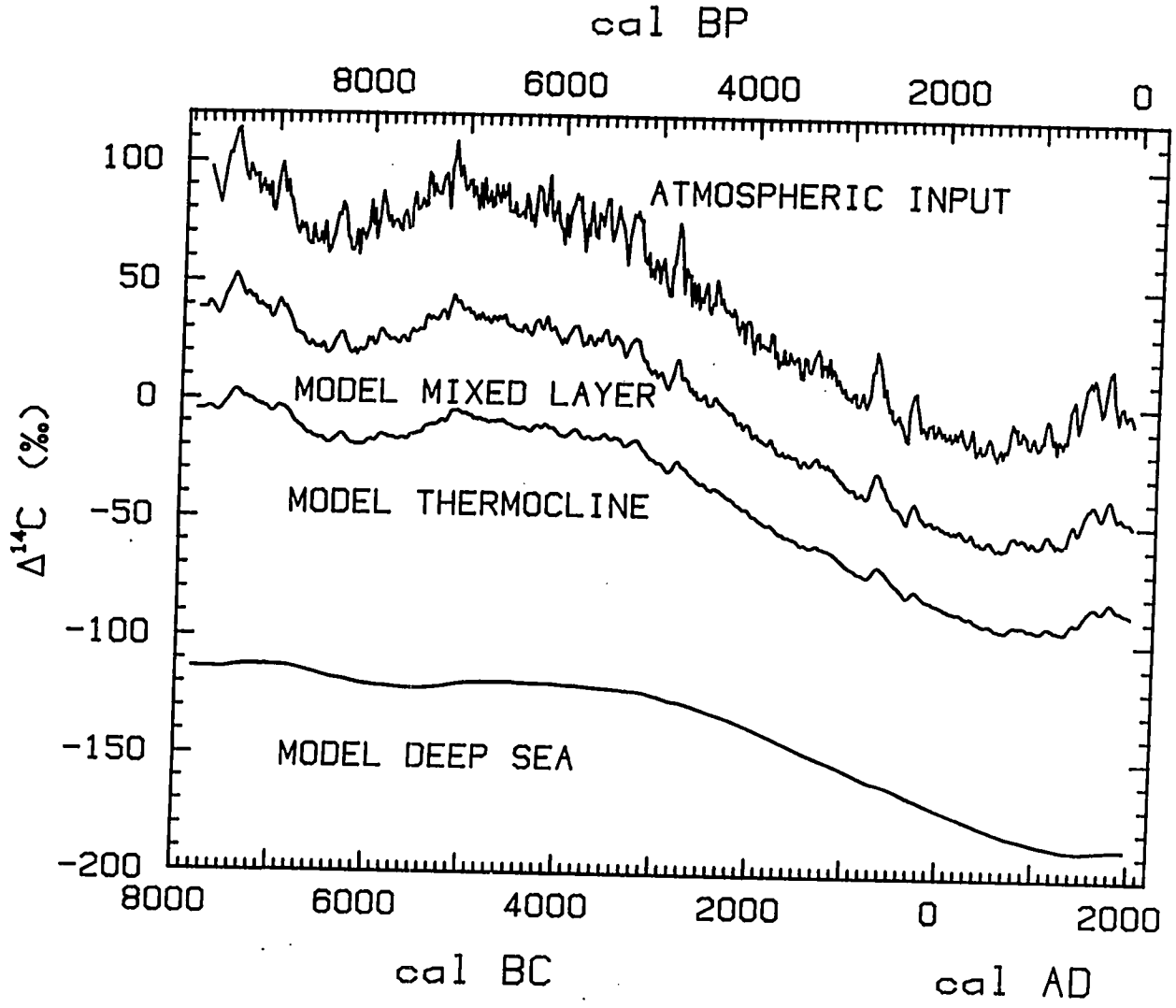
cal BP
8000
6000
4000
2000
0
100
50
0
-50
-100
-150
-200
$\Delta^{14}C$ (‰)
ATMOSPHERIC INPUT
MODEL MIXED LAYER
MODEL THERMOCLINE
MODEL DEEP SEA
8000
6000
4000
2000
0
2000
cal BC
cal AD

Figure 2.4: Reservoir $\Delta^{14}C$ declines associated with a hypothetical instantaneous drop in ^{14}C production rate. The Q step function (in units of ^{14}C atoms s^{-1} cm_E^{-2}) generates the reservoir $\Delta^{14}C$ responses shown in heavy lines. For comparison, the light lines are the atmospheric (tree-ring) $\Delta^{14}C$ record and the oceanic $\Delta^{14}C$ histories associated with the deconvolved $Q(^{14}C)$ scenario.

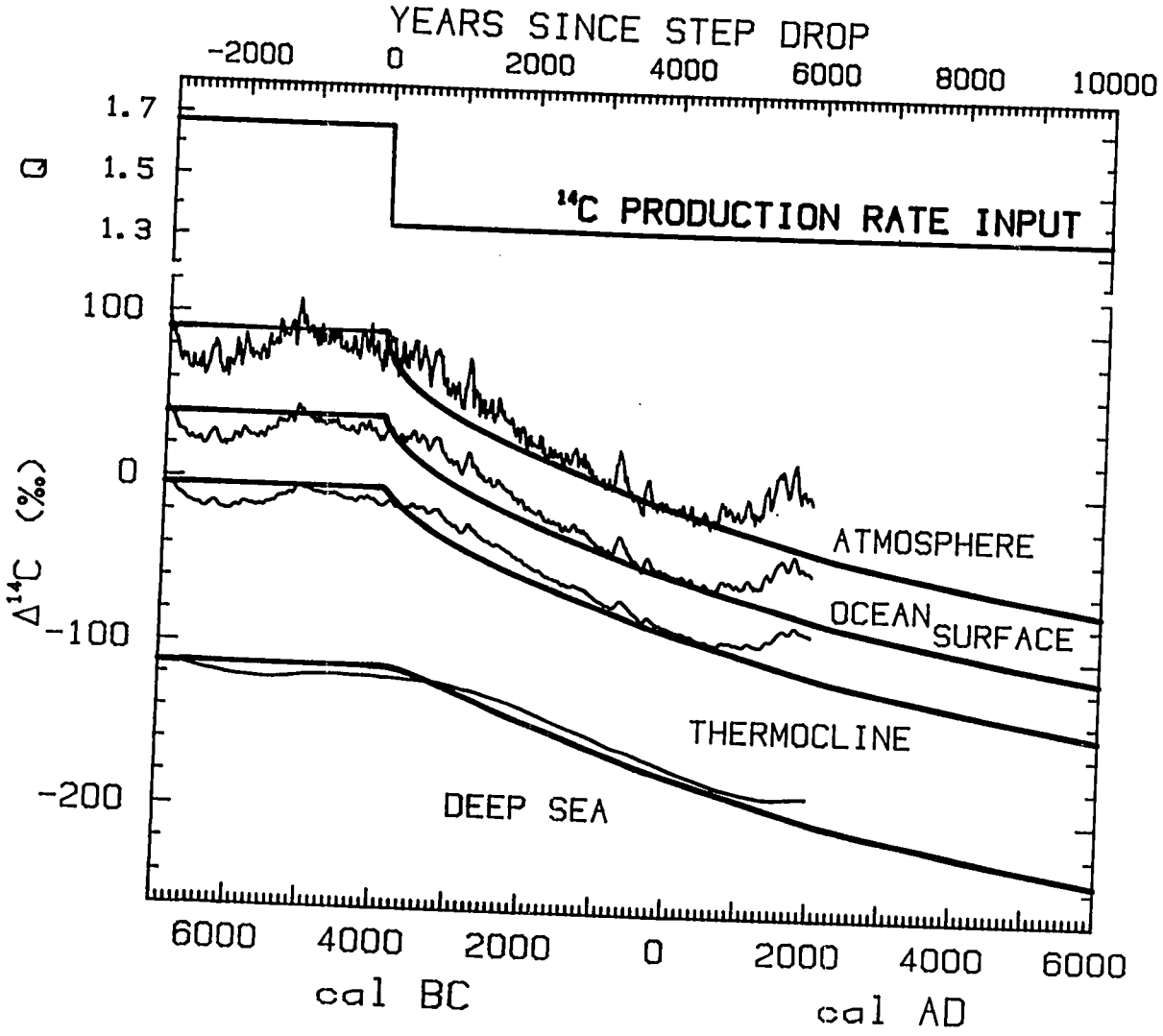
YEARS SINCE STEP DROP
-2000
0
2000
4000
6000
8000
10000
Q
1.7
1.5
1.3
^{14}C PRODUCTION RATE INPUT
100
0
-100
-200
Δ^{14}C (‰)
ATMOSPHERE
OCEAN SURFACE
THERMOCLINE
DEEP SEA
6000
4000
2000
0
2000
4000
6000
cal BC
cal AD

is strictly constant; however, lags and attenuations impart a low-level noise to the model ventilation index MVI (see section 1.4 for definitions).

The secondary variation in the model ventilation index is displayed in figure 2.5 which compares the trend in model ventilation index with the foram-derived trend in surface/bottom ocean ^{14}C age-differences from the South China Sea (Andrée et al. 1986b). The model curves are plotted against the left axis scaling MVI; the foram data are associated with the right axis scaling the foram ventilation index FVI (see section 1.4 for description of the foram analysis). The scales only differ by a shift of 310 yrs that allows the AD 1830 model surface/deep ocean age difference of 1275 ^{14}C yrs to match the estimated pre-anthropogenic surface/bottom water age difference in the South China Sea of 1585 ± 150 yrs. This offset in recent "baseline" values may partially be explained by geographic idiosyncrasies and/or inherent interpretative difference between MVI and FVI. The former represents the ^{14}C age difference between global-average ocean surface water and all marine layers below one km while the latter measures ^{14}C age differences between surface and bottom water (specifically at 2 km depth) in the South China Sea. The shift does not interfere with a comparison of ventilation trends.

The trend in MVI (solid line in figure 2.5) falls within the uncertainty of the foram data. The late Holocene decrease of 200 ^{14}C yrs in MVI results from the lag in deep ocean response to the mid-Holocene atmospheric and surface marine $\Delta^{14}C$ decline. This artificial ventilation feature must be distinguished from the truly constant ventilation rate of 1275 yrs (ie., KVI, corresponding to the model's constant eddy diffusivity of 4000 m^2 yr^{-1} or 1.26 cm^2 s^{-1} as denoted by the solid line in the figure inset). Thus MVI and FMI are imprecise indicators of oceanic mixing rate when the ocean system experiences rapid transient $\Delta^{14}C$ redistributions driven by external (or internal) processes. The discussion

Figure 2.5: Model and foram ventilation indices (MVI and FMI, respectively). MVI is defined as the age difference (in ^{14}C yr) between the model surface ocean layer and the average model deep ocean (ie. below 1 km) and is scaled on the left axis. FVI is defined by Andrée et al. (1986b) as the age difference (in ^{14}C yr) between the planktonic foram *Globigerinoides sacculifer* and benthic foraminifera and is scaled on the right axis. FVI relates specifically to data from two sediment cores in the South China Sea (triangles and x's with one-sigma error bars). The MVI axis is shifted relative to the FVI axis in order to match their respective recent values. MVI curves are derived from the ocean $\Delta^{14}C$ histories associated with the observed atmospheric $\Delta^{14}C$ record when the deconvolved "forcing function" is: $Q(^{14}C)$ (solid line), $K_Z(^{14}C)$ (dashed line), $F(^{14}C)$ (dot-dashed line), or a combined $F,K_Z(^{14}C)$ (short-long-dashed line). Dark rectangles indicate initial "steady-state" values.
(inset) Deconvolved eddy diffusion $K_Z(^{14}C)$ required to generate the observed atmospheric $\Delta^{14}C$ record with and without equivalent changes in CO_2 gas exchange rate (short-long-dashed and dashed lines, respectively). The solid line indicates the constant K_Z value used when $Q(^{14}C)$ explains entirely the observed atmospheric $\Delta^{14}C$ record.

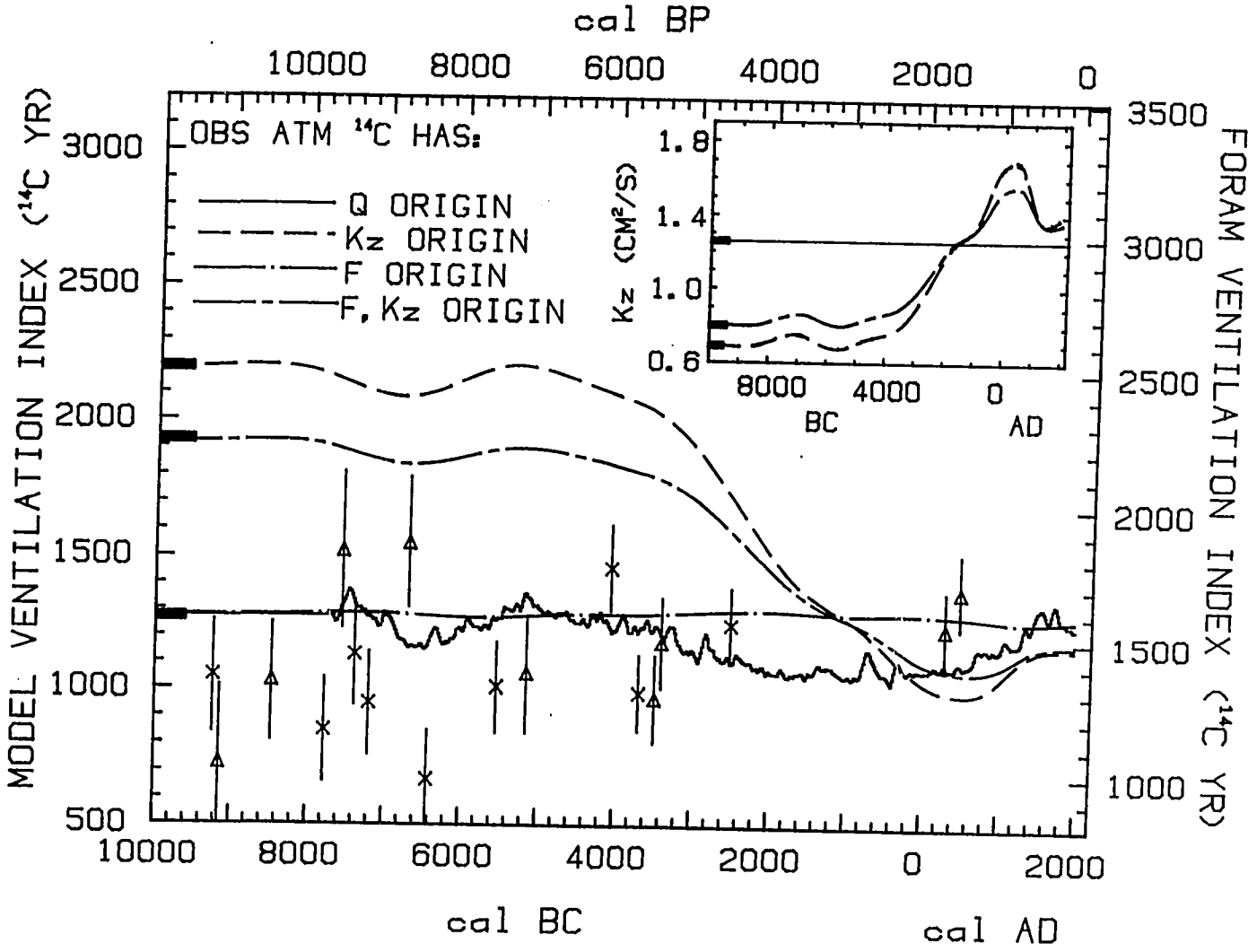
cal BP
10000
8000
6000
4000
2000
0
OBS ATM ^{14}C HAS:
Q ORIGIN
Kz ORIGIN
F ORIGIN
F, Kz ORIGIN
Kz (CM²/S)
1.8
1.4
1.0
0.6
8000
4000
0
BC
AD
MODEL VENTILATION INDEX (^{14}C YR)
3000
2500
2000
1500
1000
500
FORAM VENTILATION INDEX (^{14}C YR)
3500
3000
2500
2000
1500
1000
10000
8000
6000
4000
2000
0
2000
cal BC
cal AD

of this figure continues in section 2.2.

The century-scale atmospheric ^{14}C variations are attenuated by ca. 50% in the ocean surface layer and are fully diluted in the deep sea except for a "mega-event" near 700 BC (figures 2.3, 1.6). (The 200-yr time-averaging in figure 1.6 artificially reduces the variability.) All lags and attenuations have implications for accurate radiocarbon dating and age calibration of marine samples as detailed by Stuiver et al. (1986b). Discussion of these features continues in chapter 3.

Sensitivity of model results to revisions in tree-ring $\Delta^{14}C$

The dendrochronological dating of the older tree rings must occasionally be revised. For example, as noted in section 1.2, the chronology of the south German oak "Main 9" series was recently revised by 74 yrs inducing a relative drop of ca. 9 ‰ in the age-corrected atmospheric $\Delta^{14}C$ for a 600-yr period (bi-decades 7750 BC to 7150 BC). A correction of ca. 50 yrs is also required in another portion of the south German oak chronology. What impact can these revisions be expected to create on the conclusions derived from the "less-revised" $\Delta^{14}C$ record utilized here?

A simulation with the Q-deconvolution model using the revised Main 9 $\Delta^{14}C$ data produced only secondary alterations to the previous model-derived Holocene histories of ^{14}C production rate and oceanic $\Delta^{14}C$ (figure 2.6). The production rate is reduced on average by 3% between 7750 and 7050 BC, surface ocean $\Delta^{14}C$ is reduced on average by 6.5 ‰ between 7750 and 7130 BC, thermocline $\Delta^{14}C$ is reduced by 4 ‰ between 7750 and 7030 BC, and deep ocean $\Delta^{14}C$ is reduced by 1 ‰ between 7750 and 6130 BC. Beyond these time periods, the model differences are deemed negligible (less than 2% in Q differences, less than 2 ‰ for oceanic $\Delta^{14}C$ differences). The deeper oceanic

Figure 2.6: Comparisons of Q-deconvolution model results derived from either: (1) the original tree-ring $\Delta^{14}C$ history with the 7760 to 7220 BC calendar-age assignment (range of bi-decadal averages) for the "Heidelberg Main 9" oak chronology; or (2) the revised and expanded tree-ring $\Delta^{14}C$ history with a 7960 to 7160 BC bi-decadal range for this oak chronology. Light lines show original model results; dark lines are revised results. Left side depicts the pre-5000 BC model-deconvolved ^{14}C production rates in ^{14}C atoms per second per cm^2 of Earth surface; right side shows the alternative sets of atmospheric $\Delta^{14}C$ model inputs and model-derived oceanic $\Delta^{14}C$ histories in per mil.

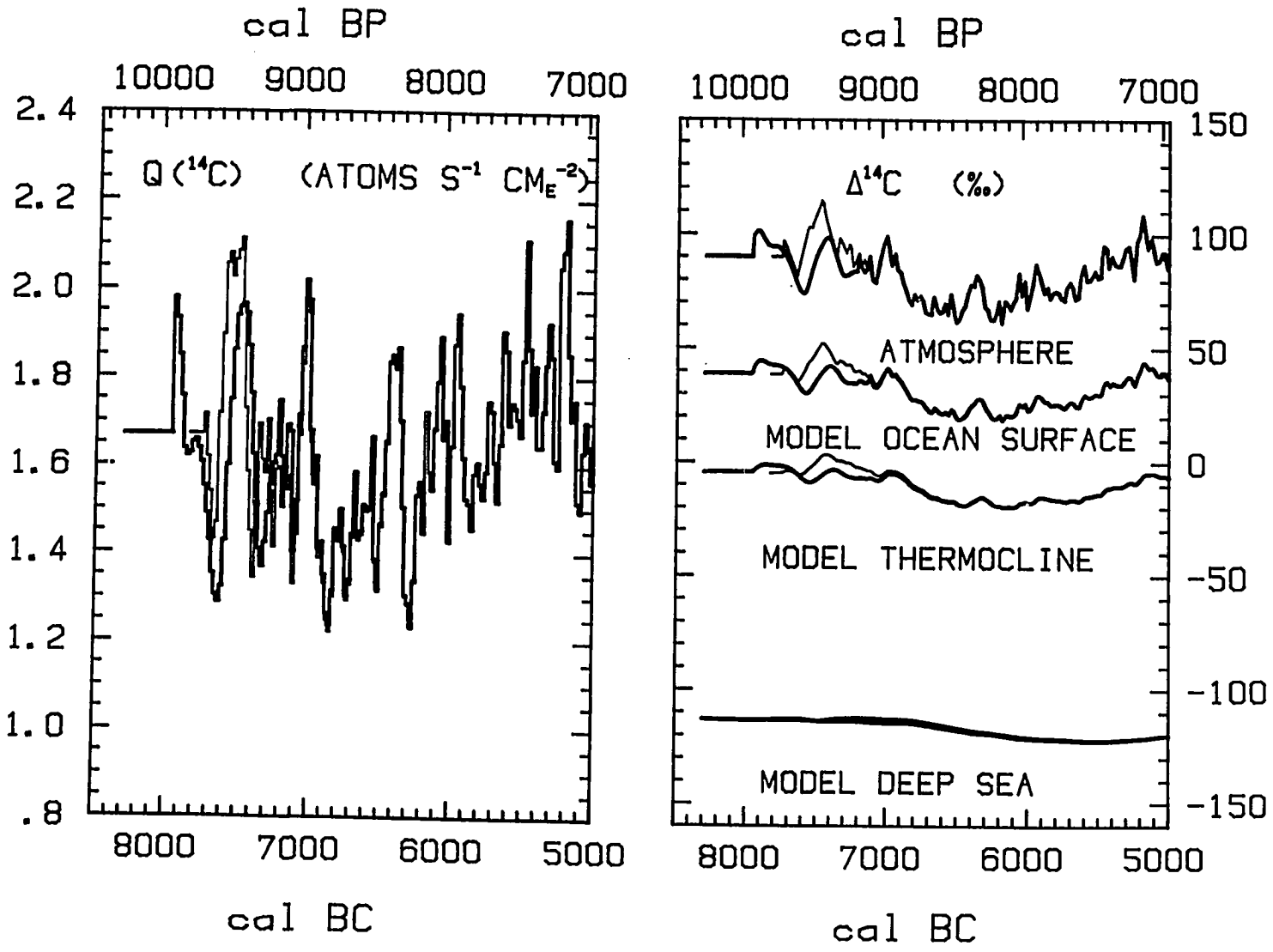
cal BP
10000
9000
8000
7000
2.4
2.2
2.0
1.8
1.6
1.4
1.2
1.0
.8
Q (^{14}C) (ATOMS S^{-1} CM$_E^{-2}$)
8000
7000
6000
5000
cal BC
cal BP
10000
9000
8000
7000
150
100
50
0
-50
-100
-150
Δ^{14}C (‰)
ATMOSPHERE
MODEL OCEAN SURFACE
MODEL THERMOCLINE
MODEL DEEP SEA
8000
7000
6000
5000
cal BC

discrepancies are longer lasting but reduced in magnitude. The spectral analysis (see chapter 4) is negligibly affected.

The greater relative drop in average Q of 3% (i.e. 30 °/oo) during the time period of the -9 °/oo correction in atmospheric $\Delta^{14}C$ is an attenuation phenomenon; the production rate must drop low enough to diminish the ^{14}C content not only in the atmosphere but also in the other reservoirs (ie. surface/thermocline ocean and terrestrial biosphere) that exchange with and influence atmospheric ^{14}C levels. However, as seen in figure 2.6, the atmospheric $\Delta^{14}C$ drop does not translate into a simple Q reduction. The $Q(^{14}C)$ deconvolved from the new atmospheric $\Delta^{14}C$ history that is attached to the same pre-Holocene initial $\Delta^{14}C$ levels is more strongly reduced during the early portion of the revised 600-yr interval and even exceeds its original values in the late portion. The balance between current reservoir $\Delta^{14}C$ levels and past ^{14}C production rates leads to complex responses in the deconvolution process.

Sensitivity of model results to initial conditions

A series of model simulations were conducted to determine the sensitivity of the Holocene $Q(^{14}C)$ and $\Delta^{14}C$ results discussed above on assumed initial pre-Holocene conditions. Similar tests were performed to gauge the sensitivity of deconvolved Holocene oceanic, geomagnetic, and ^{10}Be-related scenarios to assumed pre-Holocene conditions (see later sections).

The structure and parameterization of the simple box-diffusion model does not include some of the reservoirs and mechanisms that may be critical during glacial/interglacial changes in the carbon cycle (sections 1.2, 2.2). For example, prior to 11,000 BP (9050 BC), the model assumption of constant atmospheric CO_2 is no longer

valid (Neftel et al. 1988). To avoid some of these complications, the global carbon model was primarily utilized only to simulate transient ^{14}C system behavior after 11,000 BP.

Constant "steady-state" conditions usually initiate any model simulation. Thus, as a preliminary simplication, I tested several choices for pre-11,000 BP "steady-state" conditions. If the model results for the Holocene show little dependence on diverse "steady-state" assumptions, then a more detailed simulation of pre-Holocene ^{14}C history is not required for the present analysis. However, a preliminary simulation of variable pre-Holocene atmospheric $\Delta^{14}C$ was performed to test the implications of the 30,000-yr behavior of the global dipole moment on hypothetical model-derived Holocene ^{14}C production histories associated with geomagnetic modulation (see section 2.3).

The preferred radiocarbon chronology of figure 1.5 (see section 1.3 for discussion) was chosen to represent the pre-7750 BC atmospheric $\Delta^{14}C$ history for all standard model simulations. This radiocarbon scenario remains at a relatively stable $\Delta^{14}C$ level of 90 °/oo for the 1300 calendar yrs between 11,000 BP (9050 BC) and 9700 BP (7750 BC). In contrast, the original radiocarbon chronology of Zbinden et al. (1989) displays a deficient atmospheric $\Delta^{14}C$ history prior to 7750 BC (figure 1.2). Two strong features of this alternative scenario are (1) the $\Delta^{14}C$ levels of ca. 50 °/oo after 11,000 BP, in accord with the independent ice-layer determinations, and (2) the $\Delta^{14}C$ levels of ca. 0 °/oo in the Late Wisconsin. An antithetical scenario is an elevated pre-7750 BC atmospheric $\Delta^{14}C$ level averaging ca. 140 °/oo as proposed by Beer et al. (1988) from ice-core [^{10}Be] evidence (see section 2.4). Our adjusted Younger-Dryas radiocarbon chronology (figure 1.5) is compatible with this estimate; radiocarbon ages of $^{234}U/^{230}Th$-dated corals (Bard et al. 1990) also indicate high pre-Holocene $\Delta^{14}C$ levels of 200 °/oo or more (figure 2.22).

The basic sensitivity tests were simplified (figure 2.7 upper right) such that four "steady-state" atmospheric $\Delta^{14}C$ levels of 0, 50, 90, and 140 °/oo were alternatively

Figure 2.7: Deconvolved model ^{14}C production rates required to generate the post-7750 BC tree-ring $\Delta^{14}C$ record attached onto 4 hypothetical pre-7750 BC atmospheric $\Delta^{14}C$ histories. The 4 atmospheric records commence with "steady-state" $\Delta^{14}C$ levels of 0, 50, 90, or 140 ‰ prior to 11,000 BP (9050 BC) and then advance linearly to the beginning of the tree-ring record (upper right panel). The ocean exchange parameters K_z (upper left panel) and F remain constant. The lettering of the 4 deconvolved Q histories (bottom panel) corresponds to the respectively lettered atmospheric scenarios.

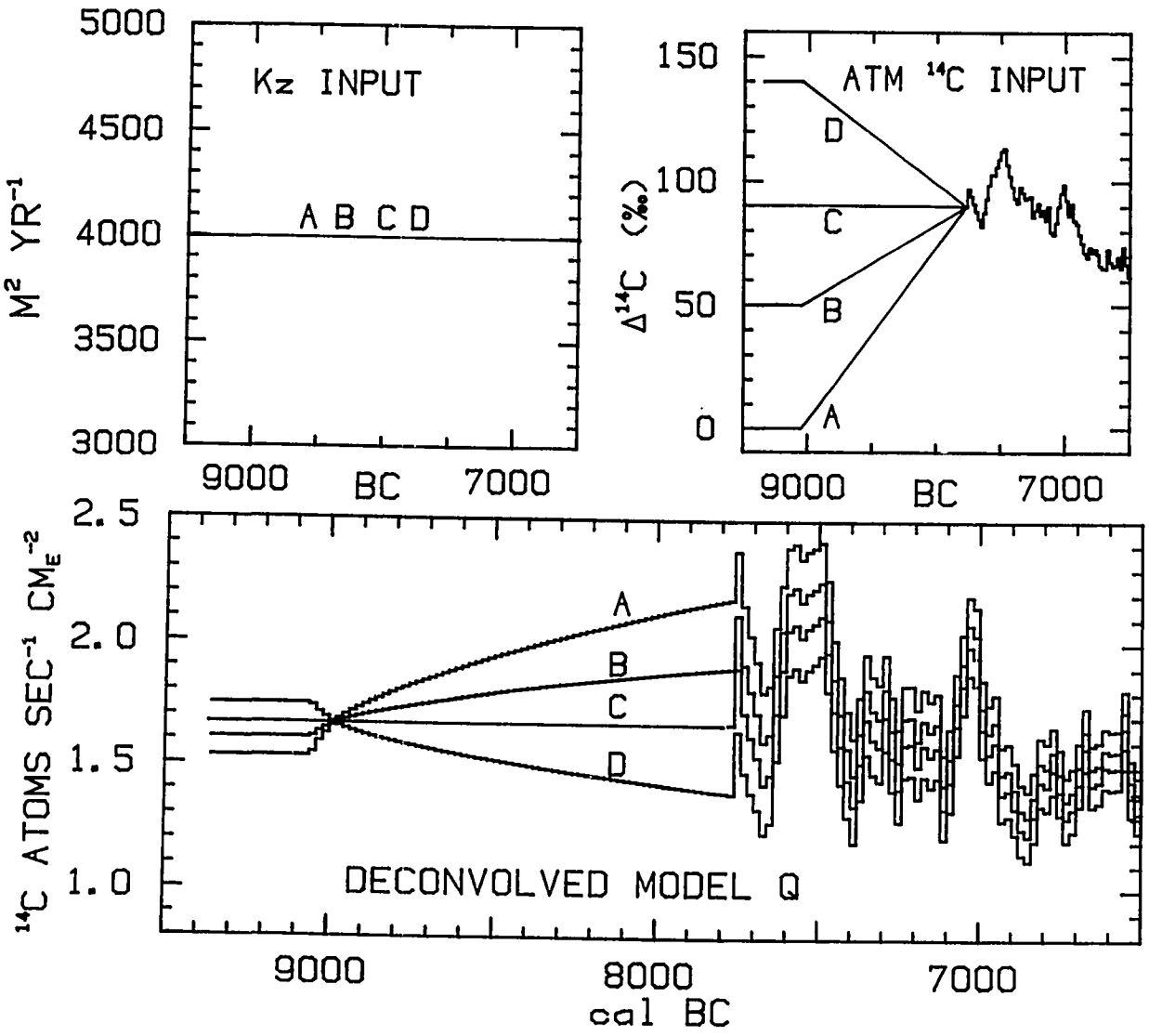
Kz INPUT
A B C D
M² YR⁻¹
5000
4500
4000
3500
3000
9000
BC
7000
ATM ¹⁴C INPUT
D
C
B
A
Δ¹⁴C (‰)
150
100
50
0
9000
BC
7000
¹⁴C ATOMS SEC⁻¹ CM_E⁻²
2.5
2.0
1.5
1.0
A
B
C
D
DECONVOLVED MODEL Q
9000
8000
7000
cal BC

assumed prior to 11,000 BP; atmospheric $\Delta^{14}C$ then advanced linearly to 90‰ at the commencement of the tree-ring $\Delta^{14}C$ record at 9700 BP (7750 BC). The *cause(s)* of these alternative $\Delta^{14}C$ trends may be deconvolved as ^{14}C production rate changes, climate-related fluctuations in air-sea gas exchange or ocean ventilation, or a combination of these factors. Here I consider the implications for Holocene model results of the alternative ^{14}C production rate scenarios needed to produce the observed (tree-ring) atmospheric $\Delta^{14}C$ record when linked to the four hypothetical pre-7750 BC $\Delta^{14}C$ histories shown in figure 2.7. Ocean parameters remain constant at standard values during these tests (as denoted by the horizontal line in figure 2.7 upper left).

Because of radiocarbon's half-life of 5730 yrs, past "steady-state" levels of production can have a lasting effect on reservoir ^{14}C contents. As noted above, several half-lives are required before the memory of a prior "steady state" production is nearly eliminated through redistribution and decay. However, a substantial proportion of the discrepancies in model results that derive from different initial Q conditions disappears in one half-life (ie. 5000 yrs). The four deconvolved ^{14}C production histories and the associated trends in oceanic ^{14}C contents are shown in figure 2.7 (bottom) and figure 2.8 (left), respectively.

In order to produce the observed post-7750 BC $\Delta^{14}C$ record, ^{14}C production rates must generally be greater if the global ^{14}C system is recovering from lower pre-Holocene "steady-state" production. Such Holocene production rates are required to maintain a relatively high level of atmospheric ^{14}C activity against a historically depleted ocean and terrestrial biosphere. For example, when initial production is 4% lower than the standard simulation in order to generate a pre-Holocene atmospheric $\Delta^{14}C_o$ of 50 ‰, the deconvolved $Q(^{14}C)$ is subsequently 14% greater in 7750 BC. As shown in figure 2.7,

Figure 2.8: Model and foram ventilation indices (MVI and FVI, respectively). Definitions and left and right axes alignments are as described in figure 2.5. Left axis scales model curves in *both* left and right half of figure; right axis scales foram data on *both* sides as well. The lettered MVI curves on the left are associated with the 4 identically-lettered deconvolved ^{14}C production histories displayed in figure 2.7. The lettered MVI curves on the right are associated with the 4 identically-lettered deconvolved eddy diffusion histories displayed in figure 2.13. The foram data are as described in figure 2.5.

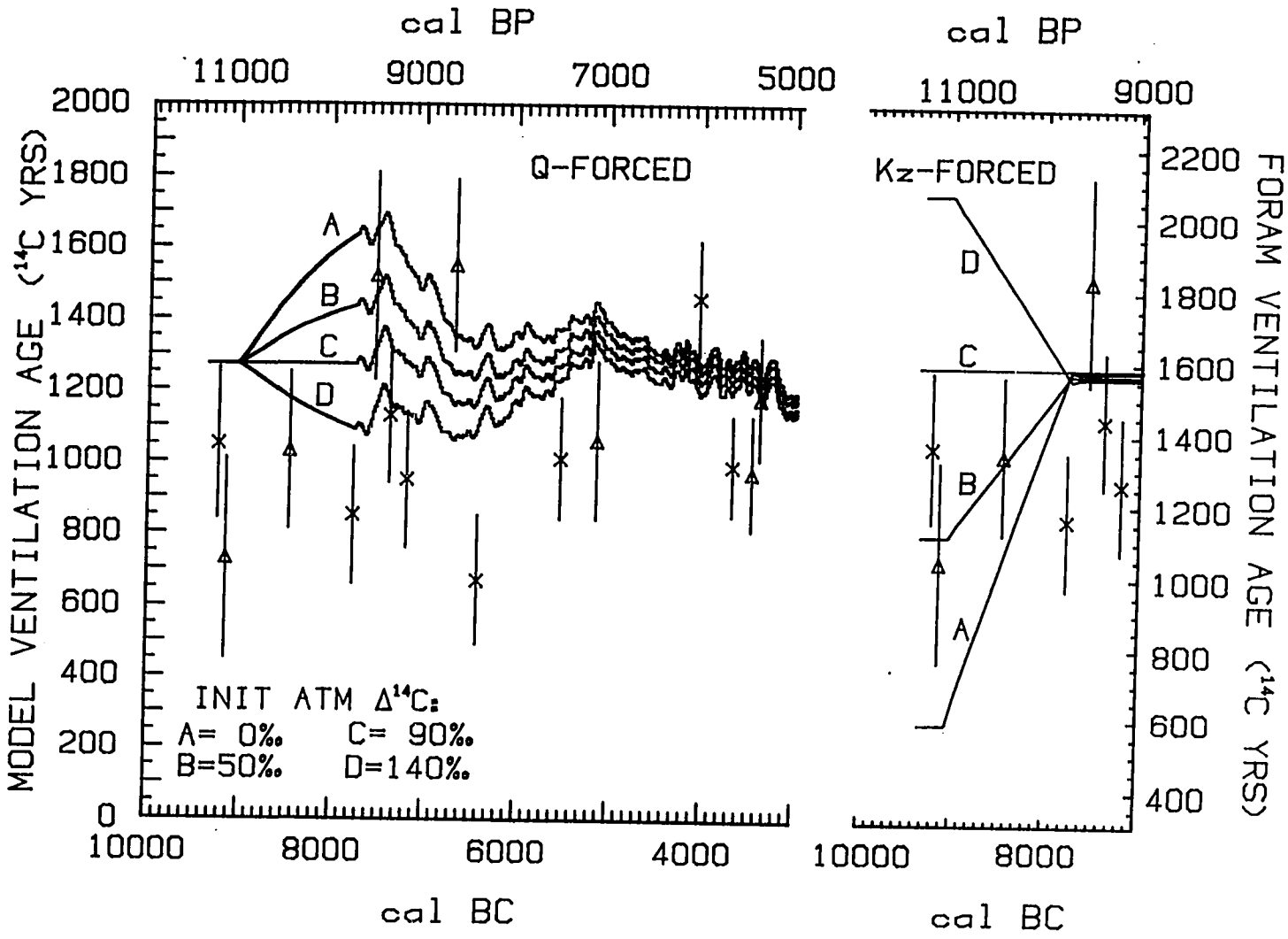
cal BP
11000
9000
7000
5000
2000
1800
1600
1400
1200
1000
800
600
400
200
0
MODEL VENTILATION AGE (14C YRS)
Q-FORCED
A
B
C
D
INIT ATM Δ14C:
A= 0‰ C= 90‰
B=50‰ D=140‰
10000
8000
6000
4000
cal BC
cal BP
11000
9000
Kz-FORCED
D
C
B
A
2200
2000
1800
1600
1400
1200
1000
800
600
400
FORAM VENTILATION AGE (14C YRS)
10000
8000
cal BC

the lowest "steady-state" level of production (curve A) results in the highest compensatory Holocene production rates. However, by 4000 BC the differences among $Q(^{14}C)$ histories deconvolved from alternative pre-Holocene "steady states" dwindles considerably (eg. the difference between $Q(^{14}C)$ from the $\Delta^{14}C_o$ scenarios of 90 ‰ and 50 ‰ is only 1.3%). These changes to the long-term trend in deconvolved $Q(^{14}C)$ have important implications for the proper normalization of geomagnetic- and ^{10}Be-related ^{14}C production rate histories (see sections 2.3 and 2.4), but do not, in themselves, affect any conclusions stated above.

Deconvolved century-scale $Q(^{14}C)$ features in the early Holocene are secondarily affected by the alternative choices for initial production conditions. The magnitude of a century-scale Q digression depends on past production levels because, as for the longer-term trend, the background history incorporated into all the reservoir $\Delta^{14}C$ contents in contact with the atmosphere determines the additional production required to produce an observed Maunder- or Spörer-type event. However, the detrended patterns (see chapter 3) and the spectral analysis (see chapter 4) of the alternative $Q(^{14}C)$ records are essentially equivalent (eg. for the scenario with $\Delta^{14}C_o$ = 50‰, only the 420 yr periodicity from the Burg method is modified by 2 yrs).

The time interval involved in these hypothetical transitions from a "steady-state" condition to a fixed atmospheric $\Delta^{14}C$ record has a significant influence on the deconvolved ^{14}C production rates. For example, if the ^{14}C system is allowed twice as much time (ie. 2600 yrs) to progress from an initial "steady state" to the observed $\Delta^{14}C$ level in 7750 BC, then the deconvolved ^{14}C production rate need be less enhanced at that time. For the case of $\Delta^{14}C_o$ of 50 ‰, $Q(^{14}C)$ in 7750 BC is only 8% rather than 12% greater than in the standard simulation if the transition from initial conditions began in

12,300 BP (10,350 BC). The slower pace spreads out the elevated production levels, allowing a reduced *rate* of production at any specific time. Partially counteracting the mitigating effect from the increased time available for production is the greater involvement of deeper oceanic reservoirs that requires an enhanced production rate (ie. a transitional period twice as long does not reduce the requisite production rate fully by 50%). The duration of the transition period is less influential when climatic changes are responsible (see next section).

The deep ocean responds more slowly to a long-term change in ^{14}C production; nearly all of the perturbation in model ventilation age (figure 2.8) is the result of the lag in the deep ocean. The recovery from this artificial production-induced digression is essentially complete in 4000 yrs (eg. the increase in ventilation age of scenario B over scenario C is 12% in 7750 BC but only 2% by 4000 BC). As noted for the deconvolved $Q(^{14}C)$ histories, the transient perturbation response is less severe when the ^{14}C system has more time to adjust to the transitional forcing. For example, the MVI discrepancy between scenarios B and C is reduced 40 yrs (25%) if the transition from initial conditions is 2600 rather than 1300 yrs. Still, even with the possibility of an increased transition period, the MVI response to scenario A (ie. the scenario with a production-induced pre-Holocene $\Delta^{14}C_o$ of 0 ‰) appears too diametrically opposed to the foram data to be feasible.

In summary, if the considered pre-Holocene atmospheric $\Delta^{14}C_o$ levels derive from ^{14}C production rate variations, then moderate adjustments will ensue in the early Holocene model-dependent ^{14}C production rate curve and oceanic $\Delta^{14}C$ histories. The Q analysis detailed above is unaffected by these secondary alterations. The $Q(^{14}C)$ modifications are important to consider when geomagnetic- and ^{10}Be-based ^{14}C production histories are reconstructed (see sections 2.3 and 2.4). Spectral analysis of

higher-frequency Q features is insensitive to the assumed pre-Holocene conditions. Finally, for 3 of the pre-Holocene "steady state" scenarios, model and foram ventilation indices are compatible; only with a production-forced deficiency in pre-Holocene atmospheric $\Delta^{14}C_o$ of 0 ‰ do model oceanic $\Delta^{14}C$ trends conflict with the available foram radiocarbon evidence.

Sensitivity to model exchange parameterization

The deconvolved ^{14}C production rate and oceanic $\Delta^{14}C$ responses will be affected by modifications to reservoir exchange rates or burdens (contents). Since reservoir burdens are usually determined by specific exchange parameters, adjustments in one model parameter create associated changes in other features. Four sets of simulations were performed to gauge the sensitivity of model results to oceanic exchange rates (F and K), model surface ocean $\Delta^{14}C$ level, the vertically-uniform $[\sum CO_2]$ of the model ocean, and air-sea and air-land fractionation processes.

Broecker et al. (1980) have synthesized and reviewed the information available for parameterization, calibration and validation of global carbon models of varying complexity. Bomb radiocarbon inventories endorse F values between 19 and 24 moles CO_2 m^{-2} yr^{-1} in the AD 1960's when atmospheric CO_2 was approximately 325 ppm (or between 16.5 and 21 moles CO_2 m^{-2} yr^{-1} for our pre-industrial atmospheric CO_2 level of 280 ppm). The bomb ^{14}C inventories are also compatible with a K_z range of 1.9 to 3.3 cm^2 s^{-1} (6000 to 10,400 m^2 yr^{-1}). Natural radiocarbon inventories, surface ocean ^{222}Rn deficits, and oceanic ^{3}H penetration depths indicate model parameter ranges for F of 16 to 21 moles CO_2 m^{-2} yr^{-1} and for K_z of 1.25 to 1.7 cm^2 s^{-1} (4000 m^2 yr^{-1} to 5400 m^2 yr^{-1}).

If F is re-parameterized as 24 moles CO_2 m^{-2} yr^{-1} while retaining standard values for

the other parameters and initial conditions, the model simulates for AD 1830 a surface layer $\Delta^{14}C$ deficiency of 40 ‰ rather than 50 ‰ relative to the contemporaneous atmospheric ^{14}C content. The deep sea is also 10 ‰ less depleted in AD 1830 than in the "standard" case; as a result, the model ventilation age is not modified. In addition, the oceanic $\Delta^{14}C$ reservoirs are always within ca. 2 ‰ of a constant 10 ‰ constant shift from their "standard" histories during the entire Holocene (figure 4 in Stuiver et al., 1986b). The constancy of this offset means that the relative millennium-scale trends and century-scale patterns in oceanic $\Delta^{14}C$ are virtually unaffected by the reparameterization. The oceanic offset of 80 ^{14}C yrs (10 ‰) will be important, however, to the proper calibration of marine radiocarbon age samples if historical information is unavailable for normalizing the model calibration curves to the $\Delta^{14}C$ characteristics of the sample site (Stuiver et al. 1986b). In order to balance the greater oceanic ^{14}C reservoir, the deconvolved ^{14}C production rate history is shifted almost uniformly by +1% (10 ‰) during the entire simulation.

The diffusivity K_z was also re-parameterized to 2.2 $cm^2\ s^{-1}$ (6950 $m^2\ yr^{-1}$) as suggested by the synthesis of estimates in Broecker et al. (1980). This enhanced mixing increases the deep ocean $\Delta^{14}C$ content by 60 ‰ while drawing down the surface mixed layer $\Delta^{14}C$ by ca. 4 ‰. If F is also re-parameterized to 20 moles $CO_2\ m^{-2}\ yr^{-1}$, the model conforms with the calibration criteria of a 50 ‰ depleted surface ocean relative to the atmospheric ^{14}C contents in AD 1830. The Holocene $\Delta^{14}C$ history of the surface mixed layer that results from this alternative combination of F and K_z was found to vary by less than 1 ‰ from the standard case. On the other hand, the deep ocean is younger (initial "steady-state" MVI = 750 instead of 1275 ^{14}C yrs) and also responds more quickly to the Holocene-scale atmospheric $\Delta^{14}C$ decline, thus "aging" 80 ^{14}C yrs (ie. becoming only 50 ‰ enriched) relative to the standard case during the 3000 BC to present

transitional period. The associated MVI curve can be re-normalized to the foram data in figure 2.5 by shifting the left axis such that the AD 1830 MVI "base line" of ca. 800 ^{14}C yrs matches the FVI "base line" of 1585 ^{14}C yrs; the new MVI trend closely resembles the standard model curve in figure 2.5 except for its offset of -80 ^{14}C yrs in the first half of the Holocene.

The greater eddy diffusivity of 2.2 $cm^2\ s^{-1}$ generates a deep ocean $\Delta^{14}C$ level of -140 °/oo for the 19th century, a much greater ^{14}C content than the -180 °/oo that measurements indicate (eg. Oeschger et al. 1975, Siegenthaler 1989). Since the enriched deep ocean $\Delta^{14}C$ content of this K_z parameterization does not conform to our calibration criteria (see section 1.4), this simulation was deemed inappropriate for deconvolving ^{14}C production rates, and its implications were not pursued further. An alternative model strategy would be to employ an enhanced diffusivity for the thermocline layers only (Stuiver 1980a).

Whereas changes have been considered in oceanic ^{14}C relative to a fixed ^{12}C content, the ocean's $\sum CO_2$ content can be re-parameterized as well. In this way "steady-state" $\Delta^{14}C$ (a measure of $^{14}C/^{12}C$) levels may remain unchanged while absolute quantities of ^{14}C vary with ^{12}C. As a sensitivity test, the model's vertically-uniform $[\sum CO_2]$ was re-parameterized to reflect the lower surface ocean concentration of 2.05 moles m^{-3} rather than the average ocean value of 2.31 moles m^{-3} (Takahashi et al. 1981). The analogous "equivalent mixed layer depth" ZEQ becomes 66.8 m rather than 59 m relative to an atmospheric CO_2 content of 280 ppm (see Bacastow and Björkström, 1981, section 2.2 for discussion).

The diminished oceanic carbon reservoir (for both ^{12}C and ^{14}C) induces a general 10% decrease in ^{14}C production rate but negligibly influences *relative* millennium-scale Q trends. After detrending, the percentage century-scale $\Delta Q/Q_t$ variations are only enhanced

3%, ie. about 10% relative to their original 30% ranges (see chapter 3). The diminished oceanic ^{14}C content also weakens the absolute decay rate, causing a slight (5 °/oo) rise in the $\Delta^{14}C$ levels of all oceanic layers. Relative oceanic $\Delta^{14}C$ variations, however, remain essentially unchanged and, with slight adjustments in the F and K_Z parameters, the model ocean can be finely tuned to again precisely meet our calibration criteria (see section 1.4).

The use of fractionation-corrected $\Delta^{14}C$ values in the global model effectively eliminates the need for explicit fractionation factors in air-sea and air-land interactions. However the strengths of the decay process and the ^{14}C production rate depend on the *absolute* ^{14}C contents, especially in the large oceanic reservoir. When the fractionation-induced enhancement (relative to the atmosphere) of isotopic carbon in the oceans and the fractionation-induced depletion of isotopic carbon in the terrestrial biosphere is "corrected" by normalization to a standard ^{13}C content, the absolute rates of decay and production will be affected.

In their landmark modeling paper, Oeschger et al. (1975) noted that some secondary modifications will ensue when ^{13}C inhomogeneities are fully incorporated into the calculations of absolute reservoir ^{14}C contents. With assigned $\delta^{13}C$ values of -7 °/oo for the atmosphere, -25 °/oo for the terrestrial biosphere, and 0.92 °/oo for the ocean (as determined by the chosen air-sea fractionation factors), the initial steady-state ^{14}C production rate of the box-diffusion ^{14}C model utilized here is elevated by ca. 4% (ie. Q = 1.74 rather than 1.67 ^{14}C atoms $cm_E^{-2}\ s^{-1}$ at the start of the simulation). The greater Q is required to balance the enhanced oceanic ^{14}C contents (increased ca. 5%) and atmospheric ^{14}C (increased ca. 4%).

More realism could be instilled in the model by explicitly including a marine particulate flux. The marine ^{13}C vertical profile consists of a relatively enriched surface ocean and depleted subsurface ocean due to biological activity and this ^{13}C distribution

will modify the secondary adjustments just considered. Of course, a variable rather than fixed ^{13}C distribution ultimately allows the most precise representation of the ^{14}C system as well. Because the *relative* variations in ^{14}C time series are fairly robust to shifts in the absolute levels of ^{14}C contents (influencing only production and decay rates modestly), I did not pursue the fractionation effects in further detail here.

Sensitivity to additional model CO_2 and ^{14}C reservoirs

The incorporation of the large long-term CO_2 and ^{14}C storage reservoirs in marine sediments and terrestrial soils will generally enhance the deconvolved ^{14}C production rates necessary to balance the decay in the global ^{14}C system. Such an increase would make the model Q more compatible with the Q's derived from neutron flux measurements (Damon 1988; see also sections 2.3 and 4.4). *Relative* variations in production rate will be less affected when an additional ^{14}C reservoir "scales up" the Q variations required to produce the observed atmospheric $\Delta^{14}C$ history (see Lazear et al. 1980 for a discussion of the "model DC gain"). However, as noted above, attenuation factors relating relative atmospheric $\Delta^{14}C$ fluctuations to causal ^{14}C production fluctuations are dependent on the specific reservoir interchanges controlling the residence times of atmospheric $^{14}CO_2$.

To test the impact on absolute and relative Q and $\Delta^{14}C$ variations of the addition of $^{14}CO_2$ reservoirs onto the basic global box-diffusion structure, a longer-storage terrestrial subfossil carbon pool was incorporated into the model; to test the maximum possible effect on the attenuation factor, this box was parameterized to interact directly with the atmospheric reservoir. The reservoir contained alternatively 970 or 3000 GT (ie. gigatons or 10^{15} gm) of carbon, the extremes of the burden estimates in Olson et al. (1985). A slow gross exchange flux of 1 GT C yr^{-1} (net flux = 0) yields alternative reservoir residence times of 970 and 3000 yrs. The model initial conditions and other exchange

parameters were unchanged.

The model simulations with long-term terrestrial storage of 970 yrs or 3000 yrs respectively deconvolved ^{14}C production rates 3% and 7.5% greater than the standard model results. The relative millennium-scale Q trends are essentially identical with the standard Q curve and the relative century-scale Q patterns are noticeably modified only for the simulation with the greater subfossil pool. After detrending (see section 3.1 for details), the century-scale Q variations are reduced about 7% relative to their original ranges. In other words, the attenuation factor H for century-scale Maunder-type perturbations is .058 instead of .052, a secondary modification. The reason for the increase in H appears to stem from the fact that the atmospheric $^{14}CO_2$ residence time is little changed (shortened by .02 yrs) with the additional air-land flux; as a consequence, the ^{14}C production rate needs to change less (than a simple "scaling up" would indicate) because the atmosphere efficiently retains the newly produced ^{14}C with only an additional slow leakage. The history of the ocean ^{14}C reservoir is unaffected by the additional long-storage terrestrial reservoir.

The estimated Q of 2.2 ^{14}C atoms cm_E^{-2} s^{-1} derived from neutron flux measurements over recent solar cycles (see compilation of Damon 1988) is 40% greater than "base-line" model Q (for atmospheric $\Delta^{14}C$ = o/oo); about 20,000 kg of additional reservoir ^{14}C contents are required to generally elevate the deconvolved Q levels by 40%. If a single terrestrial sedimentary reservoir is assumed for simplicity to be responsible for most of this additional ^{14}C, an infinite pairing of reservoir residence times and ^{12}C contents will yield the necessary ^{14}C mass. For example, a (well-mixed) terrestrial reservoir with a residence time τ of 10,000 yrs and a ^{12}C burden of 33,000 Gtons (and thus a carbon flux of 3.3 GT/yr) will have an absolute ^{14}C content of 20,000 kg with $\Delta^{14}C$ being ca.-550 o/oo; a sedimentary reservoir with τ of 1,000,000 yrs and a ^{12}C

burden of 1,800,000 Gtons has the same ^{14}C content with $\Delta^{14}C$ being -990 o/oo.

Damon (1988) estimates the size of carbon reservoirs that potentially contain enough ^{14}C to raise the total decay of the global ^{14}C system to 2.2 ^{14}C atoms cm_E^{-2} s^{-1}. From his tables and references, I calculated an "effective" ^{12}C reservoir not considered in the box-diffusion model utilized here. My computations indicate that Damon's sedimentary (and other unconsidered) reservoirs contain ca. 30,000,000 Gtons of ^{12}C with an average residence time of ca. 17,000,000 yrs; although the $^{14}C/^{12}C$ ratio are therefore extremely low ($\Delta^{14}C$ is -999.5 o/oo) the total ^{14}C burden amassed is 20,000 kg. The impact of this added burden, based on limited and uncertain evidence, was modeled as an "exteme" case.

The *relative* Q variations deconvolved from the tree-ring $\Delta^{14}C$ record and a box-diffusion model containing such a well-mixed terrestrial reservoir with Damon's criteria have the same basic pattern as but are significantly reduced (generally by 25%) on both the century- and millennium-scale from the standard Q history described above. The absolute Q record is, of course, also increased by 40%. However, this "maximum" increase in ^{14}C requires more research before acceptance.

A large marine sedimentary ^{14}C sink requires an increase in air-sea CO_2 exchange to balance additional oceanic ^{14}C decay. Yet my calibrated model F agrees with other estimates and the implications of additional marine sinks have not been further pursued.

2.2 Implications of a climate (atmosphere/ocean) origin for reservoir $\Delta^{14}C$ variations

Could the climate system have generated the millennium-scale trends in reservoir $\Delta^{14}C$ if the ^{14}C production rate has remained constant during the Holocene? In this

section, the variations in oceanic vertical mixing and air-sea CO_2 gas exchange rate required to produce, alone or in conjunction, the long-term atmospheric (tree-ring) $\Delta^{14}C$ record are derived from the global K_Z-, F- and F,K_Z-deconvolution models described in the first chapter. The hypothetical histories $K_Z(^{14}C)$, $F(^{14}C)$ and $F,K_Z(^{14}C)$ have been subsequently applied as forcing functions in a model version that produces an atmospheric $\Delta^{14}C$ record. A match between the original atmospheric $\Delta^{14}C$ record and the regenerated record has confirmed the veracity of the deconvolution procedure in each case.

The oceanic $\Delta^{14}C$ variations implicated in these climate-induced parameter digressions allow, by comparison to the foram data already described, an evaluation of the three postulated climate scenarios. Microparticle concentrations in ice cores that span the Holocene infer global wind conditions that, because of the wind-dependence in air-sea CO_2 exchange rate, can be compared to the model scenarios as well.

In addition to the basic analysis outlined above, the impact of pre-Holocene *climatic* conditions on the Holocene model $\Delta^{14}C$ curves is tested in a similar fashion as was the influence of pre-Holocene ^{14}C production rates in the previous section. As will be discovered, the global ^{14}C system has a much shorter memory for the redistribution of ^{14}C within reservoirs than for changes in ^{14}C production.

Finally, other potential climatic explanations for long-term $\Delta^{14}C$ variation will be briefly considered.

Variable eddy diffusion and reservoir $\Delta^{14}C$ trends

In the K_Z-deconvolution model, specified time histories of both ^{14}C production rate and atmospheric $\Delta^{14}C$ are input functions that force a compatible transient history in eddy diffusion. More specifically, the K_Z parameter for the entire vertical profile is recalculated for every time step such that the vertical redistribution of oceanic ^{14}C will compensate,

through its effect on surface ocean $\Delta^{14}C$, for any discrepancy between the assigned ^{14}C production rate history and the observed atmospheric $\Delta^{14}C$ record.

To test the sensitivity of atmospheric $\Delta^{14}C$ solely to the internal oceanic mixing process, a static Holocene ^{14}C production rate Q_C was chosen. The average deconvolved ^{14}C production back to 500 cal BP (AD 1440 - 1980) is 1.55 atoms s^{-1} cm_E^{-2}. In the K_Z-deconvolution model, this recent value for the ^{14}C production rate is assumed to apply throughout the Holocene and a varying eddy diffusion becomes the sole factor responsible for the atmospheric $\Delta^{14}C$ record. In section 2.5, the atmospheric $\Delta^{14}C$ observations are reconciled to *joint* changes in oceanic mixing and non-constant ^{14}C production histories derived from geomagnetic or ^{10}Be information.

A smoothed atmospheric $\Delta^{14}C$ curve is used as the other model input in addition to the ^{14}C production rate. The high-frequency variability in the original bi-decadal tree-ring $\Delta^{14}C$ cannot be explained solely by variations in eddy diffusion because the model deconvolves inordinate vacillations in K_Z that quickly become unstable. The "400-yr spline" of atmospheric $\Delta^{14}C$ shown in figure 1.1 could aptly represent the millennium-scale $\Delta^{14}C$ trends, but a moderately smoother curve was chosen to serve as model input (figure 2.9, short-short-long dashed line). The basic insights gained from the analysis below are not sensitive to these options for long-term atmospheric $\Delta^{14}C$ although the quantitative aspects will be secondarily affected.

To explain this choice for the long-term atmospheric $\Delta^{14}C$ curve, I must jump ahead and briefly describe the coarse resolution geomagnetic record that will be involved in several modeling analyses. The smoother atmospheric $\Delta^{14}C$ curve is a "least common denominator" that facilitates the assessment of the relative contributions of climate, ^{14}C production and combinations of both. In order to properly measure the relative roles of climate and ^{14}C production, all potential forcing mechanisms must be associated with a

Figure 2.9: Model-derived reservoir $\Delta^{14}C$ histories. The surface mixed layer and deep ocean $\Delta^{14}C$ curves are generated when the long-term atmospheric $\Delta^{14}C$ record (short-short-long dashed line; see text for derivation) was assumed to originate through: (1) ^{14}C production rate variations (yielding the solid marine curves), (2) eddy diffusivity variations (yielding the dashed marine curves), or (3) air/sea CO_2 exchange rate variations (yielding the dot-dashed marine curves). The deep sea curves are averages for the 5 model ocean boxes below one km depth.

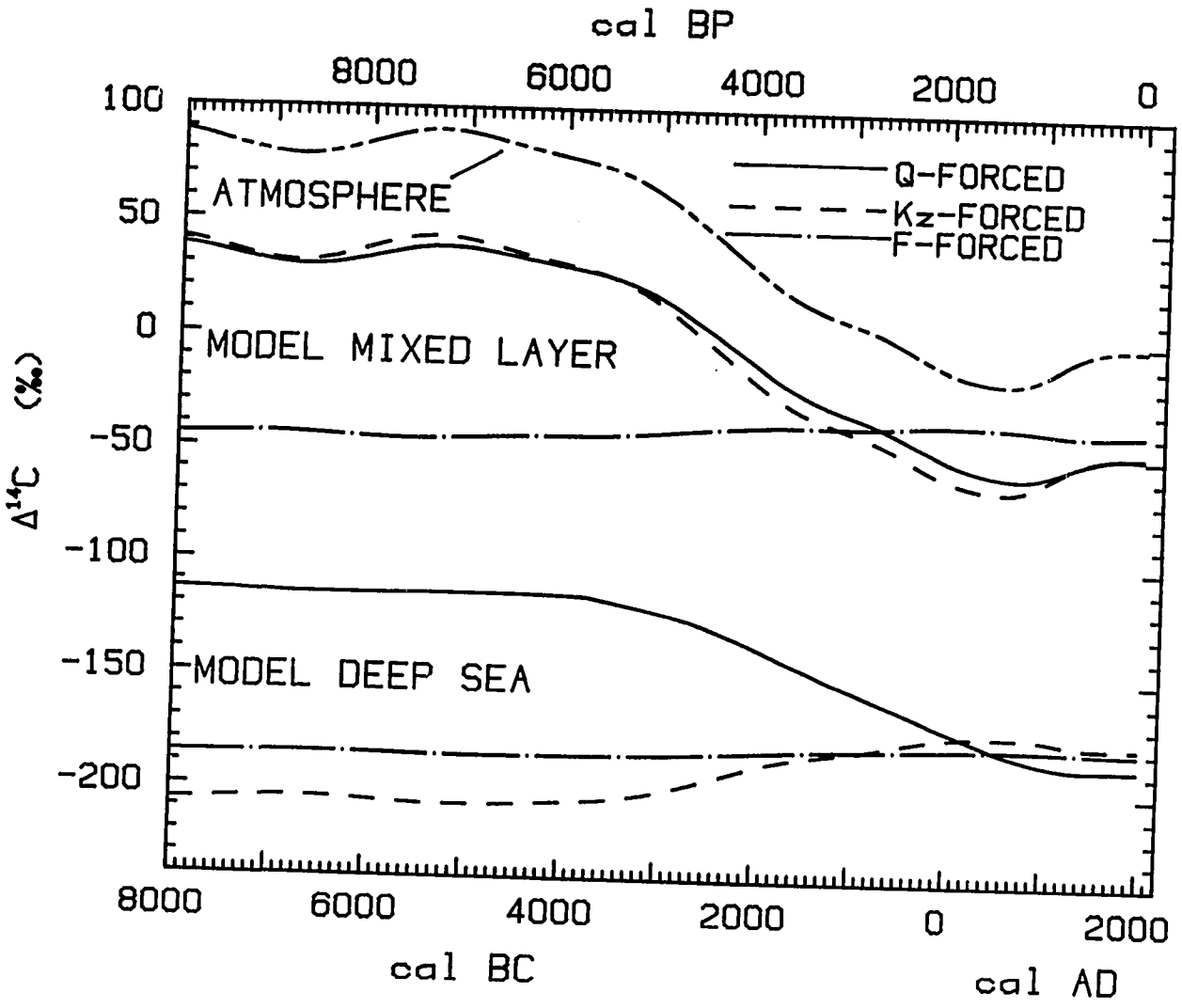
cal BP
8000
6000
4000
2000
0
100
50
0
-50
-100
-150
-200
ATMOSPHERE
MODEL MIXED LAYER
MODEL DEEP SEA
Q-FORCED
Kz-FORCED
F-FORCED
Δ14C (‰)
8000
6000
4000
2000
0
2000
cal BC
cal AD

common atmospheric $\Delta^{14}C$ history. The long-term variation in the geomagnetic dipole moment is conceivably the overwhelming influence on millennium-scale atmospheric $\Delta^{14}C$ change through its effect on ^{14}C production (section 2.3); the dipole data are averaged over 500-yr intervals for the past 4000 calendar years and 1000-yr intervals for the earlier Holocene (figure 2.15). Thus the Q(^{14}C) record, deconvolved in the previous section, was averaged over identical time intervals as the geomagnetic averages and used in the Q-forcing model to produce a "standardized" atmospheric $\Delta^{14}C$ record of comparable resolution as the model-derived $\Delta^{14}C$ record that will be generated by the dipole-related production rate Q(DM) in section 2.3. This "standard" low-frequency record of atmospheric $\Delta^{14}C$ captures the fundamental trends of the bi-decadal observations as shown by the comparison in figure 2.21 of the upper smooth solid curve (identical to the atmospheric curve in figure 2.9) and the bi-decadal bar curve. The use of one atmospheric $\Delta^{14}C$ record standardizes the resolution of all deconvolved source functions and allows combinations of sources to be simulated. Section 2.3 contains additional details not necessary for the current discussion.

The deconvolved history of eddy diffusion required to explain the long-term trend in atmospheric $\Delta^{14}C$ without ^{14}C production rate changes is depicted in the inset to figure 2.5 (equi-dashed line). The corresponding changes in surface and deep ocean $\Delta^{14}C$ are shown in figure 2.9 (equi-dashed line) with the resultant model ventilation history displayed in figure 2.5 (equi-dashed line). Figure 2.10 provides a more detailed depiction of the changes in the oceanic vertical $\Delta^{14}C$ profile that accompany the atmospheric $\Delta^{14}C$ trend when eddy diffusion is the driving variable. The time resolution of this latter figure was drawn out, for clarity, into two-hundred year averages.

To maintain a steady-state atmospheric ^{14}C content, the net flux of atmospheric ^{14}C

Figure 2.10: The history of oceanic vertical $\Delta^{14}C$ profile associated with variations in eddy diffusivity required to produce the long-term Holocene trend in atmospheric $\Delta^{14}C$. Each "horizontal" line represents one of the 43 model ocean boxes. The time intervals between "vertical" lines span 200 years.

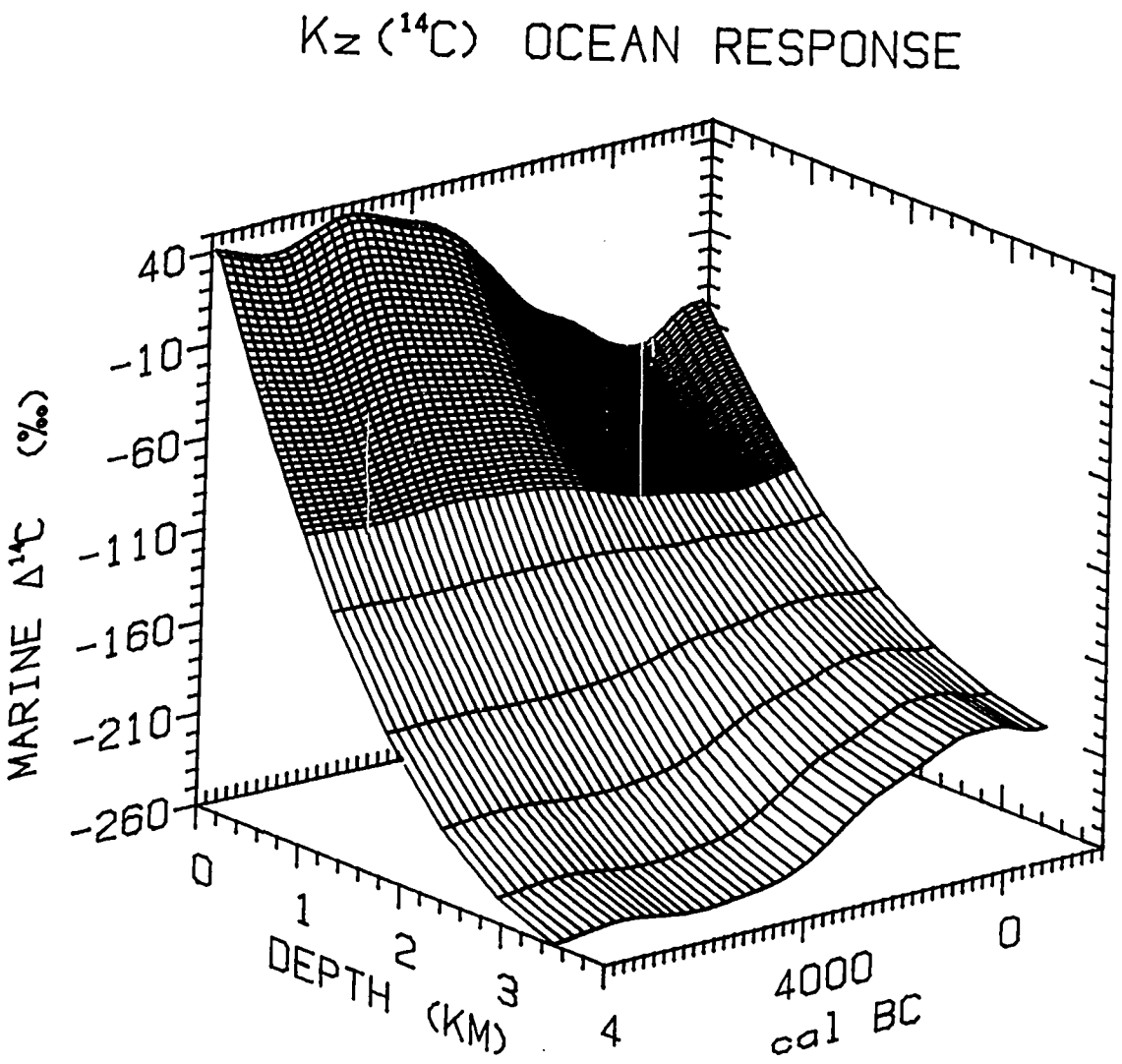
Kz (14C) OCEAN RESPONSE
MARINE Δ14C (‰)
40
-10
-60
-110
-160
-210
-260
0
1
2
3
4
DEPTH (KM)
4000
0
cal BC

into the ocean must equal the production of new ^{14}C in the atmosphere (neglecting the minimal net flux into the model's terrestrial biosphere and the negligible decay rate). Since CO_2 air-sea gas exchange remains constant, the driving factor behind the "pumping" of $^{14}CO_2$ into the ocean is the relative surface ocean $\Delta^{14}C$ depletion. When production is also assumed constant but steady-state atmospheric $\Delta^{14}C$ is greater by 90 ‰, then the surface ocean must also have increased by 90 ‰ to maintain the same net flux of ^{14}C into the ocean. In order to raise the surface ocean ^{14}C content, less ^{14}C must be transported into the deeper ocean, ie. vertical mixing must be reduced. Thus, when variable K_Z is the origin of atmospheric $\Delta^{14}C$ change, such change is controlled indirectly through the effect on surface ocean $\Delta^{14}C$ of strengthened or weakened penetration of ^{14}C into the deeper ocean; because of rapid air-sea exchange (ie. short atmospheric ^{14}C residence time), variations in surface layer $\Delta^{14}C$ are generally paralleled by the atmospheric ^{14}C reservoir (ie. nearly at steady-state).

The correlation between atmospheric $\Delta^{14}C$ and surface ocean $\Delta^{14}C$ (figure 2.9 upper equi-dashed line) is even closer than when production rate changes forced the atmospheric and surface ocean $\Delta^{14}C$ trends (upper solid line). The oceanic lag and attenuation involved in the Q-forced scenario introduce a greater variability in the simulation's atmosphere-surface ocean $\Delta^{14}C$ difference ($s = \pm 4$ ‰) than when the forcing is directed *by* the oceanic reservoir ($s = \pm 0.4$ ‰). Because an increase in upper ocean ^{14}C content now requires a decrease rather than an induced increase in deep ocean ^{14}C concentration, the "steady-state" deep ocean $\Delta^{14}C$ is 10% (100 ‰) lower than during a Q-forced scenario (figure 2.9, lower dashed and solid lines). The variations in the vertical oceanic $\Delta^{14}C$ gradient are fully depicted in figure 2.10.

The low-frequency variability of atmospheric $\Delta^{14}C$ is more sensitive to ^{14}C

production changes than internal oceanic mixing. When production is constant at 1.55 ^{14}C atoms s^{-1} cm_E^{-2}, the initial atmospheric $\Delta^{14}C$ level of 90 ‰ requires a substantial reduction in $K_Z(^{14}C)$ of 45% to 0.7 cm^2 s^{-1} or 2200 m^2 yr^{-1} (equi-dashed line, figure 2.5 inset); when K_Z is fixed at 1.26 cm^2 s^{-1} or 4000 m^2 yr^{-1}(solid line, figure 2.5 inset), the initial production of 1.67 ^{14}C atoms s^{-1} cm_E^{-2} is only 7.5% enhanced relative to Q_C. The magnified eddy diffusion change is a complicated consequence of the equation governing the vertical profile of oceanic ^{14}C. The diffusion process operates on the concentration gradient for the entire ocean, a more oblique influence on atmospheric $\Delta^{14}C$ than direct changes in ^{14}C production within the atmosphere.

The 10% decline in atmospheric $\Delta^{14}C$ from 5000 BC to AD 500 requires eddy diffusion to increase 140% to a maximum of 1.7 cm^2 s^{-1} or 5350 m^2 yr^{-1} in AD 400 (figure 2.5 inset). Diffusivity changes do not show a simple proportionality with variations in atmospheric $\Delta^{14}C$; this nonlinearity results from the greater changes in K_Z required as the concentration gradient diminishes (see "steady-state" discussion below) and from the specific past history in oceanic ventilation that is incorporated into the deconvolution process.

The deep ocean $\Delta^{14}C$ trend induced by a surface ocean $\Delta^{14}C$ history forced "from above" is contrary to the deep ocean trend produced when vertical oceanic mixing forces a similar surface $\Delta^{14}C$ history "from below" (figures 2.9, 1.6, and 2.10). The K_Z-forced redistribution of oceanic ^{14}C yields a distinct history for the model ventilation index that is incongruous with the foram ^{14}C evidence (figure 2.5, equi-dashed line). Specifically, the simulation's surface/deep ocean ^{14}C age differences in the early Holocene are 1000 ^{14}C yrs greater than, and beyond the range of, the (normalized) Holocene trend in oceanic ventilation indicated by the foram ^{14}C measurements of Andrée et al. (1986b).

The true ventilation index KVI, derived directly from $K_Z(^{14}C)$ through equation

1.12, differs secondarily from the apparent ventilation rate represented by MVI. The former index exceeds the latter by 100 ^{14}C yrs during the 3000 - 2000 BC period when, because of the rapid increase in $K_Z(^{14}C)$, true changes in oceanic mixing outpace the adjustment time of the deep ocean. At all other times, MVI more closely reflects the model ocean's actual concurrent mixing rate. Since a direct measure of KVI is unavailable, the apparent ventilation index MVI is the proper quantity to compare to the ostensible ventilation history derived from the foram data.

To test the sensitivity of model results to the value of the constant Holocene ^{14}C production rate, I chose an alternative value for Q_c of 1.46 ^{14}C atoms s^{-1} cm_E^{-2}, the average $Q(^{14}C)$ during the recent AD 1800-1860 period. Although this production rate is only 6% less than our preferred choice for Q_c, the initial "steady-state" $K_Z(^{14}C)$ necessary to maintain an atmospheric $\Delta^{14}C$ content of 90 ‰ in conjunction with this production level is 30% lower than before (K_Z = 0.5 cm^2 s^{-1} or 1600 m^2 yr^{-1}). From this reduced production rate for Q_c and the observed long-term trend in atmospheric $\Delta^{14}C$, a history of more subdued K_Z variations is deconvolved which never exceeds 0.95 cm^2 s^{-1} (or 3000 m^2 yr^{-1}), a maximum achieved in the time interval from 400 BC to AD 500. Thus the entire K_Z history falls at least 25% below the base-line K_Z level of 1.26 cm^2 s^{-1} (or 4000 m^2 yr^{-1}) derived for the recent preanthropogenic period from the observed vertical profile in oceanic $\Delta^{14}C$.

The oceanic ^{14}C vertical gradient associated with the diminished production rate and eddy diffusivity is relatively steep: the initial "steady-state" deep ocean $\Delta^{14}C$ value is -270 ‰ and resultant MVI is 3000 ^{14}C yrs BP. Thus the oceanic distribution of ^{14}C and, as a consequence, the atmospheric ^{14}C content are more sensitive to variations in K_Z which operate on the ^{14}C gradient. In this way, the absolute magnitude of and relative range in deconvolved K_Z variations depend acutely on the assumed constant value for the

^{14}C production rate during the Holocene.

Because this alternative choice for Q_C produces a history of ocean mixing inconsistent with recent observations, it was not considered a suitable value for the constant Holocene ^{14}C production level, and the associated deconvolution of a K_Z record was not regarded further. However, the recent K_Z history deconvolved from the preferred choice for Q_C also mismatches, by 8%, the base-line level K_Z for the 19th century (figure 2.5 inset). A "fine-tuning" of Q_C to correct this secondary discrepancy is probably unwarranted because of the large uncertainties in the "base-line" K_Z related to: (1) the limited measurements of deep ocean $\Delta^{14}C$ and the simple averaging of its geographic variability (eg. Oeschger et al. 1975, Killough 1980); (2) the incorporation of all vertical exchange processes including advection, diffusion, and particle flux into one mixing parameter despite their distinctive effects on the shape of the vertical ^{14}C profile (eg. Broecker et al. 1978); and (3) the assumption of steady-state conditions for the oceanic ^{14}C vertical profile of the 19th century which is not strictly valid, as shown, for example, in figures 2.9, 1.6, and 2.10. A refinement in Q_C (ie. a reduction in Q_C less extreme than the alternative value tested above) would serve only to *increase* the early Holocene discrepancy between MVI and the foram evidence, and thus does not compromise our conclusions.

Thus the changes in ocean ventilation rate (in the guise of K_Z variations) required to explain the millennium-scale trends in atmospheric $\Delta^{14}C$ during the Holocene produce an oceanic $\Delta^{14}C$ history that is not compatible with the available foram ^{14}C data. The assumed constancy in Holocene ^{14}C production rate also contradicts the variable ^{14}C production implied by long-term archaeomagnetic data and ice-core ^{10}Be concentrations (see sections 2.3 and 2.4). For these reasons, we reject an oceanic mixing origin for long-term reservoir $\Delta^{14}C$ variation.

Variable CO_2 gas exchange rate and reservoir $\Delta^{14}C$ change

In the F-deconvolution model, specified time histories of both ^{14}C production rate and atmospheric $\Delta^{14}C$ are input functions that force a compatible transient history in the air-sea CO_2 gas exchange rate. The net air-sea flux of CO_2 remains at zero, that is, the CO_2 invasion and evasion rates always balance. However, a net air-sea flux of $^{14}CO_2$ exists when atmospheric and oceanic ^{14}C concentrations differ (see equation 1.2), and this flux varies with the strength of the exchange rate F and the magnitude of the air-sea ^{14}C disparity.

When the Holocene ^{14}C production rate is assumed constant at 1.55 ^{14}C atoms s^{-1} cm_E^{-2}, the early Holocene gas exchange rate F(^{14}C) is reduced 60% from its recent "base-line" value of 19 moles CO_2 m^{-2} yr^{-1} to 7 moles CO_2 m^{-2} yr^{-1} in order to maintain an enriched "steady-state" atmospheric $\Delta^{14}C$ of 90 o/oo (figure 2.11, dot-dash line). As noted above, under constant climate conditions (ie. constant F and K_Z), an increase in ^{14}C production of 7.5% is required to sustain the same initial atmospheric ^{14}C enrichment. Thus, as in the case of variable K_Z, the atmospheric $\Delta^{14}C$ is less sensitive (by a factor of 8) to fluctuations in air-sea gas exchange than to production rate variations.

In contrast to the ventilation scenario, *both* surface and deep ocean $\Delta^{14}C$ remain nearly constant during the long-term atmospheric ^{14}C decline (figure 2.9, dot-dash lines). The constancy in ^{14}C production induces a more stable deep ocean $\Delta^{14}C$ history during the Holocene than when Q variability is assumed to drive the ^{14}C system. When internal oceanic mixing is also considered to be constant (at 4000 m^2 yr^{-1}), the model surface ocean ^{14}C remains invariable as well, locked into an oceanic vertical ^{14}C gradient maintained by the stable exchange rate with the large stable ^{14}C reservoir of the deeper ocean (figure 2.12). Variations in the internal distribution of oceanic ^{14}C are not required for atmospheric $\Delta^{14}C$ change in this F-induced scenario, only deviations in the exchange

Figure 2.11: Model-generated air-sea CO_2 exchange histories required to produce the long-term atmospheric $\Delta^{14}C$ record (see figure 2.9) coupled with a constant ^{14}C production rate (dot-dashed line) or with the ^{14}C production rate history derived from geomagnetic evidence (dashed line) or ^{10}Be data (dotted line). The solid line indicates the gas exchange rate assumed when the atmospheric $\Delta^{14}C$ record is generated strictly from ^{14}C production variations. The linear relationship of Broecker et al. (1985a) for the velocity dependence of gas exchange rates translates these F values (left axis) into global wind speeds (right axis).

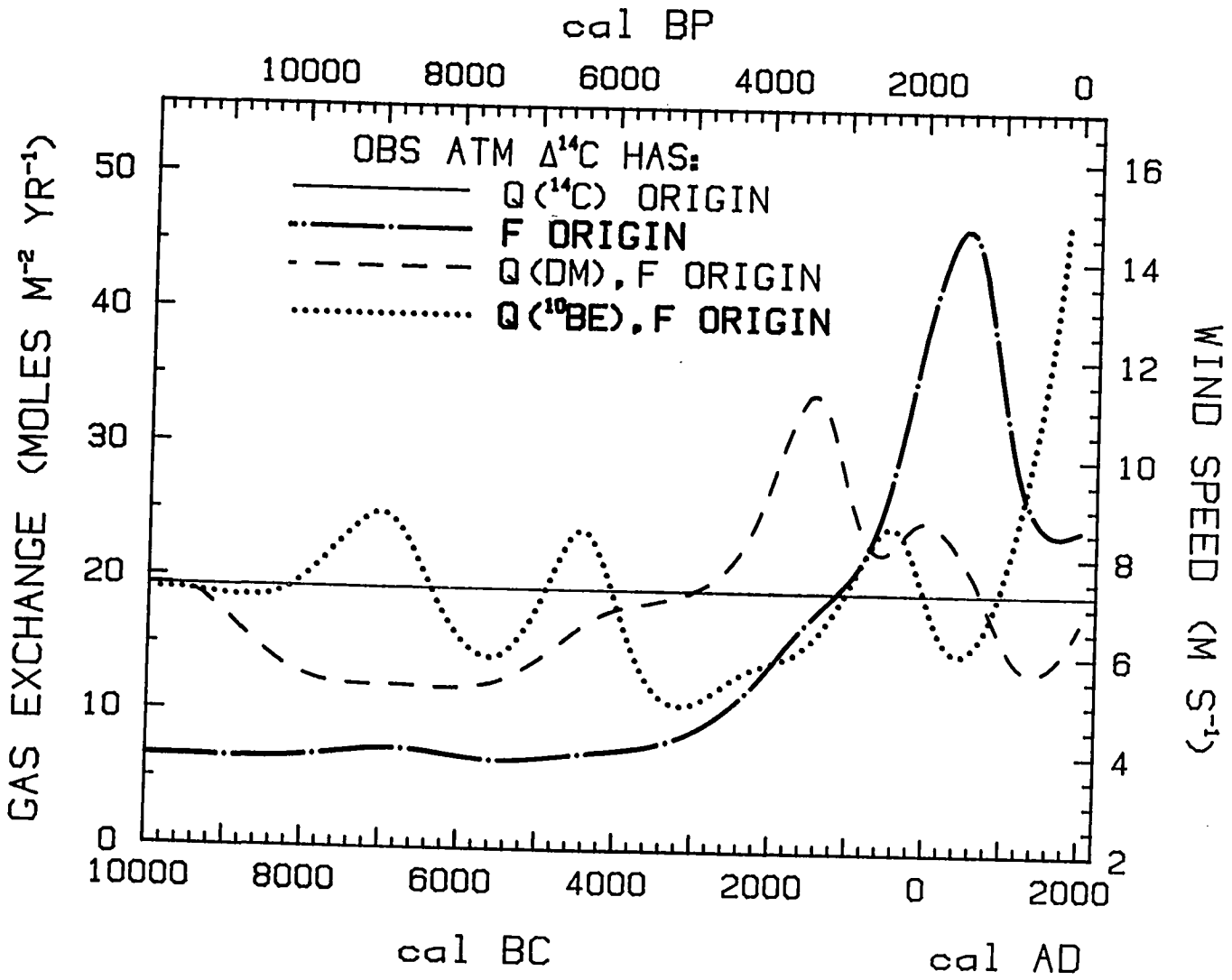
cal BP
10000
8000
6000
4000
2000
0
OBS ATM Δ14C HAS:
Q(14C) ORIGIN
F ORIGIN
Q(DM), F ORIGIN
Q(10BE), F ORIGIN
GAS EXCHANGE (MOLES M-2 YR-1)
WIND SPEED (M S-1)
50
40
30
20
10
0
16
14
12
10
8
6
4
2
10000
8000
6000
4000
2000
0
2000
cal BC
cal AD

Figure 2.12: The history of oceanic vertical $\Delta^{14}C$ profile associated with variations in air-sea CO_2 exchange rate required to produce the long-term Holocene trend in atmospheric $\Delta^{14}C$. Each "horizontal" line represents one of the 43 model ocean boxes. The time intervals between "vertical" lines span 200 years.

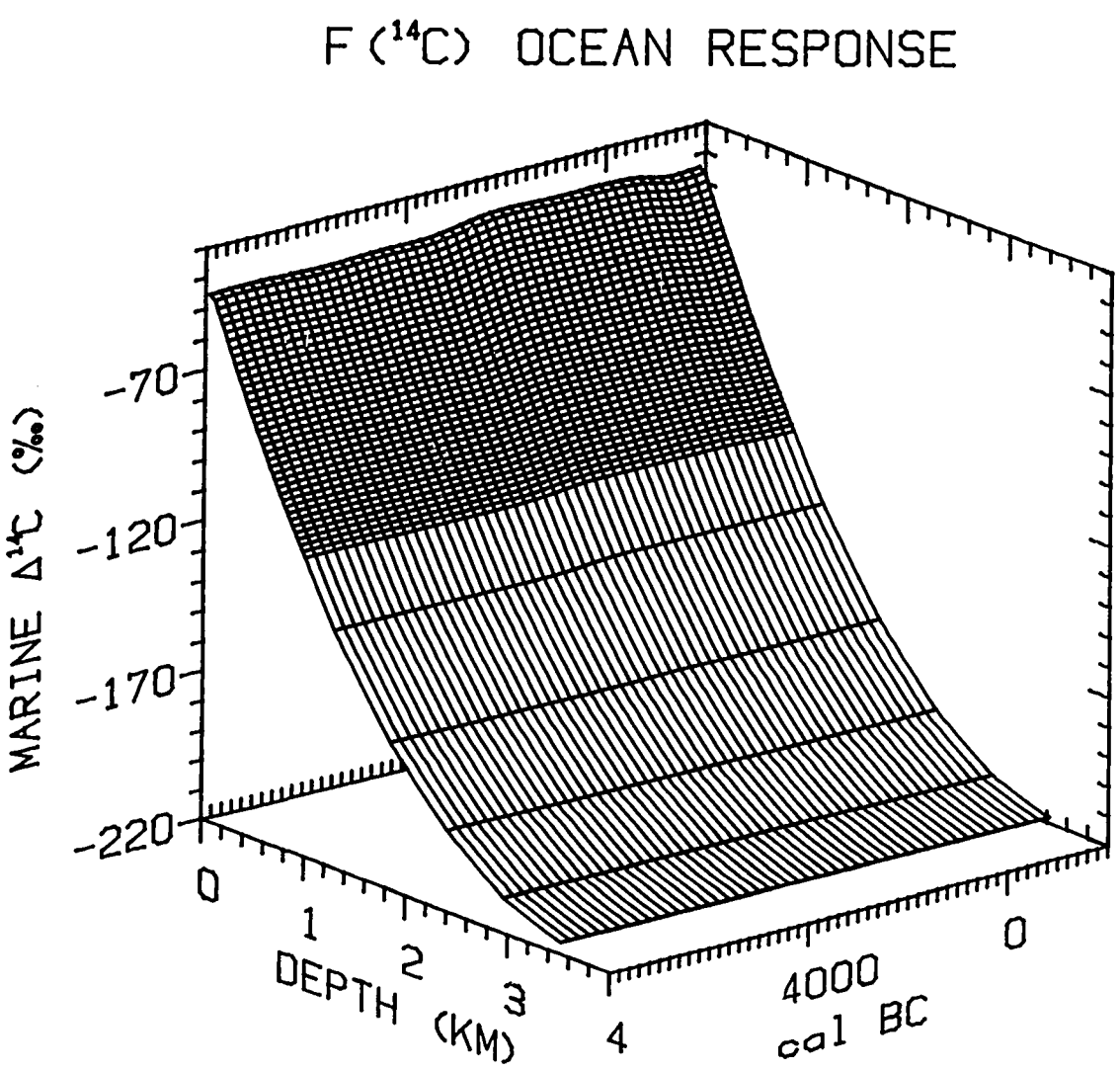
F (^{14}C) OCEAN RESPONSE
MARINE Δ^{14}C (‰)
-70
-120
-170
-220
0
1
2
3
4
DEPTH (KM)
4000
0
cal BC

rate between the small model atmosphere (containing 1.4% of global carbon and 1.7% of global ^{14}C) and immense model ocean (with 94% of global carbon and 93% of global ^{14}C).

The precision of the state and rate variables in the F-deconvolution model was doubled in order to detect the modest changes in these quantities when the ocean reservoir is subjected to such reduced ^{14}C perturbations. Whereas, in an F-deconvolution simulation including a variable production rate (see section 2.5), the net atmosphere and thermocline fluxes with the surface ocean reservoir differ at any time step by as much as 40%, these differences are reduced to 4% or less when the production rate is constant.

The diminished sensitivity of atmospheric $\Delta^{14}C$ change to air-sea gas exchange rate relative to production variations is a consequence of the altered difference between invasion and evasion ^{14}C fluxes that accompanies F changes. If "steady-state" production rate of atmospheric ^{14}C is reduced 7.5%, the net flux of atmospheric ^{14}C must be similarly reduced (neglecting decay and exchange with the terrestrial biosphere). However, such a ^{14}C flux reduction *increases* the difference between atmospheric $\Delta^{14}C$ and surface ocean $\Delta^{14}C$ by ca. 7.5% or 75 °/oo (cf. figure 2.9) necessitating a greater reduction in F to counterbalance the larger ^{14}C differential. In equation format, letting Q = F (1.0 - .95), the discussed change becomes (1-.075) Q = x F (1.0 - (.95-.075)) where x, the factor representing the fractional change in F, can be calculated as .37 (ie. a 63% reduction).

The F-deconvolution model simulates a gas exchange rate remaining nearly constant during the first half of the Holocene, then rising sharply to a peak of 46 moles CO_2 m^{-2} yr^{-1} in AD 500 in order to adequately increase the rate of oceanic uptake to draw down the atmospheric ^{14}C content as observed in the long-term trend (figure 2.11, dot-dash line).

This 550% amplification of F results from the simultaneous contraction in the air-sea $\Delta^{14}C$ difference (ie. difference between the short-short-long dashed line and dot-dashed line in figure 2.9). The air-sea CO_2 exchange must "work" harder when atmospheric and surface ocean ^{14}C concentrations are closer. As the atmospheric $\Delta^{14}C$ trend again ascends after AD 500, the gas exchange rate drops to a level near the "base-line" value assumed under constant climate conditions (solid line in figure 2.11).

Broecker et al. (1985a, 1986) summarize the evidence for the wind-speed dependence of air-sea piston velocity and CO_2 invasion rate. Wind/wave tunnel studies and ocean isotopic (natural ^{14}C, bomb ^{14}C, ^{222}Rn, ^{3}H) evidence generally accord with the linear dependency determined from experiments using an introduced tracer (SF_6) in a lake (Wanninkhof et al. 1985, Broecker et al. 1985a). The theory of gas transfer continues to develop and the exact wind-speed dependency, especially for winds greater than 13 m s^{-1}, is still unsettled (eg. Liss and Merlivat 1986). Satellite measurements of global winds have been utilized to test proposed relationships (eg. Erickson 1989). The dependency presented in Broecker et al. (1985a) remains a valid approximation.

The linear equation and an alternative nonlinear equation fit to the lake data are presented in Broecker et al. (1985a) as: P.V. = 2.2 (w.s. - 2) and P.V. = .22 $(w.s.)^2$ where "P.V." is the piston velocity of SF_6 in cm hr^{-1} and "w.s." is wind speed in m s^{-1}. The piston velocity for SF_6 differs from CO_2 as determined by their diagnostic molecular diffusivities and kinematic viscosities (cf. Wanninkhof et al. 1985). P.V. of SF_6 is converted in figure 11 of Broecker et al. (1985a) into a CO_2 invasion rate (equivalent to F) in moles m^{-2} yr^{-1} that can be represented by the equations: F = 3.7 (w.s. - 2) and F = .37 $(w.s.)^2$. Both relationships associate a gas exchange of 19 moles CO_2 m^{-2} yr^{-1} with a wind speed of 7.2 m s^{-1}, a value that accords with the mean scalar wind speed estimated for the present world ocean (Broecker et al. 1985a, Table 8, from the atlas data of

Esbensen and Kushnir 1981). The linear equation was used to rescale the CO_2 exchange flux in figure 2.11 (left axis) into a measure of mean global wind speeds (right axis).

Winds drive the k_v component of air-sea gas transfer rather than F directly. A model piston velocity of 4.6 m day^{-1} (19 cm $hour^{-1}$) is associated with the "base-line" gas exchange of 19 moles CO_2 m^2 yr^{-1}, as calculated from the invasion rate equation: $F = k_v S pCO_2$ where k_v is the piston velocity in m yr^{-1}, S is the solubility in water of CO_2 equal to ca. 40 moles m^{-3} atm^{-1} (Broecker and Peng 1974), and pCO_2 is the partial pressure of CO_2 equal to 280 ppm in our preindustrial atmospheric reservoir. The wind-speed dependency for F derived by Broecker et al. (1985a) partially reflects the enhanced atmospheric pCO_2 of ca. 325 ppm during the GEOSECS measuring period. Thus a correction of 280/325 should be applied to the two equations for the wind dependence of CO_2 exchange rate, expanding the wind-speed axis in figure 2.11 by 16%. However, the "base-line" gas exchange of 19 moles CO_2 m^{-2} yr^{-1} then corresponds to an inflated mean global wind speed of 8 m s^{-1}. The original F relationships presented in Broecker et al. (1985a) were retained to derive conservative estimates for the global wind-speed scenario associated with the deconvolved F history.

The deconvolved Holocene CO_2 exchange rate varies from 60% less to 140% more than the "base-line" level (figure 2.11). If climate-related variations in air-sea CO_2 gas exchange are responsible for the long-term trends in atmospheric $\Delta^{14}C$, the linear and nonlinear relationships stated above require low mean global winds of 4 or 4.5 m s^{-1}, respectively, during the early Holocene and maximum speeds of 14.5 or 11 m s^{-1}, respectively, near AD 500.

Microparticle concentrations in ice cores are related to snow accumulation rate, volcanic activity, available dust sources such as deserts and exposed continental shelves, and global wind strengths. Holocene microparticle concentrations in ice cores from both

the North and South Pole regions are dramatically reduced (by factors of 2.5 to 30) from their concentrations during the late-glacial stage (Petit et al. 1981). The seasonal resolution of the microparticle analyses especially for the later Holocene (see references compiled in Petit et al. 1981) convincingly establishes the uniformity in the low concentration levels during the Holocene. If, as Petit et al. (1981) infer, the higher late-glacial microparticle concentrations were induced in part by a 50% increase in regional and global wind speeds (to perhaps 11 m s^{-1}), then the late Holocene wind strength exhibited in figure 2.11 for the variable F scenario should be reflected in a late Holocene inflation in microparticle concentration by perhaps an order or magnitude. Thus the microparticle evidence does not support the changes in global wind speeds required for an air-sea exchange-rate origin for the Holocene-scale trend in atmospheric $\Delta^{14}C$.

The grain-size distribution of aeolian-marine dust in sediment cores from the subtropical Atlantic reflects in part the strength of the trade winds; variations in these winds, in turn, may indicate changes in atmospheric circulation on a global scale. From such data, Sarnthein et al. (1987) have reconstructed a 50,000-yr history of trade wind speeds, the Holocene portion of which displays more variablility than the microparticle concentrations indicate. This record, as well as the remaining model curves in figure 2.11, will be discussed in section 2.5. Here I will only note that the proposed Holocene pattern in trade winds is converse to the modeled F trend compatible with the long-term atmospheric $\Delta^{14}C$ curve.

The ocean is unresponsive to variations in F, showing only secondary changes at the surface during the rapid late-Holocene increase in gas exchange rate (figure 2.12). Surface ocean $\Delta^{14}C$ remains near -50 ‰ while deep ocean $\Delta^{14}C$ is stable near -180 ‰. Therefore the model ventilation index is nearly constant at 1275 ^{14}C yrs throughout the Holocene (figure 2.5, dot-dash line). Such a scenario for oceanic behavior cannot be

rejected by comparison with the foram ^{14}C data.

The preferred choice for the constant production rate (Q_c = 1.55 ^{14}C atoms s^{-1} cm_E^{-2}) generated a recent gas exchange rate (24 moles CO_2 m^{-2} yr^{-1}) similar to the "base-line" estimate (figure 2.11); the simulation's recent oceanic $\Delta^{14}C$ values also conform to the inferred pre-anthropogenic ^{14}C profile. The alternative choice for the constant production rate (Q_c = 1.46 ^{14}C atoms s^{-1} cm_e^{-2}; see above), together with the observed long-term trend in atmospheric $\Delta^{14}C$, deconvolves a Holocene history of dramatically diminished gas exchange rates that are never stronger than 50% of the "base-line" rate of 19 moles CO_2 m^{-2} yr^{-1}. As discussed in regard to the K_Z scenario, the value for Q_c might be adjusted to match the deconvolved recent F history with the "base-line" value, but this modification does not alter the basic pattern in the modeled F nor its deficiencies noted above.

In conclusion, the Holocene history of mean global wind speeds that is required to explain (through variations in air-sea CO_2 exchange rate F) the millennium-scale trends in atmospheric $\Delta^{14}C$ is not supported by independent evidence such as the microparticle concentrations in ice cores or the dust grain sizes in ocean sediment cores. Although we reject a variable F as the sole mechanism driving the Holocene trend in atmospheric $\Delta^{14}C$, the influences of a variable F combined with variations in ocean ventilation or in ^{14}C production rates were also investigated (see next subsection and section 2.5).

Coincident variations in diffusivity and gas exchange

Climatic regimes are characterized by many features including atmospheric and oceanic circulation rates which may be interrelated in complex ways. One proposed climate "interconnection" (eg. Lal 1985) prescribes that, when the meridional temperature gradient is reduced such that less poleward heat transport is required (during warmer

climatic periods), atmospheric winds become weaker (thus model F decreases) and the oceanic thermohaline circulation diminishes (thus model K_Z decreases as well). Although this simple relationship accords with some model analyses favoring enhanced oceanic ventilation rates during glacial stages (eg. Broecker and Takahashi 1984), the cessation of North Atlantic Deep Water Formation during glacial times is also convincingly in evidence (eg. Broecker et al. 1985b).

A single-parameter concept for ocean ventilation is difficult to retain for extensive climate variations on a glacial/interglacial scale; high-latitude processes in both hemispheres (eg. Toggweiler and Sarmiento 1985, Wenk and Siegenthaler 1985) and intermediate/deep water mixing rates (Boyle 1988) are important features to incorporate into global carbon models. However, for climatic changes within the Holocene, the K_Z parameter is a practical concept; and simpler joint changes in climatic variables, such as the F,K_Z-covariance proposed above, may occur.

A global ^{14}C model was programmed to deconvolve concomitant and equivalent relative changes in air-sea CO_2 exchange rate and vertical oceanic mixing that are compatible with specific records of atmospheric $\Delta^{14}C$ and ^{14}C production. Specifically, the F,K_Z-deconvolution model recalculates, at every time step, the gas exchange rate necessary to balance the atmospheric $\Delta^{14}C$ record and the assumed ^{14}C production rate; the K_Z parameter is recalculated simultaneously to reflect the same relative change as between the updated and prior F values. In this way, the requisite climatic perturbations were partitioned equally between wind-driven exchange at the air-sea boundary and internal oceanic mixing. Although the reality of this interrelated climate scenario cannot be verified, the model simulation allows an assessment of the strength and direction of potential "feedbacks" of equivalent multi-parameter changes on atmospheric $\Delta^{14}C$.

The previously described long-term atmospheric $\Delta^{14}C$ trend and preferred ^{14}C

production-rate constant served to "force" the joint exchange-parameter histories during the Holocene. The initial "steady-state" atmospheric $\Delta^{14}C$ of 90 ‰ is maintained by a "steady-state" gas exchange rate and eddy diffusivity that are 36% below "base-line" conditions (ie. F = 12 moles CO_2 m^{-2} yr^{-1} and K_Z = 2550 m^2 yr^{-1}).

The K_Z history that accompanies the equivalent relative variations in F closely resembles the K_Z history that would alone explain the long-term atmospheric $\Delta^{14}C$ trend; however, relative to the "base-line" level, the early Holocene reduction in K_Z is only 85% as low and the maximum K_Z near AD 500 is only 60% as high as the latter K_Z variations (figure 2.5 inset, short-long dashed line). Analogously, the gas exchange history from the F,K_Z-deconvolution follows the same trend as the F history that alone would explain the Holocene-scale atmospheric $\Delta^{14}C$ record, but the early Holocene depression in F is only 60% as low and the peak at AD 500 is only *20%* as high as the latter record. When the atmospheric ^{14}C forcing is split equally, both F and K_Z vary from -37% to +25% (relative to their respective "base lines") during the Holocene.

When relative variations in F and K_Z are simultaneous and identical, the effect on atmospheric $\Delta^{14}C$ is reinforcing: the required digressions in both exchange processes are reduced from the deconvolved histories for each parameter operating alone. But, rather than simply attenuating the variance in each history by 50%, the reinforcement more severely affects the Holocene trend in the CO_2 exchange rate. This asymmetry is primarily explained by the greater sensitivity of atmospheric $\Delta^{14}C$ to variations in K_Z compared to F, as apparent from the different "steady-state" responses discussed above. When equivalent relative variations in F and K_Z are responsible for atmospheric $\Delta^{14}C$ change, the stronger influence of K_Z on atmospheric $\Delta^{14}C$ translates into a greater contraction of the F trend from its solo pattern.

The transience in the joint histories complicates the explanation because the F and K_Z

response at any time step is linked not only to the atmospheric ^{14}C content but also to the oceanic ^{14}C profile derived from the past histories in these exchange processes. The problem of interpreting the "feedback" effects for joint parameter variations is further compounded because, as noted before, the sensitivity of atmospheric $\Delta^{14}C$ to changes in K_Z and F at any point in time is also a function of the magnitude of the oceanic vertical ^{14}C gradient and of the atmosphere/surface ocean ^{14}C disparity, respectively.

The model ventilation index associated with the joint F/K_Z histories described above (figure 2.5, short-long dashed line) more closely resembles the MVI curve for the unaccompanied K_Z scenario (equi-dashed line) than MVI for the unaided F scenario (dot-dashed line). Thus, even when the climate-related forcing is partitioned equally between air-sea exchange rate and internal oceanic mixing, the resultant MVI trend transgresses the range in foram ^{14}C data. Furthermore, the mean scalar wind speeds associated with the joint F/K_Z simulation, as calculated from the linear relationship of Broecker et al. (1985a), range from 5.2 m s^{-1} between 8000 and 4000 BC to a peak of 8.4 m s^{-1} at AD 500. These digressions of -25% to +20% in Holocene wind speeds are not compatible with the microparticle data described above. For these reasons, this specific joint climate scenario, comprising equivalent relative variations in F and K_Z, is also rejected as the explanation for long-term atmospheric $\Delta^{14}C$ variation.

Sensitivity of model results to initial conditions

The four hypothetical pre-Holocene histories in atmospheric $\Delta^{14}C$ described in section 2.1 were again utilized to test the sensitivity of model results to initial conditions (figure 2.13, upper right panel). However, we now assume that each of these four alternative trends has a climatic origin and derives from Pleistocene/Holocene transitions in K_Z or F. As in the climatic deconvolutions discussed above, the ^{14}C production rate is

Figure 2.13: Deconvolved model eddy diffusivities required to generate 4 hypothetical pre-7750 BC atmospheric $\Delta^{14}C$ histories. The 4 atmospheric records commence with "steady-state" $\Delta^{14}C$ levels of 0, 50, 90, or 140 ‰ prior to 11,000 BP (9050 BC) and then advance linearly to the 90 ‰ level assigned to the beginning of the tree-ring record (upper right panel). The ^{14}C production rate remains constant (upper left panel). The lettering of the 4 deconvolved K_z histories (bottom panel) corresponds to the respectively lettered atmospheric scenarios.

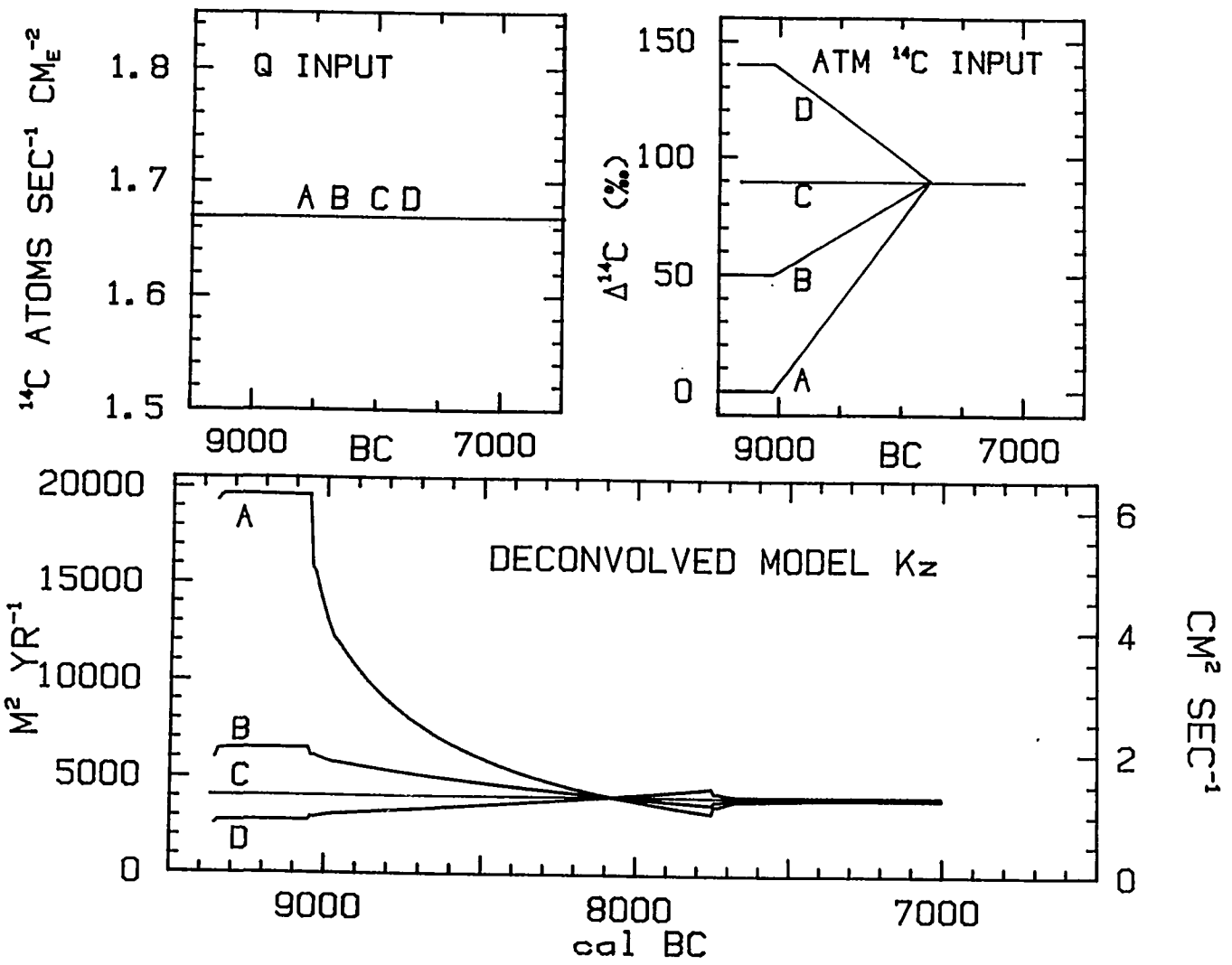
Q INPUT
A B C D
^{14}C ATOMS SEC^{-1} CM_E^{-2}
1.8
1.7
1.6
1.5
9000
BC
7000
ATM ^{14}C INPUT
D
C
B
A
$\Delta^{14}C$ (‰)
150
100
50
0
9000
BC
7000
DECONVOLVED MODEL Kz
A
B
C
D
M^2 YR^{-1}
20000
15000
10000
5000
0
CM^2 SEC^{-1}
6
4
2
0
9000
8000
7000
cal BC

assumed constant during the simulation (figure 2.13, left upper panel). I chose a Q_c value of 1.67 ^{14}C atoms s^{-1} cm_E^{-2} because this production rate maintains an early Holocene atmospheric $\Delta^{14}C$ level of 90 °/oo if K_z and F represent the standard "base-line" conditions of 4000 m^2 yr^{-1} and 19 moles CO_2 m^{-2} yr^{-1}, respectively. In this way, we can test the influence of different climate-related pre-11,000 BP (9050 BC) "steady states" in K_z and F on the hypothetical Holocene histories of these parameters presented above.

The $K_z(^{14}C)$ trends derived from the K_z-deconvolution model are conversely related to the assumed atmospheric $\Delta^{14}C$ record (figure 2.13, lower panel). As noted before, oceanic mixing must diminish in order to permit more ^{14}C to remain in the atmosphere and surface ocean. If a change in K_z was responsible for a hypothetical pre-11,000 BP atmospheric $\Delta^{14}C$ level of 0 °/oo (but not for the Holocene variations in atmospheric $\Delta^{14}C$), then K_z must have been 20,000 m^2 yr^{-1} prior to 11,000 BP only to decrease swiftly to "base-line" values at the start of the tree-ring $\Delta^{14}C$ record in 7750 BC. The analogous "steady-state" K_z values for alternative atmospheric $\Delta^{14}C$ levels of 50, 90, and 140 /oo are 6500, 4000, and 2800 m^2 yr^{-1}, respectively. In all cases, the recovery curve from these initial mixing rates to the standard "steady-state" Holocene diffusivity is constrained by the transition period in atmospheric $\Delta^{14}C$ with little perturbation effects on the post-7750 BC K_z deconvolution.

Model ventilation ages of 275, 800, 1275 and 1750 ^{14}C yrs (figure 2.8, right) are derived from the oceanic $\Delta^{14}C$ changes induced by the four hypothetical K_z histories which are required to explain the alternative atmospheric $\Delta^{14}C$ "steady states" of 0, 50, 90, and 140 °/oo, respectively. The most extreme MVI curves (associated with scenarios A and D) transgress the foram ^{14}C observations. Thus these two pre-Holocene atmospheric $\Delta^{14}C$ scenarios are not convincingly explained by variations in ocean mixing.

The oceanic $\Delta^{14}C$ responses to the same set of pre-Holocene atmospheric $\Delta^{14}C$ scenarios have contrasting natures when the assumed driving mechanism is variable ^{14}C production or variable eddy diffusion (figure 2.8, left vs. right side). If Q is entirely responsible for the changes in pre-Holocene atmospheric $\Delta^{14}C$, the memory of past ^{14}C production continues to affect the ^{14}C contents of the ocean (and terrestrial biosphere) well after the alternative pre-Holocene atmospheric $\Delta^{14}C$ transitions have occurred. If K_z is entirely responsible for the changes in pre-Holocene atmospheric $\Delta^{14}C$, the oceanic recovery (ie. the redistribution of the oceanic ^{14}C contents) is rapid enough that the impact on the Holocene ^{14}C system is negligible.

Generalizing from these distinctive responses, if pre-Holocene variations in atmospheric $\Delta^{14}C$ -- no matter how extreme -- were induced by climatic events rather than ^{14}C production changes, such variations make a minimal impression on the Holocene ^{14}C system. The pre-Holocene digressions in eddy diffusion need not be considered for an accurate portrayal of the early Holocene K_z history; the deconvolution of Q for the early Holocene, however, depends more sensitively on the Q changes that have come before. The fundamentally different responses reflect the ability of the deep ocean with a ventilation rate of ca. 1000 yrs to recover more quickly from a climate-induced *redistribution* in reservoir ^{14}C than to eject previously *produced* ^{14}C with a mean life of ca. 8000 yrs.

The slow 100 °/oo long-term decline in atmospheric $\Delta^{14}C$ during the Holocene, then, cannot merely represent a recovery from pre-Holocene climatic conditions. The ice-age simulation of Toggweiler and Sarmiento (1985), for example, indicates that an atmospheric $\Delta^{14}C$ level of ca. 100 °/oo may have accompanied reduced oceanic ventilation. However, this climate-induced enrichment could not have alone caused the elevated $\Delta^{14}C$ levels of the early Holocene because the atmospheric recovery would have

been much more rapid than observed. An increased ^{14}C production rate or climatic variations during the Holocene are implicated by the slow atmospheric ^{14}C decline. The greater oceanic ventilation time of ca. 1750 ^{14}C yrs for the simulated glacial ocean of Toggweiler and Sarmiento is not evident in the early Holocene foram ^{14}C data but this absence is expected because the Holocene marine reservoirs will also recover quickly from their pre-Holocene conditions.

The Q- and K_Z-forced model ventilation curves represent inherently different reactions of the oceanic ^{14}C system to disturbance. Each Q-forced MVI curve reflects the transient adjustment of the ocean system operating to re-establish its *equilibrium* ^{14}C configuration which, in association with K_Z, is identical (KVI = 1275 ^{14}C yrs) before, during and after the atmospheric $\Delta^{14}C$ transition. These MVI curves are functions of the magnitude *and* duration of the atmospheric $\Delta^{14}C$ transition; as noted above, the perturbation in the oceanic ^{14}C profile is less pronounced when the linear recovery from the hypothetical pre-Holocene "steady-state" atmosphere is simulated as more gradual.

In contrast, each K_Z-forced MVI curve reflects the adjustment of the ocean system operating to establish a *new* equilibrium ^{14}C configuration which varies in conjunction with the changing ocean mixing rate. Rather than being artifacts of an external Q forcing, the latter model ventilation curves represent actual changes in the oceanic ventilation rate and, in fact, closely approximate the true histories in the ventilation indices (KVI) as can be defined by the deconvolved K_Z trends (figure 2.13). Because the K_Z-forced MVI curves trace real trends in ocean mixing, a change in the duration of the transition from pre-Holocene "steady state" to standard Holocene conditions does not affect the magnitude of the MVI digression, only its timing.

The F(^{14}C) trends derived from the F-deconvolution model are conversely related to the four alternative atmospheric $\Delta^{14}C$ histories (figure 2.14). Like internal ocean mixing,

Figure 2.14: Deconvolved air-sea CO_2 exchange rates required to generate 4 hypothetical pre-7750 BC atmospheric $\Delta^{14}C$ histories. The 4 atmospheric records commence with "steady-state" $\Delta^{14}C$ levels of 0, 50, 90, or 140 ‰ prior to 11,000 BP (9050 BC) and then advance linearly to the 90 ‰ level assigned to the beginning of the tree-ring record (upper right panel). The ^{14}C production rate remains constant (upper left panel). The lettering of the 3 deconvolved F histories (bottom panel) corresponds to the respectively lettered atmospheric scenarios; atmospheric $\Delta^{14}C$ history "A" cannot be explained by variations in F (see text).

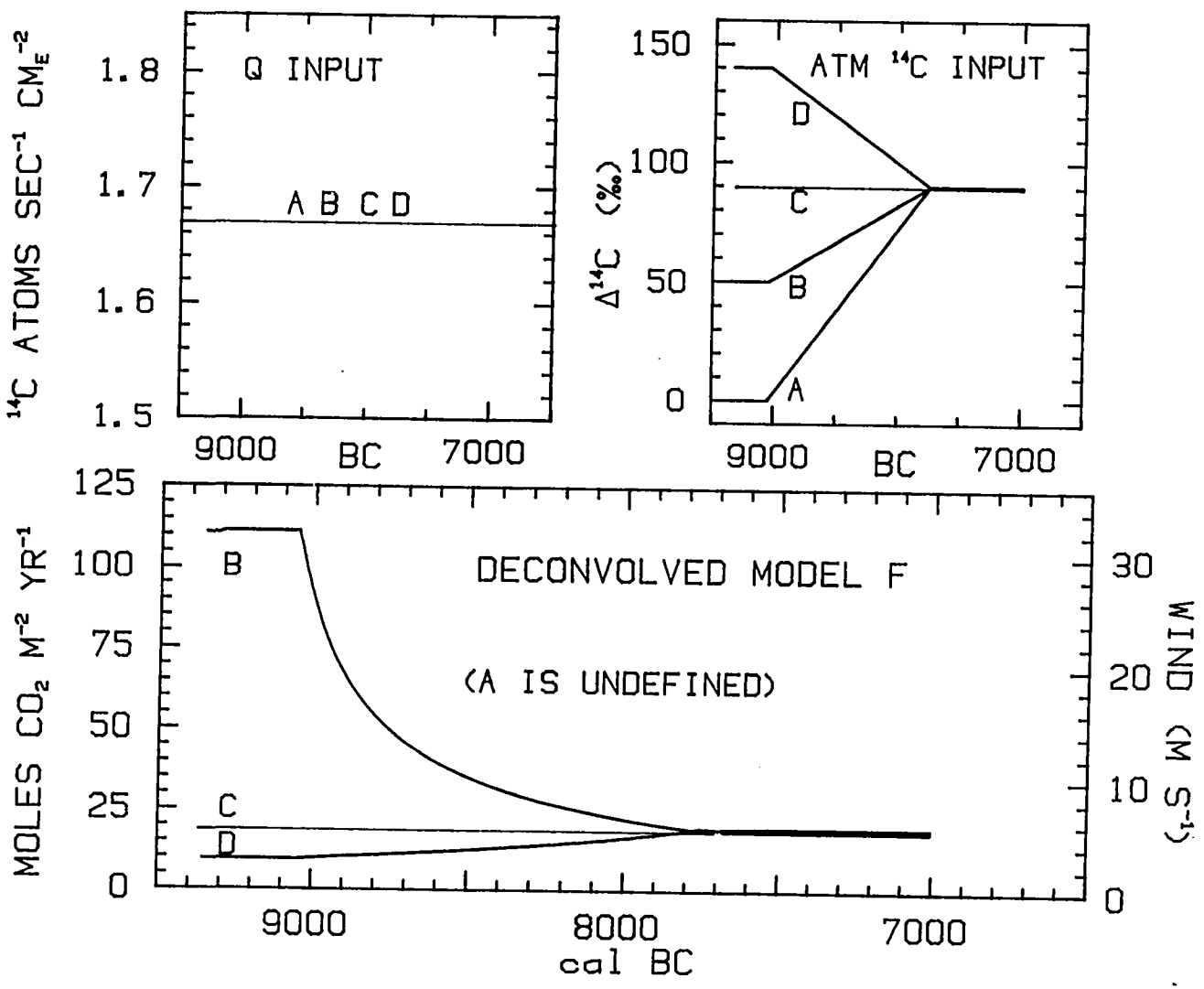
Q INPUT
A B C D
^{14}C ATOMS SEC^{-1} CM$_E^{-2}$
1.8
1.7
1.6
1.5
9000
BC
7000
ATM ^{14}C INPUT
D
C
B
A
Δ^{14}C (‰)
150
100
50
0
9000
BC
7000
DECONVOLVED MODEL F
(A IS UNDEFINED)
B
C
D
MOLES CO$_2$ M^{-2} YR^{-1}
125
100
75
50
25
0
WIND (M S^{-1})
30
20
10
0
9000
8000
7000
cal BC

the air-sea exchange rate must diminish in order to permit more ^{14}C to remain in the atmosphere. Atmospheric "steady-state" $\Delta^{14}C$ values of 50, 90, and 140 ‰ require gas exchange strengths of 110, 19, and 9 moles CO_2 m^{-2} yr^{-1}, respectively. With the level assumed for ^{14}C production rate (figure 2.14, left panel) and oceanic mixing (K_z at "base-line" conditions), a low value of 0 ‰ in atmospheric $\Delta^{14}C$ cannot be maintained by any air-sea CO_2 exchange rate. At "steady state", the ^{14}C production rate determines the ^{14}C content of the large deep ocean reservoir; the eddy diffusion, in turn, is a prime determinant of the surface ocean ^{14}C contents relative to the deeper reservoir. These restrictions impose a surface ocean ^{14}C concentration too high to permit an atmospheric $\Delta^{14}C$ of only 0 ‰ even with an infinitely large F (which equalizes the atmospheric and surface ocean $\Delta^{14}C$ values).

The influence of the atmosphere/surface ocean $\Delta^{14}C$ disparity produces a nonlinearity in the relationship of "steady-state" gas exchange to atmospheric ^{14}C level. A five percent (50 ‰) increase in the initial "steady-state" atmospheric $\Delta^{14}C$ (scenario D) requires a 50% decrease in F whereas a 4% (40 ‰) *decrease* in the initial "steady-state" atmospheric $\Delta^{14}C$ (scenario B) necessitates a 500% increase in gas exchange!

According to the linear wind-speed dependence of CO_2 gas exchange in Broecker et al. (1985a), the "steady-state" F values for scenarios B and D correspond to global wind speeds of 32 and 4.5 m s^{-1}, respectively, or deviations of +350% and -33% from "base-line" conditions. Microparticle evidence from ice cores supports late-glacial wind speeds perhaps 50% above Holocene conditions, much less extreme than required by an F-forced pre-Holocene atmospheric $\Delta^{14}C$ of 50 ‰ and contrary to the trend implied by elevated pre-Holocene atmospheric ^{14}C levels.

The histories of the model ventilation index associated with these alternative F-forced

atmospheric $\Delta^{14}C$ scenarios all vary by less than twenty ^{14}C years from the standard MVI of 1275 ^{14}C yrs. This insensitivity means that the foram ^{14}C observations do not help to distinguish or reject any of these alternatives.

In summary, if the Pleistocene/Holocene differences in atmospheric $\Delta^{14}C$ are primarily induced by climate (in the guise of exchange parameters K_Z and/or F) rather than ^{14}C production rate, the impact on the oceanic ^{14}C contents during the Holocene is insignificant. Distinct alternative pre-Holocene histories in F and K_Z have little bearing on the deconvolved Holocene trends of these parameters whereas the pre-Holocene history of ^{14}C production moderately affects the earlier portion of the deconvolved Holocene Q record. Neither the foram ^{14}C data nor the ice-core microparticle records support climatic origins for the two most extreme Pleistocene/Holocene scenarios in atmospheric $\Delta^{14}C$.

Climatic events and ^{14}C production rate changes may *both* have occurred during the time of the Pleistocene/Holocene transition. Independent proxies for ^{14}C production rate variations, such as long-term data on the geomagnetic dipole moment and ^{10}Be concentrations in ice cores, may allow the "Q component" in the atmospheric $\Delta^{14}C$ record to be extracted. The next two sections present the evidence for Holocene variations in the ^{14}C production rate. In section 2.5, the K_Z-, F-, and F,K_Z-deconvolution models are used to calculate the "residual" climate forcing required to produce the atmospheric $\Delta^{14}C$ record when a specific ^{14}C production rate is assumed. In addition, alternative couplings of Q and climate forcings are considered for the four hypothetical pre-Holocene atmospheric $\Delta^{14}C$ scenarios presented above.

Alternative roles for climate in long-term reservoir $\Delta^{14}C$ change

In addition to variations in oceanic mixing and air-sea gas exchange, a variety of other climate-related changes in the global ^{14}C system might occur during the Holocene. The

simple box-diffusion model is incapable of simulating some of these alterations while other proposed climate-induced parameter modifications are speculative and difficult to verify. A brief discussion follows of some of the climate-induced $^{14}C/^{12}C$ perturbations that were not modeled. These atmospheric $^{14}C/^{12}C$ perturbations may result primarily from atmospheric $^{12}CO_2$ variations or from changes in source $^{14}C/^{12}C$ signals directly.

Atmospheric pCO_2: Variations in atmospheric pCO_2 influence the ^{14}C exchange rates between the atmosphere, ocean, and terrestrial biosphere (see equations in section 1.4). The global carbon modeling undertaken here has assumed the constancy in ^{12}C contents of all reservoirs. Yet during the Holocene atmospheric pCO_2 changes of approximately ±7% (ie. ±20 ppm) are recorded in the ice-core CO_2 measurements from Byrd station in Antarctica (Neftel et al. 1988). Such variations may result from inbalances in the carbon exchanges represented in the box-diffusion model by F, K_Z, and B_T.

A net carbon flux from the terrestrial biosphere is implicated in at least one apparent 10-ppm digression in atmospheric CO_2 near AD 1300 (as measured in an ice core from the South Pole) provided the synchronous change in atmospheric $^{13}CO_2$ is verified by more data (Siegenthaler et al. 1988). From a 2000-yr record of decadal tree-ring $\delta^{13}C$ (assumed to reflect atmospheric $\delta^{13}C$ variations), carbon reservoir modeling has deconvolved a history of hypothetical terrestrial biospheric carbon fluxes; these fluxes would have generated Holocene atmospheric pCO_2 excursions on the order of ±10 ppm (Stuiver and Braziunas 1986, Stuiver et al. 1984). The tree-ring $\delta^{13}C$ history may instead derive from changes in atmosphere/biosphere fractionation induced by Holocene global temperature and/or humidity variations (Stuiver and Braziunas 1987); such climatic diversions might also have disturbed atmospheric pCO_2 through modifications in its exchanges with the other reservoirs.

In a one-dimensional ocean with a vertical gradient in ΣCO_2, a decrease in ocean mixing K_z without a change in particulate flux would cause a decrease in atmospheric pCO_2 because of reduced contact with the deep ocean (eg. Keir 1983, Lal 1985). However, the particulate flux co-varies with ocean mixing to strip the surface ocean of its supply of limiting nutrients (phosphate and nitrate), maintaining a steady pCO_2 in the surface ocean and, subsequently, in the atmosphere (when the global surface ocean is presumed to always lack nutrients). When K_z-independent forces alter the biological pump, eg. marine organisms incorporate a different C/P ratio or the nutrient content of the ocean is reduced by storage on submerged continental shelves, atmospheric pCO_2 can be substantially affected (as recapitulated in Broecker and Peng 1982). But, although such dramatic biological modifications may occur during glacial/interglacial transitions, these events are not expected during the Holocene. By neglecting marine biology, our box-diffusion model lacks the vertical gradient in marine ΣCO_2 (and $\Sigma^{13}CO_2$); in effect, however, the model assumes that compensatory processes such as biological pumping will counter atmospheric (and oceanic) pCO_2 variations related to changes in ocean mixing. In any case, as discussed below, pCO_2 variations have only a secondary effect on atmospheric $\Delta^{14}C$.

The oceanic processes that specifically occur in polar regions appear crucial to the explanation of atmospheric pCO_2 increase during glacial/interglacial transitions (eg. Broecker and Takahashi 1984, Toggweiler and Sarmiento 1985, Wenk and Siegenthaler 1985). The thermohaline circulation is comprised of deep water formation at high latitudes and upwelling in lower latitudes; in addition, convective interchanges between surface and deep polar waters occur during the winter season; finally, at high latitudes nutrient utilization is incomplete and potentially variable. These processes have been integrated into the fundamental ocean mixing parameter K_z in the box-diffusion model. Yet the

atmospheric pCO_2 is especially sensitive to high-latitude carbon exchanges (see below).

An indication of the distinct role of polar oceans on carbon cycling is the contrary response of atmospheric pCO_2 to greater oceanic "ventilation" when high-latitude processes are incorporated into the ocean model. In such a model, a decrease in ocean mixing (ie. themohaline ventilation) produces an *increase* in atmospheric pCO_2 through the dominant effect of high-latitude surface ocean pCO_2 on the pCO_2 of the atmosphere and low-latitude surface ocean (eg. Broecker and Takahashi 1984, Toggweiler and Sarmiento 1985). But because the lower atmospheric pCO_2 of the last glacial stage was apparently accompanied by less rather than greater deep-water formation, compensatory changes in other co-varying high-latitude processes (ie. convective interchanges and/or biological productivity) must have occurred.

Regardless of the origin for changes in atmospheric pCO_2, the pCO_2 change itself has a secondary effect on the atmospheric $\Delta^{14}C$ content. The source for this atmospheric $\Delta^{14}C$ change is the pCO_2-dependence of the air-sea gas exchange which determines the degree of communication between the atmosphere and the ^{14}C-depleted surface ocean. We have calculated before that, if atmospheric $\Delta^{14}C$ is constant and ^{14}C production decreases by 7.5%, then the air-sea invasion rate must decrease 63% (ie. by a factor of 8.5) in order to counter the greater air/surface ocean $\Delta^{14}C$ disparity. A "scaling effect" also occurs when, instead, ^{14}C production remains constant and atmospheric $\Delta^{14}C$ is allowed to vary with changes in the air-sea invasion rate. In this case we find that a 7% increase in F (induced by a 20 ppm increase in atmospheric -- and surface ocean -- pCO_2 in equation 1.1) generates only a 3.5 ‰ *decrease* in atmospheric $\Delta^{14}C$ (a reduction factor of -1/20).

The insensitivity of atmospheric $\Delta^{14}C$ to variations in F and, thus, atmospheric pCO_2 is explained by: (1) the constancy in the net $^{14}CO_2$ gas flux, equivalent to F (R_a -

R_S), required at "steady state" if ^{14}C production remains constant and (2) the essential stability of the ^{14}C contents of the ocean (and thus R_S) when the ^{14}C production is unchanged. To maintain a constant net $^{14}CO_2$ gas flux, a 7% increase in F must be balanced by a ca. 7% reduction in (R_a - R_S). Inserting the pre-disturbance values for relative ^{14}C activities yields: F (1 - .95) = 1.07 F (1 + x - .95) where x represents the fractional increase in the atmospheric relative ^{14}C activity required to balance the new and old invasion rates. The solution for x is -(.05)(.07)/1.07 or -3.5 ‰. Thus a variation in atmospheric pCO_2 of ±20 ppm produces only a minor deviation in the atmospheric $\Delta^{14}C$ level.

$^{14}C/^{12}C$ signals: As demonstrated by the deconvolution modeling presented above, air/sea gas exchange and other oceanic processes not only affect atmospheric $\Delta^{14}C$ secondarily through their control on atmospheric pCO_2 but are capable of a profound influence on atmospheric ^{14}C because of the ^{14}C deficiency in the oceanic reservoir. Several reservoirs with distinct $^{14}C/^{12}C$ signals (eg. polar oceans, terrestrial peatlands, and marine sediments) are not incorporated into the present structure of the box-diffusion model and are discussed briefly here.

The box and box-diffusion models without a high-latitude ocean reservoir produce a 10% increase in atmospheric $\Delta^{14}C$ for a 50% reduction in K_Z (Keir 1983; our results above). The box models that incorporate polar processes show a similar total sensitivity of atmospheric $\Delta^{14}C$ to combined components of ocean mixing despite the inclusion of a polar oceanic source of more deficient $\Delta^{14}C$ to the atmospheric reservoir (Wenk and Siegenthaler 1985, Toggweiler and Sarmiento 1985). The deficiency in high-latitude surface ocean $\Delta^{14}C$ is as extreme as ≤ -100 ‰ (eg. data compilations of Bard et al. 1989 and Stuiver and Braziunas 1985, preanthropogenic reconstruction of Broecker et al.

1985a). Yet atmospheric $\Delta^{14}C$ response to a change in ocean ventilation is unaffected by this feature.

The reason that a high-latitude oceanic outcrop has a significantly greater effect on atmospheric pCO_2 than on atmospheric ^{14}C is discussed in section 1.4. The high-latitude box models demonstrate that the sensitivity of atmospheric $\Delta^{14}C$ to changes in thermohaline circulation is about twice its sensitivity to high-latitude convective interchanges.

The CO_2 gas exchange between the polar surface ocean and the atmosphere is also missing in the simple box-diffusion model. High-latitude F has a disproportionate influence on atmospheric ^{14}C because of the greater high-latitude air-sea $\Delta^{14}C$ disparity. But the limited surface area of the polar outcrop counters this greater sensitivity. A box model yields a 25 ‰ increase in atmospheric $\Delta^{14}C$ for a 50% reduction in the high-latitude air-sea CO_2 exchange (Lal and Venkatavaradan 1970). This scaling factor of 1/20 matches the total scaling factor for the sensitivity of atmospheric $\Delta^{14}C$ to the globally-averaged air-sea gas exchange rate (discussed above). Thus climate-induced variations in polar air-sea exchanges have only an equivalent influence on atmospheric $\Delta^{14}C$.

In a one-dimensional ocean model, changes in marine production require co-variations in the ocean mixing parameter (except during major glacial/interglacial disturbances in nutrient dynamics). However, the particulate flux in the polar ocean is not nutrient-limited and may independently influence atmospheric $\Delta^{14}C$. Doubling the high-latitude particulate flux, however, only increases atmospheric $\Delta^{14}C$ by 3 ‰ (Wenk and Siegenthaler 1985), likely because of its influence on atmospheric pCO_2 (see above). The large refractory pool of oceanic dissolved organic carbon (DOC) may play a critical role in carbon cycling (eg. Sarmiento et al. 1988) but its ^{14}C and ^{12}C characteristics are controversial at present (Toggweiler 1988).

Obviously a one-dimensional ocean model lacks features required to properly simulate carbon system variations during a glacial/interglacial transition; the dynamics of such processes can only be treated distinctly in a transient ocean model with explicit high-latitude reservoirs. Yet, for the Holocene, carbon system variations are less extreme and K_Z may remain a valid statistical entity for the combination of physical processes that govern internal ocean mixing.

Variations in the terrestrial biosphere have a nominal effect on atmospheric $\Delta^{14}C$ primarily through changes in the atmospheric CO_2 content as discussed above. An imbalance in atmospheric exchange with older terrestrial carbon reservoirs in which most ^{14}C has decayed has a greater potential for modifying long-term atmospheric $\Delta^{14}C$. Carbon accumulation and release rates in peatlands and coastal wetlands may vary significantly with climatic and sea-level changes during the Holocene (Olson et al. 1985, Zoltai and Vitt 1990). The details on size and associated fluxes for these reservoirs are still speculative (Olson et al. 1985, Damon 1988) and this mechanism for long-term Holocene trends in atmospheric $\Delta^{14}C$ was not incorporated into the global carbon model.

Carbon in the upper 8 cm of marine sediments generally has ages of several thousand radiocarbon yrs because bioturbation mixes in older carbon from deeper sediment layers (Keir 1984). The extensive dissolution of marine sediments could decrease oceanic and atmospheric $\Delta^{14}C$ by introducing ΣCO_2 that is deficient in ^{14}C into the active system (Lal 1985, Lal et al. 1990). Indeed Keir (1984) suggests the occurrence of a mid-Holocene millennium-scale dissolution event, synchronous with enhanced coral reef growth, in order to explain anomalously old ^{14}C ages in the carbonate profiles of sub-lysocline Pacific sediment cores. Although my own modeling efforts did not include a simulation of such an event, the calculations of Lal (1985) indicate that a mid-Holocene dissolution peak and/or increase in river influx of dead carbon can explain the atmospheric $\Delta^{14}C$ decline

but that substantial flux perturbations are required with respect to prior "steady-state" conditions. Because the existence of a dissolution event is based on equivocal evidence with alternative explanations such as mechanical erosion or sedimentation rate change (Keir 1984), the proper timing and magnitude of the proposed flux perturbations is highly speculative.

Lal and co-authors remain strong proponents of a dominant climatic influence on Holocene-scale atmospheric $\Delta^{14}C$ variations because of the lack of viable alternatives. The geomagnetic evidence has large uncertainties and contains an enigmatic phase lag that hinders comparison with the ^{14}C production rate hypothetically associated with the atmospheric $\Delta^{14}C$ record; the ^{10}Be concentrations in ice cores appear to contradict the geomagnetic evidence of long-term Q variations (Lal 1985, Lal et al. 1990). We hope to show, however, that both the global dipole data and ice-core [^{10}Be] records strongly support a geomagnetic origin for millennium-scale Holocene variations in ^{14}C production and atmospheric $\Delta^{14}C$ (see section 2.3 and 2.4).

2.3 Evidence from the geomagnetic dipole moment for a production rate origin for reservoir $\Delta^{14}C$ variations

The theoretical basis for a geomagnetic influence on ^{14}C production was outlined in section 1.1 and will be detailed in the following pages. The measured long-term trend in the dipole moment is here converted to a trend in ^{14}C production rate, Q(DM), for comparison with the trend in ^{14}C production rate, Q(^{14}C), deconvolved from the atmospheric (tree-ring) $\Delta^{14}C$ record. The model-determined Q(^{14}C) history assumes no significant climatic changes to the carbon cycle during the Holocene. The derivation of

Q(DM) and its similarity to the smoothed Q(14C) curve is assessed before discussing the apparent "residual" influence of climate in section 2.5.

Geomagnetic dipole moment data

The global archeomagnetic intensity data on the dipole moment are reproduced from Merrill and McElhinney (1983) in figure 2.15. Samples consist largely of pottery and bricks associated with ashes from kilns and fireplaces whose radiocarbon ages are measured and calibrated to calendar ages. Past dipole moments are determined from the samples' thermoremanent magnetization (TRM) and are reported in units of A m^2 where A signifies amperes (one A m^2 being equivalent with 1000 Gauss cm^3 in the cgs system). The figure lists the number of samples incorporated into each averaged result (squares with ±2-sigma dipole ranges). The horizontal bar for each result represents the calendar interval it comprises.

The dipole data were originally grouped into 500-yr intervals and 1000-yr intervals before and after 4000 cal BP, respectively. However, in figure 2.15, the results prior to the 6500 ± 500 BP average have been recalibrated using a revised calibration method and, subsequently, the calendar intervals have expanded moderately. The proper assignment of calendar ages to the dipole data is critical in establishing that the problematic phase shift between the mid-Holocene declines of Q(DM) and the smoothed Q(^{14}C) cannot be eliminated simply by a revised calibration of these data (see below).

I recalibrated each average result and its calendar range by first reversing the original calibration procedure (described by McElhinny and Senanayake, 1982) in order to regenerate the original ^{14}C ages that would be associated with these averaged results. To produce new estimates for the calendar ages of the averaged results and their ranges, I then applied a new calibration program (Stuiver and Reimer 1986); or, for samples older than

Figure 2.15: Dipole moment averages in units of 10^{22} ampere-meter^2 from Merrill and McElhinny (1983). Number of samples comprising each average is indicated. The older data has been recalibrated (see text).

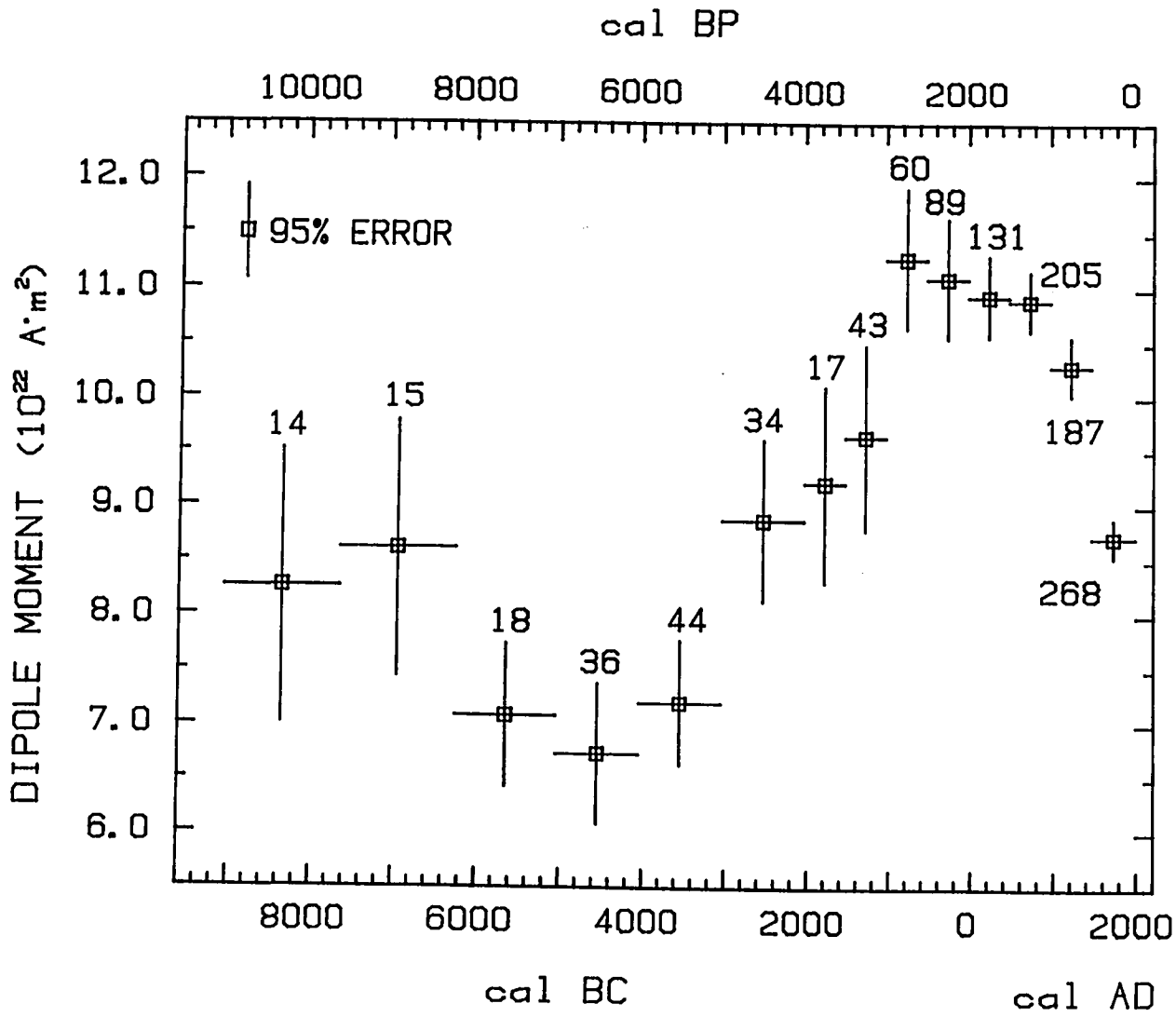
cal BP
10000
8000
6000
4000
2000
0
12.0
11.0
10.0
9.0
8.0
7.0
6.0
DIPOLE MOMENT (10^{22} A·m^2)
95% ERROR
14
15
18
36
44
34
17
43
60
89
131
205
187
268
8000
6000
4000
2000
0
2000
cal BC
cal AD

8100 ^{14}C yrs BP, I applied the linear equation x = 1.05R + 470 approximating the preliminary observed relationship between radiocarbon ages, R, and calendar ages, x, of older materials (Stuiver et al. 1986a). Ideally, the calendar age of each of the 1161 archeomagnetic samples should be recalibrated instead of merely the averaged results, but I decided to take this less precise first-order approach.

As a result of the recalibration, the averaged dipole results at 7500±500 B.P., 8500±500 B.P., 9500±500 B.P., 10,500±500 B.P., and 11,500±500 B.P. are reassigned calendar ages of, respectively, 7600±600 B.P. (5650 B.C.), 8900±700 B.P. (6950 B.C.), 10,300±700 B.P. (8350 B.C.), 11,500±500 B.P. (9550 B.C.), and 12,500±500 B.P. (10,550 B.C.). I will hereafter refer to the dipole data according to these recalibrated times. The averaged dipole results for the two latter intervals (not shown on figure 2.15) are highly uncertain, being based on only a few samples, and were not used in the standard model simulations. Including them, however, affected the model results insignificantly (see below).

The dipole moment in AD 1950 is 8.065 x 10^{22} A m^2 (Sternberg and Damon 1983) and the average dipole moment for the last ten 1000-yr intervals (now recalibrated in figure 2.15 to span 11,000 calendar years) is 8.75 x 10^{22} A m^2 (McElhinny and Senanayake 1982). Sporadic analyses undertaken since AD 1835 show that dipole intensity has decreased ca. 5% in a linear fashion to AD 1980 (Merrill and McElhinny, 1983, their fig. 2.10).

Since the geographic coverage of the TRM samples emphasizes the European region, changes in the local non-dipole field may color the data (McElhinny and Senanayake 1982). From an analysis of the relative timing in the millennial-scale intensity trends from separate geographic regions, Aitken et al. (1989) suggest that a major component of such

intensity records could be a westward-drifting non-dipole disturbance. McElhinny and Senanayake (1982) contend that long-term averaging, as they have done, removes much of the non-dipole influence. Relative paleointensity data from marine sediments support the general character of the data trend in figure 2.15 (Tauxe and Valet 1989). However, between ca. 4000 BC and AD 1000 when the phase difference between the rise in the dipole moment and the decline in atmospheric $\Delta^{14}C$ is critical for the acceptance of a geomagnetic influence on long-term $\Delta^{14}C$, the intensities of the European TRM samples differ notably from the marine sediments (Tauxe and Valet 1989; see figure 2.22) and from limited TRM data for the rest of the world (McElhinny and Senanayake 1982, figure 1). Keeping these limitations in mind, the dipole moment data in figure 2.15 are considered here still the best representation available for the millennial-scale dipole moment and is used to generate the long-term dipole-related ^{14}C production rate Q(DM).

Finally, as mentioned in section 1.2, although the sinusoidal characteristics of the dipole trend and the long-term tree-ring $\Delta^{14}C$ record were emphasized by some earlier researchers, the dipole moment need not be inherently sinusoidal (eg. Merrill and McElhinny 1983). The limited *pre-Holocene* intensity data do not exhibit a sinusoidal trend (Merrill and McElhinny 1983; Tauxe and Valet 1989; also see below). Some modelers have approximated Q(DM) with a sinusoid (eg. Keir 1983) but, in this study, the geomagnetic ^{14}C production rate will be more directly related to the dipole moment measurements.

Relationship of Q to geomagnetic dipole moment

The complex dependence of the penetrating cosmic-ray flux on the strength of the geomagnetic field can be accurately represented, for intensities ranging from 70% to 300% of the current dipole moment, by a simple relationship in which ^{14}C production rate varies

with the inverse square of the dipole moment (Elsasser et al. 1956, Wada and Inoue 1966, Ramaty 1967). The equation is:

$$Q/Q_0 = \sqrt{(DM_0/DM)} \quad \text{or} \quad Q = c_1/\sqrt{DM} \tag{2.1}$$

where Q is the ^{14}C production rate in ^{14}C atoms per second per cm^2 of Earth surface, DM is the geomagnetic dipole moment in units of 10^{22} A m^2, Q_0 is a specified production rate related to DM_0 which is a specified dipole moment, and c_1 is a constant scaling factor algebraically equivalent to Q_0 times $\sqrt{DM_0}$. Estimates of the precise exponent for DM in relationship (2.1) vary from -.52 to -.47 or -.49 (the latter alternatives reflecting differential sensitivities at solar maximum and minimum sunspots, respectively); as in Ramaty (1967) and Lingenfelter and Ramaty (1970), an average estimate of -.50 is chosen here.

As noted above, the simple approximation fails at high and low dipole moments relative to the present field; but the Holocene results displayed in figure 2.15 are within 80% and 200% of the present dipole moment, thus qualifying for use in equation (2.1). The low geomagnetic field strength indicated for the 20,000 calendar yrs prior to the Holocene requires that a more complicated formulation be applied to calculate the ^{14}C production rates (see subsection below). During this period of low paleointensity measurements, the sensitivity of Q to DM is reduced; the maximum possible Q, for a hypothetical DM equal to zero, is only about twice the current ^{14}C production (Wada and Inoue 1966).

A proper value for c_1 is required to convert dipole observations to hypothetical ^{14}C production rates. Two related difficulties are (1) accurate estimates for Q_0 and DM_0 and (2) consideration of the additional influence on Q of variable solar wind modulation, SW,

on different time scales during the Holocene. Extended times of low sunspot numbers like the Maunder Minimum of the 17th century may theoretically lead to increases in ^{14}C production by 30% or more depending on the contemporaneous geomagnetic field strength (eg. Lal 1988, Table V). If DM_O and Q_O were measured during this Maunder time interval and converted to the constant of proportionality c_1 (= $Q_O\sqrt{DM_O}$), then equation (2.1) would overestimate the sensitivity of Q to DM levels at times when solar modulation was more "average". Because variations in SW are not incorporated, relationship (2.1) and the geomagnetic intensity record can be expected to generate a Q(DM) history comparable to the long-term trend in Q(^{14}C) only if the average level of solar modulation has remained the same as for the time period from which Q_O and DM_O were selected.

From theoretical considerations, Castagnoli and Lal (1980) and Lal (1988) explicitly describe and quantify the separate influences of solar activity and geomagnetic field strength in producing relative variations in ^{14}C production rate. The relative Q variations are assigned absolute values by normalizing to and extrapolating from neutron flux measurements and theoretical estimates for the associated ^{14}C production rates (eg. Lingenfelter 1963, Lingenfelter and Ramaty 1970) during two sets of recent minima and maxima times in the ca. 11-yr solar cycle. The limited neutron flux data produce substantial uncertainties of ca. 20% in the estimated absolute ^{14}C production rates. For example, Lingenfelter and Ramaty (1970) calculate ^{14}C production rates, in units of ^{14}C atoms per sec per cm^2 of Earth surface, of 2.42±.48 for the solar minimum in AD 1953-54, 1.93±.39 for the solar maximum in AD 1957-58, and 2.2±.4 for the average over the 3 solar cycles from AD 1937 to 1967. Extrapolating the regression between sunspot numbers and ^{14}C production rates calculated from neutron flux estimates, Lingenfelter (1963) estimated an average Q of 2.50±.50 over the 10 solar cycles from AD 1844 to 1954.

Lal (1988) suggests that a typical ca. 11-yr solar cycle yields an average ^{14}C production rate of 2.56 with a range of .94 between solar minimum and maximum; for extreme solar minimum (e.g. the Maunder period) and extreme solar maximum, Lal proposes that the range in ^{14}C production is 1.80 with an average rate of 2.72. Damon (1988) compiled the various estimates for ^{14}C production rates calculated from neutron flux data for the AD 1965 solar minimum and AD 1969 solar maximum.; six independently published estimates converge on respective Q's of 2.47±.19 and 2.02±.13. In contrast, O'Brien (1979) calculates a substantially lower average ^{14}C production rate of 1.75 from AD 1937 to 1970. O'Brien defends his results as more physically valid and accurate because his theoretical calculations are not normalized to limited thermal neutron measurements as done by, for example, Lingenfelter and Ramaty (1970); however, he utilizes data on proton and alpha particle spectra which also have limitations.

The recent ^{14}C production rates deconvolved from the tree-ring ^{14}C database and the modeling efforts here are significantly lower than the calculations based on neutron flux estimates. For example, $Q(^{14}C)$ in AD 1950 is 1.37 and the average for the interval of ca. 12 solar cycles from AD 1820 to 1960 is 1.44. The long-term trend, Q_t, in model ^{14}C production rate has nearly the same values as $Q(^{14}C)$ for these two time periods. The post-AD 1840 model production rates cannot, however, be treated as simple functions of the tree-ring ^{14}C history since these recent production rates were deconvolved from reconstructed "natural" atmospheric $\Delta^{14}C$ levels, in turn based on previous model determinations incorporating dipole and solar modulation factors (Stuiver and Quay 1981). A detailed discussion of these complications is presented in section 4.4. In any case, figure 2.1 (left-hand scale) clearly demonstrates that nearly all of the model ^{14}C production rates throughout the Holocene are significantly lower than the neutron-flux based estimates of ca. 2.0.

All of the researchers discussed here refer to DM_O and Q_O as the *current* dipole moment and ^{14}C production rate, respectively. However, which of the above Q estimates should be selected in order to calculate c_1 for generating a Holocene Q(DM) history? If the dipole moment and ^{14}C production rate occurring exactly at AD 1950 are used to determine c_1 (eg. Sternberg and Damon 1983), then the postulated Q(DM) record approximates the true long-term trend in ^{14}C production rate only if average Holocene solar activity is well represented by its AD 1950 level. If DM_O and Q_O are averages for longer time intervals, then the variable solar component has more likely been averaged out for use of equation (2.1). For example, better choices for DM_O and Q_O might be the average dipole analyses and neutron-flux based ^{14}C production estimates for AD 1937 to 1967 of 8.41×10^{22} and 2.2, respectively). Still, as noted by Castagnoli and Lal (1983), solar activity for the last 200 years appears significantly different from the solar variations for the previous 200 years. How representative of standard Holocene conditions will be a 3 solar-cycle or even a 10 solar-cycle average in ^{14}C production rate?

For these reasons, a different approach was employed to determine c_1. Values for DM_O and Q_O were derived from the *multi-century* average dipole moments described above and from averages for the $Q(^{14}C)$ history spanning the same time intervals. Such 500-yr and 1000-yr averages are assumed here to be long enough to balance exceptionally high with low solar modulation events and, thus, remove the solar influence on ^{14}C production from consideration. Also, in this way, c_1 and subsequently Q(DM) are "normalized" to the lower model ^{14}C production rates, a record covering the entire Holocene, rather than the higher production levels determined from the limited neutron flux measurements of the recent past. This normalization is appropriate since the purpose is to judge compatibility in the relative trends of the hypothetical Q(DM) and $Q(^{14}C)$ records rather than to compare absolute values. I contend that if the lower deconvolved

^{14}C production rate history is scaled up through the computer modeling to match the production estimates normalized to neutron flux data (by increasing ^{14}C reservoirs in the deconvolution model), the relative changes in $Q(^{14}C)$ will be only moderately affected (see section 2.1 for detailed discussion). Therefore, absolute differences are of secondary importance.

Several variations in the normalization procedure were considered. First, c_1 can be derived from the dipole moment measurements and the model-derived ^{14}C production rates averaged for the last ca. 500 years, ie. AD 1450 to 1980 (the most recent datum point in figure 2.15). However, as noted above, the post-AD 1840 model ^{14}C production rates are only indirectly determined. Furthermore, each multi-century average of paleointensity determinations only approximates the *global* dipole moment because it is biased toward the regional geomagnetic field characteristics of the majority of its sample sites (McElhinny and Senanayake 1982, Aitken et al. 1989). A temporal bias in the paleointensity averages may also exist because, whereas each multi-century $Q(^{14}C)$ average equally weighs each bi-decade within its time interval, the limited dipole data for each multi-century average may be concentrated within certain subperiods. As noted before, the terrestrial paleointensity averages show moderate differences to paleointensity measurements in marine sediments, an independent estimate of "global" geomagnetic variations (Tauxe and Valet 1989). Perhaps as a result of these limitations, the c_1 chosen in this fashion produces a pre-AD 1450 Q(DM) history significantly offset from the comparable trend in $Q(^{14}C)$.

Some of the influence of inconstant solar modulation and the regional geomagnetic bias may be removed by using more than one pair of multi-century $Q(^{14}C)$ and DM averages to determine c_1. I decided that utilizing all 14 dipole averages in figure 2.15 and the contemporaneous $Q(^{14}C)$ averages in order to define a c_1 was the most effective

method for assessing the role of geomagnetism in influencing *relative* multi-century-scale changes in ^{14}C production during the Holocene. In computing the c_1 which produced the best possible match between the Holocene DM and $Q(^{14}C)$ records, I treated all 14 points equivalently (in effect, favoring the 500-yr averages of the later Holocene with larger sample numbers and minimizing the 1000-yr averages with sparse data).

A c_1 of 4.39 applied to the DM averages in figure 2.15 through equation (2.1) yielded the best χ^2 fit between the 14 derivative Q(DM) values and their corresponding $Q(^{14}C)$ averages (figure 2.16, squares and bar curve, respectively). The correlation coefficient is r=.76 and the probability of no correlation (eg. Bevington 1969) is p=.002 for number of samples n=14. The standard deviations for the average dipole moments were converted into standard deviations in Q(DM) by calculating the propagation of error (Bevington 1969). The error propagation associated with equation (2.1) is:

$$S_{Q(DM)} = (.5\, Q\, S_{DM}) / DM \qquad (2.2)$$

where $S_{Q(DM)}$ and S_{DM} are the respective standard deviations of the dipole-related ^{14}C production rate and the measured dipole moment.

Alternatively, c_1 may be simply chosen so that the 14-point Q(DM) average (= c_1 $(1/\sqrt{DM_1} + 1/\sqrt{DM_2} + ... + 1/\sqrt{DM_{14}})/14$) equals the corresponding $Q(^{14}C)$ average. The results are nearly identical since alternate c_1 equals 4.40. However, if a value for c_1 is generated by combining the 14-point average $\underline{DM}$ ("DM_0" = $(DM_1 + DM_2 + ... DM_{14})/14$ = 9.20) with the analogous $Q(^{14}C)$ average ("Q_0" = 1.46), the calculated c_1 ($=Q_0\sqrt{DM_0}$) is 4.44, slightly different from the other estimates because of the nonlinearity in equation (2.1). Although the difference in calculated proportionalities is only 1%, the atmospheric $\Delta^{14}C$ record is a sensitive scale reflecting small changes in Q forcing (a 1%

increase in Q will produce an equivalent 1%, ie. 10 ‰, increase in atmospheric $\Delta^{14}C$ at steady-state). Therefore, c_1 must be carefully estimated and the χ^2 method allows a proper comparison of the relative long-term ^{14}C production rate trends and their carbon cycle implications.

The geomagnetic role in multi-century ^{14}C production rates

Ideally, if geomagnetic modulation is the driving force behind the multi-century- to millennium-scale trend in ^{14}C production, the Q(DM) history would be identical to $Q(^{14}C)$ in figure 2.16. The correlation is strong enough (see above) to suggest that dipole influence is a strong component of the $Q(^{14}C)$ record; however, discrepancies exist which appear to produce a ca. 900-yr phase difference between the two calculated production records. A phase lag of this magnitude is expected between millennial-scale *atmospheric* $\Delta^{14}C$ changes and low-frequency variations in the 14C production rate due to rate-limiting exchanges between carbon reservoirs (Houtermans et al. 1973), but such carbon-cycle delays cannot explain the discrepancies between alternative production rate records in themselves. In fact, contentions of Lal (1985) and Lal et al. (1990) indicate a mostly fortuitous similarity between the hypothetical trends in dipole-related ^{14}C production rate and in the production history deconvolved from the tree-ring $\Delta^{14}C$ observations assuming constant climatic influences; Lal asserts that climate-related changes in the global carbon cycle can explain the major features of the millennium-scale and century-scale Holocene variations in atmospheric $\Delta^{14}C$.

I have discussed elsewhere (see sections 2.2 and 3.3) the potential roles of variations in several carbon-cycle exchange parameters, controlled by climate, in producing the observed longer-term fluctuations in atmospheric $\Delta^{14}C$ during the Holocene. I concluded

Figure 2.16: ^{14}C production rates: (1) Q(DM) derived from the dipole moment averages using equation (2.1) with $c_1 = 4.39$ (squares); (2) Q(^{14}C) deconvolved from the global carbon model and averaged for the same time intervals as the dipole data (bar graph); (3) interpolating spline through Q(DM) (dashed line); (4) interpolating spline through Q(^{14}C) averages (smooth solid line); (5) ^{14}C production rate for AD 1950 as derived from the measured dipole moment in AD 1950 using equation (2.1) and $c_1 = 4.39$ (triangle). The right-hand scale indicates the relative ^{14}C production with respect to the Q(^{14}C) average for the last 500 yrs.

(inset): The ± one-sigma error range of 20 ^{14}C production rate histories generated randomly with a gaussian probability about the Q(DM) averages (shaded area). Axes and symbols are the same as in main figure.

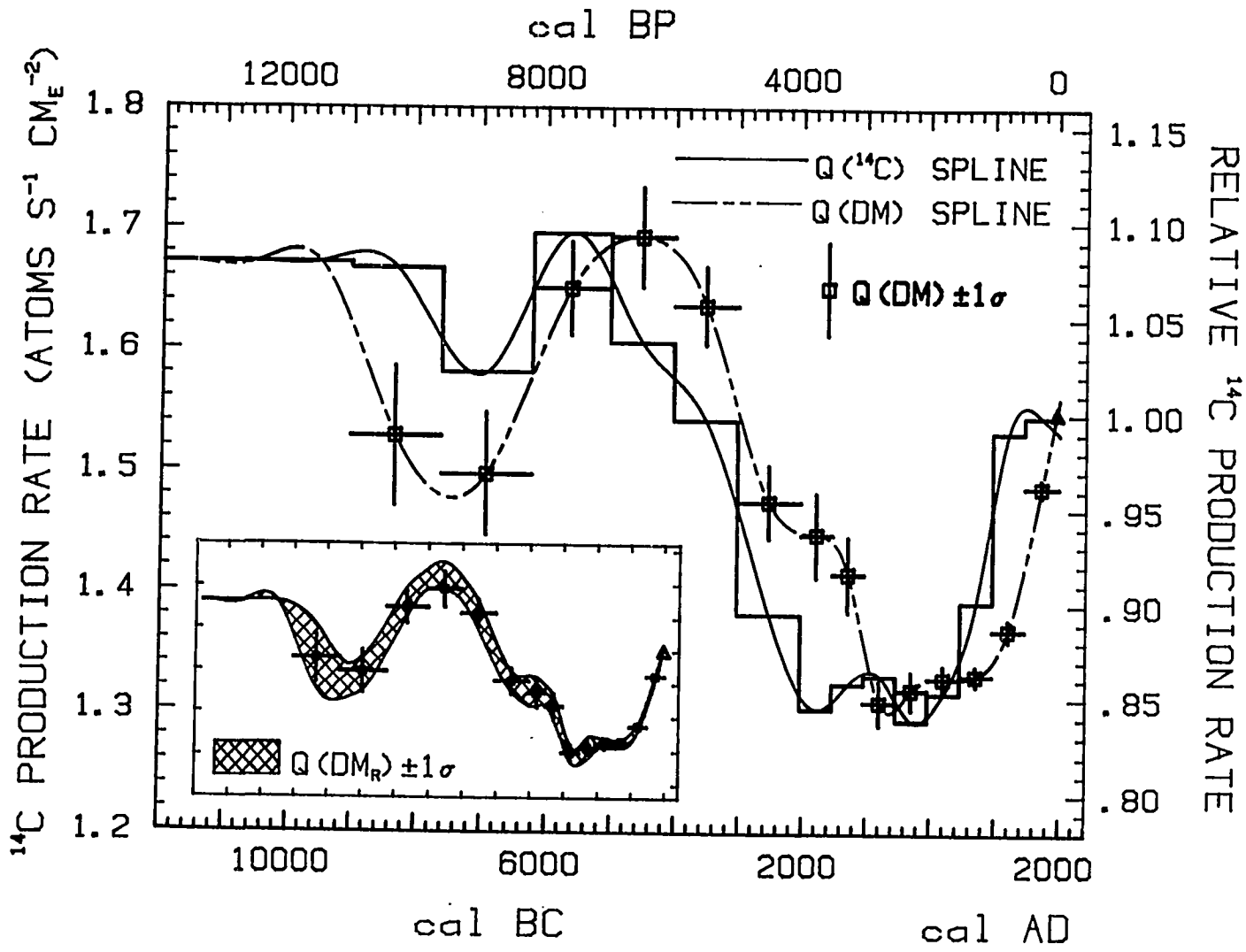
cal BP
12000
8000
4000
0
1.8
1.7
1.6
1.5
1.4
1.3
1.2
^{14}C PRODUCTION RATE (ATOMS S^{-1} CM$_E^{-2}$)
1.15
1.10
1.05
1.00
.95
.90
.85
.80
RELATIVE ^{14}C PRODUCTION RATE
Q (^{14}C) SPLINE
Q (DM) SPLINE
Q (DM) ±1σ
Q (DM$_R$) ±1σ
10000
6000
2000
2000
cal BC
cal AD

that the evidence did not support the degree of climate change required, as an alternative for major ^{14}C production variations, in order to generate the low-frequency atmospheric $\Delta^{14}C$ record; the role of other climate scenarios (Lal 1985, Lal et al. 1990) for such ^{14}C change is still speculative (section 2.2). Rather, climate may be a secondary player in millennial-scale atmospheric $\Delta^{14}C$ change, explaining some of the discrepancy between the dipole-derived and "constant-climate" ^{14}C production rates, ie. compensating for the stronger dipole-derived production in the middle of the Holocene and the weaker dipole-derived production in the late Holocene (see section 2.5).

If one accepts the applicability of equation (2.1) and the strong correlation in figure 2.16 as evidence that the geomagnetic field is primarily responsible for the long-term trend in ^{14}C production rate, the secondary differences in the two ^{14}C production records may originate in several ways already mentioned. Changes in the ventilation of the deep ocean cannot be ruled out as invalidating the "constant-climate" assumption of the $Q(^{14}C)$ record (section 2.5); limitations of the dipole data may create irregularities in the Q(DM) record; and/or multi-century-scale variations in solar modulation may complicate the application of equation (2.1).

The ^{14}C production rate derived from the ^{10}Be concentrations in a Greenland ice core, $Q(^{10}Be)$, compares favorably with the $Q(^{14}C)$ record of figure 2.16 when averaged for the same time periods (see section 2.4). The millennium-scale as well as the century-scale fluctuations in ^{10}Be appear to have the same origin as the ^{14}C variations. Through equation (2.1), the $Q(^{10}Be)$ and $Q(^{14}C)$ averages were converted to hypothetical dipole moments, $DM(^{10}Be)$ and $DM(^{14}C)$ respectively, and compared with the averaged dipole moment measurements (figure 2.26). All three records are correlated, suggesting a common origin, but $DM(^{10}Be)$ and $DM(^{14}C)$ show the strongest affinity (section 2.4),

which may mean that limitations in the dipole measurements contribute to their discrepancies with the other two "dipole proxies". These conclusions contradict the argument, discussed below, that the history of ice-core ^{10}Be concentrations does not exhibit a geomagnetic influence (Lal et al. 1990).

The computation of Q(DM) assumes the same "average" solar modulation on balance during 500-yr or 1000-yr time intervals whereas Q(^{14}C) may reflect a higher or lower than "average" solar influence in addition to the geomagnetic modulation. For example, over the last 500 years, reduced solar modulation during the Maunder and Spörer sunspot Minima may have increased ^{14}C production rate more than the "average" solar modulation for other multi-century intervals through the Holocene. This additional forcing, then, might explain part of the enhanced Q(^{14}C) average relative to Q(DM) for the last 500 years.

I tried to quantify the potential interference of long-term solar modulation on the 500-yr and 1000-yr intervals in atmospheric $\Delta^{14}C$. The Q(^{14}C) record is characterized by an asymmetric variability with more century-scale peaks than troughs imprinted on a history of more restricted variations (figure 2.1). If all variations are interpreted as primarily solar-induced, then the Q(^{14}C) record can be considered to consist of (1) periods of reduced variability (ie. no peaks) and solar modulation that is high relative to the Holocene "average", interrupted by (2) times of greater variability (ie. peaks) during which solar modulation is relatively low. As a consequence, Q(^{14}C) averages should exceed Q(DM) averages during periods of reduced variability in Q(^{14}C) if solar modulation explains the discrepancies in figure 2.16. Indeed the percentage difference between Q(^{14}C) and Q(DM) shows some correlation (r = .21) with increased variability of Q(^{14}C) but the weak association suggests a minimal influence. Either solar modulation manifests itself in different ways than through the "scatter" in Q(^{14}C) or other factors account for the ^{14}C

production rate discrepancies.

In summary, the correlation between the theoretical dipole-related ^{14}C production rate and the model-deconvolved "constant-climate" ^{14}C production rate that is required to generate the observed atmospheric $\Delta^{14}C$ record indicates a strong geomagnetic component behind the long-term history in the global ^{14}C system. This conclusion is supported by ^{10}Be evidence, while carbon reservoir modeling indicates that climate-related oceanic change is not a feasible substitute as a forcing mechanism. Climate may play a secondary role in explaining the discrepancies between the ideal dipole-related ^{14}C production rate and the deconvolved "constant-climate" rate; however, a more likely candidate for causing the discrepancies is the amalgamation of uncertainties in the determination of average dipole moments and their derivation into average ^{14}C production rates.

Q(^{14}C) and Q(DM) splines for global model runs

The Holocene ^{14}C production rate changes are integrated, attenuated, and lagged when recorded as atmospheric and oceanic $\Delta^{14}C$ variations in shells, sediments, tree-rings, or other carbon repositories. These three effects significantly redefine the appearance of the ^{14}C time series from the hypothetical input functions. The translation of the dipole-derived ^{14}C production rate history into associated dipole-related atmospheric and oceanic $\Delta^{14}C$ variations allows a direct comparison with the time series which constitute the available evidence that is observed and measured. The large standard deviations in Q(DM) averages in figure 2.16 (minimum indicators of the uncertainties in these averages as discussed above) should be appropriately converted into a range of modeled atmospheric and oceanic $\Delta^{14}C$ histories. In this way, we can identify the specific data intervals that are incongruent with the supposition that the geomagnetic field is the primary influence on long-term ^{14}C variations; the implications of this hypothesis

can be evaluated directly against the observations.

I chose an interpolating spline to convert Q(DM) into a smooth input function, $Q(DM)_S$ (figure 2.16, dashed line), to force $\Delta^{14}C$ variations in the forward carbon reservoir model with constant exchange parameters. An interpolating spline, $Q(^{14}C)_S$ (figure 2.16, solid smooth curve), was also generated for the averaged hypothetical "constant-climate" ^{14}C production rate record in order to produce model reservoir $\Delta^{14}C$ variations with the same resolution and reduced variability as the dipole-related model output. The deviations in these dipole-related reservoir changes, $\Delta^{14}C(DM)_S$, are accurately measured only against a "constant-climate" baseline, $\Delta^{14}C_S$, that had been produced through an identical process. The reduction of high-frequency "noise" in the forcing function can theoretically alter the long-term trends in reservoir $\Delta^{14}C$ because of delayed ocean responses; however, the close correspondence after the early Holocene between atmospheric $\Delta^{14}C_S$ and the trend in the original $\Delta^{14}C$ observations (figure 2.21, upper solid smooth curve and bar curve, respectively) is evidence that such an effect is minimal here.

The first 1000-yr average for both records is at 8350 BC. A steady-state ^{14}C production rate of 1.67 atoms s^{-1} cm_E^{-2} was assigned to three earlier "averages" at 9550, 10,550 and 11,550 BC before calculating the interpolating splines from 11,550 BC through all averages to AD 1710. Through these splines, each model run is forced at the beginning with 2000 yrs of nearly constant ^{14}C production. This production rate level was chosen to yield a steady-state atmospheric $\Delta^{14}C$ of 90 ‰ for both cases.

The interpolating splines were extended to AD 1990 by extrapolation from their slopes at AD 1710. Both splines fortuitously converge near the instantaneous value for ^{14}C production in AD 1950 of 1.55 atoms s^{-1} cm_E^{-2} (figure 2.16, triangle) calculated from the observed dipole moment (see above) and the preferred c_1. However, similar

end-points in ^{14}C production rate histories do not insure close levels in modeled reservoir $\Delta^{14}C$ at this time. As noted above, atmospheric and oceanic $\Delta^{14}C$ are functions of recent and past ^{14}C production rate history.

The dipole-forced history of $\Delta^{14}C$ variations in global carbon reservoirs must start with the same initial conditions that were assumed when deconvolving the "constant-climate" ^{14}C production rate because: (1) the absolute magnitude of the deconvolved ^{14}C production rate variations depends on the "steady-state" production that determines the initial ^{14}C content in the global system, and (2) through c_1 the dipole-related production history is normalized to the absolute values of the deconvolved ^{14}C production record. In other words, Holocene $Q(^{14}C)$ fluctuations have been derived from the variations in atmospheric $\Delta^{14}C$ *and* the memory of past conditions which have been integrated into the global (primarily oceanic) ^{14}C reservoirs. For example, early Holocene $Q(^{14}C)$ levels must be higher, as compensation, if the *pre-Holocene* "steady-state" ^{14}C production rate produced a much lower "steady-state" atmospheric $\Delta^{14}C$ than the previously assumed 90 ‰ level. An infinite number of deconvolved $Q(^{14}C)$ histories is possible depending on the assumed initial conditions; any c_1-related Q(DM) record reflects the initial conditions of the specific $Q(^{14}C)$ record to which it has been normalized. The reconstruction and implications of alternative initial conditions is discussed in a following subsection.

In addition to the sensitivity tests of model results to assumed initial conditions, the impacts of other modifications to the production forcing function were investigated. First, the steady-state Q(DM) values at 9550 and 10,550 BC were replaced with ^{14}C production rates derived (through equation (2.1) and the preferred c_1) from the dipole moment averages for these times in Merrill and McElhinny (1983). I considered these dipole averages too uncertain (based on 2 and 5 measurements, respectively) to routinely use but decided to test their potential influence on the model results. The same initial conditions at

and prior to 11,550 BC were assumed and an interpolating spline was generated exactly as before.

Because the errors in the dipole moment cause large uncertainties in the production rate forcing function, I wished to translate these ambiguities into consequent uncertainties in the modeled reservoir $\Delta^{14}C$ records. Model runs using Q(DM) plus one-sigma in one case and minus one-sigma in another case simulate scenarios that are too improbable to provide a realistic one-sigma spread in the results. Instead I created 20 dipole moment records generated randomly with a normal (gaussian) distribution about each original dipole data average (figure 2.17). The random number generator was programmed in order that random points had a 66% probability of lying within the one-sigma range and a 95% probability of falling within 2-sigma. Each of the 20 sets of 14 "randomized" dipole moments was converted to ^{14}C production rate histories through equation (2.1) and c_1, and interpolating splines were determined assuming the same initial conditions as the original Q(DM).

The ability of the 20 randomized Q(DM) records to accurately reflect the uncertainties in the original dipole averages was judged by calculating the mean and error of the mean of the 20 ^{14}C production rate records, $Q(DM_R)\pm 1s$, for each bi-decade. These statistics were compared to the standard errors in the original data averages (figure 2.16 inset). The match is generally excellent except near 4550 BC where, by chance, the distribution of random points has a significantly asymmetrial distribution around the original data average (figure 2.17). The 20 randomized forcing functions produced 20 reservoir $\Delta^{14}C$ histories from which running means and errors in the means were calculated. These "model error ranges", then, directly reflect the one-sigma uncertainty in the original dipole measurements.

Figure 2.17: Average dipole moments (diamonds with ± one-sigma error bars). About each dipole average, 20 points (circles) were generated randomly with a gaussian probability.

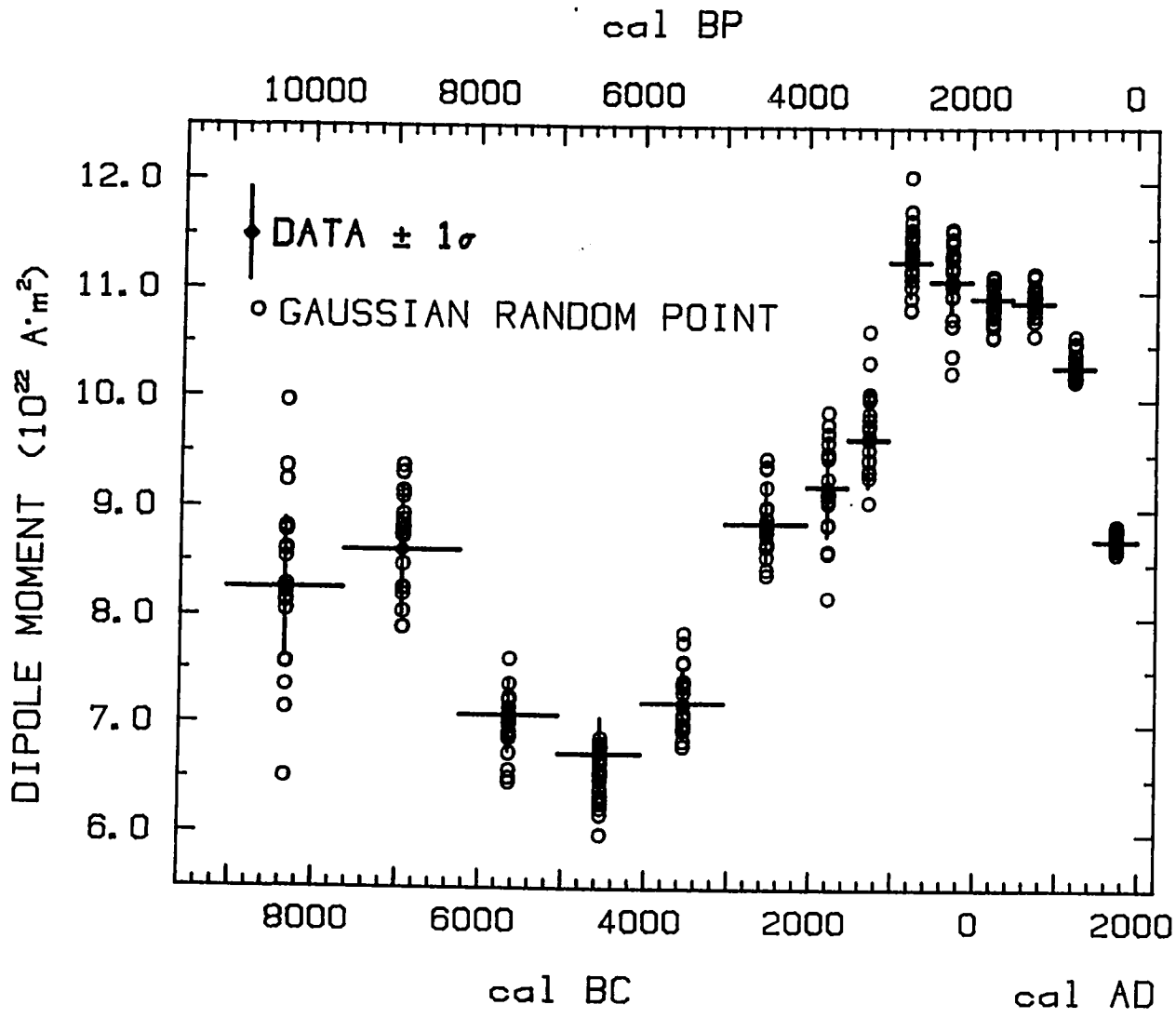
cal BP
10000
8000
6000
4000
2000
0
12.0
11.0
10.0
9.0
8.0
7.0
6.0
DIPOLE MOMENT (10^{22} A·m^2)
DATA ± 1σ
GAUSSIAN RANDOM POINT
8000
6000
4000
2000
0
2000
cal BC
cal AD

The geomagnetic imprint on atmospheric and oceanic $\Delta^{14}C$

The splines for the "constant-climate" ^{14}C production rate and the original and 20 randomized dipole-related ^{14}C production rates served as inputs for the forward global carbon model, each model run possessing constant and identical ocean parameterization. The resulting atmospheric and oceanic $\Delta^{14}C$ histories closely resemble one another with some important secondary discrepancies.

The mean and error of the mean for the 20 $Q(DM_R)$ model runs yielded the "model error ranges" which are compared to the tree-ring $\Delta^{14}C$ record in figure 2.18 (shading and bar curve, respectively). Prior to 4500 BC and after AD 1000 the dipole-related production is apparently too weak to produce the observed atmospheric levels; the ostensible "phase shift" between the atmospheric curves from 3000 BC to AD 600 originates, according to this model interpretation, from a dipole-related production that is stronger than required. The early Holocene offset in the dipole-related atmospheric $\Delta^{14}C$ curve is somewhat understated in figure 2.18; for reasons discussed below, the difference between dipole-related atmospheric $\Delta^{14}C(DM)_S$ and the "constant climate" baseline $\Delta^{14}C_S$ of identical resolution is more pronounced than the discrepancy of $\Delta^{14}C(DM)_S$ with the original bi-decadal tree-ring record (figure 2.21 and below).

Beginning about 5000 BC, the tree-ring $\Delta^{14}C$ record exhibits a broad decline of ca. 110 °/oo; the dipole-induced atmospheric $\Delta^{14}C$ curve shows a nearly equivalent drop of ca. 90 °/oo after ca. 4000 BC. I contend that the similarity in amplitude shown here strongly supports more than a coincidental relationship between the approximated global dipole moment record and long-term fluctuations in ^{14}C.

The most recent histories (last 1000 yrs) of the two atmospheric $\Delta^{14}C$ curves do not match (figure 2.18). The great difference between the Q(DM) and $Q(^{14}C)$ records for the

Figure 2.18: Atmospheric $\Delta^{14}C$ measured in tree rings (bar graph) and forced in the global carbon model by the 20 "randomized" dipole-derived ^{14}C production rate histories described in the text (shading indicates model ranges corresponding to ± one-sigma in the 20 modeled $\Delta^{14}C$ trend lines). A steady-state ^{14}C production is assumed prior to 9550 BC that yields an atmospheric $\Delta^{14}C_0$ of 90 ‰.
(inset): Atmospheric $\Delta^{14}C$ measured in tree rings (bar graph) and forced in the global carbon model by the dipole-derived production rate history with an assumed $\Delta^{14}C_0$ of 50 ‰ (dashed line).

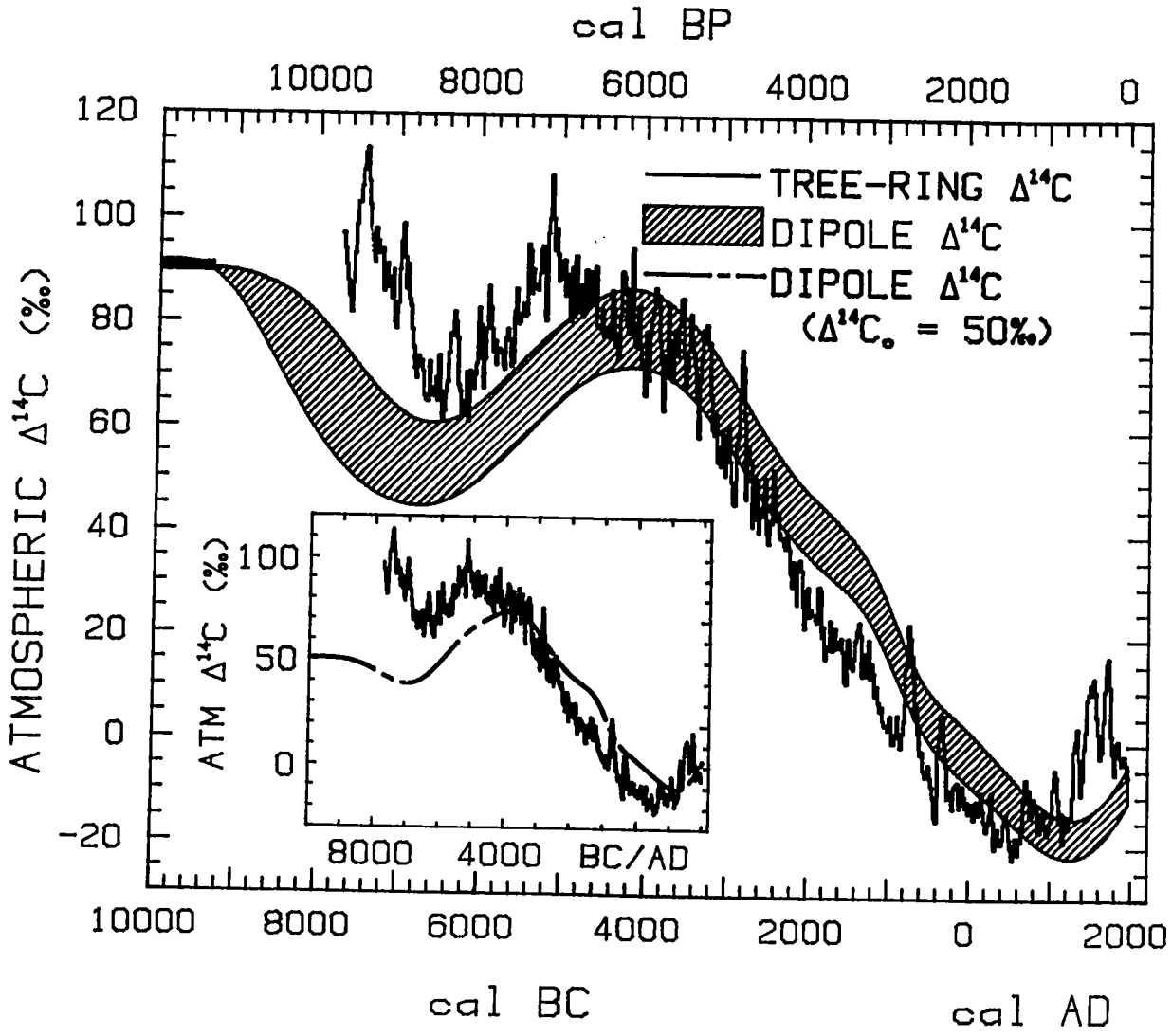
cal BP
10000
8000
6000
4000
2000
0
120
100
80
60
40
20
0
-20
ATMOSPHERIC Δ14C (‰)
TREE-RING Δ14C
DIPOLE Δ14C
DIPOLE Δ14C
(Δ14C0 = 50‰)
ATM Δ14C (‰)
100
50
0
8000
4000
BC/AD
10000
8000
6000
4000
2000
0
2000
cal BC
cal AD

last 1500 years (figure 2.16), especially the disparity at AD 1200 (ie. AD 950 - 1450), prevents recent compatibility in the reservoir $\Delta^{14}C$ curves. An alternative c_1 that reconciles the recent dipole-derived and deconvolved "constant climate" ^{14}C production rates will also considerably enhance the mid-Holocene discrepancies between these ^{14}C production rates and between their corresponding atmospheric $\Delta^{14}C$ trends. Modification of the pre-11,000 BP model initial conditions has a significantly reduced effect on model reservoir histories for recent centuries (see next subsection). Because of the potential inaccuracies (enumerated above) in determining (1) average multi-century dipole moments, (2) related ^{14}C production rates, and (3) a smooth production rate trend, the disparity in the recent trends cannot carry too much weight and I have not pursued, by model adjustment, a perfect correspondence between records of the last 1000 years. Climatic change during this time interval, the so-called Little Ice Age of ca. AD 1550 to 1800 (eg. Grove, 1988), may be responsible for a portion of the disparity (see section 2.5).

If the geomagnetic forcing function $Q(DM)_S$ incorporates two earlier dipole measurements at 9550 BC and 10,550 BC and assumes conventional initial conditions (atmospheric $\Delta^{14}C_o$ = 90 ‰) prior to 11,550 BC, the subsequent model atmospheric $\Delta^{14}C$ trend for the Holocene is negligibly altered from the one discussed so far. In a later subsection, I consider the implications for Holocene ^{14}C production rates and atmospheric $\Delta^{14}C$ of the even more uncertain dipole record for the last 30,000 calendar years.

The model ^{14}C ventilation age trends associated with the dipole-related and "constant climate" ^{14}C production rate histories are shown in figure 2.19 (shading and bar curve respectively). As before, the model results are normalized to the foraminifera data (Andrée et al. 1986b) by matching recent ventilation ^{14}C ages. The model oceanic ^{14}C trends are very similar to one another and are consistent with the observations within the relatively

Figure 2.19: Ventilation indices in ^{14}C yrs. Left axis scales the model ventilation index MVI (model deep ocean - model surface ocean). The bar graph is the MVI history associated with the deconvolved "constant climate" ^{14}C production rate; the shaded trend shows the MVI ranges associated with the 20 "randomized" dipole-related ^{14}C production histories, all with assumed atmospheric $\Delta^{14}C_o$ of 90 °/oo. Right axis scales the foram ventilation index FVI (mixed benthics ^{14}C ages - planktonic *Globigerinoides sacculifer* ^{14}C ages) of Andrée et al. (1986a). Symbols denote measured FVI data (± 1-sigma) from the South China Sea. The FVI scale is shifted -310 ^{14}C yrs relative to the MVI scale in order to match the AD 1830 MVI value of 1275 yrs with the recent preanthropogenic FVI of 1585 yrs.

(inset): Dashed line is the MVI associated with a dipole-related ^{14}C production history normalized for atmospheric $\Delta^{14}C_o$ = 50°/oo. All scales and other symbols are identical to the main figure.

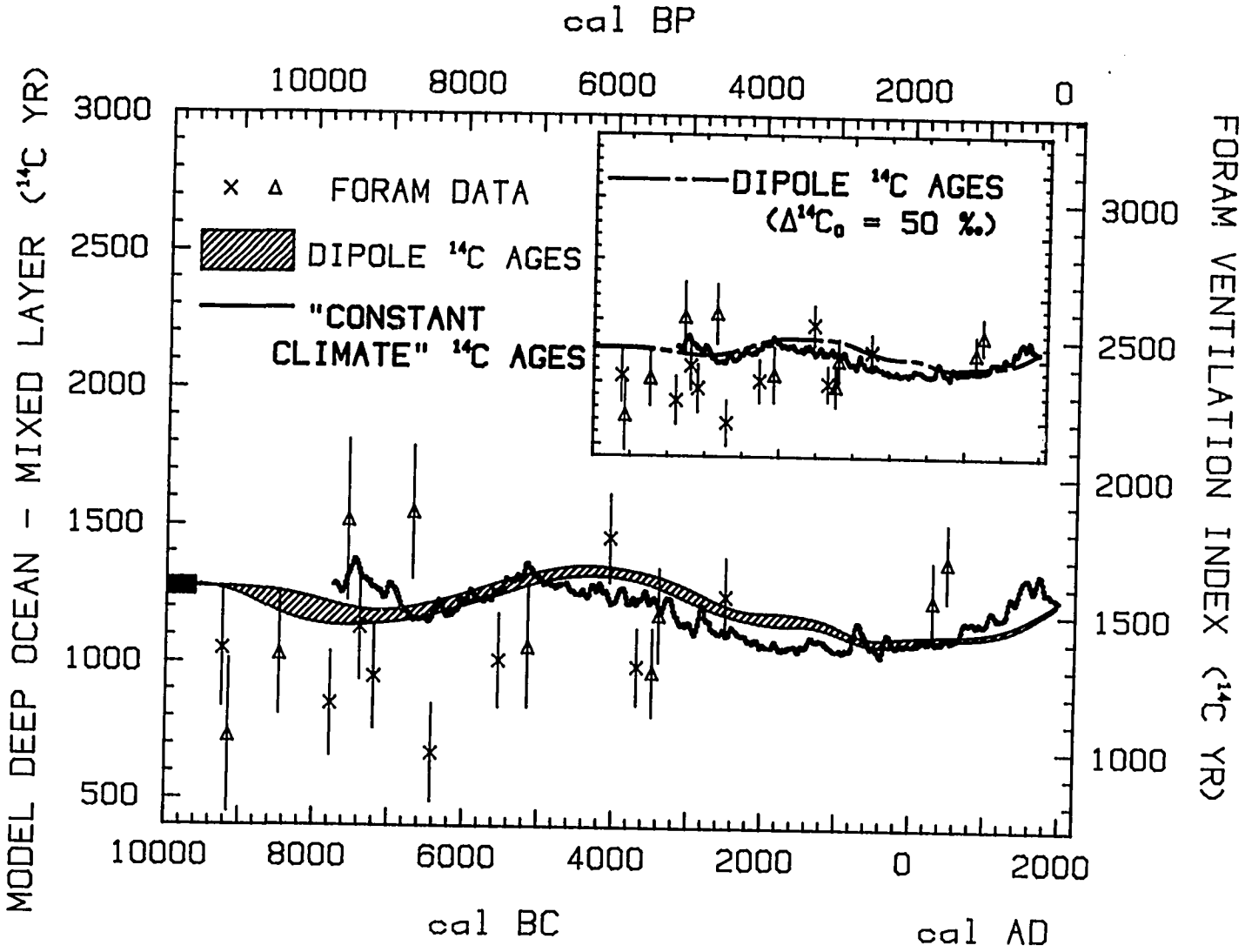
cal BP
10000
8000
6000
4000
2000
0
3000
2500
2000
1500
1000
500
MODEL DEEP OCEAN - MIXED LAYER (^{14}C YR)
FORAM VENTILATION INDEX (^{14}C YR)
× △ FORAM DATA
DIPOLE ^{14}C AGES
"CONSTANT CLIMATE" ^{14}C AGES
DIPOLE ^{14}C AGES ($\Delta^{14}C_0$ = 50 ‰)
10000
8000
6000
4000
2000
0
2000
cal BC
cal AD

large uncertainties.

As concluded before, with some allowance for additional fallibility in the Holocene dipole trend beyond the statistical uncertainties, the good agreement between the dipole-derived reservoir $\Delta^{14}C$ changes for the Holocene and the ^{14}C observations suggests that the geomagnetic field is the primary force behind millennial-scale ^{14}C fluctuations. Changing ocean parameters might be secondary contributors to long-term ^{14}C variation. Climate especially may play a role in the early Holocene during recovery from the Late Wisconsin subage. The extent of change needed in oceanic parameters to compensate for the discrepancies between $\Delta^{14}C(DM)_S$ and $\Delta^{14}C_S$ in order to create a perfect match is discussed in section 2.5.

Finally, the higher frequency $\Delta^{14}C$ variations were re-introduced into the long-term dipole-related atmospheric trend in order to regenerate a "complete" atmospheric $\Delta^{14}C$ record. The short-term features incorporated into the model-derived $\Delta^{14}C(DM)_S$ trend are composed of the deviations of the bi-decadal tree-ring $\Delta^{14}C$ record from the identically-derived $\Delta^{14}C_S$ trend (see trend lines in figure 2.21). If the long-term ^{14}C production rate is solely a function of the dipole moment and is accurately derived by the calculations above, then the resulting complete curve (figure 2.20 curve B) represents a $\Delta^{14}C$ history that has been "corrected" for long-term climatic change.

In section 2.1, a spline closely approximating a 400-yr moving average was chosen to represent the long-term non-solar history of the atmospheric $\Delta^{14}C$ record. Assuming that the "complete" dipole-related atmospheric $\Delta^{14}C$ record eliminates long-term climatic influences, an analogous spline of this latter record (figure 2.20, curve B in lower right panel) represents a multi-century trend purely induced by the geomagnetic field. In other words, the finer resolution of the bi-decadal tree-ring $\Delta^{14}C$ record has been utilized to

Figure 2.20: Atmospheric $\Delta^{14}C$ histories. Curve A (upper left panel) is the observed $\Delta^{14}C$ record; curve B (upper right) is compiled by superimposing the high-frequency $\Delta^{14}C$ fluctuations of curve A (see text) onto the long-term $\Delta^{14}C$ trend derived through the Q-forced model from the dipole-related ^{14}C production history with assumed atmospheric $\Delta^{14}C_o$ of 90 ‰; curve C (lower left) is the same as B with assumed atmospheric $\Delta^{14}C_o$ of 50 ‰. Smoothing splines (approximating 400-yr moving averages) of curves A, B, and C are compared in the lower right panel.

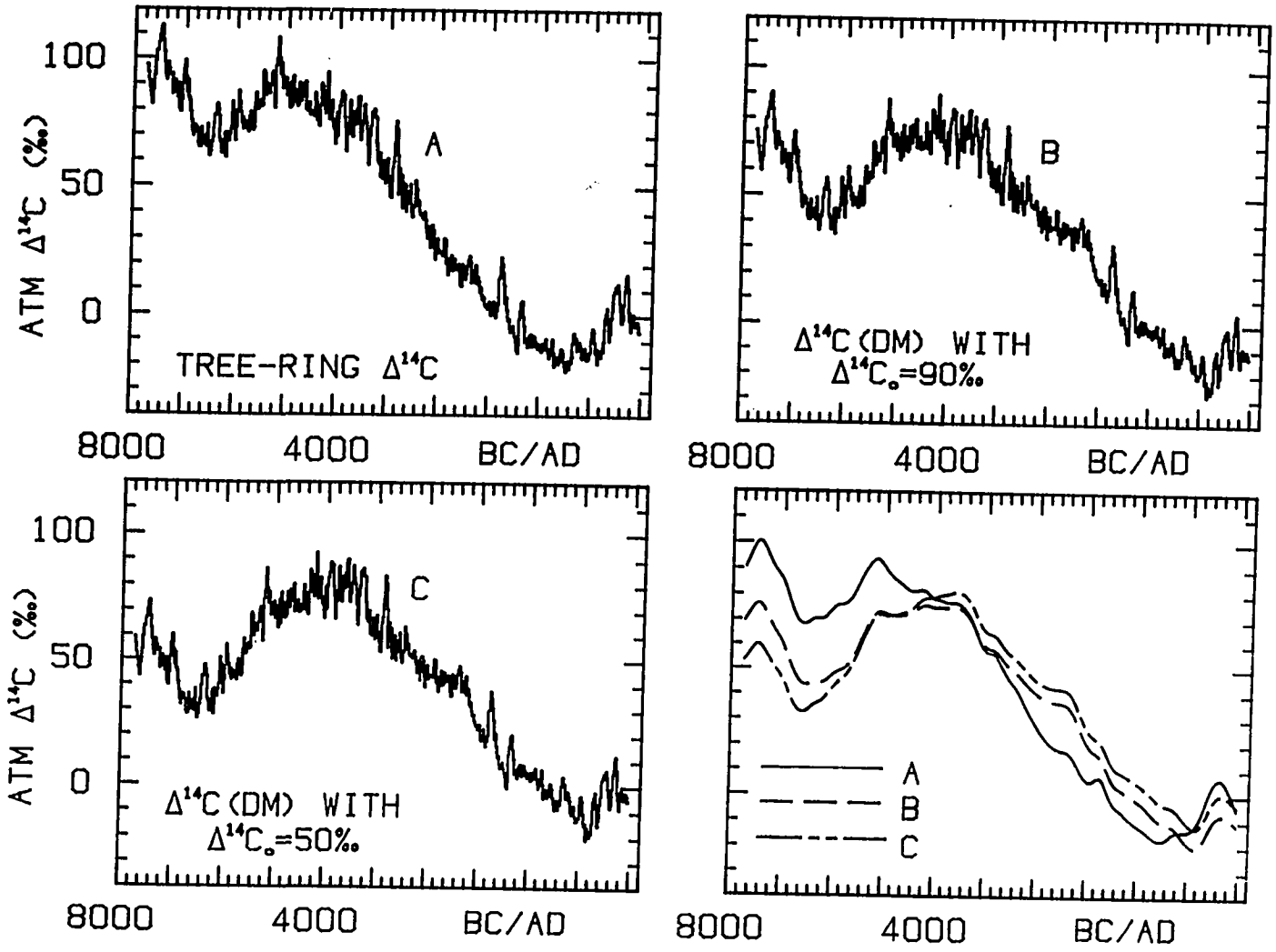
100
50
0
ATM Δ14C (‰)
A
TREE-RING Δ14C
8000
4000
BC/AD
B
Δ14C (DM) WITH
Δ14C₀=90‰
C
Δ14C (DM) WITH
Δ14C₀=50‰
A
B
C

estimate hypothetical geomagnetic variations with periodicities of ca. 400 -800 yrs which are too short to be detected by the poorer resolution dipole moment data. This spline will be useful for comparison with the higher resolution ^{10}Be record in the next section.

Sensitivity of model results to assumed initial conditions

Systematic sensitivity analyses involving model initial conditions were presented in section 2.1 for alternative pre-Holocene "steady state" ^{14}C production rates and in section 2.2 for alternative pre-Holocene "steady state" oceanic conditions. Initial scenarios involving different climatic and ^{14}C production rate "steady state" combinations will be discussed in section 2.5. These analyses all attach different initial conditions to model simulations associated with the *tree-ring* $\Delta^{14}C$ record. Here I test the repercussions of an alternative initial steady-state on the *dipole-related* ^{14}C curves. Specifically, if the pre-Holocene steady-state ^{14}C production rate prior to the Holocene Q(DM) record produced an atmospheric $\Delta^{14}C$ level of 50 °/oo rather than the assumed 90 °/oo, how severely would the model-derived reservoir $\Delta^{14}C$ curves be affected?

Lal et al. (1990) stress the sensitivity of dipole-induced atmospheric $\Delta^{14}C$ to assumed pre-Holocene "steady-state" conditions. A ±10% different steady-state ^{14}C production level is appended to the beginning of an independent Holocene Q(DM) history. In each case, the *Holocene* Q(DM) history is identical and "normalized to today's value" (Lal et al., figure 8). Indeed, when using this approach, I find a similar effect on the atmospheric $\Delta^{14}C$ record as does Lal et al. For example, if the initial ^{14}C production rate is reduced by 4% to yield a lower "steady-state" atmospheric $\Delta^{14}C$ of 50 °/oo but the rest of Q(DM) remains the same, the consequent dipole-related atmospheric $\Delta^{14}C$ curve will drop as well. The initial ^{14}C conditions becomes less influential as the Holocene

transpires; the difference between the atmospheric $\Delta^{14}C$ curves with initial atmospheric $\Delta^{14}C_o$ at 90 ‰ and at 50 ‰ will be less than 15 ‰ by the present.

However, the normalization procedure of choosing c_1 to best fit the dipole-related Holocene Q(DM) history to the deconvolved Q(^{14}C) record results in a more complex but generally compensatory model response to changes in pre-Holocene initial conditions. As explained above, the Q(DM) record must be matched (through c_1) to a "constant climate" Q(^{14}C) with the same initial steady-state conditions proposed for Q(DM). Thus, calculation of a $\Delta^{14}C$(DM) history with an alternative pre-Holocene steady-state level requires a six-step procedure: (1) attach the alternative steady-state $\Delta^{14}C_o$ to the Holocene tree-ring $\Delta^{14}C$ record, (2) deconvolve the ^{14}C production rate required to generate this atmospheric $\Delta^{14}C$ record in the global carbon model with constant oceanic parameterization, (3) average the deconvolved bi-decadal ^{14}C production record to mirror the temporal resolution of the dipole moment averages, (4) choose a c_1 that yields the best χ^2 fit of the dipole-dependent Q(DM) record to the new Holocene Q(^{14}C) history, (5) generate a new smooth input function $Q(DM)_S$, and (6) use $Q(DM)_S$ in the global carbon model to force new reservoir $\Delta^{14}C$ trends.

Figure 2.21 and its inset depict the alternative ^{14}C production rate histories and atmospheric $\Delta^{14}C$ curves associated with initial "steady-state" ^{14}C production rates of 1.67 ^{14}C atoms s^{-1} cm_E^{-2} ($\Delta^{14}C_o$ = 90 ‰) and 1.60 ^{14}C atoms s^{-1} cm_E^{-2} ($\Delta^{14}C_o$ = 50 ‰). The smooth solid lines depict the model results linked to the tree-ring $\Delta^{14}C$ record while the dashed and dotted line are trends tied to the dipole moment data. The deconvolved ^{14}C production rates have been averaged for the same time intervals as the averaged dipole measurements and all curves in the inset are interpolating splines of these averages (analogous to the curves in figure 2.16). Through the global carbon model, these ^{14}C production trends subsequently forced the smooth atmospheric $\Delta^{14}C$ curves

Figure 2.21: Observed and modeled atmospheric $\Delta^{14}C$ trends: bar graph is the bi-decadal tree-ring $\Delta^{14}C$ record; upper solid line is the atmospheric $\Delta^{14}C$ trend derived, through the Q-forced model, from production rate curve (1) in the inset; lower solid line, dashed line, and dotted line are derived, respectively, from curves (2), (3) and (4) in the inset.

(inset): Interpolating splines of ^{14}C production rate records: (1) lower solid line that begins higher at 1.67 is based on the deconvolved Q(^{14}C) which has assumed atmospheric $\Delta^{14}C_0$ of 90 °/oo; (2) upper solid line that begins at 1.61 is based on the deconvolved Q(^{14}C) which has assumed atmospheric $\Delta^{14}C_0$ of 50 °/oo; (3) dashed line is based on dipole-related Q(DM) normalized to curve (1); (4) dotted line is based on dipole-related Q(DM) normalized to curve (2). Text explains normalization procedure.

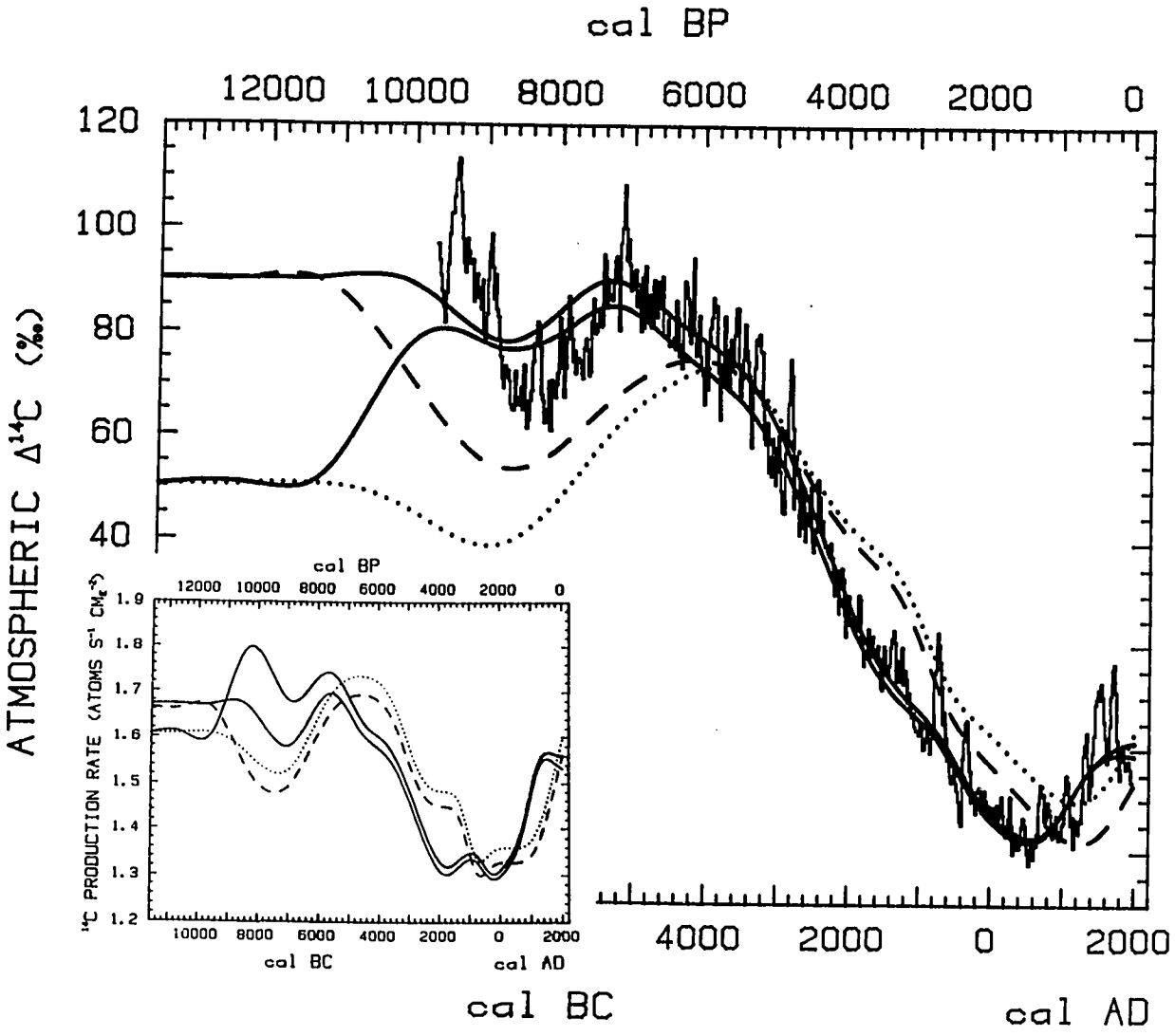
cal BP
12000 10000 8000 6000 4000 2000 0
120
100
80
60
40
ATMOSPHERIC Δ14C (‰)
4000 2000 0 2000
cal BC
cal AD
cal BP
12000 10000 8000 6000 4000 2000 0
14C PRODUCTION RATE (ATOMS S-1 CM-2)
1.9
1.8
1.7
1.6
1.5
1.4
1.3
1.2
10000 8000 6000 4000 2000 0 2000
cal BC
cal AD

shown in the main figure.

Holocene ^{14}C production rates must be higher to generate the same observed tree-ring $\Delta^{14}C$ history if the pre-Holocene initial steady-state ^{14}C production is lower (ie. in the inset, the solid curve that begins at 1.60 ^{14}C atoms s^{-1} cm_E^{-2} crosses over and remains *above* the solid curve that begins at the higher initial production rate of 1.67 ^{14}C atoms s^{-1} cm_E^{-2}). The corresponding atmospheric $\Delta^{14}C$ curves should be equivalent after 7750 BC and pass through the higher resolution tree-ring $\Delta^{14}C$ record (bar curve in figure 2.21). Because the deconvolved bi-decadal ^{14}C production records are somewhat recast by the averaging and splining process, the $Q(^{14}C)_S$ forcing functions produce smooth atmospheric $\Delta^{14}C$ records out of phase with the original tree-ring $\Delta^{14}C$ variations during the early Holocene. Except in the early Holocene, however, the two atmospheric $\Delta^{14}C_S$ curves adequately trace the trend in the original data.

As discussed above, the discrepancies in the dipole-related reservoir $\Delta^{14}C$ trends are accurately measured only against identically derived reservoir $\Delta^{14}C_S$ trends rather than the original tree-ring $\Delta^{14}C$ data. Thus, for the model simulations with $\Delta^{14}C_o$ at 90 °/oo, the actual divergence in atmospheric $\Delta^{14}C(DM)_S$ (dashed line in figure 2.21), with respect to $\Delta^{14}C_S$ (upper solid line in figure 2.21), is greater than indicated by its direct comparison to the tree-ring $\Delta^{14}C$ record. For this reason, dipole-related discrepancies are always quantified here relative to the reservoir $\Delta^{14}C_S$ base lines.

For the alternative scenario with initial steady-state atmospheric $\Delta^{14}C$ of 50 °/oo, the dipole-related atmospheric $\Delta^{14}C$ trend (dotted line in figure 2.21) is, during the last half of the Holocene, *above* the modeled $\Delta^{14}C(DM)_S$ trend which has begun with a greater initial atmospheric $\Delta^{14}C$. This inversion stems from the higher Holocene Q(DM) levels for the lower pre-Holocene initial condition, these levels resulting, in turn, from the 2.5%

higher c_1 (=4.50) derived for the χ^2 fit to higher Holocene Q(^{14}C) levels (figure 2.21 inset). Thus, when the constant of proportionality in equation (2.1) is determined by the model ^{14}C production rate history for the entire Holocene rather than the estimated geomagnetic, solar, and neutron flux conditions for only recent decades (eg. Lal et al. 1990), pre-Holocene "steady-state" conditions have a decidedly weaker impact on model-derived Holocene Δ^{14}C trends.

For simple comparison with the model results based on standard assumptions, the insets to figures 2.18 and 2.19 show the atmospheric and oceanic Δ^{14}C histories associated with the 4% lower pre-Holocene "steady-state" ^{14}C production rate and resulting atmospheric $\Delta^{14}C_O$ of 50 ‰. The short-term Δ^{14}C fluctuations are also re-introduced into the alternative atmospheric $\Delta^{14}C(DM)_S$ curve by transferring onto this curve the differences between the bi-decadal Δ^{14}C observations and the $\Delta^{14}C_S$ baseline for the 50 ‰ scenario. The derivative curve is displayed in figure 2.20 (bar graph C). The 400-yr spline for curve C closely resembles the analogous splines for the observations and the other dipole-related record associated with the standard initial conditions (lower right panel of figure 2.20).

Although I did not explicitly model the impact of other possible initial "steady states" on the dipole-related Holocene Δ^{14}C trends, clearly the effect will be secondary as in the "50 ‰ scenario". Beer et al. (1988) prefer a *higher* pre-Holocene "steady state" ^{14}C production level which would create an atmospheric $\Delta^{14}C_O$ of 140 ‰. Using the matching approach applied here, any resulting change in modeled Holocene Δ^{14}C fluctuations will be minimal (discussed in detail in section 2.4). Recent studies have produced pre-Holocene histories (rather than "steady states") for the geomagnetic dipole moment (Tauxe and Valet 1989) and for oceanic surface Δ^{14}C (Bard et al. 1990). Although our model results for the Holocene are not significantly recast, minor changes

occur which have potentially important implications (see next subsection).

Because modeled Holocene reservoir $\Delta^{14}C$ trends are relatively insensitive to pre-Holocene "steady-state" ^{14}C production rate conditions, the good agreement between the dipole-induced Holocene histories and the available observations is favorably robust and independent of pre-Holocene uncertainties. On the other hand, this circumstance also prevents clear differentiation between hypothetical "initial conditions" based on Holocene $\Delta^{14}C$ evidence. Importantly, a proper assessment of the global ^{14}C cycle in the Late Pleistocene (Late Wisconsin) requires additional climatic information and a fundamental restructuring of the reservoir modeling; any preliminary conclusions drawn here would need to be carefully reconsidered with a more appropriate approach.

Implications of pre-Holocene geomagnetic and $\Delta^{14}C$ histories

The sensitivity analyses in the subsection above investigated the impact of assumed pre-Holocene "steady state" initial conditions on modeled reservoir $\Delta^{14}C$ trends during the Holocene. The ^{14}C production rate, reservoir exchange parameters, and consequently atmospheric $\Delta^{14}C$ are treated as constant prior to 11,500 BP (9550 BC).

The dashed lines marked "A" in the 3 panels of figure 2.22 represent the conventional "steady-state" assumption as applied to the dipole-related trends. The "A" production rate curve in the middle panel simply extends the dashed curve, $Q(DM)_S$, in figure 2.16 back 35,000 calendar years; the squares are the ^{14}C production rate values obtained from the dipole moment averages of Merrill and McElhinny (1983) using equation (2.1) with c_1 of 4.39. The upper panel displays the corresponding dipole moment averages (squares) and the implicitly assumed pre-Holocene "steady-state" geomagnetic field (dashed line A). Line A in the lower panel is $\Delta^{14}C(DM)_S$ with $\Delta^{14}C_o$ of 90 ‰ prior to 9550 BC. Different "flat A levels" in the three panels would be associated with a hypothetical pre-

Figure 2.22: (upper panel) Dipole moment data and trend lines (in units of 10^{22} A m^2). Squares are calibrated Holocene dipole averages (± 1-sigma) of Merrill and McElhinny (1983); triangles are early- and pre-Holocene dipole measurements of McElhinny and Senanayake (1982) with reported ^{14}C (and thermoluminescence) ages assumed (preliminarily) equivalent to calendar ages; asterisks are normalized relative paleointensity measurements on marine sediments (Tauxe and Valet 1989); dashed curve A is the interpolating spline through the calibrated dipole averages (squares) extended into the pre-Holocene with a dipole value that would produce, with assumed "constant climate" conditions, an atmospheric $\Delta^{14}C_o$ of 90 °/oo; solid curve B is the smoothing spline through the triangles and is linked to the Holocene portion of curve A; short-short-long dashed curve C is the same as B with a different assumed pre-30,000 BP value; short-long dashed curve D is the trend line through the asterisks and is linked to the Holocene portion of curve A; dotted curve E is the smoothing spline through the recalibrated triangles (see text).

(middle panel) ^{14}C production rates associated with the dipole moment data and trends described above. Lines and symbols are same as in the upper panel. Right axis scales production rates relative to the deconvolved "constant climate" ^{14}C production rate average back to 500 cal BP.

(lower panel) Atmospheric $\Delta^{14}C$ trends derived, through the Q-forced model, from the ^{14}C production rate histories shown in the middle panel. In addition, the bar graph is the tree-ring $\Delta^{14}C$ record and the diamonds are the atmospheric $\Delta^{14}C$ levels (± 1-sigma) calculated from the ^{14}C ages of the $^{238}U/^{230}Th$-calibrated corals (see text) of Bard et al. (1990).

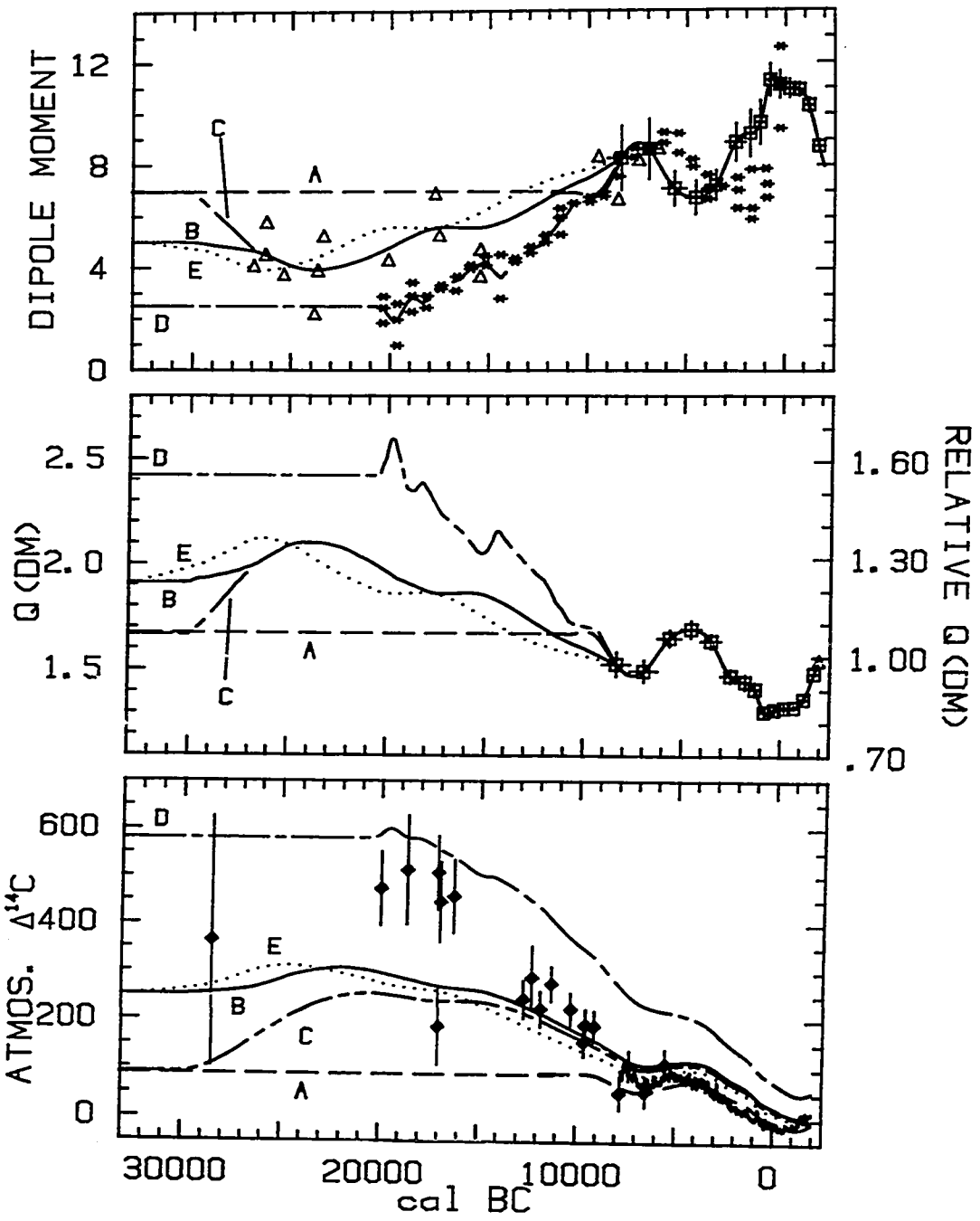
DIPOLE MOMENT
12
8
4
0
A
B
C
D
E
Q (DM)
2.5
2.0
1.5
RELATIVE Q (DM)
1.60
1.30
1.00
.70
ATMOS. Δ14C
600
400
200
0
30000
20000
10000
0
cal BC

Holocene "steady-state" $\Delta^{14}C_O$ of 50 °/oo. Also,"steady-state" ^{14}C production rate levels related to specific $\Delta^{14}C_O$ values would vary with different pre-Holocene exchange parameters and/or reservoir sizes (see section 2.5).

But pre-Holocene "conditions" are not truly at "steady-state" as demonstrated by the dipole moment histories in the upper panel of figure 2.22. A 22,000 yr record of relative paleointensity measurements on marine sediments from the North Atlantic (Tauxe and Valet 1989) indicates a nearly linear rise in the dipole moment between 20,000 and 10,000 BC (asterisks). The authors calibrated the ages of samples by assigning a date of 10,000 calendar yrs BP to the $\delta^{18}O$ digression interpreted as occurring at the Younger Dryas/Holocene transition. The conversion of sedimentary remanent intensity into a record of absolute global dipole moments requires several assumptions and normalizations; Tauxe and Valet (1989) emphasize the need for multiple marine and terrestrial records to substantiate a global dipole history. Indeed the Holocene portion of the marine record does not quite match the terrestrial dipole moment measurements (squares in the upper panel).

A trend line was drawn through the pre-8350 BC marine sediment results (long-short dashed line D) and linked to the interpolating spline of the terrestrial averages. The Holocene portion of the terrestrial record of McElhinny and Senanayake (1982) is considered here better defined as well as more complete than the marine paleointensity record and serves as the Holocene geomagnetic trend in all cases. A "steady-state" condition is assumed prior to and at the level of the earliest marine data at 20,000 BC.

The terrestrial global dipole data compiled in McElhinny and Senanayake (1982, table 4) extend well into the Late Wisconsin (triangles in figure 2.22 in addition to two data, not utilized, at 31,400 and 50,000 "thermoluminescence" yrs BP). Except for one

thermoluminescence date, the ages of the plotted samples are in ^{14}C yrs. To assign calendar dates to these pre-Holocene data points, I assumed (preliminarily) an equivalence in calendar and ^{14}C yrs BP. The modeling described below will allow the formulation of a calibration curve which will then be utilized to better approximate the calendar ages of the samples. The two most recent "uncalibrated" triangles shown in figure 2.22 represent the same data as the two earliest "calibrated" squares; the 500 and 900 yr discrepancies illustrate the magnitudes of the missing calibration factors at the time of the early Holocene.

A smoothing spline was determined on the pre-Holocene terrestrial dipole data with the two measurements at 15,400 BC from the same site weighted singly (solid curve B). The spline was linked to the previously determined interpolating spline for the Holocene dipole averages. I tested the impact of different assumed "steady states" before the earliest data at 27,000 BC by choosing two alternative geomagnetic initial conditions prior to 30,000 BC. The dipole moment either remains at the low strength indicated by the measured pre-Holocene levels (solid curve B) or commences at the same strength as the pre-Holocene level implied in the standard model scenarios with atmospheric $\Delta^{14}C_0$ of 90 o/oo (short-short-long dashed curve C). The dipole data are eventually recalibrated (as described below) and re-splined to determine a better calendar history of pre-Holocene dipole variations (dotted curve E).

In order to convert the geomagnetic trend lines shown in the upper panel of figure 2.22 into ^{14}C production rate histories, the six-step procedure for determining Holocene Q(DM), as outlined in the subsection above, might be applied to the extended time interval of the past 35,000 yrs. As part of this procedure, a ^{14}C production rate, $Q(^{14}C)$, is deconvolved from an observed atmospheric (or oceanic) $\Delta^{14}C$ history for the past 35,000 years. Then new estimates of c_1 in equation (2.1) are calculated that produce the best χ^2

fit, with respect to the $Q(^{14}C)$ history of the past 35,000 yrs, of each c_1-dependent Q(DM) record based on each dipole moment trend in upper figure 2.22. For several reasons, this procedure cannot currently be applied to this longer time interval.

First, conflicting evidence for the atmospheric $\Delta^{14}C$ history of the past 35,000 yrs prevents us from deconvolving a reliable estimate of $Q(^{14}C)$. Zbinden et al. (1989) present lake sediment evidence indicating generally lower levels in atmospheric $\Delta^{14}C$ during the several thousand years prior to the Holocene. Barbetti (1980) compiled over 20 measurements on atmospheric $\Delta^{14}C$ for the past 40,000 yrs which were dated by thermoluminescence or $^{230}Th/^{238}U$ disequilibrium techniques. The data points scatter widely between 50 °/oo and 700 °/oo with large uncertainties and no definite trend. From ^{14}C determinations on a stalagmite independently dated using the $^{230}Th/^{238}U$ disequilibrium method, Vogel (1983) calculates 4 atmospheric $\Delta^{14}C$ levels that include values of ca. 500 °/oo at 19,000 BP, ca. -100 °/oo at 29,500 BP and ca. 1000 °/oo at 35,000 BP.

Bard et al. (1990) use ^{14}C and $^{230}Th/^{234}U$ dating on coral cores to derive a well defined sequence of surface ocean $\Delta^{14}C$ levels with excellent calendar resolution back to 30,000 BP. By applying a reservoir correction of 400 ^{14}C yrs to the conventional ^{14}C ages, Bard et al. convert these results into atmospheric $\Delta^{14}C$ levels (diamonds with one-sigma errors in lower figure 2.22). The very late glacial $\Delta^{14}C$ levels indicated by the corals differ by ca. 200 °/oo from the lower contemporaneous lake sediment $\Delta^{14}C$ values determined by Zbinden et al. (1989). If the reservoir correction were zero rather than 400 yrs, the coral-derived atmospheric $\Delta^{14}C$ levels would only be reduced by 50 °/oo. Thus a consistent pre-Holocene atmospheric $\Delta^{14}C$ story is wanting.

A second essential for the proper deconvolution of a pre-Holocene $Q(^{14}C)$ history is the appropriate simulation of pre-Holocene carbon reservoir sizes and exchange

parameters. Glacial conditions for these variables are debatable; potential changes in oceanic parameters are considered in section 2.5. Even with suitable adjustments in F and K_Z, however, the global box-diffusion model presented here cannot adequately simulate the pre-Holocene-to-present carbon cycle because the model lacks features (eg. high-latitude oceanic reservoirs and processes) critical to the glacial/Holocene carbon cycle transition. Such modifications were not pursued in the present work.

Finally, a third complication in the conversion of DM data into Q(DM) records is the failure of the simple inverse square-root relationship of equation (2.1) for global dipole moments less than ca. 70% of the current value (Wada and Inoue 1966). Thus, as dipole trends fall farther below ca. 5.5 A m^2, the corresponding ^{14}C production rates will be increasingly less than predicted by equation (2.1), achieving a maximum level (at DM = 0) of double the current rate.

Despite these serious limitations, it is still possible to estimate the potential influence of alternative pre-Holocene dipole histories on model-derived atmospheric $\Delta^{14}C$ curves for the Holocene. The standard approach assumed a "steady-state" pre-Holocene ^{14}C production rate that generated a steady atmospheric $\Delta^{14}C_o$ of 90 o/oo under standard assumptions for exchange rates (curve A in middle and lower panel of figure 2.22). The subsequently deconvolved Holocene Q(^{14}C) record and the dipole-derived Q(DM) record were found to best match if the proportionality constant c_1 in equation (2.1) was 4.39. As a preliminary step, the alternative pre-Holocene Q(DM) histories described above were converted to Q(DM) curves (B, C, and D in middle panel of figure 2.22) using equation (2.1) with the same value for c_1. After 8350 BC, all curves are identical. Figure 1 of Wada and Inoue (1966) was utilized, after normalization to c_1, to estimate Q(DM) levels for the time intervals with lower dipole moments when equation (2.1) becomes imprecise.

The atmospheric $\Delta^{14}C$ histories produced by the forward global carbon model from

these three Q(DM) scenarios are all higher during the Holocene than the observed tree-ring $\Delta^{14}C$ record (lower panel of figure 2.22). The curves B and C associated with the terrestrial dipole measurements are both 3% too high, on average, during the Holocene while curve D from the marine dipole record is 10% above the tree-ring $\Delta^{14}C$ data on average. The minimal difference between curves B and C after 20,000 BC illustrates the reduced impact on the global ^{14}C cycle of alternative "steady-state" ^{14}C production rates beyond two ^{14}C half-lives or about 10,000 yrs. I do not further discuss curve C.

The ^{14}C activities associated with $\Delta^{14}C$ curves B and D were reduced by 3% and 10% respectively in order to match the averages of these atmospheric $\Delta^{14}C$ trends during the Holocene with the average tree-ring $\Delta^{14}C$. The adjusted B and D trends are again depicted as a solid curve and short-long dashed curve, respectively, in the upper inset of figure 2.23. These proportional reductions in atmospheric ^{14}C have a similar effect as applying a lower "effective c_1" to each dipole record. For each atmospheric history, both the average *and the range* in ^{14}C activities are diminished proportionally. Because ^{14}C production is less sensitive to the geomagnetic field changes at the lower dipole moments, the proportional decreases are not strictly valid for atmospheric $\Delta^{14}C$ levels that exceed ca. 200 ‰; but the adjustments are satisfactory for a preliminary analysis.

The revised "effective c_1" matches the average of the Holocene portion of the dipole-related atmospheric $\Delta^{14}C$ record with the tree-ring $\Delta^{14}C$ observations. As shown in the lower inset of figure 2.23, the *trend* in adjusted curve B (solid line) also fits the observed tree-ring data (bar graph). Furthermore, only moderate differences exist between $\Delta^{14}C(DM)$ derived from the Holocene dipole averages with an assumed pre-Holocene "steady-state" $\Delta^{14}C_o$ of 90 ‰ (dashed curve in lower inset) and $\Delta^{14}C(DM)$ derived from the "non-steady-state" terrestrial dipole record extended back 35,000 yrs (solid line in inset). This agreement supports the broad durability and independence of the Holocene

Figure 2.23: Radiocarbon/calendar age calibration curves. Solid, short-long dashed, and dotted curves are calculated from the respective trends in the upper inset. Dashed line represents ^{14}C/calendar age equivalence. Circles are calibrated coral data (± 1-sigma) of Bard et al. (1990).

(upper inset): Atmospheric $\Delta^{14}C$ histories are solid curve B, short-long dashed curve D, and dotted curve E from lower figure 2.22 after adjustment so that post-7750 BC averages match the corresponding average in the tree-ring $\Delta^{14}C$ observations. Circles are the atmospheric $\Delta^{14}C$ (± 1-sigma) values calculated from the ^{14}C ages of the calibrated corals of Bard et al. (1990).

(lower inset): Adjusted atmospheric $\Delta^{14}C$ curves B and E, as above, compared to dashed curve A of figure 2.22 and the Holocene tree-ring $\Delta^{14}C$ record (bar graph).

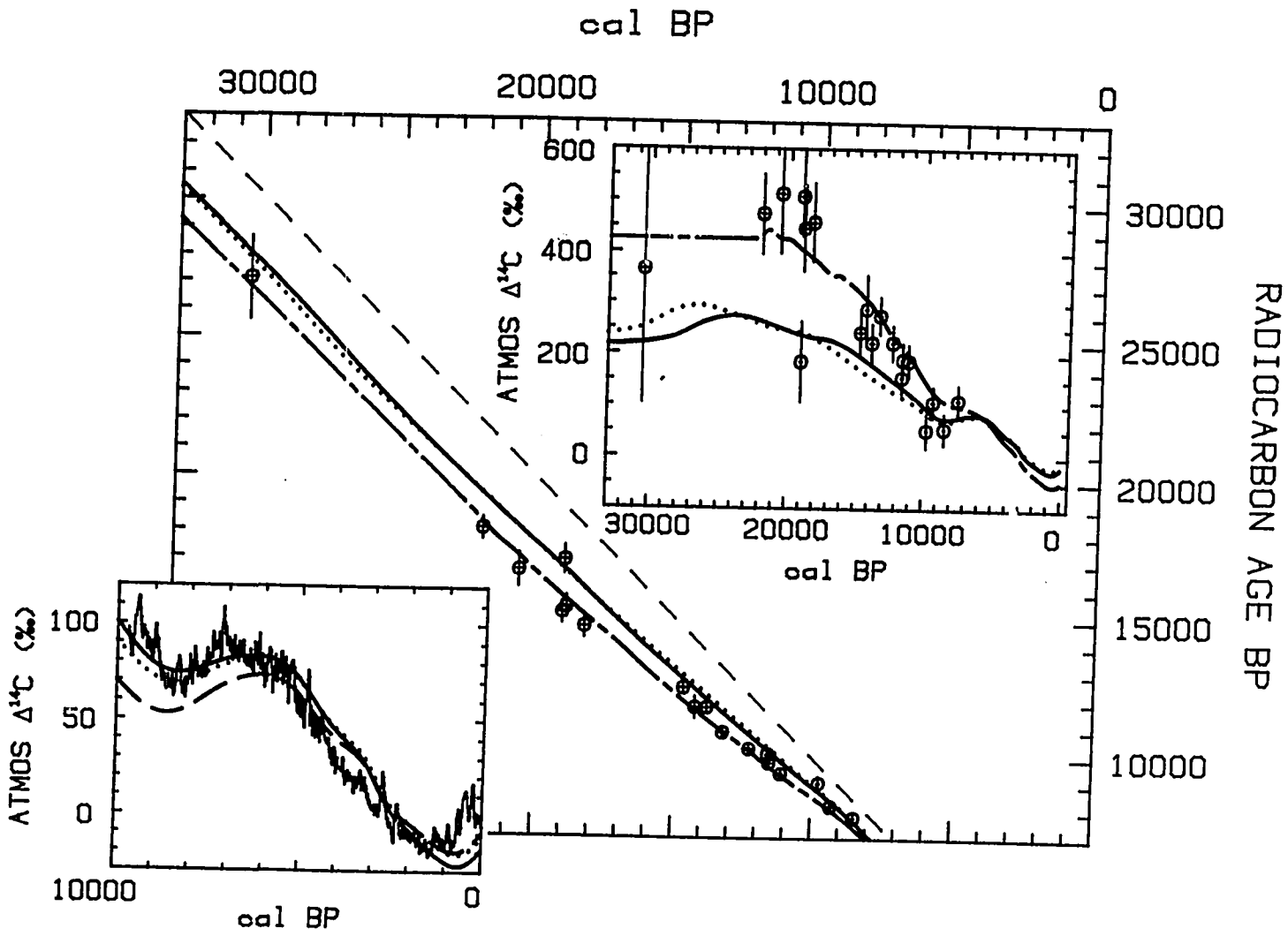
cal BP
30000
20000
10000
0
RADIOCARBON AGE BP
30000
25000
20000
15000
10000
ATMOS Δ14C (‰)
600
400
200
0
30000
20000
10000
0
cal BP
ATMOS Δ14C (‰)
100
50
0
10000
0
cal BP

$\Delta^{14}C$(DM) analysis presented above regardless of assumed pre-Holocene conditions.

These preliminary results have several important implications. The elevated pre-Holocene dipole-induced ^{14}C production rates of scenario B generate an atmospheric $\Delta^{14}C$ history that even better fits the early Holocene observations than the standard $\Delta^{14}C$(DM) derived above (lower inset of figure 2.23). In this way, our earlier conclusion that the long-term trend in atmospheric $\Delta^{14}C$ appears to be primarily produced by changes in the global dipole moment is reinforced by this excellent fit of the extended $\Delta^{14}C$(DM) with the Holocene observations. This early Holocene match also implies that climate plays a minor role in producing any of the long-term changes in the global ^{14}C system even near the glacial/Holocene transition.

Secondly, the coral measurements of elevated pre-Holocene $\Delta^{14}C$ levels are compatible with the dipole-induced long-term $\Delta^{14}C$ scenarios while the lake sediment $\Delta^{14}C$ history is discordant with this evidence. This independent support for the coral evidence dictates a re-evaluation of the assumptions behind the lake sediment $\Delta^{14}C$ history (see section 1.3). Again another implication is that climate is a secondary factor in global ^{14}C change during the late Wisconsin.

Evidence is still ambiguous for deciding between the terrestrial and the marine measurements as alternative representatives of the pre-Holocene global dipole moment. The atmospheric $\Delta^{14}C$ scenario associated with the pre-Holocene marine paleointensity data of Tauxe and Valet (1989) better matches the coral measurements of Bard et al. (1990) as shown in the upper inset of figure 2.23. But the Holocene portion of this atmospheric $\Delta^{14}C$ trend is much steeper than the tree-ring $\Delta^{14}C$ record; the early and late Holocene $\Delta^{14}C$(DM) trend is ca. 50 ‰ too high and too low, respectively. The extended atmospheric $\Delta^{14}C$ curve based on the dipole measurements of McElhinny and

Senanayake (1982) more closely resembles the tree-ring $\Delta^{14}C$ record but deviates from the pre-Holocene coral data.

This dilemma may be partially resolved by the proper determination of the proportionality constant c_1 that quantifies the geomagnetic field's influence on the global ^{14}C production rate. Because our preliminary analysis supports the veracity of the coral $\Delta^{14}C$ measurements, a simple atmospheric $\Delta^{14}C$ curve based on this data might be utilized to deconvolve a pre-Holocene $Q(^{14}C)$ record which would subsequently permit a direct calculation of c_1. Also required is a global ^{14}C model designed to realistically simulate both glacial and Holocene oceanic/terrestrial conditions. On the other hand, as noted above, climate would appear to be a limited factor in prescribing ^{14}C changes at least during the past 20,000 yrs.

The two preliminary dipole-derived atmospheric $\Delta^{14}C$ curves B and D (figure 2.23, upper inset) were converted into calendar histories of radiocarbon ages (main figure 2.23). The reservoir-corrected ^{14}C ages of the coral samples are also plotted. Both calibration curves show substantial deviation from a ^{14}C/calendar age equivalence (dashed line in main figure). As before, the trend associated with the marine paleointensity record has a moderately better agreement with the coral data of Bard et al. (1990) than the trend derived from the terrestrial data of McElhinny and Senanayake (1982). The former calibration curve has been artificially extended prior to 22,000 BP by assuming an arbitrary "steady state" dipole moment and constant atmospheric $\Delta^{14}C$ level as discussed above. Thus this early portion of calibration curve D is a modeling choice not directly based on observations.

The ^{14}C ages of the dipole moment data of McElhinny and Senanayake (1982) were calibrated to calendar ages according to the first-generation calibration curve B derived from this "uncalibrated" terrestrial record. This calibration shifted the calendar ages of the

older dipole samples by ca. 2500 yrs. A new smoothing spline was calculated for the newly calibrated pre-Holocene data and linked to the interpolating spline through the previously calibrated Holocene dipole averages (dotted curve E in figure 2.22, upper panel). Each step of the procedure described above was repeated to generate a calibrated Q(DM) history (figure 2.22, middle panel), an atmospheric $\Delta^{14}C$ history (figure 2.22, lower panel), an adjusted atmospheric $\Delta^{14}C$ curve (figure 2.23, upper and lower insets), and a revised calibration curve (dotted line in main figure 2.23) associated with the "re-calibrated" dipole moment data of McElhinny and Senanayake (1982). Only minor differences exist between the first- and second-generation calibration curves B and E.

As a preliminary calibration aid, the correlated radiocarbon and calendar ages, as derived from the calibration curves in figure 2.23, are listed in Table 2.1. The first column of calendar ages is based on the revised calibration curve E. For radiocarbon ages younger than 12,000 BP, we prefer the calibration derived from the adjusted high-resolution ^{14}C history defined by lake sediments and tree rings (section 1.3). These recommended calendar ages are listed in Table 1.1.

2.4 Evidence from Greenland ^{10}Be concentrations for a production rate origin for reservoir $\Delta^{14}C$ variations

The production of ^{10}Be and ^{14}C

Entering the upper atmosphere, cosmic rays (primarily galactic particles such as high-energy protons) collide with and fragment molecules like oxygen and nitrogen into ^{10}Be and other nuclear fragments in "spallation events". Therefore the ^{10}Be production rate should respond to geomagnetic and solar modulations of cosmic radiation in a similar

TABLE 2.1

CALENDAR YR - RADIOCARBON YR AGE CALIBRATION DERIVED FROM:

(1) THE MCELHINNY/SENANAYAKE PRE-HOLOCENE DIPOLE SCENARIO

(2) THE TAUXE/VALET PRE-HOLOCENE DIPOLE SCENARIO

^{14}C AGE	CAL AGE 1	CAL AGE 2	AVERAGE CAL AGE
28000	30500		
27000	29500		
26000	28500		
25000	27500		
24000	26600		
23000	25600		
22000	24600		
21000	23600		
20000	22500		
19000	21500	22500	22000*
18000	20400	21500	21000*
17000	19300	20400	19800*
16000	18200	19300	18700*
15000	17100	18100	17600*
14000	16000	16900	16500*
13000	14900	15800	15400*
12000	13700	14600	14200*

*Recommended calibration

fashion as ^{14}C production. If variations in atmospheric $\Delta^{14}C$ do indeed result solely from production rate changes without the influence of variable climate, then a close correlation between the histories of ^{10}Be production and ^{14}C production is expected.

However, an important difference exists in the genesis of these cosmogenic isotopes (Lal and Peters, 1967). The production of ^{10}Be is *directly* related to the cosmic influx through spallation events while ^{14}C nuclei primarily originate *indirectly* from the galactic flux through the capture by atmospheric nitrogen of thermal (slow) neutrons in the nuclear reaction $^{14}N(n,p)^{14}C$. These neutrons are energetic spallation products which have subsequently lost energy. The leakage of neutrons from the upper atmosphere before thermalization and capture by ^{14}N reduces the absolute ^{14}C production rate. Because of these distinct origins, geomagnetic and solar variations produce different relative changes in ^{10}Be and ^{14}C production rates.

Lal (1988) has tabulated expected changes in nuclear disintegrations (proportional to ^{10}Be production rates) and ^{14}C production rates for variations in the global dipole moment and in solar activity. For a variation in the dipole moment, DM, from half to double its present level, ^{10}Be production varies ca. ± 66% from its average rate while ^{14}C production varies ca. ± 70% from its average rate. Since Holocene variations in DM are less than half this extreme, the long-term production trends in ^{10}Be and ^{14}C should be more than 93% (66/70) alike despite differences in formation processes.

Using Lal's (1988) proposed average level and Maunder-Minimum level of solar activity, the expected relative increases in ^{10}Be and ^{14}C production are 20% and 30%, respectively. Thus, according to this analysis, century-scale peaks in ^{10}Be are expected to be only 66% (20/30) as extreme as the corresponding ^{14}C peaks. This result is very sensitive to the debatable choice for the typical century-scale range in solar activity.

Evidence for *comparable* relative amplitudes has also been cited (eg. Beer et al. 1988). Thus the exact disparity is uncertain but must at least be considered qualitatively when comparing relative ^{10}Be and ^{14}C production rates.

Cosmogenic ^{10}Be quickly attaches to aerosols and is removed from the atmosphere in precipitation (atmospheric residence time ≈ 1-2 yrs). When the precipitate is snow, a history of changes in the low concentrations of ^{10}Be can be preserved in ice layers and measured by accelerator mass spectrometry. A ^{10}Be concentration record from the 1370-meter Camp Century, Greenland ice core spans the pre-AD 1800 Holocene and a portion of the late Pleistocene (Beer et al. 1988). The ice-flow model for dating the ice layers was tuned to produce dates of AD 1700 for the Maunder Minimum ^{10}Be excursion and 9050 BC for the $\delta^{18}O$ change at the end of the Younger Dryas. The post-AD 1180 ^{10}Be concentration measurements from the Milcent, Greenland ice core were incorporated into the final ^{10}Be record.

In order to treat this ^{10}Be concentration record as a direct proxy for a ^{14}C production rate history, several associations must be valid: (1) the relative changes in ice-core ^{10}Be concentrations reflect global-scale atmospheric ^{10}Be variations rather than regional climatic events; (2) the atmospheric ^{10}Be variations accurately reflect ^{10}Be production rate variations; and (3) ^{10}Be production rate changes are equivalent to ^{14}C production rate changes. With respect to the third assumption, already noted is the possibility that typical century-scale changes in ^{10}Be production rate are significantly less than corresponding ^{14}C production rate changes.

The veracity of the first assumption is also unsettled. Because post-7000 BC fluctuations in ^{10}Be and $\delta^{18}O$ (a climate indicator) in the Greenland cores do not correlate, Beer et al. (1988) contend that climate-induced changes in ice accumulation rates are not responsible for the recorded variations in ^{10}Be concentration. Lal (1987), in

contrast, argues that ^{10}Be concentration variations on all time scales may primarily originate through climatic changes in precipitation rates, tropopause height, and the latitudinal position of principal stratosphere-troposphere exchange. A significant correlation between Q(^{14}C) and [^{10}Be] would strongly support a production-rate rather than climatic origin for ^{10}Be variations because climate influences each elemental cycle distinctly. While precipitation controls the permanent removal of atmospheric ^{10}Be, wind speeds and temperatures are important in setting the CO_2 gas exchange rate that dominates the removal (and return) of atmospheric ^{14}C. The pre-7000 BC Greenland ice record is not considered below because ^{10}Be and $\delta^{18}O$ variations do correlate and the role of climate is potentially much greater in creating ice-layer [^{10}Be] fluctuations.

In regard to the second assumption, do atmospheric ^{10}Be variations translate into production rate changes without frequency-dependent modification? As discussed in section 2.1, atmospheric $\Delta^{14}C$ variations are attenuated with respect to causal ^{14}C production rate changes through the reservoir exchanges that govern the atmospheric ^{14}C burden of ca. 100 yrs of production and its residence time of 7 yrs (eg. Houtermans 1966). In contrast, the shorter atmospheric residence time of ^{10}Be and the permanence of its removal process provide less chance for attenuation. For example, Beer et al. (1985) estimate that an 11-yr cycle in ^{10}Be production is attenuated only ca. 20%. Thus the attenuation factor H(^{10}Be) is 0.8 whereas H(^{14}C) for a comparable sinusoidal 11-yr cycle is .008 (see section 2.1). Longer-term periodic fluctuations in ^{10}Be (and ^{14}C) production are even less attenuated in the atmospheric signal.

I applied the simple 2-box model of Houtermans (1966) to the global ^{10}Be cycle by stipulating: (1) an atmospheric residence time T_1 of 1, 2, or 3 yrs, (2) a decay half-life of 1.5×10^6 yr, and (3) no return flux of ^{10}Be removed from the atmosphere. For $T_1 = 1$ yr, H(^{10}Be) was calculated to be ca. 0.85 and 1.00 for periodic ^{10}Be production rate

variations of 10 yrs and 100 yrs, respectively. For production variations of the same periods, H(^{10}Be) was, respectively, 0.62 and 0.99 for T_1 = 2 yrs, and 0.47 and 0.98 for T_1 = 3 yrs. Thus, for century-scale and millennial-scale variations, an insignificant attenuation of the ^{10}Be production rate signal occurs in the derivative atmospheric ^{10}Be record.

To summarize the above discussion of assumptions, the *Holocene-scale* trends in ^{14}C and ^{10}Be production rates should be theoretically equivalent within a few percent while *century-scale* ^{10}Be production variations are expected to be weaker than contemporaneous ^{14}C production variations by as much as 33%. Except for rapid decade-scale variations, atmospheric ^{10}Be fluctuations reflect production rate changes with little attenuation. Lastly, a strong correlation between Q(^{14}C) and Q(^{10}Be) would eliminate climate as a major factor in the ice-core ^{10}Be concentration history. Here Q(^{10}Be) represents the ^{14}C production history derived from the ^{10}Be concentration record.

Figures 2.24 and 2.25 compare the relative variations in the model-deconvolved ^{14}C production rate with the relative variations in observed ^{10}Be concentrations presented in figure 2 of Beer et al. (1988). Variations are scaled relative to the post-7000 BC average in Q(^{14}C) of 1.48 ^{14}C atoms s^{-1} cm_E^{-2} and the post-7000 BC average in [^{10}Be] of 1.20 x 10^4 atoms g^{-1}, respectively. The pre-7000 BC [^{10}Be] has been set at the same relative level as the standard pre-7750 BC "steady-state" Q(^{14}C) of 1.67 ^{14}C atoms s^{-1} cm_E^{-2}. I have ignored, for the moment, the potential inaccuracies of the three assumptions investigated above and equate the relative [^{10}Be] variations with ^{14}C production rate changes.

The long-term ^{14}C and ^{10}Be trends and century-scale features show a close correspondence both in timing and magnitude. When the ^{10}Be curve is subdivided into

Figure 2.24: Variations in ^{14}C production rate and ^{10}Be concentration relative to their respective post-7000 BC averages. The ^{14}C production rate history (bar graph) was deconvolved from the tree-ring $\Delta^{14}C$ record using the global carbon model with constant exchange parameters; the [^{10}Be] history (heavy line) was measured from Greenland ice cores by Beer et al. (1988). Both curves assume a pre-data constant relative level 12.5% above the post-7000 BC average.

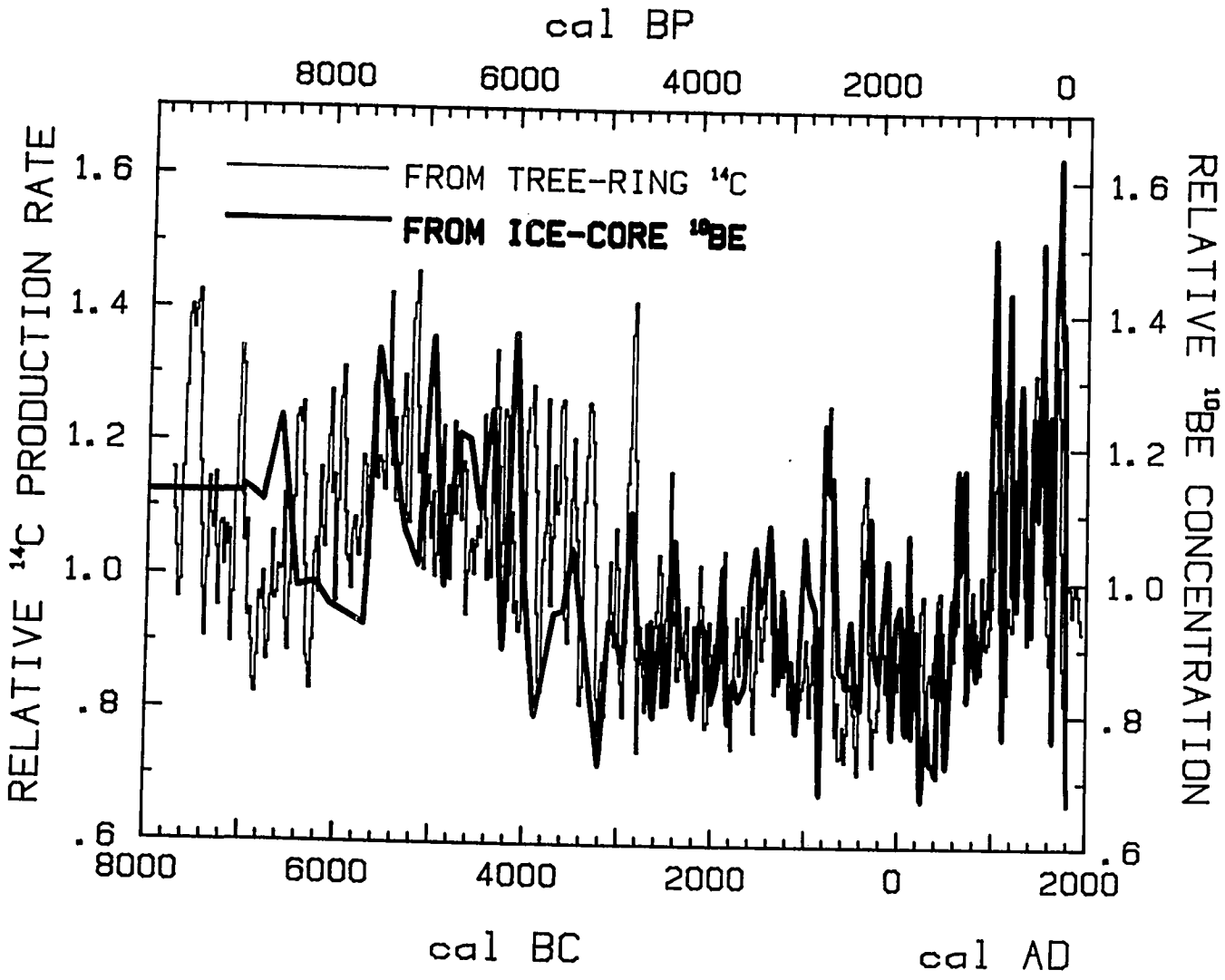
cal BP
8000
6000
4000
2000
0
FROM TREE-RING ^{14}C
FROM ICE-CORE ^{10}BE
RELATIVE ^{14}C PRODUCTION RATE
RELATIVE ^{10}BE CONCENTRATION
1.6
1.4
1.2
1.0
.8
.6
8000
6000
4000
2000
0
2000
cal BC
cal AD

Figure 2.25: Variations in ^{14}C production rate and ^{10}Be concentration relative to their respective post-7000 BC averages. See figure 2.24.

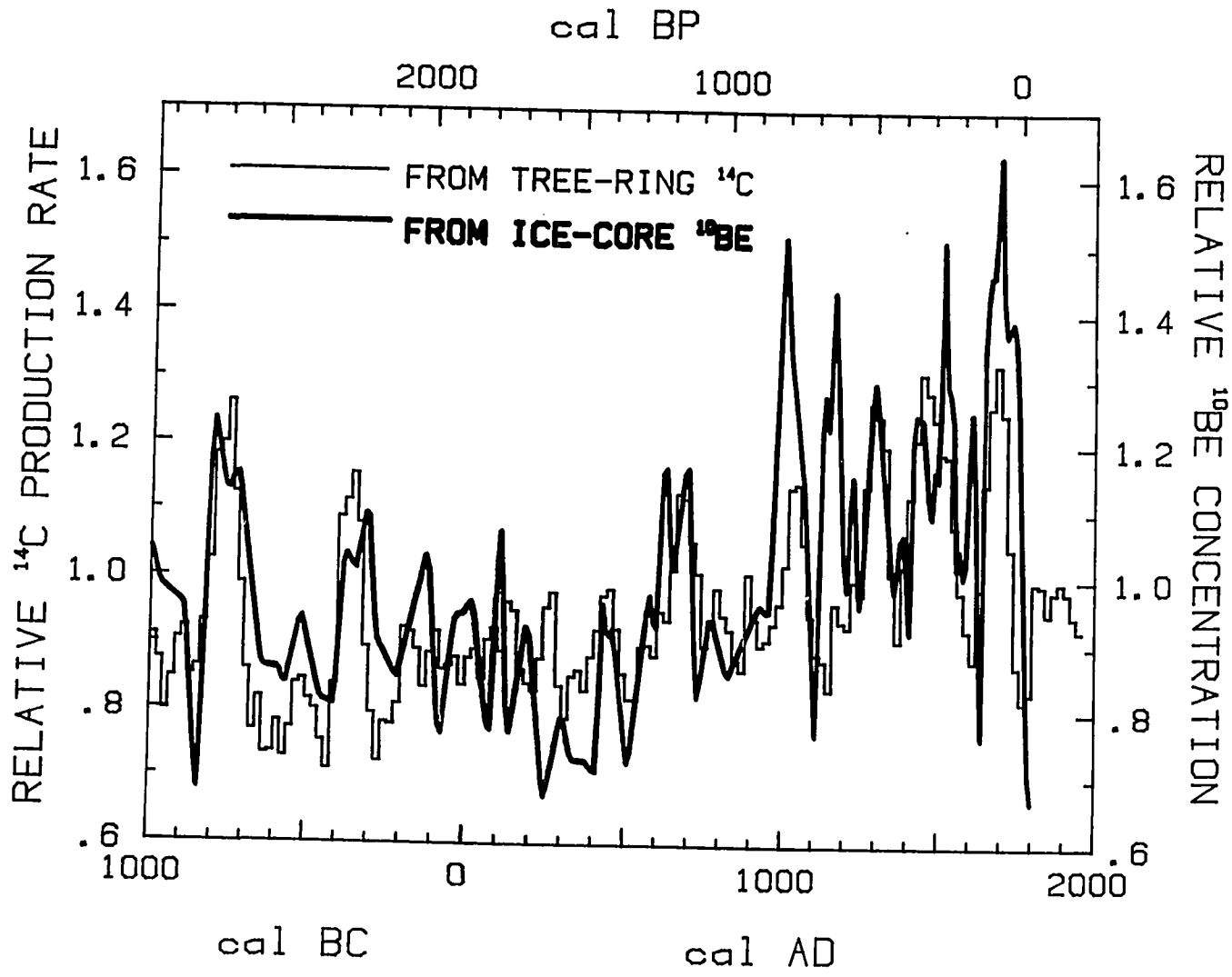
cal BP
2000
1000
0
FROM TREE-RING ^{14}C
FROM ICE-CORE ^{10}BE
RELATIVE ^{14}C PRODUCTION RATE
RELATIVE ^{10}BE CONCENTRATION
1.6
1.4
1.2
1.0
.8
.6
1000
0
1000
2000
cal BC
cal AD

the same bi-decadal intervals as the ^{14}C record, the correlation coefficient is .47 for the entire post-7000 BC comparison and .67 for the post-1000 BC portions (figure 2.25). Averaging both curves in 200-yr intervals leads to correlation coefficients of .70 and .86, respectively, for the post-7000 BC and post-1000 BC time periods.

Both records have flat long-term trends between 3500 BC and AD 500. Earlier researchers contrasted the flat ^{10}Be record with the long-term "sinusoidal" trend in tree-ring $\Delta^{14}C$; the decreasing $\Delta^{14}C$ trend of the last half of the Holocene appeared to require a different origin than contemporary geomagnetic influence because of the stability of the ^{10}Be trend. It is apparent from figure 2.24 (in which ^{14}C production rate itself is compared to the ^{10}Be data) that, on the contrary, the long-term ^{10}Be and ^{14}C trends do not need separate explanations because the two derived production rate curves match closely, especially after 3500 BC. This affinity suggests a common (geomagnetic) origin for the Holocene-scale trends in these two cosmogenic isotopes; discrepancies between these curves and the dipole moment record more likely stem from inaccuracies in the geomagnetic data than from a climatic cause (see below). Clearly, a direct comparison of production rate histories is an instructive approach.

A discrepancy between the two long-term curves occurs in the 4500-3500 BC time period; the deconvolved ^{14}C production rate, $Q(^{14}C)$, declines more gradually than the ^{14}C production rate, $Q(^{10}Be)$, indicated by the $[^{10}Be]$ data. However, the coarser resolution of the pre-3500 BC $[^{10}Be]$ record may prevent detection of some of the finer features visible in the ^{14}C record and may artificially produce the apparent offset in rates at 4500-3500 BC. This apparent disparity in production rates creates a longer-lasting distinction between the $\Delta^{14}C$ history derived from $Q(^{10}Be)$ and the observed ^{14}C record (see below). Again the direct comparison of production rates is critical to evaluating the

agreement between corresponding reservoir $\Delta^{14}C$ histories.

The relative amplitudes of the century-scale ^{10}Be variations range from 25% less to 15% greater than their ^{14}C counterparts, with many pairs of comparable peaks (figures 2.24, 2.25). If indeed century-scale ^{10}Be production rate changes should be weaker than associated fluctuations in ^{14}C production rate, then apparently these [^{10}Be] variations have frequently been enhanced perhaps through climatic factors as described above. However, this behavior is not consistent; the augmentation is greatest during the last 1000 years. Extrapolating a strong climatic signal to all century-scale ^{10}Be variations from the behavior of only the Maunder Minimum (Lal et al. 1990) appears to be premature.

The Q(^{14}C) and Q(^{10}Be) histories were averaged over the same calendar intervals as the global dipole moment data (Merrill and McElhinny 1983) and were then converted, using equation (2.1), into corresponding dipole moment averages DM(^{14}C) and DM(^{10}Be) (figure 2.26). As detailed above, a constant of proportionality $c_1 = 4.39$ yields the best match between the fourteen Holocene Q(^{14}C) and Q(DM) averages; this c_1 was employed to calculate the dipole moment values necessary to entirely explain the 14 averages of the deconvolved ^{14}C production rate. A value for c_1 of 4.35 was similarly derived to best fit the Q(^{10}Be) averages to their Q(DM) counterparts. Because the Q(^{10}Be) record spans less time than Q(^{14}C), only 11 averages could be calculated and converted into the corresponding dipole moments required to geomagnetically explain the [^{10}Be] observations.

The DM(^{14}C) averages correlate more strongly with the measured dipole moments than do the DM(^{10}Be) averages ($r = .76$ and .37, respectively). In fact, the DM(^{10}Be) record has a much greater affinity to the DM(^{14}C) record ($r = .71$) than to the dipole data. Both isotopic records exhibit a "phase shift" with the mid-Holocene rise in the dipole record. As argued above, because climate should influence each isotopic cycle distinctly,

Figure 2.26: Measured and isotope-deduced dipole moment averages. Diamonds are the dipole moment averages of Merrill and McElhinny (1983) with horizontal bars denoting the representative time intervals; crossed squares are the dipole moments derived from the deconvolved "constant climate" ^{14}C production rates averaged for the same time intervals; triangles are the dipole moments derived from the ^{14}C production rates inferred from [^{10}Be] variations averaged for these time intervals. Text contains details of derivations.

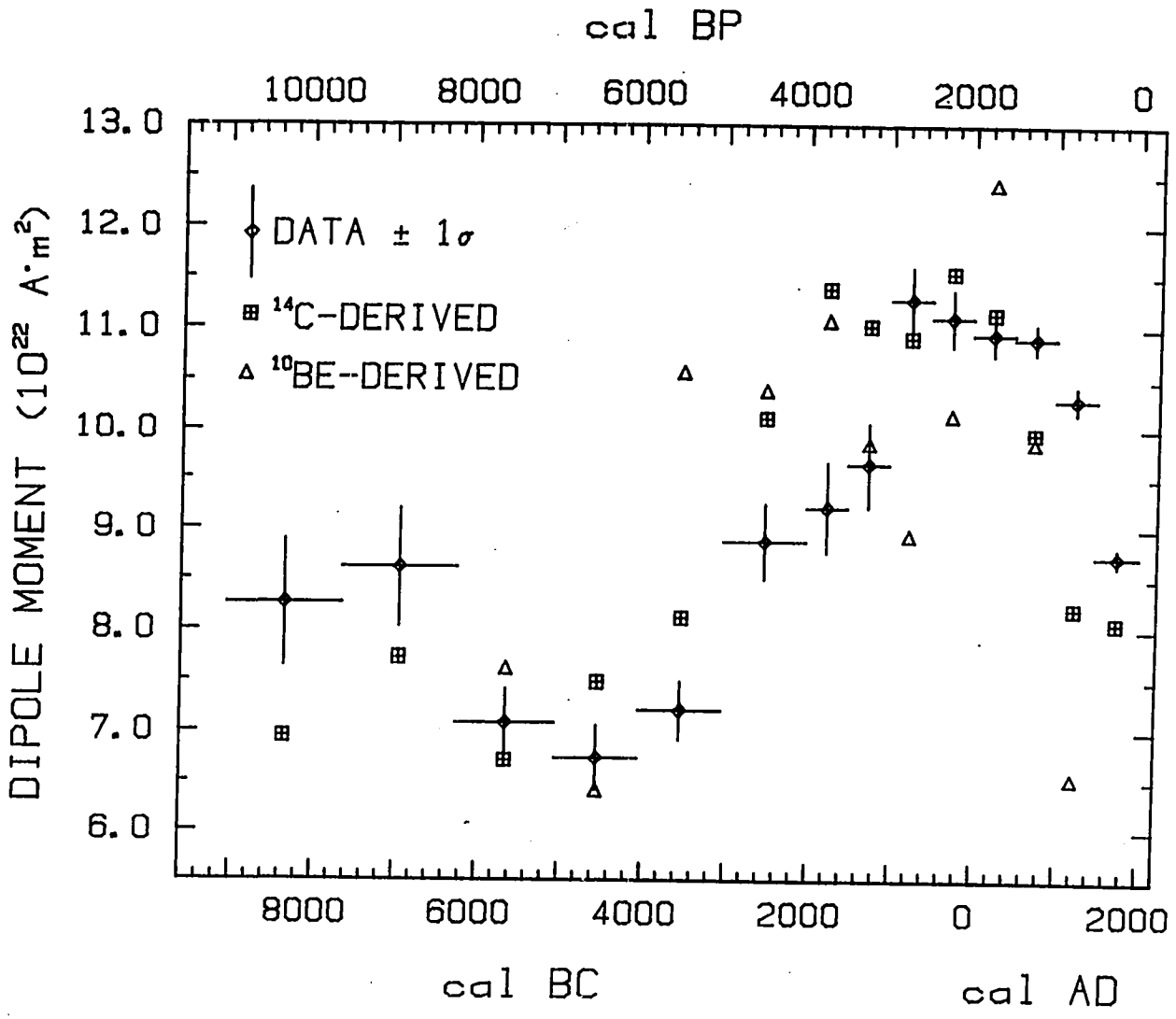
cal BP
10000
8000
6000
4000
2000
0
13.0
12.0
11.0
10.0
9.0
8.0
7.0
6.0
DIPOLE MOMENT (10^22 A·m^2)
DATA ± 1σ
14C-DERIVED
10BE-DERIVED
8000
6000
4000
2000
0
2000
cal BC
cal AD

the similarities in the isotopic Holocene-scale trends suggest a limited role for climatic change in creating these histories. Indeed these isotopic records may be better proxies for Holocene-scale geomagnetic variations than the uncertain dipole data (see section 2.3); the high resolution, continuous ^{14}C record may be the best choice. As a second explanation, perhaps a solar component is responsible for the apparent mutual deviations in the isotope-derived dipole averages from the measurements.

Finally, the higher frequencies were reintroduced to the Q(DM) record to reconstruct a "complete" ^{14}C production rate history to be compared with the independent Q(^{10}Be) record (figure 2.27). Bi-decadal dipole-related ^{14}C production rate records with initial "steady-state" atmospheric $\Delta^{14}C_o$ levels of 90 ‰ and 50 ‰ were deconvolved from the global carbon model; the atmospheric $\Delta^{14}C$ records used to force the deconvolution model are the bi-decadal reconstructions of $\Delta^{14}C$(DM) shown in figure 2.20.

Ideally, the ^{14}C production rates derived from such dipole-related $\Delta^{14}C$ reconstructions represent the "true" history of production unencumbered by any "false" climatic signal included in the *observed* $\Delta^{14}C$ record. Assuming the veracity of the measured dipole averages, then the dipole-related curves have been "corrected" for the climate factors (eg. changes in air-sea CO_2 gas exchange or oceanic ventilation rate) that are superimposed on the geomagnetic component in the tree-ring $\Delta^{14}C$ observations.

However, the original Q(^{14}C) curve (figure 2.27, upper left panel) correlates better with the independently measured production rate proxy, [^{10}Be] (lower right panel), than either "ocean-corrected" production record (remaining panels). The correlation coefficients for the fit of the post-7000 BC and post-1000 BC Q(^{10}Be) record with analogous temporal portions of Q(^{14}C) are .47 and .67 respectively, and with analogous temporal portions of Q(DM) having $\Delta^{14}C_o$ = 90 ‰ are .33 and .56 respectively, with

Figure 2.27: Model-derived relative short- and long-term ^{14}C production rate variations compared to the ice-core [^{10}Be] record. Upper left panel shows the ^{14}C production history derived from the tree-ring $\Delta^{14}C$ record with assumed "constant climate" conditions and a pre-Holocene "steady-state" atmospheric $\Delta^{14}C_o$ of 90 ‰; upper right panel shows the dipole-related ^{14}C production trend deconvolved from the reconstructed atmospheric $\Delta^{14}C$ curve B in figure 2.20 with assumed $\Delta^{14}C_o$ of 90 ‰; lower left panel shows the dipole-related ^{14}C production trend deconvolved from curve C in figure 2.20 with assumed $\Delta^{14}C_o$ of 50 ‰; lower right panel displays the relative [^{10}Be] measurements of Beer et al. (1988).

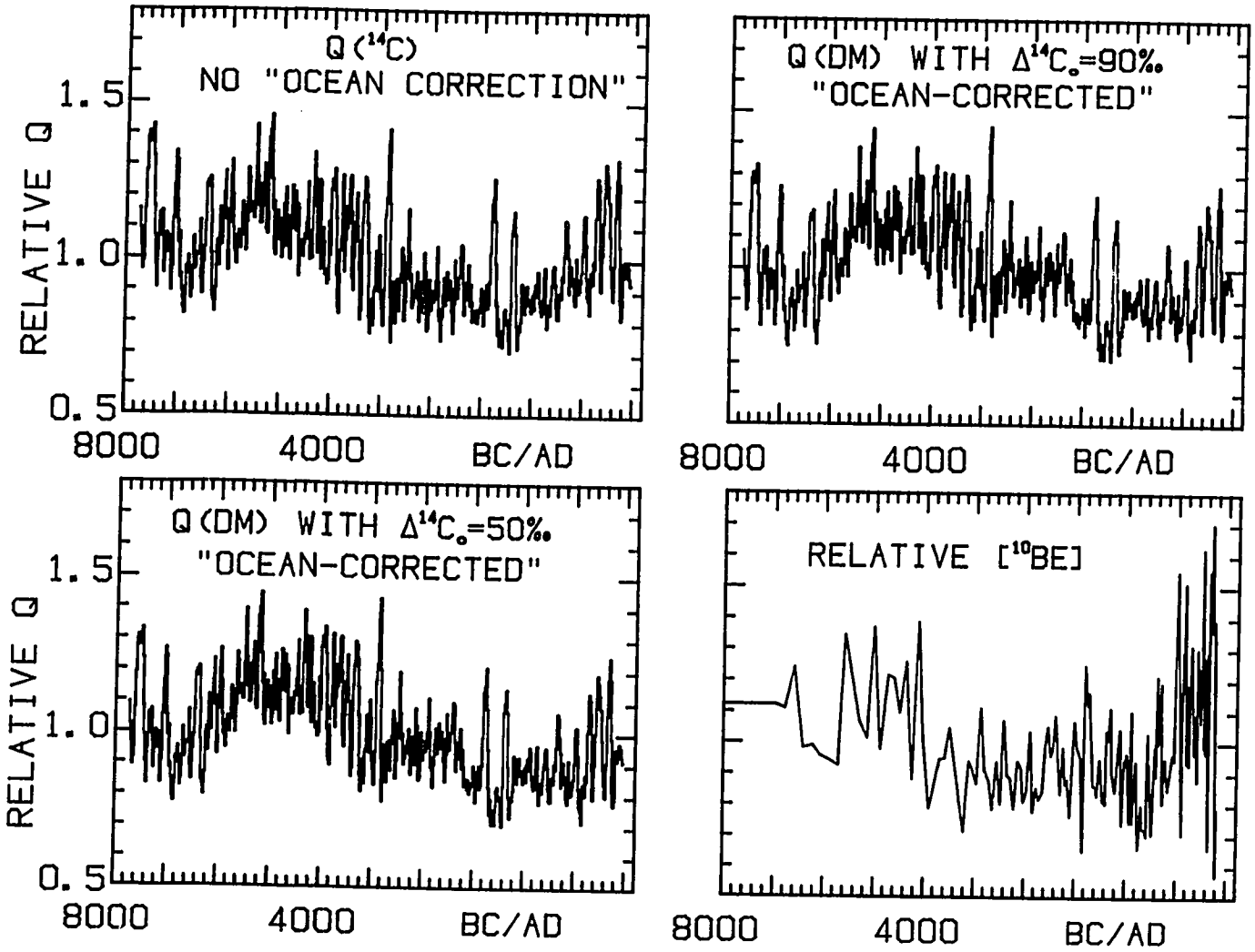
Q(14C)
NO "OCEAN CORRECTION"
RELATIVE Q
1.5
1.0
0.5
8000
4000
BC/AD
Q(DM) WITH Δ14C0=90‰
"OCEAN-CORRECTED"
8000
4000
BC/AD
Q(DM) WITH Δ14C0=50‰
"OCEAN-CORRECTED"
RELATIVE Q
1.5
1.0
0.5
8000
4000
BC/AD
RELATIVE [10BE]
8000
4000
BC/AD

analogous temporal portions of Q(DM) having $\Delta^{14}C_o$ = 50 o/oo are .35 and .56 respectively. As discussed above, climate is likely to influence ice-core [^{10}Be] differently than tree-ring Δ^{14}C; thus, the poor fit of the "corrected" records to Q(^{10}Be) suggests that the dipole moment measurements themselves may not be precise indicators of past geomagnetic activity.

Q(^{10}Be)-derived atmospheric and oceanic $\Delta^{14}C$

The Q(^{10}Be) history produced a series of Holocene Δ^{14}C variations in the atmospheric and oceanic reservoirs of the forward global carbon model. These model records were compared to the tree-ring and foraminifera observations discussed above. Beer et al. (1988) have performed the same model simulation with an input production function normalized differently (see below). As a result, our interpretations do not completely agree.

The atmospheric and oceanic Δ^{14}C histories derived from the ice-core ^{10}Be record are closely similar to the measured ^{14}C trends (figure 2.28 and inset). The atmospheric Δ^{14}C(^{10}Be) trend drops more rapidly, followed by a more gradual decline, in the mid-Holocene than the tree-ring Δ^{14}C data. However, the different slopes are attributable to the production rate discrepancies during 4500 - 3500 BC, as discussed above. The disparity may originate artificially from the limited resolution of the ice-core [^{10}Be] record during this time interval. Reservoir Δ^{14}C integrates the past history of ^{14}C production rate changes, thus prolonging the influence of short-term disparities in production rate levels. For this reason, I am less concerned with the digression of Δ^{14}C(^{10}Be) from observations during the mid-Holocene; I think the direct comparison of production rate histories better tests the agreement in isotopic signals than the indirect comparison of the

Figure 2.28: Tree-ring $\Delta^{14}C$ record (bar graph) and model-derived atmospheric $\Delta^{14}C$ (heavy line) based on the ^{14}C production rate history inferred from the ice-core [^{10}Be] record.
(inset): Holocene histories of the model ventilation index (in ^{14}C yrs). The MVI record denoted by the light bar graph is associated with the deconvolved "constant climate" ^{14}C production rate; the MVI record denoted by the heavy line is associated with the ^{14}C production history inferred from ^{10}Be data. The symbols show the foram ventilation indices of Andrée et al. (1986a) after adjustment by -310 ^{14}C yrs (see figure 2.19).

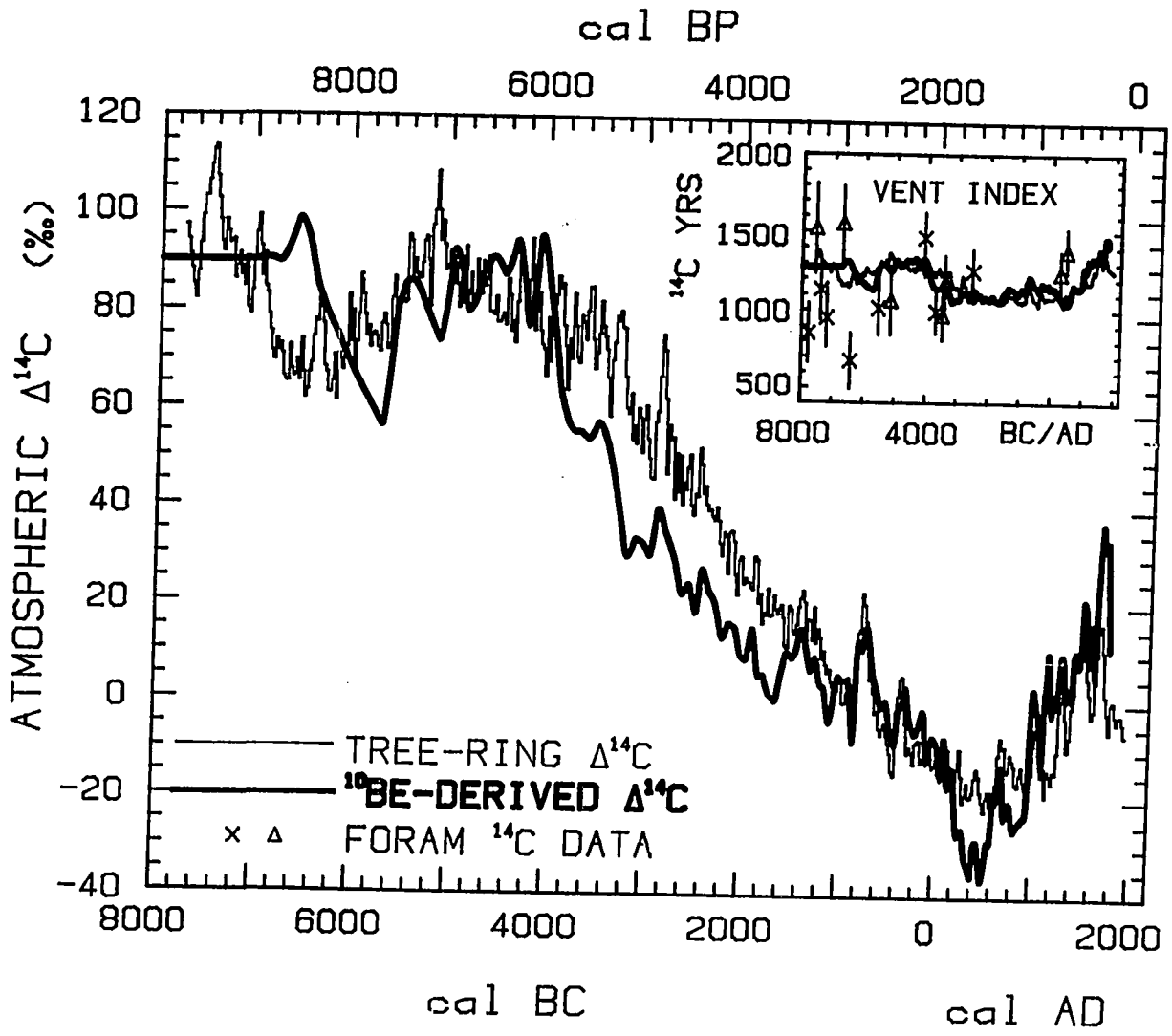
cal BP
8000
6000
4000
2000
0
120
100
80
60
40
20
0
-20
-40
ATMOSPHERIC Δ14C (‰)
2000
1500
1000
500
14C YRS
VENT INDEX
8000
4000
BC/AD
TREE-RING Δ14C
10BE-DERIVED Δ14C
FORAM 14C DATA
8000
6000
4000
2000
0
2000
cal BC
cal AD

integrated reservoir changes associated with them.

Beer et al. (1988) demonstrate that the slope in the mid-Holocene tree-ring $\Delta^{14}C$ can be accurately reproduced by a ^{10}Be-forced global carbon model if (1) the post-7000 BC $Q(^{10}Be)$ record is normalized to produce an average $\Delta^{14}C(^{10}Be)$ from AD 1 - 1000 that is equivalent to the average observations, and (2) the pre-Holocene $Q(^{10}Be)$ is set at 20% higher than the average post-7000 BC production level. This latter stipulation leads to a pre-7000 BC "steady-state" atmospheric $\Delta^{14}C$ of 140 ‰. I replicate their atmospheric $\Delta^{14}C$ curve by setting average post-7000 BC $Q(^{10}Be)$ at 1.45 ^{14}C atoms s^{-1} cm_E^{-2} (ie. 2% lower than in my preferred simulation above) and using a 20% higher pre-7000 BC "steady-state" production rate. Under these conditions, the model $\Delta^{14}C$ curve mimics the mid-Holocene decline in atmospheric $\Delta^{14}C$ but substantially exceeds the early Holocene observations between 7750 and 4000 BC and the late Holocene observations after AD 1000.

As explained above, the fit of the mid-Holocene atmospheric $\Delta^{14}C$ decline is assigned secondary importance in my analysis. As well, in our modeling approach, the observed mid-Holocene $\Delta^{14}C$ decline cannot be simulated regardless of the selected initial "steady-state" production rate. The reason relates, in comparison to the method of Beer et al. (1988), to the one less degree of freedom available in the choice of an average Holocene ^{14}C production rate and the initial "steady-state" ^{14}C production level. These two quantities are interrelated because the Holocene portion of the *deconvolved* ^{14}C production rate reflects the assumed initial conditions. When the post-7000 BC [^{10}Be] record is normalized to the independent post-7000 BC $Q(^{14}C)$ record, a specific initial "steady state" is subsumed. Changing the initial conditions requires changing the post-7000 BC normalization as well. The renormalization counters much of the effect of

alternative initial conditions (see next subsection for example). Since absolute Holocene ^{14}C production records are not available and proxy records like [^{10}Be] must be normalized in some fashion, the modeling approach with the fewest degrees of freedom is likely more reliable.

Figure 2.29 compares the smoothed trends of the atmospheric $\Delta^{14}C$ histories derived from the geomagnetic data (see section 2.3), the [^{10}Be] record, and the $\Delta^{14}C$ observations. Splines of the latter two atmospheric curves were designed to approximate 400-yr moving averages; the dipole-related $\Delta^{14}C$ record was generated, through the global carbon model, by a ^{14}C production rate spline with coarser resolution (shown in figure 2.21). When the two independent simulated atmospheric $\Delta^{14}C$ trends are averaged, the resultant trend line strongly correlates (r = .99) with the splined observations (figure 2.29 inset). Since the [^{10}Be] record ends in AD 1800, the ^{10}Be trend cannot be compared with the AD 1800 - 1950 segments of the two other trends.

The different resolutions and derivations of the smoothed $\Delta^{14}C$ curves have a negligible effect on the strong correlation. For example, a "400-yr" spline of the model forcing function, Q(^{10}Be), will produce an atmospheric $\Delta^{14}C(^{10}Be)$ record virtually identical to the "400-yr" spline as calculated directly on the original model output, ie. the ^{10}Be-derived atmospheric $\Delta^{14}C$ in figure 2.28. Secondly, if splines with the same coarser resolution of the dipole-related ^{14}C production rate are derived for the other two forcing functions, the model-generated atmospheric $\Delta^{14}C$ trends show a comparable correlation.

The oceanic $\Delta^{14}C(^{10}Be)$ trend can barely be distinguished from the oceanic $\Delta^{14}C$ trend associated with a "production rate origin" to the observed atmospheric (tree-ring) $\Delta^{14}C$ record (figure 2.28 inset). The wide scatter in the foraminifera ventilation indices prevents any detailed analysis of oceanic discrepancies. The published foram ventilation

Figure 2.29: Atmospheric $\Delta^{14}C$ trends: (1) "400-yr" spline of tree-ring $\Delta^{14}C$ data (solid line); (2) atmospheric trend derived from splined dipole-related ^{14}C production history (dashed line); and (3) "400-yr" spline of model-derived atmospheric $\Delta^{14}C$ variations from the ^{14}C production rate inferred from the ice-core ^{10}Be record (short-long dashed line).

(inset): Atmospheric $\Delta^{14}C$ trend averaged from curves (2) and (3) in main figure (short-short-long dashed line) compared to the "400-yr" spline of tree-ring $\Delta^{14}C$ data (solid line).

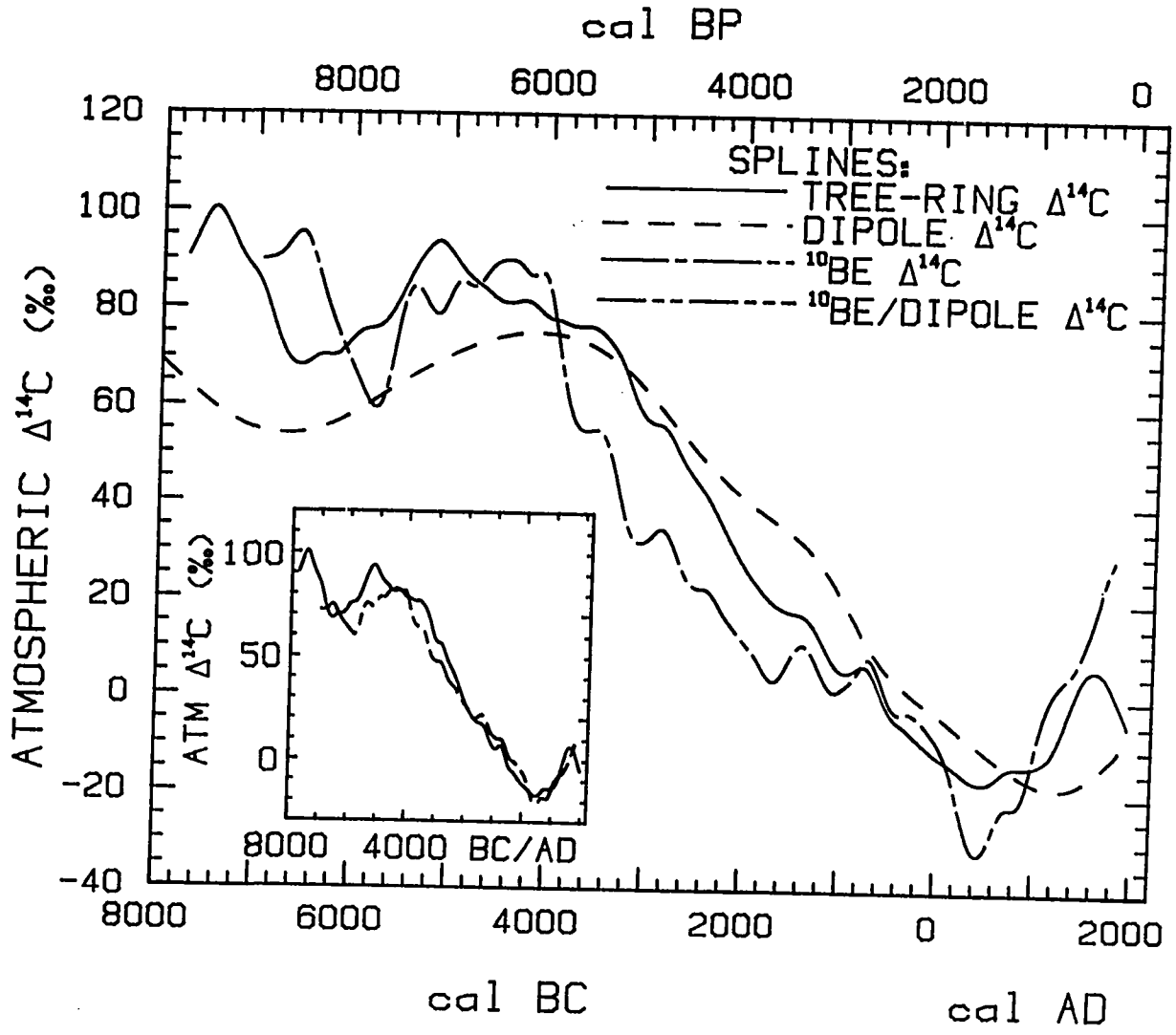
cal BP
8000
6000
4000
2000
0
120
100
80
60
40
20
0
-20
-40
ATMOSPHERIC Δ14C (‰)
SPLINES:
TREE-RING Δ14C
DIPOLE Δ14C
10BE Δ14C
10BE/DIPOLE Δ14C
ATM Δ14C (‰)
100
50
0
8000
4000
BC/AD
8000
6000
4000
2000
0
2000
cal BC
cal AD

indices (Andrée et al. 1986b) have been shifted in the figure by -310 yrs to normalize the recent value of the foram ventilation index to the recent model ventilation index (see chapter 1).

Sensitivity of model results to assumed initial conditions

To test the sensitivity of the Holocene $\Delta^{14}C(^{10}Be)$ simulations to assumed pre-Holocene initial "steady-state" conditions, the modeling procedure described above was repeated with a pre-Holocene "steady-state" atmospheric $\Delta^{14}C_o$ of 50 ‰. As indicated above, the model results are insensitive to any choice of lower *or* higher initial atmospheric $\Delta^{14}C$ levels.

A ^{14}C production history is derived from a data set (such as the dipole measurements or the ^{10}Be concentrations) which contains relative variations to be normalized to the absolute ^{14}C production rate deconvolved from the tree-ring $\Delta^{14}C$ observations. As itemized in section 2.3, several steps are required to simulate a new choice in initial conditions. As a first step, the newly assumed pre-Holocene steady-state conditions are attached to the Holocene tree-ring $\Delta^{14}C$ record and a new "constant climate" ^{14}C production rate history is deconvolved. Secondly, the relative variations in the independent data set are fit (on average) to the deconvolved $Q(^{14}C)$ record over their mutual time interval. Finally, the normalized production rate function derived from the independent data set with the *jointly assumed* initial conditions can serve as model input to generate reservoir $\Delta^{14}C$ trends. In this way, the effect on model-derived reservoir $\Delta^{14}C$ histories may be minimized by the renormalization of the Holocene ^{14}C production forcing function that partially compensates for the new initial pre-Holocene conditions. The normalization insures that average $Q(^{14}C)$ and $Q(^{10}Be)$ match but the strength of the

correlation between the records is essentially not a function of this fitting procedure.

As shown above, the post-7000 BC Q(^{10}Be) record closely matches the deconvolved Q(^{14}C) history. If the pre-9050 BC (11,000 BP) ^{14}C production rate is set 4% lower (to produce an atmospheric $\Delta^{14}C_o$ of 50 °/oo), the average post-7000 BC deconvolved ^{14}C production rate increases by 1.5% to 1.50 ^{14}C atoms s^{-1} cm_E^{-2}. With an analogous pre-7000 BC production rate history and a post-Holocene average increased 1.5%, the renormalized Q(^{10}Be) record produces a post-7000 BC atmospheric Δ^{14}C trend nearly identical to the curve in figure 2.28 derived for $\Delta^{14}C_o$ of 90 °/oo.

A similar test of alternative initial conditions was performed for the dipole-derived ^{14}C production rate record Q(DM) in section 2.3. In this case, however, the modeled Holocene reservoir Δ^{14}C trends changed moderately in the early Holocene (figure 2.21). In contrast to Q(DM), the Q(^{10}Be) record closely matches Q(^{14}C), even in the early Holocene, and alternative initial conditions have much less impact on the early Holocene reservoir trends.

The normalization approach employed here creates an insensitivity of Holocene model output to pre-Holocene conditions. Beer et al. (1988), in contrast, find an acute sensitivity of the atmospheric Δ^{14}C trend to assumed initial conditions. The reason relates to the independence of two parameters in Beer et al.'s approach. The average post-7000 BC Q(^{10}Be) level is adjusted to produce an atmospheric Δ^{14}C in agreement with observations during an arbitrary time period (AD 1 - 1000) and then *independently* the initial pre-Holocene production rate is selected to accurately reproduce the observed mid-Holocene decline in atmospheric Δ^{14}C.

Although the fit between observed and modeled atmospheric Δ^{14}C trends looks impressive in Beer et al. (1988), the corresponding Q(^{10}Be) trend will not match the Q(^{14}C) history that would be deconvolved from the atmospheric Δ^{14}C record under the

same initial conditions. Our one less degree of freedom assures that the two ^{14}C production rate records will match even though the consequent reservoir $\Delta^{14}C$ curves may show secondary differences. Because [^{10}Be] and dipole data are strictly proxies for ^{14}C production rate changes, we emphasize the comparison of production trends rather than reservoir trends in this analysis. As noted above, reservoir trends will integrate and prolong some of the short-term discrepancies in production rates, obscuring the source of disagreement.

Only when data for the *absolute* ^{14}C production rates of past millennia are available can this data truly be treated as independent of the $\Delta^{14}C$ record.

2.5 Implications of a multiple origin for reservoir $\Delta^{14}C$ variations

In the preceding two sections, strong evidence has implicated ^{14}C production rate variations in the origin of the millennium-scale Holocene trends in atmospheric $\Delta^{14}C$. At the same time, discrepancies were noted between the observed atmospheric $\Delta^{14}C$ history and the two atmospheric $\Delta^{14}C$ curves derived from the geomagnetic data and the ice-core [^{10}Be] history. One inexpedient disparity is the apparent mid-Holocene "phase shift" of several hundred years between atmospheric $\Delta^{14}C$(DM) and tree-ring observations (figure 2.18), although the "phase shift" is opposite in sign between atmospheric $\Delta^{14}C(^{10}Be)$ and the observations (figure 2.28).

In a series of model simulations, climate was assumed to represent the residual component necessary to explain the secondary discrepancies between the observed long-term atmospheric $\Delta^{14}C$ history and the $\Delta^{14}C$ trend generated by either the dipole- or ^{10}Be-derived ^{14}C production rate function. The deconvolved climate component (in the

guise of long-term variations in K_Z, F, or a combination of both) is compared to the evidence of foram ventilation indices, ice-core microparticle concentrations, and grain-size distributions in marine sediments, all previously described. The purpose is to determine whether the deconvolved climate scenarios are reasonable explanations for the discrepancies or whether uncertainties in the geomagnetic or ^{10}Be data are more likely responsible for the mismatches.

As in previous sections, the influence of initial conditions on model results is considered. In addition, an analysis is presented of harmonious combinations of ^{14}C production rate levels and climate conditions for specific pre-Holocene levels of "steady-state" atmospheric $\Delta^{14}C$.

Climate change as an explanation for ambiguities in production rate-forced reservoir $\Delta^{14}C$ histories

Climate histories were derived, from the K_Z-, F-, and F,K_Z-deconvolution models, that compensate for incongruities between the observed long-term atmospheric $\Delta^{14}C$ trend and a prescribed ^{14}C production rate history. In section 2.2, these models were similarly utilized to deconvolve climate-related parameter variations in accord with a *constant* ^{14}C production rate during the Holocene. The following analysis is identical except that model input consists of the variable ^{14}C production rate determined from the geomagnetic or ^{10}Be data.

The long-term trend in atmospheric $\Delta^{14}C$ is represented in all simulations by the smoothed curve described in section 2.2 (shown as the dark solid curve in the upper right panels of figure 2.30 and 2.31). As explained previously, the ^{14}C production rate history $Q(^{14}C)$ that perfectly explains, without climate variation, the tree-ring $\Delta^{14}C$ observations

Figure 2.30: (upper left panel) ^{14}C production history derived from ice-core ^{10}Be concentrations without smoothing (light line) and after averaging and splining as described in the text (heavy line).

(upper right panel) Atmospheric $\Delta^{14}C$ history represented by the tree-ring $\Delta^{14}C$ observations (light line) and regenerated from the averaged and splined ^{14}C production history deconvolved from the tree-ring $\Delta^{14}C$ observations (heavy line).

(lower panel) Eddy diffusion record deconvolved to produce, in tandem with the smoothed ^{14}C production history shown in the upper left panel, the smoothed atmospheric $\Delta^{14}C$ curve in the upper right panel. A pre-Holocene atmospheric $\Delta^{14}C$ of 90 ‰ is assumed.

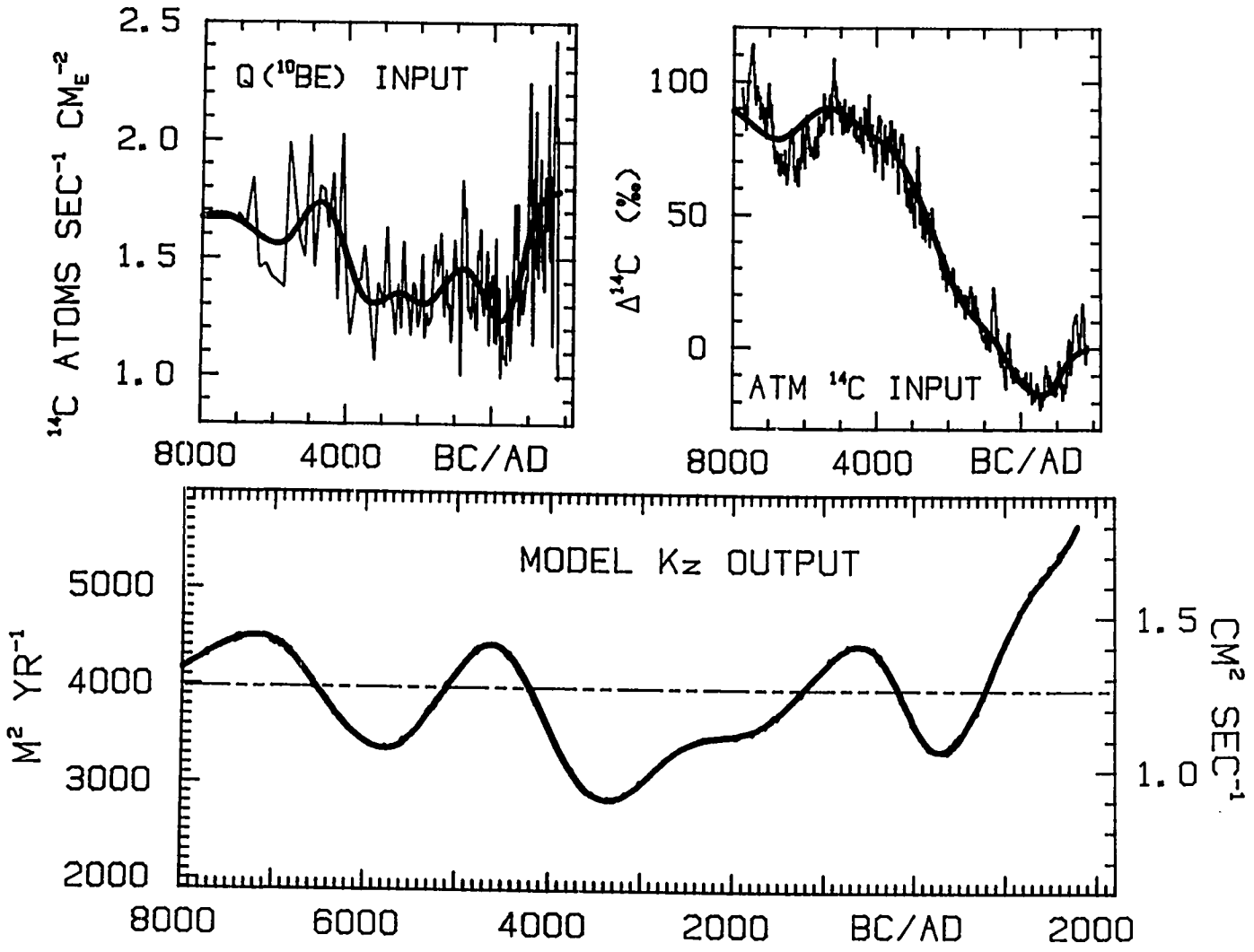
Q (^{10}BE) INPUT
^{14}C ATOMS SEC^{-1} CM$_E^{-2}$
2.5
2.0
1.5
1.0
8000
4000
BC/AD
ATM ^{14}C INPUT
Δ^{14}C (‰)
100
50
0
MODEL Kz OUTPUT
M^2 YR^{-1}
5000
4000
3000
2000
CM^2 SEC^{-1}
1.5
1.0
6000
2000

Figure 2.31: (upper left panel) ^{14}C production history derived from the global dipole data of McElhinny and Senanayake (1982) when the pre-Holocene "steady-state" atmospheric $\Delta^{14}C$ is 90 ‰ (solid line) or 50 ‰ (dot-dashed line). These production trends depend on the value for the proportionality factor c_1 which partially reflects the prescribed initial conditions (see text).

(upper right panel) Atmospheric $\Delta^{14}C$ history represented by the tree-ring $\Delta^{14}C$ observations (light line) or regenerated from the averaged and splined ^{14}C production history deconvolved from the tree-ring $\Delta^{14}C$ observations when the pre-Holocene $\Delta^{14}C_0$ is 90 ‰ (heavy solid line) or 50‰ (dot-dashed line).

(lower panel) Eddy diffusion records deconvolved to produce, in tandem with the respective smoothed ^{14}C production histories shown in the upper left panel, the respective smoothed atmospheric $\Delta^{14}C$ curves in the upper right panel. Either a pre-Holocene atmospheric $\Delta^{14}C$ of 90 ‰ (solid line) or 50 ‰ (dot-dashed line) is assumed.

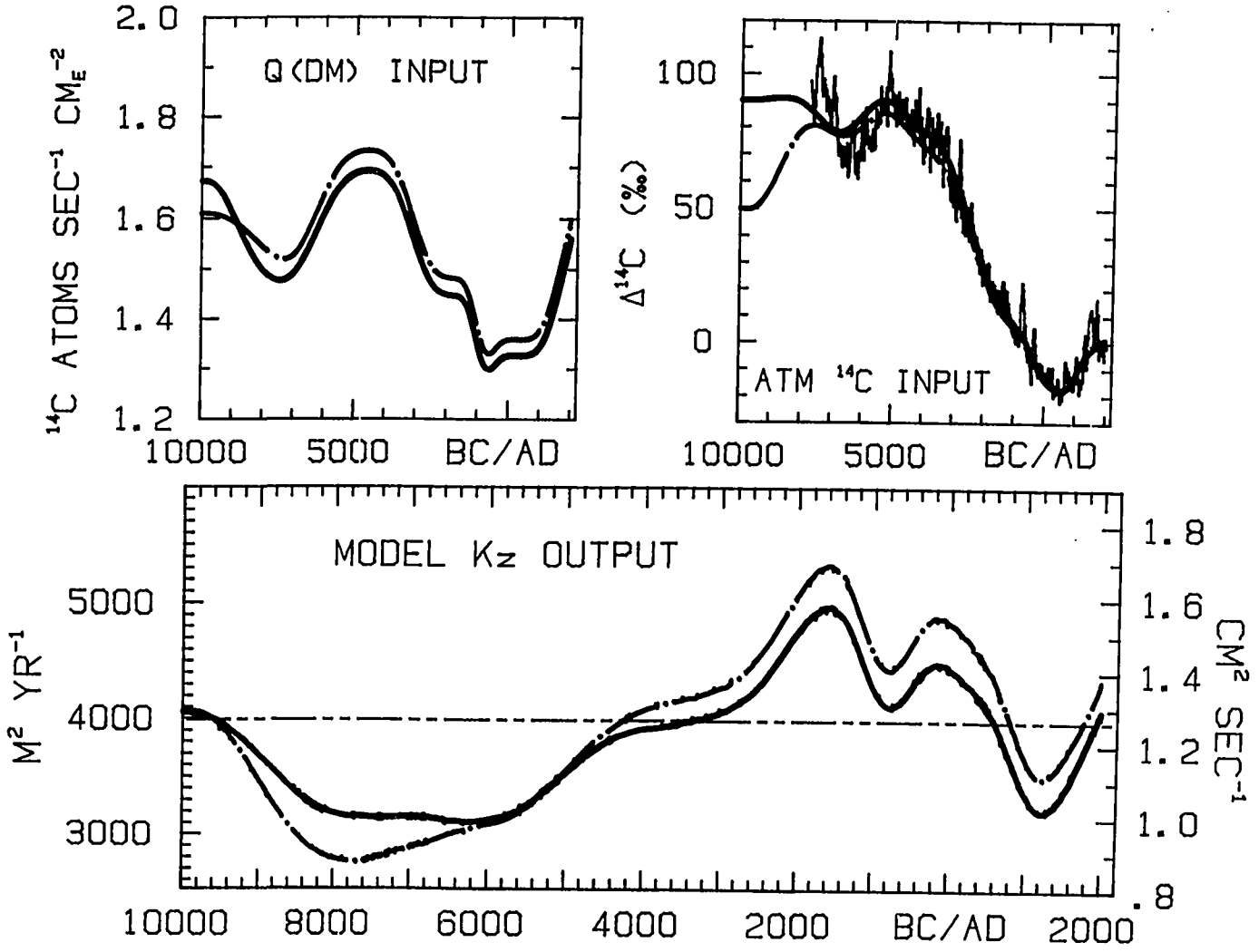
Q(DM) INPUT
^{14}C ATOMS SEC^{-1} CM$_E^{-2}$
2.0
1.8
1.6
1.4
1.2
10000
5000
BC/AD
ATM ^{14}C INPUT
$\Delta^{14}C$ (‰)
100
50
0
MODEL Kz OUTPUT
M^2 YR^{-1}
5000
4000
3000
CM^2 SEC^{-1}
1.8
1.6
1.4
1.2
1.0
.8
10000
8000
6000
4000
2000
BC/AD
2000

was averaged over identical intervals as the geomagnetic data; an interpolating spline converted these averages into a smooth record $Q(^{14}C)_S$ to compare with the hypothetical dipole-derived ^{14}C production history Q(DM) of analogous resolution; the averaging and splining process leads to a moderate phase shift between the early Holocene portion of the tree-ring $\Delta^{14}C$ record and the smoothed atmospheric $\Delta^{14}C$ history regenerated from the $Q(^{14}C)_S$ curve. However, this smoothed atmospheric $\Delta^{14}C$ curve is more appropriately compared to the dipole-related atmospheric $\Delta^{14}C$ history of similar derivation than the original tree-ring data, and this curve is also appropriately selected as the model input to couple with ^{14}C production functions of equivalent resolution in order to derive the proper residual co-variations in climate.

The ice-core [^{10}Be] data (Beer et al. 1988) were similarly averaged for the same time intervals as the geomagnetic data, and an interpolating spline was formulated through these averages (figure 2.30, dark solid line in upper left panel). As in previous simulations with production rate histories, the initial "steady-state" atmospheric $\Delta^{14}C$ of 90 °/oo is assumed for the "standard" simulation and is associated with elevated "steady-state" production rates of ca. 1.67 ^{14}C atoms s^{-1} cm_E^{-2}. The dipole-related ^{14}C production rate history associated with "standard" initial conditions is displayed as the solid line in figure 2.31 (upper left panel) whereas the dot-dashed line portrays an alternative Q(DM) compatible with atmospheric $\Delta^{14}C_o$ of 50 °/oo (see section 2.3). A full discussion of alternative initial conditions is presented below.

The deconvolved eddy diffusivity trends compatible with the prescribed atmospheric and production rate records deviate by extremes of ca. ±25% from the "base-line" value (lower panels in figures 2.30 and 2.31). The dipole-related model $K_Z(DM)$ is weaker in the earlier Holocene when a reduced flux of ^{14}C into the deep ocean must compensate for

a production rate Q(DM) that is insufficient to maintain the observed atmospheric $\Delta^{14}C$ level under "base-line" climate conditions. In contrast, ocean mixing is required to be enhanced during the later Holocene. The K_Z(DM) scenario resembles the $K_Z(^{14}C)$ history that would explain the long-term atmospheric $\Delta^{14}C$ trends *without* ^{14}C production changes but the K_Z(DM) digressions are only half as extreme (figure 2.33 inset). The most recent deconvolved K_Z(DM) of ca. 4000 $m^2\ yr^{-1}$ is consistent with the reconstructed 19th-century "base-line" eddy diffusion estimate.

The model-derived $K_Z(^{10}Be)$ record has a different character and is more variable than K_Z(DM) although the magnitude of their digressions is similar. Unlike recent K_Z(DM), the final value (in AD 1800) for $K_Z(^{10}Be)$ significantly exceeds the "base line" for modern conditions. This discrepancy, however, can be partially attributed to an artificial enhancement in recent ice-core [^{10}Be] associated with a $\delta^{18}O$-indicated change in snow accumulation rate during the Maunder Minimum period of AD 1645 to 1715 (Beer et al. 1988). The post-7000 BC [^{10}Be] record does not correlate with climate-related $\delta^{18}O$ variations, as mentioned in section 2.4, except during this one time interval. The "corrected" recent [^{10}Be] record is less elevated (Beer et al. 1988, figure 6) such that the corrected (ie. reduced) inconsistency between recent $Q(^{10}Be)$ and atmospheric $\Delta^{14}C$ will require less contribution from an enhanced ocean mixing parameter.

The marine $\Delta^{14}C$ histories associated with these residual climate scenarios are shown in figure 2.32. Whether forced by variations in ^{14}C production, internal ocean mixing, or a combination of these, the surface ocean $\Delta^{14}C$ follows a similar trend. As discussed in section 2.2, K_Z influences atmospheric $\Delta^{14}C$ through the surface ocean ^{14}C content which is closely tracked by the atmospheric ^{14}C reservoir under "base-line" conditions for the air-sea CO_2 exchange rate. The converse is also true: the surface ocean closely tracks the atmosphere when ^{14}C production variations force the ^{14}C system under "base-

Figure 2.32: Model-derived reservoir $\Delta^{14}C$ histories. The surface mixed layer and deep ocean $\Delta^{14}C$ curves are generated when the long-term atmospheric $\Delta^{14}C$ record (short-short-long dashed line; see text for derivation) was assumed to originate through: (1) ^{14}C production rate variations (yielding the solid marine curves), (2) eddy diffusivity variations (yielding the dot-dashed marine curves), (3) the dipole-related ^{14}C production history Q(DM) in combination with eddy diffusivity variations (yielding the dashed marine curves) or (4) the ^{10}Be-related ^{14}C production history Q(^{10}Be) in partnership with eddy diffusivity variations (yielding the dotted marine curves). The deep sea curves are averages for the 5 model ocean boxes below one km depth. All simulations assume a pre-Holocene "steady-state" atmospheric $\Delta^{14}C$ of 90 ‰.

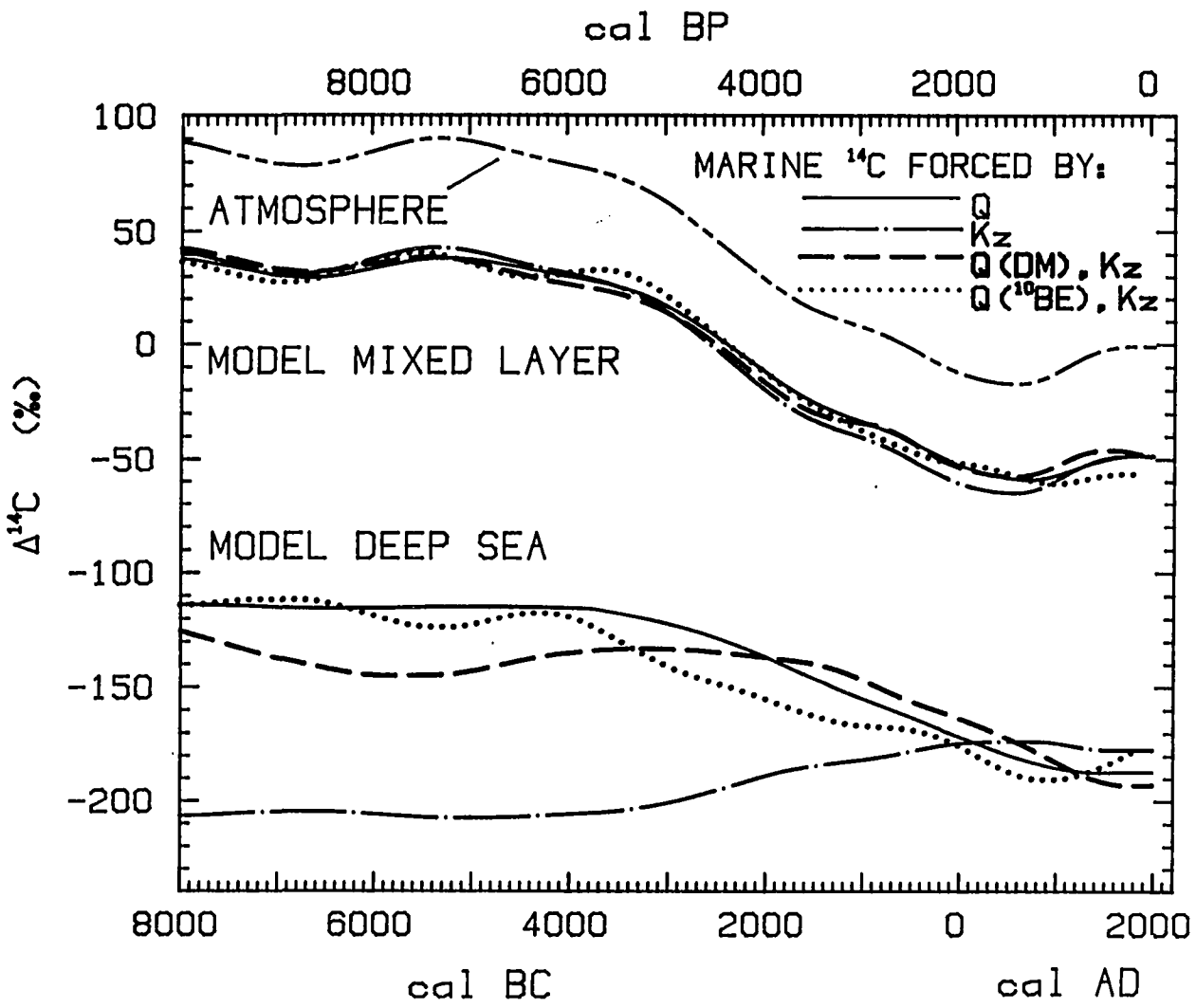
cal BP
8000
6000
4000
2000
0
100
50
0
-50
-100
-150
-200
Δ14C (‰)
ATMOSPHERE
MODEL MIXED LAYER
MODEL DEEP SEA
MARINE 14C FORCED BY:
Q
Kz
Q (DM), Kz
Q (10BE), Kz
8000
6000
4000
2000
0
2000
cal BC
cal AD

line" F conditions.

The deep ocean, however, responds antithetically to K_Z- and Q-forcings because a K_Z perturbation enhancing atmospheric $\Delta^{14}C$ requires a greater isolation (less ^{14}C transfer) between the surface and deep ocean while a Q perturbation with the same atmospheric $\Delta^{14}C$ effect results in greater ^{14}C penetration into the deep ocean. The absolute value for "steady-state" $\Delta^{14}C$ in the large deep-ocean reservoir depends on the ^{14}C production rate. The close correspondence between the model deep sea $\Delta^{14}C$ curve associated with constant ocean mixing (solid line in figure 2.32) and the two curves related to residual ocean mixing (dashed line for K_Z(DM) and dotted line for $K_Z(^{10}Be)$) reflects the strong similarities in ^{14}C production rate histories. In the early Holocene the deep-sea correspondence also derives from the assumption that all three of these Q histories start at the same initial "steady-state" level (see discussion below).

The model ventilation histories for the residual climate scenarios fall within the scatter of the foram ^{14}C measurements after appropriate normalization of the indices (figure 2.33). The residual K_Z component for the Q(DM) record generates a ventilation history that varies ± 200 ^{14}C yrs during the Holocene; the K_Z trend associated with the $Q(^{10}Be)$ record produces a similar but more subdued ventilation history. Thus a compensatory role for internal ocean mixing in the discrepancies between the long-term atmospheric $\Delta^{14}C$ curve and independent ^{14}C production rate trends is compatible with the foram ^{14}C evidence. However, this evidence currently does not impose strong enough constraints on ocean mixing scenarios to allow a definitive appraisal of the residual role of ocean mixing. For example, the ventilation trend associated with the dipole-related ^{14}C production history and compensatory K_Z variations barely conforms to the earlier Holocene foram data and critical measurements are lacking for the past 4000 calendar yrs.

Figure 2.33: Model and foram ventilation indices (MVI and FMI, respectively). Left axis scales the model ventilation index MVI (model deep ocean - model surface ocean). MVI curves are derived from the ocean $\Delta^{14}C$ histories associated with the observed atmospheric $\Delta^{14}C$ record when the deconvolved "forcing function" is: $Q(^{14}C)$ (solid line), $K_Z(^{14}C)$ (dot-dashed line), Q(DM) combined with K_Z(DM) (dashed line), or $Q(^{10}Be)$ combined with $K_Z(^{10}Be)$ (dotted line). Dark rectangles indicate initial "steady-state" values. Right axis scales the foram ventilation index FVI (mixed benthics ^{14}C ages - planktonic *Globigerinoides sacculifer* ^{14}C ages) of Andrée et al. (1986b). Symbols denote measured FVI data (± 1-sigma) from the South China Sea. The FVI scale is shifted -310 ^{14}C yrs relative to the MVI scale in order to match the AD 1830 MVI value of 1275 yrs with the recent preanthropogenic FVI of 1585 yrs.

(inset) Deconvolved eddy diffusion histories corresponding to the four scenarios described and displayed (with the same respective line styles) in the main figure.

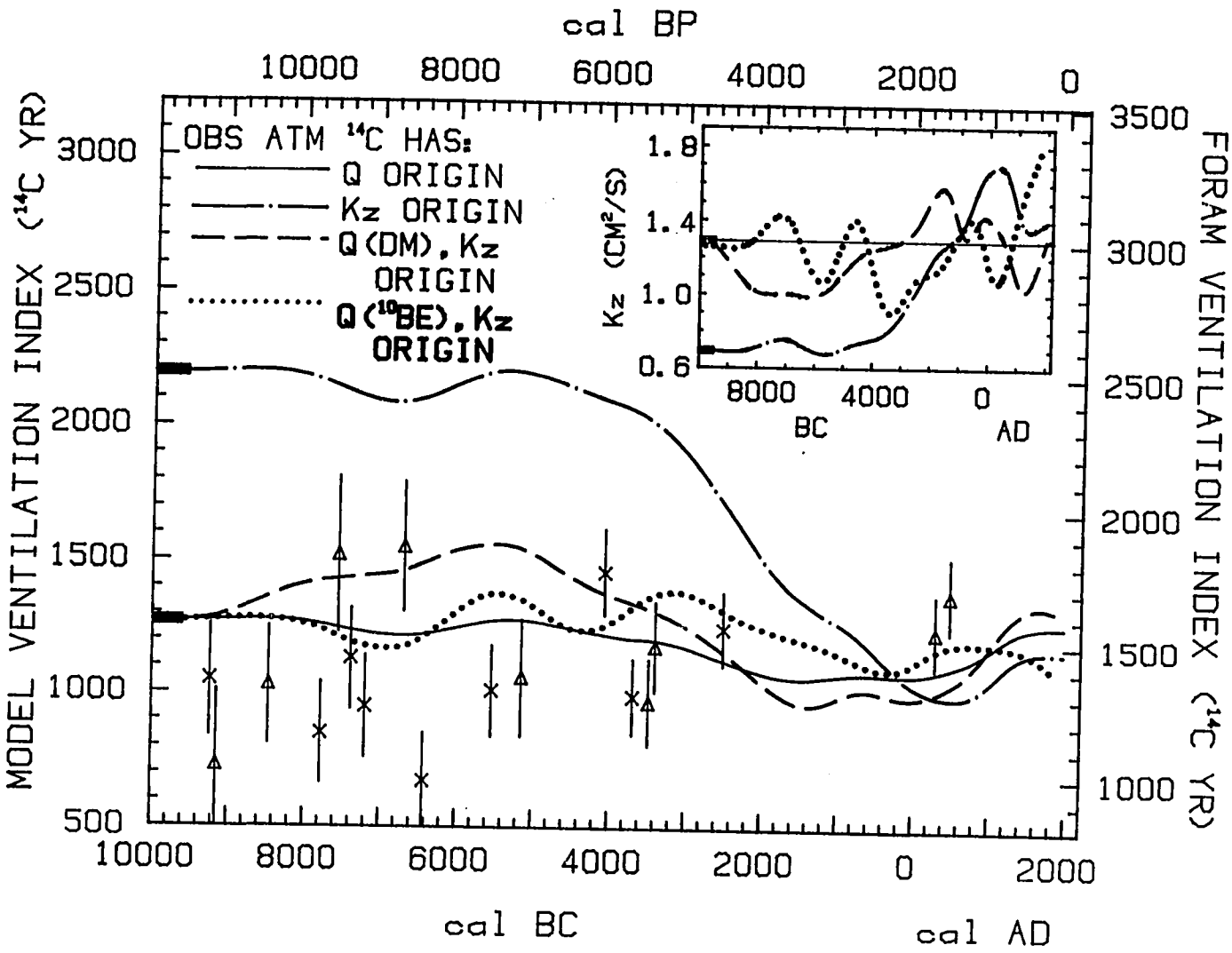
cal BP
10000
8000
6000
4000
2000
0
OBS ATM ^{14}C HAS:
Q ORIGIN
Kz ORIGIN
Q(DM), Kz ORIGIN
Q(^{10}BE), Kz ORIGIN
Kz (CM²/S)
1.8
1.4
1.0
0.6
8000
4000
0
BC
AD
MODEL VENTILATION INDEX (^{14}C YR)
3000
2500
2000
1500
1000
500
FORAM VENTILATION INDEX (^{14}C YR)
3500
3000
2500
2000
1500
1000
10000
8000
6000
4000
2000
0
2000
cal BC
cal AD

In order to assess the potential impact of large uncertainties in the Q(DM) history (see figure 2.16) on the associated K_Z(DM) trend, I followed the procedure described previously for translating standard errors in model input into error ranges in model output. Thus each of the twenty ^{14}C production rate histories derived from the "randomized" dipole-moment records (see section 2.3) served to force a compatible K_Z scenario. The running means and errors in the means in these twenty $K_Z(DM_R)$ curves were then calculated to produce an estimate of the uncertainty in the residual K_Z trend (figure 2.34). The error range for the K_Z(DM) does not alter the above interpretation; this record falls marginally within the spread of the foram ^{14}C data.

Analogously, air-sea CO_2 exchange histories F(DM) and F(^{10}Be) were deconvolved to explain the discrepancies between the long-term atmospheric $\Delta^{14}C$ record and either the dipole- or ^{10}Be-related ^{14}C production history. Each simulation began with the standard initial conditions of atmospheric $\Delta^{14}C_0$ = 90 ‰, Q = 1.67 ^{14}C atoms s^{-1} cm_E^{-2}, and F = 19 moles CO_2 m^2 yr^{-1}.

The digressions in the deconvolved residual F(DM) and F(^{10}Be) histories are less extreme than the F excursions necessary to explain the long-term atmospheric $\Delta^{14}C$ trend without ^{14}C production rate variations (figure 2.11). Air-sea CO_2 exchange varies by ca. ± 10% when it compensates for "deficiencies" in Q(DM); the air-sea flux is reduced in the earlier Holocene and enhanced in the later Holocene. The Q(DM) history between 2000 and 1000 BC (figure 2.31, upper left panel) is too constant to create the observed decline in atmospheric $\Delta^{14}C$ (figure 2.31, upper right panel) necessitating a compensatory increase in air-sea exchange to deplete the atmospheric ^{14}C reservoir (figure 2.11, dashed curve). The recent F(DM) value of 16 moles CO_2 m^{-2} yr^{-1} approaches "base-line" conditions. The configuration of the residual F(DM) trend matches the deconvolved

Figure 2.34: (upper panel) The residual K_Z history required to produce, in tandem with the dipole-related ^{14}C production history, the long-term trend in atmospheric $\Delta^{14}C$. The shaded region corresponds to the running mean and error of the mean for the 20 K_Z histories deconvolved from the 20 "randomized" dipole-related ^{14}C production histories. The dashed line indicates the K_Z value when climate is assumed constant.
(lower panel) Ventilation indices in ^{14}C yrs (see description of axes for figure 2.33). The dashed line is the MVI history associated with the deconvolved "constant climate" ^{14}C production rate; the shaded trend shows the MVI ranges associated with the 20 "randomized" dipole-related ^{14}C production histories, all with assumed atmospheric $\Delta^{14}C_0$ of 90 ‰.

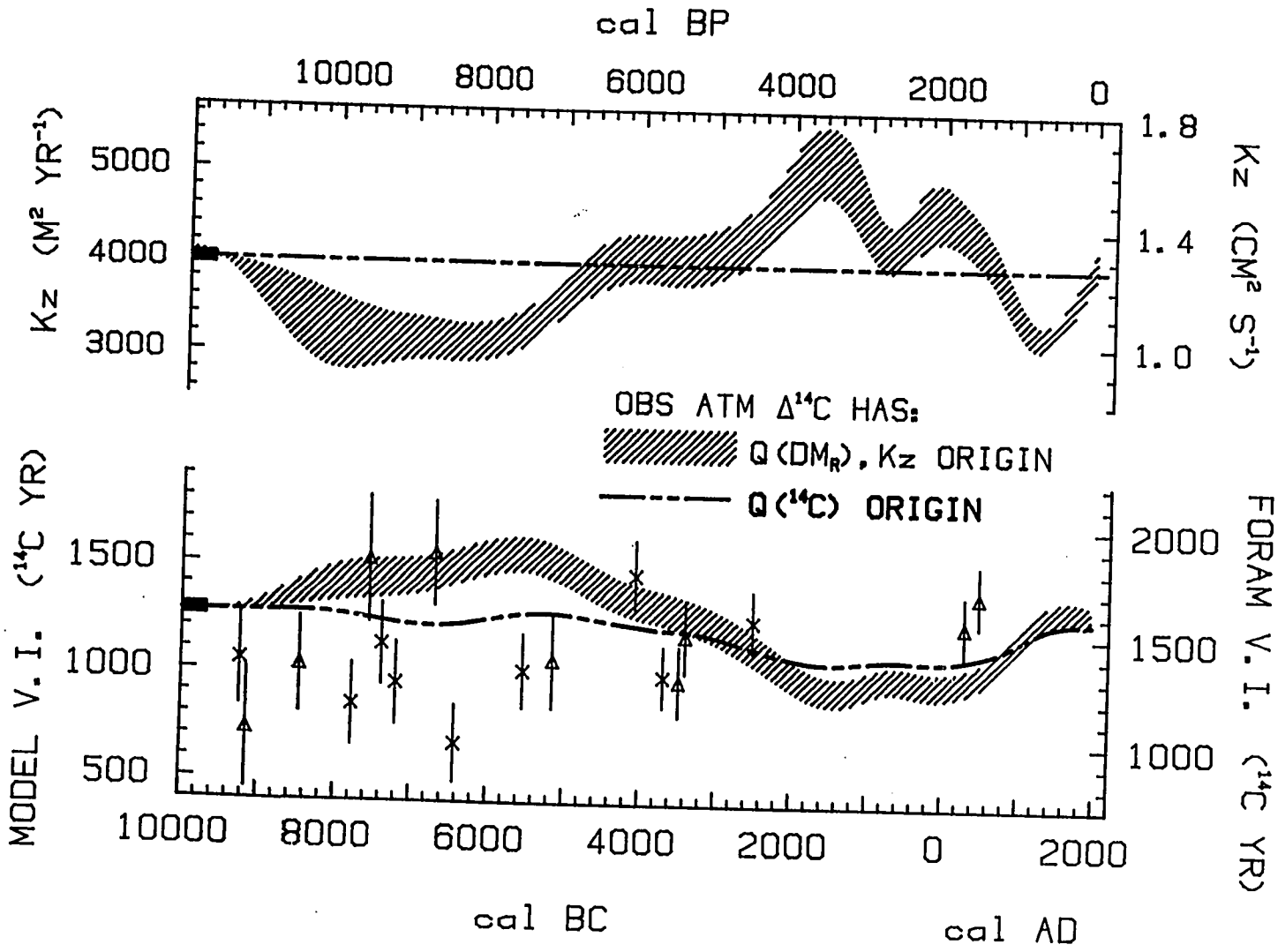
cal BP
10000
8000
6000
4000
2000
0
Kz (M² YR⁻¹)
5000
4000
3000
Kz (CM² S⁻¹)
1.8
1.4
1.0
OBS ATM Δ¹⁴C HAS:
Q(DMR), Kz ORIGIN
Q(¹⁴C) ORIGIN
MODEL V.I. (¹⁴C YR)
1500
1000
500
FORAM V.I. (¹⁴C YR)
2000
1500
1000
10000
8000
6000
4000
2000
0
2000
cal BC
cal AD

K_Z(DM) trend because compensatory oceanic uptake of atmospheric ^{14}C requires similar responses in both of these climate-related parameters.

The deconvolved F(^{10}Be) history also has the same configuration as the K_Z(^{10}Be) trend. This residual air-sea exchange history is more variable but less extreme than the F(DM) trend; the enhanced F values approaching AD 1800 are again primarily explained by the climate artifact in the recent increase in the ice-core ^{10}Be data.

The linear wind-dependence of the air-sea CO_2 flux, as defined in Broecker et al. (1985a), translates the F(DM) variations into extremes of -30% and +60% in global wind speeds during the Holocene (figure 2.11, right axis). This wind speed history conflicts with the relative stability in Holocene winds indicated by ice-core microparticle concentrations (see section 2.2). The model error ranges associated with the residual gas exchange scenario are calculated statistically for the twenty simulations utilizing the twenty "randomized" dipole-related ^{14}C production histories (figure 2.35, shaded trend). Clearly the large uncertainties in the dipole data make possible more subdued compensatory F histories which are more consonant with the microparticle evidence. Deconvolved F is especially sensitive to dipole uncertainties during the period of enhanced fluxes near 1500 BC when the reduced difference between atmospheric and surface ocean ^{14}C contents requires greater relative fluctuations in F in order to influence atmospheric $\Delta^{14}C$ (note the scale differences between figures 2.35 and 2.11).

The global wind speeds which corresponds to residual F(^{10}Be) are relatively greater than "base-line" conditions at several times during the Holocene. The grain-size distributions of aeolian-marine dust are translated into a 50,000-yr history of trade winds by Sarnthein et al. (1987), as noted in section 2.2; compared to F(^{10}Be), the Holocene portion of this trade wind history has similar but more pronounced peaks in wind strength

Figure 2.35: Model-generated air-sea CO_2 exchange histories required to produce the long-term atmospheric $\Delta^{14}C$ record (see figure 2.32) coupled with the ^{14}C production rate history derived from geomagnetic evidence (shaded curve) or ^{10}Be data (dotted line). The shading corresponds to the running mean and error of the mean for the 20 F histories deconvolved from the 20 "randomized" dipole-related ^{14}C production histories. The linear relationship of Broecker et al. (1985a) for the velocity dependence of gas exchange rates translates these F values (left axis) into global wind speeds (right axis). The history of trade winds as derived from grain-size distributions of aeolian-marine dust in Atlantic sediments by Sarnthein et al. (1987) are also plotted against the right axis.

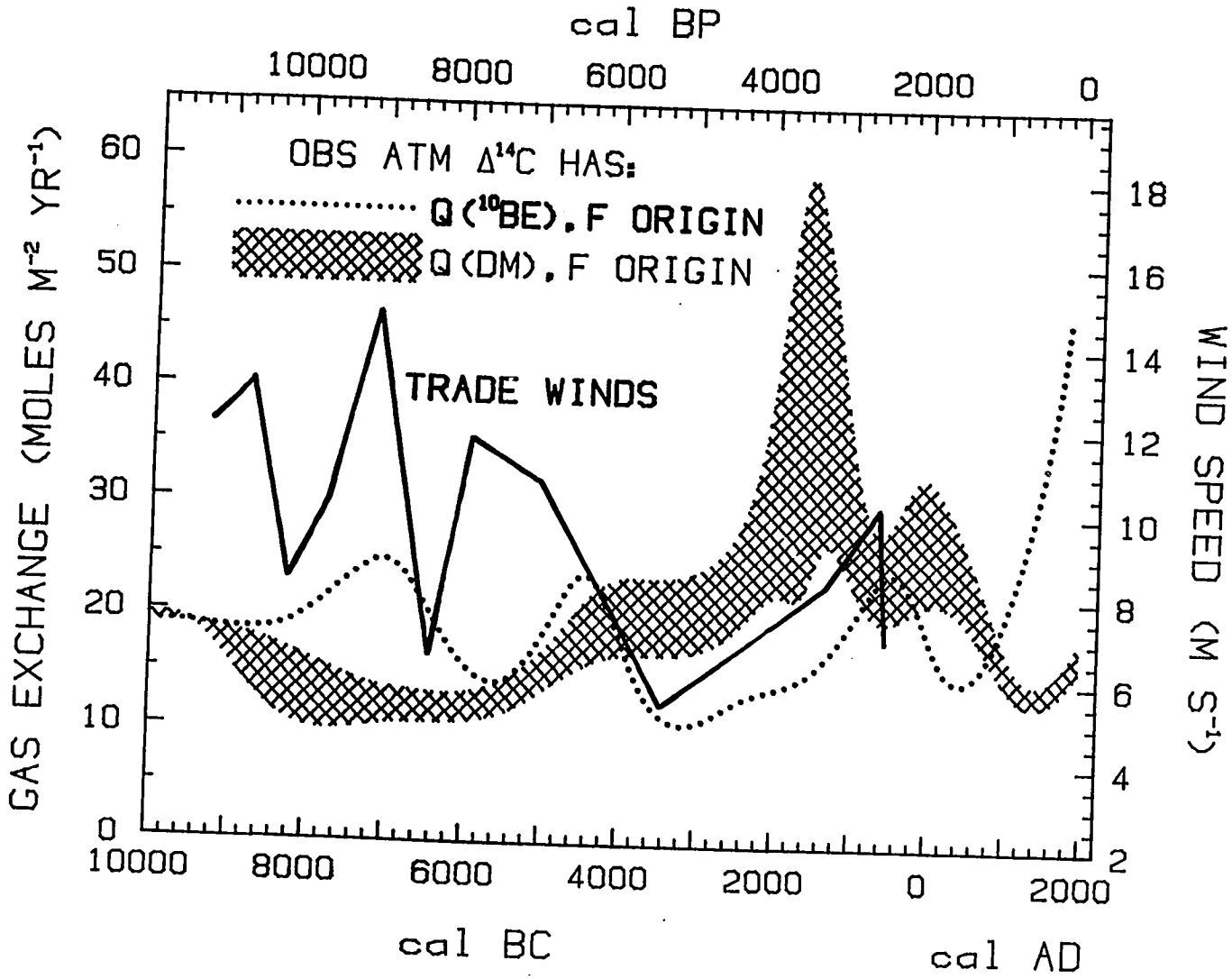
cal BP
10000
8000
6000
4000
2000
0
OBS ATM Δ14C HAS:
Q(10BE).F ORIGIN
Q(DM).F ORIGIN
TRADE WINDS
GAS EXCHANGE (MOLES M-2 YR-1)
WIND SPEED (M S-1)
60
50
40
30
20
10
0
18
16
14
12
10
8
6
4
2
10000
8000
6000
4000
2000
0
2000
cal BC
cal AD

(figure 2.35). However, the global wind speed axis may not apply to the trade winds which may be more susceptible to "climate changes" than mean *global* winds. Glacial trade winds are proposed to be 20 to 30 m s^{-1} (Sarnthein et al. 1987), a factor of 2 or 3 greater than the estimated global glacial winds of 11 m s^{-1} (Petit et al. 1981). If the relative variations in trade winds are reduced by a factor of 3 in figure 2.35, then the similarity between F(^{10}Be) and this independent data set improves.

Thus, whereas the residual ocean mixing scenarios were compatible with the available ocean ^{14}C data, a variable air-sea CO_2 exchange rate is a more qualified solution to discrepancies between the proposed ^{14}C production rate trends and the observed atmospheric Δ^{14}C record. The uncertainties in the dipole data must play a role if the deconvolved F(DM) is to accord with the stable Holocene wind speed history indicated by microparticle concentrations; the deconvolved F(^{10}Be) differs from F(DM) but resembles, perhaps coincidentally, a reconstructed trade wind history which may or may not reflect changes in mean global winds. Clearly, variations in Holocene air-sea fluxes can only account for minimal discrepancies between any proposed ^{14}C production rate and the perfect production history (ie. Q(^{14}C)) required to generate, without climate intervention, the observed long-term atmospheric Δ^{14}C record.

The model ventilation trends associated with these residual F histories fall within the scatter of the foram ^{14}C data. As discussed in section 2.2, variations at the air-sea interface have little impact on apparent oceanic ventilation ages; the MVI trend associated with combined Q- and F-forcing of the marine ^{14}C profile only secondarily differs from the MVI history generated by Q forcing alone (figure 2.5). Thus the insensitivity of the marine ^{14}C profile to variations in air-sea CO_2 flux and the limitations of the foram ^{14}C data prevent a definitive assessment of the role of F in long-term atmospheric Δ^{14}C

variation.

Eddy diffusion and air-sea exchange were also varied simultaneously in simulations that deconvolved compensatory climate change. When K_Z and F together compensate for discrepancies between Q(^{14}C) and either Q(^{10}Be) or Q(DM), their deconvolved histories resemble but are more subdued than the deconvolved histories of K_Z or F acting individually to nullify discrepancies. Holocene co-variations of K_Z and F range from -20% to +10% of "base-line" conditions. The modeled ventilation history conforms to the foram ^{14}C data within the uncertainties. The variations in gas exchange rate translate into mean global wind speeds more consonant with the Holocene wind stability inferred by the microparticle data.

Thus, a hypothetical climate scenario comprising equivalent relative changes in ocean mixing and air-sea CO_2 exchange (perhaps related to the meridional temperature gradient) conforms to the independent evidence cited above. Feedbacks related to the model's surface ocean ^{14}C content allow F to more effectively influence atmospheric Δ^{14}C during the early Holocene (because F has a more direct impact than K_Z on the atmosphere) and K_Z to be relatively more effective during the later Holocene (when the proximity of atmospheric and surface ocean Δ^{14}C reduces the impact of F changes).

In summary, variable ocean mixing is a viable explanation for the differences between the observed long-term atmospheric Δ^{14}C trend and the model Δ^{14}C trend generated by either the dipole- or ^{10}Be-related ^{14}C production history. However, because the deconvolved variations in K_Z(DM) are inconsistent with the digressions of K_Z(^{10}Be), the uncertainties and limited resolutions of the geomagnetic and/or [^{10}Be] data must also contribute to the perceived discrepancies. Even as a residual component, the required variations in the air-sea CO_2 exchange rate are extreme and unsupported by the microparticle evidence unless contemporaneous variations in ocean mixing occur or, once

again, the uncertainties in the production records account for most of the disparity.

Steady-state solutions of model equations and implications for pre-Holocene combinations of Q and climate

The model equations determine the steady-state ^{14}C production that is compatible with prescribed atmospheric $\Delta^{14}C$ levels and reservoir parameters. I applied these equations to specifically calculate the range in ^{14}C production rates that will yield, under a variety of climatic conditions, the atmospheric $\Delta^{14}C$ levels of the four alternative pre-Holocene "steady states" described above. If, for example, the late glacial (eg. ≈15,000 - 11,000 cal BP) air-sea CO_2 exchange rate and internal ocean mixing were assumed to be twice as strong as Holocene "base-line" conditions, what ^{14}C production rate is required to maintain an atmospheric $\Delta^{14}C$ level of 90 ‰?

The steady-state solutions to the model equations are displayed graphically in figure 2.36. The average model-derived ^{14}C production rate of the last 500 yrs was chosen as the reference value, i.e. $Q_R = 1.55$ ^{14}C atoms s^{-1} cm_E^{-2}. The model's steady-state atmospheric $\Delta^{14}C$ level is more sensitive to climate conditions (F and K_Z changes) as $\Delta^{14}C$ increases and more sensitive to ^{14}C production rate changes at lower $\Delta^{14}C$ values.

A range of pre-Holocene atmospheric $\Delta^{14}C$ levels between the preferred initial values of 90 ‰ and 50 ‰ and a range of late glacial winds and ocean ventilation rates up to twice "base-line" intensity are associated at steady state with the range of elevated ^{14}C production rates shown by the shaded areas in figure 2.36. Doubled global wind speeds correspond, according to the linear relationship in Broecker et al. (1985a), to an F flux of 45 moles CO_2 m^{-2} yr^{-1}; a ventilation ^{14}C age reduction by a factor of two translates into a K_Z increase to 8400 m^2 yr^{-1}. With the stipulated pre-Holocene atmospheric $\Delta^{14}C$ and climate conditions, ^{14}C production at steady state is required to function between 103%

Figure 2.36: Steady-state combinations of atmospheric $\Delta^{14}C$, ^{14}C production rate, and either K_Z (upper panel) or F (lower panel) in the global ^{14}C model. The reference ^{14}C production rate Q_R is 1.55 ^{14}C atoms s^{-1} cm_E^{-2}. The K_Z axis has units of $m^2\ yr^{-1}$; the F axis has units of moles $CO_2\ m^{-2}\ yr^{-1}$. In the upper panel, F is assigned the "base-line" value of 19 moles $CO_2\ m^{-2}\ yr^{-1}$ in the model equations while, in the lower panel, K_Z is assigned the "base-line" value of 4000 $m^2\ yr^{-1}$. The shaded areas show a hypothetical range of atmospheric $\Delta^{14}C$, K_Z, and F during the late glacial stage (≈ 11,000 - 15,000 BP).

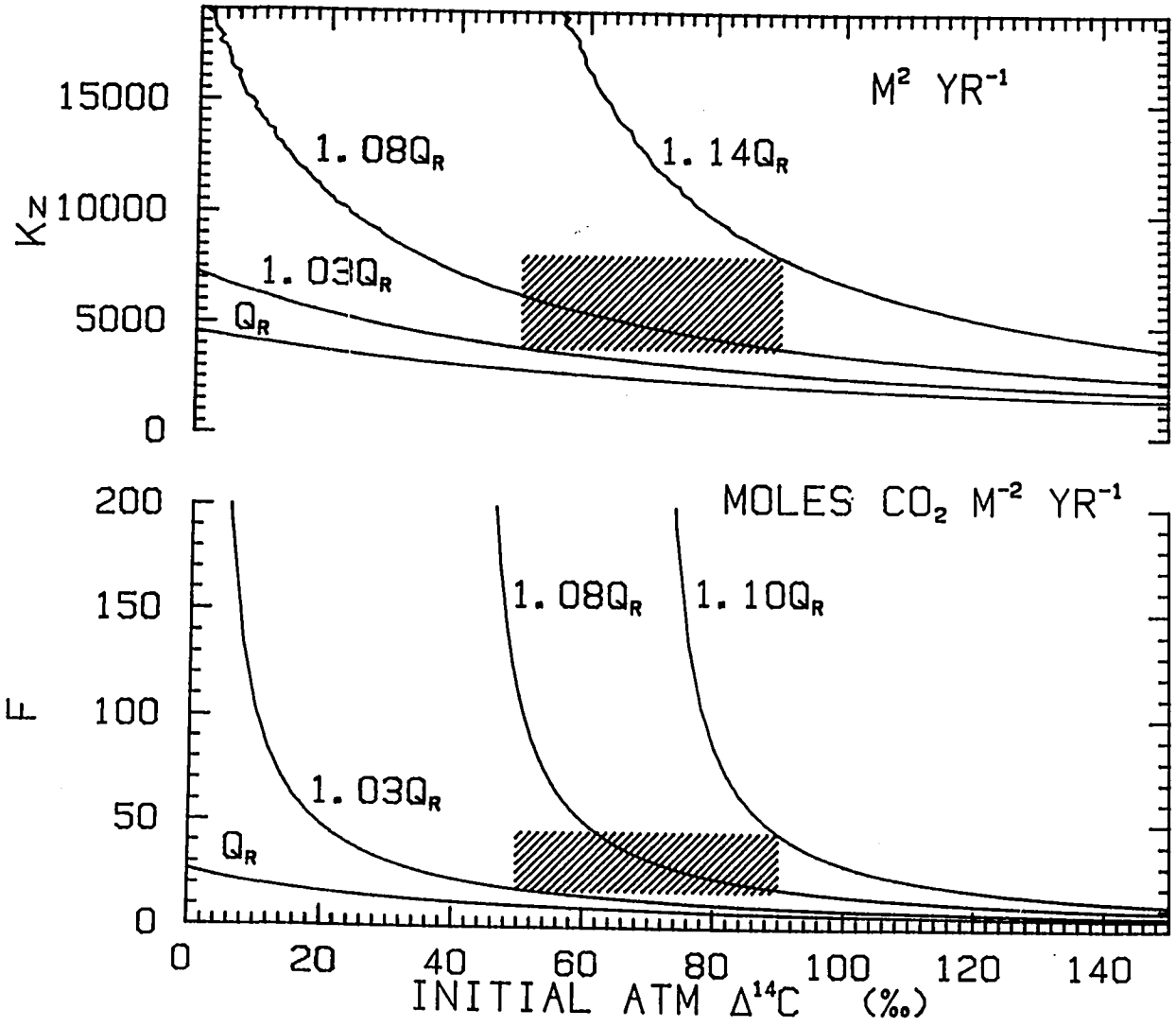
15000
10000
5000
0
K_N
M^2 YR^{-1}
$1.08Q_R$
$1.14Q_R$
$1.03Q_R$
Q_R
200
150
100
50
0
F
MOLES CO_2 M^{-2} YR^{-1}
$1.08Q_R$
$1.10Q_R$
$1.03Q_R$
Q_R
0
20
40
60
80
100
120
140
INITIAL ATM $\Delta^{14}C$ (‰)

and 110% of the current rate. The initial (pre-11,000 BP) ^{14}C production rate of $1.08Q_R$ assumed for all standard simulations passes through the center of this range.

The range of climate conditions selected here for the late glacial stage serves primarily to illustrate the relationship between the strength of the oceanic sink for atmospheric ^{14}C and the rate of ^{14}C production. The reservoir parameters during this transitional period between glacial and interglacial stages were not constant (ie. at "steady state") since this time interval comprises several climatically-distinct chronozones (eg. Bølling, Older Dryas, Allerød, Younger Dryas). Even the nature of ocean circulation within chronozones is currently debated (eg. Fairbanks 1989). The basis for the chosen parameter range rests on two preliminary observations: (1) global wind speeds were generally in transition from glacial to Holocene conditions during this interval of several thousand calendar yrs (eg. Petit et al. 1981), and (2) foram ventilation indices from the Pacific Ocean appear significantly younger on average during this time period (figure 2.5; Andrée et al. 1986b; Shackleton et al. 1988), suggesting enhanced ocean mixing.

During *full* glacial conditions, however, much evidence suggests that North Atlantic Deep Water (NADW) formation was substantially reduced (eg. references compiled in Broecker et al. 1985b). Ocean box modeling indicates that convective interchanges at high latitudes also greatly diminished during the last glacial stage (eg. Toggweiler and Sarmiento 1985). The absence of NADW formation is perhaps equivalent to a K_z reduction by a factor of 2 (eg. Siegenthaler et al. 1980); the associated model ventilation index increases by 85%. This greater model ventilation time accords with (but also exceeds) the elevated foram ventilation indices observed for the pre-15,000 cal BP glacial Atlantic and Pacific Oceans (Shackleton et al. 1988, Broecker et al. 1988b).

A full glacial wind speed 50% above the Holocene "base-line" and a full glacial eddy

diffusion half its assumed Holocene value are compatible with a lower ^{14}C production rate of $.95Q_R$, provided atmospheric $\Delta^{14}C_o$ is 90 ‰ and the other components of the global ^{14}C system remained unchanged. Thus lower ^{14}C production rates are necessary to maintain higher atmospheric $\Delta^{14}C$ levels with a reduced oceanic sink. Under such climatic conditions, the pre-Holocene geomagnetic data of Merrill and McElhinny (1983) displayed in figure 2.22 (top panel) will translate into greater atmospheric $\Delta^{14}C$ levels that are more concordant with the ^{14}C data of Bard et al. (1990) shown in figure 2.22 (lower panel). For example, the standard pre-Holocene ^{14}C production of $1.08Q_R$ produces an atmospheric $\Delta^{14}C_o$ of 230 ‰. But a more refined ocean model is clearly required to accurately simulate the glacial and transitional ^{14}C cycle.

Figure 2.36 demonstrates graphically why a change in the air-sea CO_2 flux cannot explain a hypothetical atmospheric $\Delta^{14}C_o$ of 0 ‰ (see section 2.2). With any initial "steady-state" ^{14}C production rate more than 3% greater than the reference level, F approaches infinity.

Sensitivity of model results to assumed initial conditions

In past sections, I tested the sensitivity of modeled Holocene trends in ^{14}C production, reservoir $\Delta^{14}C$, and climate-related exchange parameters to several alternative initial levels for atmospheric $\Delta^{14}C$. These $\Delta^{14}C_o$ scenarios were assumed to reflect ^{14}C production changes or climate changes but not *both* . As demonstrated in figure 2.36, an infinite pairing of climatic conditions and ^{14}C production levels will produce any specified "steady-state" atmospheric ^{14}C content.

Below we demonstrate that the impact of alternative combinations of pre-Holocene $Q(^{14}C)$, $K_Z(^{14}C)$, and $F(^{14}C)$ values on Holocene model results is generally significant in the early Holocene and negligible during the remainder of the model-generated record.

Pre-Holocene conditions, however, do affect the entire Holocene histories of the dipole- and ^{10}Be-related ^{14}C production records, Q(DM) and Q(^{10}Be) respectively. The reason is that these "independent" records are nonetheless adjusted to match the Holocene-length average of Q(^{14}C) deconvolved from the tree-ring $\Delta^{14}C$ record under the same pre-Holocene conditions (see sections 2.3 and 2.4). As a result the residual K_Z(DM), K_Z(^{10}Be), F(DM) and F(^{10}Be) variations during the entire Holocene are also influenced by pre-Holocene assumptions.

In a series of model simulations discussed above, we set pre-Holocene climate conditions to Holocene "base-line" values and allowed the ^{14}C production rate to solely explain four alternatives for atmospheric $\Delta^{14}C_o$ (see section 2.1). The impact of changes in the initial "steady-state" ^{14}C production rate to model results for marine ^{14}C was restricted primarily to the early Holocene (figure 2.8, left side). When alternative "steady states" in climate (through K_Z) determined the four atmospheric $\Delta^{14}C_o$ scenarios (see section 2.2), the modeled Holocene trends in marine ^{14}C are unaffected because the global ^{14}C system has a relatively short memory (on the order of 1000 yrs) for changes in the ocean reservoir parameters (figure 2.8, right side) When pre-Holocene climate and ^{14}C production levels are co-varied (to produce a specified atmospheric $\Delta^{14}C$ level), the consequences for marine ^{14}C trends are again limited to the early Holocene.

As a simple example, figure 2.37 shows the joint effect of one alternative set of pre-Holocene climate and ^{14}C production conditions on Holocene model results. The Q-deconvolution model was modified to include a pre-Holocene climate change but climate after 7750 BC is assumed constant. In this simulation a "steady-state" $\Delta^{14}C_o$ of 90 ‰ is prescribed prior to 7750 BC and then a ^{14}C production history is derived from the observed atmospheric (tree-ring) $\Delta^{14}C$. In accordance with the speculation that stronger internal oceanic mixing characterized the late glacial stage (≈ 15,000 - 11,000 cal BP), the

Figure 2.37: (upper panel) Bi-decadal ^{14}C production rates necessary to generate, without Holocene climate change, the atmospheric (tree-ring) $\Delta^{14}C$ observations. The pre-7750 BC (9700 BP) atmospheric $\Delta^{14}C$ value is assumed constant at 90 ‰. In one case, the pre-7750 BC eddy diffusion is assigned the "base-line" value of 4000 $m^2\ yr^{-1}$ (light line); in the second case, K_z declines linearly from a pre-11,000 BP "steady state" of 8400 $m^2\ yr^{-1}$ to the post-9700 BP "base line" of 4000 $m^2\ yr^{-1}$ (heavy line).

(lower panel) Ventilation indices in ^{14}C yrs (see description of axes for figure 2.33). The light and heavy lines are the MVI histories reflecting the K_z scenarios associated with ^{14}C production rates denoted respectively in the upper panel.

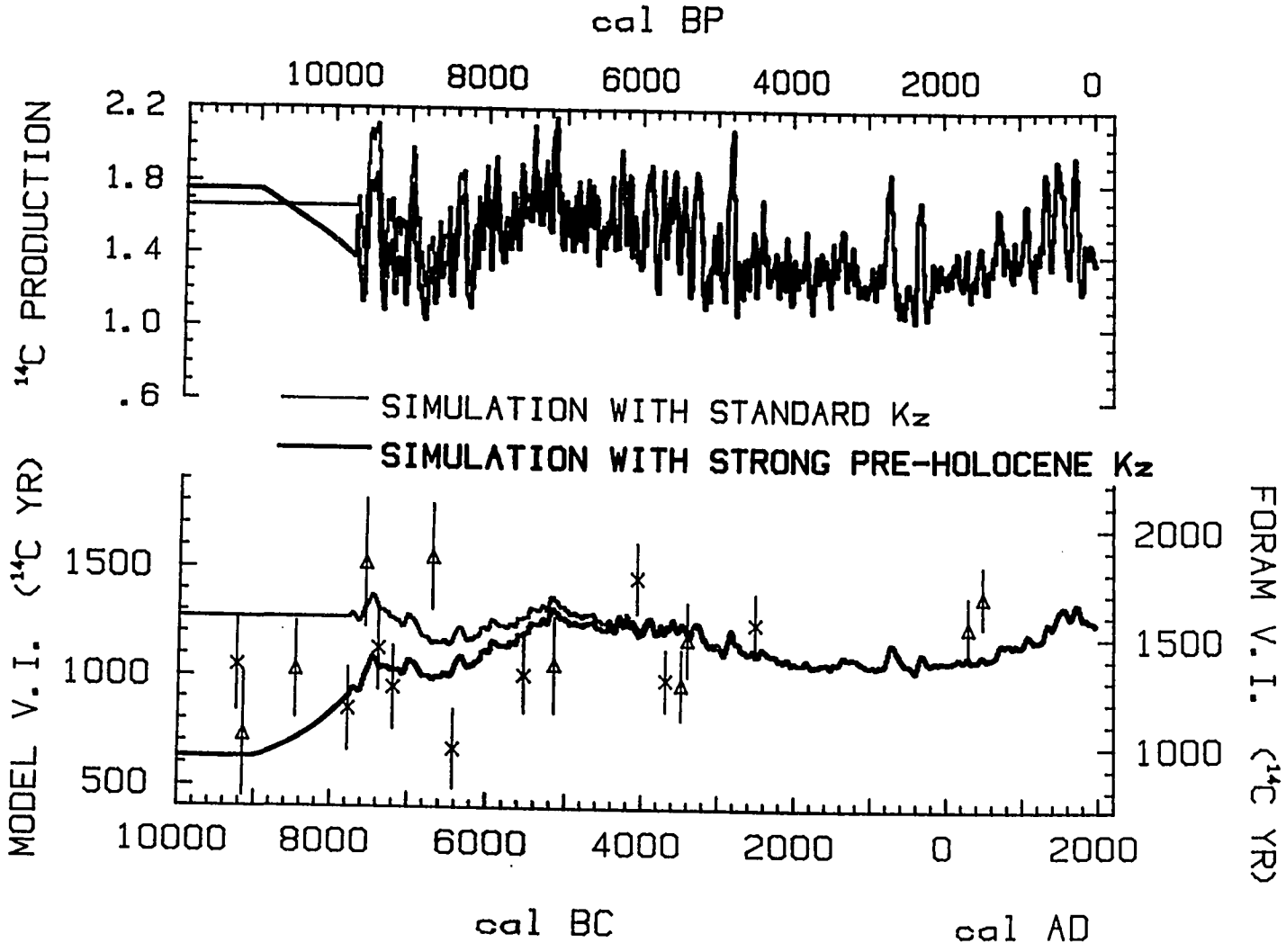
cal BP
10000
8000
6000
4000
2000
0
2.2
1.8
1.4
1.0
.6
^{14}C PRODUCTION
SIMULATION WITH STANDARD Kz
SIMULATION WITH STRONG PRE-HOLOCENE Kz
MODEL V.I. (^{14}C YR)
1500
1000
500
2000
1500
1000
FORAM V.I. (^{14}C YR)
10000
8000
6000
4000
2000
0
2000
cal BC
cal AD

eddy diffusion parameter was assigned a pre-11,000 cal BP (9050 BC) value of 8400 m^2 yr^{-1} and was linearly decreased to a steady "base line" of 4000 m^2 yr^{-1} by the beginning of the tree-ring $\Delta^{14}C$ record in 9700 cal BP (7750 BC). The pre-7750 BC "steady-state" level of 90 ‰ in atmospheric $\Delta^{14}C$ is maintained by an elevated production rate of 1.76 ^{14}C atoms s^{-1} cm_E^{-2} which subsequently diminishes in response to the prescribed reduction in K_Z.

The early Holocene $Q(^{14}C)$ which follows the K_Z change (figure 2.37, heavy line in top half) is less than the alternative $Q(^{14}C)$ deconvolved without climate variation (figure 2.37, light line in top half) because a greater pre-Holocene ^{14}C production rate supplies more ^{14}C to the pre-Holocene deeper ocean, mitigating the strength of the Holocene oceanic ^{14}C sink for several thousand years. However, the alternative ^{14}C production records and model ventilation histories (figure 2.37, lower half) rapidly converge to equivalent trends, respectively, with no lingering effects.

In the above example, climate is assigned no residual role during the Holocene; the ^{14}C production rate $Q(^{14}C)$ is assumed to be solely responsible for the post-7750 BC atmospheric $\Delta^{14}C$ record. When the dipole- or ^{10}Be-related ^{14}C production histories are reconciled with the observed atmospheric $\Delta^{14}C$ trend by a deconvolution of the appropriate residual K_Z and/or F variations, the model results for the *entire* Holocene depend more sensitively on the prescribed pre-Holocene conditions. The explanation rests on the recalculation of c_1.

Preliminarily, we consider the influence on the Holocene histories of K_Z(DM) and F(DM) of alternative pre-Holocene production rates (and associated atmospheric $\Delta^{14}C$ levels) without the influence of alternative pre-Holocene climates (ie. an initial "base-line" climate is assumed as in the deconvolutions above). As a first step, we note that an

alternative pre-Holocene "steady state" atmospheric $\Delta^{14}C$ of 50 ‰ produces an early Holocene $Q(^{14}C)$ history which differs from the standard $Q(^{14}C)$ with $\Delta^{14}C_o$ of 90 ‰ (scenarios B and C in figure 2.7). This alternative $Q(^{14}C)$ was appropriately averaged and splined in order that a proportionality factor c_1 could be calculated to convert the global dipole data into a dipole-related production rate Q(DM) *specifically associated with a prescribed $\Delta^{14}C_o$ of 50 ‰* (see section 2.3 and figure 2.21 inset). Because c_1 is modified slightly when the new initial conditions alter the deconvolved $Q(^{14}C)$ for the early Holocene, the c_1-dependent Q(DM) for the *entire* Holocene is shifted (figure 2.31, dot-dashed line in upper left panel). When this alternative ^{14}C production record serves as model input in the K_Z-deconvolution model together with the appropriate atmospheric $\Delta^{14}C$ trend (figure 2.31, dot-dashed curve in upper right panel; see also figure 2.31 and explanation in section 2.3), the variations in the deconvolved residual K_Z(DM) history are modified throughout the Holocene (figure 2.31, bottom panel).

The exhibited K_Z modifications translate into secondary changes in the MVI history and do not compromise the conclusions presented above. The c_1 calculation that defines Q(DM) compensates lower pre-Holocene production rates with higher *Holocene* production levels; in this way, the influence of pre-Holocene conditions on Holocene model results for K_Z, marine ^{14}C and MVI are always minimized.

The same alternative Q(DM) requires more extreme transformations in deconvolved residual air-sea exchange; the peak in F(DM) at 1500 BC is now more than 50 moles CO_2 m^{-2} yr^{-1}. The air-sea exchange rate is highly sensitive to disparities between the assumed production rate and atmospheric $\Delta^{14}C$ level when the ^{14}C difference between the atmosphere and surface ocean is minimal. Thus the calculated residual history of global wind speeds is too dependent on pre-Holocene assumptions to be conclusive. However, the patterns if not the absolute magnitudes in the Holocene residual trends of F as well as

K_Z are consistent in these sensitivity tests (eg. figure 2.31).

Finally, we can consider the effect of prescribed combinations of pre-Holocene ^{14}C production and climate on residual deconvolved K_Z(DM) and F(DM) variations during the Holocene. Again, the proportionality factor c_1 that determines Q(DM) from the dipole data must be recalculated from the Q(^{14}C) record defined by a specified set of initial conditions (eg. alternative Q(^{14}C) curves in figure 2.37). This adjustment to Q(DM) allows the Holocene production rate to compensate to an extent for the pre-Holocene climate and production conditions, mitigating the modification to the Holocene model outputs. However, with this Holocene-length c_1 adjustment, the residual K_Z(DM) and F(DM) variations are influenced over the entire Holocene rather than only the earlier portion. The consequences to K_Z(DM) are generally secondary as in the examples above, but the addition of pre-Holocene climate change will contribute to more significant early Holocene alterations in K_Z(DM). As illustrated above, the F(DM) deconvolution is more sensitive to shifts in Q(DM) related to alternative initial conditions.

The ^{10}Be-related production histories are also adjusted to match the average Holocene ^{14}C production rate deconvolved under specified climate conditions (see section 2.4). Therefore, the effects of pre-Holocene conditions on the residual F(^{10}Be) and K_Z(^{10}Be) deconvolutions are analogous to the dipole-associated example presented above.

In summary, pre-Holocene climate and ^{14}C production levels moderately influence the early Holocene portion and negligibly affect the remainder of the model results in the Q-deconvolution model. When the dipole- and ^{10}Be-derived ^{14}C production rates represent forcing factors and residual climate variations are deconvolved, the later Holocene model results can be significantly altered as well (especially in the case of F) because the renormalization of the absolute levels of these "independent" production records are influenced by the prescribed pre-Holocene conditions.

2.6 Chapter summary

The model analyses in this chapter indicate that: (1) most of the millennium-scale reservoir $\Delta^{14}C$ change is reasonably explained by variations in ^{14}C production rate as reconstructed from geomagnetic and ^{10}Be data; (2) the discrepancies (including the apparent mid-Holocene phase shift) between the atmospheric (tree-ring) $\Delta^{14}C$ observations and the atmospheric $\Delta^{14}C$ records derived through carbon cycle modeling from these reconstructed Q histories are best explained by the uncertainties and coarse resolution of one or both of these production records; and (3) Holocene climate variation may play a secondary role in producing the atmospheric $\Delta^{14}C$ record but model results are inconclusive because the deconvolution of the residual climate component (especially F) is sensitive to the prescribed initial conditions.

Table 2.2 summarizes the millennium-scale ^{14}C simulations discussed in this chapter. The first four columns list the prescribed status of each of the relevant model features in the simulations. The last column indicates whether the model results were considered to accord with the independent evidence which is available.

The first three rows represent the simulations without Holocene climate variation (both K_Z and F are constant). The reservoir $\Delta^{14}C$ histories forced solely by ^{14}C production changes are compatible with the available foram ^{14}C data. The geomagnetic- and ^{10}Be-derived ^{14}C production histories are consistent with the Holocene ^{14}C production record derived from the global ^{14}C model, indicating that climate change need not be invoked to explain the long-term features of the atmospheric $\Delta^{14}C$ record.

When ^{14}C production was assumed constant during the Holocene (next three rows), the climatic changes (in the guise of K_Z and F variations) required to produce the observed atmospheric $\Delta^{14}C$ trend are not supported by the available foram ^{14}C data, ice-core

microparticle concentrations, or grain sizes of aeolian-marine dust in Atlantic sediment cores. In addition, a constancy in the Holocene ^{14}C production rate is difficult to reconcile with the geomagnetic and ^{10}Be variations mentioned above. A discussion of other potential climate perturbations during the Holocene is presented in section 2.2. The last simulation in this set involves equivalent relative variations in K_Z and F.

Finally, the dipole- and ^{10}Be-derived ^{14}C production histories are reconciled to the observed atmospheric $\Delta^{14}C$ record by invoking a residual climatic effect. The F variations required to compensate for the disparities between the observed and the dipole- or ^{10}Be-related atmospheric $\Delta^{14}C$ records are too extreme to accord with the microparticle evidence. The compensatory K_Z variations produce marine ^{14}C trends that are compatible with the foram ^{14}C data, but the large uncertainties in this evidence do not allow a critical appraisal of the model results.

In addition, the feasibility of several alternative pre-Holocene "steady-state" assumptions and their influence on the Holocene model trends were investigated. The simulations show that pre-Holocene atmospheric $\Delta^{14}C$ levels of 90 ‰ and 50 ‰ are consistent with the pre- and early Holocene marine ^{14}C evidence while a deficient $\Delta^{14}C_o$ of 0 ‰ is not. A pre-Holocene "steady-state" atmospheric $\Delta^{14}C$ of 140 ‰ accords with the marine ^{14}C data if an elevated ^{14}C production rate is responsible but not when the internal ocean mixing or air-sea CO_2 exchange rate is considered the cause.

The assumed pre-Holocene ^{14}C production rate and climate conditions generally have a secondary influence on the deconvolved Holocene ^{14}C production and modeled reservoir $\Delta^{14}C$ trends. The global ^{14}C system has a short memory for climate variations in themselves and the impact of the pre-Holocene history of ^{14}C production is primarily limited to the earlier Holocene.

The influence of pre-Holocene climate and/or ^{14}C production levels becomes more

complex when the global dipole data or ice-core ^{10}Be concentrations are converted to represent the Holocene history of the ^{14}C production. Because we use an adjustable factor to match the dipole- and ^{10}Be-derived ^{14}C production histories, Q(DM) and Q(^{10}Be) respectively, to the average production rate Q(^{14}C) deconvolved from the tree-ring $\Delta^{14}C$ data, early Holocene digressions in Q(^{14}C) translate into Holocene-length shifts in Q(DM) and Q(^{10}Be). The repercussions of these shifts to the model-derived reservoir $\Delta^{14}C$ trends are generally secondary because the Holocene portion of the deconvolved Q(^{14}C) will compensate for the pre-Holocene portion for any specified atmospheric $\Delta^{14}C$ history. However, when climate must nullify the Holocene disparities between the atmospheric $\Delta^{14}C$ observations and dipole-induced trends, we find that the deconvolution of especially F(DM) is sensitive to the pre-Holocene assumptions because of a feedback involving the air-sea $\Delta^{14}C$ difference.

The absolute definition of c_1 and an independent conversion of the dipole data to a ^{14}C production rate, without normalization to the observed Holocene ^{14}C record, requires an understanding of the present annual-scale influence of solar activity on the present ^{14}C production rate in relation to the millennium-scale solar component in the Holocene tree-ring ^{14}C record (see section 2.3). At present, c_1 cannot be selected precisely enough on a theoretical basis and lower-frequency solar activity during the Holocene cannot be approximated adequately enough to permit an absolute calculation of a geomagnetically-defined millennium-scale ^{14}C production history.

Table 2.2

Assigned features of millennium-scale ^{14}C simulations

^{14}C production	atmos. $\Delta^{14}C$	F	K_Z	assessment
model output	tree-ring record	constant	constant	yes
geomagnetic	model output	constant	constant	yes
ice-core ^{10}Be	model output	constant	constant	yes
constant	tree-ring record	model output	constant	no
constant	tree-ring record	constant	model output	no
constant	tree-ring record	model output	model output	no
geomagnetic	tree-ring record	model output	constant	no
geomagnetic	tree-ring record	constant	model output	yes
geomagnetic	tree-ring record	model output	model output	yes
ice-core ^{10}Be	tree-ring record	model output	constant	no
ice-core ^{10}Be	tree-ring record	constant	model output	yes

CHAPTER 3. MODEL ANALYSIS OF ORIGINS FOR CENTURY-SCALE $\Delta^{14}C$ VARIATIONS

This chapter focuses on the century-scale variations in atmospheric $\Delta^{14}C$. Strong evidence indicates that these features are associated with changes in solar activity. The implications of an atmosphere-ocean origin for these features are also investigated by means of the F- and K_Z-deconvolution ^{14}C models, and the feasibility of these alternative possibilities is considered with reference to coral ^{14}C data.

3.1 The residual atmospheric ^{14}C signal

The long-term trend for bi-decadal atmospheric (tree-ring) $\Delta^{14}C$ is represented by a spline approximating a 400-yr moving average (figure 1.1). As discussed in chapter 1 and shown in figure 3.1, the removal of this curve yields a bi-decadal residual $\Delta^{14}C$ record that retains the essential characteristics of the century-scale ^{14}C features without the millennium-scale trends. As mentioned in chapter 2, periodicities in atmospheric ^{14}C greater than 500 yrs are often attributed to geomagnetic causes while higher-frequency $\Delta^{14}C$ fluctuations are often discussed in terms of solar origins (eg. Damon and Linick 1986). Therefore, the arbitrary 400-yr criterion applied to distinguish long- from short-term ^{14}C variability nevertheless appears to be a suitable preliminary step for isolating the solar influence on atmospheric ^{14}C.

Also, as mentioned in chapter 1, I prefer a spline to a direct moving average because the resulting curve is smoother and remains centered more closely on the data. In

Figure 3.1: Residual $\Delta^{14}C$ from 7760 BC to AD 1840 after removal of a spline approximating a 400-yr moving average from the bi-decadal atmospheric (tree-ring) $\Delta^{14}C$ record in figure 1.1. Maunder-type and Spörer-type century-scale $\Delta^{14}C$ fluctuations are denoted with "M" and "S", respectively. Four 680-yr intervals with similar patterns of triple oscillations are labeled "T_1" through "T_4".

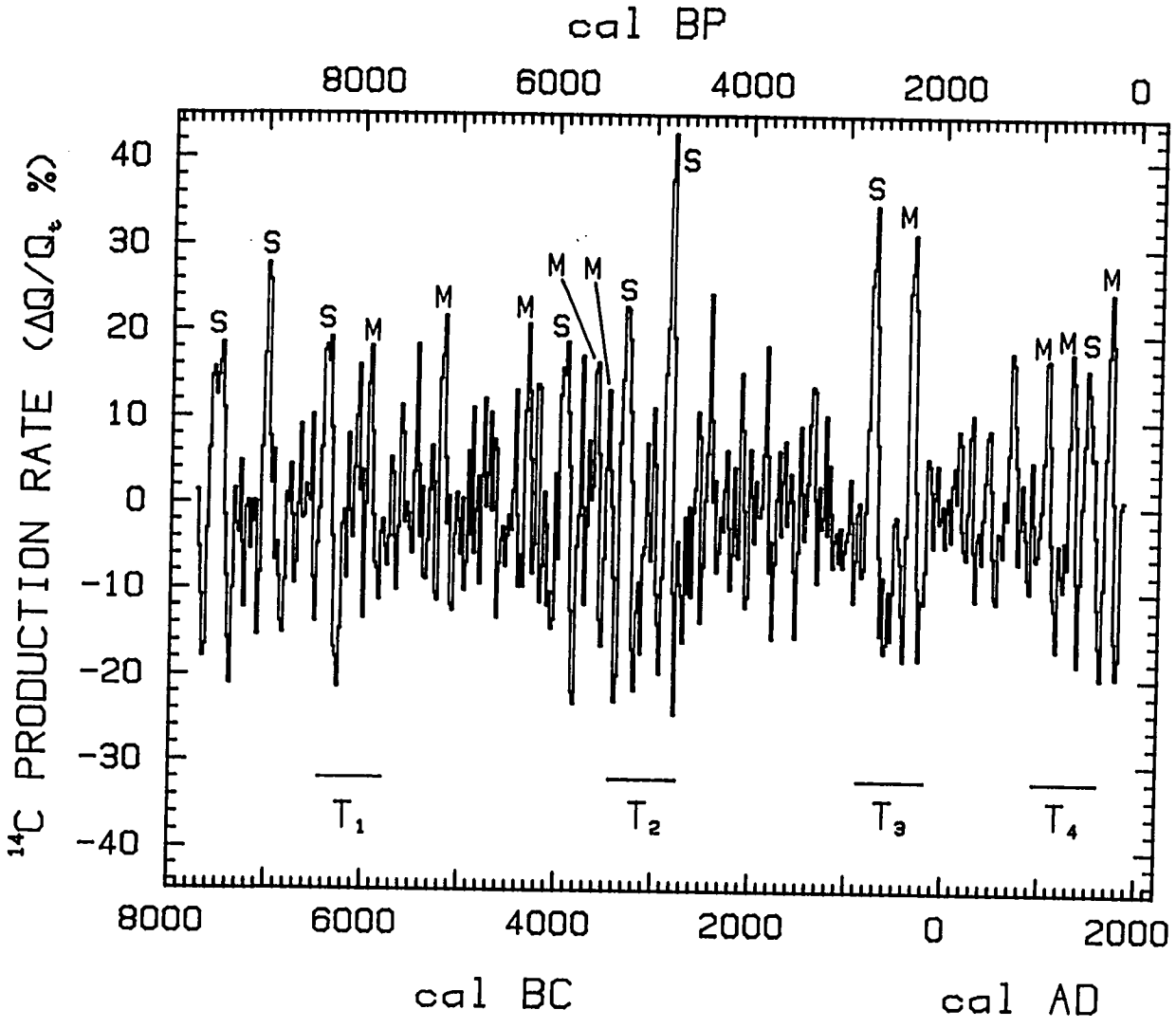
cal BP
8000
6000
4000
2000
0
40
30
20
10
0
-10
-20
-30
-40
^{14}C PRODUCTION RATE (ΔQ/Q$_t$ %)
S
M
T$_1$
T$_2$
T$_3$
T$_4$
8000
6000
4000
2000
0
2000
cal BC
cal AD

addition, low-pass filtering (eg. moving averages) cannot provide a trend line of comparable smoothing for the beginning or end of the data set. For example, a full 400-yr moving average cannot be calculated for the first or last 200 yrs of the data record. A spline does not have this limitation.

The veracity of the spline as the trend line is, unfortunately, ambiguous for the most recent portion of the ^{14}C record. The four strong century-scale digressions in atmospheric $\Delta^{14}C$ during the last 1000 calendar yrs elevate the spline (or moving average). This rise is followed by a sharp decline in the trend line in synchrony with the drop in atmospheric $\Delta^{14}C$ after the $\Delta^{14}C$ peak in AD 1710 (figure 1.1). The relatively level portion of the bi-decadal $\Delta^{14}C$ record after AD 1830 is *reconstructed* from a previous modeling interpretation (see chapters 1 and 4) but little affects the shape of the calculated spline which, for comparison, was also derived from a ^{14}C data record terminating in AD 1830. The recent decline in the "400-yr" spline contrasts with the rise in long-term atmospheric $\Delta^{14}C$ that would be compatible with the pattern of determinations of the global dipole moment available since AD 1835 (figure 2.10a in Merrill and McElhinny 1983). This discrepancy confers an ambiguity on the $\Delta^{14}C$/sunspot relationship for recent centuries (discussed in detail in chapter 4). In effect, the "elevated" spline may remove some of the solar component of the atmospheric $\Delta^{14}C$ record as well as the geomagnetic-related trend because of the close spacing of century-scale "solar events" during the past millennium.

A trend of coarser resolution represented the geomagnetic component of the atmospheric $\Delta^{14}C$ record in chapter 2 only because of the lack of higher resolution dipole data for most of the Holocene. A limitation of this coarser curve was its phase-shift in the early Holocene with respect to the original $\Delta^{14}C$ record, a consequence of the averaging

and splining process (see chapter 2). Therefore, I switch here to the more wiggly "400-yr" spline that visually is more effective in detrending the $\Delta^{14}C$ record.

Many of the residual variations in atmospheric $\Delta^{14}C$ (figure 3.1) closely resemble one of the two most recent century-scale digressions. The shorter ^{14}C digression from AD 1600 to 1800 coincides with the disappearance of sunspots during the Maunder Minimum interval of AD 1654 to 1714 (see discussion in Stuiver and Quay 1980); the longer ^{14}C digression from AD 1360 to 1640 is contemporaneous with the period of reduced naked-eye sunspot sightings during the Spörer Minimum interval of AD 1400 to 1600, also a period of infrequent aurorae (see discussion in Stuiver and Grootes 1980). The 9 "Maunder-type" $\Delta^{14}C$ events and the 8 "Spörer-type" $\Delta^{14}C$ events are labeled "M" and "S", respectively, in figure 3.1 and are described and displayed in detail in Stuiver and Braziunas (1988). These 17 events are used to calculate the average variations (figure 3.2, upper half) associated with these two prominent century-scale patterns in the residual $\Delta^{14}C$.

The emphasis of my dissertation work is the application of global carbon cycle models rather than the visual analysis of century-scale ^{14}C patterns so that the latter topic is not pursued in detail here. However, the averaged Maunder and Spörer digressions of figure 3.2 are important steps in the modeling process since these "prototypes" for century-scale atmospheric $\Delta^{14}C$ events are inputs for the global ^{14}C models that deconvolve compatible century-scale changes in atmosphere-ocean dynamics if ^{14}C production rate is assumed constant. Discussion of these curves continues in section 3.3.

In four instances, sequences of Maunder and Spörer $\Delta^{14}C$ digressions together with less prominent fluctuations in atmospheric $\Delta^{14}C$ show a consistent 680-yr pattern termed a "triplet interval" (Stuiver and Braziunas 1989). These four segments are labelled "T1" through "T4" in figure 3.1 and will be considered again in chapter 4 when the predictive

Figure 3.2: Average "Maunder-type" and "Spörer-type" century-scale digressions in residual $\Delta^{14}C$ (upper panel) and residual ^{14}C production rate (lower panel). The shaded bar-graphs in the upper panel are based on the means and standard deviations of the means calculated for the residual bi-decadal $\Delta^{14}C$ levels of the 9 "M" digressions (for the average Maunder-type event) and 8 "S" digressions (for the average Spörer-type event) marked in figure 3.1. The shaded bar-graphs in the lower panel were calculated analogously for the similarly denoted $\Delta Q/Q_t$ excursions in figure 3.4. The $\Delta Q/Q_t$ units are explained in the caption for figure 3.4. In absolute time, the average $\Delta Q/Q_t$ digressions in the lower panel lead by one bi-decade their average residual $\Delta^{14}C$ counterparts in the upper panel.

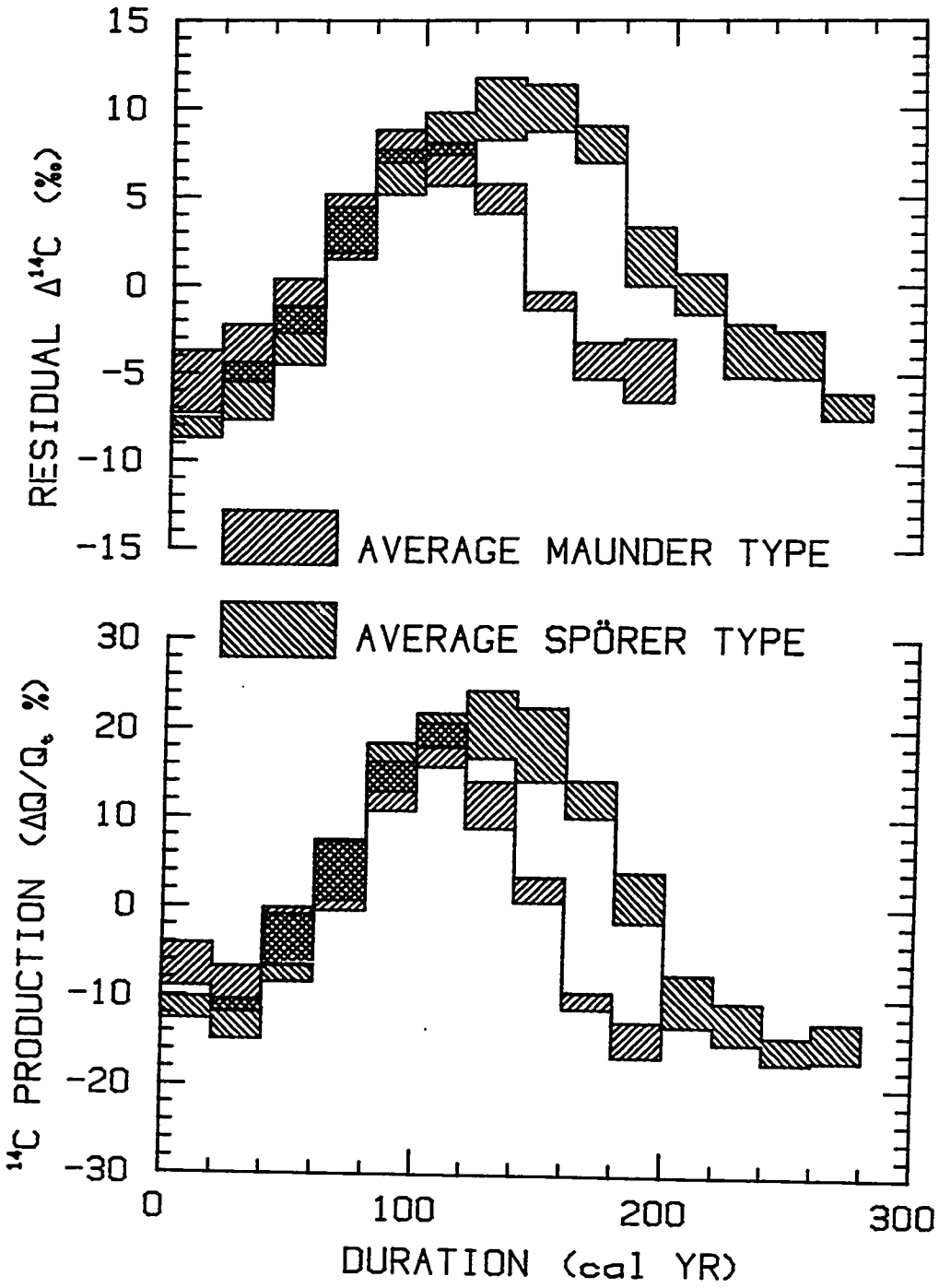
15
10
5
0
-5
-10
-15
RESIDUAL Δ14C (‰)
AVERAGE MAUNDER TYPE
AVERAGE SPÖRER TYPE
30
20
10
0
-10
-20
-30
14C PRODUCTION (ΔQ/Q0 %)
0
100
200
300
DURATION (cal YR)

capabilities of the model-derived ^{14}C production rate curve Q(^{14}C) are discussed. The expanded figures of residual bi-decadal and decadal $\Delta^{14}C$ fluctuations presented in Stuiver and Braziunas (1988) permit the common features of these "triplet intervals" to be observed.

The removal of the "400-yr" spline that was fit to the *decadal* atmospheric $\Delta^{14}C$ record (figure 2.2) produces the high resolution residual $\Delta^{14}C$ history shown in figure 3.3 (lower half). Again, the details of this record are exhibited in the expanded figures in Stuiver and Braziunas (1988).

3.2 Implications of a production rate origin for century-scale reservoir $\Delta^{14}C$ variations

As mentioned above, the correlation of recent century-scale atmospheric $\Delta^{14}C$ variations with changes in solar activity as reflected in records of sunspot observations, auroral frequencies, and geomagnetic Aa indices strongly supports a solar origin for these $\Delta^{14}C$ fluctuations. By analogy, the 15 other century-scale patterns in the Holocene that resemble the recent Maunder or Spörer ^{14}C digression would also originate through solar modulation of ^{14}C production. The magnetic properties of the solar wind theoretically interact with the charged particles of the galactic radiation impinging on the Earth's atmosphere (eg. Stuiver and Quay 1980). In this way, increased solar activity reduces the atmospheric penetration of cosmic rays and, subsequently, the production of radiocarbon from high-energy neutrons generated in cosmic ray-induced spallation events. Thus ^{14}C production responds inversely to variations in solar activity for reasons that similarly

Figure 3.3: Residual decadal ^{14}C production-rate variations (upper graph) and residual decadal atmospheric (tree-ring) $\Delta^{14}C$ values (lower graph). The residual $\Delta^{14}C$ record was derived from the decadal $\Delta^{14}C$ measurements between 2500 BC and AD 1860 after removal of a spline approximating a 400-yr moving average (shown in figure 2.2). Units of $\Delta Q/Q_t$ for the residual ^{14}C production curve are defined as the percent differences between the model-derived decadal $Q(^{14}C)$ record and the long-term trend Q_t represented by a spline approximating a 400-yr moving average (see figure 2.2).

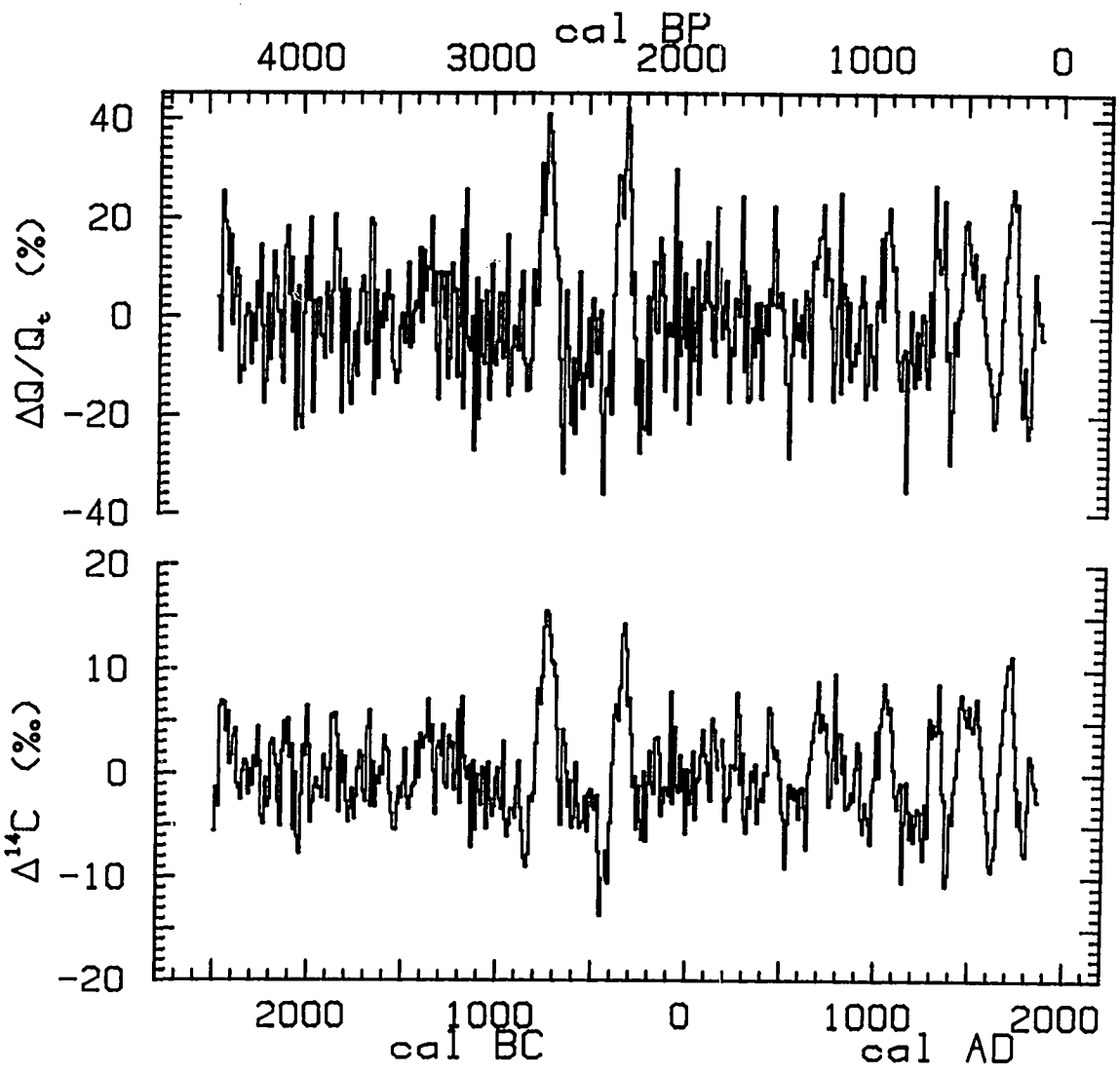
cal BP
4000
3000
2000
1000
0
40
20
0
-20
-40
ΔQ/Q (%)
20
10
0
-10
-20
Δ14C (‰)
2000
1000
0
1000
2000
cal BC
cal AD

explain its inverse relationship to changes in the strength of the magnetic field lines associated with the global dipole.

The close correlation between model-derived century-scale ^{14}C production rate variations and ice-core ^{10}Be fluctuations provides additional support for the proposition of a production rate (solar) origin for the century-scale atmospheric $\Delta^{14}C$ record (figure 2.25 and discussion in section 2.4). In this comparison of the $Q(^{14}C)$ curve with the normalized [^{10}Be] measurements, the solar and geomagnetic forcings together account for the 45% covariance (r = .67) in the post-1000 BC records. As discussed in section 2.4, the uncertainties in the ^{14}C and ^{10}Be measurements as well as some climatic influences might explain the residual variances in these two records.

Detrended century-scale ^{14}C production rate variations

To delete the long-term (assumed geomagnetic) component from the bi-decadal ^{14}C production history, a "400-yr" spline (figure 2.1) was removed from the model-derived $Q(^{14}C)$ record. The dipole moment will, however, continue to contribute to the absolute magnitude of the residual variations in the ^{14}C production rate. For example, when the global dipole moment is lower, the millennium-scale trend *and* century-scale digressions will be enhanced (eg. Lal 1988). To fully remove the geomagnetic influence, the residual ^{14}C production rate variations are expressed as percentage changes relative to the long-term trend Q_t represented by the "400-yr" spline. Thus the variations shown in the residual Q record (figure 3.4) have units of $\Delta Q/Q_t \times 100$ where $\Delta Q = Q(^{14}C) - Q_t$ and $Q(^{14}C)$ is the original model-derived ^{14}C production rate.

The 17 century-scale $\Delta Q/Q_t$ fluctuations associated with the Maunder- or Spörer-type atmospheric $\Delta^{14}C$ patterns noted above are marked analogously with "M" or "S".

Figure 3.4: Detrended ^{14}C production-rate variations from 7740 BC to AD 1840. Units of $\Delta Q/Q_t$ are defined as the percent differences between the model-derived bi-decadal $Q(^{14}C)$ record and the long-term trend Q_t represented by a spline approximating a 400-yr moving average (see figure 2.1). Maunder-type and Spörer-type century-scale fluctuations are denoted with "M" and "S", respectively. Four 680-yr intervals with similar patterns of triple oscillations are labeled "T_1" through "T_4".

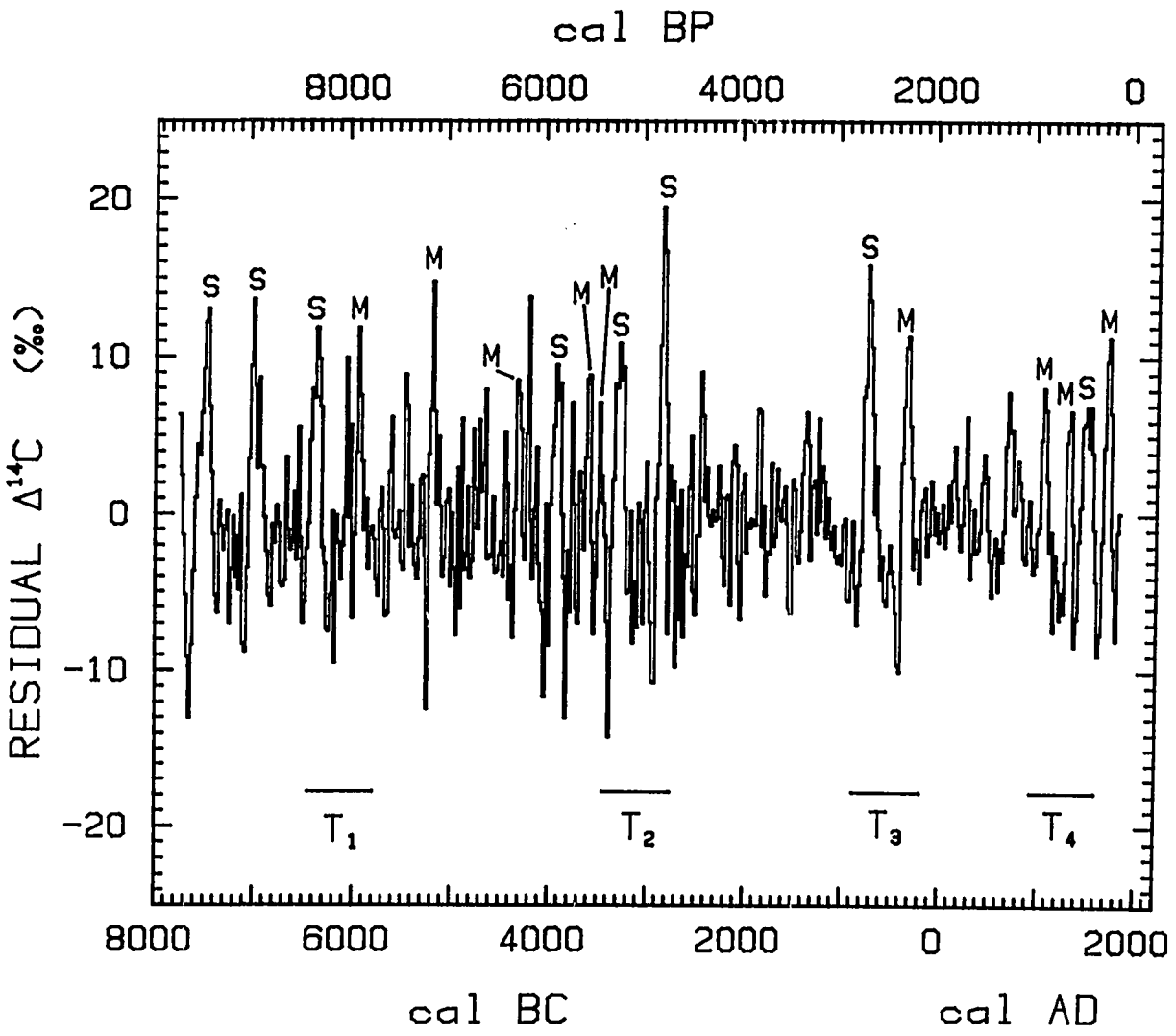
cal BP
8000
6000
4000
2000
0
20
10
0
-10
-20
RESIDUAL Δ14C (‰)
S
S
S
M
M
M
S
M
M
S
M
S
S
M
M
M
S
M
M
S
T1
T2
T3
T4
8000
6000
4000
2000
0
2000
cal BC
cal AD

Average Maunder- and Spörer-type ^{14}C production fluctuations are estimated by calculating the mean and error of the mean for the two categories of these 17 events (figure 3.2, lower half). The $\Delta Q/Q_t$ "triplet intervals" are also identified in figure 3.4. The expanded figures in Stuiver and Braziunas (1988) display the details of the detrended bi-decadal Q variations as well as those of the detrended decadal Q variations shown in figure 3.3 (upper half).

In order to assign uncertainties to the bi-decadal and decadal century-scale $\Delta Q/Q_t$ patterns exhibited in the detrended curves, I tested the sensitivity of the model-derived ^{14}C production history to the uncertainties in the bi-decadal and decadal atmospheric (tree-ring) $\Delta^{14}C$ measurements. As noted in chapter 1, the typical precision of the post-5200 BC tree-ring $\Delta^{14}C$ record (both bi-decadal and decadal) is 2 °/oo while the earlier record has an average precision of 5 °/oo. A change of 5 or 2 °/oo in any bi-decadal $\Delta^{14}C$ value affects the model-derived (and detrended) $\Delta Q/Q_t$ history for a 140 year duration. Such changes of 5 and 2 °/oo in an atmospheric $\Delta^{14}C$ bi-decade translate into sudden $\Delta Q/Q_t$ changes of 6-8% and 3%, respectively, which are followed by much reduced *converse* effects in ensuing bi-decades. This antithetical system behavior occurs as the ^{14}C pulse events stored in the surface ocean and terrestrial biota continue to feed back into the atmospheric reservoir and temporarily displace the ^{14}C production required by the deconvolution process. Passing over some of these complexities, the uncertainty in the bi-decadal $\Delta Q/Q_t$ record can be generally estimated as ± 8% prior to 5200 BC and ± 3% thereafter.

The $\Delta Q/Q_t$ history is more sensitive to the precision of the *decadal* tree-ring $\Delta^{14}C$ data. A ± 2 °/oo shift in any decadal $\Delta^{14}C$ value produces a contemporaneous adjustment, after detrending, of ± 5-7% in decadal $\Delta Q/Q_t$ with a much reduced converse

effect during the ensuing 100 yrs. The greater sensitivity of deconvolved Q to decadal $\Delta^{14}C$ changes derives from the closer spacing in the $\Delta^{14}C$ data. A change in atmospheric $\Delta^{14}C$ level during a 20 yr period requires less adjustment in ^{14}C production than the same change over a period of 10 years.

The detrended $\Delta Q/Q_t$ history is the appropriate record to compare with sunspot observations and other data that reflect solar activity levels. The frequency-related attenuation of ^{14}C production rates obscures the solar dependence of atmospheric $\Delta^{14}C$ observations directly, as discussed in chapter 2. If climate can be eliminated as a significant influence on century-scale ^{14}C variation (see section 3.3), the residual $\Delta Q/Q_t$ record, deconvolved through the global ^{14}C modeling efforts described above, can reveal patterns and periodicities in solar activity (see chapter 4). This $\Delta Q/Q_t$ record has also been utilized to determine a paleo-sunspot curve and a "sunspot prognosis" for coming centuries (chapter 4).

As mentioned in section 2.1, the detrended $\Delta Q/Q_t$ history is relatively insensitive to adjustments in model exchange constants (ie. F and K_z values) and reservoir sizes (ie. oceanic $\sum CO_2$ concentration and long-term terrestrial storage). The removal of the millennium-scale Q trends and the representation of higher-frequency Q variations on a percentage scale yields a consistent pattern of residual ^{14}C production variations valid for a reasonable range of model parameterizations.

According to figure 3.2, a typical century-scale atmospheric $\Delta^{14}C$ variation of 15 ‰ corresponds to a 30% digression in ^{14}C production. An attenuation factor of .05 is consistent with the modeling discussion in section 2.1. Alternatively, the global ^{14}C model can also be utilized to deconvolve "average ^{14}C production rates" directly from the average Maunder- and Spörer-type atmospheric $\Delta^{14}C$ fluctuations in figure 3.2. However, when the trend in atmospheric $\Delta^{14}C$ is constrained to match either mid-line of

the average Maunder- or Spörer-type variation in the Q-deconvolution model (ie. the mid-line of the shaded area), the resultant $\Delta Q/Q_t$ digressions are 15% less extreme than the $\Delta Q/Q_t$ changes detrended from the original $Q(^{14}C)$ history (and shown in figure 3.2, lower half). Thus the average Maunder- and Spörer-related ^{14}C production rate variations are 25% of base line when superimposed on the steady-state long-term "Q_t" trend but are 30% when deconvolved and detrended from the actual variable atmospheric $\Delta^{14}C$ record.

In these simulations, the model exchange parameters F and K_z were fixed at the standard values of 19 moles CO_2 m^{-2} yr^{-1} and 4000 m^2 yr^{-1}, respectively, and the initial ^{14}C production rate was assigned a "steady-state" level (analogous to Q_t) necessary to maintain a constant atmospheric $\Delta^{14}C$ level at the beginning of the century-scale $\Delta^{14}C$ variation. The steady-state start of the Maunder $\Delta^{14}C$ event at -5.5 ‰ and the steady-state start of the Spörer $\Delta^{14}C$ event at -8 ‰ both require initial Q values of approximately 1.52 ^{14}C atoms cm_E^{-2} s^{-1}. These initial conditions were retained in all the simulations presented in this chapter and their limitations are important to consider here.

The difference of 5% in the average century-scale $\Delta Q/Q_t$ variations stems from the low choice for the steady-state ^{14}C production curve. The average Maunder- and Spörer-type $\Delta^{14}C$ digressions in reality start *below* the long-term curve represented by Q_t (as the negative $\Delta^{14}C$ levels indicate); these century-scale events begin with a decline in $\Delta^{14}C$ away from the long-term trend. An initial decline, followed by a positive century-scale digression in $\Delta^{14}C$, will produce a greater century-scale range in $\Delta Q/Q_t$ for the same reason that succeeding $\Delta Q/Q_t$ levels responded inversely to data shifts in the uncertainty tests described above. By raising the initial steady-state Q levels in the century-scale simulations, the range in $\Delta Q/Q_t$ can be adjusted. However, I elected to use the initial steady-state Q values enumerated above in all the century-scale ^{14}C simulations because these initial Q levels assume nothing about pre-Maunder and pre-Spörer $\Delta^{14}C$ history and

are accurate enough for the deconvolution comparisons presented below.

Oceanic $\Delta^{14}C$ response to century-scale Q-forcing

Figure 3.5 illustrates the oceanic $\Delta^{14}C$ behavior associated with Maunder- and Spörer-type atmospheric ^{14}C events if these events originate solely from ^{14}C production rate variations. During this millennium, an especially busy time in the global ^{14}C system, the long-term trends in reservoir $\Delta^{14}C$ are subdued while the higher-frequency variations are numerous. As noted in chapter 2, a century-scale Q-forced atmospheric $\Delta^{14}C$ event is accompanied by a similar but weaker and delayed $\Delta^{14}C$ fluctuation in the surface ocean. The three oceanic $\Delta^{14}C$ events that are labeled in figure 3.5 exhibit variations of 5, 7.5, and 5 ‰, representing attenuations of ca. 33% with respect to the corresponding atmospheric $\Delta^{14}C$ variations. These three surface ocean digressions lag their atmospheric $\Delta^{14}C$ counterparts by 20 yrs. The exact attenuation and delay in the mixed layer reservoir is a function of the magnitude and timing of marine and terrestrial ^{14}C uptake and of the rate at which excess surface ocean ^{14}C is distributed to greater oceanic depths. At the 750 m level of the one-dimensional model ocean, the century-scale variability is delayed by 50 yrs and the perturbations are nearly dissipated (figure 3.5).

The differences in magnitudes and phases in the Q-forced century-scale atmospheric and oceanic $\Delta^{14}C$ histories complicate the dating of marine materials. For example, the "reservoir age correction" (the difference between ^{14}C ages of contemporaneous organic materials grown in the atmosphere and another carbon reservoir) for surface ocean samples varies by ± 100 ^{14}C yr during the Holocene as calculated from the surface ocean $\Delta^{14}C$ history derived from the one-dimensional model (figure 9A in Stuiver et al. 1986b). A marine calibration curve based on such model results is available in a practical computer program (Stuiver and Reimer 1986).

Figure 3.5: Fluctuations in the oceanic vertical $\Delta^{14}C$ profile associated with the variations in ^{14}C production rate required to produce the observed atmospheric (tree-ring) $\Delta^{14}C$ record between 4500 and 3500 BC. The top "horizontal" line in each column represents the oceanic mixed layer with the remaining "horizontal" lines showing the history of the upper 27 boxes of the model thermocline. The bi-decadal $\Delta^{14}C$ record has been interpolated to decadal spacing for visual effect. The oceanic digressions associated with Maunder- and Spörer-type atmospheric $\Delta^{14}C$ variations are labeled as "M" and "S", respectively.

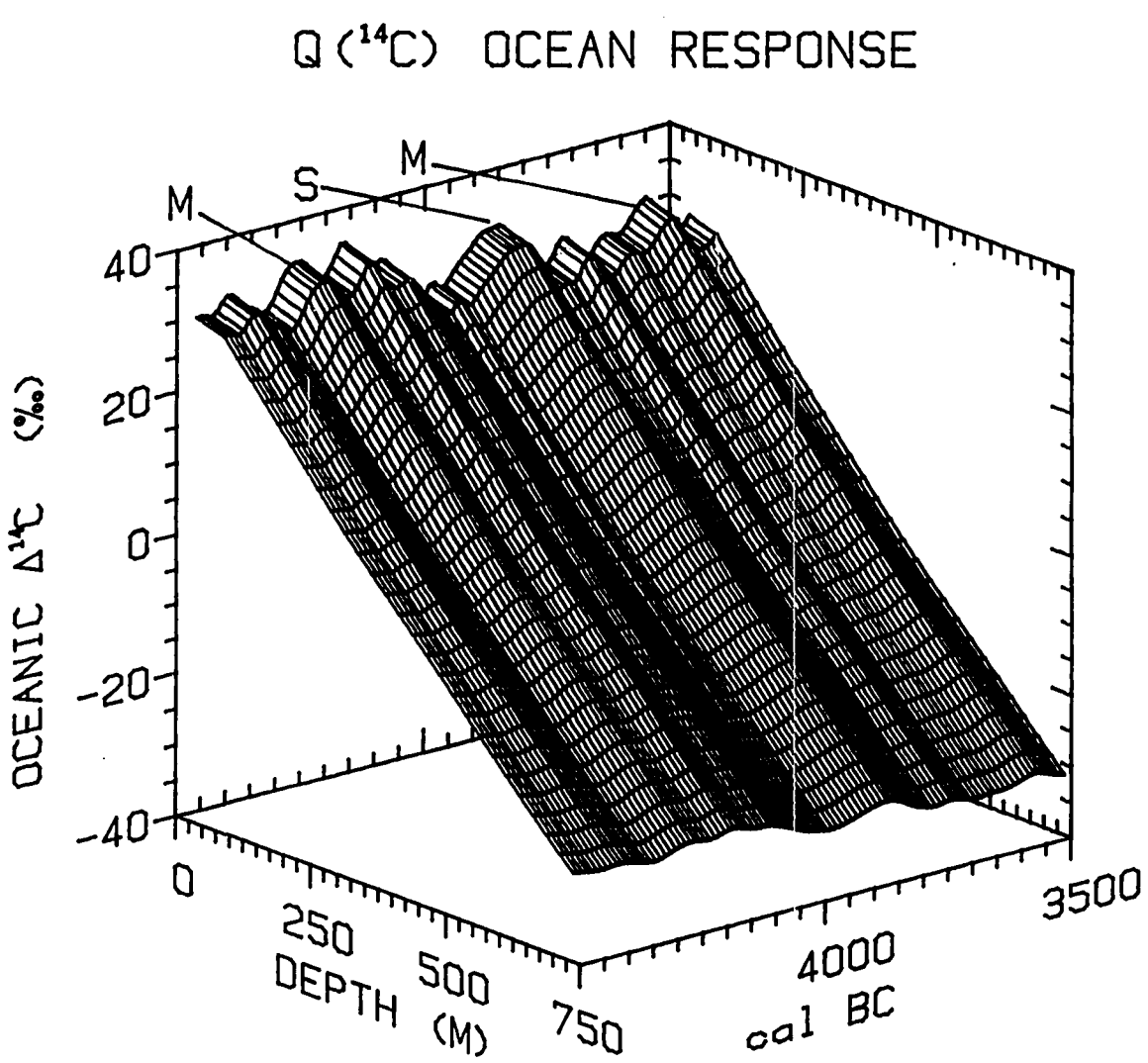
Q (^{14}C) OCEAN RESPONSE
M
S
M
40
20
0
-20
-40
OCEANIC Δ^{14}C (‰)
0
250
500
750
DEPTH (M)
3500
4000
cal BC

Figure 3.6 (upper panel) displays the "average" Q-forced oceanic Spörer-type $\Delta^{14}C$ event associated with the average Spörer-type atmospheric $\Delta^{14}C$ digression shown in figure 3.2 (ie. the mid-line of the shaded boxes). As stated above, the exchange parameters F and K_Z were fixed at standard values in the Q-deconvolution model and the initial ^{14}C production was set at 1.52 ^{14}C atoms cm_E^{-2} s^{-1} to yield a steady-state atmospheric $\Delta^{14}C$ value of -8 °/oo prior to the Spörer digression. Surface ocean $\Delta^{14}C$ increases ca. 10 °/oo before the excess ^{14}C gradually dissipates into the deeper ocean (with about a 3 °/oo surface ocean excess remaining after 300 yrs). This oceanic response to a Q-related Spörer-type atmospheric $\Delta^{14}C$ event will be contrasted with the oceanic behavior simulated when variations in the exchange parameters F or K_Z are instead responsible for century-scale atmospheric $\Delta^{14}C$ change (section 3.3).

3.3 Implications of a climate (atmosphere/ocean) origin for century-scale reservoir $\Delta^{14}C$ variations

Although convincing evidence suggests that the two common century-type oscillations in atmospheric $\Delta^{14}C$ originate from changes in ^{14}C production rates related to solar activity variations, digressions in reservoir exchange rates may also influence atmospheric $\Delta^{14}C$. In this section, we consider some of the atmospheric and oceanic evidence for variations in carbon reservoir dynamics which could produce Maunder- or Spörer-type excursions in atmospheric $\Delta^{14}C$.

Reasonable evidence and careful analysis exist both supporting a correlation between century-scale atmospheric $\Delta^{14}C$ variation and Holocene climate change (eg. Eddy 1977,

Figure 3.6: Histories of oceanic ^{14}C profiles associated with the average Spörer-type atmospheric $\Delta^{14}C$ digression when this digression is forced in the global reservoir model by changes in: (1) ^{14}C production rate $Q(^{14}C)$ (upper panel), (2) eddy diffusion $K_z(^{14}C)$ (left lower panel), or (3) air-sea CO_2 exchange rate $F(^{14}C)$ (right lower panel). The "horizontal" lines represent $\Delta^{14}C$ trends in model ocean boxes as explained in figure 3.5. The modeling assumptions and initial conditions are discussed in the text.

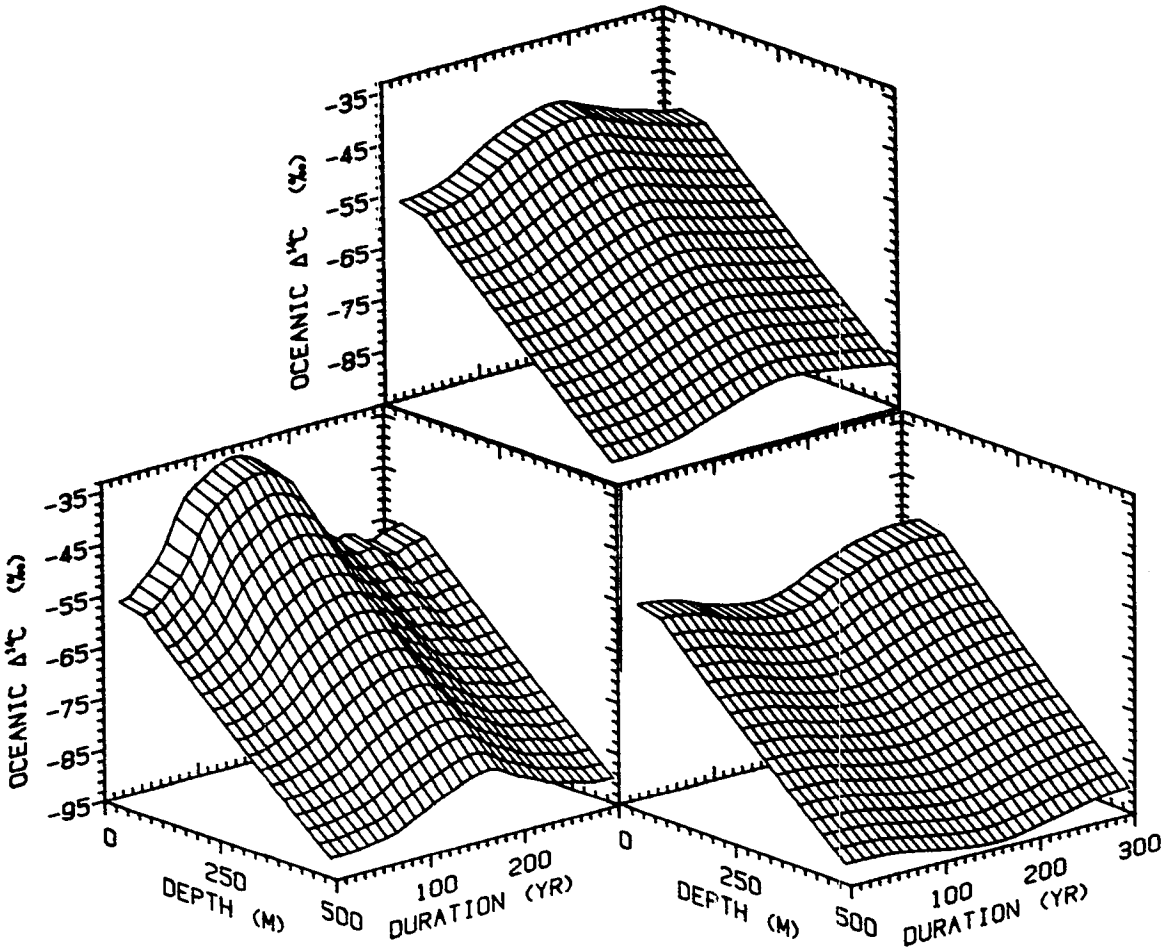
OCEANIC Δ¹³C (‰)
-35
-45
-55
-65
-75
-85
-95
0
250
500
DEPTH (M)
100
200
300
DURATION (YR)

Wigley 1988) and contradicting a consistent relationship (eg. Stuiver 1980b). The "Little Ice Age" in western Europe approximately coincides with the Maunder Minimum in sunspot activity (and maximum in ^{14}C production) but closer inspection reveals inconsistencies in the decadal timing of climatic and ^{14}C variations (Stuiver 1980b). The ^{14}C/climate association for the recent Maunder ^{14}C event is thus equivocal, and the contemporaneity of ^{14}C/climate variations for the earlier Holocene is even more difficult to assess.

Although the correlation of century-scale ^{14}C and Holocene climate records is uncertain, century-scale atmospheric $\Delta^{14}C$ variations can theoretically originate from changes in atmosphere-ocean dynamics. Greater communication between the atmospheric and surface or deeper oceanic carbon reservoirs depletes atmospheric ^{14}C because of the decay-related $^{14}C/^{12}C$ deficiency in oceanic carbon. In addition, the associated increase in atmospheric CO_2 (because of the greater deeper ocean pCO_2) works to diminish the atmospheric ^{14}C level by enhancing air-sea ^{14}C exchange fluxes (see section 2.2). On the other hand, weakened communication between these reservoirs should raise atmospheric $\Delta^{14}C$.

As an added complication, some climate-related changes may be continuous while others may involve sudden deviations at certain threshold levels. Rapid (century-scale) alterations between bi-stable modes of climate are proposed as explanations for sudden synchronous oscillations in ice-core $\delta^{18}O$ and CO_2 variations during the last glacial stage (eg. Oeschger and Stauffer 1986) perhaps related to the apparent switching on and off of North Atlantic Deep Water formation (Broecker et al. 1985b). Modeling studies support a bi-stability in Atlantic thermohaline circulation (Manabe and Stouffer 1988).

As discussed in section 2.2, Holocene atmospheric pCO_2 apparently varied as much

as ± 7% (ie. by ± 20 ppm or ± 40 gigatons of carbon) on a scale of centuries if the fluctuations in ice-core CO_2 measurements from Byrd station in Antarctica are confirmed (Neftel et al. 1988). An increase in atmospheric CO_2 of 20 ppm will produce a decrease in atmospheric $\Delta^{14}C$ of 3.5 °/oo (section 2.2). If, in addition, the source for the atmospheric CO_2 increase is the oceanic thermocline with $\Delta^{14}C$ of -100 °/oo, then a simple mass balance shows that atmospheric $\Delta^{14}C$ will decline an additional 6.5 °/oo. A total 10 °/oo decline or rise (if such a source of CO_2 is instead "closed off") represents two-thirds of the typical $\Delta^{14}C$ range associated with century-scale Maunder- and Spörer-type events. Is there physical evidence of such a mechanism influencing atmospheric carbon contents?

Gaudry et al. (1987) estimate that 6 gigatons of CO_2 (ie. 1.6 GT of carbon) were released into the atmosphere during the 1982-1983 El Niño event. The authors speculate that the continental biomass is responsible for part of this release. A sustained "reverse El Niño event" of 100 yrs duration that generated an emission from the oceanic thermocline of 100 yr x (1.6 GT carbon / 2 yr) = 80 GT of carbon would increase atmospheric $\Delta^{14}C$ by up to 18.5 °/oo and atmospheric pCO_2 by up to 40 ppm as a result of the effects discussed above. This "maximum" ^{14}C estimate assumes that the full carbon release originates in the thermocline. Furthermore, an increase in atmospheric $\delta^{13}C$ will accompany a "closed off" carbon release from the thermocline (with its pCO_2 content enriched by ^{13}C-deficient biological remineralization) and partially counter any rise in ^{14}C incorporated in the fractionation-corrected $\Delta^{14}C$ term. Therefore, this mechanism for generating century-scale atmospheric $\Delta^{14}C$ digressions requires profound changes in atmospheric pCO_2 and in oceanic upwelling which do not readily match current knowledge.

In place of mass balance calculations, the F- and K_z-deconvolution models are

utilized below to further determine the implications of variations in atmosphere/ocean dynamics as controls on century-scale $\Delta^{14}C$. Wind-driven air-sea CO_2 exchange (the F model parameter) does not affect atmospheric pCO_2; we also neglect atmospheric pCO_2 changes that might be associated with variations in internal oceanic mixing (the K_Z model parameter) although variable oceanic pCO_2 will secondarily change the trends in the model-derived oceanic $\Delta^{14}C$ curves. These trends will be compared to available coral ^{14}C data in order to assess the potential for F or K_Z changes to induce the observed century-scale atmospheric $\Delta^{14}C$ digressions.

The transient trends in air-sea CO_2 exchange and internal oceanic mixing, $F(^{14}C)$ and $K_Z(^{14}C)$ respectively, were deconvolved with the century-scale atmospheric $\Delta^{14}C$ history constrained to match either the average Maunder or Spörer-type atmospheric $\Delta^{14}C$ digression of figure 3.2. The ^{14}C production rate was assumed constant at 1.52 ^{14}C atoms cm_E^{-2} s^{-1} during each atmospheric digression and the initial reservoir exchange parameters at the start of the Maunder- or Spörer-type event were set at their standard values of F = 19 moles m^{-2} yr^{-1} and K_Z = 4000 m^2 yr^{-1} (see section 3.2). The validity of the deconvolved parameter histories was verified by successfully regenerating the average atmospheric $\Delta^{14}C$ excursions in the conventional "forward" version of the global ^{14}C model with the previously derived $F(^{14}C)$ and $K_Z(^{14}C)$ curves serving as model inputs.

To simulate sudden transitions in climate-related reservoir exchanges, F and K_Z were allowed to change instantaneously to new values for a specified time interval after which they were instantaneously returned to their original strengths. These step-function inputs for F and K_Z were adjusted until the atmospheric $\Delta^{14}C$ digressions derived from the conventional "forward" ^{14}C model best fit the observed average Maunder- and Spörer-type atmospheric $\Delta^{14}C$ curves. Various combinations for the magnitudes and durations of

these step functions might yield similar atmospheric $\Delta^{14}C$ curves, but I only wish to investigate the feasibility in principle for such sudden climatic switches (see below). The same initial conditions were applied in these simulations as those denoted above.

An association between century-scale ^{14}C and Holocene climate might also result if century-scale variations in solar activity (reflected in the $\Delta Q/Q_t$ record) significantly influence global climate. However, small century-scale changes in solar irradiance require an unidentified amplifying mechanism to affect global climate (see chapter 4). Although co-variations in ^{14}C production and reservoir exchange parameters (F and K_z) were investigated on a millennial timescale (section 2.5), I did not model joint century-scale changes in (solar-related) ^{14}C production and (assumedly solar-related) climate change because of the lack of an independent proxy record for either ^{14}C production or century-scale climate variation. When a higher precision ice-core ^{10}Be record can serve as a proxy for century-scale ^{14}C production, perhaps global modeling can be applied to isolate any residual solar-related climate signal in the atmospheric $\Delta^{14}C$ record.

Variable gas exchange and century-scale ^{14}C change

The trend in air-sea CO_2 exchange that is compatible with the average Maunder-type atmospheric $\Delta^{14}C$ excursion consists of a century-scale 30% decrease in $F(^{14}C)$ (from 19 to 13 moles CO_2 m^{-2} yr^{-1}); this trend is somewhat less than the 40% decline in $F(^{14}C)$ (to 11.5 moles CO_2 m^{-2} yr^{-1}) compatible with the longer Spörer-type $\Delta^{14}C$ excursion (figure 3.7). In both cases, a slight increase in $F(^{14}C)$ (to 20 moles CO_2 m^{-2} yr^{-1}) is required in the final bi-decades of the event in order to produce the rapid return of atmospheric $\Delta^{14}C$ to pre-event conditions (note the sharp atmospheric $\Delta^{14}C$ declines in figure 3.2). As shown below, the late enhancement of $F(^{14}C)$ compensates for the inertia in the oceanic thermocline in its recovery from the $\Delta^{14}C$ perturbation.

Figure 3.7: The histories of air-sea CO_2 exchange rate required to explain the average Maunder-type and Spörer-type atmospheric $\Delta^{14}C$ digressions when ^{14}C production and internal oceanic mixing are constant. These deconvolved $F(^{14}C)$ curves translate into variations in global wind speed (right axis) as defined by the linear relationship in Broecker et al. (1985a). Other modeling assumptions and initial conditions are discussed in the text.

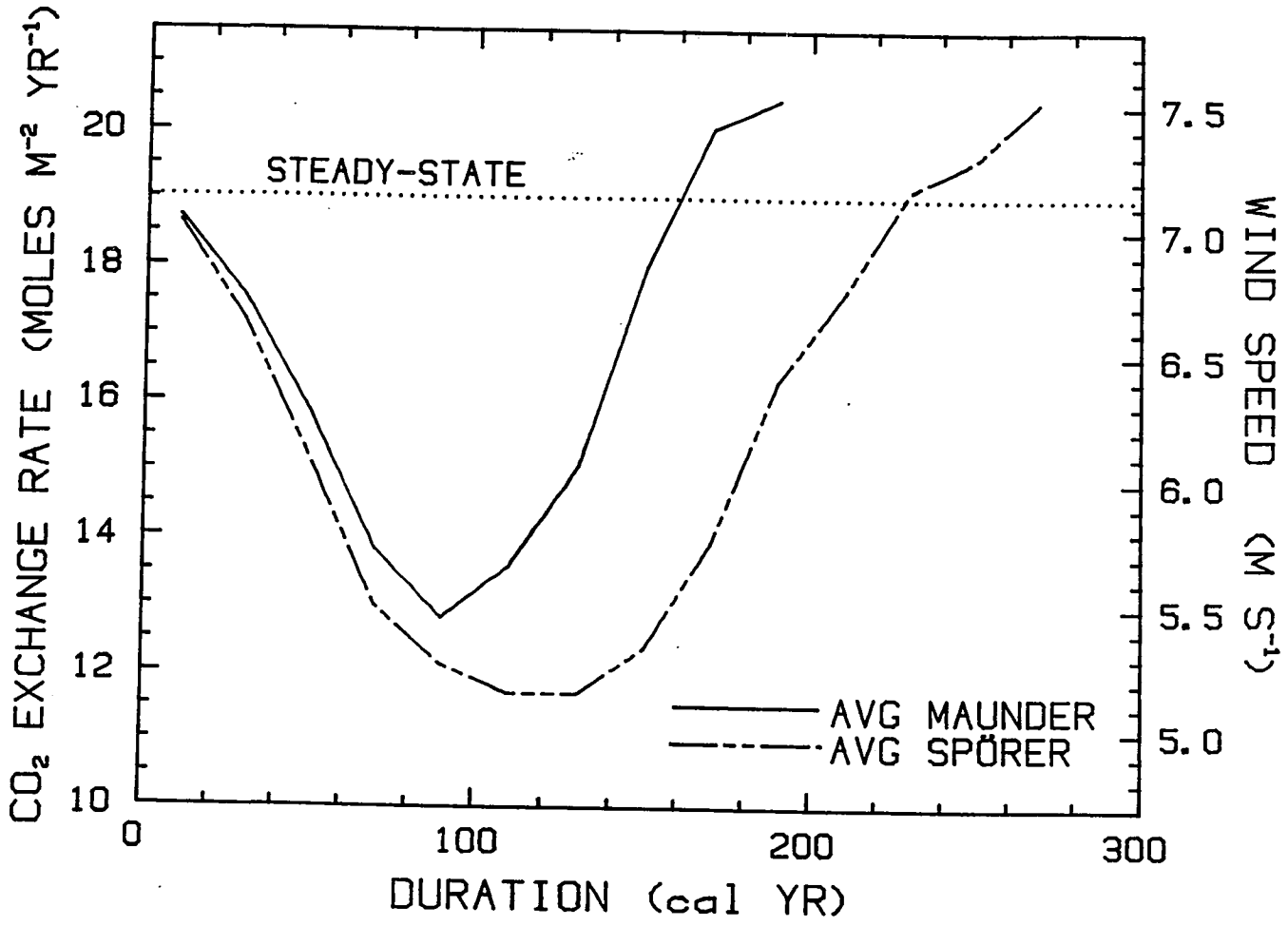
STEADY-STATE
AVG MAUNDER
AVG SPÖRER
CO_2 EXCHANGE RATE (MOLES M^{-2} YR^{-1})
WIND SPEED (M S^{-1})
DURATION (cal YR)
10
12
14
16
18
20
5.0
5.5
6.0
6.5
7.0
7.5
0
100
200
300

The decline in air-sea gas exchange permits more ^{14}C to remain in the atmosphere and less to be transported into the surface ocean. As a result, surface ocean $\Delta^{14}C$ decreases about 4 ‰ during, for example, the Spörer event but recovers rapidly to within 2 ‰ of pre-event levels at the end of the atmospheric $\Delta^{14}C$ digression (figure 3.6, lower right panel). The oceanic $\Delta^{14}C$ decline is mild relative to the atmospheric $\Delta^{14}C$ increase of 15 ‰ because internal oceanic mixing distributes the ^{14}C deficiency throughout the thermocline. On the other hand, the swiftness in the recovery of atmospheric $\Delta^{14}C$ requires a slight "overshoot" in $F(^{14}C)$ and an increase in surface ocean $\Delta^{14}C$ while the vertical ^{14}C profile in the thermocline lags in its return to pre-event conditions (figure 3.6).

The variation in model ventilation index MVI which accompanies this upper ocean perturbation parallels the surface ocean $\Delta^{14}C$ history (figure 3.8, curve S/F for the F-forced Spörer scenario). The MVI term is defined as the difference between ^{14}C age of the model surface ocean and of the average model deep ocean below 1 km depth (ie. below the model thermocline). An apparent decrease in ventilation time of 50 ^{14}C yrs occurs even though, since K_Z does not vary in this simulation, the true ventilation index (KVI) remains constant at 1275 ^{14}C yrs.

The observed oceanic uptake of excess ^{14}C produced during nuclear weapons testing in the 1950's and 1960's is compatible with a greater rate of upper oceanic mixing than the K_Z value of 1.25 $cm^2\ s^{-1}$ (4000 $m^2\ yr^{-1}$) derived from the natural vertical distribution of ^{14}C in the entire ocean. As a sensitivity test for the F-deconvolution simulation, the K_Z constant was reset to be 2.2 $cm^2\ s^{-1}$ (6940 $m^2\ yr^{-1}$), as calibrated to fit the bomb ^{14}C total oceanic inventory and surface content (Broecker et al. 1980). The steady-state ^{14}C production must be increased to 1.60 ^{14}C atoms $cm_E^{-2}\ s^{-1}$ in this simulation in order to

Figure 3.8: The histories in model ventilation index MVI associated with the alternative forcings of the average Maunder- and Spörer-type atmospheric $\Delta^{14}C$ digressions in figure 3.2. The MVI term is defined in the text. The M/Q and S/Q bi-decadal curves are derived from the Q-forced model ocean variations during the Maunder- and Spörer-type events, respectively; the M/F and S/F curves are analogously related to F-forced model ocean variations and the M/K and S/K curves are similarly related to K_Z-forced model ocean variations. The dotted line denotes the steady-state MVI of 1275 ^{14}C yrs for all simulations.

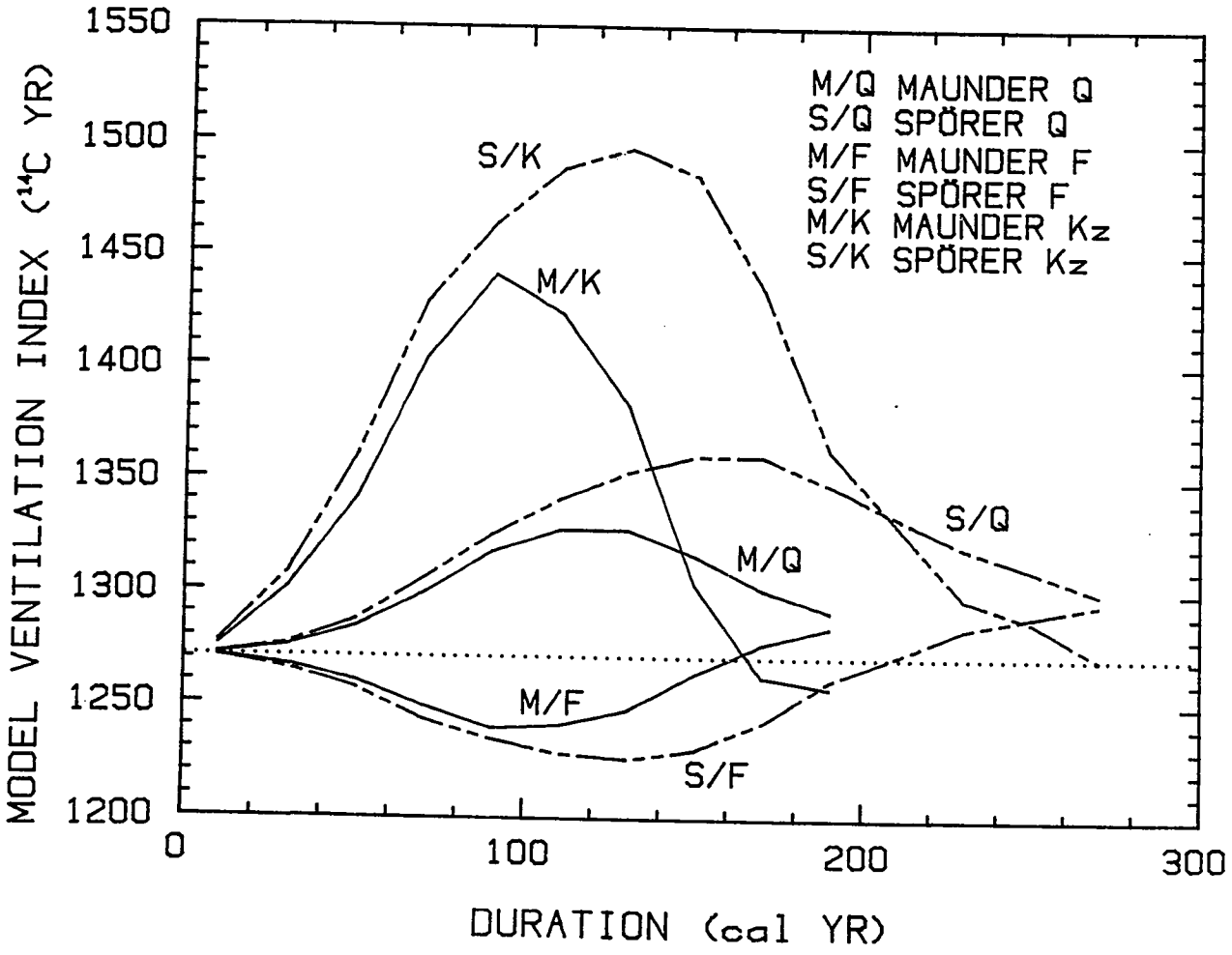
1550
1500
1450
1400
1350
1300
1250
1200
0
100
200
300
MODEL VENTILATION INDEX (^{14}C YR)
DURATION (cal YR)
M/Q MAUNDER Q
S/Q SPÖRER Q
M/F MAUNDER F
S/F SPÖRER F
M/K MAUNDER Kz
S/K SPÖRER Kz
S/K
M/K
S/Q
M/Q
M/F
S/F

maintain the same pre-event atmospheric $\Delta^{14}C$ level as observed. However, the decline in $F(^{14}C)$ is affected less than 3% by this greater oceanic mixing because of the dominant effect of air-sea gas exchange rate in controlling century-scale atmospheric $\Delta^{14}C$ variations.

As a second sensitivity test, F and K_Z were forced to covary in the same relative proportions (in the F,K_Z-deconvolution model described in chapters 1 and 2) as joint agents generating either the observed Maunder and Spörer-type atmospheric $\Delta^{14}C$ excursion. The decline in $F(^{14}C)$ is alleviated only 33% in these scenarios, once again demonstrating the greater potential for variations in CO_2 gas exchange to affect atmospheric ^{14}C in comparison to the more indirect role of internal oceanic mixing. As concluded in section 2.2, relative variations in F appear to have approximately twice the impact on atmospheric ^{14}C as the same relative K_Z variations.

As before, the $F(^{14}C)$ curve can serve as an index of global wind speed history by applying a simple linear relationship for the wind-speed dependence of air-sea CO_2 exchange (Broecker et al. 1985a). The century-scale decline in global wind speeds implied by this relationship (figure 3.7, right axis) is approximately 20% lasting about 80 yrs for the Maunder-type ^{14}C perturbation and 30% over a 120 yr interval for the Spörer-type ^{14}C perturbation. Such excursions represent significant digressions; for comparison, global wind speed is estimated to have generally declined about 50% at the beginning of the present interglacial Holocene epoch from its magnitude during the last glacial stage (Petit et al. 1981). Microparticle evidence does not support such extreme Holocene variations (see section 2.2) but are any other relevant atmospheric records available?

Global wind speeds also have an influence on two quantities with high resolution records in ice cores, $\delta^{18}O$ and d (ie. deuterium excess which equals $\delta D - 8\,\delta^{18}O$); these

records may therefore contain independent information on century-scale wind variations. Unfortunately for this study, other variables play important roles as well in determining the time histories of these tracers. The dependence of $\delta^{18}O$ and d on temperature-related equilibrium fractionation of evaporation and condensation, wind-related kinetic fractionation, and relative humidity complicates the interpretation of these climatic tracers with the latter association generally being dominant (Merlivat and Jouzel 1979, Jouzel et al. 1982).

Our estimated current global wind average of 7.2 m s^{-1} falls in the transitional range between a "smooth" and "rough" wind regime (figure 2 in Merlivat and Jouzel 1979). According to the equations presented in Jouzel et al. (1982), a 3 m s^{-1} reduction in global winds (as accompanies an F-forced Maunder or Spörer event) changes the $\delta^{18}O$ of the first precipitate in a given air mass by 0 ‰ in the smooth regime, by 0.18 ‰ in the rough regime, and by -0.9 ‰ in a transition of smooth to rough wind regimes. Thus the expected wind-driven $\delta^{18}O$ variations are ambiguous. The expected d variations are likewise equivocal with changes, for the three cases stipulated above, of 0, 1.3, and -6.4 ‰, respectively. Unless pre-event global wind conditions clearly fall in one of the two wind regimes and unless the influence of other variables such as relative humidity can be isolated, the use of ice-core $\delta^{18}O$ and d as high-resolution tracers of past wind conditions is very limited.

The step-function variations in F that approximately produce the Maunder and Spörer atmospheric $\Delta^{14}C$ events are similar in magnitude and duration to the transient $F(^{14}C)$ histories derived above. A 35% decrease in F (down to 12.5 moles CO_2 m^{-2} yr^{-1}) for 80 years duration (between "year 50" and "year 130" of the atmospheric Maunder event) results in an atmospheric $\Delta^{14}C$ perturbation that resembles the average Maunder $\Delta^{14}C$ fluctuation (figure 3.9). A 40% decrease in F (down to 11.5 moles CO_2 m^{-2} yr^{-1}) for

Figure 3.9: Bi-decadal atmospheric $\Delta^{14}C$ histories (dark lines) derived from step changes in air-sea CO_2 exchange rate designed to produce the basic features of the common century-scale atmospheric $\Delta^{14}C$ digressions. For comparison, the observed average Maunder- and Spörer-type atmospheric $\Delta^{14}C$ excursions (shaded areas) are reproduced from figure 3.2.

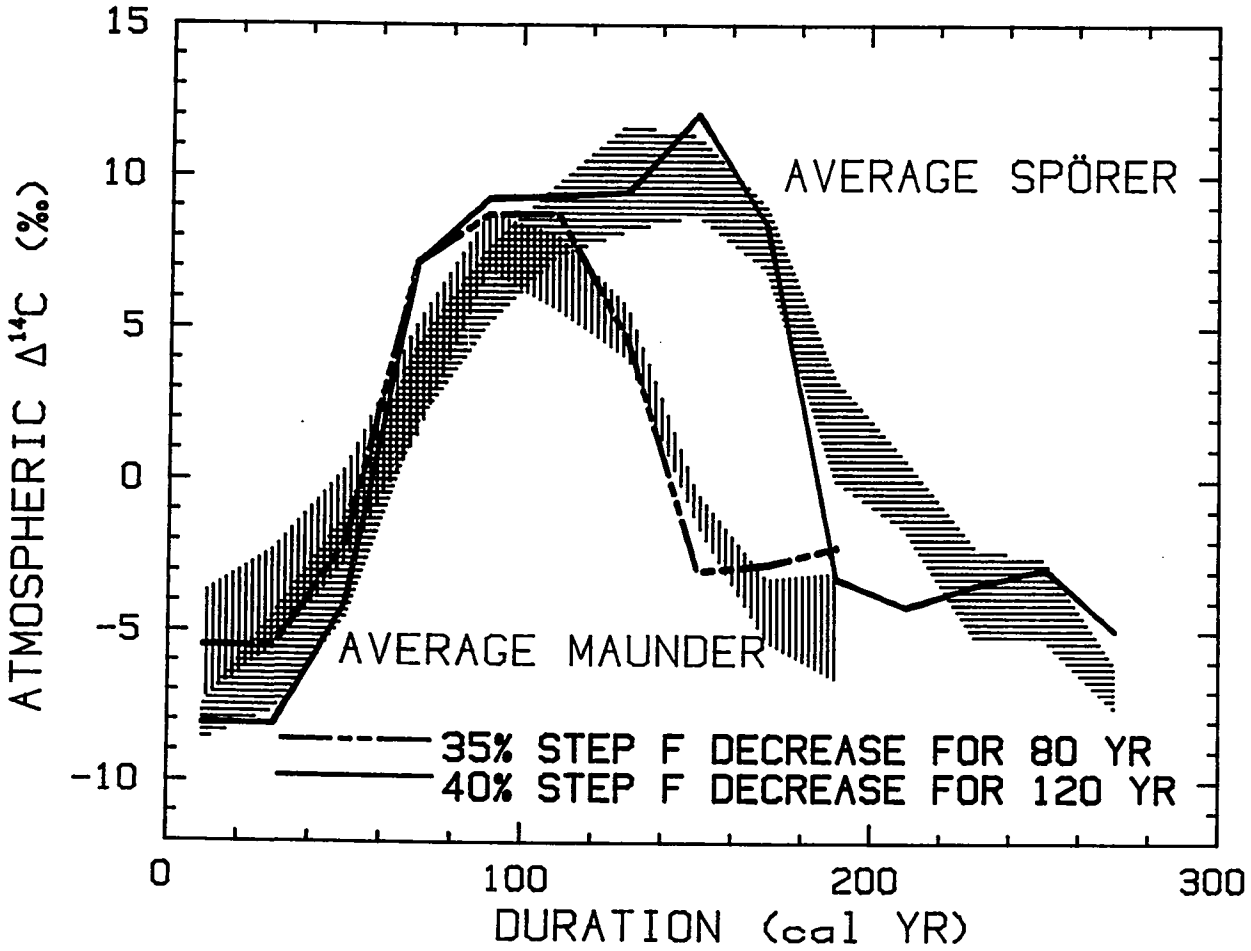
15
10
5
0
-5
-10
ATMOSPHERIC Δ14C (‰)
AVERAGE SPÖRER
AVERAGE MAUNDER
35% STEP F DECREASE FOR 80 YR
40% STEP F DECREASE FOR 120 YR
0
100
200
300
DURATION (cal YR)

120 years duration (between "year 50" and "year 170" of the Spörer event) likewise is compatible with the average Spörer-type atmospheric $\Delta^{14}C$ perturbation although the modeled recovery in atmospheric $\Delta^{14}C$ is steeper than observed (figure 3.9). The oceanic ^{14}C response to these parameter step-changes resembles the curves displayed above for the progressive $F(^{14}C)$ histories. Therefore, the same analysis and criticisms apply. In contrast, the outcome of a step change in K_Z will be shown to differ dramatically from that of its progressive counterpart.

Variable diffusivity and oceanic ^{14}C change

The modeling approach and analysis of the deconvolution of $K_Z(^{14}C)$ parallels the $F(^{14}C)$ discussion above. However, the curves used to represent the average Maunder- and Spörer-type atmospheric $\Delta^{14}C$ oscillations were slightly redefined to prevent the failure of the K_Z-deconvolution model. Whereas, for the F simulations, the continuous curves that characterized the average Maunder and Spörer atmospheric constraints consisted of linear interpolations of the bi-decadal $\Delta^{14}C$ records in figure 3.2, interpolating *splines* were instead used in the K_Z simulations to force a smoother transition from each average bi-decadal $\Delta^{14}C$ to the next. Otherwise, the deconvolution of undefined $K_Z(^{14}C)$ values occasionally occurred when changes in internal oceanic mixing were required to produce the instantaneous slope breaks in the atmospheric $\Delta^{14}C$ record derived by a simple linear interpolation. Except for this minimal adjustment in the atmospheric $\Delta^{14}C$ inputs, the other century-scale model assumptions and initial conditions remained the same.

The variations in $K_Z(^{14}C)$ necessary to produce the two average century-scale excursions in atmospheric $\Delta^{14}C$ are more complicated than the $F(^{14}C)$ variations

deconvolved above. A Maunder-type atmospheric $\Delta^{14}C$ fluctuation requires a 50% decrease in $K_Z(^{14}C)$ (from 4000 $m^2\ yr^{-1}$ to 2000 $m^2\ yr^{-1}$) followed by a 50% increase in $K_Z(^{14}C)$ (peaking at 5850 moles $m^{-2}\ yr^{-1}$) before a return to steady-state conditions (figure 3.10). The Spörer-type atmospheric $\Delta^{14}C$ fluctuation requires a 50% decrease in $K_Z(^{14}C)$ as well with a subsequent rise in $K(^{14}C)$ of 25% (to 5150 $m^2\ yr^{-1}$) before returning to base-line conditions (figure 3.10). Because the exchange parameter K_Z directly affects the entire oceanic distribution of ^{14}C, the return to pre-event atmospheric ^{14}C levels requires a strong antithetical digression in K_Z to nullify the original perturbation (see below).

The initial decline in internal oceanic mixing restricts the transfer of ^{14}C into deeper oceanic layers, in this way causing the ^{14}C rise in the surface ocean which is responsible for producing the century-scale elevation in atmospheric $\Delta^{14}C$. The surface ocean $\Delta^{14}C$ peak during the Spörer event is 20 ‰ above initial conditions and the average thermocline $\Delta^{14}C$ also increases by 8 ‰ (figure 3.6, lower left panel). The deep ocean ^{14}C reservoir, on the other hand, becomes on average 5 ‰ more depleted because of the reduced transport of ^{14}C from the surface. In contrast, the hypothetical Spörer-related excursion in air-sea CO_2 exchange rate insignificantly affects the deep ocean.

As previously noted by Druffel (1982), the $\Delta^{14}C$ digression in the surface ocean must equal or exceed the atmospheric $\Delta^{14}C$ change when the oceanic reservoir drives this change. The model results show that a 20 ‰ increase in the surface ocean is required to produce a rise of 15 ‰ in atmospheric $\Delta^{14}C$. The difference of 5 ‰ partly reflects the importance of the longer-term (τ_2 = 80 yr) terrestrial biota as a ^{14}C sink. The surface ocean must supply sufficient ^{14}C to produce positive $\Delta^{14}C$ digressions in both the atmospheric and terrestrial reservoirs since the latter acts to mitigate any atmospheric ^{14}C perturbation by removing a portion of it.

Figure 3.10: The histories of eddy diffusivity required to explain the average Maunder-type and Spörer-type atmospheric $\Delta^{14}C$ digressions when ^{14}C production and air-sea CO_2 exchange rate are constant. These deconvolved $K_Z(^{14}C)$ curves translate into variations in instantaneous ventilation index KVI (right axis) as defined by the equation 1.12 in chapter 1. Other modeling assumptions and initial conditions are discussed in the text.

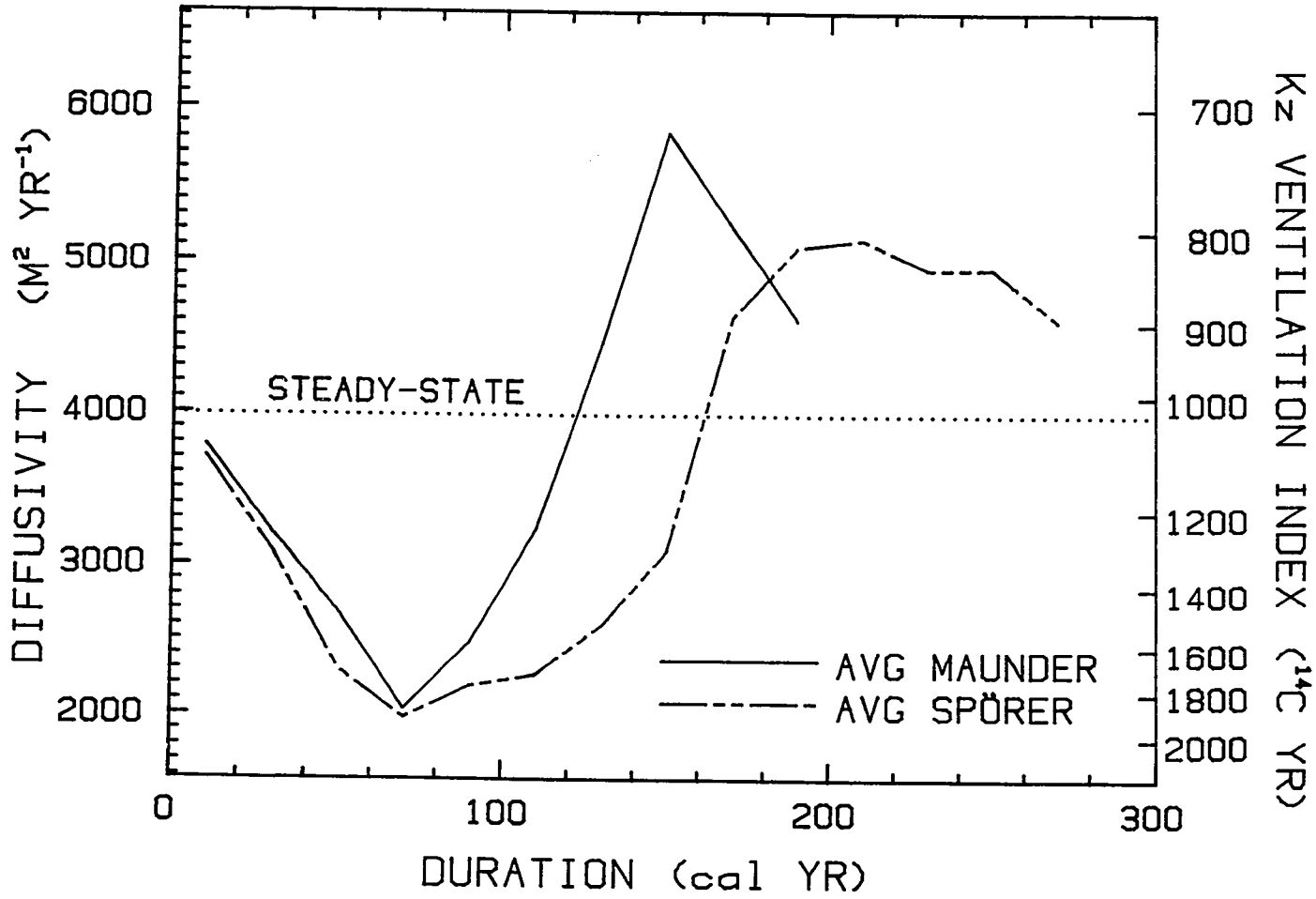
DIFFUSIVITY (M² YR⁻¹)
6000
5000
4000
3000
2000
STEADY-STATE
AVG MAUNDER
AVG SPÖRER
0
100
200
300
DURATION (cal YR)
Kz VENTILATION INDEX (¹⁴C YR)
700
800
900
1000
1200
1400
1600
1800
2000

The ventilation index from the ^{14}C "circulation tracer" suggests that the turn-over time of the ocean reservoir with respect to water fluxes has an order of magnitude of 1000 yrs. The relaxation time of the ocean in response to an oceanic ^{14}C perturbation event will have this same order of magnitude. Unlike the variations in $F(^{14}C)$, the $K_Z(^{14}C)$ changes significantly affect the entire vertical distribution of oceanic ^{14}C. Thus a simple return of $K_Z(^{14}C)$ to its "base-line" value is not sufficient to force oceanic and atmospheric ^{14}C back to pre-perturbation conditions; a significant compensatory digression (figure 3.10) in internal mixing for an extended period of time (ca. 100 yrs) is necessary to recover the ^{14}C system promptly to a resemblance of initial steady-state conditions (figure 3.6).

The long relaxation time of the model ocean is apparent when step changes in K_Z are fit to the Maunder- or Spörer-type atmospheric $\Delta^{14}C$ fluctuations. A 45% step decrease in K_Z (to 2200 $m^2\ yr^{-1}$) for 80 yrs duration results in an increase in atmospheric $\Delta^{14}C$ of the proper magnitude and slope for an average Maunder event while a similar step decrease in K_Z (to 2250 $m^2\ yr^{-1}$) for 120 yrs duration is compatible with the first half of the atmospheric Spörer event (figure 3.11). However, after the simple step return of K_Z to its pre-perturbation value, hundreds of years are required before atmospheric $\Delta^{14}C$ will be permitted by the slow recovery of the perturbed model ocean to return to its pre-event level (figure 3.11). Thus a simple switching mechanism for decreasing ocean ventilation over a specific time interval cannot produce the relatively rapid excursions and restorations of the century-scale atmospheric $\Delta^{14}C$ events.

The variations in the model ventilation index MVI which accompany the progressive K_Z changes in figure 3.10 significantly differ from the MVI histories associated with the ^{14}C production changes or air-sea CO_2 flux changes necessary to alternatively produce the century-scale atmospheric $\Delta^{14}C$ excursions (figure 3.8). Ocean ventilation truly varies

Figure 3.11: Bi-decadal atmospheric $\Delta^{14}C$ histories (dark lines) derived from step changes in internal oceanic mixing designed to produce the basic features of the common century-scale atmospheric $\Delta^{14}C$ digressions. For comparison, the observed average Maunder- and Spörer-type atmospheric $\Delta^{14}C$ excursions (shaded areas) are reproduced from figure 3.2. Although the specified step decreases in K_Z can provide suitable rises in atmospheric $\Delta^{14}C$, a K_Z step return to its initial level will allow the atmosphere to only slowly recover from its perturbed $\Delta^{14}C$ condition.

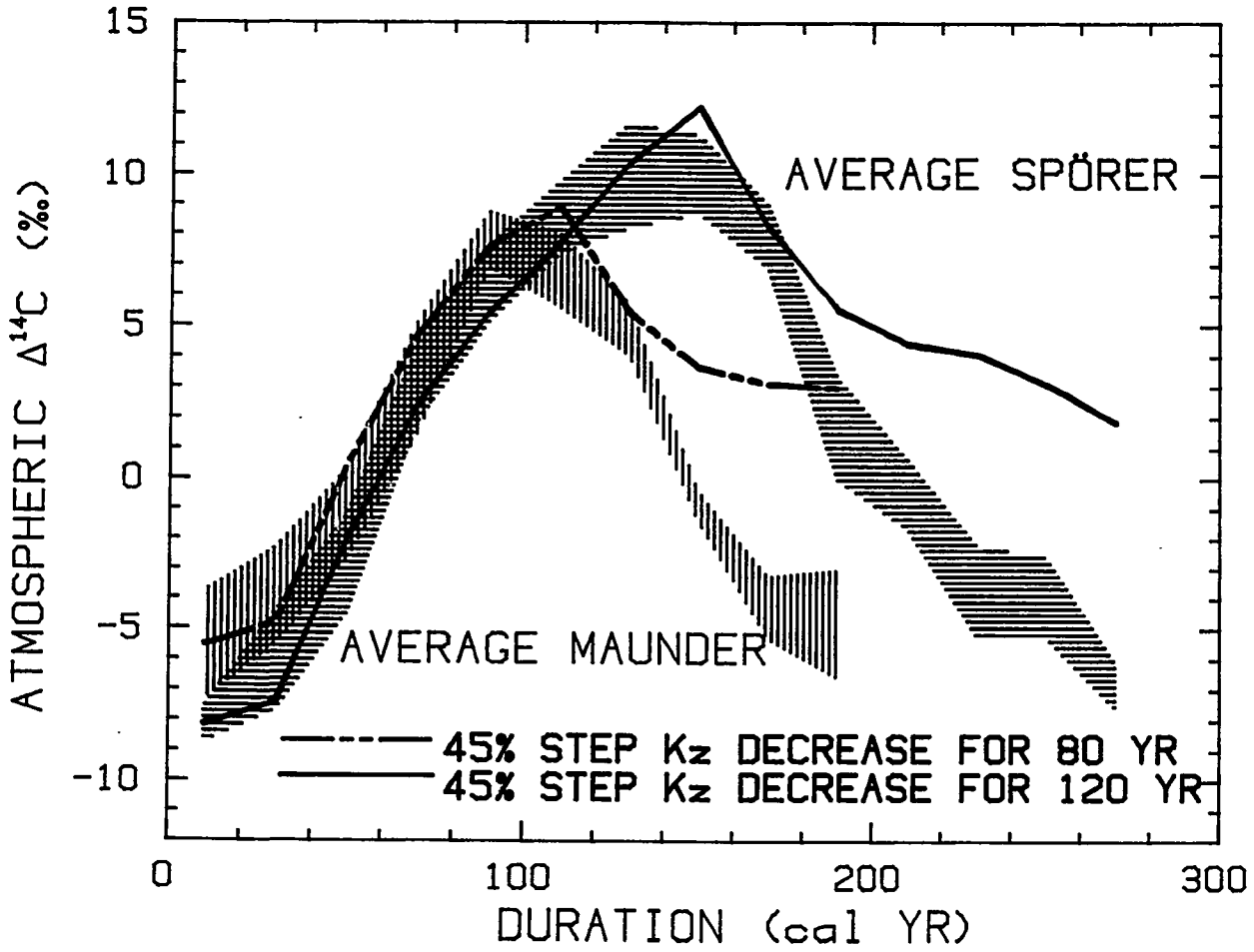
15
10
5
0
-5
-10
ATMOSPHERIC Δ14C (‰)
AVERAGE SPÖRER
AVERAGE MAUNDER
45% STEP Kz DECREASE FOR 80 YR
45% STEP Kz DECREASE FOR 120 YR
0
100
200
300
DURATION (cal YR)

only during the $K_Z(^{14}C)$ simulations; the apparent ventilation changes that comprise the other MVI histories only reflect the lag in the deeper oceanic ^{14}C reservoir in responding to variations in other reservoirs in the ^{14}C system. However, a K_Z-related MVI curve also does not accurately represent the history of $K_Z(^{14}C)$ when the ocean is not at steady state; for example, the enhancement in ocean mixing required to restore the pre-perturbation oceanic ^{14}C profile is not recorded by this index.

The ventilation index directly defined by $K_Z(^{14}C)$ is scaled on the right axis in figure 3.10. This ventilation index, KVI, denotes the difference in ^{14}C age between the surface and subsurface ocean reservoirs for a steady-state oceanic ^{14}C profile defined by the model equations and the instantaneous value for $K_Z(^{14}C)$ (see chapter 1). The Maunder-related $K_Z(^{14}C)$ history translates into an 85% increase in ocean ventilation time (from a "base-line" value of 1025 ^{14}C yrs to a maximum of 1890 ^{14}C yrs) which is followed by a 30% reduction in ocean ventilation time (to 720 ^{14}C yrs) before its return to initial conditions (figure 3.10). The Spörer event produces a similar increase in KVI succeeded by an extended 20% reduction in "instantaneous ventilation time" (to 810 ^{14}C yrs).

The "true" ventilation scenarios contrast sharply with the MVI trends based on the actual $\Delta^{14}C$ changes in the model ocean reservoirs (figure 3.8). Yet an MVI trend, like an FVI trend from foram ^{14}C measurements (section 1.4), is the mixing signal, however imperfect, that is available in oceanic records and is an important indication of instability in the ^{14}C system. The KVI and MVI "base lines" (and digressions) are offset because the definition of MVI does not include the thermocline in the calculation of the deeper ocean ^{14}C age; multiplication by a factor of 1025/1275 to adjust MVI allows a more direct comparison of these two indices.

Comparison of modeled ocean histories and coral ^{14}C data

The three alternative mechanisms considered for century-scale atmospheric ^{14}C digressions each result in distinct upper ocean $\Delta^{14}C$ variations (figure 3.6). For comparison, the annual resolution of coral growth bands has provided a detailed history of surface ocean $\Delta^{14}C$ change in the Florida Straits during the atmospheric Maunder ^{14}C event of AD 1600 to 1800 (Druffel 1982). The ^{14}C measurements on three coral cores collected in ocean waters of the Gulf Stream system (Druffel and Linick 1978; Druffel 1980, 1982) together represent a high resolution record of surface ocean $\Delta^{14}C$ spanning more than 3 centuries and place in perspective the Maunder-related ocean ^{14}C signal (figure 3.12).

A 20-yr moving average was calculated for the coral data after contemporaneous samples were averaged and the record was interpolated to annual spacing. This trend-line (figure 3.12, solid line) is elevated as much as 6 ‰ during the Maunder interval with respect to the persistent "base-line" level of ca. -49 ‰. The bi-decadal $\Delta^{14}C$ trend for the model surface ocean associated with a Q-forced atmospheric ^{14}C history exhibits a similar multicentury trend with a 6 ‰ rise during the Maunder event (dashed line). The offset in curves may reflect the difference between the global-average surface ocean $\Delta^{14}C$ of the model and the influences of specific regional exchange processes on the coral $\Delta^{14}C$ records. The concept of similar but offset $\Delta^{14}C$ histories for different surface ocean regions is elaborated in Stuiver et al. (1986b). The 20th-century decline in coral $\Delta^{14}C$ is associated with recent fossil-fuel emissions of dead carbon ($\Delta^{14}C$ = -1000 ‰); this anthropogenic effect was deleted for the global ^{14}C simulations (section 1.2).

The alternative model surface-ocean $\Delta^{14}C$ histories produced by the deconvolved Maunder-related variations in air-sea gas exchange or eddy diffusivity do not resemble the observed ^{14}C trend (figure 3.13). A smoothing spline between AD 1644 and 1811 was

Figure 3.12: $\Delta^{14}C$ measurements in annual growth bands of corals from Gulf Stream waters (symbols ± 1-sigma counting errors) compared to the Q-forced model surface ocean history (dashed line) excerpted from the full Holocene simulation displayed in figure 2.3. The dark solid line is a 20-yr moving average of the coral data after contemporaneous points were averaged and the record was interpolated to single year spacing.

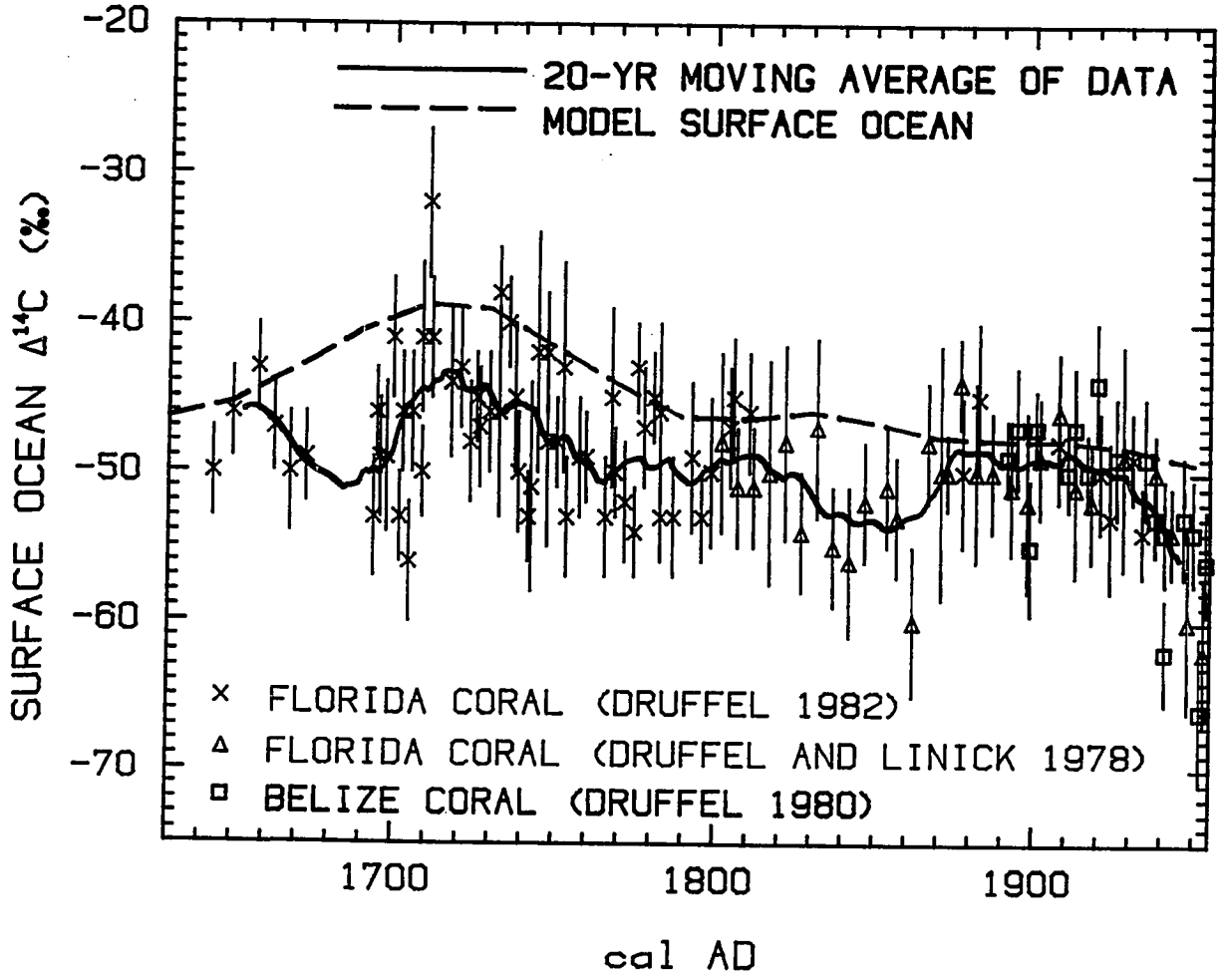
20-YR MOVING AVERAGE OF DATA
MODEL SURFACE OCEAN
FLORIDA CORAL (DRUFFEL 1982)
FLORIDA CORAL (DRUFFEL AND LINICK 1978)
BELIZE CORAL (DRUFFEL 1980)
SURFACE OCEAN Δ14C (‰)
-20
-30
-40
-50
-60
-70
1700
1800
1900
cal AD

Figure 3.13: The alternative model surface ocean $\Delta^{14}C$ trends associated with a Maunder-type atmospheric $\Delta^{14}C$ excursion compared to the available coral $\Delta^{14}C$ data spanning the last Maunder ^{14}C event (AD 1600 to 1800 in the atmosphere). The coral data is represented by a smoothing spline (dotted line) with an uncertainty range of ± 1.5 ‰ (shaded area) calculated for the AD 1680 to 1800 interval (see text for details). The Q-forced surface ocean $\Delta^{14}C$ curve (solid line) is excerpted from the full Holocene simulation shown in figure 2.3; the K_Z- and F-forced surface ocean $\Delta^{14}C$ curves (equi-dashed and short-short-long dashed line, respectively) are derived from the century-scale perturbation simulations linked to the average Maunder-type atmospheric $\Delta^{14}C$ digression. All curves are shifted slightly for direct comparison to the coral trend (see text).

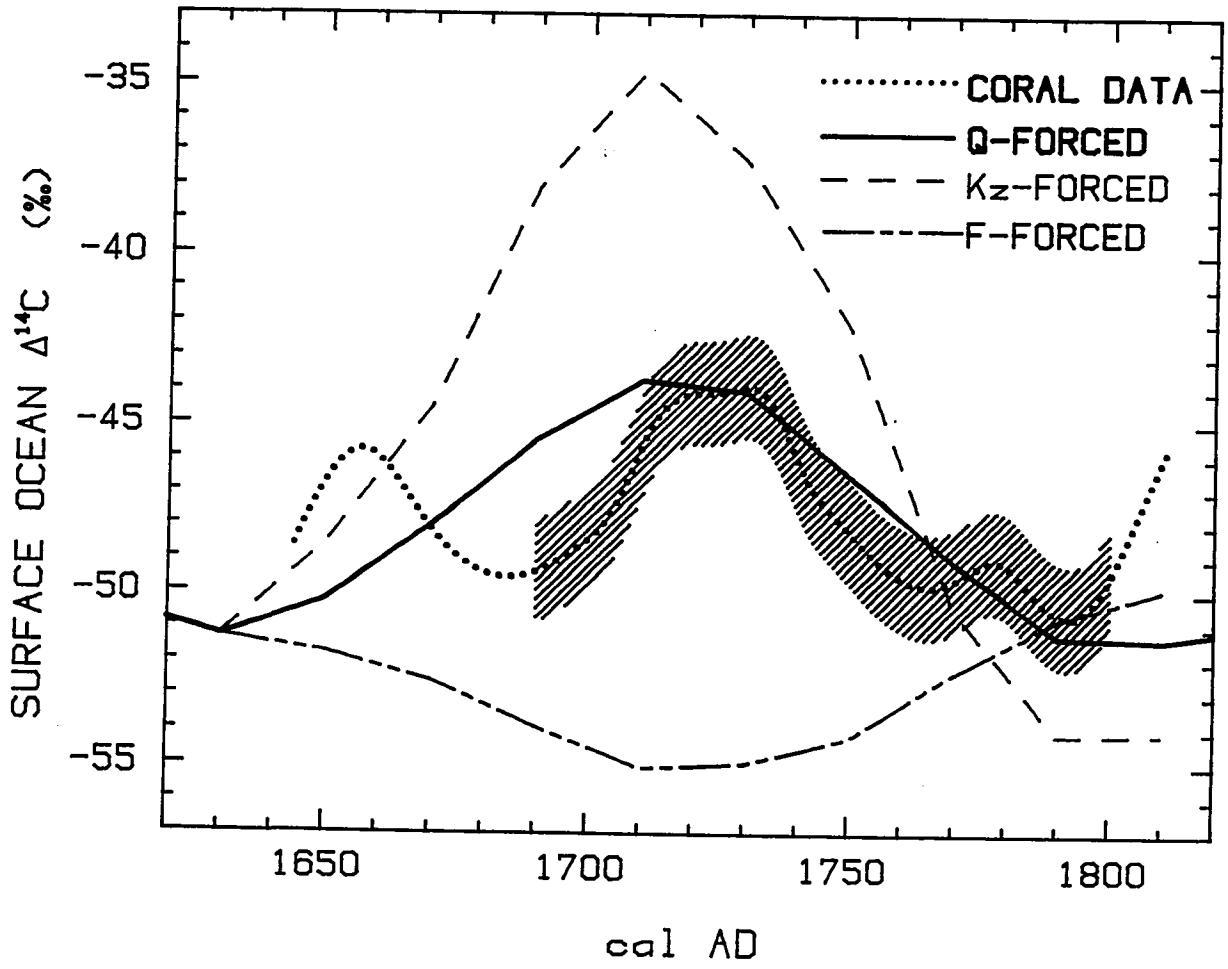
CORAL DATA
Q-FORCED
Kz-FORCED
F-FORCED
SURFACE OCEAN Δ14C (‰)
-35
-40
-45
-50
-55
1650
1700
1750
1800
cal AD

fit to the coral data of the one core that spans the Maunder interval (dotted line). An uncertainty of ± 1.5 ‰ (shaded area) was estimated for the well-represented data interval between AD 1680 to 1810 by calculating and averaging the standard errors of the means for the ^{14}C data within bi-decadal bins. The Q-forced surface ocean trend is part of the complete Holocene simulation discussed in chapter 2 (eg. figures 2.3 and 3.12); this trend has been depressed by 5 ‰ in order to match the mean of the coral spline and permit a direct comparison. The F- and K_Z-forced surface ocean $\Delta^{14}C$ curves, derived from the century-scale perturbation simulations above, were each adjusted by ca. -1 ‰ in order that all the curves have the same initial $\Delta^{14}C$ value at the beginning of the Maunder-related model oceanic digression in AD 1630.

Thus the coral $\Delta^{14}C$ data from the Gulf Stream system are consistent only with the hypothetical model surface-ocean $\Delta^{14}C$ history that is associated with a century-scale change in ^{14}C production rate. The ocean trends induced by climate-related F and K_Z changes clearly transgress the data uncertainties. None of the model curves, however, accurately replicates the first portion of the available coral record (figure 3.13). A more definitive analysis must await the existence of oceanic data records representing different ocean regions at times contemporaneous with the century-scale digressions in atmospheric $\Delta^{14}C$. More refined oceanic ^{14}C models that simulate specific regional mixing processes (eg. Toggweiler et al. 1989) will also be important.

3.4 Chapter summary

The detrended atmospheric $\Delta^{14}C$ record contains two common century-scale digressions during the Holocene. The 9 identified Maunder-type $\Delta^{14}C$ events on average

consist of +15 °/oo excursions lasting 200 yrs while the 8 Spörer-type $\Delta^{14}C$ events comprise excursions of similar magnitude but lasting 280 yrs. The Q-deconvolution simulations show that these atmospheric digressions can be generated by century-scale ^{14}C production rate increases of 30% if climate variables are assumed constant. The timing and magnitude of the deconvolved century-scale $Q(^{14}C)$ variations are consistent with the hypothetical ^{14}C production changes derived from ice-core [^{10}Be] fluctuations, and the correlation of the recent portions of these records with indices of solar activity ascribes a strong solar component to their origin.

The modeled ocean history associated with century-scale ^{14}C production variations is consistent with the limited coral $\Delta^{14}C$ data spanning the last Maunder event. In contrast, the coral $\Delta^{14}C$ trend differs significantly from the F-forced and K_Z-forced surface ocean histories required in the climatic explanations for the century-scale atmospheric $\Delta^{14}C$ digressions. In addition, the century-scale variations in global wind speeds that correspond to the deconvolved CO_2 exchange rates necessary to yield the atmospheric $\Delta^{14}C$ excursions are not evident in the ice-core microparticle record. Thus the available evidence supports only a production rate (solar) origin for century-scale atmospheric ^{14}C variations.

A switch mechanism for climatic events was considered by employing a step change for K_Z and F in the century-scale simulations. The notion of sudden climate change at threshold levels is currently receiving attention to explain the apparent turning on and off of deep water formation during and concluding the last glacial stage; a climatic switch may potentially account for El Niño/Southern Oscillation cycles. Although a step change in F is possible as a force behind century-scale atmospheric $\Delta^{14}C$ change, the recovery times for Maunder- and Spörer-type atmospheric ^{14}C events are too rapid to be explained by simple step changes in internal ocean mixing.

CHAPTER 4. SPECTRAL ANALYSIS AND INTERPRETATION OF MODEL-DERIVED ^{14}C PRODUCTION RATES

The modeling analysis presented in chapters 2 and 3 has indicated that millennium- and century-scale atmospheric $\Delta^{14}C$ variations during the Holocene originate primarily from fluctuations in ^{14}C production rates rather than climatic changes. The periodic nature of these fluctuations in ^{14}C production rate is subsequently investigated through several spectral techniques and the findings are discussed in terms of solar dynamics. In addition, a visual inspection of the detrended Q(^{14}C) history reveals a repetitive pattern in ca. 30% of this Holocene record. This information and the spectral analysis are utilized to tentatively extend the history of solar activity into the past and future.

4.1 Description of spectral techniques

In this section, I will briefly address the strengths and weaknesses of the several spectral techniques used here to assess the cyclic nature of the ^{14}C production rate variations. Spectral methods consist of two classical approaches, the direct Fourier analysis/periodogram method and the indirect Blackman/Tukey power spectrum analysis, as well as two filtering approaches, the autoregressive Maximum Entropy Method (MEM) using either the Burg or FABNE algorithm.

Four complementary methods

Classical Fourier analysis projects a time series onto orthogonal (i.e. uncorrelated)

axes consisting of sine waves that are harmonics of a fundamental period equal to the total length (duration), T, of the data series. Least-squares estimates of the amplitude and phase associated with each harmonic frequency can be calculated from these projections (transforms). The periodogram constitutes the total energy of the time series at each harmonic frequency. This energy is proportional to the square of the estimated amplitude of the forcing signal at that frequency. The corresponding power spectral density (PSD) at each frequency is the energy divided by the total number of observations, N. Spectral results are usually presented graphically as plots of PSD versus frequency. The fast Fourier transform (FFT) is a computationally efficient algorithm that derives the periodogram by adjusting (padding) N to be highly composite (eg. to be a power of 2). Our FFT program is based on the algorithm in Singleton (1969).

The periodogram is unstable without some tapering (windowing). A spectral window can be applied to the Fourier transforms or, equivalently, a data window can be applied to the original time series. Various windows have been proposed to reduce sidelobe distortion, i.e. the presence of spurious PSD peaks by leakage of the power from strong harmonic and nonharmonic frequencies into other neighboring frequencies. We use a split cosine bell window to taper 20% of the data (10% on each end), a percentage generally recommended (Bloomfield 1976).

The average resolution in the cycles determined by Fourier analysis are usually estimated as 1/T (e.g. Kay and Marple 1981). Resolution as great as 1/(4T) using FFT has also been claimed (e.g. Wolff 1976) whereas others have argued that resolution may be much less in practice (e.g. Marple 1987, Sonett and Suess 1984). Windows reduce sidelobes but may coarsen resolution (e.g. Marple 1987). An additional caution is that the above resolution is an *average* of a range of potential resolutions dependent on the relative phases of the frequencies of the input signals. For example, by varying relative phases,

Marple (1977) found a 10-fold range in resolution for an artificial data set consisting of two sinusoids without noise. I have here adopted the 1/T rule-of-thumb for the average resolution in the periodogram spectral results.

As suggested by the 1/T maxim, a limitation of the periodogram approach is the poor spectral resolution (broad peaks) for relatively short data sets. Another limitation in this spectral technique is the assumption that the data set can be fully represented by a fundamental sinusoidal cycle equal to the data length and by its higher harmonics. In effect, the periodogram is a least squares fit of an overtone series to the data set (Kay and Marple 1981). Stochastic noise is not considered.

The periodogram can be calculated indirectly from the autocovariance function of the time series for *all* lags j up to N-1. The second spectral technique, the Blackman/Tukey approach (known also as power spectrum analysis, generalized harmonic analysis, or the correlogram method), estimates power spectral density by selecting a maximum lag, J, *less than* N-1. This "lag windowing" serves to smooth the periodogram and emphasize the persistent features. To reduce sidelobes, the lags in the autocovariance function or, equivalently, the original data values are weighted. Our power spectrum approach follows the procedure outlined in Mitchell et al. (1966) in which the data are initially smoothed with a 3-point weighted moving average (Hamming window).

The various windows in both Fourier techniques are subjective choices. A "lag window" of 10-30% of the total data length is often recommended (e.g. Mitchell et al. 1966, Kane 1977, Marple 1987) although successful results on artificial data have been shown for J up to 80% of N as well (Kane 1977). Rather than limiting the choice of J to one fixed proportion, we used a range of maximum lags (10-50% of N) to assess the spectral characteristics of the $Q(^{14}C)$ record. The periodogram can be considered a special case of Blackman/Tukey power spectrum analysis with the lag window set at 100% of the

data length.

A horizontal PSD spectrum (all spectral estimates equal) indicates purely random variation or "white noise". A PSD spectrum that decays exponentially from low to high frequencies indicates persistence, or "Markov red noise", in the time series (Mitchell et al. 1966). Our power spectrum program calculates this red noise spectrum and determines the relative significance of any periodicities (PSD peaks) with respect to it. The 95% confidence level above the red noise spectrum is incorporated into our power spectrum plots as an upper limit against which to compare the significance of PSD peaks. As discussed in Mitchell et al. (1966), a more stringent level of confidence (up to 99%) is actually required to consider cycles significant if they are not expected from theory or not present in other data series.

The average resolution of the power spectrum approach is comparable to the periodogram approach at ca. 1/T, although data windowing can affect resolution by as much as 20% (Marple 1982, fig. 2). The resolution increases with increases in maximum lag but the statistical stability decreases (Mitchell et al. 1966). In this way, lag windowing is a compromise: as J increases, resolution becomes finer (i.e. the spectrum is peakier) but the statistical significance of the spectral peaks may drop with respect to the red noise spectrum. The resolution is roughly proportional to maximum lag at least above 20% of the data length (Marple 1982, fig. 2) so that a range in maximum lags of 10-50% generally corresponds to a fining in resolution by a factor of 5.

In addition to the subjectivity involved in window selection, the power spectrum approach has other limitations that require its cautious interpretation. Spurious PSD peaks may result from leakage through window sidelobes if the true power is associated with a non-sinusoidal cycle such as a pulse. A square-wave cycle can result in spurious PSD peaks at harmonics of the actual period. A broad PSD peak may indicate a cycle with an

irregular periodicity. Information on relative phases is unavailable with this technique.

The third spectral technique, the maximum entropy method (MEM), is not restricted to harmonics of the data length and, as importantly, considers the stochastic element of time series. Because of MEM's treatment of the time series outside the window, this method has greater frequency resolution than the Fourier techniques and no sidelobe leakage. While the Fourier analyses assume data values equal to zero beyond the specified taper interval, MEM assumes the greatest randomness, or maximum entropy, for the extrapolated time series. In this way, the PSD spectrum for MEM is not smoothed and resolution is generally sharp enough to separate spectral peaks that would coalesce into a broad peak in Fourier analysis.

As Skilling (1984) elegantly and concisely summarizes: "Maximum entropy always selects the simplest possible result, containing the bare minimum of structure needed to fit the data". And, as Olapido (1988) explains, by choosing the most unpredictable time series consistent with the known data record, MEM "sets out to express our ignorance of the power spectral density of the underlying stochastic process".

The model equation for this approach is:

$$x_t = \sum a_m x_{t-m} + e \qquad (4.1)$$

where x is a residual data value (by deducting the mean of the time series) at some time t as denoted by its subscript; $\sum$ is a summation from m = 1 to m = M, the model's autoregressive (AR) order; the a_m's represent the autoregressive coefficients or weights; and e is a stochastic noise term with zero mean. In short, the time series model is a linear autoregression in which each datum x_t is a weighted sum of M past data points mixed with random noise.

Two algorithms for efficiently implementing MEM are designated as Burg (named after its originator) and FABNE (i.e.,"forward and/or backward normal equations"). For a specified model AR order, the algorithms select the autoregressive coefficients that produce the best least-squares fit between model prediction and data, that is "minimize the prediction error power". The Burg algorithm (e.g. Ulrych and Bishop 1975) constrains the chosen AR coefficients for model order M to satisfy the Levinson recursion, an autocorrelative relationship to the calculated coefficients for the model order M-1. The FABNE algorithm (e.g. Barrodale and Erickson 1980 a,b) recalculates the AR coefficients for each chosen model order without imposing a recursive constraint. The PSD values are then calculated from the autoregressive coefficients and the variance of the noise. Details on all these procedures are provided in Kay and Marple (1981).

Despite the superiority of some MEM features over Fourier techniques, MEM has its own deficiencies. One severe handicap is that, in contrast to the Fourier methods discussed above, MEM PSD peak heights have no relation to true amplitudes of the cycles. Using an artificial data set with equal-amplitude input signals, Kane and Trivedi (1985) found that MEM PSD peaks accurately located the signal periods but peak heights varied by an order of magnitude. Another MEM imperfection, as discussed below, is the subjectivity required in selecting the optimum model AR order (also called the LPEF, Length of the Prediction Error Filter), a choice to which the PSD spectra is sensitive.

For signal periods longer than 20% of the data length, the Burg algorithm can result in inaccurate frequency estimates (shifts up to ca. 25%) and peak-splitting (Kane and Trivedi 1982). The FABNE algorithm requires more computation time than the Burg algorithm but, as supported by tests with artificial data sets, FABNE is more accurate with less peak-splitting (Kane and Trivedi 1985, Kay and Marple 1981). This difference in behavior is especially critical for data series which are short in comparison to the

frequencies of interest. However, in resolving century-scale cycles for the 9600-yr Q(^{14}C) record, we expect a general consensus between algorithms. For example, Barrodale and Erickson (1980a) find that Burg and FABNE will yield nearly identical spectral estimates for sinusoids with 15 or more cycles contained in the data length (equivalent to periods under 640 yrs in the Q record). In my own comparison described below, the Burg and FABNE algorithms demonstrate little difference in century-scale PSD peaks for a range of model AR choices from M = 20 to 100 (4% to 20% of the Q record).

The relative phasing of the input signals, the level of random noise, and the nature of the mechanism generating the time series also influence the veracity of the MEM spectral results. With respect to the first matter, although PSD peak accuracy can be sensitive to the relative phase of cycles, phasing is of much less importance for longer data sets such as the 9600-yr model Q record considered here (Kay and Marple 1981, Kane and Trivedi 1982).

Addressing the second influence, Chen and Stegen (1974) and Kane (1977) found that Burg PSD peaks retain good resolution with Gaussian white noise up to 30-40% of the signal but often lose resolution and accuracy at higher noise levels. In the latter case, a longer data set or increased model AR order can return the spectrum to an acceptable form. Since several dominant frequencies explain 50% of the variance in the Q(^{14}C) time series (see below) and the century-scale fluctuations are clearly evident within the noise, we estimate a signal-to-noise ratio (SNR) below 1.0 (ie. noise equivalent to or weaker than the signal in the time series). Again, the accuracies of longer MEM-derived periodicities are more influenced by a moderate noise level than the shorter century-scale PSD peaks of interest here. The validity of our conclusions are supported by my own experiments with FFT and MEM spectral analyses of artificial data sets at varying noise levels (see below).

Thirdly, the incompatibility of the autoregressive model with the mechanism

generating the data set may also undermine the validity of the MEM analysis (Treitel et al. 1977). Unfortunately, identification of the nature of the generating process is usually unachievable. This inadequacy is a major reason to compare different spectral approaches as done here.

Resolution of MEM Burg and FABNE spectral peaks is argued to be 1/(2T), or twice that of the classical Fourier analyses (Ulrych and Bishop 1975, Kane and Trivedi 1982), but MEM resolution has also been claimed to be much less in practice, ca. 3.5/T (Sonett and Suess 1984). In a series of publications, Marple (1977, 1982, 1987) calculates the resolution as 1/(xT) where x is an empirically determined equation which increases proportionately with model AR order (as a fraction of N) and with the cube-root of SNR:

$$x \approx (M/N)\,(\,SNR\,(M+1)\,)^{0.31} \qquad (4.2)$$

Thus MEM resolution is relatively insensitive to changes in SNR but linearly affected by the chosen model AR order. Using this equation with N = 480 (the number of bi-decades in a 9600 yr Q record) and an estimated SNR of 1.0, we calculate that our MEM spectral resolution is better than the FFT approach if AR is above 120 and worse than the FFT technique when the model AR order is below 120. At a model AR order of 20 (one of our choices below), the resolution is approximately 10/T. The resolutions of the various Fourier and MEM analyses are evident graphically by the relative smoothness of the PSD spectra (in other words, in the bandwidths of the PSD peaks).

The choice of autoregressive model order

Because of the sensitivity of MEM spectral results to model AR order, the choice of optimum LPEF is critical. Too low a model AR order causes too smooth a spectrum while

a high AR, although better able to resolve the relatively long periods, also often produces splitting and spurious PSD peaks at higher frequencies. Olapido (1988) lists 11 popular criteria in AR order selection. Various rules-of-thumb in choosing the LPEF fix the model AR order at anywhere from 20% to 100% of the total number of observations while other formulae select an optimum AR order contingent on how well each model order fits the data. Kay and Marple (1981) suggest a maximum model AR order of 50% because of the problem of spurious peaks, and they select 25% for their standard MEM examples. Kane (1979) proposes a dual approach in which shorter periods are resolved using model AR orders less than 50% of the total data set while longer periodicities are resolved at higher LPEF's. Presently, however, no consensus exists on the proper criteria to use in choosing the optimum model AR order and a subjective decision is required (e.g. Kay and Marple 1981, Press et al. 1986, Olapido 1988).

The least squares fit of model to data improves with increasing model AR order, that is the minimized "prediction error power" continues to decrease. However, the uncertainty in estimating AR coefficients increases with greater model AR order. The Akaike (1969) final prediction error (FPE) is the most popular of a number of criteria which attempt to quantify the compensation between the degree of model fit and the parameter uncertainty to select the optimum order for the autoregressive model. Akaike's criterion is defined as:

$$FPE_M = ((N+M+1)/(N-M-1)) R_M \qquad (4.3)$$

where M is the model autoregressive order, N is the total number of observations, and R_M is the mean square of the residuals of the least squares fit of the model to the data. When M is too low for a good model fit to the data, R_M will be relatively large; if the AR

order is unnecessarily large, the term in parentheses (representing the parameter inaccuracy) will increase faster than R_M decreases. The optimum M corresponds to the absolute minimum FPE.

Kane and Trivedi (1982) investigated the reliability of the FPE criterion. In a test study with an artificial data set of 101 single-yr values and high SNR, they found that the FPE choice of optimum model AR order (M/N = 18% in this case) allowed both Burg and FABNE to accurately identify periodicities of 5, 10, and 20 yrs. These cycles are 5%, 10%, and 20% of the data length. The equivalent periods in a 101-item bi-decadal data set are 100 (= 20 x 5), 200, and 400 yrs, respectively. If these results are pertinent for an analogous 480-item bi-decadal record, being the total number of observations in the Holocene Q(^{14}C) record, cycles below 1920 yrs (20% x 9600) should be accurately identified using the FPE criterion.

In other studies with real geophysical time series, the FPE criterion has been criticized as yielding too low a model order (e.g. Sonett 1984). A smoothed spectrum may result which masks important spectral details. This objection applies especially when the process being modeled is not purely autoregressive (e.g. Kay and Marple 1981). The FPE criterion may underestimate the proper model AR order for a time series controlled by harmonic processes with a high SNR (references in Kay and Marple 1981). Noise appears to play a devious role because Kane (1979) showed that, when 30% noise was introduced into an artificial sinusoidal data set, the Burg algorithm was accurate at a lower model AR order.

Several test studies demonstrate that relatively low model AR orders can yield true spectra. Barrodale and Erickson (1980a) and Akaike (1969) show that FABNE can be accurate at M < 4% of N. Kane and Trivedi (1985) also demonstrate with artificial data that MEM provides reliable spectral results at model AR orders of 8%, and that the

FABNE algorithm is more accurate with less splitting than the Burg. A model AR order must be high enough that the MEM analysis of the residual record (i.e. data minus model time series) displays a white noise spectrum (e.g. Sonett 1984). Akaike (1969), in introducing the FPE criterion, found that the FPE-selected model AR orders, at ca. 3% of N for several time series, resulted in the required white noise residual spectra. In analyzing an 8400-yr decadal atmospheric ^{14}C time series, Sonett (1984) determined that model AR orders as low as 6% (M = 50) produced residual white noise spectra.

Other studies are less encouraging. Kane and Trivedi (1985), although supporting the use of the FPE criterion in theory, were not pleased with the simple MEM spectrum generated at the FPE-selected model AR order in their FABNE analysis of the sunspot record. The analysis identified only a single PSD peak at an 11-yr periodicity. They instead favored the more detailed spectra produced with a model AR order of 30% to 50% of the data length primarily because it showed more peaks in common with other spectral studies. In another test case, Kane and Trivedi (1982) endorsed selection of a model AR order of 30% because, only at that AR order, did MEM properly produce PSD peaks having equal amplitudes for an artificial data set of equal-strength input signals.

For the 9600-yr Q(^{14}C) record specifically, the FPE criterion yields a low optimum model AR order of 20 (equivalent to 4% of the total number of observations). An MEM model AR order of 4% falls far below the other popular rules-of-thumb favoring use of 30-50% of the data length. In view of the general lack of consensus on the proper model AR order, the MEM results for this range of model orders are considered here as well.

Therefore, the <u>complete</u> MEM analytical routine, resembling Olapido's (1988) approach, consists of choosing the Akaike Final Prediction Error (FPE) criterion to designate a suitable model AR order for spectral analysis but then utilizing the results of a range (4%-50%) of model AR orders to put in context the initial PSD findings. Spectral

peaks maintaining their integrity without shifting or splitting over a range of model AR orders are considered reliable. The results are plotted in "split plots" (expression by M. Stuiver) showing the significant PSD periods identified at specific model AR orders.

4.2 The periodic nature of Holocene Q(^{14}C) variations

To assess the periodic nature of the model-derived ^{14}C production history, all four spectral approaches discussed above were compared. Classical Fourier analysis is performed with the FFT program, the Blackman/Tukey power spectrum approach is executed at lags of 10-50% of the total number of bi-decadal observations, and the MEM Burg and FABNE analyses are carried out systematically with AR model orders up to 50% and 20% of the total number of observations, respectively. Special consideration is assigned to the optimum AR model order defined by the FPE criterion. Olapido (1988) successfully employs a similar full analytical approach on climate data.

The MEM FABNE algorithm generally has superior accuracy and resolving power for data records that are relatively short with respect to the frequencies of interest, but, for the century-scale periodicities considered below, a concurrence of all spectral approaches is expected when analyzing the long 9600-yr Q(^{14}C) record. Agreement among these 4 methods will corroborate the spectral results. The tenacity of identified cycles is tested through comparison of spectral results from a wide range of lags in the power spectrum approach and from a wide range of model AR orders in the MEM analyses. Differences among methods will help to define the true uncertainties in the spectral results; these differences also provide some insights into the limitations of specific spectral techniques.

After the application of the four spectral techniques to determine the dominant cycles

in the Q(^{14}C) record with and without its long-term trend (ie. the "400-yr" spline in figure 2.1), the principal frequencies are adjusted and assigned amplitudes and relative phases by least-squares fit of the detrended Q(^{14}C) history to a set of sinuosoidal variations. In addition, a recurrent 680-yr pattern (a characteristic triple fluctuation or "triplet") appears at irregular intervals in 30% of the detrended Q(^{14}C) record as identified by visual inspection of this record on an expanded timescale (Stuiver and Braziunas 1988, 1989). Least-squares sinusoidal fits to the "triplet" and "intertriplet" intervals in the detrended Q(^{14}C) variations are determined as well.

Spectral analysis of the Q(^{14}C) record

At the FPE_M-selected model AR order 20, the MEM FABNE analysis of the Q(^{14}C) record (without removal of the long-term trend) produces a PSD spectrum with peaks at 420, 218, 143, and 85 yrs, corresponding to 4 of the first 5 harmonics of a fundamental period of 420 yrs (figure 4.1). A minor feature in the spectrum is apparent at the fifth harmonic (106 yrs) as well. This spectrum corresponds to a relatively low model AR order (equivalent to 4% of the total number of observations) and thus smooths over the finer scale "peakiness" characterizing PSD spectra for higher model AR orders (see below). The MEM Burg analysis produces a PSD spectrum with identical peak periodicities at a model AR order of 20.

The resolution of the identified frequencies may be estimated conservatively as ca. ± 3.5/T where T is the duration of the data set (Sonett and Suess 1984). Using this criterion, the four principal periods identified by MEM FABNE on the 9600-yr Q(^{14}C) record correspond to ranges of 364-499, 202-237, 136-151, and 82-88 yrs. Even more expansive are the ranges that correspond to the resolution estimate of ± 10/T based on

Figure 4.1: PSD results for the Maximum Entropy Method (MEM) analysis (using the FABNE algorithm) of the 9600-yr bi-decadal ^{14}C production rate record without trend removal. Spectral power is normalized to equal 1.0 for the highest spectral feature of the total spectrum. The MEM analysis is based on a model AR order of 20 corresponding to the Akaike (1969) absolute minimum FPE_M criterion.

(inset) Comparison of observed peak periodicities in the $Q(^{14}C)$ record and the harmonics of a 420-yr cycle (depicted by the hyperbolic line). The vertical lines represent the $\pm 3.5/T$ resolution limits of the observed periodicities (circles) as discussed in the text; no vertical lines are shown when the calculated range is less than the size of the symbol.

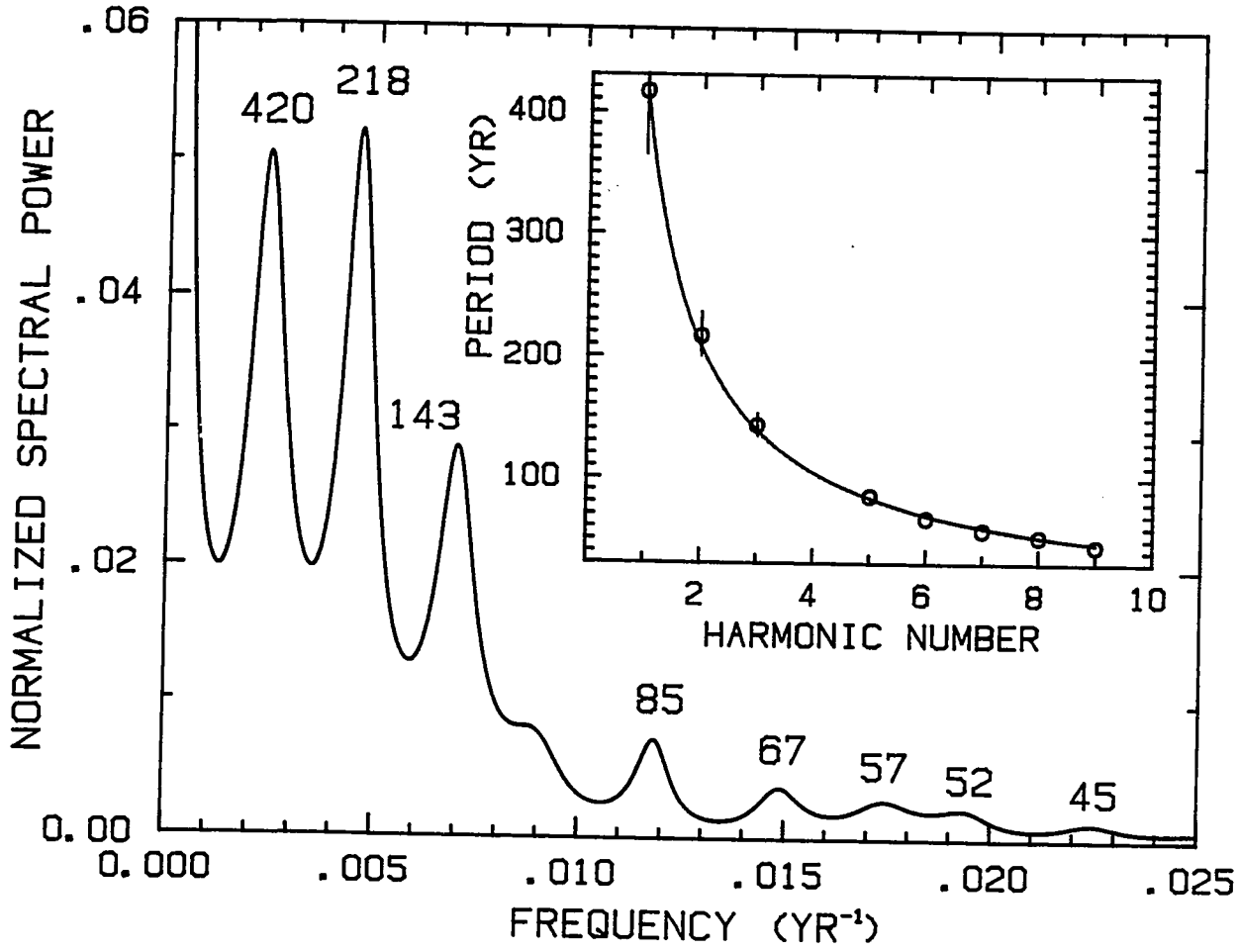
.06
.04
.02
0.00
NORMALIZED SPECTRAL POWER
420
218
143
85
67
57
52
45
0.000
.005
.010
.015
.020
.025
FREQUENCY (YR⁻¹)
PERIOD (YR)
400
300
200
100
2
4
6
8
10
HARMONIC NUMBER

equation (4.2): 292-747, 178-282, 124-168, and 78-93 yrs. The application of equation (4.2), however, requires several assumptions on signal and noise characteristics (Marple 1977, 1982, 1987) which are difficult to certify. With any criteria, the three shorter periodicities are better defined and, as the total number of ^{14}C observations increases, all spectral peaks become better resolved. As discussed above, however, the relative *amplitudes* of these periodicities cannot be ascertained from the MEM approach.

At the recommended maximum lag of 20% (see section 4.1), the power spectrum analysis of $Q(^{14}C)$ identifies virtually the same four periodicities as the MEM spectrum (figure 4.2, lower panel). However, only the 213-yr and 148-yr PSD peaks are statistically significant at the 95% confidence level above the red noise spectrum whereas the PSD peak with the 405-yr periodicity is much less important. The power spectrum also displays a significant PSD peak at 124 yrs which does not conform to a simple harmonic interpretation.

A greater number of PSD peaks appear at higher model AR orders in the MEM analyses and at higher maximum lags in the power spectrum. At a maximum lag of 50%, the power spectrum exhibits the same PSD pattern but some of the principal peaks have become split (figure 4.2, upper panel). For example, the 213-yr periodicity is now identified as two significant PSD peaks at 229 and 204 yrs and the 405-yr periodicity is replaced by three peaks at 505, 457, and 355 yrs. Millennium-scale cycles are represented in this analysis by PSD peaks that are very low relative to the red noise spectrum. Since the periodigram can be considered a special case of power spectrum analysis with the lag window set at 100% (see section 4.1), the FFT method produces a highly spiky spectrum although many of the PSD peaks are again clustered near the same major periods identified in the smoother power spectra and MEM analyses (see below).

The MEM Burg analysis at the higher model AR order of 120 (equivalent to 25% of

Figure 4.2: Power spectrum analysis of the 9600-yr bi-decadal ^{14}C production rate record without trend removal. The lower panel displays the PSD spectrum determined with a maximum lag (or "lag window") of 96, ie. 20% of the total number of bi-decadal observations (see text), whereas the upper panel displays the PSD spectrum corresponding to a maximum lag of 240 or 50% of the total number of bi-decadal observations. The upper and lower dashed lines indicate the 95% and 5% confidence limits relative to the calculated red noise spectrum (solid smooth curve).

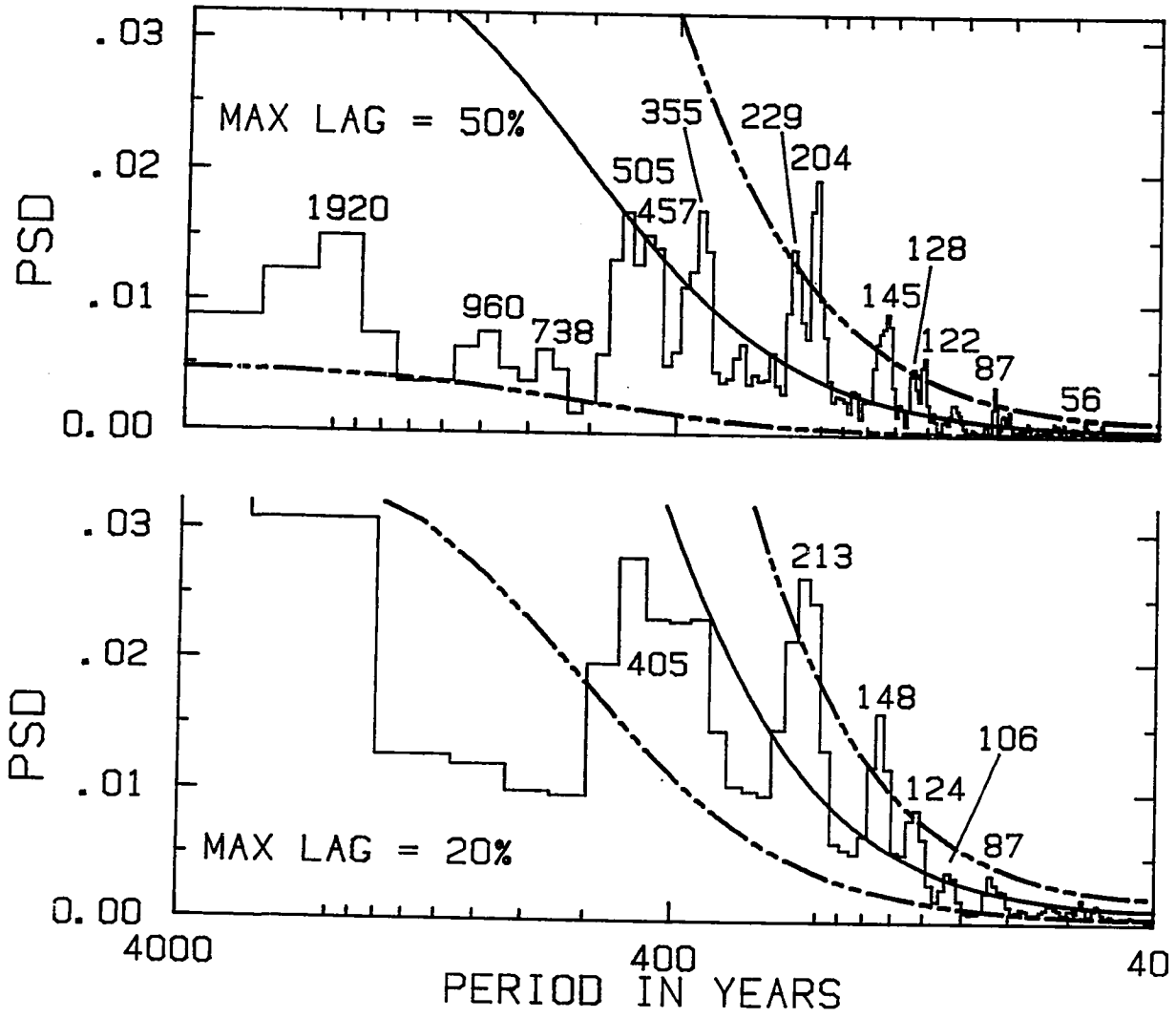
.03
.02
.01
0.00
PSD
MAX LAG = 50%
1920
960
738
505
457
355
229
204
128
145
122
87
56
.03
.02
.01
0.00
PSD
MAX LAG = 20%
405
213
148
106
124
87
4000
400
40
PERIOD IN YEARS

N) exhibits clusters of PSD peaks around the four periodicities (414, 216, 142, and 85 yrs) identified at the model AR order of 20 (figure 4.3). The former model AR order corresponds to the informal N/4 criterion of Kay and Marple (1981) while the latter is associated with the absolute minimum FPE_M value. The Burg analysis presented here was performed on the model-derived $Q(^{14}C)$ history based on the revised tree-ring (atmospheric) $\Delta^{14}C$ record which incorporates the 74-yr shift in the "Heidelberg Main 9" tree (see sections 1.2 and 2.1 and figure 2.6). Thus this minor adjustment to the early portion of the Holocene $\Delta^{14}C$ record insignificantly influences the PSD spectrum (cf. figure 4.1).

The spectral transition from the harmonic PSD periodicities to the PSD peak clusters in the $Q(^{14}C)$ record is presented graphically in figure 4.4 for the 1000- to 77-yr portion of the Burg PSD spectrum. Model AR orders advance in steps of 5 following the PSD spectrum in the foreground comprising the four distinct harmonic periodicities at the model AR order of 20. Figure 4.5 identifies, at model AR orders up to 240 (ie. 50% of the total observations), those peak periodicities (between 60 and 550 yrs) with a relative power spectral density exceeding .007. This "cut-off" PSD level was subjectively selected because it most clearly distinguishes the prominent PSD peaks in figure 4.4 from the "background" spectrum. Table 4.1 tabulates the PSD periodicities (significant at PSD > 0.007) for selected model AR orders.

The splitting of PSD peaks with increasing model AR order complicates the simple harmonic interpretation of $Q(^{14}C)$ periodicities. Importantly, the systematic presentation of spectra over a range of model AR orders delineates those periodicities most robust to model AR assumptions. Both the 216-yr and 143-yr harmonic are apparent throughout the entire AR range of Burg spectral curves (figures 4.4 and 4.5 and Table 4.1). Although the peak cluster associated with the 88-yr periodicity loses spectral power after model AR

Figure 4.3: PSD results for the Maximum Entropy Method (MEM) analysis (using the Burg algorithm) of the (revised) 9600-yr bi-decadal ^{14}C production rate record without trend removal. One PSD spectrum (heavy line and numbers) is derived for a model AR order of 20 corresponding to the Akaike (1969) absolute minimum FPE_M criterion; the other PSD spectrum (light line and numbers) is derived for a model AR order of 120 based on the informal N/4 criterion of Kay and Marple (1981). In both cases, power spectral density is normalized to equal 1.0 for the highest spectral feature of the total spectrum.

(inset) Calculated Final Prediction Error (FPE_M) of equation (4.3) for model AR orders (M) up to 50% of the total observations. Troughs in the relative FPE_M pattern indicate the preferred model AR orders. The FPE_M units relate to the mean square of the residuals of a least squares fit of model and data; FPE_M can be made unitless by division of FPE_0 (see Akaike 1969) but the relative FPE_M pattern remains unchanged.

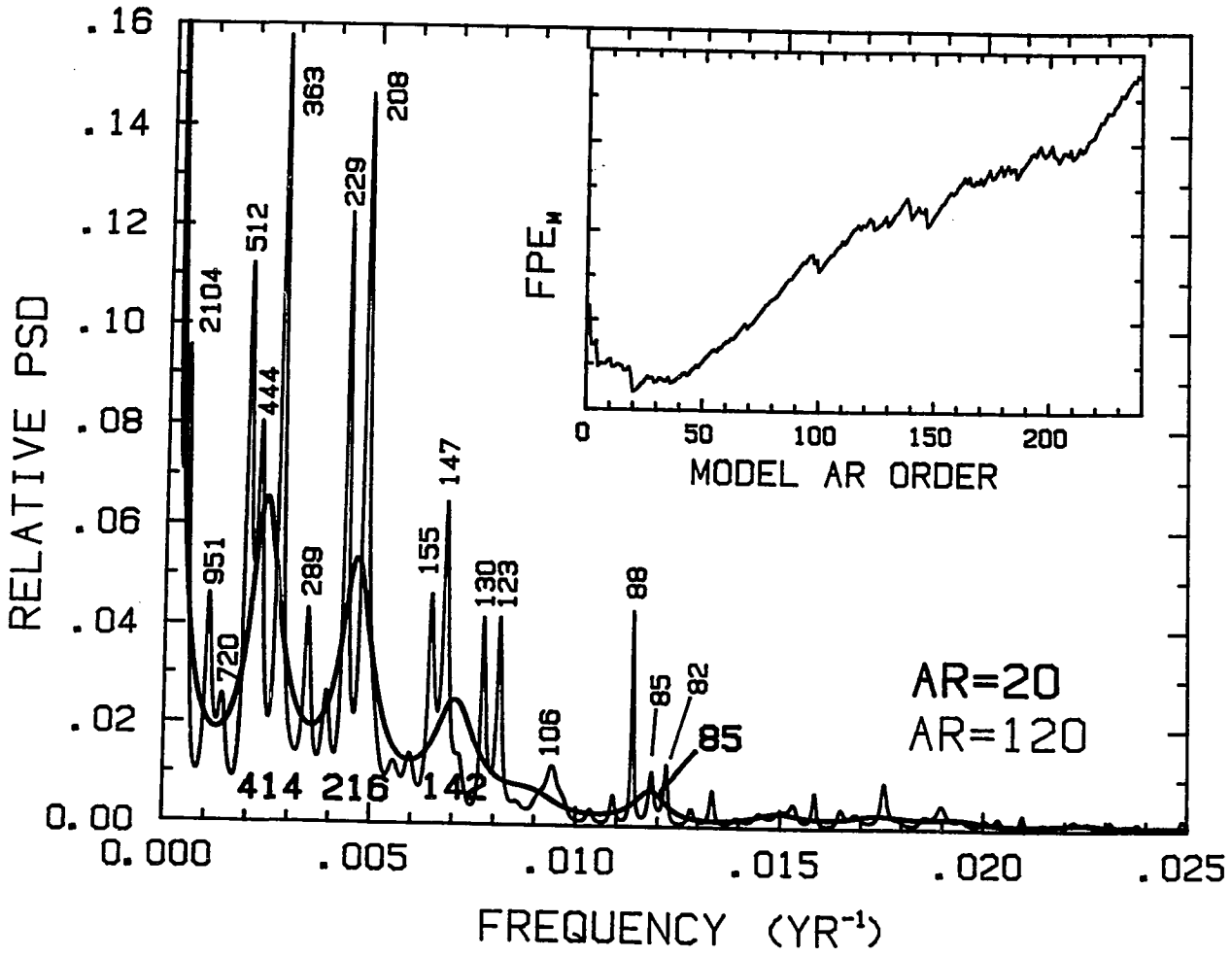
RELATIVE PSD
.16
.14
.12
.10
.08
.06
.04
.02
0.00
0.000
.005
.010
.015
.020
.025
FREQUENCY (YR⁻¹)
2104
512
363
229
208
444
951
720
289
155
147
130
123
106
88
85
82
85
414
216
142
AR=20
AR=120
FPE_M
0
50
100
150
200
MODEL AR ORDER

Figure 4.4: PSD results for selected model AR orders (every fifth order between 20 and 120) corresponding to the MEM (Burg) analysis of the (revised) 9600-yr bi-decadal ^{14}C production rate record without trend removal. Each relative PSD spectrum is normalized as in figure 4.3; most spectral features plot below 0.12 relative PSD units (vertical axis).

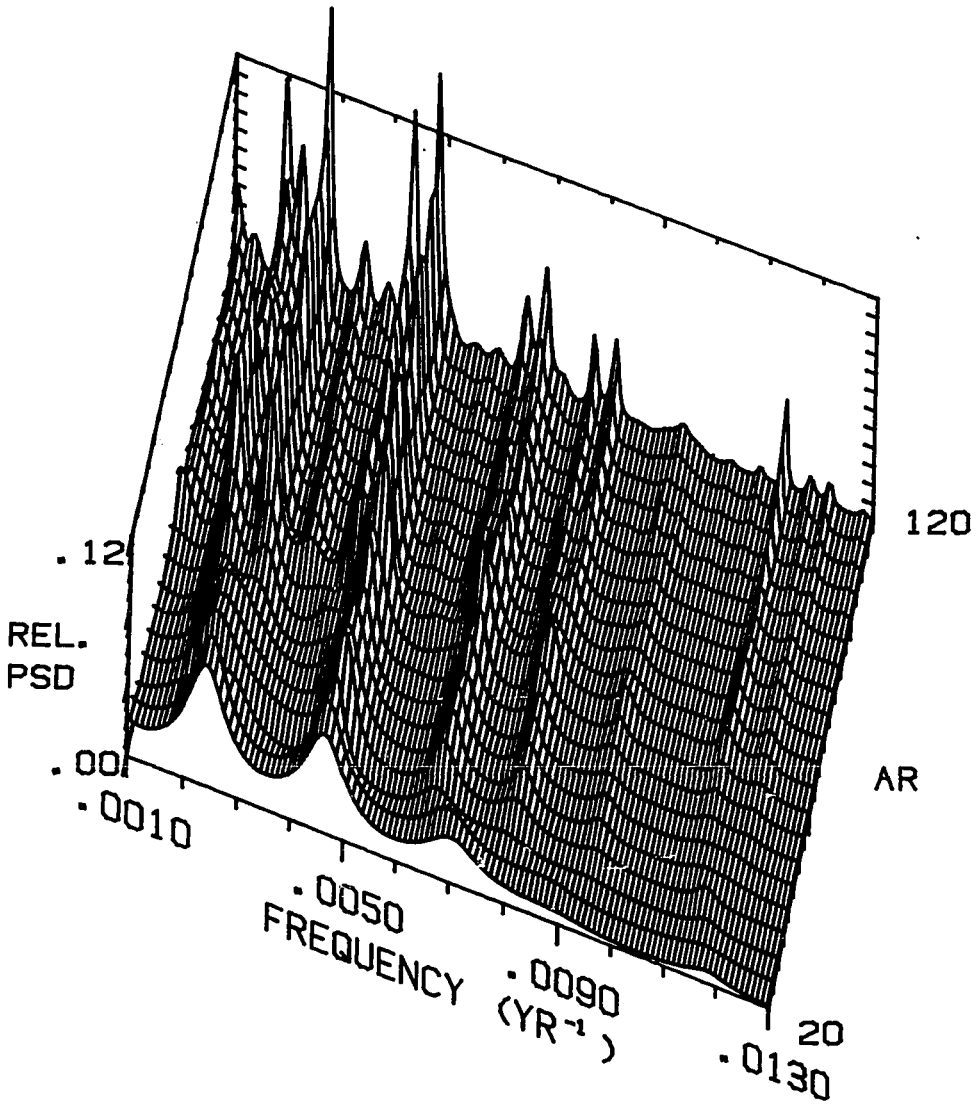
.12
REL.
PSD
.00
.0010
.0050
FREQUENCY
.0090
(YR-1)
.0130
120
AR
20

Figure 4.5: A "split plot" identifying the spectral peak features exceeding a relative PSD of .007 in the MEM (Burg) analyses of (revised) Q(^{14}C). Model AR orders are listed as absolute numbers and may be converted to percentages of total number of observations (N = 480) with multiplication by 100/480. The plot spans only the range of periodicities from 60 to 550 yrs.

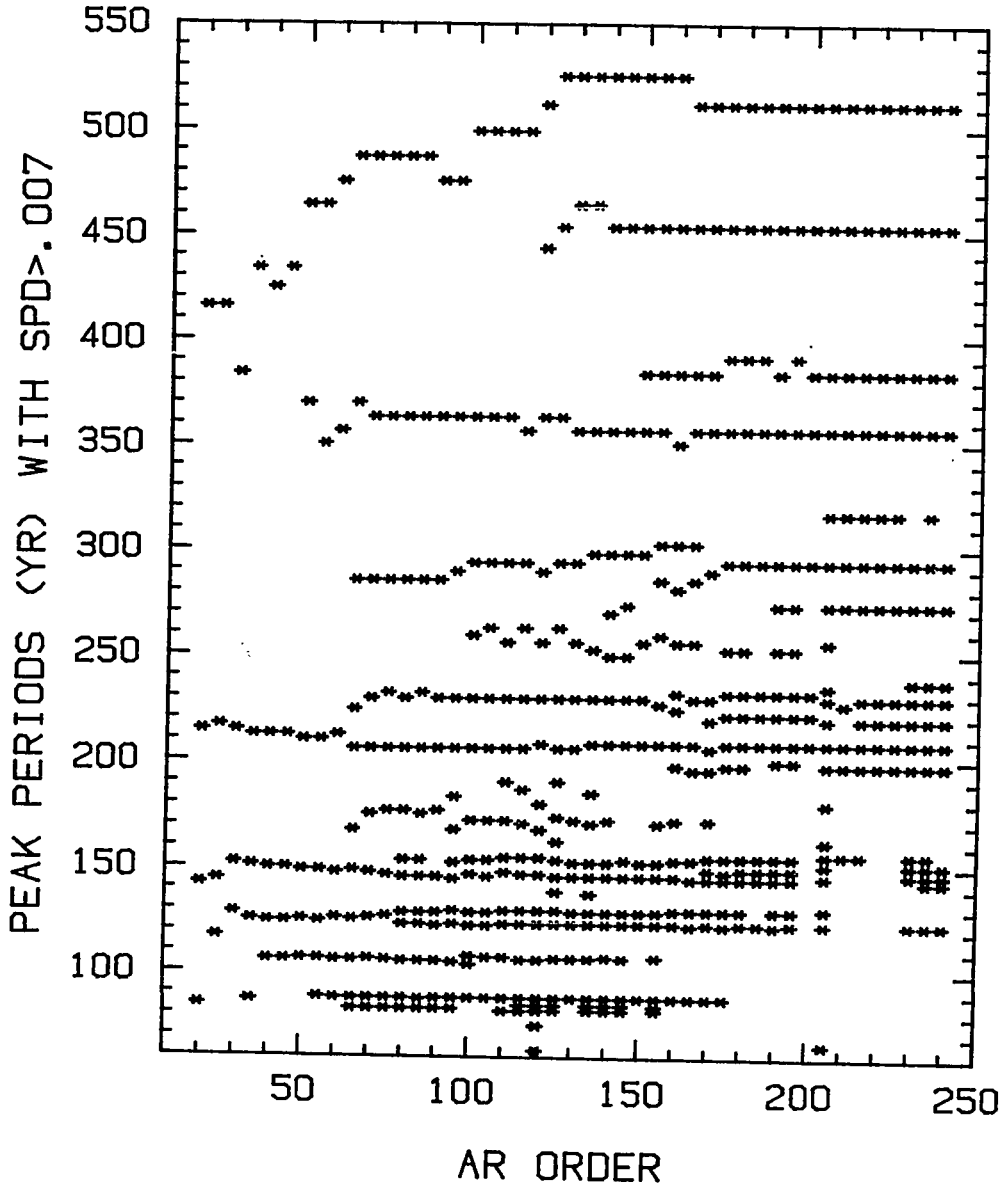
BURG: 9600-YR BIDEC Q
PEAK PERIODS (YR) WITH SPD>.007
550
500
450
400
350
300
250
200
150
100
50
100
150
200
250
AR ORDER

TABLE 4.1

PEAK PERIODICITIES WITH PSD > .007 AS IDENTIFIED BY MEM (BURG) ANALYSIS OF THE BI-DECADAL Q(^{14}C) RECORD

MODEL AR ORDERS:	PERIODICITIES:										
20							414				
60						475		356			
120	12395	2104	951	720	512	444		363	289	256	
180	9995	2221	975	740	512	454	391	356	294	253	232
240	9995	2161	975		512	454	384	356	294	273	238
20			216					142			
60			212				148		126		106
120	229		208		180	168	155	147		130	123 106
180		222	208	198			155	149	145	130	123
240	229	219	208	198			151	147	144		123
20		85									
60	88										
120	88	85	82	75	63	57					
180											
240											

order 120 (as do all spikes in the PSD spectrum), the cluster signal nevertheless is visible (below PSD of .007) through model AR order of 240 (N/2). The 414-yr cycle, however, splits at a relatively low AR order and is eventually replaced at model AR orders of 120 or greater by at least three PSD peaks with periodicities at ca. 510, 450, and 350 yrs.

The "split plot" of figure 4.5 not only identifies the PSD peaks that persist at a range of model AR orders in the spectral analyses but also represents a "spectral fingerprint" with which other spectral techniques and the spectral analyses of other time series can conveniently be compared. The "split plots" of the power spectrum method and MEM Burg analysis of $Q(^{14}C)$ have strong similarities when maximum lags are superposed on model AR orders that represent equivalent percentages of the total observations (Stuiver and Braziunas 1990). Also, "split plots" of PSD spectra for long high-resolution climate records allow spectral similarities between ^{14}C production rates and climate to be investigated (M. Stuiver, in progress). In this way, the spectral components of separate time series can be compared without the need to specify the "correct" interpretation of their periodic natures.

The MEM Burg analysis was repeated on the detrended ^{14}C production variations (ie. $\Delta Q/Q_t$) derived from both the revised and pre-revised $Q(^{14}C)$ records. The PSD results, displayed in figure 4.6 for the revised $\Delta Q/Q_t$ history, demonstrate that the removal of a spline approximating a 400-yr moving average has a nominal effect on the identity of the significant century-scale periodicities. At the same model AR orders, the PSD spectra for $Q(^{14}C)$ and $\Delta Q/Q_t$ show essentially the same structure (figure 4.3 vs. 4.6). However the PSD spectrum for the $\Delta Q/Q_t$ record lacks the low-frequency rise associated with the millennium-scale features of the original $Q(^{14}C)$ record; without the long-term trend, the normalized spectral power also enhances the PSD levels of the harmonic PSD peaks for model AR order 20 relative to the higher order spectrum. The secondary nature of these

Figure 4.6: PSD results for the Maximum Entropy Method (MEM) analysis (using the Burg algorithm) of the (revised) 9600-yr bi-decadal ^{14}C production rate record after trend removal. One PSD spectrum (heavy line and numbers) is derived for a model AR order of 20; the other PSD spectrum (light line and numbers) is derived for a model AR order of 120. In both cases, power spectral density is normalized to equal 1.0 for the highest spectral feature of the total spectrum.

(inset) Calculated Final Prediction Error (FPE_M) of equation (4.3) for model AR orders (M) up to 50% of the total number of observations. See figure 4.3 inset for additional comments.

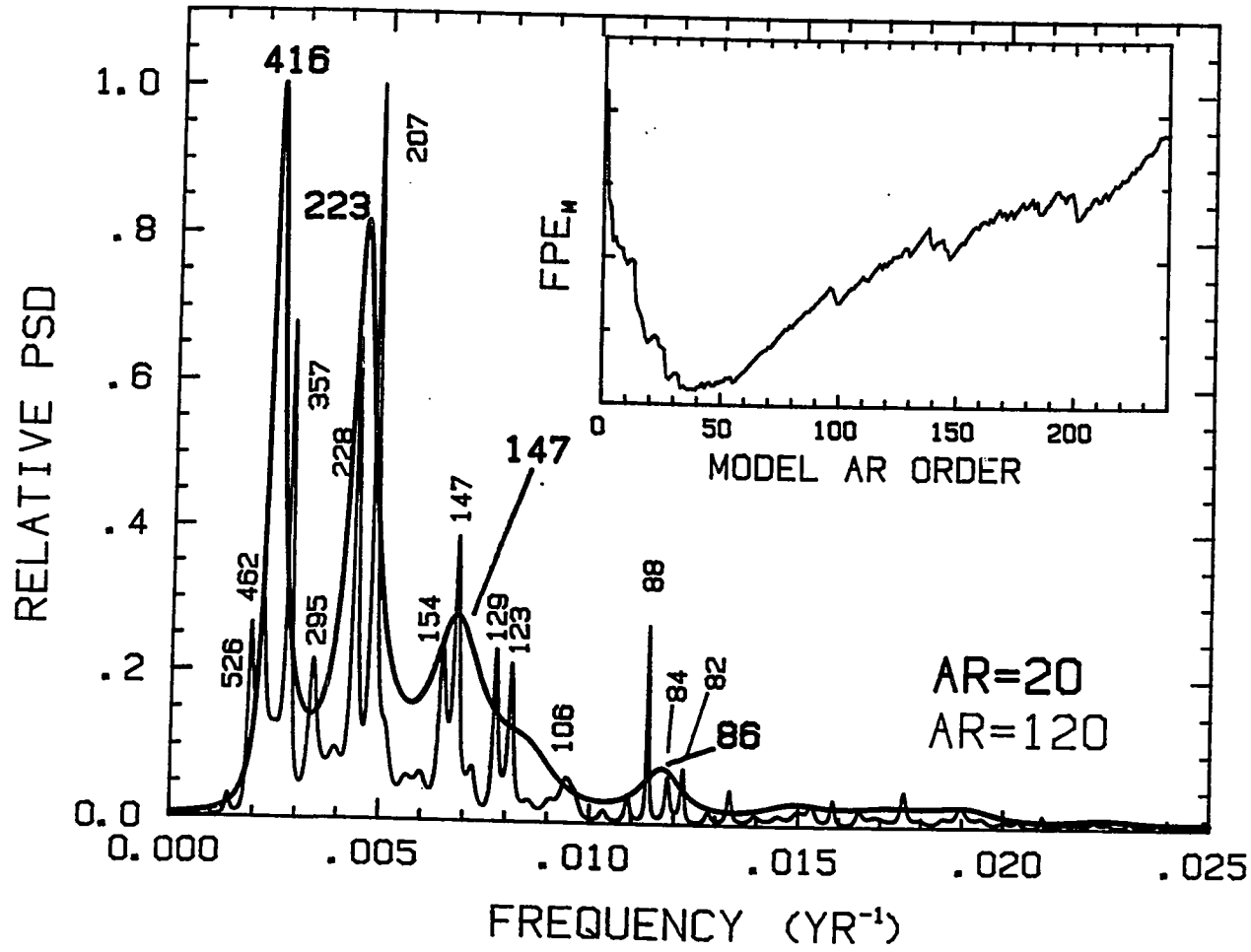
RELATIVE PSD
1.0
.8
.6
.4
.2
0.0
0.000
.005
.010
.015
.020
.025
FREQUENCY (YR⁻¹)
416
223
207
357
228
147
147
462
526
295
154
129
123
106
88
84
82
86
AR=20
AR=120
FPE_M
0
50
100
150
200
MODEL AR ORDER

distinctions concurs with the comprehensive study of Kane (1977) in which low pass and high pass filterings of artificial data sets were found to insignificantly affect the PSD results (except the amplitudes) associated with the Fourier, Blackman/Tukey, or MEM (Burg) spectral methods.

The removal of the spline from the $Q(^{14}C)$ record has, however, another consequence for the interpretation of the MEM Burg spectral results. The absolute minimum value for FPE_M shifts to a higher AR order of 39 in the MEM analysis of the $\Delta Q/Q_t$ record (figure 4.6 inset). The PSD spectrum associated with this higher order varies from its simpler harmonic structure displayed at model AR order of 20. A PSD spike with two peaks at 519 and 386 yrs replaces the 416-yr periodicity and the remaining PSD spectrum exhibits strong peaks at 213, 149, 125, 106, and 87 yrs. Thus an additional harmonic of the 416-yr period becomes identified (at 106 yrs) but the other new peaks compromise the harmonic interpretation. This PSD spectrum is not specifically shown but closely resembles the Burg-derived curve on the $Q(^{14}C)$ record displayed in figure 4.4 at model AR order of 40.

Different time intervals in the Holocene ^{14}C production history appear to be characterized by distinctive periodic behavior. The MEM FABNE analyses on four equal divisions of the $\Delta Q/Q_t$ record reveal that, whereas the PSD peaks around 200 and 150 yrs are defined throughout the Holocene, the 85-yr periodicity is primarily restricted to the 5360 to 2960 BC segment (figure 4.7). A PSD peak corresponding to a 400-yr cycle is not visible in any of these arbitrary subdivisions, contradicting the harmonic interpretation based on the MEM analysis for the entire time series. Each chosen model AR order corresponds to a local minimum in FPE_M that occurs near the informal AR selection criterion of N/4 (Kay and Marple 1981). In this way, the PSD spectrum of each time interval exhibits a similar degree of structure.

Figure 4.7: PSD results for the Maximum Entropy Method (MEM) analysis (using the FABNE algorithm) on four equal subsections of the 9600-yr bi-decadal ^{14}C production rate record after trend removal. Each spectral plot is labeled with the time interval spanned by the $\Delta Q/Q_t$ subsection and the selected model AR order (a local minimum in FPE_M near N/4). As in previous figures, spectral power is normalized to equal 1.0 for the highest spectral feature in each case.

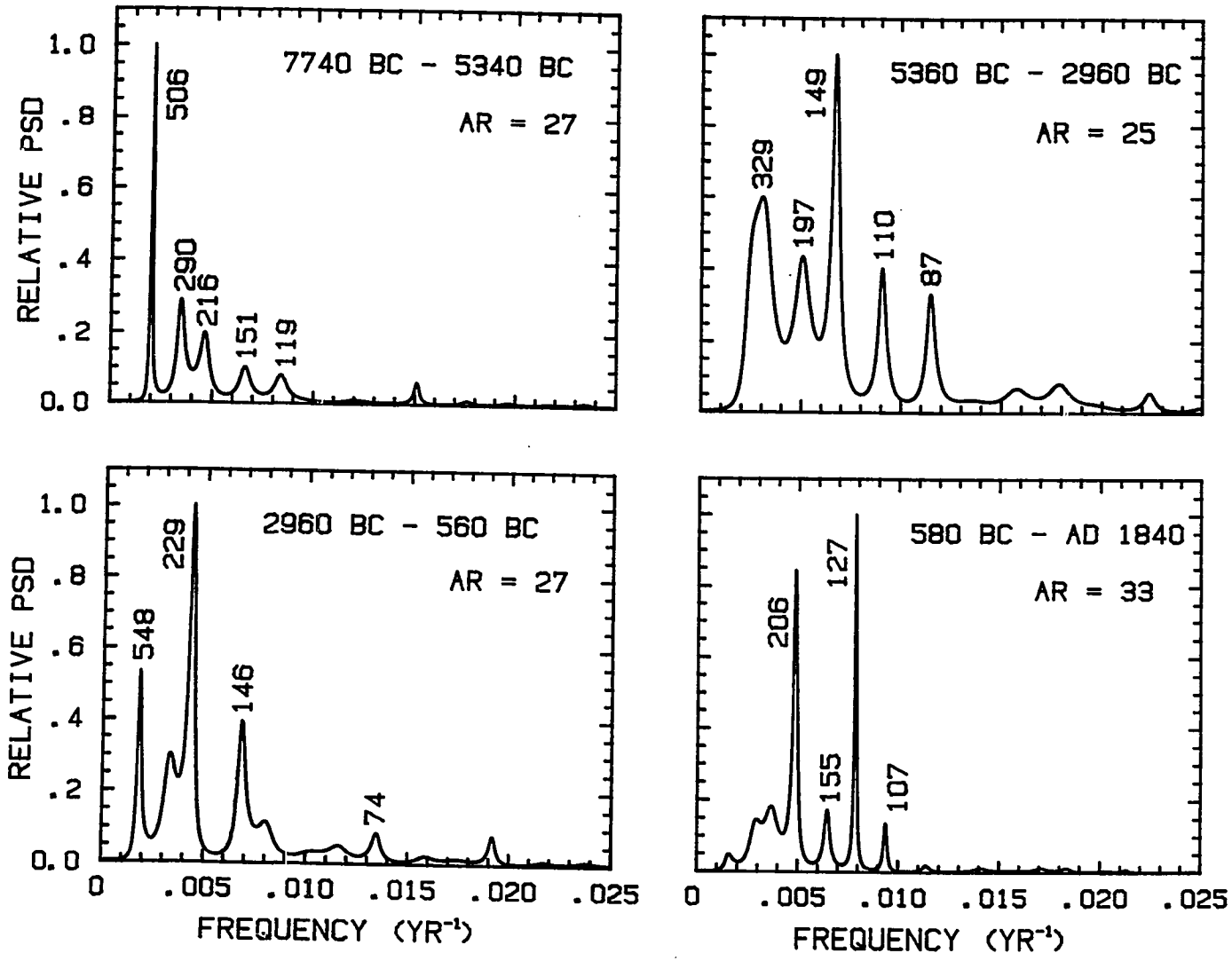
7740 BC - 5340 BC
AR = 27
506
290
216
151
119
5360 BC - 2960 BC
AR = 25
329
197
149
110
87
2960 BC - 560 BC
AR = 27
548
229
146
74
580 BC - AD 1840
AR = 33
206
155
127
107
RELATIVE PSD
1.0
.8
.6
.4
.2
0.0
0
.005
.010
.015
.020
.025
FREQUENCY (YR⁻¹)

A strong periodicity of 127 yrs in the most recent quarter of the $\Delta Q/Q_t$ record is consistent with the 130-yr oscillation identified in another solar activity index, the historical record of aurorae, between 1550 BC and AD 1700 (Attolini et al. 1988); however, the prominent 88-yr auroral cycle does not have a counterpart in the MEM FABNE analysis of the most recent time interval. The "missing fourth harmonic" at ca. 105 yrs also appears in half of the $\Delta Q/Q_t$ record when subdivided in this fashion.

These frequency differences in the MEM analyses of $\Delta Q/Q_t$ subsets can be evaluated in the context of other evidence of nonstationarity in ^{14}C time series. For example, Neftel et al. (1981) recognize amplitude variations and phase shifts in the 200-yr and 150-yr periodicities of the 8000-yr La Jolla tree-ring (atmospheric) $\Delta^{14}C$ record by means of a Fourier analysis on a 2000-yr "moving window" of the time series. Sonett (1984) re-examines the La Jolla $\Delta^{14}C$ record and finds spectral evidence for amplitude, frequency or phase modulation of the 200-yr cycle by a millennium-scale periodic component and for nonstationarity in the $\Delta^{14}C$ time series in general. The spectral inconstancies in ^{14}C history are not assessed in detail here but two distinct behavior patterns in $\Delta Q/Q_t$ have been visually identified (Stuiver and Braziunas 1989) and incorporated into the full analysis of patterns in the 9600-yr detrended ^{14}C production record (see below)

As discussed in section 2.1, atmospheric $\Delta^{14}C$ variations are attenuated and delayed with respect to the ^{14}C production rate signal. Thus spectral investigations of reservoir $\Delta^{14}C$ histories (eg. Neftel et al. 1981; Sonett 1984) are complicated by distortions of relative amplitudes and phases by the global ^{14}C system. The derivation of Q signal frequencies in the $\Delta^{14}C$ record may be confused as well by climate-induced variations in carbon reservoir sizes and exchanges (which, however, are also not taken into account in the Q-deconvolution process). The impact of attenuation and lag factors on PSD spectra was examined using an artificial time series (see next subsection).

Despite the effects of such complications, the calculated spectral properties of the atmospheric (tree-ring) $\Delta^{14}C$ record are fundamentally consistent with the PSD spectra derived above on the ^{14}C production histories. Figure 4.8 shows the FFT analysis of the 9600-yr atmospheric (tree-ring) $\Delta^{14}C$ time series. In this example, a spline approximating a 1000-yr moving average is subtracted from the original data as an alternative method of trend removal prior to spectral analysis. The structure of the FFT spectrum on residual atmospheric $\Delta^{14}C$ closely resembles the power spectrum results for $Q(^{14}C)$ at 50% maximum lag (figure 4.2, upper panel). PSD peaks with millennium-scale periodicities of 960 and 2400 yrs are also identified in the FFT spectrum; however, power spectrum analyses indicate that these longer-term features are not significant components of ^{14}C records.

Spectral tests on artificial ^{14}C time series

Several spectral tests were devised to permit a better assessment of the PSD results on the ^{14}C time series presented above. The four issues addressed are: (1) the relationship of relative PSD peak height to relative signal amplitude; (2) "beat" phenomena; (3) the expected differences between PSD spectra on time series of ^{14}C production, atmospheric $\Delta^{14}C$ and oceanic $\Delta^{14}C$; and (4) potential sources for spurious harmonics in PSD spectra. Some of these test analyses essentially repeat previous investigations but focus on the operation of the specific spectral programs applied here and the veracity of relatively low model AR orders.

Spectral analyses on artificial time series have often been observed to behave differently than analyses on actual geophysical data (eg. Kay and Marple 1981, p. 1395). Therefore, although the tests below clearly illustrate some of the weaknesses and strengths of the different spectral methods, the investigations are limited in scope and applicability

Figure 4.8: PSD results for fast Fourier transform (FFT) analysis of the 9600-yr atmospheric $\Delta^{14}C$ record after trend removal. The detrending of this ^{14}C time series prior to spectral analysis differs from all previous examples in that the long-term trend is represented by a spline approximating a 1000-yr moving average. Spectral power is normalized to equal 1.0 for the highest spectral feature in the spectrum (505-yr peak).

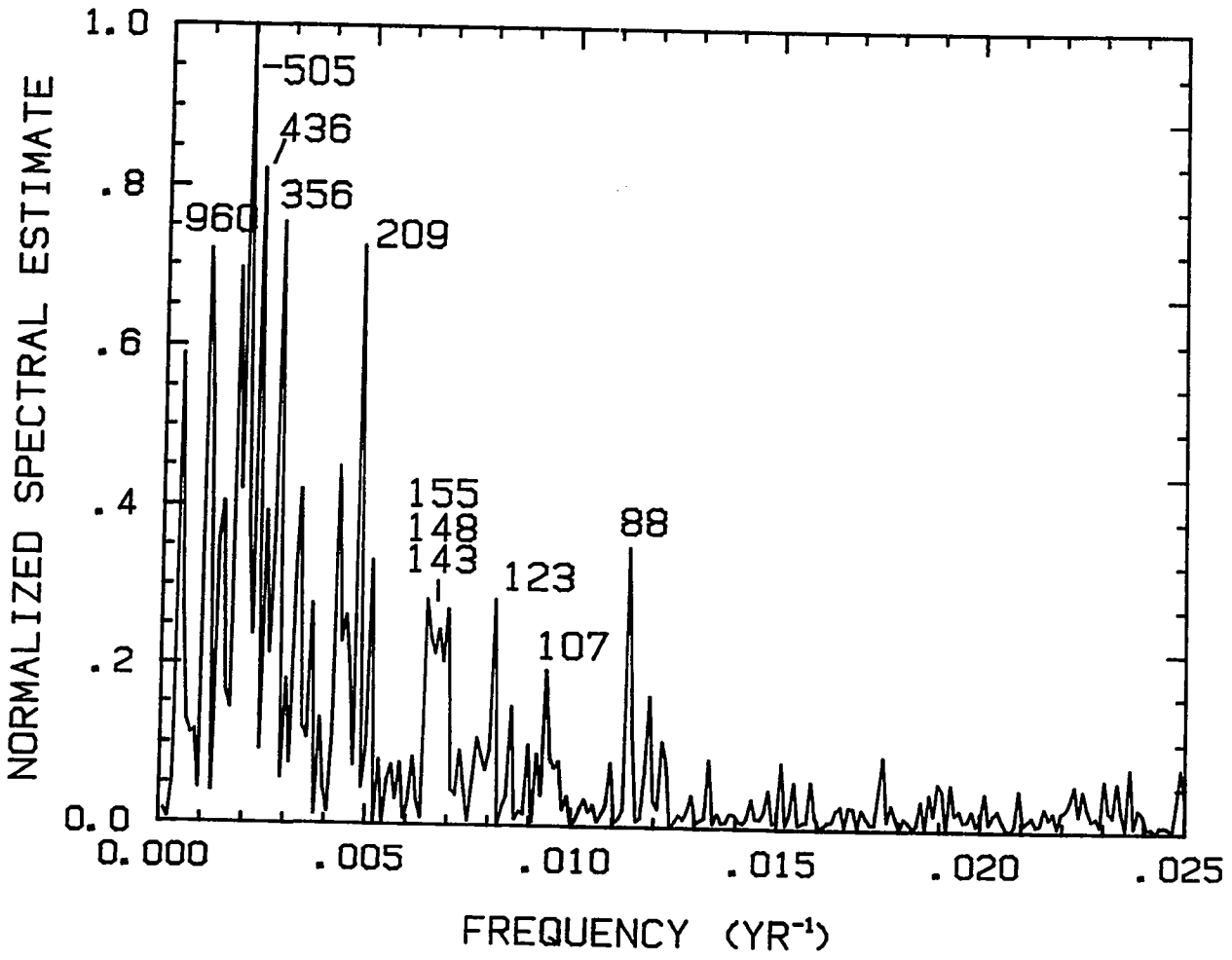
1.0
.8
.6
.4
.2
0.0
NORMALIZED SPECTRAL ESTIMATE
505
436
356
960
209
155
148
143
123
107
88
0.000
.005
.010
.015
.020
.025
FREQUENCY (YR-1)

and their conclusions must be related with caution to the interpretation of the actual ^{14}C-related PSD spectra.

In the first series of tests, the ability of the classical and MEM spectral approaches to properly identify frequencies and amplitudes was assessed with artificial time series comprised of 350 bi-decades, 20 uniformly spaced frequency signals with amplitudes of unity, and an adjustable level of background noise. The frequency signals ranged from 1/2500 yr^{-1} to 1/92 yr^{-1} in steps of .00055 yr^{-1} (figure 4.9 inset). Random numbers with a gaussian distribution characterized by one sigma of either ± .001 or ± 2.0 units were added to the signal to represent high signal-to-noise (SNR) and low signal-to-noise levels, respectively. PSD spectra of these two alternative time series were derived from FFT and MEM (Burg) analysis, and the accuracy of these two spectral approaches and the effects of noise level were evaluated.

The resultant PSD spectra are displayed in figures 4.9, 4.10, 4.11, and 4.12. Both spectral approaches accurately locate the signal frequencies but vary substantially in their responses to noise levels. The FFT spectrum most closely regenerates the equality in signal amplitudes but exhibits a reduction in accuracy when noise level is increased (figures 4.9 and 4.10). The effect is opposite in the MEM Burg analysis which produces a greater range in PSD peak heights when background noise is lower (figures 4.11 and 4.12). These results confirm the inferiority of MEM Burg analysis in identifying amplitudes and the sometimes devious role of background noise as mentioned in section 4.1.

In both Burg analyses described above, the model AR order (equivalent to approximately 50% of N) was selected by application of the Akaike FPE_M criterion. With artificial time series, the chosen model AR orders were generally higher than for the actual ^{14}C data sets. When a relatively low model AR of 4% is arbitrarily selected in the MEM

Figure 4.9: PSD results for FFT analysis of an artificial 7000-yr bi-decadal time series with relatively high signal-to-noise ratio (SNR). The figure inset shows the 20 uniformly- spaced signal frequencies with amplitudes of 1.0 units; a low background level of gaussian random noise with one sigma of ± .001 units has been added.

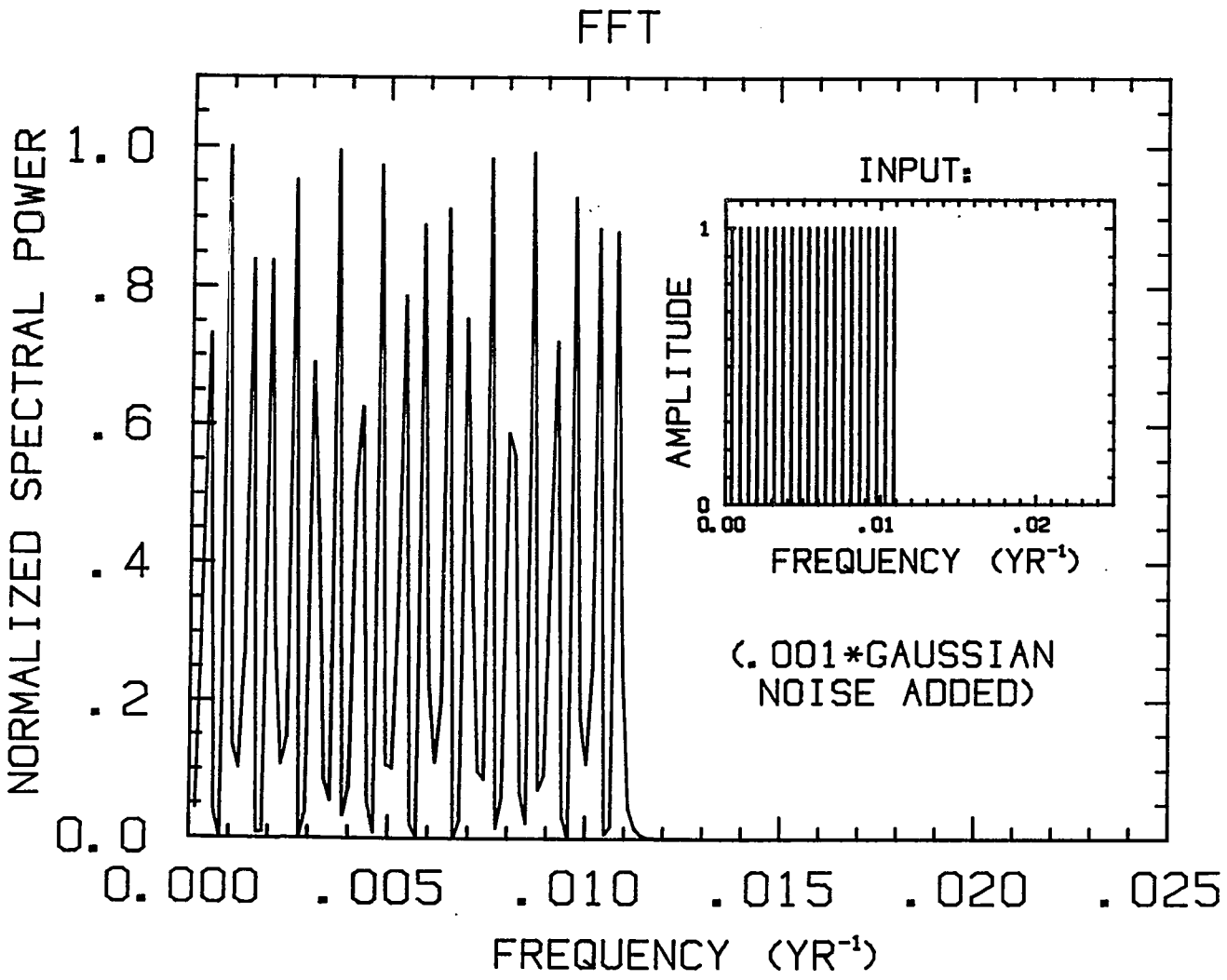
FFT
NORMALIZED SPECTRAL POWER
1.0
.8
.6
.4
.2
0.0
0.000
.005
.010
.015
.020
.025
FREQUENCY (YR⁻¹)
INPUT:
AMPLITUDE
1
0
0.00
.01
.02
FREQUENCY (YR⁻¹)
(.001*GAUSSIAN
NOISE ADDED)

Figure 4.10: PSD results for FFT analysis of an artificial 7000-yr bi-decadal time series with relatively low SNR ratio. A high background level of gaussian random noise with one sigma of ± 2.0 units has been added. See figure 4.9 for additional information.

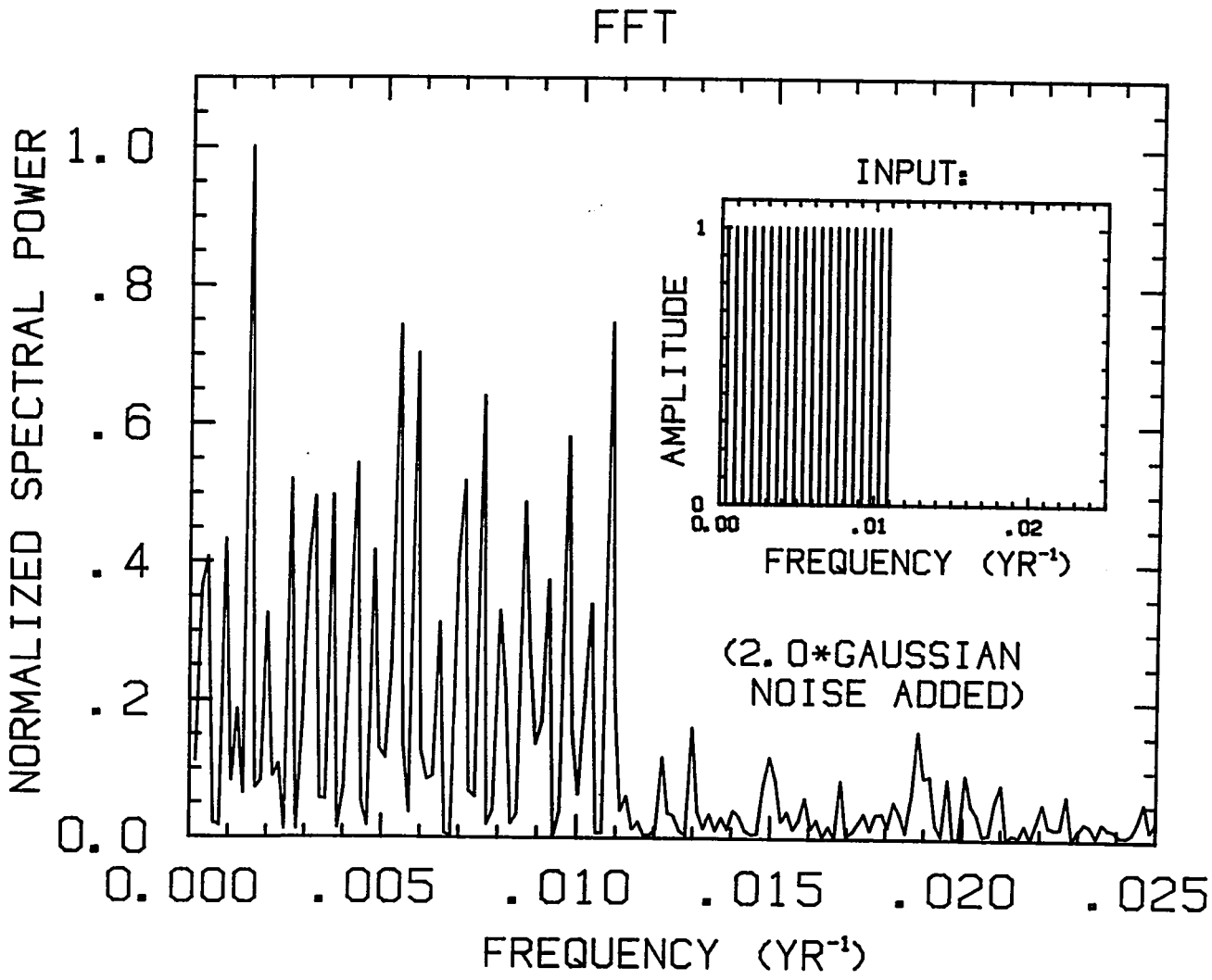
FFT
NORMALIZED SPECTRAL POWER
1.0
.8
.6
.4
.2
0.0
0.000
.005
.010
.015
.020
.025
FREQUENCY (YR⁻¹)
INPUT:
AMPLITUDE
1
0
0.00
.01
.02
FREQUENCY (YR⁻¹)
(2.0*GAUSSIAN
NOISE ADDED)

Figure 4.11: PSD results for MEM (Burg) analysis of an artificial 7000-yr bi-decadal time series with relatively high SNR ratio. The model AR order of 174 (or ca. 50% of the total number of observations) corresponds to the absolute minimum FPE_M value. Other details as in figure 4.9.

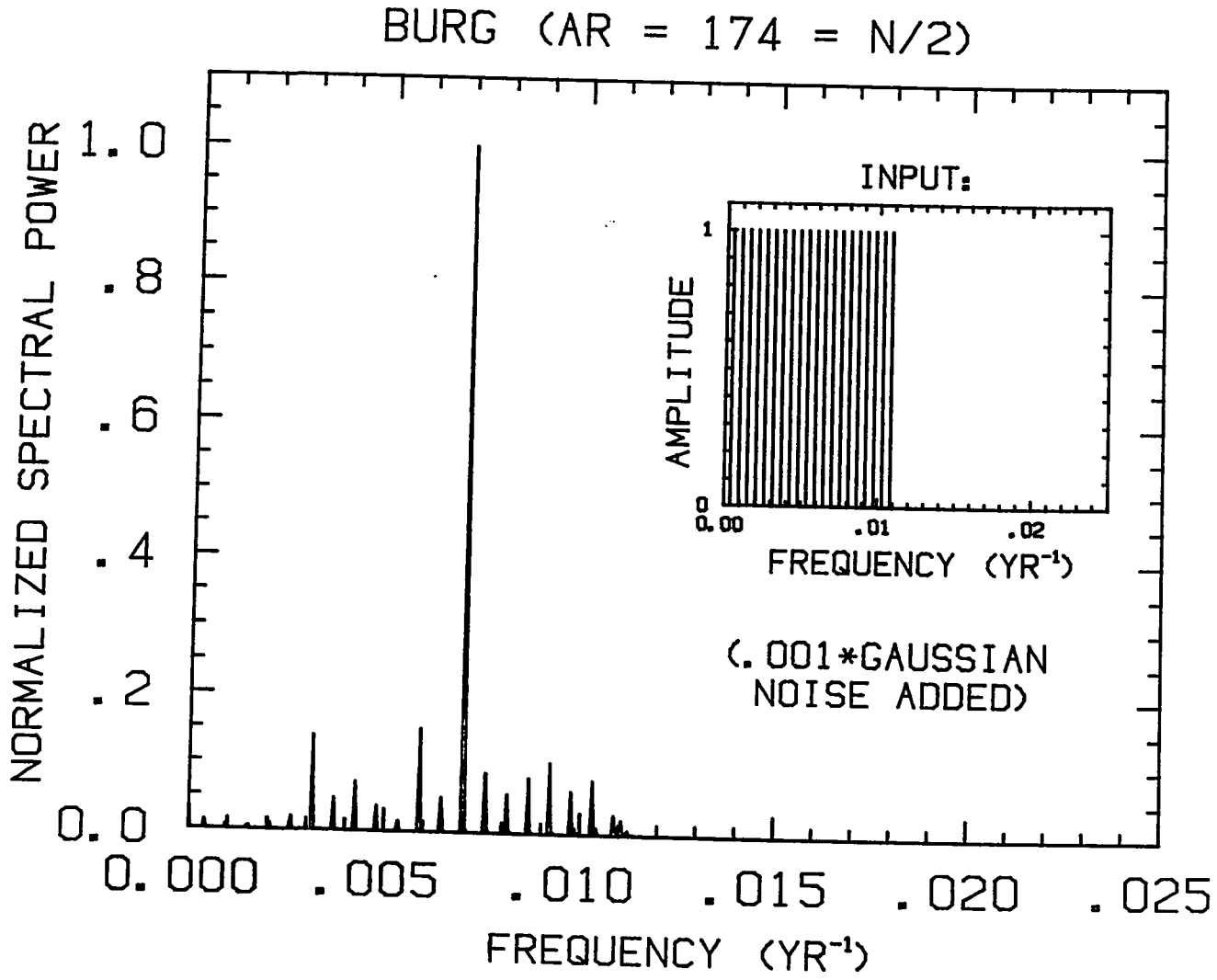
BURG (AR = 174 = N/2)
NORMALIZED SPECTRAL POWER
1.0
.8
.6
.4
.2
0.0
0.000
.005
.010
.015
.020
.025
FREQUENCY (YR⁻¹)
INPUT:
AMPLITUDE
1
0
0.00
.01
.02
FREQUENCY (YR⁻¹)
(.001*GAUSSIAN
NOISE ADDED)

Figure 4.12: PSD results for MEM (Burg) analysis of an artificial 7000-yr bi-decadal time series with relatively low SNR ratio. The model AR order of 172 (or ca. 50% of the total number of observations) corresponds to the absolute minimum FPE_M value. Other details as in figure 4.10.

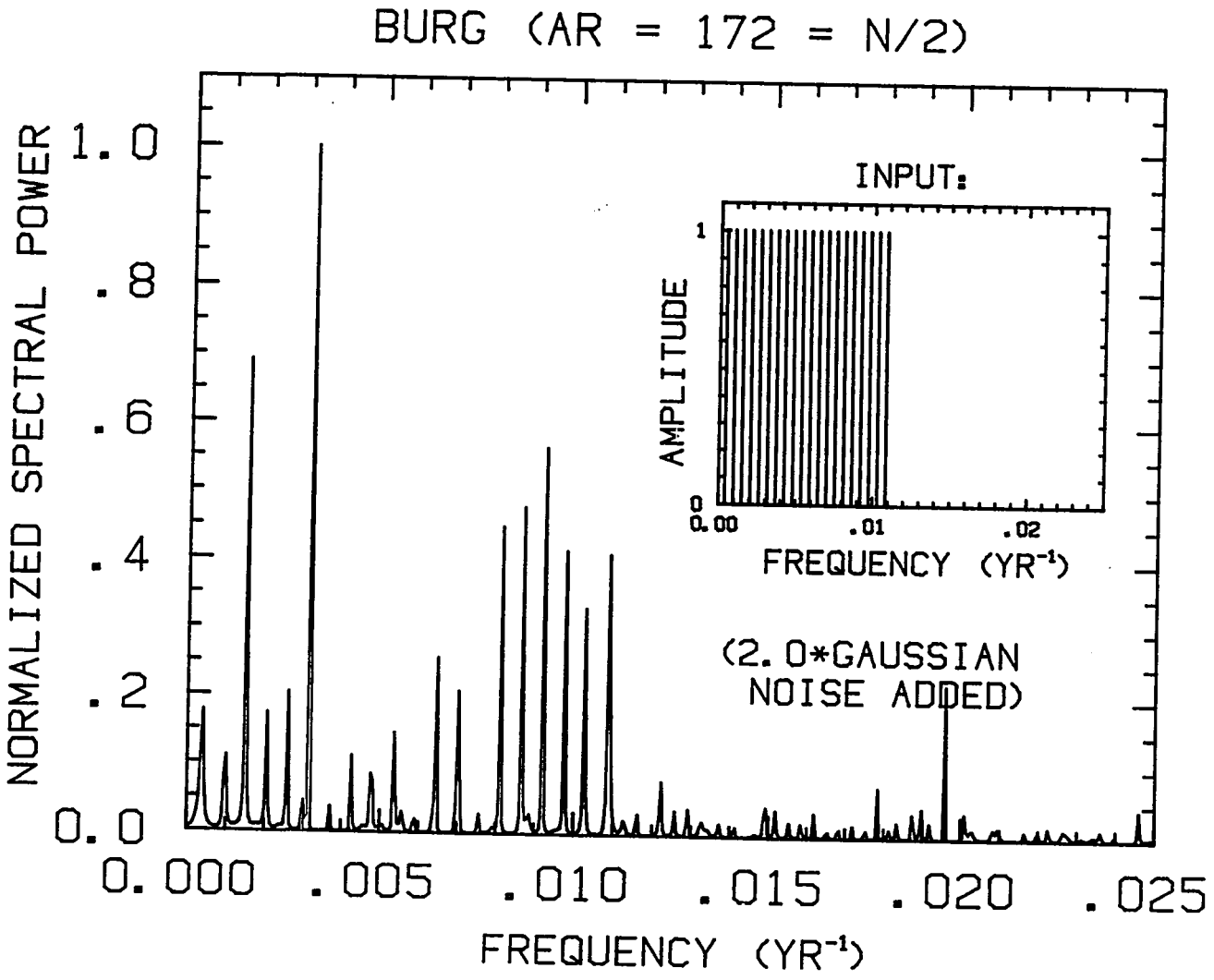
BURG (AR = 172 = N/2)
NORMALIZED SPECTRAL POWER
1.0
.8
.6
.4
.2
0.0
0.000
.005
.010
.015
.020
.025
FREQUENCY (YR⁻¹)
INPUT:
AMPLITUDE
1
0
0.00
.01
.02
FREQUENCY (YR⁻¹)
(2.0*GAUSSIAN
NOISE ADDED)

(Burg) analysis of the above artificial time series with low SNR, spectral resolution is lost and the peak PSD frequencies (corresponding to periodicities of 605, 196, 97, 67, and 53 yrs), although evenly spaced, do not reflect the original signal frequencies. Thus, in this case, a low model AR order fails to identify the many periodicities in the time series but also does not generate a false series of PSD harmonics with the loss in resolution.

Distinct sinusoidal periodicities in a time series can combine to produce a pattern of "beats". A "beat" occurs when two higher frequency cycles (f_1 and f_2) of similar duration interfere to produce an apparent longer-period amplitude modulation (of frequency $f_3 = (f_1-f_2)/2$) of a relatively short cycle (of frequency $f_4 = (f_1+f_2)/2$). Spectral analysis techniques ideally identify only genuine periodicities although, as noted above, windowing will complicate the spectra. With an artificial single-yr data set, Kane and Trivedi (1985) demonstrated that the MEM spectrum does not exhibit a fictitious longer periodicity (f_3 = 1/120 yr^{-1} in this case) resulting from the beating of two proximate higher frequencies (f_1 = 1/10 yr^{-1} and f_2 = 1/12 yr^{-1}).

I also investigated the effects of signal interference on FFT and MEM spectra. For a 480-item bi-decadal time series composed of equal-strength signal periodicities of 218 ($=1/f_1$) and 185 ($=1/f_2$) yrs with and without background noise, neither FFT nor MEM (Burg) analysis (at a model AR order of 25%) produced "beat"-related PSD peaks at 2400 ($=1/f_3$) or 200 ($=1/f_4$) yrs. However, for a data set comprising the *decadal averages* of a similar length single-yr time series with signal periodicities of 11.9 ($=1/f_1$) and 10.4 ($1/f_2$) yrs, FFT and MEM (Burg) analysis (at model AR order of 50%) identified a strong PSD peak cluster at 65 yrs (perhaps coincidentally near $2/f_3$). Clearly the ability to identify higher signal frequencies is compromised when time series are averaged; whether signal interference truly contributes to the PSD spectra of lower frequencies in these averaged time series was not pursued further here.

To investigate the authenticity of the four MEM-derived harmonics, spectral analyses were performed on several 480-item bi-decadal time series with one or more of these harmonic periodicities. The first artificial data set comprised equal-strength sinusoidal signal periodicities of 414, 216, 142, and 85 yrs and, in a series of tests, the standard deviation of the gaussian random noise ranged from .001 to 1.0 units of the signal amplitudes. Both MEM Burg and FABNE analyses accurately identified the four signal frequencies in all cases with generally no extraneous PSD peaks. However, MEM-identified PSD peak heights for the signal frequencies differed by up to 3 orders of magnitude, with both algorithms producing less divergent PSD peak heights when noise level was greater. MEM analyses at model AR orders of 20 appeared equally reliable as those analyses at FPE_M-selected model AR orders of 10-20% of the total number of observations.

To evaluate the influence of attenuation factors on the spectral analysis of atmospheric and oceanic $\Delta^{14}C$ histories in comparison to the spectral analysis of the original Q forcing function, the artificial bi-decadal time series above was converted to a "$\Delta Q/Q_t$ record" with which to generate associated reservoir $\Delta^{14}C$ variations in the conventional ^{14}C model. The "base-line" Q was set at 1.55 ^{14}C atoms sec^{-1} cm_E^{-2} to match the average $Q(^{14}C)$ back to 500 cal BP and each of the four sinusoidal signals was assigned an amplitude of ±30% relative to this "base line" in order to simulate century-scale $\Delta Q/Q_t$ variations. The gaussian probability distribution of the added random noise had a standard deviation equivalent to the signal amplitudes.

The four signal periodicities were accurately identified by the FFT and the MEM (Burg) analysis (at the FPE_M-selected model AR order of 18%) in the model-derived atmospheric $\Delta^{14}C$ record. Since the atmosphere acts as a low-pass filter for Q variations, the lower-frequency signals are expected to be attenuated less (see section 2.1); the 414-yr

cycle should appear relatively stronger in the spectral analysis of the atmospheric $\Delta^{14}C$ record than in the original Q time series. Indeed, in this spectral test, the FFT analysis assigns the most spectral power to the PSD peak for this cycle, but the MEM analysis does not. As demonstrated above, both methods fail to accurately reproduce relative signal amplitudes; any theoretical distinctions between the PSD spectra of the Q and atmospheric $\Delta^{14}C$ records are overwhelmed by this intrinsic deficiency in the methods.

The ocean reservoirs analogously respond as low-pass filters with respect to their atmospheric-forced $\Delta^{14}C$ variations; and indeed, in the spectral analyses of the artificial oceanic time series, the frequency-dependent amplitude attenuations of the signals are more definitive. For example, the FFT analysis accurately identifies the four signal frequencies in all ocean reservoirs but assigns relative spectral power to the respective PSD peaks in the ratio of 6/2.5/1/1 in the model-derived surface ocean time series, in the ratio of 24/6/2/1 for the thermocline time series and in the ratio of 1770/80/3.5/1 for the deep sea time series. The MEM Burg analysis also shows the greater relative strength of the slower periodicity in the ocean reservoirs.

Neither FFT nor MEM (Burg) analysis produced fictitious harmonics in the PSD spectrum for a 480-item bi-decadal time series consisting of only a 440-yr (T_1) sinusoidal cycle and "equivalent" random noise. Also, when the time series consisted of a 440- and 220-yr sinusoidal cycle (with relative phases offset either 0^o or 45^o) and random noise, higher harmonics were not present in the PSD spectra produced by these two methods. The preceding analyses were repeated, with equivalent results, on a time series with sinusoidal signal periodicities at $T_1/2$ and $T_1/3$.

However, when the signal shape is not sinusoidal, both spectral methods did produce significant PSD peaks at harmonics of the signal periodicity. For example, the FFT analysis of a time series with a 440-yr ($=T_1$) rectangular cycle generates additional PSD

peaks at 145 ($T_1/3$), 88 ($T_1/5$), 63 ($T_1/7$), and 49 ($T_1/9$) yrs. The spectral power of each of these false harmonics was less than 10% of the primary PSD peak at 440 yrs. The MEM (Burg) analysis produced PSD peaks at 219 ($T_1/2$), 155 ($T_1/3$), and 63 (ca. $T_1/7$) yrs with more than 10% of the spectral power of the strongest PSD peak at 475 (T_1) yrs. For a time series with equal-amplitude rectangular cycles of 440 (T_1) and 220 ($T_1/2$) yrs, FFT analysis generated PSD periodicities at 444, 222, 145 ($T_1/3$), 110 ($T_1/4$), 88 ($T_1/5$), 73 ($T_1/6$), 63 ($T_1/7$), 55 ($T_1/8$), 49 ($T_1/9$) and 44 ($T_1/10$) yrs. The 222-yr PSD peak had 80% of the spectral power of the 444-yr PSD peak while the PSD heights of the fictitious harmonics were generally below 5% relative to this peak. At model AR order of 100 (no absolute minimum FPE_M is attained), MEM (Burg) identified these same harmonic periodicities with the stronger PSD peaks at periods of 63 and 444 yrs.

Therefore, spurious PSD peaks at harmonic frequencies can be generated by a rectangular input signal resulting perhaps from step changes between two modes of solar behavior. The tests performed above, however, indicate that the PSD peaks for these fictitious harmonics generally have low spectral power compared to the primary frequencies, especially in the FFT analysis. The substantial strengths of the harmonic PSD peaks derived from all four spectral techniques are inconsistent with such an indirect origin. Thus, in the curve fitting procedure below, the primary harmonic frequencies identified by spectral analyses are treated tentatively as reflections of true sinusoidal signals in solar activity. In section 4.3, theories for patterns in solar activity are reviewed and the notions of harmonic or bi-modal solar behavior are considered in this perspective.

Sinusoidal curves fit to the Q(^{14}C) record

As demonstrated above, the MEM FABNE algorithm may accurately identify signal periodicities but MEM yields no information on phases and amplitudes of these cycles. In

order to determine these quantities and to "fine-tune" the most prominent frequencies indicated by spectral analyses, a suite of sinusoids was fit to the Q(^{14}C) record by standard least squares regression. The equation fit to the time series was:

$$f(t) = A_0 + \sum r_k \cos (2\pi t/T_k + \varnothing_k)$$
$$= A_0 + \sum r_k \cos (2\pi/T_k (t + L_k)) \qquad (4.4)$$

where f(t) is the sinusoidal model equation at year t in calendar time (with negative numbers for BC dates), A_0 is the average value of the time series, r_k and $\varnothing_k$ represent the fitted amplitudes and phases of each of the k cycles, and each T_k is a period determined by the MEM analysis and fine-tuned in the least-squares regression. The lag term L_k is equivalent to $(\varnothing_k T_k/2\pi)$. A similar fitting procedure was utilized by Kane and Trivedi (1985) and Cohen and Lintz (1974) to refine their spectral analyses.

This approach produces the following equation for the strongest sinusoidal representation of the entire $\Delta Q/Q_t$ record that incorporates the four harmonic periodicities identified in the spectral analyses above:

$$\Delta Q/Q_t\,(\%) = -0.1 + 4.3 \cos (2\pi/207\ (t + 7638))$$
$$+ 2.7 \cos (2\pi/446\ (t + 7738))$$
$$+ 2.6 \cos (2\pi/152\ (t + 7752))$$
$$+ 1.7 \cos (2\pi/88\ \ (t + 7746)) \qquad (4.5)$$

This cosine approximation explains 15% of the variance in the original $\Delta Q/Q_t$ record since the correlation coefficient between these time series is .39. The fitted curve (heavy line in figure 4.13, panel A) appears to represent the amplitudes of the higher frequency

Figure 4.13: Comparisons between percentage $\Delta Q/Q_t$ variations -- derived from Q deconvolution of the tree-ring (atmospheric) $\Delta^{14}C$ record -- and sinusoidal curves designed to approximate all or portions of the $\Delta Q/Q_t$ record. Panel "A" compares the $\Delta Q/Q_t$ record (light bar graph) with the cosine curve (smooth heavy line) defined by equation (4.5) based on the adjusted periodicities identified by MEM FABNE on $\Delta Q/Q_t$. Panel "B" compares the triplet portions of the $\Delta Q/Q_t$ record (light bar graph with horizontal sections for intertriplet intervals) with the cosine curve (smooth heavy line) defined by equation (4.6) based on the adjusted periodicities identified by MEM FABNE on the triplet intervals of $\Delta Q/Q_t$. Panel "C" compares the intertriplet portions of the $\Delta Q/Q_t$ record (light bar graph with horizontal sections for triplet intervals) with the cosine curve (smooth heavy line) defined by equation (4.7) based on the adjusted periodicities identified by MEM FABNE on the intertriplet intervals of $\Delta Q/Q_t$. Panel "D" compares the $\Delta Q/Q_t$ record (light bar graph) with the cosine curve (smooth heavy line) defined by equation (4.8) based on the Fourier analysis of $\Delta Q/Q_t$.

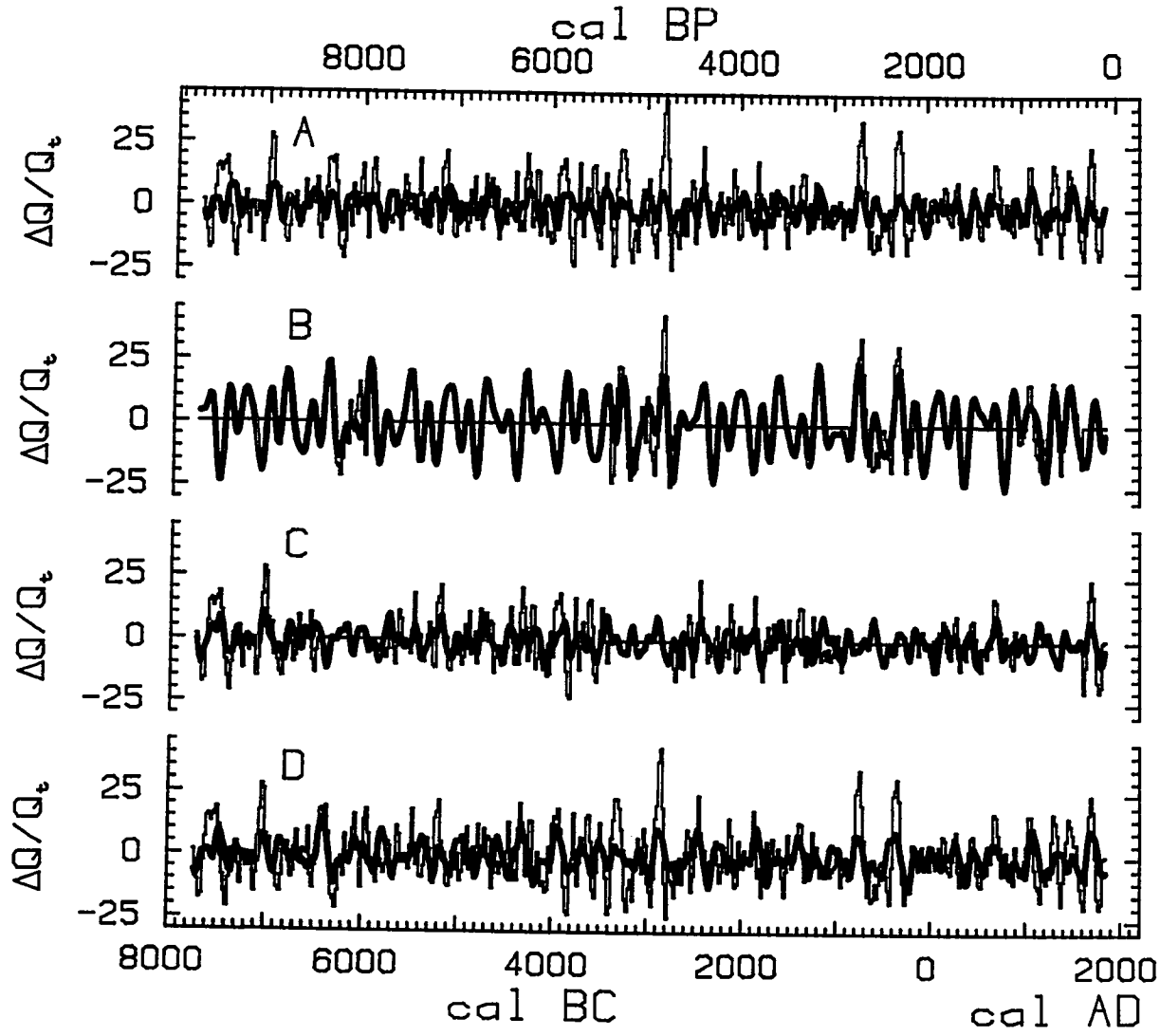
cal BP
8000
6000
4000
2000
0
A
B
C
D
ΔQ/Q
25
0
-25
8000
6000
4000
2000
0
2000
cal BC
cal AD

variations in the $\Delta Q/Q_t$ record (light bar graph in figure 4.13, panel A) better than the stronger deviations associated with the major century-scale patterns. The ca. 400-yr rectangular signal that best correlates with the $\Delta Q/Q_t$ record was analogously "fine-tuned" to a periodicity of 445 yrs and an amplitude of 2.2%. This fitted curve, however, only explains 4% of the variance in $\Delta Q/Q_t$ ($r = .20$).

The Fourier analysis and, as noted above, the power spectrum approach (at a maximum lag of 50% of the total number of observations) replace the apparent 400-yr PSD peak with several proximate periodicities. The periodicities, amplitudes and phase lags derived directly from the Fourier analysis provide this alternative suite of sinusoidal cycles:

$$\begin{aligned}\Delta Q/Q_t\,(\%) = {} & -0.1 + 4.1 \cos(2\pi/208\,(t + 7663)) \\ & + 3.4 \cos(2\pi/355\,(t + 7850)) \\ & + 2.9 \cos(2\pi/299\,(t + 7596)) \\ & + 2.6 \cos(2\pi/152\,(t + 7760)) \\ & + 2.4 \cos(2\pi/504\,(t + 7948)) \\ & + 1.7 \cos(2\pi/88\ \ (t + 7746))\end{aligned} \qquad (4.6)$$

In this case, the correlation between cosine approximation and $\Delta Q/Q_t$ record improves ($r = .48$) with 23% of the variance in the original time series now explained. This sinusoidal curve more accurately reproduces both higher and lower frequency $\Delta Q/Q_t$ variations (figure 4.13, panel D). These results are not surprising since additional periodicities in the cosine approximation are generally expected to enhance these statistics. The latter equation, however, does not conform to a harmonic interpretation for the spectral components in the residual $\Delta Q/Q_t$ record. At present, the geophysical theories and

available spectral evidence of solar activity do not permit a definitive selection between these two (or other) mathematical approximations for solar behavior (see section 4.3).

A consistent 680-yr pattern comprised of 3 century-scale oscillations (a "triplet") appears four times in the $\Delta Q/Q_t$ time series (figure 3.4) representing 28% of the total record length (Stuiver and Braziunas 1989). The common features of the triplet intervals are apparent when the timescale is amplified (Stuiver and Braziunas 1988, figure 4, and Stuiver and Braziunas 1989, figure 3a). Although the triplet pattern occurs at irregular intervals in the $\Delta Q/Q_t$ record (6480 - 5800 BC, 3420 - 2740 BC, 880 - 200 BC, and AD 920 - 1600), three sinusoidal cycles, maintaining the same relative phases, can explain more than 50% of the variance associated with these triplet $\Delta Q/Q_t$ intervals. Thus this hypothetical mode of solar behavior, concealed or replaced during long intervals of solar history, nonetheless seems regulated by a hidden clock.

The fitted curve for the triplet intervals is:

$$\begin{aligned} \Delta Q/Q_t\,(\%) = {} & 0.4 + 11.2 \cos (2\pi/207\ (t + 7633)) \\ & + 8.8 \cos (2\pi/435\ (t + 7732)) \\ & + 5.6 \cos (2\pi/148\ (t + 7734)) \\ & + 2.9 \cos (2\pi/87\ \ (t + 7718)) \end{aligned} \qquad (4.7)$$

These four periodicities were initially identified by MEM (FABNE) spectral analysis (at the FPE_M-selected model AR order of 26) on the $\Delta Q/Q_t$ triplets sequentially spaced at the proper intervals (light bar graph of triplet intervals joined by a horizontal line in figure 4.13, panel B). Nearly the same harmonic periodicities are associated with the triplet behavior as with the entire $\Delta Q/Q_t$ record. The signal amplitudes are greater (heavy line in figure 4.13, panel B) and the refined cosine approximation explains 55% of the variance

of the triplet mode (r = .74). The 207-yr sinusoid alone accounts for 31% of the variance; the three longest cycles produce virtually all of the correlation. The correlation coefficients of the fitted curve with individual triplet intervals and other portions of the $\Delta Q/Q_t$ record are displayed in Stuiver and Braziunas (1989, figure 3b).

The MEM (FABNE) spectral analysis of the remaining $\Delta Q/Q_t$ variations, ie. the "intertriplet" intervals, generates PSD peaks at 444 (=T_1), 250 (ca. $T_1/2$), 148 ($T_1/3$), 115 ($T_1/4$) and 88 yrs ($T_1/5$) for the FPE_M-selected model AR order of 19. Thus a set of harmonic frequencies is also identified in the intertriplet intervals. The following equation is the refined cosine approximation, as fit to the sequence of $\Delta Q/Q_t$ intertriplets at properly spaced intervals (light bar graph of intertriplet intervals joined by a horizontal line in figure 4.13, panel C):

$$\begin{aligned}\Delta Q/Q_t\,(\%) = {} & -0.3 + 4.3 \cos(2\pi/256\,(t + 7787)) \\ & + 3.4 \cos(2\pi/143\,(t + 7757)) \\ & + 2.8 \cos(2\pi/456\,(t + 7514)) \\ & + 2.2 \cos(2\pi/118\,(t + 7737)) \\ & + 1.9 \cos(2\pi/88\ \ (t + 7749))\end{aligned} \qquad (4.8)$$

These periodicities explain 28% of the variance in the intertriplet portions of the $\Delta Q/Q_t$ record (r = .53). The 118-yr and 88-yr cycle are secondary components of the fit since the first three cycles individually explain 12%, 7%, and 5% of the signal variance, respectively. Amplitudes in this equation are weaker than in the triplet cosine approximation because the intertriplet portions of the $\Delta Q/Q_t$ record are characterized by more subdued fluctuations (light bar graph in figure 4.13, panel C). The 143-yr periodicity, however, gains in relative strength when comparing the intertriplet to the

triplet suite of sinusoids. The fitted intertriplet curve (excluding the 118-yr cycle) is shown in panel C of figure 4.13 (heavy line).

Thus harmonic periodicities can reproduce a significant portion of the model-derived Holocene record of ^{14}C production rate changes when this record is first classified into two behavioral modes defined by observed longer-term $\Delta Q/Q_t$ patterns. In this way, a visual inspection of the detrended $Q(^{14}C)$ record is a valuable complement to standard spectral analyses. However, the veracity of this interpretation of ^{14}C production history requires supporting evidence from other spectral studies and from geophysical models of solar behavior. The concepts of century-scale solar harmonics and "triplet" solar behavior are, at present, only testable working hypotheses that modestly offer relatively simple explanations for a collection of observations with a complex appearance (see next section). The systematic survey of $Q(^{14}C)$ spectral properties conducted above at least provides an initial reference point for future investigations.

4.3 Evidence and theories for solar periodicities

The spectral analyses above indicate that the Holocene $Q(^{14}C)$ record contains persistent century-scale variations. The periods identified by MEM (FABNE) analysis at the FPE_M-selected model AR order of 20 are 420, 218, 143, and 85 yrs, which correspond to four of the first 5 harmonics of a fundamental period of 420 yrs. Spectral tests (section 4.1) suggest that a model AR order of 20 (4% of the total number of observations) will accurately identify periodicities that are 4% or less (ie. under 400 yrs) in a bi-decadal 9600-yr record. Such harmonic cycles (after "fine-tuning" and differentiation into "triplet" and "intertriplet" categories) can explain a significant portion of the variance

in the ^{14}C production record.

If, as argued above, century-scale ^{14}C production variations originate through solar modulation, harmonic ^{14}C periodicities (if real) may reflect harmonic solar processes or may result from the shape and/or interference of solar cycles at a variety of timescales. Since the criteria for selecting model AR orders or lags in spectral analyses continue to be questioned, the validity of these hypothetical solar-related harmonics and their potential source(s) can only be assessed by reviewing the current understanding of periodicities and processes in solar activity.

Century-scale cycles and models for solar activity

"Solar activity" refers to the transient phenomena of the solar atmosphere such as sunspots, faculae, flares, and coronal holes. In theory, these features are surface expressions of the sun's unsettled "heliomagnetic" activity. The solar (ie. helio-)magnetic dynamo is widely thought to be induced by electric currents in the sun's molten core (eg. Sofia et al. 1985), a process similarly responsible in theory for the earth's geomagnetic dynamo. In the sun's convective zone (the outer third of its radius), heliomagnetic field lines become twisted along with the ionized solar gases through mixing by convective motions and differential solar rotation (being faster at the solar equator). These field lines can become concentrated in places and break through the solar surface as sunspots. Flares may erupt from areas of strong magnetic activity, and solar flare activity is correlated with relative number of sunspots on the solar surface.

Flares and coronal holes directly affect the solar wind, the flux of particles (primarily protons and electrons) that streams off from the solar corona (eg. Friedman 1986). The magnetic fields associated with the charged particles of the solar wind interfere with the penetration of galactic cosmic rays into the earth's atmosphere and, therefore, modulate

neutron-derived ^{14}C production rates (see sections 1.1 and 3.2). "Gusts" in the solar wind also interact with the Earth's magnetic field to produce geomagnetic storms and to increase auroral luminosities. These associations explain the high correlation of the 11-yr cycle in the appearance and disappearance of sunspots with variations in other measures of solar activity such as auroral luminosities, geomagnetic *Aa* indices, neutron fluxes and ^{14}C production rates (eg. Stuiver and Quay 1980).

In addition to a strong and nearly stable 11.2-yr cycle in annual relative sunspot numbers, evident in nearly 3 centuries of telescopic observations, several other periodicities in solar activity phenomena have been widely established. The 22-yr Hale magnetic cycle derives from the reversal in polarity of the heliomagnetic dynamo after each 11-yr sunspot cycle. On a short time scale, geomagnetic storms occasionally exhibit a periodicity of 27 days. The 80- to 90-yr "Gleissberg cycle" observed in maximum number of sunspots per 11-yr cycle (e.g. Gleissberg 1939) matches the periodicity of 88.4 yrs determined by MEM (Burg) spectral analysis on 1000 yrs of auroral sightings (Feynman and Fougere 1984); a periodicity of 88 yrs has been reported in a more recent analysis of sunspots (Cole 1973) and this cycle may correlate with variations in solar diameter as well (Sofia et al. 1985). As discussed above, our own spectral analysis also identifies an 85-yr periodicity in $Q(^{14}C)$.

In addition, less indisputable periodicities in solar activity phenomena have been reported. MEM (Burg) analysis of annual sunspot numbers from AD 1844 to 1971 identified a 179-yr periodicity (Cohen and Lintz 1974) while comparison of expected times of 11.06-yr solar cycle maxima with available sunspot evidence between AD 300 and 1968 suggests that the *phase* of this sunspot cycle has a 190-yr nonsinusoidal periodicity (Cole 1973). In their MEM Burg and FABNE approaches, Kane and Trivedi

(1985) combined lower and higher model AR orders to determine longer and shorter periodicities, respectively, in the annual sunspot record from AD 1749 to 1971. In addition to significant PSD peaks around 11 yrs, century-scale periodicities identified at various model AR orders included cycles at ca. 84, 90, 108, 133 and 143 yrs.

Power spectrum analysis of the record between AD 1 and 1731 of historical aurorae, another proxy for solar activity, revealed prominent periodicities of 132, 88 and 44 yrs (Atollini et al. 1988). The power spectrum approach was also applied to the thermoluminescence (TL) intensity profile of an Ionian Sea sediment core (Castagnoli et al. 1989). The TL time series represents AD 170 to 1977 according to the calculated sedimentation rate in the core and contains two periodicities of 10.8 and 12.06 yrs whose interference produces a 206-yr amplitude modulation of a 11.4-yr carrier wave. Although the geophysical explanation linking the TL intensity with solar activity is very speculative, the similar periodicities associated with these two phenomena suggests a connection (Castagnoli et al. 1989). My own FFT and MEM (Burg) analyses of another potential solar proxy, the Greenland {^{10}Be} record reported in Beer et al. (1988), identify a multitude of century-scale cycles (including 436, 229, 200, 171, 137) but the uneven temporal spacing of the measurements is an added complication.

Previous spectral investigations of atmospheric Δ^{14}C data sets (of shorter duration than the ^{14}C time series considered here) have revealed, in addition to other cycles, the periodicities of 400 yrs (FFT analysis in Sonett 1984), 200 yrs (FFT analysis in Neftel et al. 1981 and Sonett 1984; power spectrum analysis in Stuiver 1983), 130-155 yrs (FFT analysis in Neftel et al. 1981 and Sonett 1984; cyclogram approach in Attolini et al. 1988), and 86 yrs (cyclogram approach in Attolini et al. 1988). Longer-scale Δ^{14}C patterns with similarities to the above identified "triplet" variations have been described as part of a 2200-2600 yr quasi-periodic amplitude modulation of the 200-yr cycle (Hood and

Jirikowic 1990, Sonett 1984). Such a 2000-yr amplitude modulation has also been considered as an explanation for the "suggestion" of century-scale harmonics including the 400-yr (2000/5) and 200-yr (2000/10) periodicities in an FFT analysis of the 8400-yr LaJolla tree-ring $\Delta^{14}C$ record (Sonett 1984).

Geophysical explanations have been proposed for the established 11-yr sunspot cycle and/or other apparent (e.g. century-scale) periodicities in solar activity phenomena. Since the 27-day geomagnetic storm periodicity coincides with the sun's rotational period, this short-term cycle is thought to be associated with solar wind streams emanating from coronal holes that point toward the earth once each solar rotation. Although the timing mechanisms controlling the durations of the 11-yr sunspot cycle and 22-yr Hale cycle have not been precisely defined, many researchers suggest that these cycles originate entirely within the sun's convective zone from the regular twisting and untwisting of magnetic field lines (e.g. Sofia et al. 1985). However, this conventional theory (the magnetohydrodynamic model) has occasionally been challenged with implications for century-scale solar cycles (see below).

Century-scale sunspot periodicities, as well as the 11-yr cycle, have been linked to the solar tidal effects caused by planetary gravitational attractions. Sunspots result when the sun transfers angular momentum outward in response to these planetary influences. Jose (1965) found a strong correlation between the 179-yr variation in the sun's motion relative to the center of mass of the solar system and variations in sunspot numbers between AD 1610 and 1957. However, these tidal forces are calculated to be weak and unable to explain, for example, the Maunder Minimum behavior of the sun (Smythe and Eddy 1977).

Century-scale sunspot periodicities have also been interpreted as "beat" phenomena originating from the interference of decade-scale solar cycles. Applying the MEM (Burg)

technique, Cohen and Lintz (1974) reported periodicities of 9.9 and 11.2 yrs in a 12-month running average of the sunspot record (AD 1750-1971) and suggest that interference by these two cycles produces a lower-frequency sunspot period of 179 yrs as a beat phenomenon. The exact lengths of these periodicities have been fine-tuned using the same least-squares approach described above. In another analysis, Hill (1977) employed a modified Fourier method (with an inferred resolution of 1/20T) to discover three closely-spaced periodicities near 22 yrs in the monthly sunspot record from AD 1749 to 1975. Hill calculated that a millennium-scale beat periodicity of 1045 ± 200 yrs in sunspots will be associated with these decade-scale cycles.

The Blackman/Tukey power spectrum approach, employed by Cole (1973) on the AD 1700-1969 annual sunspot record, yielded clusters of PSD peaks centered around periodicities of 88, 11 and 5.75 yrs. Cole proposed a complex scenario in which the two genuine solar cycles are 10.45 yrs and 11.8 yrs; an additional amplitude modulation of 11.9 yrs on the ca. 11-yr sunspot periodicity explains the peak groups at 88 and 5.75 yr as artificial "sidebands" (at frequencies of $1/11 \pm 1/11.9\ yr^{-1}$). In this case, the amplitude modulation is interpreted as a primary solar process but spectral analysis identified those frequencies (ca. 88 and 5.75 yrs) which *could* have produced such an amplitude modulation.

Wolff (1976) listed 25 sunspot cycles ranging from 3 to 180 yrs -- identified in earlier spectral analyses by Currie (1973) and Cole (1973) -- and explained 15 of these periodicities, including the 11-yr cycle, as beats associated with month-scale "harmonic" solar processes operating throughout the entire mass of the sun. Unlike the conventional magnetohydrodynamic model linking solar activity to the influence of differential rotation on magnetic field lines in the sun's convective zone (the outer 2% of its mass), ordinary gas dynamics throughout the sun were considered responsible for sunspot cycles. Wolff

proposed that "the Sun is vibrating like a bell", ie. oscillating in a system of rigid rotational modes each with a month-scale periodicity related (via an "harmonic index") to a fundamental 25.8-day cycle. Slower solar activity periodicities of 178, 89, 59, and 11.9 yr were explained as beat phenomena resulting from various interferences of combinations of the higher-frequency "harmonic" cycles.

Sakurai (1984) also questioned the traditional theory that processes governing solar activity variations are restricted to the sun's convective layer. A *quasi-bienniel* component to the 11-yr sunspot cycle matches the 2.2-yr variation in solar neutrino flux. Currie (1973) earlier noted a 25.7 month periodicity in sunspots but interpreted it only as an harmonic of the 11-yr cycle. Sakurai theorized that its correlation with the solar neutrino flux (emanating from the solar core) indicates a significant connection between physical processes occurring in the inner and outer portions of the sun (perhaps through radial movements of the convective zone's lower boundary). These ideas do not specifically address century-scale solar activity variations but suggest that the traditional magnetohydrodynamic model may need reconsideration.

Century-scale *harmonic* periodicities in solar activity phenomena would be important clues for understanding solar processes. But, although the solar globe "rings" with small-amplitude vibrations on time scales of hours or less (eg. Friedman 1986), the existence of month-scale (Wolff 1976) not to mention century-scale solar harmonics has not been widely established. A few theories for century-scale harmonics observed in specific periodic analyses have been presented. For example, as noted above, the "suggestion" of harmonics in the FFT analysis of tree-ring $\Delta^{14}C$ has been hypothetically associated with a millennium-scale amplitude modulation of a fundamental century-scale cycle (Sonett 1984).

As discussed above, harmonics in the PSD spectrum may indicate a nonsinusoidal

cycle like an impulse or square wave rather than a "ringing" sun. Solar activity has been characterized as episodic and intermediate between sinusoidal and pulsating in nature (eg. De Meyer 1981). Cole (1973), for example, found 190-yr and 94.5-yr periodicities in the phase of the 11-yr sunspot cycle and concluded that the latter periodicity is an harmonic cycle indicating the non-sinusoidal nature of the former periodicity. Using MEM (Burg) analysis (with model AR orders ranging from 26 to 52%) on mean monthly sunspot numbers from AD 1749 to 1957, Currie (1973) identified the first four harmonics of the 11-yr cycle and associated no primary significance to them.

Century-scale harmonic periodicities, then, may result from the nonsinusoidal character of a primary solar signal or from the millennium-scale amplitude modulation of such a signal. In addition, the interference of higher-frequency cycles can theoretically produce century-scale "beat" periodicities. These phenomena may be responsible at least in part for the apparent century-scale harmonics identified in the spectral analyses in section 4.2. At present, evidence is lacking that these harmonics result directly from primary solar forcing processes.

Information on higher-frequency Q(^{14}C) variations near 11 yrs would be valuable for defining the extent of signal interference in creating longer-term ^{14}C periodicities. Unfortunately, such information is lost in the bi-decadal (or decadal) averaging of the tree-ring Δ^{14}C and the associated model-derived Q(^{14}C) records utilized here. The attenuation factor of .008 for decade-scale atmospheric Δ^{14}C variations forced by changes in ^{14}C production rate (section 2.1) leads to a weak tree-ring signal but spectral analyses on high-resolution single-year ^{14}C measurements are still likely to provide additional insights into solar processes on several timescales.

Alternative models for variations in solar activity may be tested by comparing model predictions with observations. Some of the mathematical and/or theoretical solar models

published prior to solar cycle 21 (AD 1976 - 1986) were applied to predict the maximum sunspot number and timing of this 11-yr sunspot cycle. Almost none of these models successfully approximates the sunspot maximum of ca. 155 which occurred in AD 1979 (McKinnon 1987/1988, Goswami et al. 1988).

For example, interpreting some solar variations as beat phenomena, Cole (1973) and Cohen and Lintz (1974) forecast a maximum sunspot number of 50-60 in AD 1981; the solar model with planetary influences (Jose 1965) predicts a low maximum around 30 in ca. AD 1981. The mathematical (curve-fitting) models fare somewhat better with forecasts of <100 (several models in Kane and Trivedi 1985) and 130-200 in AD 1981 or 1982 (Hill 1977). Based on alternative mathematical models, De Meyer (1981) concludes that sunspot behavior is unpredictable. The forecasts of additional investigations are discussed by Gleissberg (1971) and Kane and Trivedi (1985). Predictions based on "triplet" and "intertriplet" solar behavior are presented in section 4.4.

The role of millennium-scale cycles in Q(^{14}C) and solar models

As mentioned in section 1.2, the sinusoidal appearance of both the post-6500 BC tree-ring $\Delta^{14}C$ record and geomagnetic data suggested to earlier researchers that the global dipole moment was inherently sinusoidal and that the Holocene $\Delta^{14}C$ record contained a cyclic "grand trend". Estimates for this long-term periodicity generally fell between 10,000 and 13,000 cal yrs (eg. references in Carmi et al. 1984). Using the MEM (FABNE) approach on 67 century averages of post-5400 BC tree-ring $\Delta^{14}C$ measurements, Carmi et al. (1984) found a PSD peak at 13,200 yrs, identical to the periodicity derived by a least-squares fit of a sine curve to the 9700-yr $\Delta^{14}C$ record (see section 1.2).

However, the early and pre-Holocene geomagnetic and $\Delta^{14}C$ data (see section 2.3)

as well as current geomagnetic theory (eg. Merrill and McElhinny 1983) do not support the existence of a sinusoidal cycle on this timescale. The spectral analyses presented in section 4.2 do not identify any Holocene-scale periodicities in $Q(^{14}C)$. If the MEM (FABNE) approach on century averages is performed on an abbreviated post-5400 BC $Q(^{14}C)$ record, a "grand trend" of ca. 11,000 yrs is indeed generated in the PSD spectrum at the FPE_M-selected model AR order of 26; however, when the century averages of the $Q(^{14}C)$ record span the full 9700 yrs of tree-ring data now available, the FABNE analysis reveals PSD peak periodicities at only 500 and 200 yrs (at the FPE_M-chosen model AR order of 8). For these reasons, the identification and implications of a Holocene-scale sinusoidal cycle need not be further considered here.

A pattern suggesting a ca. 2500-yr cycle is visible in tree-ring $\Delta^{14}C$ data and has been interpreted as indicating a link between solar and climate change (Denton and Karlén 1973, Eddy 1977). Fourier analysis also identifies a periodicity with a ca. 2000-yr magnitude in $\Delta^{14}C$ time series (Houtermans 1971; Sonett 1984; low-frequency PSD peak in figure 4.8). Damon and Linick (1986) advocate a geomagnetic origin for a 2400-yr ^{14}C cycle (and its harmonics) in association with the westward drift of the nondipole field. In contrast, Hood and Jirikowic (1990) find evidence of a ca. 2400-yr amplitude modulation for century-scale variations in solar activity time series (ie. sunspot numbers and auroral occurrences) as well as the $\Delta^{14}C$ record and thus propose a *solar* origin for this millennium-scale periodicity. A specific physical model for this solar phenomenon is not proposed.

Yet the MEM analyses presented in section 4.2 did not identify a millennium-scale periodicity in the $Q(^{14}C)$ record (at the FPE_M-selected model AR orders) and the power spectrum analysis displayed only an insignificant PSD peak at this periodicity (figure 4.2). Furthermore, the MEM (Burg) analysis of the spline Q_t, representing the geomagnetic

component of the Q(^{14}C) record in the detrending procedures above, does not define any PSD peaks in this long-term trend. The ca. 2400-yr Δ^{14}C cycle described by Hood and Jirikowic (1990) has very small amplitude (ca. 4 ‰) and its presence also seems difficult to ascertain in the relatively short solar activity records, ie. the 1000-yr auroral and 300-yr sunspot time series. Therefore, a solar or geomagnetic cycle at this timescale has not been pursued in any detail here.

The proper identification of millennium-scale ^{14}C trends and an understanding of their solar and/or geomagnetic origins is important, however, in order to accurately quantify the solar component in the model-derived Q(^{14}C) history and apply the Q(^{14}C)/solar relationship to reconstructing or predicting variations in solar behavior. At present, the information on century-scale patterns and periodicities in Q(^{14}C) at least allows a good first-order quantification of this solar component (section 4.4).

4.4 Applications of the model-derived Q(^{14}C) history

A linear relationship between relative sunspot numbers and model-derived ^{14}C production rates can be calculated from the present modeling efforts and compared with earlier computations. An important, and unresolved, perplexity in the accurate quantification of a Q/solar association involves the proper removal of the geomagnetic component of the Q(^{14}C) record. This issue is addressed below.

With an approximate relationship between variations in solar activity and ^{14}C production rate, the 9700-yr Q(^{14}C) history can be converted into a time series of past solar change valuable for comparison with past climate records. In addition, the hypothetical "triplet" and "intertriplet" periodicities that explain significant portions of the

variance in the model-derived ^{14}C production history can be projected into approaching centuries in order to estimate the solar change contemporaneous with the anticipated human-forced "greenhouse effect".

Removal of the geomagnetic component in Q(^{14}C)

A distinction between the earlier modeling efforts of Stuiver and Quay (1980, 1981) and the current approach involves the treatment of the geomagnetic trend in ^{14}C production rate over recent centuries. Since this trend is independent of the solar modulation of ^{14}C production rates, its influence on Q(^{14}C) must be removed before the linear regression with relative sunspot numbers is calculated. In previous studies, atmospheric (tree-ring) $\Delta^{14}C$ was corrected, prior to the Q deconvolution in the global ^{14}C reservoir model, using a Holocene-scale sinusoidal approximation for the geomagnetic component in $\Delta^{14}C$ (Houtermans 1971, Stuiver and Quay 1980). Such a sinusoidal representation generates a rising long-term trend in atmospheric $\Delta^{14}C$ over recent centuries and ascribes a relatively strong residual $\Delta^{14}C$ enhancement to the solar-induced Maunder and Spörer events of the past millennium (figures 2 and 3 in Houtermans 1971; dotted line in figure 1.1)

In contrast, the long-term trend in ^{14}C production rate is calculated here directly from Q(^{14}C), *after* its deconvolution, and arbitrarily designated (section 3.1) as a spline approximating a 400-yr moving average (Q_t in figures 2.1 and 4.14). Contrary to the sinusoidal representation, this spline is elevated by the persistently high ^{14}C production rates after AD 1200 and precipitously declines with general Q(^{14}C) levels after AD 1500 (short-long dashed line in figure 4.14). As a result, the AD 1700 - 1840 residual Q(^{14}C) (ie. $\Delta Q/Q_t$) levels are significantly higher than previously estimated. Since this specific interval in $\Delta Q/Q_t$ is regressed against sunspot numbers to derive a Q/solar relationship, the

Figure 4.14: Variations and trends in ^{14}C production rate since AD 500: (1) $Q(^{14}C)$ (bar graph) is deconvolved from the bi-decadal tree-ring (atmospheric) $\Delta^{14}C$ record in which the "natural" variations of the post-AD 1840 interval ("fossil fuel period") are reconstructed from previous ^{14}C carbon modeling (Stuiver and Quay 1981); (2) $Q(^{14}C)_S$ (equi-dashed line) is an interpolating spline through 500-yr averages of $Q(^{14}C)$ (see text for details); (3) Q_t (short-long dashed line) is the "400-yr" spline conventionally employed here as the long-term trend removed from the $Q(^{14}C)$ record in order to derive $\Delta Q/Q_t$ variations; (4) $Q(DM)_{OBS}$ (heavy solid line) is the post-AD 1835 ^{14}C production history defined by the well-documented decline in the global dipole moment (Merrill and McElhinny 1983) and equation (2.1) with c_1 of 4.39; (5) $Q(DM)_S$ is an interpolating spline through the ^{14}C production rates defined by 500-yr averages of the global dipole moment and equation (2.1) (see text for details). The vertical dots separate the period of natural ^{14}C variations (left) from the period in which natural ^{14}C variations have been reconstructed to remove the influence of fossil fuel CO_2 (right).

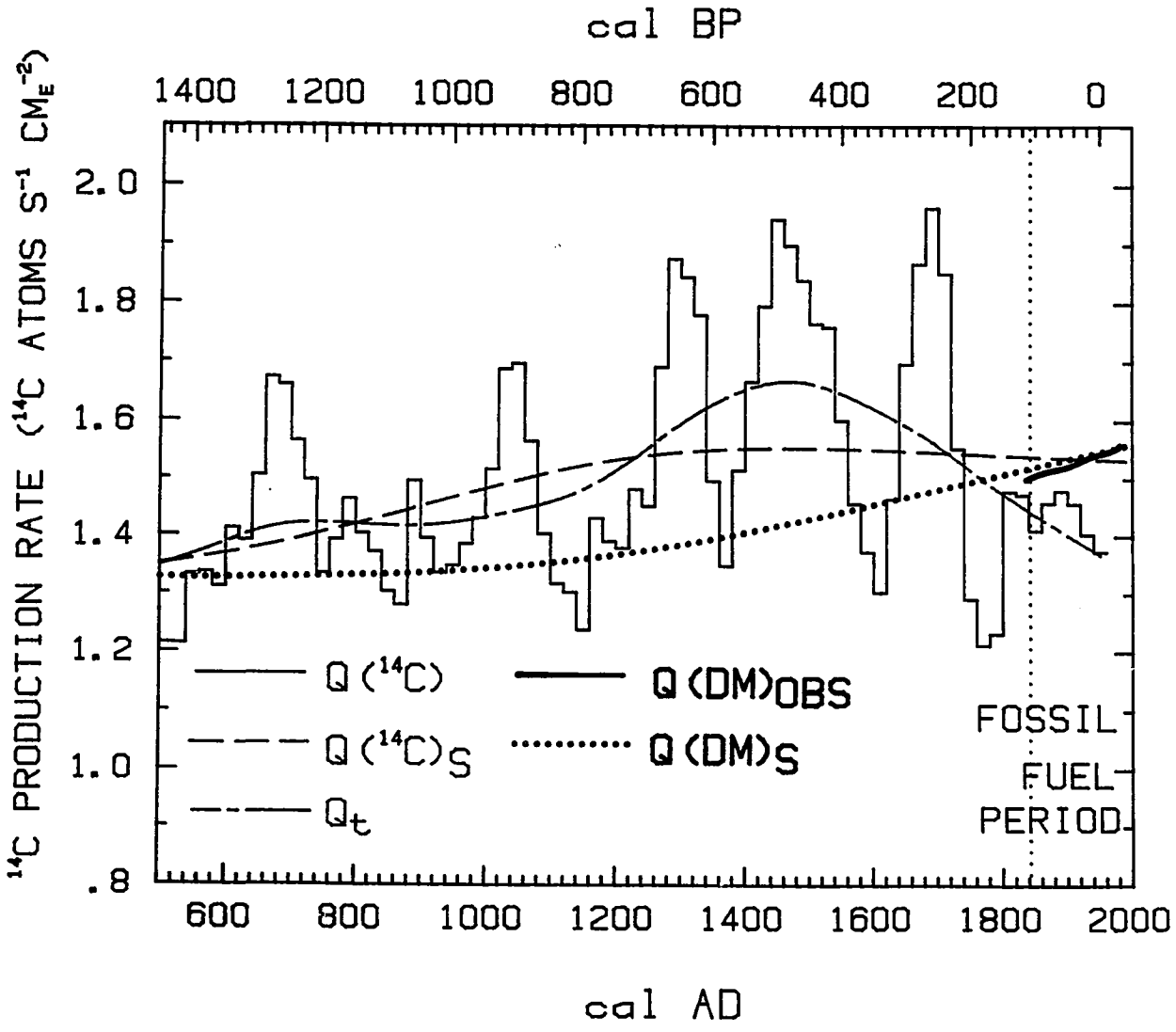
cal BP
1400
1200
1000
800
600
400
200
0
^{14}C PRODUCTION RATE (^{14}C ATOMS S^{-1} CM$_E^{-2}$)
2.0
1.8
1.6
1.4
1.2
1.0
.8
Q (^{14}C)
Q (^{14}C)$_S$
Q_t
Q (DM)$_{OBS}$
Q (DM)$_S$
FOSSIL
FUEL
PERIOD
600
800
1000
1200
1400
1600
1800
2000
cal AD

new treatment of the long-term trend has important implications for the computation of a new paleosunspot record.

The observed steady decline in the global dipole moment measured since AD 1835 (figure 10a in Merrill and McElhinny 1983) translates into a Q trend with positive slope (heavy solid line in figure 4.14) as derived from equation 2.1 with c_1 of 4.39. This short segment, $Q(DM)_{OBS}$, agrees with the final portion of the Holocene-length geomagnetic-related Q history, $Q(DM)_S$, calculated from the 500-yr and 1000-yr dipole moment averages on archaeological samples (dashed line in figure 2.16 and dotted line in figure 4.14).

The long-term Q curve, $Q(^{14}C)_S$, determined for analogous 500-yr and 1000-yr averages of $Q(^{14}C)$ is at least similar to these dipole-related trends after AD 1835 (smooth solid line in figure 2.16 and equi-dashed line in figure 4.14) whereas the "preferred geomagnetic trend" used here, Q_t, is contrary in behavior. In the crucial AD 1700 to 1840 interval (spanning the time of well-recorded sunspot information and pre-anthropogenic $\Delta^{14}C$ with associated $Q(^{14}C)$ values), three noticably different choices for the long-term trend are possible and the discrepancies among these choices become even greater extending back over the past millennium (figure 4.14).

The post-AD 1840 interval is labeled as the "fossil fuel period" in which natural $\Delta^{14}C$ levels (and thus deconvolved $Q(^{14}C)$ values) have been *reconstructed* using the earlier modeling results of Stuiver and Quay (1981). Actually, AD 1840-1900 atmospheric $\Delta^{14}C$ levels were only secondarily affected by fossil fuel release and were "corrected" only minimally. As noted in section 3.1, this "artificial" portion of $Q(^{14}C)$ (post-AD 1840 bar graph in figure 4.14) was found to have negligible influence on the determination of the Q_t spline. This most recent $Q(^{14}C)$ history represents only a first approximation for removal of the fossil fuel effect and does not affect the calculations below.

With Q_t chosen as the geomagnetic trend in $Q(^{14}C)$, the calculated Q/sunspot regression derived from the AD 1700 to 1840 interval has an identical slope as previous computations (Stuiver and Quay 1980, 1981) but a substantially shifted intercept (see below). Although this shift has implications for absolute paleosunspot numbers, the *relative* variations in solar history reconstructed here are not as sensitive to the choice for the long-term Q trend and are valuable for comparison with Holocene climate records. A more rigorous treatment of the geomagnetic component in recent Q variations must wait until higher-resolution information on the pre-AD 1835 global dipole moment becomes available.

As noted in section 3.2, the relative century- and decade-scale variations in ^{14}C production are influenced by the geomagnetic field even if the millennium-scale trend is removed from the $Q(^{14}C)$ record. Therefore, the residual Q record is expressed here in terms of percentage changes relative to the long-term trend, ie. $\Delta Q/Q_t \times 100$ where $\Delta Q = Q(^{14}C)-Q_t$. In this way, the geomagnetic effect is fully deleted from Q variations on all timescales.

Relationship between ^{14}C production and sunspot numbers

Assuming that residual ^{14}C production rates for the 18th and 19th centuries are solely tied to solar activity as reflected in sunspot numbers, a linear relationship between these two quantities can be derived in order to determine a hypothetical paleosunspot record for the Holocene and, in addition, to project solar activity into the next centuries. Such curves have limited value because (1) the sensitivity of ^{14}C production rates to sunspot variations (averaged over 11-yr solar cycles) is different in each of the last 3 centuries (Q being determined from measured neutron fluxes for the 20th century and model-derived for prior

centuries); (2) sunspot variations underestimate the range of solar activity associated with century-scale changes in ^{14}C production rates because solar activity continues to fluctuate below the threshold of zero sunspots; and (3) future sunspot numbers and, subsequently, solar activity have so far not been convincingly predicted at time scales greater than several years by any model or empirical relationship. Details on considerations 1 and 2 can be found in Stuiver and Quay (1980). Argument 3 was discussed in section 4.3.

Despite these and other limitations discussed more below, it is still worthwhile to complement previous attempts to quantify the solar modulation of ^{14}C production (Stuiver and Quay 1980, 1981) with a cautious analysis of the Holocene-length bi-decadal model results. I find that the present determinations agree well with the earlier calculations based on decadal and annual ^{14}C data and allow a preliminary extension of model-derived solar activity into past millennia and future centuries.

Sunspot numbers since AD 1700 have convincingly oscillated on average with an 11.1 yr cyclicity (eg. McKinnon 1987/1988). Sunspot numbers are currently increasing as part of the 27th cycle recorded since AD 1700 (formally denoted as cycle no. 22 since AD 1755). Sunspots numbers remained near or at zero between AD 1645 and 1715 (the Maunder Minimum) but were observed in greater numbers at several intervals between AD 1611 and 1645 (Eddy 1976). The 11-yr cycle is not readily apparent in the pre-AD 1700 sunspot record because of the record's discontinuity and/or the low level of sunspot activity.

For the interval AD 1720 to 1860, Stuiver and Quay (1980) found a relationship between decadal model-derived $Q(^{14}C)$ (based on decadal tree-ring $\Delta^{14}C$) and decadal sunspot numbers S_d (i.e. sunspot numbers averaged for each solar cycle and then interpolated to cover the same decadal intervals as the tree-ring ^{14}C measurements) such that: $\Delta Q/Q_a$ (%) = 10.5 - .53 S_d. The term on the left represents the percentage variation

in $Q(^{14}C)$ relative to the average Q (Q_a=1.57 atoms s^{-1} cm_E^{-2}) for the entire ^{14}C measurement interval AD 1000 to 1860. Multiplication by Q_a and differentiation yields $d\,Q/d\,S_d$ = -.0083 for AD 1720 to 1860 but this slope differs substantially for each century individually. A second analysis with annual tree-ring $\Delta^{14}C$ data gives $d\,Q/d\,S_c$ = -.0062 for AD 1723 to 1855 where S_c represents sunspot numbers averaged over each ca. 11-yr solar cycle (Stuiver and Quay 1981). In this case, the model-derived annual ^{14}C production rates were also averaged over the duration of each specific sunspot cycle before determining the best linear correlation. Thus an exact and constant value (if any) for the relationship of ^{14}C production to sunspot numbers has not been confirmed.

A Q/sunspot relationship is here calculated from the bi-decadal $\Delta Q/Q_t$ variations derived from the present modeling efforts. The linear correlation has limitations because (1) the coarser resolution obscures the 11-yr cyclicity (annual sunspot numbers being averaged over the same 20-yr intervals as the $\Delta Q/Q_t$ results) and (2) the uncertainty of the regression increases (with only 7 bi-decades comprising the interval AD 1700 to 1840). Nevertheless, the regression results support the analyses summarized above. The new calculation incorporates the recently revised sunspot numbers of McKinnon (1987/1988). The best linear correlation between sunspot numbers and model-derived ^{14}C production rates yields the relationship $\Delta Q/Q_t$ (%) = 21.0 - .59S_b (r=-.65 ; probability of no correlation = .12) where S_b is the 20-yr average of annual sunspot numbers for the same bi-decadal intervals as the production rate determinations. For AD 1700 - 1840, average Q_t is 1.50 atoms s^{-1} cm_E^{-2} and therefore $d\,Q/d\,S_b$ = -.0083, equivalent to the decadal results above.

In a preliminary analysis using annual tree-ring $\Delta^{14}C$ data and a more complex interhemispheric reservoir model that deconvolves global $Q(^{14}C)$ from the strictly northern hemispheric ^{14}C measurements (Stuiver and Braziunas, in preparation), the

calculated relationship is $\Delta Q/Q_t$ (%) = 20 - .55S_c. This more refined modeling approach again yields a nearly identical dependence for ^{14}C production on solar activity.

As seen in the upper half of figure 4.15, bi-decadal sunspot numbers calculated from the above regression compare favorably with observed cycle-averaged sunspot numbers (dark and light lines respectively). The apparent lag in the model-related curve is required by the linear correlation to compensate for the missing mid-18th century dip in model-related sunspot numbers. A corresponding, but narrow, peak in the decadal tree-ring $\Delta^{14}C$ record was obliterated by the coarser 20-yr averaging (see Stuiver and Braziunas, 1988, figures 1a and 2a for comparison of the bi-decadal and decadal tree-ring $\Delta^{14}C$ records).

The model-related sunspot curve is also extended to AD 1950 (dotted line in upper half of figure 4.15) by applying the same Q/sunspot relationship to the ^{14}C production rates derived from the model for the post-AD 1840 time period. The post-AD 1840 $\Delta Q/Q_t$ record, as explained above, is deconvolved from reconstructed natural $\Delta^{14}C$ variations (that is, without the industrial decline in atmospheric $\Delta^{14}C$) which in turn are based on observed sunspot numbers and the $d\,Q/d\,S_c$ relationship of Stuiver and Quay (1981). Thus the discrepancies between the dotted line and the observations partially arise from the different slopes of the bi-decadal relationship calculated here and the linear regression in Stuiver and Quay (1981) used to initially approximate post-AD 1840 "natural" atmospheric $\Delta^{14}C$ values (and associated $Q(^{14}C)$ values). The coarse bi-decadal averaging of $\Delta^{14}C$ also smoothes the $Q(^{14}C)$ and regression-derived sunspot curves. The "natural" post-AD 1840 $\Delta^{14}C$ record can be recalculated using the Q/sunspot relationship derived here.

The choice between $d\,Q/d\,S_b$ of -.0083 and $d\,Q/d\,S_c$ of -.0062 as a better estimate of solar influence on ^{14}C is difficult. Stuiver and Quay (1981) show that the better defined $d\,Q/d\,S_c$ dependency produces a post-AD 1840 atmospheric $\Delta^{14}C$ curve in

Figure 4.15: (upper) Observed sunspot numbers averaged over ca. 11-yr sunspot cycles (light line) and bi-decadal sunspot numbers calculated from a linear regression between sunspot numbers and model-derived ^{14}C production rates of AD 1700 to 1840 (heavy line). The calculated post-AD 1840 curve is dashed because the ^{14}C production rates were modeled using "natural" atmospheric $\Delta^{14}C$ values derived, in turn, from a previously published sunspot/Q regression. See text for discussion.

(lower) Observed sunspot numbers averaged over ca. 11-yr sunspot cycles (light line) and bi-decadal sunspot numbers calculated from ^{14}C production rates associated with the hypothetical "triplet" and "intertriplet" modes of solar behavior (dashed line and dotted line, respectively).

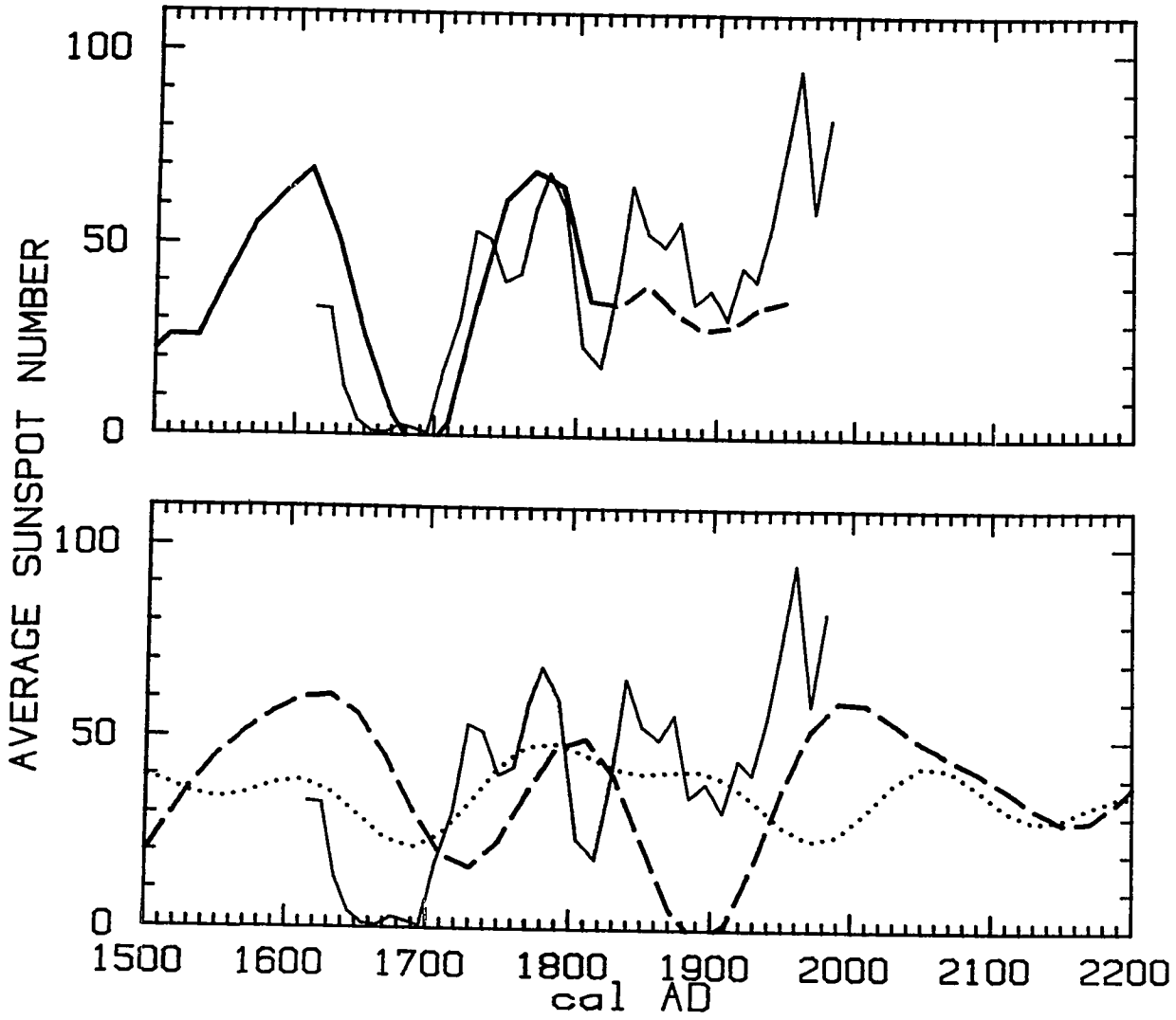
100
50
0
AVERAGE SUNSPOT NUMBER
100
50
0
1500
1600
1700
1800
1900
2000
2100
2200
cal AD

excellent agreement with the observed atmospheric $\Delta^{14}C$ record when estimates of fossil-fuel CO_2 release are incorporated into the modeling. However, the first regression matches other decadal and bi-decadal analyses. Apparently, with a limited data base (spanning AD 1700-1840 in sunspots and model-derived Q), the calculated dependencies are sensitive to data resolution and manipulation. Future modeling efforts with annual pre- and post-AD 1840 $\Delta^{14}C$ measurements as well as closer consideration of the options for the long-term geomagnetic trend should help resolve these discrepancies.

Paleosunspots and future solar activity

Sunspot numbers back to 7730 BC (figure 4.16) were calculated from the model-derived $\Delta Q/Q_t$ record and the bi-decadal ^{14}C production rate/sunspot relationship defined above. The average bi-decadal sunspot number for the entire pre-anthropogenic 9600-yr record is 36. The observed annual sunspot numbers average to 39 for AD 1611 - 1988 and 49 for the AD 1700 - 1988 interval since the Maunder Minimum. Thus recent solar activity, even including the Maunder Minimum, is greater than the model-derived average activity for the Holocene.

Unlike the earlier decadal results of Stuiver and Quay (1980, figure 13), the sunspot curve presented here shows only one instance of total disappearance of sunspots over the last millennium. Although this disparity is partly a consequence of the coarser data resolution, the new sunspot curve is also "elevated" as a result of the different treatment of the geomagnetic trend. In the new linear relationship, a relative ^{14}C production rate increase of 21% over "base line" corresponds to the disappearance of sunspots in contrast to the 10.5% intercept for zero sunspots in the original regression. This shift results because Q_t is lower between AD 1700 and 1840 than the "base line" originally assumed for the geomagnetic component in ^{14}C production rates.

Figure 4.16: Calculated sunspot numbers for bi-decades 7730 BC to AD 1830 based on model-derived ^{14}C production rates for this time period and a linear regression between observed sunspot numbers and model ^{14}C production rates from AD 1700 to 1840.

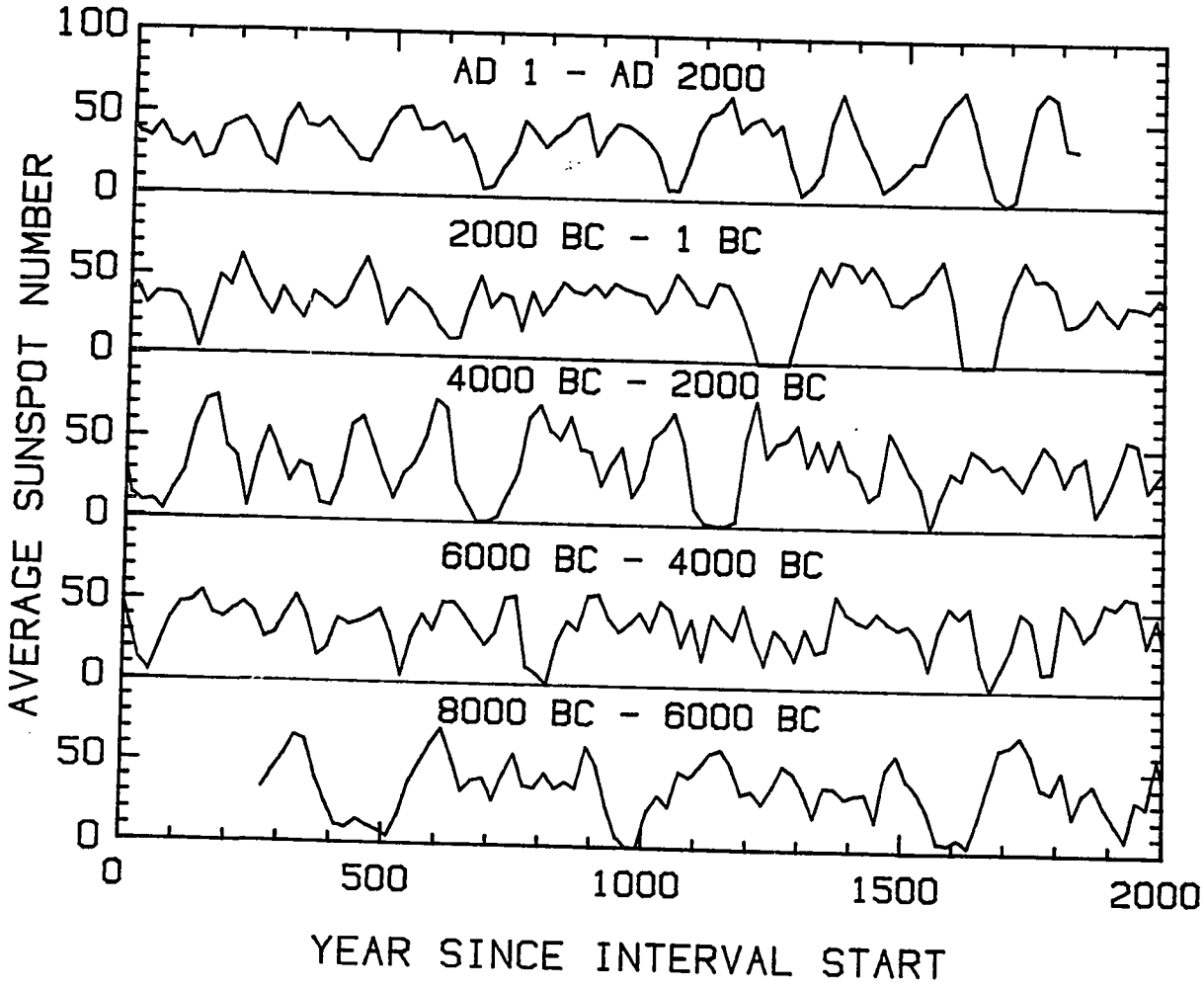
AD 1 - AD 2000
2000 BC - 1 BC
4000 BC - 2000 BC
6000 BC - 4000 BC
8000 BC - 6000 BC
AVERAGE SUNSPOT NUMBER
100
50
0
0
500
1000
1500
2000
YEAR SINCE INTERVAL START

In addition, the Q_t spline is drawn up by the more extreme century-scale excursions in ^{14}C production (smooth trend in figure 2.1), moderating the strength of the residual $\Delta Q/Q_t$ fluctuations which are defined here as solar-related. Specific to the last millennium, the peak in Q_t at AD 1450 (figures 2.1 and 4.14) significantly reduces the residual Spörer variation in ^{14}C production and consequently elevates model-related sunspot numbers in comparison to the analysis of Stuiver and Quay (1980 figure 13). The new Q/sunspot relationship implies that sunspot numbers were even greater than pre-telescopic observations (Clark and Stephenson, 1978, graphically presented in Stuiver and Quay, 1980 figure 8) than previously determined.

Stuiver and Quay (1980) also calculated a relationship between the recent history of ^{14}C production rates (derived from neutron flux measurements between AD 1937 and 1970) and the time series of geomagnetic Aa indices, another solar activity proxy. Because the AD 1867 - 1968 observations of geomagnetic Aa indices are restricted to the anthropogenic period, a relationship between the variations in this proxy and model-derived $\Delta Q/Q_t$ cannot be directly calculated. Stuiver and Quay determine a linear relationship between the observed Aa indices and percentage Q change ($\Delta Q/"Q_t"$ where the long-term trend is here equated to the Q corresponding to average AD 1868 - 1967 Aa index) with an intercept of $\Delta Q/Q_t = 22.9\%$ for Aa indices of zero. By quantifying the correlation between variations, averaged over solar cycles, in sunspot numbers and Aa indices, Stuiver and Quay refine the relationship between Q and sunspots for the AD 1868 to 1967 time period. According to this regression, when no sunspots are present, the percentage increase in Q over the "base line" is 11%.

The 11% intercept for the AD 1868 - 1967 Q/sunspot regression based on the associations of observed sunspots, Aa indices, and Q variations (calculated from neutron flux measurements) is inconsistent with the 21% intercept determined here from the AD

1700 - 1840 sunspot numbers and model-derived $\Delta Q/Q_t$ history. The difference between $\Delta Q/Q_t$ at the zero thresholds in sunspots and Aa indices is calculated now as only 22.9 - 21 = 2% rather than 22.9 - 11 = 12%. However, this discrepancy partly reflects the offset of Q_t from the Q corresponding to the average in Aa indices for the AD 1868 - 1967 time interval. The "artificial" extension of Q_t between AD 1860 and 1960 is about 2.5% below the average $Q(^{14}C)$ levels during this interval (figure 4.14); if the Q/Aa equation of Stuiver and Quay is renormalized on this lower "base line", the intercept in the Q/Aa equation increases to 25.5% and the difference in zero thresholds in sunspots and Aa indices increases to 4.5%. Unfortunately, since the post-AD 1840 $Q(^{14}C)$ levels are deconvolved from reconstructed $\Delta^{14}C$ values incorporating the earlier modeling assumptions, this normalization procedure is not very satisfying.

The lack of common extended time intervals in the records being correlated with relative sunspot numbers (ie. AD 1937 - 1970 for Q from neutron flux measurements, AD 1868 - 1967 for Aa indices, AD 1700 - 1860 for natural model-derived $Q(^{14}C)$ variations) limits direct correlations between these quantities. Differences in "base line" assumptions appear to explain a portion of the intercept discrepancy described above. Another consideration is that the Q/sunspot relationship of the current century may inherently differ significantly from the relationship in the recent past. An additional complication is the proper discrimination of the geomagnetic from the solar component of the declining trend in Q variations between AD 1937 and 1970 (figure 1 in Stuiver and Quay 1980). Any geomagnetic component should be removed before the relationships between Q, Aa indices, and sunspot numbers are derived.

After the considerations outlined above, I conclude that the bi-decadal Q/sunspot relationship derived here is an excellent qualitative index of Holocene paleosunspots but, because we have an incomplete understanding of the nature of the long-term geomagnetic

trend, the specific sunspot numbers of figure 4.16 must be applied with caution. Refinement and further discussion of earlier studies will be best undertaken when long-term (multi-century) annual $\Delta^{14}C$ and $Q(^{14}C)$ histories are utilized in place of the coarse bi-decadal analysis presented here.

Although a simple decomposition of the entire residual $Q(^{14}C)$ record into its 3 predominant cycles only explains 15% of its variance, separate representation of the "triplet" and "intertriplet" portions of the record by individual equations composed of only a few sinusoidal periods can account for 50% and 25%, respectively, of the variance of the $\Delta Q/Q_t$ record during each of these 2 modes of behavior (see section 4.2). A prediction of future solar activity can be made on the basis of each of these equations (after conversion to sunspot numbers using the bi-decadal regression), i.e. by assuming either mode of solar behavior for the next century.

In figure 4.15 (lower half), the triplet and intertriplet cyclicities are compared to the telescopic sunspot observations and are projected into the next two centuries (dashed and dotted line, respectively). Although neither curve has a strong affinity to AD 1630 - 1970 bi-decadal sunspot numbers ($r = -.20$ and $+.34$, respectively), at least coming solar activity can be predicted *if* the Sun behaves in one of these two modes. Both curves indicate average to above-average solar activity for the next two centuries but with a slow decline in sunspot numbers after AD 2050. Triplet behavior produces sunspot numbers averaging 50 for AD 2000 - 2100 and 41 for AD 2000 - 2200. These sunspot numbers exceed the Holocene average of 35 for triplet behavior and are comparable to the observed sunspot activity of the last few centuries (see above). Intertriplet behavior results in average sunspot numbers of 39 for AD 2000 - 2100 and 35 for AD 2000 - 2200. These levels are comparable to recent observations and to the average intertriplet sunspot number of 36 for the 9600-yr record.

In summary, observed solar activity since AD 1700 is ca. 33% greater than the average model-related solar activity for the Holocene. The simple calculations above suggest that sunspot numbers for the coming century will be comparable to or exceed recent observations. If this forecast is true, impending solar activity will enhance rather than mitigate the anticipated global warming due to fossil fuel emissions and deforestation fluxes of CO_2 and release of other "greenhouse" gases into the atmosphere. However, this prediction has many limitations as discussed above. In addition, the degree of solar influence on global climate change and the mechanisms involved are uncertain (eg. Pittock 1978, 1980; Stuiver 1980b; Wigley 1988; van Loon and Labitzke 1988; Stothers 1989).

4.5 Chapter summary

Spectral analyses of the deconvolved 9600-yr history of ^{14}C production rate variations (with and without trend removal) generate spectral power at the harmonics of a 420-yr cycle. At a relatively low model autoregressive order (ie. 4% of the total number of observations N), the MEM approach identifies century-scale periodicities at 420, 218, 143, and 85 yrs; at a higher model AR order (eg. 25% of N), the PSD spectrum exhibits clusters of peaks near these four periods as well as spectral power at ca. 123 and 106 yrs. The model AR order for the first analysis was selected using the Akaike FPE criterion whereas the alternative model AR order conforms to a frequently cited N/4 "rule-of-thumb". In both cases, the PSD spectra show strong peaks grouped near the harmonics of a fundamental 420-yr cycle.

Power spectrum and FFT analyses on the same time series confirm the general nature of these results. At a range of maximum lags from N/5 to N/2, the power spectrum

approach identifies statistically significant periodicities (at or near the 95% confidence level above the red noise spectrum) of ca. 213, 148, 124, and 87 yrs. Also present, but below the 95% confidence level, is a 405-yr PSD peak which splits into 3 periodicities of 355, 457, and 505 yrs as the maximum lag increases. The FFT analysis produces similar PSD peaks as the power spectrum analysis at maximum lag of N/2.

The MEM analysis of each quarter of the Q(^{14}C) time series produces distinct PSD spectra, indicating nonstationarity in the record. Visual inspection of the detrended $\Delta Q/Q_t$ time series reveals four 680-yr intervals with a common pattern of triple oscillations. More than 50% of the variance associated with this hypothetical "triplet behavior" is explained by 4 sinusoidal cycles (at 435, 207, 148 and 87 yrs), identified by MEM spectral analysis and fit by least squares regression to the triplet portions of the $\Delta Q/Q_t$ time series. Another suite of "harmonic" sinusoids (at 456, 256, 143, 118 and 88 yrs) explain nearly 30% of the variance in the remaining segments (or "intertriplet" intervals) of the $\Delta Q/Q_t$ record. The least-squares approach allows phases and amplitudes to be assigned to the "fine-tuned" periodicities initially identified by MEM spectral analysis.

Century-scale periodicities in ^{14}C production rate history may reflect primary harmonic processes in a "ringing" sun, but this conjecture so far lacks strong theoretical or empirical support. Spectral tests on artificial time series show that such harmonics may also result from a nonsinusoidal forcing function like a square wave. Amplitude modulation of a 200-yr ^{14}C cycle has also been proposed as a source for century-scale harmonics present in a PSD spectrum. Century-scale periodicities at approximately the first five harmonics of a 400-yr cycle have been noted, at least individually, in other records of solar activity phenomena such as relative sunspot numbers, geomagnetic Aa indices, and auroral frequencies. Such cycles in sunspots have sometimes been interpreted as "beats" derived from the interference of decade- or month-scale solar

periodicities.

The linear regression ($\Delta Q/Q_t$ (%) = 21.0 - .59S_b) between residual ^{14}C production $\Delta Q/Q_t$ and bi-decadal sunspot numbers S_b for the 7 bi-decades from AD 1700 to 1840 allows the full $\Delta Q/Q_t$ time series to be converted into a preliminary history of relative sunspot numbers back to 7730 BC. The average bi-decadal sunspot number for the entire pre-anthropogenic 9600-yr record is 36, lower than the average of 49 for the annual sunspot numbers observed since the Maunder Minimum (ie. between AD 1700 and 1988).

When the fitted sinusoidal curves representing solar "triplet" and "intertriplet" behavior in $\Delta Q/Q_t$ are extrapolated into the coming century and converted to relative sunspot numbers through the bi-decadal Q/sunspot regression, higher than average solar activity is predicted in both cases. Triplet behavior produces sunspot numbers averaging 50 for AD 2000 - 2100 whereas intertriplet behavior results in average sunspot numbers of 39 for this time period.

The accurate quantification of the relationship between ^{14}C production and solar activity depends on the proper identification of the geomagnetic component in the model-derived Q(^{14}C) time series and in the Q history calculated since AD 1937 from neutron flux measurements. The geomagnetic trend is treated here as a spline Q_t approximating a 400-yr moving average of the Q(^{14}C) time series. This interpretation may underestimate the solar-induced variations in ^{14}C production because the 400-yr spline closely tracks and thus "neutralizes" a portion of the multi-century trends in Q(^{14}C). As a result, intervals lacking sunspots (on a bi-decadal resolution) are rare in the Holocene including during the reconstructed Maunder and Spörer Minima. In addition, the relative depression in Q_t between AD 1700 and 1840 produces a zero-sunspot intercept for the Q/sunspot regression that requires a relatively substantial 21% positive fluctuation in $\Delta Q/Q_t$ to denote

a disappearance of sunspots.

As a consequence of this definition of the geomagnetic component in Q(^{14}C), the most recent portion of the Q_t spline contrasts with the Q trend expected from changes in the global dipole moment recorded since AD 1835. This inconsistency and the previous concerns qualify the acceptance of the Q/sunspot regression derived here. A more precise quantification of the solar influence on ^{14}C production requires an extended geomagnetic database and a higher resolution (annual) Δ^{14}C record. However, the paleosunspot curve and solar activity prognosis presented above are useful, at the least, as qualitative indices of bi-decadal to century-scale variations in solar behavior.

CHAPTER 5. CONCLUSIONS AND FINAL REMARKS

The model analyses of chapters 2 and 3 indicate that millennium- and century-scale atmospheric $\Delta^{14}C$ variations during the Holocene are more likely explained by fluctuations in ^{14}C production rate (Q) rather than changes in air-sea CO_2 exchange rate (F) or internal ocean mixing (parameterized as an "eddy diffusivity" K_Z). This conclusion remains fundamentally intact over a reasonable range of modeling choices that involve alternative pre-Holocene (initial) conditions, exchange parameterizations, and reservoir modifications.

On both the millennial and centennial timescale, the relative variations in Greenland (Camp Century) ice-core ^{10}Be concentrations over the past 9000 yrs correlate strongly with the relative Q fluctuations required to produce the atmospheric (tree-ring) $\Delta^{14}C$ record if F and K_Z are constant. This [^{10}Be] record primarily reflects changes in ^{10}Be production, a process which theoretically responds to geomagnetic and solar modulations of cosmic radiation in a similar fashion as ^{14}C production. Since the *relative* variations in Q during the Holocene are only secondarily affected by the postulated pre-Holocene model ^{14}C conditions, the correlation between the relative [^{10}Be] record and model-deconvolved Q is comparatively insensitive to these conditions; the preferred choice of a steady-state atmospheric $\Delta^{14}C$ level of 90 °/oo prior to 11,000 cal BP produces a good post-7000 BC match between Q and [^{10}Be].

A discrepancy between the Q and [^{10}Be] curves during the 4500-3500 BC millennium may derive from the limited ^{10}Be measurements presently available for this time interval. This short-term discrepancy in production rates can create a more extended offset in atmospheric $\Delta^{14}C$ histories (when [^{10}Be] is utilized in the ^{14}C reservoir model

as a proxy for ^{14}C production variations) because of the long-term memory in the global ^{14}C system as it integrates past Q variations. This prolonged influence of a short-term mid-Holocene disparity does not require a reconsideration of initial conditions (as proposed by Beer et al. 1988).

The Q record derived theoretically from the 11,000-yr time series of average global dipole moments also correlates strongly with the Q history required by the tree-ring $\Delta^{14}C$ record if Holocene climatic conditions (ie. F and K_Z) have remained constant. The scaling factor (c_1) relating Q to the dipole moment is chosen to produce the best χ^2 fit between the 14 dipole-related Q values and the model-derived Q averages for identical time intervals. Whereas the value of c_1 has previously been based on estimates for the "current" dipole moment and ^{14}C production rate (eg. Sternberg and Damon 1983), the alternative approach utilized here better minimizes the effects of multi-century solar modulation in the model-derived Q and of regional geomagnetic bias in individual dipole averages.

Assumed initial $\Delta^{14}C$ conditions affect the model-derived Q history and thus c_1 as well, but the correlation between *relative* variations in the dipole- and model-derived Q histories is only secondarily affected by any c_1 renormalization. For example, if pre-Holocene atmospheric $\Delta^{14}C$ is fixed at 50 ‰ rather than 90 ‰, Holocene ^{14}C production rates must be a few percent higher, on average, to generate the same observed tree-ring $\Delta^{14}C$ history; the c_1 factor is 2.5% higher for this alternative model scenario and thus both dipole- and model-derived Q histories are elevated. The correlation between the two records is only secondarily affected.

Another consequence of this Holocene-length normalization procedure is a generally antithetical response of dipole-related reservoir $\Delta^{14}C$ variations to pre-Holocene ^{14}C conditions. Increased pre-Holocene Q levels result in lower Holocene c_1-derived Q values on average, serving to partially compensate for the alternative initial conditions. This

dependency contrasts with modeling approaches that absolutely define c_1 according to "current" conditions and find a much greater sensitivity of Holocene atmospheric $\Delta^{14}C$ levels to postulated pre-Holocene geomagnetic and $\Delta^{14}C$ levels (eg. Lal et al. 1990). Dipole-related Q values are treated here as *relative* variations to be normalized to a model-derived absolute Q record determined in turn by the observed Holocene tree-ring ^{14}C data and a specifically assumed pre-Holocene ^{14}C scenario.

In addition to investigating the sensitivity of model results to a range of alternative "steady-state" conditions prior to 11,000 cal BP, several hypothetical pre-Holocene Q *histories* were calculated theoretically from the dipole moment data available for the past 20,000 to 30,000 yrs (Merrill and McElhinny 1983, Tauxe and Valet 1989). In these preliminary analyses, the climate-related exchange parameters F and K_Z were held constant since, compared to pre-Holocene ^{14}C production variations, pre-Holocene climate variations should not strongly affect the Holocene portions of the model reservoir $\Delta^{14}C$ curves. The essential validity of the notions of a generally reduced pre-Holocene dipole moment, of the prominence of the geomagnetic influence on ^{14}C production, and of the secondary role of climate in the atmospheric $\Delta^{14}C$ record are all underscored by: (1) the general agreement between the pre-Holocene $^{234}U/^{230}Th$-calibrated $\Delta^{14}C$ observations from Barbados corals (Bard et al. 1990) and the elevated modeled atmospheric $\Delta^{14}C$ histories derived from the dipole-related Q scenarios; and (2) the closer agreement between the early Holocene tree-ring and dipole-derived $\Delta^{14}C$ records (lower inset of figure 2.23) when the pre-Holocene dipole moment depression is incorporated into the simulations.

The correlation of recent century-scale atmospheric $\Delta^{14}C$ variations with changes in solar activity as reflected in records of sunspot observations, auroral frequencies and geomagnetic Aa indices strongly supports a solar origin for these $\Delta^{14}C$ fluctuations. By analogy, 15 other century-scale patterns in the Holocene that resemble the ^{14}C digressions

during the recent Maunder and Spörer sunspot minima also originate through solar modulation of ^{14}C production. As mentioned above, the close correlation between model-derived century-scale ^{14}C production rate variations and ice-core [^{10}Be] variations is additional support for such a production rate origin.

If, as an alternative, the Holocene ^{14}C production rate is considered constant in the global ^{14}C simulations, a climate (ie. F or K_Z) origin for millennium- and century-scale atmospheric $\Delta^{14}C$ variations has implications difficult to reconcile with some of the available independent paleoclimatic evidence. The Holocene history of mean global wind speeds that is required to explain (through variations in F) the millennium-scale trends in atmospheric $\Delta^{14}C$ is not supported by the time series of microparticle concentrations in ice cores (Petit et al. 1981) or the dust grain sizes in subtropical Atlantic sediment cores (Sarnthein et al. 1987). The changes in ocean ventilation rate (in the guise of K_Z variations) that are required to explain these same atmospheric $\Delta^{14}C$ trends produce an oceanic $\Delta^{14}C$ history that is not compatible with the available foram ^{14}C data (Andreé et al. 1986b). Coral ^{14}C data from the Gulf Stream system during the recent Maunder sunspot minimum (eg. Druffel 1982) are consistent with the model surface-ocean $\Delta^{14}C$ history generated by a century-scale change in ^{14}C production rate but conflict with marine $\Delta^{14}C$ histories forced by F or K_Z changes.

The simulations presented here of *transient* variations in Q, F, and K_Z provide important information supplementary to model analyses of alternative *steady-state* scenarios (eg. Siegenthaler et al. 1980). Past rates of ^{14}C production have a lasting effect on atmospheric and oceanic ^{14}C contents while climatic (F or K_Z) variations have more temporary impacts on reservoir $\Delta^{14}C$ levels. These fundamentally different behaviors result because the deep ocean, with a ventilation rate of ca. 1000 yrs, can recover more quickly from a climate-induced redistribution in reservoir $\Delta^{14}C$ than it can purge

previously produced ^{14}C with a mean life of ca. 8000 yrs. Thus pre-Holocene climatic events make a minimal impression on the Holocene ^{14}C system. For example, although at least one steady-state reconstruction of glacial conditions suggests that an atmospheric $\Delta^{14}C$ increase of 100 ‰ may be caused by adjustments in reservoir exchange rates alone (Toggweiler and Sarmiento 1985), the atmospheric $\Delta^{14}C$ decline of 100 ‰ during the Holocene is too slow to represent only a recovery from such pre-Holocene climatic digressions. Holocene climate events or changing ^{14}C production rates are implicated as well in this long-lasting 100 ‰ drop.

The global ^{14}C model was also programmed to deconvolve identical and simultaneous relative variations in F and K_Z consistent with the tree-ring $\Delta^{14}C$ record and a constant ^{14}C production rate. Interrelated shifts in atmospheric and oceanic circulation may occur with changes in the meridional tropospheric temperature gradient. However, carbon cycle modeling shows that this specific joint F/K_Z scenario implies Holocene wind speeds and ventilation indices that are not compatible (on a millennial timescale at least) with the paleoclimatic data mentioned above. In general, the rate of ocean mixing influences atmospheric $\Delta^{14}C$ strongly enough that variations in air-sea CO_2 exchange are more greatly attenuated in comparison to its "solo" scenario when equivalent relative variations in F and K_Z are both responsible for atmospheric $\Delta^{14}C$ change. Transient simulations are necessary to recognize the changing impact of "feedback" effects for joint parameter variations; "feedback" effects are sensitive, at any point in time, to the contemporaneous oceanic vertical ^{14}C gradient and the atmosphere/surface ocean ^{14}C disparity.

In a series of model simulations, climate (in the guise of variations in K_Z, F, or a combination of both) was assumed to represent the *residual* component necessary to explain the secondary discrepancies between the observed long-term atmospheric $\Delta^{14}C$

history and the $\Delta^{14}C$ trend generated by either the dipole- or ^{10}Be-derived ^{14}C production rate function.

A compensatory role for internal ocean mixing is compatible with the foram ^{14}C ventilation history, but deconvolved long-term variations in residual K_Z differ significantly for the two production functions. This inconsistency tied to alternative ^{14}C production proxies that should ideally match (provided that a variable millennium-scale solar component in the [^{10}Be] record does not exist) indicates that the uncertainties and limited resolutions of the geomagnetic and/or [^{10}Be] data must also contribute to the secondary discrepancies. The deconvolved residual global wind speed history conflicts with the relative stability in Holocene winds indicated by ice-core microparticle concentrations unless contemporaneous variations in ocean mixing occur or, once again, the uncertainties in the production records account for most of the disparities with the long-term tree-ring $\Delta^{14}C$ record. Transient simulations are required to properly apportion such multiple influences on the Holocene history of atmospheric $\Delta^{14}C$.

In summary, the modeling analysis indicates that millennium- and century-scale atmospheric $\Delta^{14}C$ variations during the Holocene originate primarily from fluctuations in ^{14}C production rates (as modulated primarily by geomagnetic dipole variations on a millennial-scale and by solar wind variations on a century-scale) rather than climatic changes.

The 9600-yr history of ^{14}C production rates, deconvolved from atmospheric $\Delta^{14}C$ variations assuming constant climate, was subsequently analyzed for periodic behavior using four spectral techniques (Fourier analysis, power spectrum analysis, and the autoregressive Maximum Entropy Method (MEM) applying either the Burg or FABNE algorithm). Generally these analyses on the full Q record, with and without the removal of the long-term Q trend (represented by a spline approximating a 400-yr moving average),

generate spectral power at the harmonics of a 420-yr cycle, eg. the MEM-identified periodicities at 420, 218, 143, and 85 yrs. However, MEM analyses of different quarters of the Q time series produce distinct PSD spectra, and a visual inspection of the detrended time series suggests that 30% of the Q record exhibits a common pattern of triple oscillations ("triplet behavior") distinguishable from the remaining intervals ("intertriplet behavior").

Although the identified century-scale periodicities in Q may reflect primary harmonic processes in a "ringing" sun, this conjecture presently lacks strong theoretical or empirical support. Such century-scale periodicities in the PSD spectra of ^{14}C and other solar-associated time series may also originate from nonsinusoidal signal behavior, amplitude modulation of a primary century-scale cycle, or "beat" interference among higher-frequency primary cycles.

The linear regression ($\Delta Q/Q_t$ (%) = 21.0 - 0.59S_b) between residual ^{14}C production $\Delta Q/Q_t$ and bi-decadal sunspot numbers S_b for the 7 bi-decades from AD 1700 to 1840 allows the full $\Delta Q/Q_t$ times series to be converted into a preliminary history of relative sunspot numbers back to 7730 BC. "Triplet" and "intertriplet" sunspot behavior can also be projected into future centuries when a least squares approach is employed to assign phases and amplitudes to the "fine-tuned" $\Delta Q/Q_t$ periodicities initially identified by MEM spectral analysis. Average relative sunspot numbers of 50 and 39 are forecast for 21st-century triplet and intertriplet solar behavior, respectively, whereas the average reconstructed sunspot number for the Holocene is 36 and the average observed sunspot number between AD 1700 and 1988 is 49. These model-related sunspot curves are, however, best treated as qualitative indices of solar activity; more precise quantitative sunspot estimates require extended high-resolution geomagnetic information in order to define (and remove) its long-term effect on ^{14}C production and extended high-resolution

$\Delta^{14}C$ data in order to refine the relationship of Q to sunspots associated with ca. 11-yr solar cycles.

The modeling analyses presented here reach similar conclusions as previous model investigations that simulate alternative steady-state conditions in the global ^{14}C system; the performed spectral analyses produce similar results as previous studies on ^{14}C time series. This dissertation supplements these studies (and specifically expands on the earlier efforts of Stuiver and Quay 1980, 1981) by: (1) utilizing for the first time a 9600-yr bi-decadal ^{14}C time series; (2) deconvolving, not only a hypothetical Q history for the Holocene, but also transient F and K_z scenarios for comparison to paleoclimatic time series; (3) converting the long-term dipole moment and ice-core ^{10}Be data into Q histories through a normalization procedure that avoids the limitations of using short-term "current" measurements; (4) deconvolving transient climatic histories as potential "residual" explanations for the discrepancies between the tree-ring $\Delta^{14}C$ record and either the dipole- or ^{10}Be-derived Q proxy; (5) determining the duration and magnitude of the impact of alternative pre-Holocene conditions on Holocene simulations; (6) systematically assessing the periodic nature of ^{14}C variations through comparison of four spectral techniques with a range of functional configurations (eg. maximum lags or model orders); and (7) deriving a sunspot/Q relationship after application of a new empirical approach to remove the long-term geomagnetic effects on Q.

Some ^{14}C production rate and climatic scenarios have not been considered. For example, estimates of production rate variations in cosmogenic ^{3}He during the Holocene (Kurz et al. 1990) potentially represent another independent Q proxy but these preliminary measurements have large uncertainties and a coarse resolution (although the long-term ^{3}He production trend is very similar in appearance to the ^{14}C-, ^{10}Be- and dipole-derived Q trends). The rate of ^{14}C production can also be influenced by supernovae explosions

which contribute to the galactic cosmic-ray flux in addition to producing gamma-ray bursts. The isotopic geochemistry of meteorites and lunar samples indicate a relatively stable cosmic-ray flux on timescales of 10^6 yrs (references in Damon et al., 1978); however, deviations on shorter timescales could theoretically explain a portion of the long-term variations in atmospheric ^{14}C (Lingenfelter and Ramaty 1970). Because of the limited evidence and the ability of other factors (ie. geomagnetic variations) to explain the millennium-scale changes in atmospheric $\Delta^{14}C$, I have not further considered this potential influence on the ^{14}C system.

Changes in climate-related variables other than F and K_z might force atmospheric $\Delta^{14}C$ variations during the Holocene. Although transient histories for additional climate scenarios are not specifically simulated, the influences of several potential climate factors are at least considered in steady-state terms in section 2.2. Variations in reservoir $^{12}CO_2$ contents are capable of affecting atmospheric $\Delta^{14}C$ during the Holocene as well as during glacial/interglacial transitions; new high-resolution atmospheric CO_2 databases for the Holocene, as derived from ice cores, will permit such CO_2 variations to be considered (together with an explicit treatment of high-latitude ocean processes) in order to refine the modeling analyses presented here. Also, the geomagnetic and solar influences on ^{14}C production and atmospheric $\Delta^{14}C$ are treated here strictly as *alternatives* to climatic change; if, as proposed by some researchers, geomagnetic and/or solar variations also *cause* measurable changes in climate, coincident reservoir and production rate variations may act *in unison* to produce atmospheric $\Delta^{14}C$ variations. However, the evidence for such correlations between climate and ^{14}C variations is limited (eg. references at end of section 4.5), and the modeling analysis here has neglected any secondary climatic feedback effects that might interfere with the direct deconvolution of Q from the atmospheric $\Delta^{14}C$ record.

Despite their preliminary nature, the results of this global carbon cycle modeling hopefully represent another incremental step in understanding the complexities and information contained in ^{14}C time series.

LIST OF REFERENCES

Aitken, M.J., Allsop, A.L., Bussell, G.D., and Winter, M.B., 1989. Geomagnetic intensity variation during the last 4000 years. Phys. Earth Planet. Interiors **56**: 49-58.

Akaike, H., 1969. Fitting autoregressive models for prediction. Ann. Inst. Statist. Math. **21**: 243-247.

Andrée, M., Beer, J., Loetscher, H.P., Moor, E., Oeschger, H., Bonani, G., Hofmann, H.J., Morenzoni, E., Nessi, M., Suter, M., Wölfli, W., 1986a. Dating polar ice by ^{14}C accelerator mass spectrometry. Radiocarbon **28**: 417-423.

Andrée, M., Oeschger, H., Broecker, W., Beavan, N., Klas, M., Mix, A., Bonani, G., Hofmann, H.J., Suter, M., Woelfli, W., Peng, T.-H., 1986b. Limits on the ventilation rate for the deep ocean over the last 12000 years. Climate Dynamics **1**: 53-62.

Attolini, M.R., Galli, M., and Nanni, T., 1988. Long and short cycles in solar activity during the last millennia. In Secular Solar and Geomagnetic Variations in the Last 10,000 Years, eds. F.R. Stephenson and A.W. Wolfendale, p. 49-68. Kluwer Academic Publishers.

Bacastow, R., and Björkström, A., 1981. Comparison of ocean models for the carbon cycle. In Carbon Cycle Modelling, ed. B. Bolin, SCOPE **16**: 29-79. Wiley.

Baes, Jr., C.F., Björkström, A., and Mulholland, P.J., 1985. Uptake of carbon dioxide by the oceans. In Atmospheric Carbon Dioxide and the Global Carbon Cycle, ed. J.R. Trabalka, U.S. Dept. of Energy Carbon Dioxide Rsch. Div. DOE/ER-0239, p. 81-111.

Barbetti, M., 1980. Geomagnetic strength over the last 50,000 years and changes in atmospheric ^{14}C concentration: Emerging trends. Radiocarbon **22**: 192-199.

Bard, E., 1988. Correction of accelerator mass spectrometry ^{14}C ages measured in planktonic foraminifera: Paleoceanographic implications. Paleoceanography **3**: 635-645.

Bard, E., Labeyrie, L., Arnold, M., Labracherie, M., Pichon, J.-J., Duprat, J., and Duplessy, J.-C., 1989. AMS-^{14}C ages measured in deep sea cores from the southern ocean: Implications for sedimentation rates during isotope stage 2. Quat. Rsch. **31**: 309-317.

Bard, E., Hamelin, B., Fairbanks, R.G., and Zindler, A., 1990. Calibration of the ^{14}C timescale over the past 30,000 years using mass spectrometric U-Th ages from Barbados corals. Nature **345**: 405-410.

Barrodale, I., and Erickson, R.E., 1980a. Algorithms for least-squares linear prediction and maximum entropy spectral analysis -- part I: theory. Geophysics **45**: 420-432.

Barrodale, I., and Erickson, R.E., 1980b. Algorithms for least-squares linear prediction and maximum entropy spectral analysis -- part II: fortran program. Geophysics **45**: 433-446.

Becker, B., and Kromer, B., 1986. Extension of the Holocene denrochronology by the preboreal pine series, 8800 to 10,100 BP. Radiocarbon **28**: 961-967.

Beer, J., Andrée, M., Oeschger, H., Stauffer, B., Balzer, R., Bonani, G., Stoller, Ch., Suter, M., Wölfli, W., and Finkel, R.C., 1985. ^{10}Be variations in polar ice cores. In Greenland Ice Core: Geophysics, Geochemistry, and the Environment, eds. C.C. Langway, Jr., H. Oeschger, and W. Dansgaard, Geophysical Monograph **33**: 66-70. Washington, D.C., American Geophysical Union.

Beer, J., Siegenthaler, U., Bonani, G., Finkel, R.C., Oeschger, H., Suter, M., Wölfli,

W., 1988. Information on past solar activity and geomagnetism from ^{10}Be in the Camp Century ice core. Nature **331**: 675-679.

Bevington, P.R., 1969. Data Reduction and Error Analysis for the Physical Sciences. McGraw-Hill. 336 pp.

Bloomfield, P., 1976. Fourier analysis of time series: an introduction. New York, Wiley & Sons. 258 pp.

Bolin, B., and Rodhe, H., 1973. A note on the concepts of age distribution and transit time in natural reservoirs. Tellus **25**: 58-62.

Boyle, E.A., 1988. The role of vertical chemical fractionation in controlling Late Quaternary atmospheric carbon dioxide. Jl. Geophys. Rsch. **93**: 15,701-15,714.

Broecker, W.S., and Denton, G.H., 1989. The role of ocean-atmosphere reorganizations in glacial cycles. Geochim. et Cosmochim. Acta **53**: 2465-2501.

Broecker, W.S., and Peng, T.-H., 1974. Gas exchange rates between air and sea. Tellus **26**: 21-35.

Broecker, W.S., and Peng., T.-H., 1982. Tracers in the Sea. 690 pp. Columbia University, New York: Eldigio Press.

Broecker, W.S., and Takahashi, T., 1984. Is there a tie between atmospheric CO_2 content and ocean circulation? In Climate Processes and Climate Sensitivity, eds. J. Hansen and T. Takahashi, Geophys. Monogr. Ser. **29**: 314-326.

Broecker, W.S., Peng, T.-H., and Stuiver, M., 1978. An estimate of the upwelling rate in the Equatorial Atlantic based on the distribution of bomb radiocarbon. Jl. Geophys. Rsch. **83**: 6179-6186.

Broecker, W.S., Peng, T.-H., and Engh, R., 1980. Modeling the carbon system. Radiocarbon **22**: 565-598.

Broecker, W.S., Peng, T.-H., Ostlund, G., and Stuiver, M., 1985a. The distribution of

bomb radiocarbon in the ocean. Jl. Geophys. Rsch. **90**: 6953-6970.

Broecker, W.S., Peteet, D.M., and Rind, D., 1985b. Does the ocean-atmosphere system have more than one stable model of operation? Nature **315**: 21-26.

Broecker, W.S., Ledwell, J.R., Takahashi, T., Weiss, R., Merlivat, L., Memery, L., Peng, T.-H., Jahne, B., and Munnich, K.O., 1986. Isotopic versus micrometeorologic ocean CO_2 fluxes: A serious conflict. Jl. Geophys. Rsch. **91**: 10,517-10,527.

Broecker, W.S., Andree, M., Wolfli, W., Oeschger, H., Bonanai, G., Kennett, J., and Peteet, D., 1988a. The chronology of the last deglaciation: Implications to the cause of the Younger Dryas event. Paleocean. **3**: 1-19.

Broecker, W.S., Andree, M., Bonani, G., Wolfli, W., Oeschger, H., Klas, M., Mix, A., and Curry, W., 1988b. Preliminary estimates for the radiocarbon age of deep water in the glacial ocean. Paleocean. **3**: 659-669.

Bruns, M., Rhein, M., Linick, T.W., and Suess, H.E., 1983. The atmospheric ^{14}C level in the 7th millenium BC. In ^{14}C and Archaeology, eds. W.G. Mook and H.T. Waterbolk, p. 511-516. Strasbourg, Council of Europe.

Carmi, I., Sirkes, Z., and Magaritz, M., 1984. Radiocarbon -- a direct calculation of the period of the grand trend. Radiocarbon **26**: 149-151.

Castagnoli, G., and Lal, D., 1980. Solar modulation effects in terrestrial production of carbon-14. Radiocarbon **22**: 133-158.

Castagnoli, G.C., Bonino, G., and Provenzale, A., 1989. The 206-year cycle in tree ring radiocarbon data and in the thermoluminescence profile of a recent sea sediment. Jl. Geophys. Rsch. **94**: 11,971-11,976.

Chen, W.Y., and Stegen, G.R., 1974. Experiments with maximum entropy power spectra of sinusoids. J.G.R. **79**: 3019-3022.

Clark, D.H., and Stephenson, F.R., 1978. An interpretation of the pre-telescopic sunspot records from the Orient. Royal Astron. Soc. Quart. Jl. **19**: 388-402.

Cohen, T.J., and Lintz, KP.R., 1974. Long term periodicities in the sunspot cycle. Nature **250**: 398-400.

Cole, T.W., 1973. Periodicities in solar activity. Solar Physics **30**: 103-110.

Currie, R.S., 1973. Fine structure in the sunspot spectrum - 2 to 70 years. Astrophys. Space Sci. **20**: 509-518.

Curry, W.B., and Crowley, T.J., 1987. The ^{13}C of equatorial Atlantic surface waters: implications for ice age pCO_2 levels. Paleocean. **2**: 489-517.

Damon, P.E., 1988. Production and decay of radiocarbon and its modulation by geomagnetic field-solar activity changes with possible implications for global environment. In Secular Solar and Geomagnetic Variations in the Last 10,000 Years, eds. F.R. Stephenson and A.W. Wolfendale, p. 267-285. Kluwer Academic Pub.

Damon, P.E., and Linick, T.W., 1986. Geomagnetic-heliomagnetic modulation of atmospheric radiocarbon production. Radiocarbon **28**: 266-278.

Damon, P.E., Lerman, J.C., and Long, A., 1978. Temporal fluctuations of atmospheric ^{14}C: Causal factors and implications. Ann. Rev. Earth Planet. Sci. **6**: 457-494.

Damon, P.E., Sternberg, R.S., and Radnell, C.J., 1983. Modeling of atmospheric radiocarbon fluctuations for the past three centuries. Radiocarbon **25**: 249-258.

De Meyer, F., 1981. Mathematical modelling of the sunspot cycle. Solar Physics **70**: 259-272.

Denton, G.H., and Karlén, W., 1973. Holocene climatic variations -- their pattern and possible cause. Quaternary Rsch. **3**: 155-205.

Druffel, E.M., 1980. Radiocarbon in annual coral rings of Belize and Florida.

Radiocarbon **22**: 363-371.

Druffel, E.M., 1982. Banded corals: Changes in oceanic carbon-14 during the Little Ice Age. Science **218**: 13-19.

Druffel, E.M., and Linick, T.W., 1978. Radiocarbon in annual coral rings of Florida. Geophys. Rsch. Letts. **5**: 913-916.

Druffel, E.M., and Suess, H.E., 1983. On the radiocarbon record in banded corals: Exchange parameters and net transport of $^{14}CO_2$ between atmosphere and surface ocean. Jl. Geophys. Rsch. **88**: 1271-1280.

Eddy, J.A., 1976. The Maunder Minimum. Science **192**: 1189-1202.

Eddy, J.A., 1977. Climate and the changing sun. Climatic Change **1**: 173-190.

Elsasser, W., Ney, E.P., and Winckler, J.R., 1956. Cosmic-ray intensity and geomagnetism. Nature **178**: 1226-1227.

Emanuel, W.R., Killough, G.E.G., and Olson, J.S., 1981. Modelling the circulation of carbon in the world's terrestrial ecosystems. In Carbon Cycle Modelling, ed. B. Bolin, SCOPE 16, p. 335-353. Wiley & Sons.

Emanuel, W.R., Killough, G.G., Post, W.M., Shugart, H.H., and Stevenson, M.P., 1984. Computer implementation of a globally averaged model of the world carbon cycle. U.S. Dept. of Energy, Carbon Dioxide Rsch. Div. Rept. DOE/NBB-0062. 79 pp.

Erickson III, D.J., 1989. Variations in the global air-sea transfer velocity field of CO_2. Global Biogeochem. Cycles **3**: 37-41.

Esbensen, S.K., and Kushnir, Y., 1981. The heat budget of the global ocean: An atlas based on estimates from surface marine observations. Climatic Rsch. Instit. Rep. **29**. Oregon State Univ., Corvallis.

Fairbanks, R.G., 1989. A 17,000-year glacio-eustatic sea level record: influence of

glacial melting rates on the Younger Dryas event and deep-ocean circulation. Nature **342**: 637-642.

Fan, C.Y., Chen Tie-Mei, Yun Si-Xun, and Dai Kai-Mei, 1983. Radiocarbon activity variation in dated tree rings grown in Mackenzie Delta. Radiocarbon **25**: 205-212.

Ferguson, C.W., 1970. Dendrochronology of bristlecone pine, *Pinus aristata* : Establishment of a 7484-year chronology in the White Mountains of eastern-central California, U.S.A. In Radiocarbon Variations and Absolute Chronology, ed. I.U. Olsson: 237-247. New York, Wiley & Sons.

Feynman, J., and Fougere, P.F., 1984. Eighty-eight year periodicity in solar-terrestrial phenomena confirmed. J. Geophys. Rsch. **89**: 3023-3027.

Friedman, H., 1986. Sun and Earth. New York: Scientific American Library. 251 pp.

Gaudry, A., Monfray, P., Polian, G., and Lambert, G., 1987. The 1982-1983 El Niño: A 6 billion ton CO_2 release. Tellus **39B**: 209-213.

Genthon, C., Barnola, J.M., Raynaud, D., Lorius, C., Jouzel, J., Barkov, N.I., Korotkevich, Y.S., and Kotlyakov, V.M., 1987. Vostok ice core: Climatic response to CO_2 and orbital forcing changes over the last climatic cycle. Nature **329**: 414-418.

Gleissberg, W., 1939. A long-periodic fluctuation of the sun-spot numbers. The Observatory **62**: 158-159.

Gleissberg, W., 1971. The probable behaviour of sunspot cycle 21. Solar Physics **21**: 240-245.

Goswami, J.N., McGuire, R.E., Reedy, R.C., Lal, D., Jha, R., 1988. Solar flare protons and alpha particles during the last three solar cycles. J.G.R. **93**: 7195-7205.

Grey, D.C., 1969. Geophysical mechanisms for C^{14} variations. Jl. Geophys. Rsch. **74**: 6333-6340.

Grove, J.M., 1988. The Little Ice Age. 498 pp. Methuen.

Hammer, C.U., Clausen, H.B., and Tauber, H., 1986. Ice-core dating of the Pleistocene/Holocene boundary applied to a calibration of the ^{14}C time scale. Radiocarbon **28**: 284-291.

Hill, J.R., 1977. Long term solar activity forecasting using high-resolution time spectral analysis. Nature **266**: 151-153.

Hood, L.L., and Jirikowic, J.L., 1990. Recurring variations of probably solar origin in the atmospheric $\Delta^{14}C$ time record. Geophys. Rsch. Letts. **17**: 85-88.

Houghton, R.A., Hobbie, J.E., Melillo, J.M., Moore, B., Peterson, B.J., Shaver, G.R., and Woodwell, G.M., 1983. Changes in the carbon content of terrestrial biota and soils between 1860 and 1980: A net release of CO_2 to the atmosphere. Ecological Mongr. **53**: 235-262.

Houtermans, J., 1966. On the quantitative relationships between geophysical parameters and the natural C^{14} inventory. Zeitschrift für Physik **193**: 1-12.

Houtermans, J.C., 1971. Geophysical interpretations of bristlecone pine radiocarbon measurements using a method of Fourier analysis of unequally spaced data. Dissertation, University of Bern.

Houtermans, J.C., Suess, H.E., and Oeschger, H., 1973. Reservoir models and production rate variations of natural radiocarbon. J. Geophys. Rsch. **78**: 1897-1907.

Jose, P.D., 1965. Sun's motion and sunspots. The Astronomical J. **70**: 193-200.

Jouzel, J., Merlivat, L., and Lorius, C., 1982. Deuterium excess in an East Antarctic ice core suggests higher relative humidity at the oceanic surface during the last glacial maximum. Nature **299**: 688-691.

Kane, R.P., 1977. Power spectrum analysis of solar and geophysical parameters. J.

Geomag. Geoelectr. **29**: 471-495.

Kane, R.P., 1979. Maximum entropy spectral analysis of some artificial samples. J.G.R. **84**: 965-966.

Kane, R.P., and Trivedi, N.B., 1982. Comparison of maximum entropy spectral analysis (MESA) and least-squares linear prediciton (LSLP) methods for some artificial samples. Geophysics **47**: 1731-1736.

Kane, R.P., and Trivedi, N.B., 1985. Periodicities in sunspot numbers. J. Geomag. Geoelectr. **37**: 1071-1085.

Kay, S.M., and Marple, Jr., S.L., 1981. Spectrum analysis -- a modern perspective. Proc. IEEE **69**: 1380-1419.

Keir, R.S., 1983. Reduction of thermohaline circulation during deglaciation: the effect on atmospheric radiocarbon and CO_2. Earth Planet. Sci. Letts. **64**: 445-456.

Keir, R.S., 1984. Recent increase in Pacific $CaCO_3$ dissolution: A mechanism for generating old ^{14}C ages. Marine Geol. **59**: 227-250.

Killough, G.G., 1980. A dynamic model for estimating radiation dose to the world population from releases of ^{14}C to the atmosphere. Health Physics **38**: 269-300.

Kromer, B., Rhein, M., Bruns, M., Schoch-Fischer, H., Münnich, K.O., Stuiver, M., and Becker, B., 1986. Radiocarbon calibration data for the 6th to the 8th millennia BC. Radiocarbon **28**: 954-960.

Kurz, M.D., Colodner, D., Trull, T.W., Moore, R.B., and O'Brien, K., 1990. Cosmic ray exposure dating with in situ produced cosmogenic ^{3}He: results from young Hawaiian lava flows. Earth Planet. Sci. Letts. **97**: 177-189.

Lal, D., 1985. Carbon cycle variations during the past 50,000 years: Atmospheric $^{14}C/^{12}C$ ratio as an isotopic indicator. In The Carbon Cycle and Atmospheric CO_2: Natural Variations Archean to Present, eds. E.T. Sundquist and W.S. Broecker,

Geophysical Monograph **32**: 221-233. Washington, D.C., American Geophys. Union.

Lal, D., 1987. ^{10}Be in polar ice: Data reflect changes in cosmic ray flux or polar meteorology. Geophys. Rsch. Letts. **14**: 785-788.

Lal, D., 1988. Theoretically expected variations in the terrestrial cosmic-ray production rates of isotopes. In Solar-Terrestrial Relationships and the Earth Environment in the last Millennia, ed. G.C. Castagnoli, Proc. Internat. School of Physics "Enrico Fermi", Course **XCV**: 216-233. Amsterdam, North-Holland.

Lal, D., and Peters, B., 1967. Cosmic ray produced radioactivity on the Earth. In Encyclopedia of Physics, ed. S. Flügge, **46, Pt. 2** (Cosmic Rays 2): 551-612. New York, Springer-Verlag.

Lal, D., and Venkatavaradan, V.S., 1970. Analysis of the causes of C14 variations in the atmosphere. In Radiocarbon Variations and Absolute Chronology, ed. I.U. Olsson, p. 549-569. Wiley and Sons.

Lal, D., Laffoon, M.A., and Erickson, III, D.J., 1990 (in press). Inferences about climatic changes based on $\Delta^{14}C$, $\delta^{13}C$, $CaCO_3$, pCO_2, and ^{10}Be paleodata. In Interaction of the Global Carbon and Climate Systems, ERPI Conf. Calif. Oct. 1988.

Lazear, G., Damon, P.E., and Sternberg, R., 1980. The concept of DC gain in modeling secular variations in atmospheric ^{14}C. Radiocarbon **22**: 318-327.

Lerman, J.C., Mook, W.G., and Vogel, J.C., 1970. C14 in tree rings from different localities. In Radiocarbon Variations and Absolute Chronology, ed. I.U. Olsson: 275-301. Wiley.

Lingenfelter, R.E., 1963. Production of carbon 14 by cosmic-ray neutrons. Rev. Geophys. **1**: 35-55.

Lingenfelter, R.E., and Ramaty, R., 1970. Astrophysical and geophysical variations in

C14 production. In Radiocarbon Variations and Absolute Chronology, ed. I.U. Olsson, p. 513-537. Wiley and Sons.

Linick, T.W., Suess, H.E., and Becker, B., 1985. La Jolla measurements of radiocarbon in south German oak tree-ring chronologies. Radiocarbon **27**: 20-32.

Linick, T.W., Long, A., Damon, P.E., and Ferguson, C.W., 1986. High-precision radiocarbon dating of bristlecone pine from 6554 to 5350 BC. Radiocarbon **28**: 943-953.

Liss, P.S., and Merlivat, L., 1986. Air-sea gas exchange rates: Introduction and synthesis. In The Role of Air-Sea Exchange in Geochemical Cycling, ed. P. Buat-Ménard, p. 113-127. D. Reidel Publ. Co.

Manabe, S., and Stouffer, R.J., 1988. Two stable equilibria of a coupled ocean-atmosphere model. Jl. Climate **1**: 841-866.

Marple, L., 1977. Resolution of conventional Fourier, autoregressive, and special ARMA methods of spectrum analysis. Record, 1977 IEEE Internat. Conf. on Acoustics, Speech and Signal Processing, May 9-11, 1977: 74-77.

Marple, Jr., S.L., 1982. Frequency resolution of Fourier and maximum entropy spectral estimates. Geophysics **47**: 1303-1307.

Marple, Jr., S.L., 1987. Digital spectral analysis with applications. 492 pp. New Jersey, Prentice-Hall Inc.

McElhinny, M.W., and Senanayake, W.E., 1982. Variations in the geomagnetic dipole 1: The past 50,000 years. J. Geomag. Geoelectr. **34**: 39-51.

McKinnon, J.A., 1987/1988. Sunspot numbers 1610-1985 based on "The Sunspot-Activity in the Years 1910-1960". World Data Center A for Solar-Terrestrial Physics (Boulder, CO), Report UAG-95. 112 pp. (plus supplement with sunspot numbers to September 1988). US Dept. of Commerce.

Merlivat, L., and Jouzel, J., 1979. Global climatic interpretation of the deuterium-oxygen 18 relationship for precipitation. Jl. Geophys. Rsch. **84**: 5029-5033.

Merrill, R.T., and McElhinny, M.W., 1983. The Earth's Magnetic Field. 401 pp. New York, Academic Press.

Mitchell, Jr., J.M., Dzerdzeevskii, B., Flohn, H., Hofmeyr, W.L., Lamb, H.H., Rao, K.N., and Wallén, C.C., 1966. Climatic Change. World Meteorological Organization, Technical Note No. 79. 79 pp.

Mopper, K., and Degens, E.T., 1979. Organic carbon in the ocean: Nature and cycling. In The Global Carbon Cycle, eds. B. Bolin, E.T. Degens, S. Kempe, and P. Ketner, SCOPE 13, p. 293-316. Wiley and Sons.

Neftel, A., Oeschger, H., and Suess, H.E., 1981. Secular non-random variations of cosmogenic carbon-14 in the terrestrial atmosphere. Earth Planet. Sci. Letts. **56**: 127-147.

Neftel, A., Oeschger, H., Staffelbach, T., and Stauffer, B., 1988. CO_2 record in the Byrd ice core 50,000 - 5000 years BP. Nature **331**: 609-611.

O'Brien, K., 1979. Secular variations in the production of cosmogenic isotopes in the Earth's atmosphere. Jl. Geophys. Rsch. **84**: 423-431.

Oeschger, H., 1988. The global carbon cycle, a part of the Earth system. In Solar-Terrestrial Relationships and the Earth Environment in the last Millennia, ed. G.C. Castagnoli, p. 329-352. Elsevier Science Publishers.

Oeschger, H., and Stauffer, B., 1986. Review of the history of atmospheric CO_2 recorded in ice cores. In The Changing Carbon Cycle: A Global Analysis, eds. J.R. Trabalka and D.E. Reichle, p. 89-108. Springer-Verlag.

Oeschger, H., Siegenthaler, U., Schotterer, U., and Gugelmann, A., 1975. A box diffusion model to study the carbon dioxide exchange in nature. Tellus **27**: 168-

192.

Oladipo, E.O., 1988. Spectral analysis of climatological time series: On the performance of periodogram, non-integer and maximum entropy methods. Theor. Appl. Climatol. **39**: 40-53.

Olson, J.S., Pfuderer, H.A., and Chan, Y.-H., 1978. Changes in the global carbon cycle and the biosphere. U.S. Dept. of Energy, Oak Ridge National Lab., Environ. Sci. Div. Publ. No. 1050 (ORNL/EIS-109). 154 pp.

Olson, J.S., Garrels, R.M., Berner, R.A., Armentano, T.V., Dyer, M.I., and Yaalon, D.H., 1985. The natural carbon cycle. In Atmospheric Carbon Dioxide and the Global Carbon Cycle, ed. J.R. Trabalka, p. 175-213. U.S. Dept. of Energy, DOE/ER-0239.

Oppo, D.W., Fairbanks, R.G., Gordon, A.L., and Shackleton, N.J., 1990. Late Pleistocene $\delta^{13}C$ variability. Paleocean. **5**: 43-54.

Pearson, G.W., and Stuiver, M., 1986. High-precision calibration of the radiocarbon time scale, 500 - 2500 BC. Radiocarbon **28**: 839-862.

Pearson, G.W., Pilcher, J.R., Baillie, M.B.L., Corbett, D.M., and Qua, F., 1986. High-precision ^{14}C measurement of Irish oaks to show the natural ^{14}C variations from AD 1840 to 5210 BC. Radiocarbon **28**: 911-934.

Petit, J.-R., Briat, M., and Royer, A., 1981. Ice age aerosol content from East Antarctic ice core samples and past wind strength. Nature **293**: 391-394.

Pilcher, J.R., Baillie, M.G.L., Schmidt, B., and Becker, B., 1984. A 7,272-year tree-ring chronology for western Europe. Nature **312**: 150-152.

Pittock, A.B., 1978. A critical look at long-term sun-weather relationships. Rev. Geophys. Space Physics **16**: 400-420.

Pittock, A.B., 1980. Enigmatic variations. Nature **283**: 605-606.

Press, W.H., Flannery, B.P., Teukolsky, S.A., and Vetterling, W.T., 1986. Numerical Recipes: The Art of Scientific Computing. 818 pp. Cambridge Univ. Press.

Ramaty, R., 1967. The influence of geomagnetic shielding on C^{14} production and content. In Magnetism and the Cosmos, ed. S.K. Runcorn, NATO Advanced Study Institute on PLanetary and Stellar Magnetism, 1965, Newcastle-upon-Tyne, p. 66-78. Edinburgh, Oliver and Boyd.

Raynaud, D., Chappellaz, J., Barnola, J.M., Korotkevich, Y.S., and Lorius, C., 1988. Climatic and CH_4 cycle implications of glacial-interglacial CH_4 change in the Vostok ice core. Nature **333**: 655-657.

Reinsch, C., 1967. Smoothing by spline functions. Numerische Mathematik **10**: 177-183.

Sakurai, K., 1984. The sun as an inconstant star. Space Sci. Revs. **38**: 243-279.

Sarmiento, J.L., Toggweiler, J.R., and Najjar, R., 1988. Ocean carbon-cycle dynamics and atmospheric pCO_2. Phil. Trans. R. Soc. Lond. A **325**: 3-21.

Sarnthein, M., Winn, K., and Zahn, R., 1987. Paleoproductivity of oceanic upwelling and the effect on atmospheric CO_2 and climatic change during deglaciation times. In Abrupt Climatic Change, eds. W.H. Berger and L.D. Labeyrie, p. 311-337. D. Reidel Publ. Co.

Shackleton, N.J., and Pisias, N.G., 1985. Atmospheric carbon dioxide, orbital forcing, and climate. In The Carbon Cycle and Atmospheric CO_2: Natural Variations Archean to Present, eds. E.T. Sundquist and W.S. Broecker, Geophys. Monogr. **32**: 303-317. Washington D.C., Amer. Geophys. Union.

Shackleton, N.J., Duplessy, J.-C., Armold, M., Maurice, P., Hall, M.A., and Cartlidge, J., 1988. Radiocarbon age of last glacial Pacific deep water. Nature **335**: 708-711.

Siegenthaler, U., 1983. Uptake of excess CO_2 by an outcrop-diffusion model of the ocean. Jl. Geophys. Rsch. **88**: 3599-3608.

Siegenthaler, U., 1989. Carbon-14 in the oceans. In Handbook of Environmental Isotope Geochemistry, eds. P. Fritz and J. Ch. Fontes, **3A**: 75-137. Elsevier.

Siegenthaler, U., and Münnich, K.O., 1981. $^{13}C/^{12}C$ fractionation during CO_2 transfer from air to sea. In Carbon Cycle Modelling, ed. B. Bolin, SCOPE 16, p. 249-257. Wiley and Sons.

Siegenthaler, U., and Oeschger, H., 1987. Biospheric CO_2 emissions during the past 200 years reconstructed by deconvolution of ice core data. Tellus **39B**: 140-154.

Siegenthaler, U., Heimann, M., and Oeschger, H., 1978. Model responses of the atmospheric CO_2 level and $^{13}C/^{12}C$ ratio to biogenic CO_2 input. In Carbon Dioxide, Climate, and Society, ed. J. Williams, p. 79-87. Pergamon Press.

Siegenthaler, U., Heimann, M., and Oeschger, H., 1980. ^{14}C variations caused by changes in the global carbon cycle. Radiocarbon **22**: 177-191.

Siegenthaler, U., Friedli, H., Loetscher, H., Moor, E., Neftel, A., Oeschger, H., and Stauffer, B., 1988. Stable-isotope ratios and concentration of CO_2 in air from polar ice cores. Annals of Glaciology **10**: 151-156.

Singleton, R.C., 1969. An algorithm for computing the mixed radix fast Fourier transform. I.E.E.E. Trans. on Audio and Electroacoustics **AU-17**: 93-103.

Skilling, J., 1984. The maximum entropy method. Nature **309**: 748-749.

Smythe, C.M., and Eddy, J.A., 1977. Planetary tides during the Maunder sunspot minimum. Nature **266**: 433-434.

Sofia, S., Demarque, P., and Endal, A., 1985. From solar dynamo to terrestrial climate. Amer. Scientist **73**: 326-333.

Sonett, C.P., 1984. Very long solar periods and the radiocarbon record. Rev. Geophys.

Space Phys. **22**: 239-254.

Sonett, C.P., and Suess, H.E., 1984. Correlation of bristlecone pine ring widths with atmospheric ^{14}C variations: A climate-Sun relation. Nature **307**: 141-143.

Sternberg, R.S., and Damon, P.E., 1983. Armospheric radiocarbon: Implications for the geomagnetic dipole moment. Radiocarbon **25**: 239-248.

Stothers, R.B., 1989. Volcanic eruptions and solar activity. Jl. Geophys. Rsch. **94**: 17,371-17,381.

Strömberg, B., 1985. Revision of the lateglacial Swedish varve chronology. Boreas **14**: 101-105.

Stuiver, M., 1970. Long-term C14 variations. In Radiocarbon Variations and Absolute Chronology, ed. I.U. Olsson, p. 197-213. Wiley and Sons.

Stuiver, M., 1980a. ^{14}C distribution in the Atlantic Ocean. Jl. Geophys. Rsch. **85**: 2711-2718.

Stuiver, M., 1980b. Solar variability and climatic change during the current millennium. Nature **286**: 868-871.

Stuiver, M., 1983. Statistics of the AD record of climatic and carbon isotopic change. Radiocarbon **25**: 219-228.

Stuiver, M., and Becker, B., 1986. High-precision decadal calibration of the radiocarbon time scale, AD 1950 - 2500 BC. Radiocarbon **28**: 863-910.

Stuiver, M., and Braziunas, T.F., 1985. Compilation of isotopic dates from Antarctica. Radiocarbon **27**: 117-304.

Stuiver, M., and Braziunas, T.F., 1986. Fossil fuel combustion, deforestation, climatic change and related tree-ring ^{13}C, U.S. Dept. of Energy technical report, 46 pp.

Stuiver, M., and Braziunas, T.F., 1987. Tree cellulose $^{13}C/^{12}C$ isotope ratios and climatic change. Nature **327**: 58-60.

Stuiver, M., and Braziunas, T.F., 1988. The solar component of the atmospheric ^{14}C record. In Secular Solar and Geomagnetic Variations in the Last 10,000 Years, eds. F.R. Stephenson and A.W. Wolfendale, p. 245-266. Kluwer Academic Publishers.

Stuiver, M., and Braziunas, T.F., 1989. Atmospheric ^{14}C and century-scale solar oscillations. Nature **338**: 405-408.

Stuiver, M., and Braziunas, T.F., 1990 (in press). Evidence of solar activity variations. In Climate since A.D. 1500, eds. R.S. Bradley and P.D. Jones. Unwin Hyman Publishers.

Stuiver, M., and Grootes, P.M., 1980. Trees and the ancient record of heliomagnetic cosmic ray flux modulation. In The Ancient Sun, eds. R.O. Pepin, J.A. Eddy, and R.B. Merrill, Geochim. et Cosmochim. Acta Supplement **13**: 165-173. Pergamon.

Stuiver, M., and Pearson, G.W., 1986. High-precision calibration of the radiocarbon time scale, AD 1950 - 500 BC. Radiocarbon **28**: 805-838.

Stuiver, M., and Polach, H.A., 1977. Discussion: Reporting of ^{14}C data. Radiocarbon **19**: 355-363.

Stuiver, M., and Quay, P.D., 1980. Changes in atmospheric carbon-14 attributed to a variable sun. Science **207**: 11-19.

Stuiver, M., and Quay, P.D., 1981. Atmospheric ^{14}C changes resulting from fossil fuel CO_2 release and cosmic ray flux variability. Earth Planet. Sci. Letts. **53**: 349-362.

Stuiver, M., and Reimer, P.J., 1986. A computer program for radiocarbon age calibration. Radiocarbon **28**: 1022-1030. Latest revision is available from the Quaternary Isotope Laboratory, University of Washington.

Stuiver, M., and Robinson, S.W., 1974. University of Washington GEOSECS north Atlantic carbon-14 results. Earth Planet. Sci. Letts. **23**: 87-90.

Stuiver, M., Quay, P.D., and Ostlund, H.G., 1983. Abyssal water carbon-14

distribution and the age of the world oceans. Science **219**: 849-851.

Stuiver, M., Burk, R.L., and Quay, P.D., 1984. $^{13}C/^{12}C$ ratios in tree rings and the transfer of biospheric carbon to the atmosphere. Jl. Geophys. Rsch. **89**: 11,731-11,748.

Stuiver, M., Kromer, B., Becker, B., and Ferguson, C.W., 1986a. Radiocarbon age calibration back to 13,300 years BP and the ^{14}C age matching of the German oak and US bristlecone pine chronologies. Radiocarbon **28**: 969-979.

Stuiver, M., Pearson, G.W., and Braziunas, T.F., 1986b. Radiocarbon age calibration of marine samples back to 9000 cal yr BP. Radiocarbon **28**: 980-1021.

Sundquist, E.T., 1985. Geological perspectives on carbon dioxide and the carbon cycle. In The Carbon Cycle and Atmospheric CO_2: Natural Variations Archean to Present, eds. E.T. Sundquist and W.S. Broecker, Geophys. Mongr. **32**: 5-59. Washington D.C., Amer. Geophys. Union.

Takahashi, T., Broecker, W.S., and Bainbridge, A.E., 1981. The alkalinity and total carbon dioxide concentration in the world oceans. In Carbon Cycle Modelling, ed. B. Bolin, SCOPE **16**: 271-286. Wiley.

Tauber, H., 1970. The Scandinavian varve chronology and C14 dating. In Radiocarbon Variations and Absolute Chronology, ed. I.U. Olsson, p. 173-196. Wiley and Sons.

Tauxe, L., and Valet, J.-P., 1989. Relative paleointensity of the Earth's magnetic field from marine sedimentary records: a global perspective. Phys. Earth Planet. Interiors **56**: 59-68.

Toggweiler, J.R., 1988. Deep-sea carbon, a burning issue. Nature **334**: 468.

Toggweiler, J.R., and Sarmiento, J.L., 1985. Glacial to interglacial changes in atmospheric carbon dioxide: The critical role of ocean surface water in high latitudes. In The Carbon Cycle and Atmospheric CO_2: Natural variations Archean to Present,

eds. E.T. Sundquist and W.S. Broecker, Geophys. Monograph **32**: 163-184. American Geophys. Union.

Toggweiler, J.R., Dixon, K., and Bryan, K., 1989. Simulations of radiocarbon in a coarse-resolution world ocean model. 1. Steady state prebomb distributions. Jl. Geophys. Rsch. **94**: 8217-8242.

Treitel, S., Gutowski, P.R., and Robinson, E.A., 1977. Empirical spectral analysis revisited. In Topics in Numerical Analysis III, Ed. J.J.H. Miller, p. 429-446. Academic Press.

Ulrych, T.J., and Bishop, T.N., 1975. Maximum entropy spectral analysis and autoregressive decomposition. Rev. Geophys. Space Phys. **13**: 183-200.

van Loon, H., and Labitzke, K., 1988. Association between the 11-year solar cycle, the QBO, and the atmosphere. Part II: Surface and 700 mb in the northern hemisphere in winter. Jl. Climate **1**: 905-920.

Vogel, J.C., 1983. ^{14}C variations during the upper Pleistocene. Radiocarbon **25**: 213-218.

Wada, M., and Inoue, A., 1956. Relation between the carbon 14 production rate and the geomagnetic moment. J. Geomag. Geoelectr. **18**: 485-488.

Wanninkhof, R., Ledwell, J.R., Broecker, W.S., 1985. Gas exchange - wind speed relation measured with sulfur hexafluoride on a lake. Science **227**: 1224-1226.

Wenk, T., and Siegenthaler, U., 1985. The high-latitude ocean as a control of atmospheric CO_2. In The Carbon Cycle and Atmospheric CO_2: Natural variations Archean to Present, eds. E.T. Sundquist and W.S. Broecker, Geophys. Monograph **32**: 185-194. American Geophys. Union.

Wigley, T.M.L., 1988. The climate of the past 10,000 years and the role of the sun. In Secular Solar and Geomagnetic Variations in the Last 10,000 Years, eds. F.R.

stephenson and A.W. Wolfendale, p. 209-224. Kluwer.

Wolff, C.L., 1976. Timing of solar cycles by rigid internal rotations. The Astrophys. J. **205**: 612-621.

Zbinden, H., Andree, M., Oeschger, H., Ammann, B., Lotter, A., Bonani, G., and Wölfli, W., 1989. Atmospheric radiocarbon at the end of the last glacial: An estimate based on AMS radiocarbon dates on terrestrial macrofossils from lake sediments. Radiocarbon **31** no. 3 (in press).

Zoltai, S.C., and Vitt, D.H., 1990. Holocene climatic change and the distribution of peatlands in western interior Canada. Quat. Rsch. **33**: 231-240.

BIOGRAPHICAL NOTE

Thomas Frank Braziunas was born on November 23, 1951, in Chicago, Illinois, the son of Edward and Dolores (Pommerin) Braziunas. In the early 1900's, his grandparents Frank and Petronella Braziunas emigrated from Lithuania and settled in Chicago while Herman and Agnes Pommerin emigrated from Germany to farm in Aberdeen, South Dakota.

He lived in Chicago for his first 22 years, graduating from St. Ignatius College Preparatory School in 1969. His collegiate education includes a B.A. in 1973 from the University of Chicago (Department of the Geophysical Sciences), a Paleontology M.S. in 1975 from the State University of New York at Stony Brook (Earth and Planetary Sciences Department), and a Ph.D. in 1990 from the University of Washington (Department of Geological Sciences).

In 1982 he married Jane (Tom) Braziunas and they have two children, Erik (6) and Kristin (4).